Three Dimensional Bistatic Tomography Using HDTV

Daniel J. Sego

Supervisor:

Prof. H. D. Griffiths

A dissertation submitted in fulfillment
of the requirements for the degree of

Doctor of Philosophy

of

University College London

Department of Electronic and Electrical Engineering
University College London
December, 2016

Signed Declaration

I, Daniel J. Sego, confirm that the work presented in this thesis is my own. Where information has been derived from other sources, I confirm that this has been indicated in the thesis.

Daniel J. Sego

London/Seattle December, 2016

Acknowledgements

A large debt of gratitude goes out to those whose efforts aided in the preparation of this research thesis. I acknowledge their contributions here.

To The Boeing Company whose Learning Together Program (LTP) was a major financial aid in pursuing this course of study, thank you. The benefits of LTP outweighed the ever-changing Boeing "process" that nearly resulted in this effort being abandoned. I would also like to thank the following individuals. First Dr. Gary Miller for invaluable discussions on antennas and helpful tips for FEKO and Dr. Gary Ray for the loan of one of the Ettus N200 units used for the flight test, cutting down on the out of pocket costs for the test campaign. To Dr. Yasao Kuga (University of Washington) for the use of the Ansoft Filter Design software package, University version. Also a major thank you to Dr. Tony Goodson for use of the test aircraft. I was quite unprepared, in spite of previous flight test experiences, when you handed me the fire bottle when we were ready to power up the radar off the cigarette lighter.

Thank you to University College London for the light process overhead and to my supervisor, Prof. Hugh Griffiths for his time and effort.

Most importantly, thank you to my wonderful wife of 34 years, Madeline. Your support and encouragement have been priceless as this pursuit went on through the years (as was allowing me to convert a bedroom to a radar laboratory).

Table of Contents

i		Title Page ……...…….	1
ii		Signed Declaration ...…...……	2
iii		Acknowledgements ……..……	3
iv		Table of Contents ……	4
v		List of Figures …..…….……..	6
vi		List of Tables ...……..…….……....	14
vii		List of Symbols ……..……..	15
viii		Abstract ……....……	17
1.0		**Motivation, Problem Statement and Publications** …….**.....**	19
2.0		**Research Context** ……..……..	23
	2.1	Non-cooperative Passive Bistatic Radar …….….....	23
	2.2	Passive Bistatic Radar Imaging ...….……...	27
	2.3	The Space-Frequency Aperture ...….……...	35
3.0		**Radio Frequency Reflection Tomography**	37
	3.1	Reflection Tomography as Derived from First Physical Principles ……...	37
	3.2	Radar-Centric Derivation of Tomographic Reconstruction …….	49
	3.3	Reflection Tomography Derived from Line Integrals - The Radon Transform ……..	54
4.0		**Tomographic Geometry, Waveform and Space-Frequency Trajectory**	61
	4.1	Tomographic Evaluation ……...	61
	4.2	Two Dimensional Apertures …….	69
	4.3	Three Dimensional Apertures. ……..	77
	4.4	Tomographic Imaging Dependence on Waveform ……..	80
	4.5	Reflection Tomography Image Properties ……	93
	4.6	Partial Apertures ……...	96
	4.7	Spatial Sampling Requirements ……...	103
	4.8	Combining Space (Aperture Shape) and Waveform ……	108

4.9 Doppler-based Projections and Reconstruction ……. 123
5.0 Introduction. Digital Broadcast Signals as Bistatic Illuminators for Tomography 130
5.1 DVB-T US Domestic Protocols (HDTV) ……. 132
5.2 Simulating the HDTV Waveform ……. 136
5.3 Reconstruction with Full Platform Motion Incorporated ……. 154
5.4 Direct Path Signal Influence ……. 171
5.5 Apodization …… 181
6.0 Bistatic HDTV Flight Test and Analysis 189
6.1 Bistatic Instrumentation Radar System …….. 189
6.2 Calibration ……. 226
6.3 Flight Test Design (Collection Aperture, Aircraft & Installation) . 252
6.4 Signal and Data Processing …… 268
6.5 Image Reconstruction ……..……. 289
7.0 Discussion, Conclusions and Future Work 320
8.0 References 328
9.0 Appendices 335
A HDTV Autocorrelation Approximation, Ensemble Averaged Spectrum ……. 335
B Triangle Waveform Approximation, Move-Stop-Move ……...… 339
C Frequency Domain Derivation of Cross Correlation Product in the Presence of Main Channel and Reference Channel Doppler ……... 341
D Triangle Waveform Approximation Exact Motion Solution with Doppler Compensated Reference Channel …… 347
E Large Two Dimensional Images and Apodization ……. 352

List of Figures

2.1 Topic Decomposition for the Critical Literature Review 23

3.1 Two Dimensional Scattering/Sampling Geometry 42

3.2 Graphic Representation of Generalized Fourier Slice Projection Theorem 44

3.3 Filling *k*-Space using Waveform Bandwidth 45

3.4 Filtered Back Propagation Transform Domain Coordinates 46

3.5 Reflection Tomography Geometry Definition 50

3.6 Two-Dimensional Monostatic Geometry 53

3.7 Line and Point Mappings under the 2D Linear Radon Transform 57

3.8 Example Backprojection Operation 58

4.1 Spatial Frequency Spectra in "Classical" Reflection Tomography 63

4.2 Simulated Phenomenology for Isotropic Scatterer 64

4.3 Filtered Backpropagation Point Spread Function 65

4.4 Point Spread Comparison for Two Antenna Lengths against Closed Form Result 65

4.5 Monostatic Point Spread Function – 400 MHz CW Signal 66

4.6 Spatial Spectrum Monostatic Sampling Illustrating Waveform Bandwidth 68

4.7 Windowed Annular Spatial Spectra 68

4.8 Fourier Reconstructed Examples from Figure 4.7 69

4.9 Two-Dimensional Monostatic Geometry 69

4.10 Two-Dimensional Bistatic Geometry 72

4.11 Resolution Dependency on Bistatic Angle 73

4.12 2D Resolution vs. Bistatic Angle, Constant β 74

4.13 Comparison of Monostatic to Bistatic PSF for Stationary Transmitter 75

4.14 2D Bistatic Example, Transmitter Angle Rate Twice Receiver Angle Rate 76

4.15 2D Bistatic Example - Bisector Sweeps 2π rads 76

4.16 IPR When Transmitter and Receiver Motions are Equal & Opposite 77

4.17 Definition of Tomographic, Three-Dimensional Monostatic Geometry 78

4.18 Tomographic Monostatic Geometry – Spherical Wavefront 79

4.19 Three Dimensional Bistatic Geometry Definition 80

4.20 Three Dimensional Point Spread Function for CW Waveform 85

4.21 Point Spread Function – 400 MHz Center Freq., Rectangular Pulse Waveform (a) and Cardinal Axis Response with Bandwidth as a Parameter (b) 86

4.22 PSF Cardinal Axis – 400 MHz *rect* Waveform, Match Filtered 87

4.23 Cardinal Axis Cuts - *Rect* Pulse, *Rect* Spectrum (Time Domain sinc), and Tapered *Rect* Spectrum 88

4.24 Cardinal Plane Perspective View – Pulsed Waveform with 100 MHz Bandwidth (a), and Cardinal Axis Cuts: X-Y (b) and Z (c) 89

4.25 Effects of Taper on 3D Reconstruction - Pulsed Waveform 89

4.26 Point Spread Function for LFM with Matched Filtering 90

4.27 PSF of Match Filtered LFM and Dependence on Bandwidth 90

4.28 PSF for 3D Bistatic Case 0 91

4.29 PSF for 3D Bistatic Case 1: Transmitter Elevation Angle 45 Degrees, Single Orbit with Receiver Executing Hemispherical Aperture 92

4.30 Bistatic Case 2, Offset Orbit Geometry 94

4.31 Calculated Resolution (HWHM) vs. Frequency 95

4.32 Three Dimensional Aperture - Resolution versus Frequency with Comparison to the Two-Dimensional Result 96

4.33 Geometry for Partial Aperture Response Calculations 98

4.34 2D Monostatic Resolution for Partial Apertures 98

4.35 Cross Range and Down Range Resolution & Approximations 99

4.36 Resolution Dependencies (a) Partial Azimuth, Full Elevation Aperture, (b) Horizontal Plane Resolution of Partial Elevation Aperture, (c) Vertical Axis for Partial Elevation Aperture, and d) Elevation Aperture Resolution Approximation 101

4.37 Summarized Results for Partial 2D Bistatic Apertures 102

4.38 Comparison of 2D Monostatic Resolution to Bistatic with $\beta=0^{o}$ 103

4.39 Imaging Geometry for X-Y Plane and Phase Ambiguity Derivation 104

4.40 PSF Response for X-Y Plane Demonstrating Phase Ambiguous Responses vs. Sample Spacing 105

4.41 PSF Response in X-Y plane with 3D Aperture, Sample Spacing in Azimuth as Parameter 106

4.42 PSF Response Along Z axis as a Function of Sample Spacing in Elevation 108

4.43 Spatial Frequency Representation of Two Dim. Apertures 109

4.44 Radial Cuts, Monostatic Fully-filled Spatial Spectrum and CW Spectrum 111

4.45	Three-Dimensional, Monostatic CW Aperture in *k*-space	112
4.46	Example 2D Bistatic Apertures Mapped to *k*-space	114
4.47	Rosette Trajectory and 2D PSF	117
4.48	Cardinal Axis Cuts of Rosette Space-Frequency Trajectory in Three Dimensions	118
4.49	2D Spiral Trajectory in *k*-Space and Reconstruction Results	119
4.50	Two Dimensional Example – Random Frequency vs. Position	120
4.51	3D Principal Axis Cuts of Spiral and Random Space-Frequency Trajectory	121
4.52	Random and Spiral Waveforms – Responses over Expanded Spatial Range	122
4.53	Principal Plane Contour Visualization of Reconstructed IPR	123
4.54	Analysis Geometry for Doppler-based Projections	124
4.55	Line Integral/Projection Shape for Doppler-based Sampling	126
4.56	2D Aperture Reconstruction using Doppler-based Projections	129
5.1	U. S. 8VSB (HDTV) Waveform Spectrum and Mask	133
5.2	Spectral and Temporal Properties of HDTV Signal	134
5.3	Sample HDTV Signal Statistics in the Time Domain (including phase)	135
5.4	HDTV Autocorrelation Example	136
5.5	Demonstration of Time/Waveform Dependent Resolution	136
5.6	General Bistatic Imaging Geometry	139
5.7	IPR for Randomly Drawn HDTV Simulation	143
5.8	Principal Axis Results for Randomly Drawn HDTV Simulation	143
5.9	Reconstruction Comparison: HDTV Simulation to CW	144
5.10	Extended X-Axis Reconstruction	144
5.11	Autocorrelation of the HDTV Power Spectrum – Closed Form Derivation	146
5.12	Reconstruction Using the Ensemble Average Method Compared to Monte Carlo Simulation	147
5.13	Example Spectra and Compressed Pulses for PN Codes	148
5.14	Rect Function Evaluation and Integral Limits	149
5.15	Reconstructed Cardinal Axes using PN Code Compared to HDTV Random Waveform Results (vertical offset is intentional)	151
5.16	PN Triangle Approximation Compared to HDTV Random Waveform Results	153
5.17	Extended X-Axis Reconstruction with Triangle Approximation	154
5.18	Time-BW & Platform Velocity Considerations for HDTV Signal	156

5.19 Reconstruction without Doppler Compensation – Dependence on Platform Speed 164
5.20 Reconstruction without Doppler Compensation, Z axis Only 165
5.21 Reconstruction without Doppler Compensation – Spatial Variation with Fixed Speed (185 m/sec) and Time-Bandwidth (10^4) Z axis Only 165
5.22 Reconstruction without Doppler Compensation – Dependence on Coherent Integration Time/TB Product 166
5.23 Phase Mismatch due to Platform Motion 168
5.24 Periodic Modulation of Phase Error Extent over Elevation vs. Polar Angle 169
5.25 Reconstructed Response after Doppler Compensation 170
5.26 Graphical Illustration Direct Path Imposed Noise Floor 174
5.27 Image Formed with DSB Present 176
5.28 Adaptive Beamformer Schematic and Antenna Patterns 176
5.29 Sample Sidelobe Canceller Results 178
5.30 Canceller Response over Angle – Response with Antennas Displaced 180
5.31 Reconstruction with Adaptive Canceller – Principal Plane IPR Contour View 181
5.32 Reconstruction w/ Adaptive Canceller – IPR Slice Projection View 182
5.33 Window Functions Applied in the Frequency Domain 184
5.34 Window Functions Applied to HDVT Waveform-based Reconstruction 185
5.35 SVA Assessment Against 2D Tomographic Reconstructions 188
6.1 Clutter Power vs. Range Difference, Simulated Geometry 192
6.2 Top Level Two-channel Bistatic Instrumentation System Block Diagram 193
6.3 RF Daughterboard Block Diagram 196
6.4 Peak Signal Power through Receive Cascade 198
6.5 N200 Digital Receiver Block Diagram 199
6.6 Bistatic Instrumentation System Pallet 200
6.7 Example Ambiguity Function with Reference Antenna Gain as a Parameter 202
6.8 Candidate Reference Antennas Evaluated 203
6.9 FEKO Model Cylindrical Slot Element 207
6.10 FEKO Calculated Reference Antenna Gain Pattern 209
6.11 Turnstile Antenna Design, Assembly and Test 210
6.12 Horizontally Polarized Dielectrically-loaded Rectangular Patch 213
6.13 Edge-shorted Patch Array Design 214

6.14 Horizontally Polarized, Dielectrically-loaded, Rectangular Patch 215
6.15 Fabricated Main Antenna 216
6.16 Main Antenna with Brass Ground Plane 217
6.17 Pattern Comparison - Flight Configuration to Model 218
6.18 GPS Instruments 219
6.19 Monostatic RCS and Example Scattered Field 221
6.20 Sphere Time Domain Response (from Fig. 6.1-19) 221
6.21 Two Dimensional Aperture, Monostatic Reconstruction (Wideband) 222
6.22 Two Dimen. Aperture, Monostatic Reconstruction (Narrowband) 222
6.23 Bistatic Response of a PEC Sphere 223
6.24 Bistatic Reconstruction, Perfectly Conducting Sphere (Wideband) 224
6.25 Bistatic Reconstruction, Perfectly Conducting Sphere (Narrowband) 224
6.26 Candidate Test Targets 225
6.27 Tophat Bistatic RCS at 587 MHz – Select Aspect Cuts 226
6.28 Zero Forcing Equalizer Operation 231
6.29 Calibration Perspective Block Diagram 231
6.30 Bandpass Filter Characterization 232
6.31 Zoomed Plots - Bandpass Response 232
6.32 Antenna Calibration Schematic 233
6.33 Antenna Calibration – Anechoic Chamber Setup 235
6.34 Phase Response over Angle - Reference Antenna 236
6.35 Magnitude Response over Angle - Reference Antenna 237
6.36 Phase Response over Angle - Main Antenna 237
6.37 Magnitude Response over Angle - Main Antenna 238
6.38 System Antennas Group Delay 238
6.39 Anechoic Chamber Measured Antenna Patterns 239
6.40 Adaptive Sidelobe Canceller Geometry 240
6.41 Cancellation Ratio vs. Magnitude and Phase Mismatch (after 6-26) 241
6.42 Individual Channel Response Estimates – Magnitude 245
6.43 Individual Channel Response Estimates – Phase 245
6.44 Channel Response Similarity – Amplitude and Phase 246
6.45 Ideally Matched Channels After Pulse Compression 250
6.46 Channel Alignment with and without Final Correction 251

6.47 Cessna 170 Flight Test Aircraft 253
6.48 Antenna Installation Positions 253
6.49 Main Antenna Installed 254
6.50 Reference Antenna Installed 254
6.51 Aeronautical Navigation Charts with Test Locations 255
6.52 Google Earth Scene Center Image 256
6.53 Planned (white) vs. Executed (black) Flight Trajectory 257
6.54 Collection Aperture Options 258
6.55 U. S. Radio Frequency Spectrum Allocation 100-608 MHz 262
6.56 Distribution of TV Transmitters Relative to Test Location 263
6.57 Emissions Masks U. S. Digital TV 265
6.58 Snapshot Calculated UHF/VHF Spectra with Analog Filtering 266
6.59 4^{th} and 5^{th} order Band Pass Filter Magnitude-squared Responses 267
6.60 Aliased Spectrum after 8 MHz, 5^{th} order BPF 267
6.61 Examples Adjacent Channel Signal Spectrum 269
6.62 Adjacent Transmit Channel Power Level 271
6.63 Quick-look Installed Antenna Patterns 272
6.64 Example Reference Channel Autocorrelation (Multipath Check) 273
6.65 Coordinate Frame Definitions 274
6.66 Navigation Data Processing 277
6.67 Collection Aperture Details 278
6.68 Wind Vector Estimation for Imaging Leg 279
6.69 Final Wind Vector Estimation for Imaging Leg 279
6.70 Main-Reference Antenna Projected Separation vs. Time 280
6.71 Signal Processing Flow Diagram 281
6.72 Example Pulse Compressed Result with Adaptive Sidelobe Canceller ... 284
6.73 Comparison of Compressed Result with and without Canceller - Magnitude 285
6.74 Comparison of Compressed Result with & without Canceller - Phase ... 286
6.75 Zero Delay Phase vs. Orbit/Position 288
6.76 Geometry of the Phase Artifact 289
6.77 Processed Segments of Full Aperture 289
6.78 Elevation Angle Subtended for each Orbit Segment 290
6.79 Test Image 25 Second Test Aperture Orbit 1 292

6.80 Orbit 1 2D Reconstruction: Simulated As-Flown and Flight Data 296
6.81 Orbit 2 2D Reconstruction: Simulated As-Flown and Flight Data 296
6.82 Orbit 3 2D Reconstruction: Simulated As-Flown and Flight Data 297
6.83 Orbit 4 2D Reconstruction: Simulated As-Flown and Flight Data 297
6.84 Orbit 5 2D Reconstruction: Simulated As-Flown and Flight Data 298
6.85 Orbit 6 2D Reconstruction: Simulated As-Flown and Flight Data 298
6.86 Orbit 7 2D Reconstruction: Simulated As-Flown and Flight Data 299
6.87 Orbit 8 2D Reconstruction: Simulated As-Flown and Flight Data 299
6.88 Orbit 9 2D Reconstruction: Simulated As-Flown and Flight Data 300
6.89 Nine 2D Reconstructions: Simulated As-Flown and Flight Data Focused to Z=0 301
6.90 Ideal Orbit Segment Point Spread Function (2-D Contours) 302
6.91 Point Spread Function Reconstructed from 2D Fourier Aperture 303
6.92 Ideal Orbit Segment Point Spread Function Surface 304
6.93 PSF Cuts along Cardinal and Intercardinal Axes 305
6.94 Ideal Orbit Simulation - Spatial Aperture 307
6.95 Ideal Orbit Simulation PSF - Principal Plane Reconstruction 307
6.96 Ideal Orbit Simulation PSF - Principal Plane Cuts 308
6.97 Ideal Orbit Simulation - Principal Axis Cuts and Resolution 308
6.98 As-Flown Simulated PSF - Principal Plane Reconstruction 309
6.99 As-Flown Simulated PSF - Principal Plane Cuts 310
6.100 As-Flown Simulation - Principal Axis Cuts and Resolution 310
6.101 Point Cloud PSF Representation - As-Flown Simulation 311
6.102 Point Cloud PSF Representation - As Flown Simulation 312
6.103 Flight Data Reconstruction - Volume 50540 m^3, Linear Scale 313
6.104 Flight Data Reconstruction - Perspective from Northeast of Scene 314
6.105 3D Point Cloud Scene Buildings Overlain - 3 dB dynamic range 315
6.106 Point Spread Function Resolution - Principal Plane Cuts 3 Points in Scene 316
6.107 Scene with Buildings - 3 dB dynamic range and Ground Perspective (Insert) 317
6.108 Scene from Zenith Perspective - 3 dB dynamic range 317
6.109 Scene North View near Zenith 318
6.110 Image Results and Silo Overlain on Photograph at Best Rendered Perspective 319

E.1	1.25 km x 1.25 km Image, -35 dB Taylor, Linear Scale	355
E.2	Orbit 1 Reconstruction 240 m x 240 m Image Size	356
E.3	Orbit 2 Reconstruction 240 m x 240 m Image Size	357
E.4	Orbit 3 Reconstruction 240 m x 240 m Image Size	358
E.5	Orbit 4 Reconstruction 240 m x 240 m Image Size	359
E.6	Orbit 5 Reconstruction 240 m x 240 m Image Size	360
E.7	Orbit 6 Reconstruction 240 m x 240 m Image Size	361
E.8	Orbit 7 Reconstruction 240 m x 240 m Image Size	362
E.9	Orbit 8 Reconstruction 240 m x 240 m Image Size	363
E.10	Orbit 9 Reconstruction 240 m x 240 m Image Size	364
E.11	Enlarged Area around Silo with Features Highlighted -90 degree Aperture	365
E.12	Partial Aperture Tapering - Spatial Domain	366
E.13	Partial Aperture Tapering - 2D Reconstruction no Taper and -35 dB Taylor	367
E.14	Partial Aperture Tapering - Frequency Domain	367
E.15	Apodization Results – 2D Frequency Domain Taper	368
E.16	2D Frequency Domain Taper with One Axis Constrained	368
E.17	Apodization Results – Two Dimensional Constrained Taper	369
E.18	2D Frequency Domain Taper with Both Axes Constrained	371
E.19	Images Resulting from 2D Frequency Domain Taper with Both Axes Constrained	372
E.20	1D Frequency Domain Taper with A Single Axis Constrained	373
E.21	Images Resulting from 1D Frequency Domain Taper with One Axis Constrained	374
E.22	Images Resulting from Taper Applied Along-Aperture During Reconstruction	375

List of Tables

4.1	Bandwidth Derived from Radial Δk Based on Linear Array Antenna	63
4.2	Image Metrics Comparison for Example Decoupled Bistatic Apertures	77
4.3	Waveforms Evaluated	82
4.4	Bistatic Case 1 Image Metric Compilation	93
4.5	3D Monostatic Image Quality Improvement Using Multiple Narrowband Tones	116
4.6	Image Properties of Example Rosette and Spiral Apertures in Two Dimensions	120
4.7	PSF Metrics Summary of Space-Frequency Waveforms- 3D	122
6.1	Ettus Research N200 Unit Attributes	194
6.2	Total Power Budget – Flight Experiment	195
6.3	Detail Tuner/Analog Receiver Daughterboard	196
6.4	Reference Antenna Requirements	202
6.5	Main Antenna Requirements	211
6.6	Channel Matching Results Summary	245
6.7	Measured Antenna Positions in Aircraft Coordinates	254
6.8	Emitter Listing for RFI Analysis	264
6.9	Data Preprocessing Listing	270
6.10	In-phase and Quadrature Channel Balance Results	271
6.11	Washington State Reference Network Sites	278
6.12	RMS Zero Delay Phase Error Summary by Orbit	287
6.13	Processed Orbit Segment Details	290
6.14	Times and A/C Position where ASC Condition Met	291
6.15	Resolution Estimates Derived from 2D Reconstructions	306
6.16	Three Dimensional Reconstruction Resolution Values	309

List of Symbols

α	Weight coefficient
β	Bistatic angle
$\Gamma(\tau)$	Autocorrelation of waveform envelope
δ	Unit impulse, Dirac delta, also resolution parameter
Δ_τ	Time delay to range *r*
Δk	Frequency increment, spatial frequency bandwidth
$\theta, \phi, \varphi, \eta$	Angle variables
λ	Wavelength
ρ	$2/\lambda$
σ_0	Mean reflectivity
σ	Radar cross section and standard deviation
τ	Delay
$\Im_1$	Fourier Transform operator
ϕ_m	m^{th} phase code bit
χ	Ambiguity function relating to cross correlation product
$\psi(\vec{r})$	Electromagnetic field, time domain, subscript indicates state usage
$\Psi(\omega)$	Electromagnetic field, frequency domain, subscript indicates state usage
ω	Angular frequency
A	Modulated signal and envelope
B	Backprojection operator, bandwidth
$\vec{B}$	Bistatic bisector vector
C	Voltage scalar(s)
c	Speed of light
D	Directivity
E	Electric field
f	Linear frequency
f_x, f_y	Also linear spatial frequency
F	Noise Figure (subscript refers to receiver gain stage)
$g(x,t)$	Green's function, time domain usage
$G(x, \omega)$	Green's function, frequency domain usage
H_o	Zeroth order Hankel function of the first kind
$H(\omega)$	Transfer function (component or subsystem indicated with subscript)
J_n	Bessel function of the first kind of order n
k	Wave number, spatial frequency ($2\pi/\lambda$), radians per unit distance
k_x, k_y	Two dimensional Cartesian components of wavenumber
L	SAR aperture length, system losses
n, m	Code indices (Riemann sum indices)
N_c	Number of bits (chips) in phase code sequence
O, G	Bounded reflectivity region – frequency domain
o, g	Bounded reflectivity region – spatial domain

R	Range
$\vec{r}$	Position vector, two or three dimensions
r	Distance (scalar)
$\boldsymbol{R}$	Covariance matrix
R	General autocorrelation (from context)
R	Resistance
Rot	Coordinate rotation matrix
s	Radon Transform orthogonal line distance to origin
s	Waveform (time domain)
S	Waveform (frequency domain)
$\boldsymbol{s, n, x}$	Signal, noise and measured signal-plus-noise vectors
t	Integral line contour, also time (context dependent)
u, v	Rotated Cartesian spatial variables
V	Velocity
$W(n)$	Weight vector (apodization)
$\boldsymbol{w}$	Weight vector
X	Sampled complex signal
x, y, z	Cartesian spatial variables
X, Y, Z	Cartesian axes
Z	Impedance

Abstract

Three Dimensional Bistatic Tomography Using HDTV

The thesis begins with a review of the principles of diffraction and reflection tomography; starting with the analytic solution to the inhomogeneous Helmholtz equation, after linearization by the Born approximation (the weak scatterer solution), and arriving at the Filtered Back Projection (Propagation) method of reconstruction. This is followed by a heuristic derivation more directly couched in the radar imaging context, without the rigor of the general inverse problem solution and more closely resembling an imaging turntable or inverse synthetic aperture radar. The heuristic derivation leads into the concept of the line integral and projections (the Radon Transform), followed by more general geometries where the plane wave approximation is invalid.

We proceed next to study of the dependency of reconstruction on the space-frequency trajectory, combining the spatial aperture and waveform. Two and three dimensional apertures, monostatic and bistatic, fully and sparsely sampled and including partial apertures, with controlled waveforms (CW and pulsed, with and without modulation) define the filling of *k*-space and concomitant reconstruction performance.

Theoretical developments in the first half of the thesis are applied to the specific example of bistatic tomographic imaging using High Definition Television (HDTV); the United States version of DVB-T. Modeling of the HDTV waveform using pseudonoise modulation to represent the hybrid 8VSB HDTV scheme and the move-stop-move approximation established the imaging potential, employing an idealized, isotropic

scatterer. As the move-stop-move approximation places a limitation on integration time (in cross correlation/pulse compression) due to transmitter/receiver motion, an exact solution for compensation of Doppler distortion is derived. The concept is tested with the assembly and flight test of a bistatic radar system employing software-defined radios (SDR). A three dimensional, bistatic collection aperture, exploiting an elevated commercial HDTV transmitter, is focused to demonstrate the principle. This work, to the best of our knowledge, represents a first in the formation of three dimensional images using bistatically-exploited television transmitters.

Chapter 1

Motivation, Problem Statement and Publications

There are many remote sensing applications where a need exists for high spatial resolution imaging in either two or three dimensions, and consequently this is remains an active area of radar research. When imaging at standoff distances from the object or scene of interest, one often has to contend with a line-of-sight that is partially or fully occluded over some or all of the observation geometry. This blockage may be the result of foliage occluding the scene, the imaged area/volume being in the interior of some structure, or some other screening medium was or is in place during observation. Example applications range from archaeological survey [1, 2], law enforcement [3, 4], environmental and natural resource monitoring [5], disaster response [6], and defense operations [7]. Radar systems are frequently the modality of choice for remote sensing because of 1) the ability to decouple data collection from constraints such as weather, clouds or lighting conditions, 2) possibly of operation at frequencies that propagate, at least to some degree, through intervening media, and 3) the potential to yield very large image production/area coverage rates.

Radio Frequency (RF) imaging radar systems employ Synthetic Aperture Radar (SAR) techniques to create an image in which resolution in the range dimension is realized through the waveform bandwidth and in the cross range dimension through the length of the synthetic antenna created. SAR continues to be a dynamic research topic and many algorithms have been developed to efficiently focus the synthetic aperture. Operating at lower frequencies is necessary to realize penetration of foliage (or other media) and many

monostatic imaging systems have been developed over the years. An excellent summary can be found in [8]. The evolution of RF technology has removed, or at least heavily mitigated, hardware-based limitations and wide-to-ultrawide band imaging radars have resulted. However those commercial influences which have largely served as the stimulant for component maturation and associated cost reductions, the mobile telephony/wireless services/social media markets, have created, or greatly contributed to, the constraint on low frequency radar operation. The availability in the portion of the microwave spectrum below 1.5 GHz, which would be desirable for some imaging radar operations, is very limited with spectrum allocations representing very significant commercial (and government) investment [9]. In some environments, national and international spectrum allocations may be secondary considerations (e.g., operating within underdeveloped regions), but other applications of interest would necessarily have to contend with other emitters/receivers as both threats (interferers) and victims, including critical communications links. One approach is to implement spectral notching to mitigate interference on both transmit and receive (for examples [10] and [11]). However in many regions there may be so much radio frequency interference, or keep out bands, that the degree of notching could result in unacceptable performance [12]. These complications lead to the argument for as limited an operating bandwidth as possible, dynamically, and cognitively [13], adjusting waveforms to work amongst other allocated users, or exploiting the radiations as signals of opportunity.

Bistatic radar can operate with dedicated, purpose-designed transmitters, waveforms and synchronization or it can exploit signals of opportunity that meet application specific criteria while synchronizing noncooperatively. Synthetic aperture imaging is a well established capability within the field of bistatic radar. Radar imaging requires that transmitter, receiver or both platforms are moving during aperture sampling [14], or that an ensemble of receivers are distributed around a scene such as in structural imaging [15]

or geophysical imaging [16]. The low frequency spectrum (e.g., 1 GHz and below) has large numbers of transmitters which may be suitable for exploitation for imaging use: elevated transmit locations, high radiated average power levels with wide spatial coverage. These include digital audio broadcasting (DAB) and digital television broadcasting (DVB-T in the majority of the world, HDTV in the United States and Canada). These signals are individually narrowband and strictly regulated to avoid potential interference. Bistatic radar introduces challenges not present in monostatic applications, particularly with continuous wave signals. These include relative stability of the transmit and receive system clocks, multipath presence in the reference or template signal, and direct signal breakthrough.

Exploiting a low bandwidth signal to produce high resolution images (the term "high resolution" is subjective, but here we define it as spatially resolving of the order of fifty-to-one hundred times that defined by bandwidth) requires extended synthetic apertures, *e.g.*, [17] employing tomographic techniques (recognizing the spotlight SAR-tomographic duality [18]) to reconstruct the scene. With the shape of the sampling aperture dictating the image impulse response, both two dimensional and three dimensional images are possible, as suggested by [19] and [20], which can meet our definition. In addition to resolution however, image quality is an essential attribute, arguably dominant: one manifested through the sidelobe structure of the image point spread function (PSF). Ultra-narrowband imaging produces sub-wavelength resolution in tomographic application (with an isotropic scatterer) but yields high sidelobes [21].

The main question posed in this research is whether opportunistic exploitation of commercial broadcast signals, such as U. S. format digital television (High Definition Television, HDTV) is suitable for high resolution, three dimensional imaging. This work, to the best of our knowledge, represents a first in the formation of three dimensional images using bistatically-exploited, television transmitters. A secondary aspect explored

whether the potential exists to realize both high resolution and low sidelobe operation through the exploitation of spectrally sparse waveforms in combination with the sampling aperture.

Publications and Patents derived from thesis research are listed below.

Sego, D. J., Griffiths, H. D. and Wicks, M.C., 'Waveform design for low frequency tomography', *IEEE International Waveform Diversity and Design Conference (WDD) 2010*, Niagara Falls, CA, pp230-237, 8-13 Aug. 2010.

Sego, D., Griffiths, H. D. and Wicks, M. C., 'Waveform and synthetic aperture design for low frequency tomography', *2011 UNSC-URSI National Radio Science Meeting, Special Session on Waveform Diversity: Multidisciplinary Approaches to Different Sensing Modalities*, Boulder, CO, 4-6 Jan. 2011.

Sego, D. J., Griffiths, H. D. and Wicks, M. C., "Waveform and aperture design for low frequency RF tomography', *IET Radar, Sonar and Navigation Special Issue on Waveform Diversity and Design*, Vol.5, Issue 6, pp686-696, July 2011.

Sego, D. J., Griffiths, H. D., and Wicks, M. C., 'Radar tomography using Doppler-based projections', *IEEE Radar Conference 2011*, pp403-408, Kansas City, MO, 23-27 May 2011.

Sego, D. J. and Griffiths, H. D., 'Three dimensional RF tomography using sparse waveforms', *IET Radar Conference 2012*, Glasgow U.K, pp74-80, 25-27 October 2012,

Sego, D. J. and Griffiths, H. D., 'Tomography using digital broadcast television', *IEEE Radar Conference 2014 (RadarConf '14)*, Cincinnati OH, pp285-290, 19-23 May 2014.

Sego, D. J. and Griffiths, H. D., 'Bistatic tomography using digital broadcast television – exact solution for platform motion', *RADAR 2014 SEE Radar Conference*, Lille France, pp1-6, 13-17 October 2014.

US Patent #9176226, "Radar Tomography using Doppler-based Projections", assignee: The Boeing Company, Nov 2015.

Sego, D. J. and Griffiths, H. D., 'Tomography using digital broadcast television - flight test and interim results', *IEEE Radar Conference 2016*, Philadelphia PA, pp557-562, 2-6 May 2016.

Chapter 2

Research Context

The research topic outlined in Section 1 represents a system level construct combining several distinct topics. The body of work on microwave imaging and related topics is far too large to encompass. Likewise are the broad, multi-phenomenology aspects of clinical tomographic imaging. Consequently we conduct our critical examination by addressing the specific radar sub-disciplines herein, and along the lines indicated in Figure 2.1. The perspective taken is that of more recent developments, acknowledging, but not addressing, the historical aspects of bistatic radar.

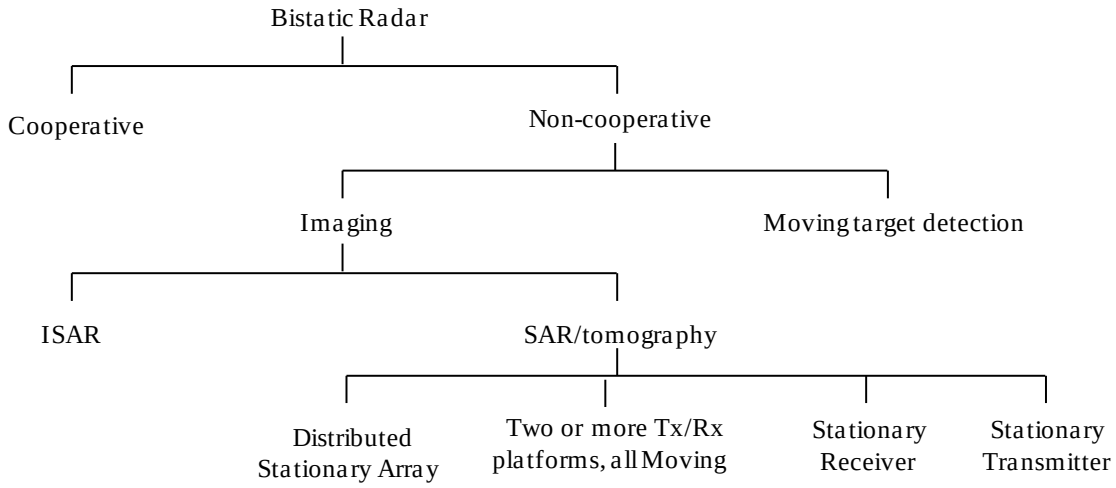

Figure 2.1. Topic Decomposition for the Critical Literature Review

2.1 Non-cooperative Passive Bistatic Radar.

Very significant amount of research into bistatic radar applications, much of which is ongoing, has demonstrated the exploitability of high power commercial transmitters (particularly digital television and radio) for surveillance as non-cooperative sources.

Transmitters are available in quantity, are relatively widely dispersed, use stable clocks for generating the signal(s), and exhibit high effective radiated power (ERP). Also, evolution to digital modulation formats eliminates the ambiguities associated with analog waveforms and with the striking similarity to noise radars, produces an ambiguity function with lower sidelobes. These features allow radar operation and employment, and research with affordable, receive-only electronics such as the software-defined radio/radar (SDR). The preponderance of the work has been performed against moving targets from stationary receivers using terrestrial sources (*e.g.*, [22] to [29] and references therein, and noting [23] as an exemplar of the class of fielded systems which includes the Thales HA100, among others). The moving targets range from aircraft to automobile traffic and vessels at sea. The underlying functional basis is the processing of a coded, modulated, continuous wave waveform with no time reference from which to measure delay, into a form from which range can be estimated is common to both imaging and moving target detection areas. This process, which employs a reference antenna to measure the direct signal path and generate a template waveform, may be considered a form of pulse compression. The cross correlation (also called ambiguity function processing) of a down-converted and coherently sampled signal containing moving targets with the synchronously sampled template signal must be steered to each Doppler hypothesis.

These works introduce and address the unique aspects of continuous wave waveform exploitation [30]: direct signal breakthrough or leakage, and multipath effects which arise from the ambiguity function processing to generate the range-Doppler predetection map (*e.g.*, multipath present in the template signal). Much of the signal processing for Passive Bistatic Radar (PBR) is common to noise radar [31]. Leakage serves to desensitize the PBR. Direct path energy received via the sidelobes of the surveillance (or main) antenna combines with the template signal to produce a very bright return at zero delay in the cross correlation result. The sidelobe levels of the compressed (e.g., cross correlated or

ambiguity function processed) data burst are a function of the time-bandwidth (TB) product: that is the bandwidth of the illuminating waveform and the coherent processing time associated with burst temporal duration. The cross correlation time sidelobes are 1/*TB* down from the zero delay response (in power). This has two main implications. The first is that the direct path signal might establish an effective noise floor well above the actual noise level of the receiver(s) [36], suppressing detection or limiting sensitivity. The second case relates to the more customary problem with thumbtack ambiguity structures of the absence of ambiguity-free range-Doppler regions [32]. The problem of leakage is addressed in several ways: shielding of the main antenna from unwanted sidelobe/backlobe energy along the direct path [26], direct path filtering [34 and citations] or through the use of spatial filtering such as an auxiliary antenna and adaptive cancellation [35].

Digital broadcast signals strongly exhibit noise-like properties and, consequently, bear a significant degree of similarity to noise radar. The presence of clutter scatterers and targets will cause the cross correlation sidelobes to add in the RMS sense, increasing net sidelobes above the 1/*TB* mean level. Alternative processing to cross correlation is described in [36], [37], and [38] where adaptive processing or mismatched filtering is introduced lower time sidelobes due to the incoherent summation of multiple scatterer responses. LMS adaptive pulse compression performed by estimating the reflectivity profile in an unknown channel is demonstrated to lower the sidelobes when the unknown channel is comprised of up to 8 scatterers [37]. Lowering time sidelobes increases effective SNR when the noise level is defined by the mean time sidelobe level. The motivation in [36] and [37] is the preprocessing of pseudo-pulses comprised of a set of contiguous samples of a noise or noise-like CW waveform in preparation for GMTI or SAR processing. An alternative approach is identified in [38] based on Least Squares adaptation. The CLEAN algorithm is proposed in [39] for range sidelobe reduction of

random noise radar compressed pulses. Point and continuous targets were simulated using a waveform consisting of 100 samples of independent Gaussian noise with a bandwidth of 150 MHz. For the case of three closely-spaced, but resolved, targets CLEAN reduced the sidelobe level by greater than 10 dB with a simulated SNR of 20 dB and by about 10 dB when the SNR was reduced to 10 dB. The CLEAN algorithm intrinsically assumes that the brightest object in the scene is a target, hence this sensitivity. In the continuous target case the application of CLEAN reduced the mean sidelobe level by 3 dB. Concomitant improvement in detection is also demonstrated for a small target in the presence of a larger, masking target.

There has been substantial progress in addressing multipath which, on the reference signal, will produce additional artifacts in the zero-Doppler profile through the pulse compression process. There are several methods evaluated and demonstrated through which this is achieved. The first is realized by exploiting the known modulation protocol. The main antenna signal is demodulated and the program content recovered. The content is then remodulated, producing a multipath free replica as the template signal [40], among others. This method has the additional advantage of elimination of the dedicated reference channel as the template signal is estimated directly from the surveillance antenna. A second approach is based on digital filtering and several variations can be found with a subset collected here. In addition to the method of [40] and references therein, there is an orthogonal subspace projection [41] which addresses the direct path, multipath as well as clutter (Extensive Cancellation Algorithm, a range-Doppler implementation). The multidimensional Constant Modulus Algorithm (with Space and Time variants) is defined in [42] to remove multipath from the reference signal. Finally, a single spatial channel lattice filter topology is employed in [43]. These methods, generally, are presented in the system context of moving target detection, though elimination of artifacts on the direct path is applicable to imaging.

2.2 Passive Bistatic Radar Imaging.

Imaging with synthetic apertures requires diversity of geometric viewing with respect to the object or scene under observation. With PBR we parse bistatic imaging using noncooperative, opportunistic waveforms into two categories. These are delimited by the method of realizing geometric diversity necessary for imaging: target motion or sensor motion (or equivalent via spatially distributed apertures). The first, target motion, is essentially Inverse Synthetic Aperture Radar (ISAR) with the specific requirement, per our decomposition, of noncooperatively exploiting transmissions of opportunity. The second we further parse into four subcategories.

- The first is defined as a constellation (distributed) of static sensors wherein each sensor may act as transmitter, receiver, or both (this may arguably considered a form of coherent MIMO, multiple-input multiple-output, imaging)
- Second an ensemble of moving sensors which can either transmit, receive or both.
- Our third category is defined by a moving transmitter/stationary receiver
- The fourth is limited to stationary transmitter/moving receiver.

We recognize that the third and fourth categories are special cases of the second.

2.2.1 ***Noncooperative ISAR***. ISAR achieves geometric diversity through rotation of an object or target with respect to the lines of sight to transmitter and receiver. We distinguish this from radio frequency instrumentation ranges wherein a target is placed on a turntable for high resolution radar cross section measurements, as in [44]. The first known suggestion of the use of television transmitters for ISAR is found in [45]. Here XPATCH was used to simulate aircraft phenomenology over 180 degrees of rotation (with symmetry). The body of the work, describing a multiple subaperture reconstruction based on what was called the Smoothed Pseudo Wigner-Ville distribution (SPWVD) but employed monostatic geometry with a frequency range of 500 MHz using L-band,

because of electromagnetic solver limitations in terms of accuracy and speed/computational complexity arguments, to emulate the UHF (broadcast) band. The accompanying issues with PBR detailed in Section 2.1 were not considered. There were several related papers by these authors, not cited here, including a multistatic variant, all published in the 2001 time frame.

The first ISAR experiment found [46] was reported in 2010, having been conducted in Japan. This work was concentrated on imaging airborne targets using a single transmit tower but with 6 adjacent channels providing a total bandwidth of 36 MHz. The bistatic angle of 68 degrees yielded a range resolution of about 5 m. A 5 second aperture was employed to produce a two dimensional image of a Boeing 777-300. A burst of research on this topic occurred in 2012 to 2014 (see, for example [47] and [48]). The latter citation incorporates a version of the CLEAN algorithm (PR-CLEAN) to enhance simulated point spread functions based on up to 9 simultaneous illuminators.

Applying PBR-based ISAR to imaging ships at sea can be found in [49] and related references. The identification of candidate targets to image is based on range-Doppler maps as described for moving targets generally in Section 2.1. As in [46] multiple channels on the same broadcast tower are coherently combined to enhance bandwidth. Candidate target complex range delay-Doppler cells are inverse processed to a range-time format using an inverse Fourier transform. From this point generally standard processing is employed for image production; motion compensation, time windowing for a stable target rotation vector followed by the cross range FFT. The final stage is described as a cross range rescaling operation. Resolution cited is 6.89 m in range and 11.4 m in cross range against large commercial shipping targets.

ISAR concepts employing satellite-based transmitters and stationary receivers have also been proposed. In [50] multistatic ISAR using geostationary satellites is proposed. The

concept exploits telecommunications transponders on geosynchronous satellites, combining the several possible bistatic pairs into a commonly registered image plane. The work builds on [51] in which only bistatic pairs are addressed. In these works the receiver is terrestrial and stationary. In geosynchronous orbit the transmitter is effectively stationary as well. We expand to "true" multistatic ISAR, distinct from pair-wise operation just noted, in Section 2.3.

2.2.2 ***Noncooperative SAR/tomography*****.** Spatial sampling diversity with respect to a fixed/stationary target (area) separates SAR from ISAR. Our decomposition of SAR/Tomography contains four subcategories: distributed stationary arrays, distributed moving arrays, moving transmitter/stationary receiver and moving receiver/stationary transmitter.

• **2.2.2.1** ***Distributed stationary array*****.** The category is represented by an array of sensor units which may transmit, receive or transmit and receive, and which are stationary. In our literature study, the first example of this class was [52]. The focus of this work is the reconstruction given the circular sensor geometry (with an ultrasonic context) in three modes. In the first each element could transit then receive (e.g. operate monostatically) and the active element would sequentially cycle around the element ring, discretely emulating a moving monostatic source. In the second mode, one element transmits and second receives. The pair has a fixed and constant angular separation (bistatic angle) and, again the active pair discretely cycle around the ring. In this work there is no discussion of the specific implementation found (e.g., cooperative/noncooperative) however it is included as exactly representing the subcategory. A radio frequency implementation for transmission (not reflection) imaging for diagnostics of living trees *in vivo* is found in [53] employing a semicircle of receivers distributed around a hypothetical tree trunk. Incident plane waves at multiple, discrete frequencies (without modulation as part of transmission) are used to reconstruct a dielectric image of the trunk in two dimensions.

Mechanization is not described but noncooperative exploitation of existing signals is distinctly an option. Set up and orientation of the receive array might be made with this specific objective. However the transmission measurement distinctly separates this work from reflection imaging approaches.

A study conducted based on exploiting wireless networks can be found in [54] where Wi-Fi based tomographic imaging is described. Like [53], this work employed the transmission modality, as opposed to reflection, and because it is attenuation-based operates without a coherent reference. The concept forms all network transmit-receive pairs performing reconstruction on moving objects after compensating for effects of static absorptive objects and environmental effects (multipath). While noncooperative, the use only of the network channel as opposed to the modulation differentiates this concept apart from the research described herein. The reconstruction methodology employs a Bayesian approach with regularization based on a maximum *a posteriori* formulation. Experimental results are presented from an array of 28, 2.4 GHz wireless routers. Image examples are presented which clearly display the position of one, and two moving human targets surrounded by the ensemble of WiFi antennas (an approximately 7 m by 7 m instrumented region). In the two object case some image splitting appears to occur. The image magnitude scale is not provided and it is not possible to judge the resolution achieved. In the single target case, and assuming the scale to be linear, ~1.5 m resolution is estimated.

There are several research examples of distributed RF tomographic imaging networks, both concepts and related experimentation, performed by the U. S. Air Force Research Laboratory (AFRL). Like [53] these studies [55], [56], [57], and references therein, employ continuous wave or ultra narrowband (UNB) waveforms with an ensemble of emplaced sources and receivers for both two- and three dimensional imaging. The mechanization can be considered as noncooperative as, in the case of commercial

broadcasts, the modulation structure is known but they employ for-purpose radar signals and do not share timing and control (as can be inferred from the means of sensor emplacement and concept of employment). However it is distinct in that no range information can be derived as the waveforms are grossly range ambiguous. The UNB implementation exploits space/geometry and frequency to fill Fourier space (see Section 2.3) to complement the spatially sparse sampling of the image scene. Solution for the forward matrix required regularization prior to reconstruction. This is distinct from the more traditional method of imaging using translation of one or both platforms with spatial sampling linked to the method of reconstruction; Doppler-based with spatial Nyquist of backprojection and the spatial phase artifact.

• **2.2.2.2** ***Moving distributed sensor array.*** Little was found in this category. A concept employing GPS multistatically from a single elevated moving receiver is described in [58]. A constellation of such transmitters would be available for exploitation by the single receiver. The GPS waveforms are exactly known, except for the unknown delay and complex amplitude but can be noncooperatively exploited. The authors describe the GPS waveform as a LFM modulated, not distinguishing between code sets for the Global Positioning System (C/A or P) nor attributing the processing to Galileo (also CDMA) or GLONASS (FDMA) so some confusion resulted in attempting to interpret the processing described. Further no indication on discriminating direct measurement from scattered, termed "indirect" was made.

A similar concept is described in a series of papers. Termed 'Space Surface Bistatic SAR – SS BSAR' [59] with no apparent association to [58], a much more complete systems description including the use of surveillance and reference antennas to generate waveforms which, when correlated, yield the bistatic range difference, is given. The test system cleverly uses a receiver mounted on a rail system on top of a 5 storey building,

and which can translate during data collection, emulating the airborne moving receiver. Image simulation results are presented in [59].

• **2.2.2.3** ***Stationary receiver/moving transmitter***. There are ample examples of bistatic imaging using a spaceborne SAR, one such is [60] and references. Again, we specifically look for examples of non-radar waveforms for noncooperative exploitation. Communications satellites in geosynchronous orbit are effectively stationary and require a moving receiver (though a geostationary transmit- geostationary receive bistatic concept is described below). There are mobile communications satellites such as Thuraya in medium earth orbit and Iridium satellites in low earth orbit which could potentially serve as transmitters. However the availability of GNSS satellites as persistent emitters of opportunity has enabled research along the lines defining this category. One was presented in the section preceding that fit that section class description. A derivative example is described in [61]. The bistatic receiver described resembles that of [59], operates against the GLONASS constellation and has an institutional relationship with the previously cited work. This research successfully produced two dimensional images from a fixed, elevated position.

• **2.2.2.4** ***Stationary transmitter/moving receiver***. There are only four known examples in this subcategory. The first, found in [62] and [63], was performed at University College London wherein an airborne receiver operating against FM radio signals successfully produced low resolution images of the English countryside, including suburban and urban terrain types. This, and related references from the author, including Ph. D. Thesis, is the first instance found for an airborne measurement campaign using PBR and commercial broadcast sources. The second [64], and related citations, was performed using the LORA system (LOw frequency RAdar, a CARABAS II follow-on system) in Sweden, exploiting DVB-T radiated from an elevated tower and producing two dimensional images from the fixed television transmitter and business jet-class airborne receiver. This effort, which

was concurrent with the research described herein, is the first known published two dimensional bistatic image using DVB-T illumination. The third known research program [65] was by researchers in Poland, carried out in 2013, after initial investigations using a ground vehicle-mounted bistatic receiving system. The final example was a concept proposed in [66] exploiting geosynchronous DAB satellites.

The airborne collection in [63] employed a low wing civil aircraft (Piper PA 28-181) with two-channel receiver which down-converted, digitally sampled and stored analog FM signals in the 88-108 MHz band. The data were processed off-line to several purposes, the relevant one here being the processing of the returns to ground clutter maps (very low resolution images). A three second aperture (linear aperture) was selected and Doppler beam sharpening employed to create clutter maps with nominal resolutions 0.33 Hz, or 100 m in cross range (at 10 km slant range), with 2 km of range resolution (derived from 200 kHz bandwidth). A key part of the processing was the use of the NLMS adaptive filter [41] to reduce direct signal breakthrough and multipath contamination. This algorithm is functionally equivalent to the two channel spatial canceller but is extended to cancel multipath returns over range and Doppler in the context of a single coherent processing interval (CPI). This methodology is reported from the perspective of moving target detection and not imaging, but is clearly satisfactory for the limited dwell associated with the DBS maps. A clear constraint on the application of the full algorithm is the coherent processing interval duration and Doppler walk which would be problematic for longer, nonlinear apertures.

Higher resolution images are reported in [64] and noncooperatively exploit DVB-T emissions. The LORA SAR collection apertures were linear and nominally 1 sec (160 m) and 13 sec (2000 m) in duration; collected from a Saberliner jet aircraft. The reconstructed scenes included transmitting antenna and had theoretical resolutions of 20 m and 5 m, respectively, with high dynamic ranges. The DVB-T signal was continuously

recorded; the system is composed of 8, 10 MHz receivers sampled with a 12 bit ADC. Image reconstruction was implemented via a fast back projection algorithm after RFI filtering and pulse compression. The method by which the reference signal is obtained for correlation processing is not detailed. Preprocessing describes the delayed and Doppler shifter ground returns being superimposed on the direct path signals. Reconstruction was aided through the application of a DEM.

The third known example of noncooperative exploitation of a fixed commercial transmitter and airborne receiver for imaging is [65]. Again, a two channel system was employed which was adapted from an earlier vehicle test which employed three antennas, one reference and two surveillance and of which only one was used for the imaging study. Details on the receiver employed are not known, nor are antenna installations clearly evident. The citation details CLEAN processing using a lattice filter to remove the direct path signal [35], [39], an approach also cited in noise radar references [31]. The test aircraft was a single-engine civil model, the PLZ-104. Short time Fourier transform (STFT) processing was employed for reconstruction, resolution estimates not presented, describing the STFT as a rudimentary method for short apertures.

The fourth and final example is perhaps the first in terms of when the concept was published. [66] describes an interesting concept wherein the anticipated proliferation of commercial Digital Audio Broadcast (DAB), provided by broadcast satellites in geosynchronous orbit, would be exploited for two dimensional imaging by placing a receive satellite in a geosynchronous orbit such that the plane of the orbit is slightly displaced from equatorial. This positioning creates the motion necessary, albeit very slowly, to construct the synthetic aperture. An aperture time of 8.3 hours at a relative speed of 2 m/sec results from this geometry. Reference signal (direct path/baseline) and correlation with the bistatically scattered terrestrial returns are processed, yielding an image resolution of 120 m by 120 m, based on a 4 MHz DAB bandwidth.

2.3 The Space-Frequency Aperture.

The passive bistatic radar does not require the introduction of new signals into the already crowded microwave spectrum, and passive receivers are immune from directional electronic countermeasures. However, in all but the most fortuitous circumstances, the available resources may not provide the necessary, or acceptable, space-frequency coverage for imaging operation. The location/distribution, operating frequency and bandwidth of transmitters when combined with potential imaging locations may be in some manner incomplete; too sparse, poor coverage or access, etc. For monostatic radar the combination of spatially variant waveform with the collection aperture can produce excellent images as we show in Section 4.8 based on a adaptation of [67] to radar from the original Magnetic Resonance Imaging (MRI) application. Here instantaneously narrow band signals were set as a function of frequency and angle over a wide tunable bandwidth over the collection aperture. Reconstruction produced point spread functions with the same resolution as full bandwidth signals and good sidelobe structure while occupying a fraction of the space-frequency domain.

The term space-frequency is used to represent locus of points, in the spatial frequency domain that is defined by the combination of the collection aperture and the composite frequency and bandwidth of the operating emitters/waveforms exploited. The application of the concept of space-frequency to passive bistatic radar is then fulfilled with the inclusion of multiple, distributed emitters with separable waveforms, potentially in concert with tailoring the collection aperture which could be comprised on multiple receivers.

As noted, Bracken, *et al* [57] describes composing the aperture in the frequency domain where λ, β (bistatic angle) and the bistatic bisector vector are used to describe the sampled Fourier space. All combinations of monostatic and bistatic pairs over frequency,

waveform and position define a space-frequency region of greater size than any constituent contribution, resulting in higher resolution than less filled sampling schemes. The combination of frequency, position and geometry can effectively produce low frequency/DC sampling, all conditioned on the target response. Cetin and Lanterman [68] model the PBR for ISAR (while using the term ’SAR’ interchangeably) assuming a noncooperative multistatic (multiple transmitter, single receiver) architecture based on VHF transmitters in the Washington, D. C. area. Simulated images of good quality, employing several reconstruction methods, are formed using the complex radar cross section generated from aircraft shapes and derived using a method of moments electromagnetic solver. The Fourier sampling pattern described in this work is another codification of the space-frequency spectrum from Bracken.

Similar concepts can be seen in the work of the Air Force Research Laboratory [69] in the creation of a tomographic test range. The employment of a thinned constellation of sensors surrounding a test scene employing RF tones as the illuminating/probing signal and collecting all source/sensor/tone (CW signal) combinations, followed by calibration and reconstruction. Planned upgrades include arbitrary waveform generation.

Chapter 3

Radio Frequency Reflection Tomography

We introduce Radio Frequency (RF) reflection tomography with three derivations that illustrate the principles and properties from three distinct perspectives. The first is the inverse problem solution derived from first physical principles. The second is an *ad hoc* derivation that develops the inverse problem using representations that will be familiar to anyone with a background in radar systems. Finally, the third is realized more from an image processing perspective, bridging elements of the first and second. Neither the second nor the third approach can be realized without the assumptions inherent in the solution developed from first principles. The value of the second and third approaches, fundamentally the concept of projections, illustrates extensions beyond what might be considered a spatial-only phenomenology of the first principles development, as can be seen with the extensions to tomography using Doppler-based projections [70].

3.1 Reflection Tomography as Derived from First Physical Principles.

In general scattering of energy from an unknown body, either acoustic or electromagnetic, is termed the *forward problem*. Given a description of the geometry of the object, the parameters representing the physical properties, and the form of the illuminating energy, the scattered fields can be found. The *inverse problem* is then the process of describing the geometry of a body given measurements of energy scattered or emitted from it. Tomography in its various forms addresses the latter.

The development of solutions to the inverse problem involving reflection tomography begins with general solutions to the scalar wave equation [71]

$$\nabla^2\Psi(r',t) - \frac{1}{c^2}\frac{\partial^2}{\partial t^2}\Psi(r',t) = s(r,t) \tag{3-1}$$

where Ψ, the general potential, represents the field at a point (*r'*, *t*) in space-time due to source *s* at (*r*, *t*=0). Daveney [72] describes the overall process in terms of Potential Scattering. While the electromagnetic scattering process is vector in nature, the inverse problem, tomographic reconstruction is scalar. Norton and Linzer [73], developing acoustic reflection tomography, ascribe this to the use of the same antenna for transmission and reception and that the signal from the receiver may be treated as the result of integrals of spherical wave fronts over the target reflectivity function, producing a scalar function of space. Further that it is a consequence of the Born approximation (more below) and monostatic operation. This latter because the antenna presumably radiates and receives the same, single polarization, eliminating any vector dependencies. In [74, eqns. 4, 5] the authors make this point through the use of a TM radiated wave and identical receive antennas, not necessarily monostatically. Cheney and Borden [75] begin their development with the scalar wave equation as a given. Soliman and Boerner [76], discussing electromagnetic wave diffraction tomography, observe that depolarization effects require that the vector wave equation would be required to be inverted; "something beyond the current state of the art".

A fundamental solution to (3-1) is realized for the class of functions for an impulse excitation

$$(\nabla^2 - \frac{1}{c^2}\frac{\partial^2}{\partial t^2})g(x,t) = -\delta(t)\delta(x) \tag{3-2}$$

This solution is, in one dimension for convenience,

$$g(x,t) = \frac{\delta(t-|x|/c)}{4\pi|x|}. \tag{3-3}$$

This solution is called an outgoing Green's function. In the frequency domain (3-2) and (3-3) become

$$(\nabla^2 + k^2)G(x,\omega) = -\delta(x) \qquad \text{and} \qquad G(x,\omega) = \frac{e^{jk|x|}}{4\pi\,|\,x\,|}. \tag{3-4}$$

The Green's function permits solutions to this class of equations for any source term [77]. The Fourier relationships for the source and potential wave functions are

$$S_\omega(r) = \frac{1}{2\pi}\int_{-\infty}^{\infty} s(r,t)e^{-j\omega t}dt \qquad (3\text{-}5), \qquad \psi_\omega(r) = \frac{1}{2\pi}\int_{-\infty}^{\infty} \Psi(r,t)e^{-j\omega t}dt. \tag{3-6}$$

Equation 3-6 suggests that solutions to (3-1) for the individual frequency components of the field can be combined to develop the overall solution. Given (3-6) the frequency dependence is implicitly retained in that which follows. Various researchers treat the temporal (frequency) dependence differently; solutions to (3-1) are multiplied by a single frequency and Fourier techniques used to address waveform [71], [78] or the waveform effects are normalized out [73] and also [78], or carried completely [75].

Now define a bounded region ***R*** of compact support, with electrical properties, refractive index (η) or permittivity (ε), permeability (μ), and conductivity (σ), as defined within an unbounded volume. The electrical properties of this larger volume are homogeneous, such that free space (constant velocity) propagation is observed. Let $\psi_{\text{total}}(\vec{r}\,)$ be the total field at any point, which is the sum of the incident field (given by the solution to the homogeneous wave equation) and field scattered by ***R***. Let the incident field be from a point source antenna in the free space region (outside of ***R***, lossless and nondispersive) and at sufficient range that the incident waveform is planar (the paraxial approximation [77]). Otherwise stated

$$\psi_{total}(\vec{r}) = \psi_{inc}(\vec{r}) + \psi_{scattered}(\vec{r}). \tag{3-7}$$

The incident wave satisfies the homogeneous Helmholtz equation

$$(\nabla^2 + k^2)\psi_{inc}(\vec{r}) = 0 \tag{3-8}$$

where *r* is a vector in $\mathbb{R}^n$ (n=1, 2, 3). For inhomogeneous media we can more generally write the wave equation as

$$(\nabla^2 + k(\vec{r})^2)\psi_{total}(\vec{r}) = 0 \tag{3-9}$$

where $k(\vec{r})$ is a scalar function that defines the reflective/refractive properties of the media. If the electrical properties of ***R*** are expressed as a deviation from those of the isotropic, homogeneous, ambient region such that $\eta(\vec{r})$ = 1+ $\eta_d(\vec{r})$, the subscript '*d*' indicating deviation, then

$$k(\vec{r}) = k_o n(\vec{r}) = k_o(1 + n_d(\vec{r})) \tag{3-10}$$

making the substitution of (3-10) into (3-9) and with some manipulation gives

$$(\nabla^2 + {k_0}^2)\psi_{total}(\vec{r}) = -O(\vec{r})\psi_{total}(\vec{r}) \tag{3-11}$$

where $O(\vec{r})$ is interpreted as the reflective (or refractive) distribution representing the object. Now substituting (3-7) and using (3-8), (3-11) can be written

$$(\nabla^2 + {k_0}^2)\psi_{scattered}(\vec{r}) = -O(\vec{r})\psi_{total}(\vec{r}). \tag{3-12}$$

As in (3-4), solutions of the form of (3-2) are sought

$$(\nabla^2 + k^2)G(\vec{r}) = -\delta(\vec{r}) \tag{3-13}$$

where $G(\vec{r})$ is a Green's function and δ represents the source. In one, two, and three dimensions the Green's function is given by

$$G(x,x') = \frac{e^{\left|jk_0 x - x'\right|}}{4\pi\left|x - x'\right|} \text{ (a)} \quad G(\vec{r},\vec{r}') = \frac{j}{4}H_0^{(1)}(k_0|\vec{r} - \vec{r}'|) \text{ (b)} \quad G(\vec{r},\vec{r}') = \frac{e^{jk_0|\vec{r}-\vec{r}'|}}{4\pi|\vec{r} - \vec{r}'|} \text{ (c).} \tag{3-14}$$

In 3-14b, H_o is the zeroth order Hankel function of the first kind. The Green's function is only a function of position $(\vec{r} - \vec{r}')$. In [78] Kak and Slaney describe $G(\vec{r} - \vec{r}')$ as a point inhomogeneity. However in equation 3-12 the scattered field is expressed as a function of the total field, itself the sum of the incident and scattered field.

A solution to (3-12) is given by the Lippman-Schwinger equation [75] relating the scattered field to the total field through an integral expression over the region of nonhomogeneous reflectivity

$$\psi_{scattered}(k,\vec{r}) = -\iiint_R G_k(\vec{r} - \vec{r}')O(\vec{r})\psi_{total}(\vec{k},r)dR. \tag{3-15}$$

If the reflectivity distribution and incident waveform are represented by a single function then equation 3-15 resembles Duhamel's function [80]. Yet another variant invokes the Green's Formula [82] to derive a similar relationship. In (3-15) we also have the scattered field recursively expressed as a function of the incident and scattered field (3.1-7). The elimination of the dependence of the scattered field on the scattered field as part of the total field is realized through application of a linearizing approximation, typically the Born approximation [72], [75], [76], and [79] or the Rytov approximation [79]. The Born approximation requires that the scattered field be much less than the incident field and can thus be ignored. Stated otherwise, there is no scatterer mutual interaction (multipath). This latter gives rise to the reference of the Born approximation as the weak scatterer approximation and is valid when $|k(n\text{-}1)D| << 1$ for n the index of refraction and D the object size. The linearizing approximation permits replacing the total field term in (3-15) with the incident field, giving.

$$\psi_{scattered}(k,\vec{r}) = -\iiint_R G_k(\vec{r}-\vec{r}')O(\vec{r})\psi_{inc}(k,\vec{r})dR \tag{3-16}$$

which is essentially a convolution integral of the Green's function with the product of the reflectivity function and the incident field. In the time domain the insertion of the Green's function into (3-16) followed by taking the inverse Fourier transform produces a result of the form

$$\psi_{scattered}(t,\vec{r}) = -\iiint_R \frac{\delta(t-(\vec{r}-\vec{r}')}{2(\vec{r}-\vec{r}')}O(\vec{r})\psi_{inc}(k,t)dR \tag{3-17}$$

The problem now becomes the reconstruction of the reflectivity distribution $O(\vec{r})$ given knowledge of the incident field and the measurements of the scattered field over a sufficient range of r and k. At this point electromagnetic arguments are essentially complete and the derivation of the inverse scattering solution is one of the collection aperture and geometry, as codified in the expansion of the Green's function. Equation 3-16 is a linear mapping of the reflectivity function to the scattered field which can be

essentially treated as the received signal from the probing field. Consider the geometry of Figure 3.1, and following the development of [71] and [78]. For convenience the geometry is considered in two dimensions.

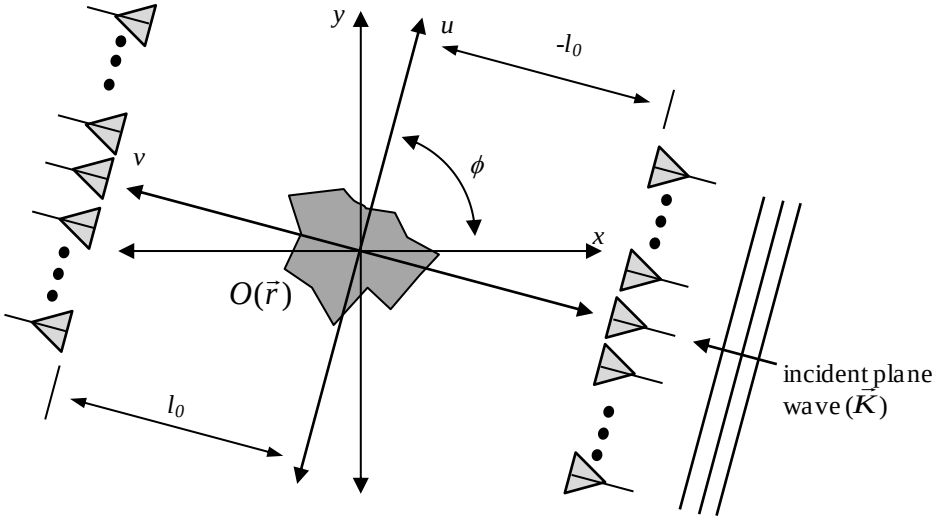

Figure 3.1. Two Dimensional Scattering/Sampling Geometry

A monochromatic plane wave is propagating in a direction given by $\vec{K}$, or

$$\psi_{inc}(\vec{r}) = e^{j\vec{K}\cdot\vec{r}} \tag{3-18}$$

where $\vec{K} = (k_x, k_y)$ satisfies the relationship

$$k_o^{\,2} = k_x^{\,2} + k_y^{\,2} \tag{3-19}$$

The practice is to now substitute the plane wave expansion (PWE) form of the Green's function into (3-14), along with eqn. 3-18. The two dimensional plane wave expansion [82] in a frame rotated against the object coordinate frame is

$$G\left(\left|\vec{r} - \vec{r}'\right|\right)_{PWE} = \frac{1}{2\pi}\int_{-\infty}^{\infty} \frac{j}{2k_v} e^{j[k_u(u-u') + k_v|v-v'|]} dk_u \tag{3-20}$$

where the PWE subscript identified the plane wave expansion, where $\vec{r} = (x, y)$, $\vec{r}' = (x', y')$, and

$$k_v = \sqrt{k_0^{\,2} - k_u^{\,2}}. \tag{3-21}$$

The plane wave expansion basically describes a cylindrical wave. This is intuitively satisfying with the earlier interpretation that the Green's function behaves as a point

inhomogeneity and one can visualize the scattered result from a plane wave and a point. In this notation, $\vec{r}'$ is the center of the outwardly propagating wave. The terms k_u and k_v serve as wave numbers in the rotated frame in Figure 3.1. We are only concerned with outwardly propagating waves that can be sampled at large *r*. The definition in (3-21) is equivalent to k_u and k_v being real-valued. If $|k_u| > k_0$ then k_v becomes imaginary (the so-called evanescent wave) which exponentially decays and can be neglected after some 10 wavelengths.

Let the direction of the incident field be along direction s_0 which is aligned with v'

$$\psi_{inc}(s_0) = e^{jk_0 v'} \tag{3-22}$$

Carrying out the substitution and rearranging the order of integration we have, for the reflected wave ($v = -l_0$)

$$\psi_{scattered}(u, v = -l_0) = \frac{j}{4\pi k_v} \int_{-\infty}^{\infty} e^{j(k_u u - k_v l_0)} \iint_{u',v'} O(u', v') e^{j[-k_u u' - (k_v - k_0)v']} du' dv' dk_u \tag{3-23}$$

In Figure 3.1 this is illustrated by the lines of sensors sampling the scattered fields. In (3-23) we have sampled along $-l_0$, for reflection tomography, this location defined such that the sampling line nowhere intersects $O(\vec{r}')$. The inner integrals in (3-23) resemble a two-dimensional Fourier transform over the reflectivity distribution in the rotated space, and so can be simplified

$$\begin{aligned} \psi_{scattered}(u, v = -l_0) &= \frac{j}{4\pi k_v} \int_{-\infty}^{\infty} o(k_u, k_0 - k_v) e^{j(k_u u - k_v l_0)} dk_u \\ o(k_u, k_v - k_0) &= \iint_{u',v'} O(u', v') e^{j[-k_u u' - (k_v - k_0)v']} du' dv' \end{aligned} \tag{3-24}$$

Equation 3-24 also includes the form of an inverse dimensional Fourier transform. Taking the transform of the scattered field (ψ - Ψ form a transform pair) with respect to k_u gives

$$\Psi_{scattered}(k_u, k_v - k_0) = \frac{j}{2k_v} e^{-jk_v l_0} o(k_u, k_v - k_0) \tag{3-25}$$

This result relates the forward (spatial) Fourier transform of the measurements of the scattered field along the line $v = -l_0$ to the arc of the reflectivity function represented in the Fourier (frequency) domain. Slaney and Kak [78] describe this as a generalization of the Fourier Slice Projection (or Slice Diffraction) Theorem, generalizing from the case of straight line propagation of X-ray transmission tomography. This is depicted in Figure 3.2. The locus of measurements for sampling in a diffraction geometry (semicircle passing through 0 in *k*-space) and a reflection geometry (the semicircle that closes the circle) are shown. For the monochromatic illuminating plane wave the radius of the circle is k_0. Measurements conducted for incident fields from 0 to 2π relative define a disk of radius $\sqrt{2k_0}$ in diffraction tomography and from $\sqrt{2k_0}$ to $2k_0$ in reflection tomography.

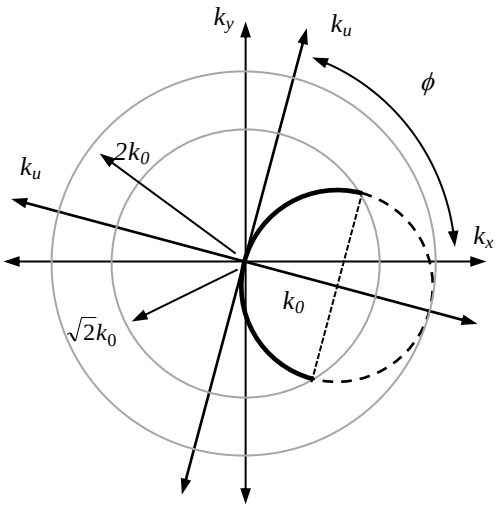

Figure 3.2. Graphic Representation of the Generalized Fourier Slice Projection Theorem

This is shown in Figure 3.2 where the dashed semicircle represents the reflection mapping and the heavy the forward scatter (diffraction). The magnitude of k_0 acts as a band pass filter for reflection tomography (yielding a torus-like shape in *k*-space when rotated overall; $\phi = 0$ to 2π) while emulating a low pass filter for transmission measurement geometries and yielding a disk of sampled spatial frequencies. Also, sampling at equally spaced intervals, which map uniformly onto k_u, produces nonuniform samples along the arc. The method assumes either an array that simultaneously samples the scattered fields or a single element that is sequentially positioned. This approach has assumed a monochromatic plane wave, or components of a waveform with wider bandwidth that has been decomposed into its Fourier frequencies. As the geometry is rotated this will result in nonuniform sampling of the object. The implication of increased bandwidth is that the

projection arc is different for each frequency. This is shown in Figure 3.3 for a limited number of discrete tones. Sampling over rotation is now denser, resulting in a more complete filling of *k*-space.

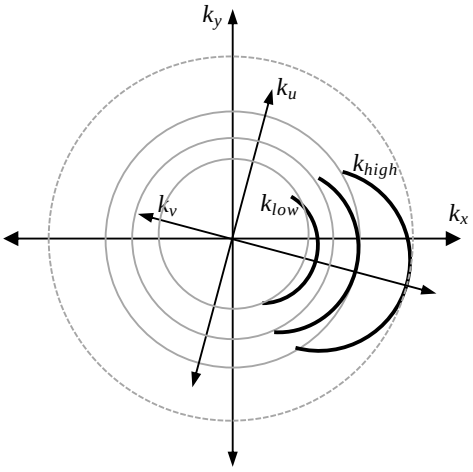

Figure 3.3. Filling *k*-Space using Waveform Bandwidth

3.1.1 ***Image reconstruction by filtered back projection***. There are a number of methods for image reconstruction given the measurement set and phenomenology just described. One is selected, filtered back projection (sometimes termed filtered back propagation), because of the similarities to the technique used extensively in the remainder of this thesis. The development of this technique, following the original approach of Daveney [83] begins with the inverse two-dimensional Fourier transform of the reflectivity distribution as one means to obtain the reflectivity distribution

$$O(\vec{r}) = O(x, y) = \frac{1}{(2\pi)^2} \int_{-\infty}^{\infty} \int_{-\infty}^{\infty} o(\overline{K}) e^{j\overline{K}\cdot\vec{r}}\, d\overline{K} \tag{3-26}$$

defined on a rectangular grid as (k_x, k_y) from (3.1-19). To overcome the need for interpolation over the rectangular basis a change of variable is made that represents *K* over circular arcs as shown in Figure 3.4, more appropriately representing the means by which the data were collected. We define $o(\overline{K})$ as the ensemble of data representing forward transform with respect to k_u of measured scattered fields along *u* at $v=-l_0$ with ϕ as a parameter, sampling as shown in Figure 3.1. We also define $\overline{K}$ as

$$\overline{K} = k_0(\vec{s} - \vec{s}_0) \tag{3-27}$$

where $\vec{s}_0 = (\cos(\phi), \sin(\phi))$ is the unit vector describing the direction of the illuminating wave and $\vec{s} = (\cos(\chi), \sin(\chi))$ the direction of the scattered wave (both interpreted relative to the non-rotated frame in Figure 3.4) is defined by the locations of elements in the receive array or sequential sampling positions. Note that for monostatic collection $\vec{s} = -\vec{s}_0$. We make a change of variable from the Cartesian wavenumber basis (k_x, k_y) in (3-26) to a coordinate frame defined by the incident and scattered angles. Using (3-27) and

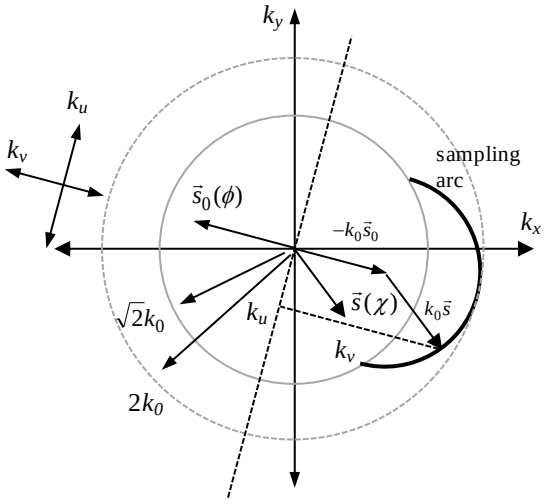

Figure 3.4. Filtered Back Propagation Transform Domain Coordinates

$$\overline{K} = k_x\hat{x} + k_y\hat{y}$$

gives

$$\begin{aligned} k_x &= k_0(\cos(\chi) - \cos(\phi)) \\ k_y &= k_0(\sin(\chi) - \sin(\phi)) \end{aligned} \tag{3-28}$$

so that the Jacobian yields

$$dk_x dk_y = \begin{vmatrix} \frac{\partial k_x}{\partial \chi} & \frac{\partial k_x}{\partial \phi} \\ \frac{\partial k_y}{\partial \chi} & \frac{\partial k_y}{\partial \phi} \end{vmatrix} = \begin{vmatrix} -k_0\sin(\chi) & k_0\sin(\phi) \\ k_0\cos(\chi) & -k_0\cos(\phi) \end{vmatrix} d\chi d\phi = (k_0\sin(\chi)k_0\cos(\phi) - k_0\cos(\chi)k_0\sin(\phi))d\chi d\phi$$

using the trigonometric angle difference identity the RHS gives

$$dk_x dk_y = k_0{}^2\sin(\chi - \phi)d\chi d\phi \text{ or } dk_x dk_y = k_0{}^2\sqrt{1-\cos^2(\chi-\phi)}d\chi d\phi$$

the cosine angle difference is expanded to give $k_0{}^2\sqrt{1-(\cos(\chi)\cos(\phi)+\sin(\chi)\sin(\phi))^2}\,d\chi d\phi$. The expression in parenthesis under the radical is also the inner product of the incident and scattered unit vectors [84]

$$dk_x dk_y = k_0{}^2\sqrt{1-(\vec{s}\bullet\vec{s}_0)^2}\,d\chi d\phi \tag{3-29}$$

where $\bullet$ indicates inner product. With this (3.1-26) becomes

$$O(\vec{r}) = \frac{1}{(2\pi)^2} k_0{}^2 \int_0^{2\pi} \int_0^{2\pi} \sqrt{1-(\vec{s} \bullet \vec{s}_0)^2}\, o(k_0(\vec{s}-\vec{s}_0)) e^{jk_0(\vec{s}-\vec{s}_0)\cdot\vec{r}}\, d\chi d\phi \qquad (3\text{-}30)$$

In diffraction tomography, with the presumption of reciprocity of scattering along reciprocal geometries (*i.e.*, 0^o to 180^o or 180^o to 360^o), there is an additional factor of 1/2 outside the integral because of the double coverage of the angle space. For reflection tomography this reciprocity cannot be assumed.

This initial transformed domain maps the data through two angles, but is not fully representative of the measurement geometry which was a distance along the transformed measurement line (k_u, as noted in Figure 3.4) and angle ϕ. A final transformation is made to overcome this. Using a trigonometric identity and asserting that χ is defined relative to the rotated frame and because the sample points lie on an arc in the frequency domain (also Figure 3.4)

$$\cos(\chi) = \frac{k_u}{k_0} \qquad \sin(\chi) = \frac{k_v}{k_0} \qquad \text{and} \qquad d\chi = -\frac{1}{k_0 k_v} dk_u \qquad (3\text{-}31)$$

This is found by interpreting $\vec{s}_0$ with respect to the rotated frame where it propagates along $\hat{v}$. The radical reduces to

$$\sqrt{1-(\vec{s} \bullet \vec{s}_0)^2} = \frac{1}{k_0}\sqrt{k_0{}^2 - k_v{}^2} = \frac{|k_u|}{k_0} \qquad (3\text{-}32)$$

The differential for the change of variable in (3-31) is found by solving for k_u, taking the derivative and solving for $d\chi$. With these substitutions the inner integral in (3.1-30) becomes

$$-\frac{1}{k_0}\int_{-k_0}^{k_0} \frac{1}{k_v} |k_u| o(k_0(\vec{s}-\vec{s}_0)) e^{jk_0(\vec{s}-\vec{s}_0)\cdot\vec{r}}\, dk_u \qquad (3\text{-}33)$$

where the integral limits are fixed by the non-evanescent wave constraint. We now use eqn. 3-25, the Fourier transform with respect to k_u of the reflection measurements made along the line at $v = -l_0$, and solve for the scattered spectrum which is then substituted into (3-24)

$$O(\vec{r}) = \frac{2k_0 j}{(2\pi)^2} e^{jk_v l_0} \int_0^{2\pi} \int_{-k_0}^{k_0} |k_u| \Psi_{scattered}(k_u, k_v - k_0) e^{jk_0(\vec{s}-\vec{s}_0)\cdot\vec{r}} dk_u d\phi \tag{3-34}$$

where the negative sign was cancelled by shifting *j* to the numerator. Finally we address the dot product using (3-31) and the definition of $\vec{s}_0$ in the rotated frame.

$$\vec{r} = \begin{bmatrix} u \\ v \end{bmatrix} \quad \vec{s} = \begin{bmatrix} \frac{k_u}{k_0} \\ \frac{k_v}{k_0} \end{bmatrix} \quad \vec{s}_0 = \begin{bmatrix} 0 \\ 1 \end{bmatrix} \qquad \text{giving} \qquad k_0(\vec{s} - \vec{s}_0) = k_u u + (k_v - k_0)v \tag{3-34}$$

Making this final substitution into (3-34) results in

$$O(\vec{r}) = \frac{2k_0 j}{(2\pi)^2} e^{jk_v l_0} \int_0^{2\pi} \int_{-k_0}^{k_0} |k_u| \Psi_{scattered}(k_u, k_v - k_0) e^{j(k_u u + (k_v - k_0)v)} dk_u d\phi \tag{3-35}$$

It is common practice to represent (3-35) in a form which illustrates the filtered backpropagation implementation. The outer integral expresses the reconstructed image in the original coordinate (*x*, *y*)

$$O(x, y) = \frac{1}{2\pi} \int_0^{2\pi} \Pi_\phi(x\cos(\phi) + y\sin(\phi), -x\sin(\phi) + y\cos(\phi)) d\phi. \tag{3-36}$$

The substitution Π_ϕ is then defined from

$$\Pi_\phi(u, v) = \frac{k_0 j}{\pi} \int_{-k_0}^{k} \Gamma_\phi(k) H(k) G_n(k) e^{jk_u u} dk_u \tag{3-37}$$

with

$$\Gamma_\phi(k) = \Psi_{scattered}(k_u, k_v - k_0) e^{jk_v l_0}$$

$$G_\eta(k) = \begin{cases} \exp[\, j(k_v - k_0)v] & |k| \le k_0 \\ 0, otherwise \end{cases}$$

$$H(k) = \begin{cases} |k_u| & |k_u| \le k_0 \\ 0, otherwise \end{cases}$$

As will be seen, the methodology in this section reduces to that of the following sections as the distributed (multiple antenna) spatial sampling is reduced to a single sensor/antenna/transducer in a monostatic, pseudo-monostatic (transmitter and receiver aligned to a common angle of incidence), or bistatic geometry; and temporal bandwidth replacing spatial bandwidth in filling *k*-space. Also the form of (3-37) will be recognized in the generalization of the Radon Transform and projections as line integrals in Section

3.3. Back propagation also has similarities to the motion compensation applied to account for non-circular or non-spherical trajectories defining the collection aperture.

This section was presented to demonstrate the justification for the use of convolution arguments concerning the interaction with radar waveforms with the target/object that will be employed in the remainder of this thesis. The first principles methodology establishes the connection between the forward and the inverse problems, generally not encountered in Radar Systems developments involving imaging modes or applications.

3.2. Radar-Centric Derivation of Tomographic Reconstruction.

Mensa presents in [21], [17] a heuristic development of tomographic reconstruction; one that leads through the Fourier Slice Projection Theorem before developing the expression for reconstruction via filtered backprojection (FBP) in two dimensions. The synthesis comes more from the radar perspective and tacitly employs the weak scattering approximation from Section 3.1, together with the far field approximation of a planar wavefront illuminating the target.

Consider the geometry in Figure 3.5. An antenna illuminates a scene that is being imaged from successive angular positions at constant range (R). A rotated coordinate frame (u, v) is overlaid on the fixed scene/object coordinate frame (x,y), with the antenna line-of-sight defined along u.

The returns from all points of constant delay, the isorange contour (aligned along v), combine coherently at the antenna terminals, *e. g*., the antenna performs integration along the line described by the locus of constant delay. The aggregate over all delay spanning the object or scene produces the projection as depicted in Figure 3.5b. The range samples defining a projection are entirely a function of the illuminating waveform bandwidth;

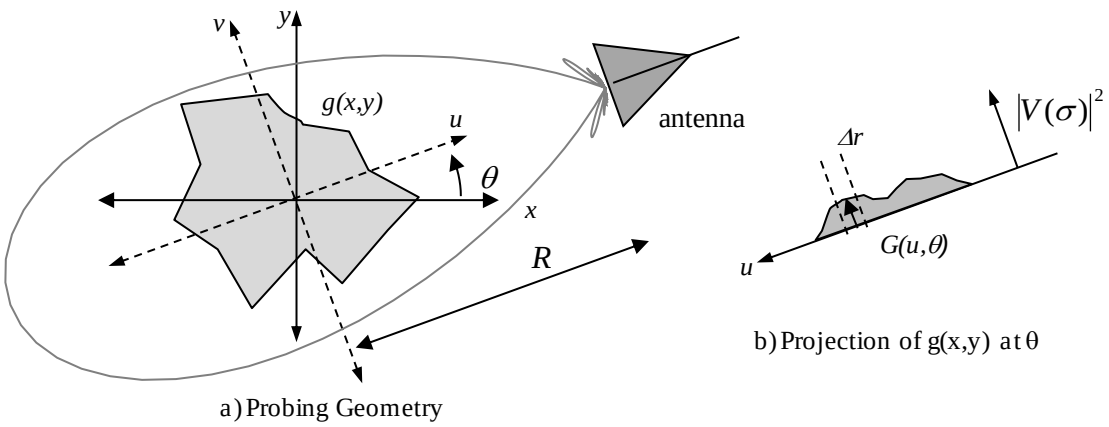

Figure 3.5. Reflection Tomography Geometry Definition

with Δr representing the bandwidth resolving power in range. As shown, the projection represents received power as a function of range. Defining the reflectivity distribution of the object as $g(x, y)$ then the projection of $g(u, v)$, a rotated form of $g(x, y)$, onto u through the action of the antenna can be written as an integral over v at angle θ, or

$$P(u,\theta) \propto \int_{-\infty}^{\infty} g(u,v)dv \tag{3-38}$$

In (3-38) we have assumed that $R>>1$ so that curvature of the isorange contour is a plane wave and the projection expressed as a line integral extending indefinitely outside the extent of the mainbeam. Note that θ is equivalent to ϕ in the previous section. The finite physical extent of the object, from a controlled test or laboratory perspective, is commonly offered to physically justify the infinite bounds on the integral. In remote sensing applications the gain response of the antenna pattern and range sampling may also be argued, though perhaps more weakly, as a justification. Note also that projections are formed normal to the line of sight in reflection tomography (Figure 3.5b), and sampled along the line of sight (also termed the projection axis) but are parallel to the propagation direction in pure transmission tomography (Figure 3.1, without scattering) and sampled orthogonally to the propagation direction.

The total signal received is given by the integral along u with a phase factor proportional

to the two way propagation distance with the assumption of a constant propagation constant $k=2\pi/\lambda$

$$G(\theta)=\int_{-\infty}^{\infty}P(u,\theta)e^{-j2ku}du=\int_{-\infty}^{\infty}\left(\int_{-\infty}^{\infty}g(u,v)dv\right)e^{-j2ku}du=\int_{-\infty}^{\infty}\int_{-\infty}^{\infty}g(u,v)e^{-j2ku}dvdu \tag{3-39}$$

and the factor of 2 is for two-way propagation (e.g., monostatic). Rotating into (u, v) in object coordinates is accomplished by the change of variable

$$\begin{bmatrix}u\\v\end{bmatrix}=\begin{bmatrix}\cos(\theta) & \sin(\theta)\\ -\sin(\theta) & \cos(\theta)\end{bmatrix}\cdot\begin{bmatrix}x\\y\end{bmatrix}. \tag{3-40}$$

Substitution into (3-40) yields an expression equivalent to the spatial Fourier transform of the object reflectivity distribution. This is

$$G(\theta)=G(\rho\cos(\theta),\rho\sin(\theta))=\int_{-\infty}^{\infty}\int_{-\infty}^{\infty}g_{\theta}(x,y)e^{-j2\pi(\rho x\cos(\theta)+y\rho\sin(\theta))}dydx \tag{3-41}$$

with $g(u, v)=g_{\phi}(x, y)$ and $\rho=2/\lambda$. The Jacobian of the variable change is unity. Equation 3-41 directly illustrates the Slice Projection theorem: the forward transform of the range projection P at angle θ, given (3-39), is equivalent to the two dimensional spatial Fourier transform of the reflectivity distribution at angle ϕ. Making the change of variable $f_y=\rho sin(\theta)$ and $f_x=\rho cos(\theta)$ gives the transform in term of spatial frequencies (f_x, f_y) as

$$G(f_x,f_y)=\int_{-\infty}^{\infty}\int_{-\infty}^{\infty}g(x,y)e^{-j2\pi(xf_x+yf_y)}dydx \tag{3-42}$$

This development is slightly altered from [21] to be consistent with conventions used throughout this thesis: we reference the projection axis (u) as the normal to the illuminating plane wavefront (along or parallel to the radar line-of-sight for the planar wavefront) whereas Mensa uses v, and we define the rotation angle measured from the object coordinate frame x axis in the polar sense toward u (Mensa referenced the negative y axis, counter-clockwise). This has the effect of producing the form of the forward Fourier transform as e^{-jkR} as used herein but results in a somewhat awkward formalism in

(3-42) with the order of integration reversed. This is addressed by letting the reflectivity distribution *g(x, y)* be a bounded region *B*. The integration is performed over the area *B*; with integral limits not functionally dependent on the integral variables then the order of integration is simply reversed.

Conversely, the inverse transform is given by

$$g(x,y) = \int_{-\infty}^{\infty}\int_{-\infty}^{\infty} G(f_x, f_y) e^{j2\pi(xf_x+yf_y)} df_x df_y \qquad (3\text{-}43)$$

where $f_x = 2/\lambda$, etc.. Equation 3-43 represents an image reconstruction given the series of forward transformed projections, measured at a discrete set of angles around the object/scene origin. The forward transformed projections are defined on a polar map in measurement space (ρ, θ) while the inverse transform is developed on a rectangular grid of spatial frequencies. For this derivation, in the narrowband approximation, the region of support of the object is a ring in spatial frequency domain (also called *k*-space), centered at the operating wavelength, going to infinitesimal thickness as the bandwidth goes to zero (continuous wave) as a circle of radius $f_x^{\,2} + f_y^{\,2} = 4/\lambda^2$, and zero elsewhere. Employing the inverse Fourier transform for reconstruction would require interpolation to avoid reconstruction errors.

Alternatively, using the spatial frequency definition a second change of variable is made in (3-41) from a rectangular to polar basis in physical/object space, given by $x=r\cos(\phi)$ and $y=r\sin(\phi)$ (Figure 3.6). From (3-41) and (3-42), $G(f_x, f_y) = G(\rho\cos(\theta),\rho\sin(\theta))$. Making the change of variable, evaluating the Jacobian ($|\rho| d\rho d\theta$) and with simplification gives a reconstruction which is the two dimensional form of filtered back projection

$$\hat{g}(r,\phi) = \int_{0}^{2\pi}\int_{-\infty}^{\infty} G(\rho,\theta)|\rho| e^{j2\pi\rho r\cos(\phi-\theta)} d\rho d\theta. \qquad (3\text{-}44)$$

This form require no interpolation in reconstruction, as is the case with the inverse two-

dimensional FFT where (k_x, k_y) define a rectangular grid). The implementation of (3-44) steers the inverse transform the projection at θ to range r corresponding to the pixel (x, y) under reconstruction and is then summed over all θ.

Note in the development of (3-44) that the customary integrand range for the angle variable $(0,\pi)$ is not employed. As noted in Section 3.1, in transmission tomography reciprocity can be argued for the path of integration wherein the same result is obtained for viewing angles θ and $\theta+\pi$, and observation over the full range of angles represents redundant measurements. Ishimaru [71] and Kak and Slaney [78] apply this argument to diffraction tomography; both electromagnetic and acoustic. In reflection tomography the angular dependence of individual scatterers representing a reflectivity distribution invalidates this argument. This is not the case when the hypothetical point scatterer (rotation angle invariant response) is employed for calculating the point spread function, but will be the case in any real environment.

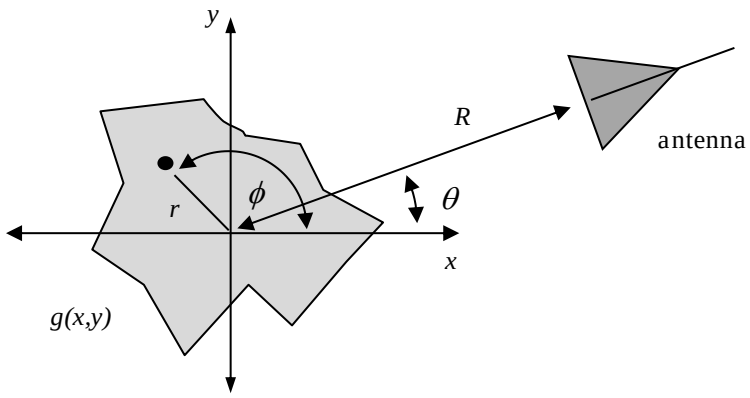

Figure 3.6. Two-Dimensional Monostatic Geometry

Figure 3.6 gives the general two-dimensional geometry that is used herein for any 2D monostatic applications. In the assignment of the spatial frequency as $f_x = 2/\lambda\cos(\theta)$ or $f_y = 2/\lambda\sin(\theta)$ (eqn. 3-42) Mensa departs from more customary definitions for spatial frequency (incorporating π). The radius of the tomographic aperture in k-space would be $k = \sqrt{k_x^{\,2} + k_y^{\,2}}$; or $k=2\pi/\lambda$, instead of $2/\lambda$, and would be more consistent with the broader

literature. Further there is a factor of 2 for the two-way propagation. Incorporating this into the wave number, then defines an aperture radius of $4\pi/\lambda$ and eqn. 3-42 becomes

$$G(k_x, k_y) = \int_{-\infty}^{\infty} \int_{-\infty}^{\infty} g(x, y) e^{-j2(xk_x + yk_y)} dxdy. \tag{3-45}$$

We see this latter definition in the description of the sampling aperture in Fourier space, for example, in [57]. Finally, the results in Section 3.1 collapse to those represented here when the sampling is performed at a single point represented by $\vec{s} = -\vec{s}_0$.

3.3 Reflection Tomography Derived from Line Integrals – The Radon Transform.

The heuristic method of Mensa in Section 3.2 invoked line integrals in his development of reflection-derived projections (eqn. 3-38). The integrals over the reflectivity distribution could be interpreted more from a radar engineering perspective, i.e., implicitly assumed the weak scatterer approximation. Likewise, the time domain integral term in the inhomogeneous wave equation solution (3-17) contains a delta function convolved with the reflectivity distribution. Mathematically, these approaches are examples of the Radon Transform [85]. This transform is a mapping from (x, y) into a new space (s, θ) defined by the integral contour form; a displacement term and a rotation. This transform was first applied to the problem of absorptive media and straight-line, transmission tomography using X-rays. The Radon Transform in two dimensions can be generalized as

$$F(T, s, \theta) = \int_{-\infty}^{\infty} \int_{-\infty}^{\infty} g(x, y) \delta(T(x, y, \theta) - s) dxdy \tag{3-46}$$

where $g(x, y)$ represents the reflectivity distribution over a bound region. Eqn. 3-46 has the general form of a convolution of a contour over the reflectivity distribution at fixed rotation angle. Here T is the functional description of the curvilinear integration path, s a propagator which affects the delta function. For a linear propagator the Radon Transform

translates lines (or linear features) in the physical domain into points in the transform domain. Conversely, the Radon Transform maps a point in physical space to a sinusoid in the transform (s,θ) domain. Examples of these mappings are given in Figure 3.7.

The two-dimensional, Cartesian Radon Transform is given by

$$G(s,\phi) = \int_{-\infty}^{\infty}\int_{-\infty}^{\infty} g(x,y)\delta(x\cos(\theta) + y\sin(\theta) - s)dxdy \qquad (3\text{-}47)$$

where s is the distance to the line $x\cos(\theta)+y\sin(\theta)$ from the origin, orthogonal to the line, at angle θ with respect to the x axis, as depicted in Figure 3.7a. Note that θ is identical to the prior section, representing the normal to the probing wavefront. Equation 3-47 generates projections by collapsing (integrating) perpendicular to s, all points along T. Figures 3.7b and 3.7c depict the mapping of a line by the Radon Transform to a point, including quantization effects due to finite array indexing. Here the 2π radian value for total rotation was used, and, as can be seen, the single defined line returns the point-pair response. The line slope is ~26 degrees, so θ normal occurs at approximately 116 and 296 deg with s roughly -5.4 and 5.4 respectively. Figures 3.7d and 3.7e demonstrate depicting an inverse-like operation where a point is mapped to a sinusoid;. Making a change of variable from a Cartesian representation to polar $(x,y) = (r\cos(\phi), r\sin(\phi))$ the expression for s becomes

$$s = r\cos(\theta - \phi). \qquad (3\text{-}48)$$

Specifically for Figure 3.7e, the point at (40,40) with origin at (32,32) yields an initial value for s (at θ=0) of 7.99, matching the initial value in the Figure. This representation, with lines mapped to points and points mapped to sinusoids, suggests the inverse processes which follow.

The Radon Transform in a rotated frame (s, u), rotated at angle θ from (x, y), is realized with the change of variable

$$\begin{bmatrix} x \\ y \end{bmatrix} = \begin{bmatrix} \cos(-\theta) & \sin(-\theta) \\ -\sin(-\theta) & \cos(-\theta) \end{bmatrix} \cdot \begin{bmatrix} s \\ u \end{bmatrix}. \tag{3-49}$$

The Jacobian associated with the change is unity so that (3-49) becomes

$$g(s,\theta) = \int_{-\infty}^{\infty}\int_{-\infty}^{\infty} g(s\cos(\theta) - u\sin(\theta), s\sin(\theta) + u\cos(\theta))\delta(s\cos^2(\theta) + s\sin^2(\theta) - s)dsdu. \tag{3-50}$$

The argument of the Dirac delta function reduces to (*s*-*s*) or identically 1. Using the filtering property of integrals of the delta function the inner integral is eliminated yielding

$$g(s,\theta) = \int_{-\infty}^{\infty} g(s\cos(\theta) - u\sin(\theta), s\sin(\theta) + u\cos(\theta))du. \tag{3-51}$$

Associated with the Radon Transform is the back projection operation. Following the method of Jain [86] the backprojection operator *B* is given by

$$B = B(g(s,\theta)) = \int_0^{2\pi} g(x\cos(\theta) + y\sin(\theta))d\theta \text{ or } B = \int_0^{2\pi} g(r\cos(\theta - \phi), \theta)d\theta. \tag{3-52}$$

The 0 to 2π range of the integral in (3-52) is a departure from the normal representation (0, π) [86], [87]. Whereas the Radon Transform "sums along rays" the backprojection operator accumulates rays through specific points. For applications where the scattering or propagation is reciprocal or symmetrical the range of the integral to π is adequate and carrying the procedure through a full 2π adds no new information, only serving to scale the result by a factor of 2. However for the reflection tomography problem we know that the majority of real objects, spheres being one exception, produce azimuthally variant responses. In many cases the azimuth response may be less than π radians, for example conducting planar areas many wavelength on a side. To maintain generality the full angular range is maintained.

The operation of the backprojection operator is demonstrated in Figure 3.8. Here a sparse scene consisting of 4 points (Figure 3.8a) is filtered by the Radon Transform producing the result in Figure 3.8b, with points 1-4 mapping onto sinusoids 1-4 representing $g(s,\theta)$. The backprojection concept is illustrated in Figure 3.8c where two horizontal slices of *g*

(Figure 3.8b), at angles 0 and 81 degrees are projected onto the locus (x, y) such that $s=x\cos(\theta) + y\sin(\theta)$ is satisfied. Figure 3.8d demonstrates this from the results in b) at three angles. The linear projection, four original points, plus ambiguous partial sums, can be seen.

The backprojection operator is not the inverse operator to the Radon Transform, but rather the adjoint. Exercising the backprojection operator on the Radon Transform of a

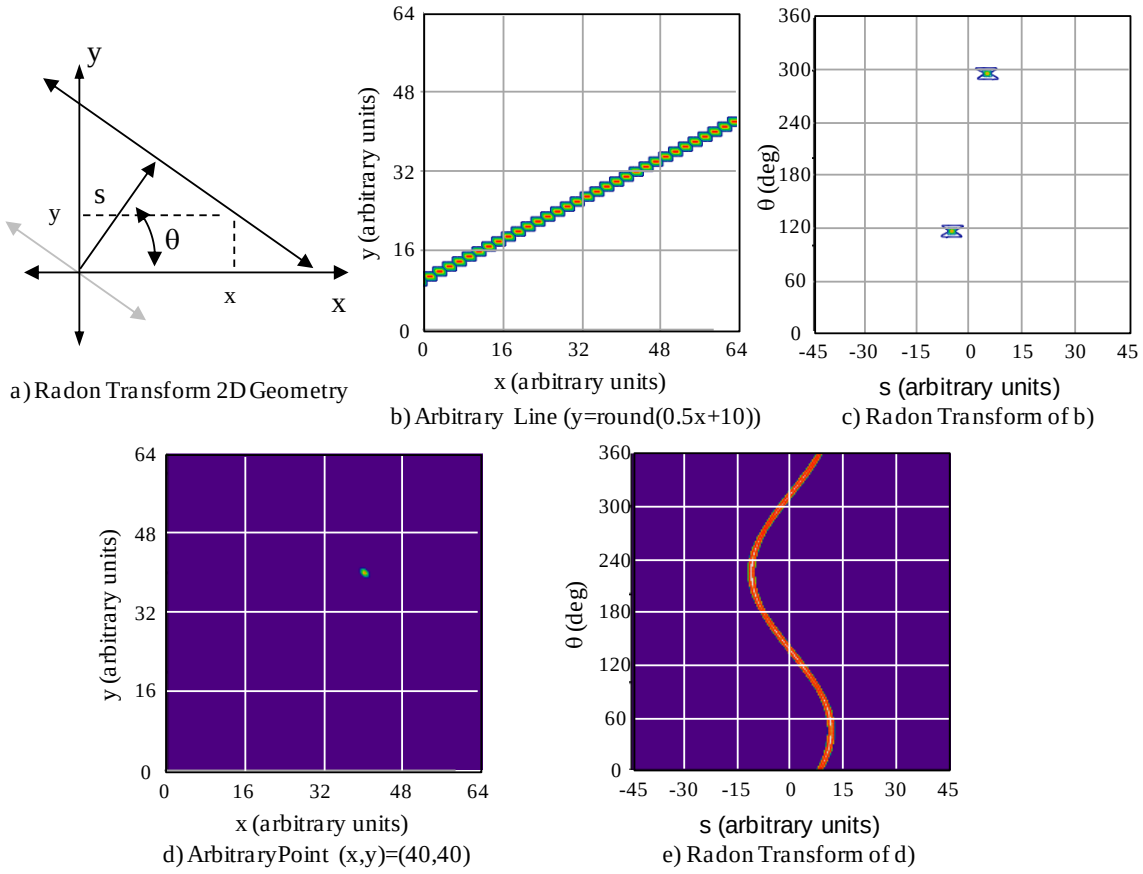

Figure 3.7. Line and Point Mappings under the 2D Linear Radon Transform

reflectivity distribution ($BR(g(x,y)$, where R represents the Radon Transform operator) produces a blurred reconstruction [86]. The blurring function is $1/\sqrt{x^2+y^2}$ that if convolved with $BR(g)$, the backprojection operator applied to the Radon transform of $g(x, y)$, will result in a reconstructed image without blurring. This two dimensional convolution can be realized using Fourier transforms. However the set of projections are generally taken along radials as the sensor is sequentially positioned or translates about

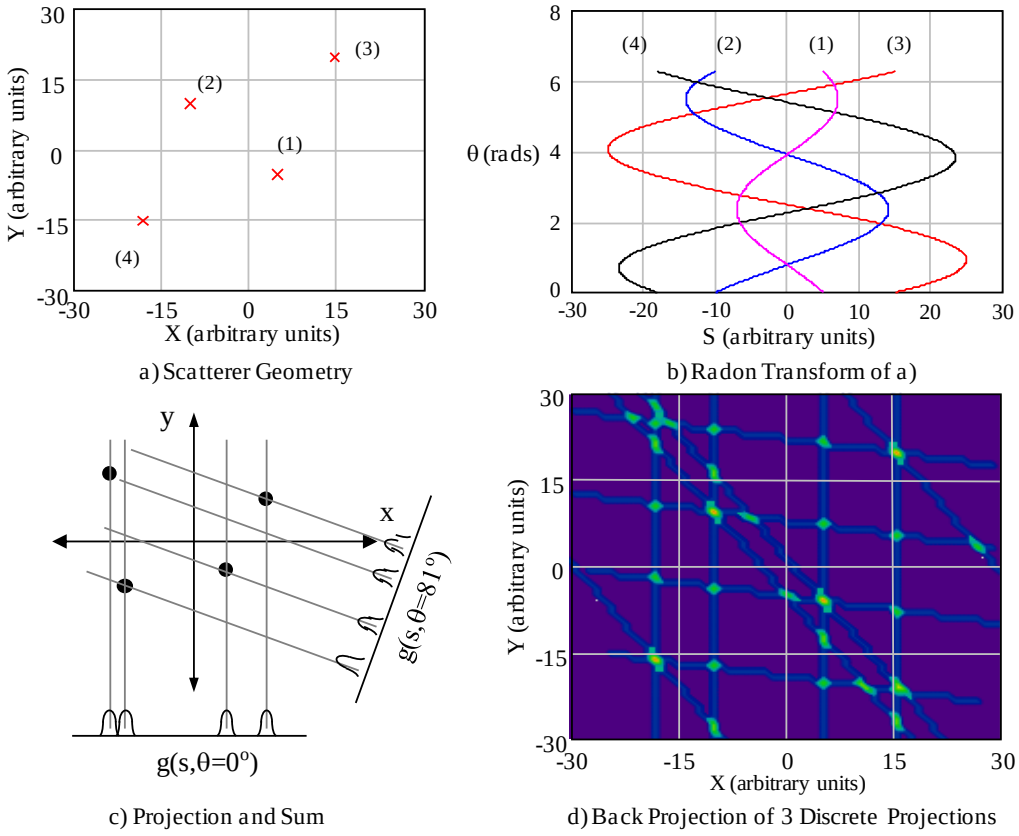

Figure 3.8. Example Backprojection Operation

the scene. This requires interpolation to match the data sample to the rectangular Fourier basis functions. To avoid interpolations, particularly for sparse collection apertures, an alternative is sought.

The Fourier transform of the Radon Transformed reflectivity ($g(s,\ \theta)$) at angle θ is given by

$$G(k,\theta) = \int_{-\infty}^{\infty} g(s,\theta) e^{-jks} ds \tag{3-53}$$

where $k=2\pi/\lambda$. Substituting 3-51 gives

$$G(k,\theta) = \int_{-\infty}^{\infty}\int_{-\infty}^{\infty} g(s\cos(\theta) - u\sin(\theta), s\sin(\theta) + u\cos(\theta)) e^{-jks} du ds \tag{3-54}$$

and making the change of variable (s, u) back to (x, y)

$$G(k,\theta) = \int_{-\infty}^{\infty}\int_{-\infty}^{\infty} g(x,y) e^{-jk(x\cos(\theta)+y\sin(\theta))} dx dy. \tag{3-55}$$

Equation 3-55 states that the one dimensional (forward) Fourier Transform of the Radon Transform of a reflectivity distribution $g(x,\ y)$ taken at fixed angle θ is equivalent to a

slice through the two-dimensional Fourier Transform of $g(x, y)$ at angle θ. Again we see the similarity to the heuristic development of Mensa (eqn. 3-41). Equation 3-55 is also a formal derivation of the Slice Projection Theorem.

Image reconstructed is accomplished using an implementation of the inverse Radon Transform (among other formulations that are to be discussed in Section 4). The inverse transform is given by [88]

$$g(x,y) = \frac{1}{2\pi^2} \int_0^{2\pi} \int_{-\infty}^{\infty} \frac{1}{x\cos(\theta) + y\sin(\theta) - s} \frac{\partial}{\partial s} g(s,\theta) ds d\theta \tag{3-56}$$

in Cartesian coordinates and

$$g(r,\phi) = \frac{1}{2\pi^2} \int_0^{2\pi} \int_{-\infty}^{\infty} \frac{1}{r\cos(\theta - \phi) - s} \frac{\partial}{\partial s} g(s,\theta) ds d\theta \tag{3-57}$$

in polar. In [86] three methods of effecting the inverse Radon transform are described: 1) convolving the blur spot with the projections, followed by backprojection, 2) convolving a filter function with the projections, followed by backprojection and, 3) taking the forward transform of the projection (slice projection operation), scaling by a filter function, then inverse transforming followed by backprojection. Method 1 is the direct inverse transform, method 2 is termed convolution backprojection while method 3 is termed filtered backprojection. The implementation of the third option is well suited to this effort and is used herein. This is given in integral form as

$$Q_\theta(s) = \int_{-\infty}^{\infty} G(k,\theta) \left|\frac{k}{\pi}\right| e^{jks} dk \qquad \text{such that} \qquad g(r,\phi) = \int_0^{2\pi} Q_\theta(s) d\theta. \tag{3-58}$$

and in operator form with

$$g(x,y) = B\Im_1^{-1}\left[\left|\frac{k}{\pi}\right| \Im_1(g(s,\theta))\right] \tag{3-59}$$

where $\Im_1$ indicates the one dimensional Fourier Transform and B the backprojection operator.

Reflection tomography has been introduced from three different perspectives: electromagnetic scattering and a more first principles approach, a radar system engineering perspective, and one more which might be considered more representative of image processing. In the next Section we examine the waveform and spatial aperture and sampling and the impact to microwave imaging using tomographic principles.

Chapter 4

Tomographic Geometry, Waveform and Space-Frequency Trajectory

Section 3 gives the basic form for image reconstruction for our evaluation of aperture concepts, waveforms and trajectories in this section; invoking the weak scatterer approximation and thereby enabling the convolution model for projections. The concept of the sampling aperture and projection of the scene into the spatial frequency domain was also introduced without discussion of the rationale. In this section we consider more general tomographic geometries.

4.1 Tomographic Evaluation.

Section 3 introduced imaging using reflection tomography without discussing the imaging performance. Performance is defined in terms of both resolution and the sidelobe qualities of the point spread function associated with a collection geometry or waveform. We complete the development by establishing the reconstruction against an isotropic scatterer (reflection properties are invariant to illuminator or receiver angular position) before expanding the evaluation to encompass waveforms and more complex space-frequency trajectories.

4.1.1 ***First principles development.*** The reflection tomography formulation in Section 3.1 could be considered a pseudomonostatic geometry: we assumed an incident plane wave impinging on the object with the plane of the wave parallel to (coplanar with) the line of

the receiving antenna array. Referring to Figure 3.1 and again considering the antenna array at $-l_0$ we arrive with the back projection solution in two dimensions (Equation 3-23)

$$g(x,y,\lambda) = \frac{2k_0 j}{(2\pi)^2} e^{jk_v l_0} \int_0^{2\pi} \int_{-k_0}^{k_0} |k_u| \Psi_{scattered}(k_u, k_v - k_0) e^{j(k_u u + (k_v - k_0)v)} dk_u d\phi \qquad (4\text{-}1)$$

with $k_v = \sqrt{{k_0}^2 - {k_u}^2}$, $u = x\cos(\phi) + y\sin(\phi)$ and $v = -x\sin(\phi) + y\cos(\phi)$, and (u,v) the rotated Cartesian coordinates from Figure 3.4. $\Psi_{scattered}$ is the forward transformed projections wherein the transform is performed along the *u* axis in Figure 3.1, at each rotated measurement position, and collected over angle. We began with the assumption of single frequency illumination and the isotropic scatterer. We also treat the length of the receive array as a parameter. The phenomenology is generated by calculating the phase at each element of the array based on the distance of the scatterer to the element. Since only the relative phase is significant, the distance to the plane wave source is arbitrary. At each angular position (1 degree receive array rotation) the spatial frequency of each element is calculated (as a pair-wise bistatic combination). The expression from Bracken [57] is used

$$K = \frac{4\pi}{\lambda} \cos\left(\frac{\beta}{2}\right) \vec{B} \qquad (4\text{-}2)$$

where β is the bistatic angle at each antenna element and $\vec{B}$ is the bistatic bisector vector. Applying (4-2) to the simulated geometry produces the spatial spectrum across the sampling array at a single position (0^o). This is shown in Figure 4.1a. In this first panel, three array lengths (number of elements) are shown based on a 400 MHz CW frequency and half-wavelength spacing. The arc subtended indicates the spatial bandwidth.

Figure 4.1b is then the ensemble of spatial spectra with rotation over 360 degrees in 1 degree increments. Figure 4.1c is a zoomed image of Figure 4.1b showing fine structure. With only a single antenna and CW frequency a very thin ring is produced as described in Section 3.2. The use of the array of distributed elements generates a spectral width which

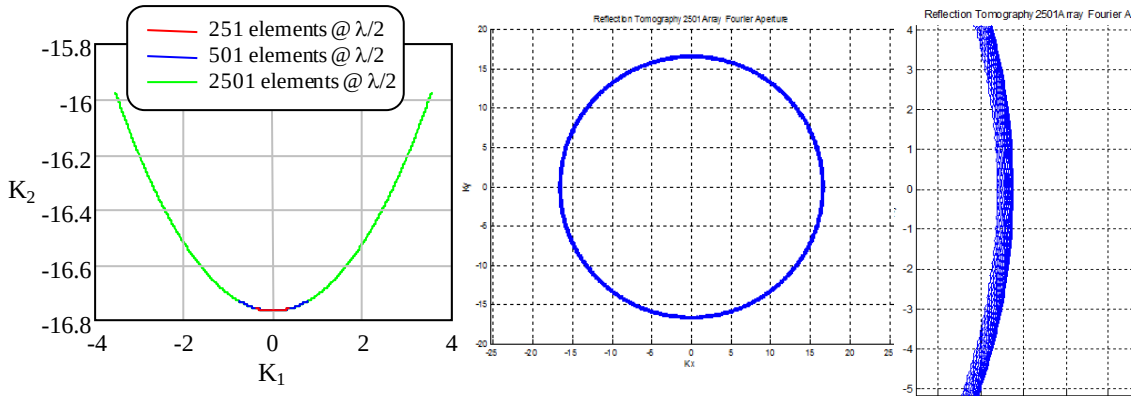

a) Sampled Spatial Spectrum Single Antenna Position

b) Spectrum of a) Over all Antenna Rotation Angles

c) Zoomed View of b)

Figure 4.1. Spatial Frequency Spectra in "Classical" Reflection Tomography

is proportional to the antenna length. With sufficiently dense sampling, an annulus is produced which, as will be shown, mimics temporal frequency. This equivalent bandwidth was calculated for a series of antenna lengths, shown in Table 4.1. 501 elements at half-lambda at 400 MHz equates to an antenna length of 187.5 m. The circular surface for the spatial frequency suggests the limitation of antenna length to realize greater bandwidth which is also evident in Table 4.1. As the antenna length goes to infinity bandwidth approaches a modest asymptote.

Antenna Length (# elements)	ΔK_2	Equivalent Bandwidth (MHz)
251	9E-04	< 0.25
501	0.037	0.88
1001	0.144	3.4
1501	0.313	7.5
2001	0.524	12.75
2501	0.792	19

Table 4.1. Bandwidth Derived from Radial Δk Based on Linear Array Antenna

Reconstruction was performed numerically (no analytic solution is known for this geometry). The CW plane wave reflecting of the point scatterer and sampled at each sensor/sampling along the ξ axis creates a phase response; which closely resembles the azimuth chirp associated with synthetic aperture radar (SAR). To illustrate, phase versus receive element number for three scatterer positions is depicted in Figure 4.2a with the spatial frequency spectrum for a single case shown in Figure 4.2b. The filtered back

propagation (back projection) result is shown in Figure 4.3 as a contour plot for a scatterer at (0.25, 0.25).

Resolution and sidelobe structure can be visualized in Figure 4.4 which presents principal axis cuts for a scatterer located at (1, 0). The receiving array was modeled as offset 100 m from the point scatterer, as was for the previous cases. Two cases are shown: 251 element antenna and one 10 times longer (both listed in Table 4.1). Overlaid on both plots is the exact response for the2D geometry with a point scatterer at origin (response shifted to overlay the numerical simulation), single antenna element, and CW waveform (the only known case where an exact solution is available - Section 4.1.2). Identifying the value of bandwidth is one of the goals of this thesis section.

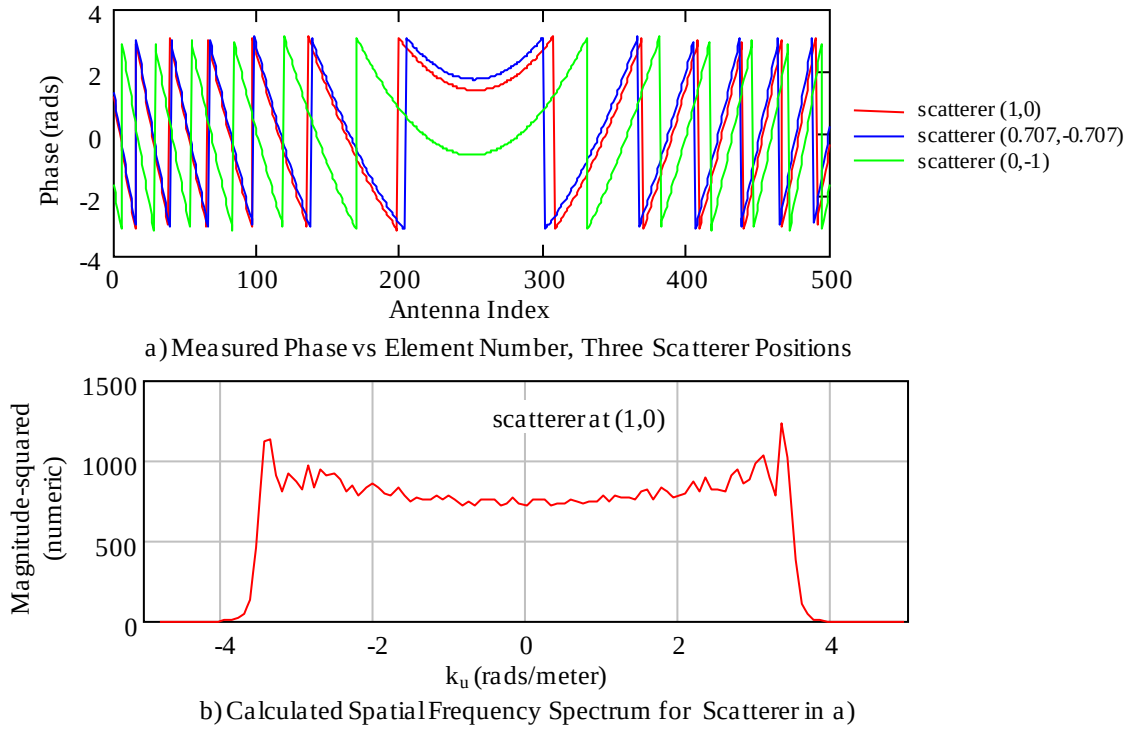

Figure 4.2. Simulated Phenomenology for Isotropic Scatterer

The modest spectral filling from this implementation of tomography and the impracticality of realizing antennas of the sizes suggested, particularly in non clinical or laboratory environment, indicate the limited utility of this implementation. Note the 1501 element array subtended 40 degrees with respect to the target.

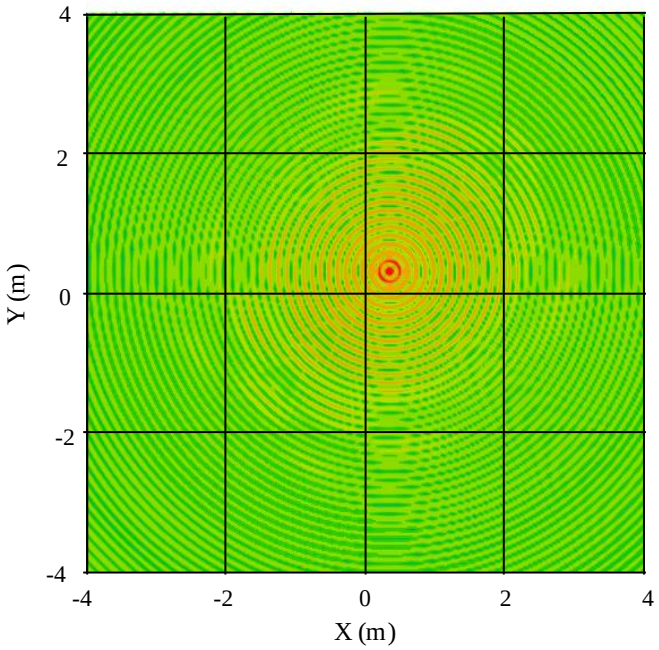

Figure 4.3. Filtered Backpropagation Point Spread Function

4.1.2 ***Single antenna monostatic geometry***. In Section 3.2 the heuristic development of Mensa represents a degenerate case from Section 4.1.1. Using only the center antenna

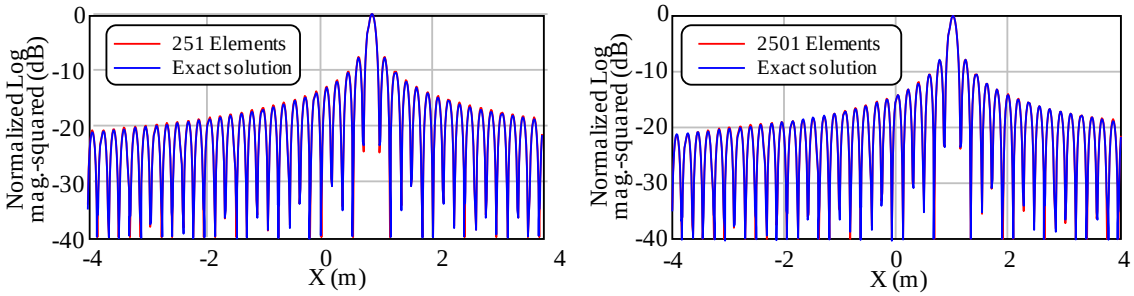

Figure 4.4. Point Spread Comparison for Two Antenna Lengths against Closed Form

element yields the same geometry as described therein. With the plane wave approximation we have the expression for reconstruction given in (3-44). With the use of an isotropic scatterer and CW frequency then (3-44) becomes

$$g(r,\phi) = \int_0^{2\pi}\int_{-\infty}^{\infty} \delta\left(\rho - \frac{2}{\lambda}\right)|\rho| e^{j2\pi\rho\cos(\phi-\theta)} d\rho d\theta. \tag{4-3}$$

Making use of an integral sifting property of the delta function gives

$$g(r,\phi) = |\rho| \int_0^{2\pi} e^{j2\pi\rho\cos(\phi-\theta)} d\theta \tag{4-4}$$

The Bessel function of the first kind integral identity[1] is

$$J_n(z) = \frac{1}{2\pi j^n} \int_0^{2\pi} e^{jz\cos(\theta)} e^{jn\theta} d\theta. \tag{4-5}$$

Setting n=0 and making the change of variable $\kappa = \phi - \theta$ and noting that the effect on the definite integral limits of a simple rotation caused by the change of variable along the closed path of the start and stop points making no difference gives

$$g(r) = \frac{4\pi}{\lambda} J_0\left(\frac{4\pi r}{\lambda}\right) \tag{4-6}$$

which is the analytical solution referred to in the previous section. Equation 4.6 is evaluated for a 400 MHz CW signal with results displayed in Figure 4.5. magnitude-squared and normalized to unity peak response with a point scatterer located at (1,1). The first Figure, 4.5a, is the response surface, with the plot z axis limited to -30 dB.

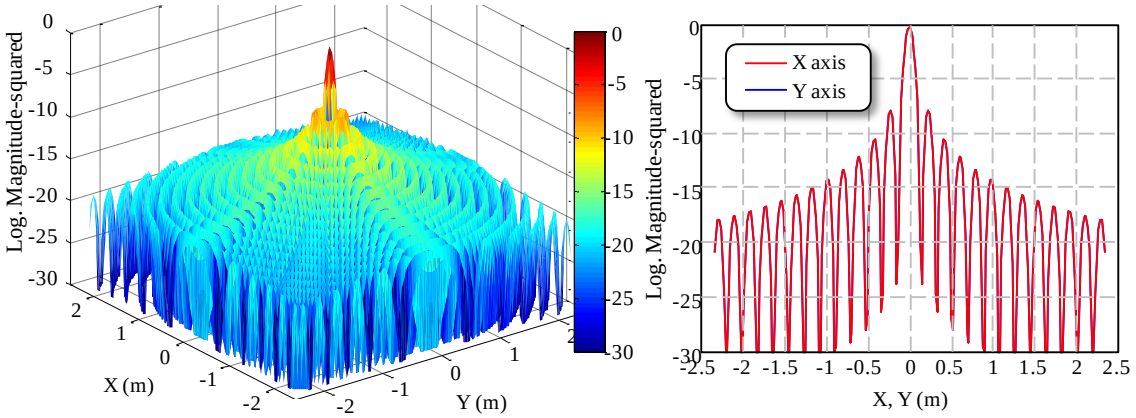

a) Response Surface b) Cardinal Axis Response

Figure 4.5. Monostatic Point Spread Function – 400 MHz CW Signal

The second Figure (4.5b) represents cuts along the cardinal axes of the scene coordinate frame, showing both X and Y axis results. There are several interesting attributes of the PSF. The first is the modest (peak) sidelobe level only 7.9 dB down, relative to the peak response, with a roll off at 3 dB per doubling of distance; basically a 1/r dependence. Secondly the spatial extent of the sidelobe structure is indefinite, which has implications when the imaged scene has a high dynamic range of reflectivity and the realizable

[1] http://mathworld.wolfram.com/BesselFunctionoftheFirstKind.html

contrast. Said otherwise, a single large scatterer could, through the sidelobe response, degrade the entire image.

As waveform bandwidth is increased due to modulating an RF carrier, the two dimensional frequency spectrum fills. At each sampling angular position (k_θ) a radial segment samples the scene. The segment length matches the waveform bandwidth. The Bracken derivation [57] applied to monostatic sampling collapses to a radial wavenumber $k_r=4\pi/\lambda$. If k_{lower} and k_{upper} define the wave numbers corresponding to the 3dB temporal frequency spectral bandwidth of the waveform, and the radar orbits around the object, then an annulus-like two-dimensional spectrum is created. An example appears in Figure 4.6. This representation is commonly applied to Synthetic Aperture Radar as well e.g., [89]

Modeling the sampled spectrum as an annulus for a 2D geometry allows the derivation of the dependency of the point spread function on temporal bandwidth using straightforward Fourier techniques (temporal bandwidth realized far more conveniently than spatial bandwidth as the noted in the previous section). Define the bandwidth (Δk) about some center frequency (k): Δk is the difference in the inner and outer radii and defines an annulus when observations are conducted over 2π radians relative to object coordinates. This is depicted in Figure 4.6. Let the annulus magnitude be such that the spectrum is one within the annulus and zero everywhere else in rectangular frequency domain coordinates. With phase equal to 0 this represents a target at the scene origin. Two cases are examined, both for 400 MHz center frequency (k=16.766, λ=0.75) with Δk=0.5 (Figure 4.7a) and Δk=2.0 (Figure 4.7b).

The inverse 2D DFT is computed, without explicit consideration of sample quantization in the frequency domain, finely sampled (Δk_x, Δk_y = 0.078, 512 samples along each axis) with a frequency range from -20 to 20. Single axis cuts of the point spread function are

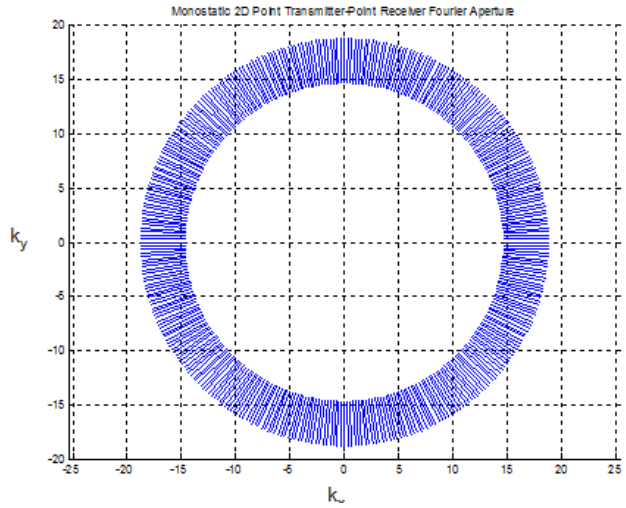

Figure 4.6. Spatial Spectrum Monostatic Sampling Illustrating Waveform Bandwidth

given in Figure 4.8 (Y=0 axis) over the spatial range -4 to 4 meters with a sample spacing of approximately $\lambda/40$. Overlain on both plots for comparison is the analytic PSF for the 2D CW (normalized). At 400 MHz Δk=0.5 is approximately equivalent to 12 MHz of

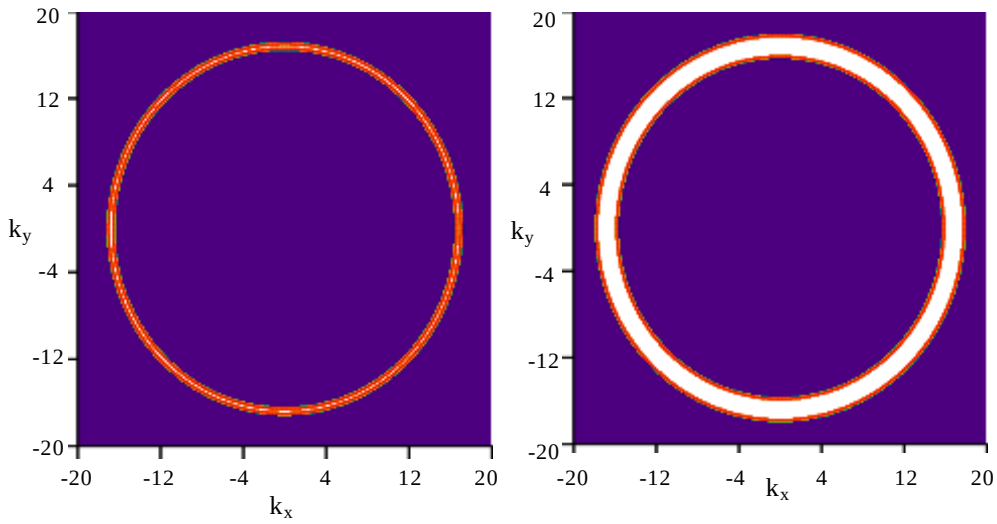

a) Δk = 0.5 b) Δk = 2.0

Figure 4.7. Windowed Annular Spatial Spectra

bandwidth, Δk=2.0 corresponds to 47.8 MHz.

The effects of the temporal bandwidth are immediately obvious. The sidelobe structure of the wider bandwidth response exhibits a sharper roll-off. The addition of bandwidth will improve the contrast of the reconstructed by reducing the effect that large scatterers can influence nearby pixels, while retaining the resolution possible from tomographic processing. 12 MHz corresponds to ~12.5 m resolution and Figure 4.7a shows only the

slightest effect over 8 the meter range plotted. The second case (Figure 4.7b) corresponds to a range resolution of 3.2 m.

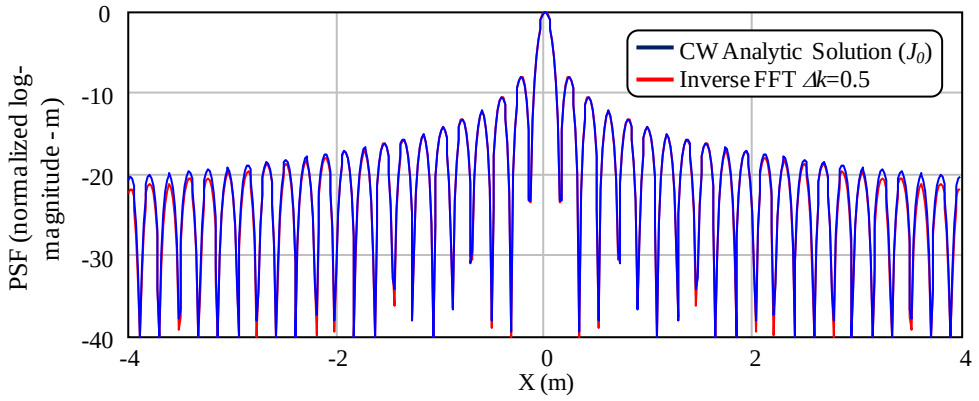

a) PSF for Low Spatial Bandwidth Compared to Single Frequency Result

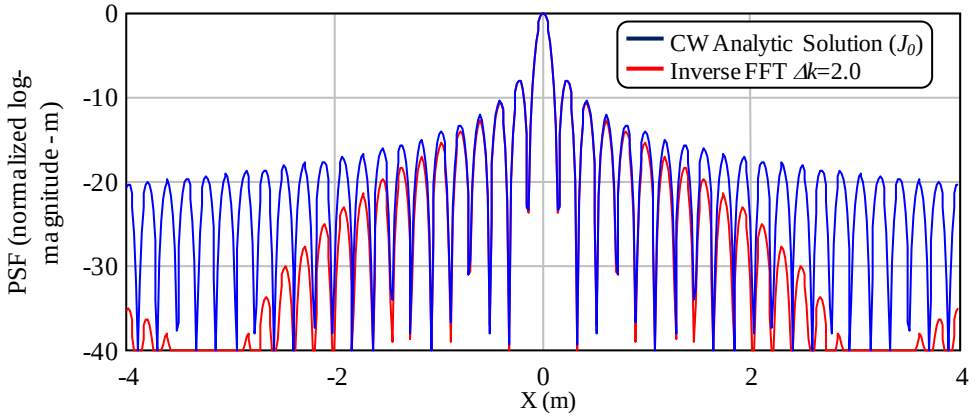

b) PSF for Higher Spatial Bandwidth Compared to Single Frequency Result

Figure 4.8. Fourier Reconstructed Examples from Figure 4.7

4.2 Two Dimensional Apertures.

We now extend to propagation across the object or scene which cannot be modeled as a plane wave, the more general case. We address the monostatic geometry before extending to the bistatic case. We model the antenna effectively as a point object which radiates a two dimensional circular wavefront, as depicted in Figure 4.9. This wavefront defines the locus of points of constant delay, the isorange contour, along which integration occurs at the receiving antenna.

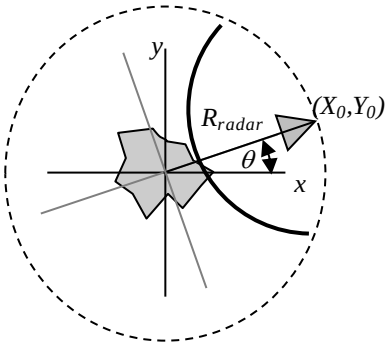

Figure 4.9. Two-Dimensional Monostatic Geometry

We begin with a generalization of the filtered back projection algorithm for reconstruction. Equation 3-58 is expressed in terms of the general Radon Transform operator *t*, line integral formalism.

$$g(r,\phi) = \int_0^{2\pi} \int_{-\infty}^{\infty} G(k,\theta) \left| \frac{k}{\pi} \right| e^{j2kt} dk d\theta. \tag{4-7}$$

4.2.1 ***Monostatic geometry***. A circular wavefront is shown in Figure 4.9 propagating outwards from a radar at (X_0, Y_0) that is executing a circular orbit around the object/scene at constant radius (R_{radar}), scattering and propagating back to the radar as a circular wavefront from each scatterer. The path of the line integral described by the transmitted wavefront, that is the locus of points of constant one-way delay, is

$$t = \sqrt{(x - X_0)^2 + (y - Y_0)^2}. \tag{4-8}$$

Defining the scatterer and radar positions in the object-centered polar coordinates, as in Figure 3.6, make the following change of variables

$$\begin{bmatrix} x \\ y \end{bmatrix} = \begin{bmatrix} r\cos(\phi) \\ r\sin(\phi) \end{bmatrix} \qquad \text{and} \qquad \begin{bmatrix} X_0 \\ Y_0 \end{bmatrix} = \begin{bmatrix} R_{radar}\cos(\theta) \\ R_{radar}\sin(\theta \end{bmatrix} \tag{4-9}$$

which gives

$$t = \sqrt{(r\cos(\phi) - R_{radar}\cos(\theta))^2 + (r\sin(\phi) - R_{radar}\sin(\theta))^2}. \tag{4-10}$$

Completing the squares, grouping terms and making use of the trigonometric sum and difference identities gives

$$t = \sqrt{r^2 + {R_{radar}}^2 - 2rR_{radar}\cos(\theta - \phi)}. \tag{4-11}$$

This is substituted into (4-7) and results in the 2D monostatic backprojection filtered expression, with a factor of 2 in the exponential term to account for two-way propagation.

This approach was suggested in [52], the earliest citation found, in which a static series of acoustic transducers (circular transducer array) surrounded the object to be imaged using a reflection-based technique. The object was in the near field, motivating the use of the circular wavefront. Instead of translating a single sensor, the sensors are operated

individually with the active unit switched sequentially around the array. This method is indistinguishable from a sequentially positioned transducer or antenna. It should be noted that we assume no effects due to platform motion occur during transmission or reception. The platform executes a move-stop-move motion pattern; stopping for transmission and reception, then moving to the next sampling position. This is addressed in greater detail in Section 5.

4.2.2 ***Bistatic geometry***. The two-dimensional bistatic aperture is a direct extension of the 2D circular wavefront, monostatic case. We show two platforms in uniform circular motion around a common origin; each at an arbitrary speed and radius, as shown in Figure 4.10. With no loss of generality, either platform may be stationary. The Figure indicates the incident and scattered wavefront, as well as the red contour indicating the bistatic range sum; the locus of points of constant bistatic delay (bistatic isorange contour). Analogous to the monostatic case, this is the physical form of the integration path for bistatic projections (sometimes referred to the as the bistatic Radon Transform [90]). The contours of integration are elliptical.

The propagation path is composed of two terms, emitter-to-scatterer and scatterer-to-receiver. Thus for the 2D geometry, to an arbitrary point (x, y) in the region to be imaged, the integration path is the sum of the two, or

$$t = t_{xmtr} + t_{rcvr} = \sqrt{(x - x_{xmtr})^2 + (y - y_{xmtr})^2} + \sqrt{(x - x_{rcvr})^2 + (y - y_{rcvr})^2}. \qquad (4\text{-}12)$$

Making the same polar substitutions as the monostatic case (expanded with the receiver term) and generally expressing the transmitter position and receiver position as arbitrary states results in

$$t = \sqrt{r^2 + R_{xmtr}{}^2 - 2rR_{xmtr}\cos(\phi - \theta_{xmtr})} + \sqrt{r^2 + R_{rcvr}{}^2 - 2rR_{rcvr}\cos(\phi - \theta_{rcvr})} \qquad (4\text{-}13)$$

where r and ϕ are again as defined in Figure 3.6. There is no platform velocity dependence in (4-13), the platforms may be at arbitrary radii and angular rates. The

instantaneous bistatic half-angle is shown in Figure 4.10. An earlier work by Mensa [17] which addressed a bistatic collection geometry in which the sensors (transmit and receive) operated synchronously (constant, fixed angle rates that yielded a constant bistatic angle). This permitted the use of the filtered backprojection derivation based on the position of the receiver and one-half the bistatic bisector angle.

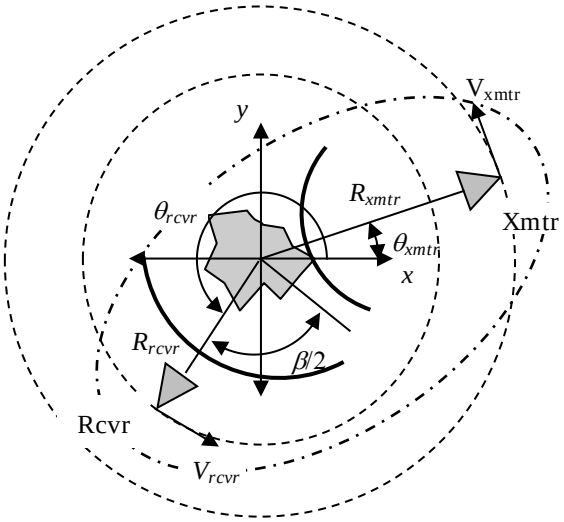

Figure 4.10. Two-Dimensional Bistatic Geometry

Extension to multistatic geometries offers a several alternatives. A single transmitter serving a multiplicity of receivers (1 transmit, *M* receive) each receiver in a unique trajectory (or the reciprocal). Alternatively, all transmit and all receive, again using orthogonal waveforms, and including each platform also functioning monostatically (this would be a moving platform analog to the stationary elements in Lo Monte, et al [59]). Image reconstruction from such a collection aperture could coherently combine images reconstituted from each unique monostatic or bistatic pair [17], [91], or form a single data matrix from which a single image is formed, as in [59], using matrix operations.

There are two geometry classes for two-dimensional bistatic apertures: those with a constant bistatic angle over the aperture and those which where this is not the controlling variable (β is a function of time/space); this latter including one platform stationary.

The first class (constant bistatic angle) requires that the angle rates of the two platforms are identical. The reconstruction derivation is an extension of that for the two dimensional monostatic geometry. Starting with equation 4-12 with the separate transmitter and

receiver positions, then defining the transmitter and receiver angles relative to the bistatic angle and the rotation angle of the bisector vector, let

$$\begin{bmatrix} x \\ y \end{bmatrix} = \begin{bmatrix} r\cos(\phi) \\ r\sin(\phi) \end{bmatrix}, \begin{bmatrix} x_{xmtr} \\ y_{xmtr} \end{bmatrix} = \begin{bmatrix} R_{radar}\cos(\theta - \beta/2) \\ R_{radar}\sin(\theta - \beta/2) \end{bmatrix} \text{ and } \begin{bmatrix} x_{rcvr} \\ y_{rcvr} \end{bmatrix} = \begin{bmatrix} R_{radar}\cos(\theta + \beta/2) \\ R_{radar}\sin(\theta + \beta/2) \end{bmatrix} \quad (4\text{-}14)$$

Inserting (4-14) into (4-12) and expanding the squares and defining θ as the rotation of the bisector with respect to the x axis

$$t = \sqrt{r^2 + {R_{xmtr}}^2 - 2rR_{xmtr}\cos(\phi - (\theta + \beta/2))} + \sqrt{r^2 + {R_{rcvr}}^2 - 2rR_{rcvr}\cos(\phi - (\theta - \beta/2))} \quad (4\text{-}15)$$

Now the angles are forced to a common angle reference/rate. For the bisector to be invariant the trajectory radius for both transmitter and receiver must be the same. In this manner (4-15) reduces to

$$t = \sqrt{r^2 + R^2 - 2rR\cos(\phi - (\theta + \beta/2))} + \sqrt{r^2 + R^2 - 2rR\cos(\phi - (\theta - \beta/2))}. \quad (4\text{-}16)$$

Now substituting (4-16) into (4-7) we can see that the inclusion of the $\beta/2$ dependency exerts an influence on the resolution. This is shown in Figure 4.11 which compares the

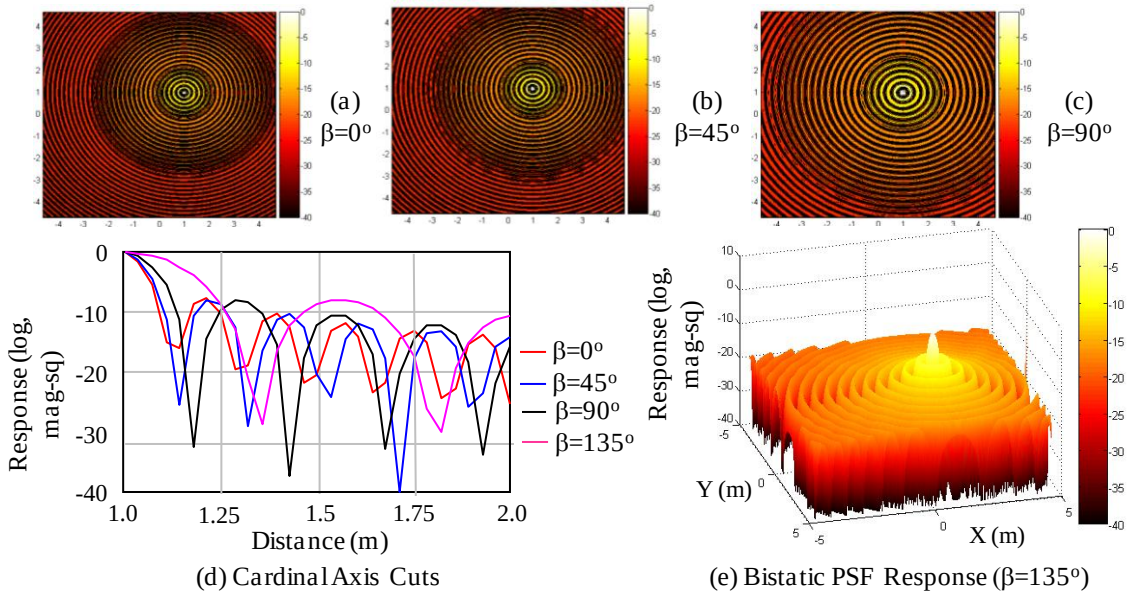

(d) Cardinal Axis Cuts (e) Bistatic PSF Response (β=135°)

Figure 4.11. Resolution Dependency on Bistatic Angle

monostatic PSF, for a CW waveform at 400 MHz, to two bistatic geometries distinguished by the bistatic angle; β=45 and 90 degrees, for the case of a point scatterer at (1, 1). Tracking the dilution of resolution is the entire response surface. The peak sidelobe level is unchanged, only the spatial response is diluted with increasing bistatic

angle. Note that in the bistatic case, the factor of two in the exponent in (4-7) is dropped as t contains full propagation dependency. Figure 4.12 summarizes resolution versus bistatic angle. The red curve represents the one-sided resolution estimated from simulation runs (half-width, half-maximum, HWHM). The blue curve is the monostatic response normalized by the cosine of the half bistatic angle.

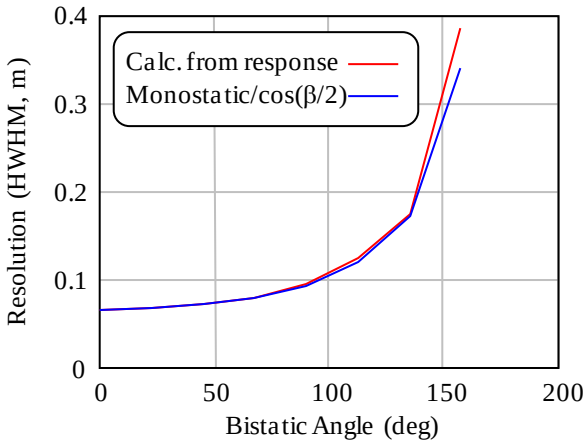

Figure 4.12. 2D Resolution vs. Bistatic Angle, Constant β

For the second class, more general bistatic geometry we begin with the special case of one platform stationary. As will be seen in Section 4.6 the motion dependency is reciprocal: the same result is obtained independently of which platform is motionless. With either the transmitter or receiver stationary, the corresponding angle (θ) becomes fixed. Let us assume a stationary transmitter and without loss of generality, let the transmitter angle be 0. Then (4-13) simplifies to

$$t = K_{xmtr} + \sqrt{r^2 + {R_{rcvr}}^2 - 2rR_{rcvr}\cos(\phi - \theta_{rcvr})} \tag{4-17}$$

where K_{xmtr} is a pixel specific constant (unvarying over the aperture). Inserting into equation (4-7), the constant term comes out of the integral and can be ignored as a simple scalar. Figure 4.13 compares the monostatic to stationary transmitter bistatic for a scatterer at the scene origin. As both axes produce identical results, only a single axis is shown. The resolution is observed to be diluted by a factor of 2 relative to monostatic. As previously done, the CW frequency is 400 MHz. The monostatic HWHM is ~0.09λ while the bistatic is ~0.18 λ.

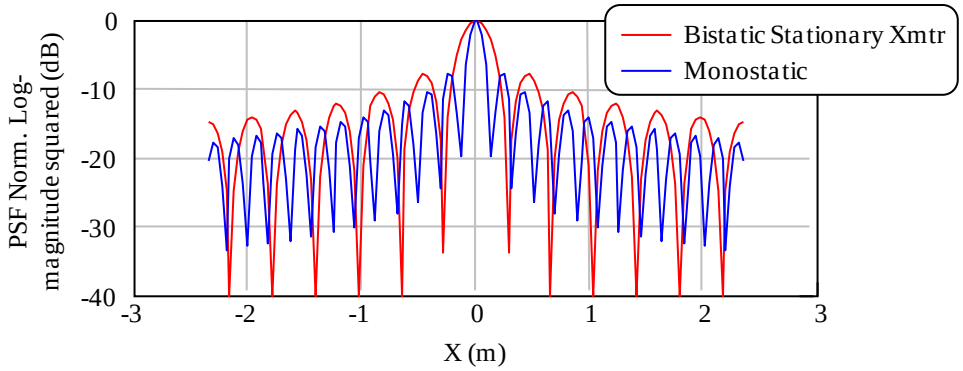

Figure 4.13. Comparison of Monostatic to Bistatic PSF for Stationary Transmitter

The more general case within the second class, and that which complicates the bistatic analysis because of the number of options, is when the transmitter and receiver trajectories are not constrained, taking on arbitrary geometries. For example the platform angle rates relative to the scene are decoupled. For this geometry we express t by parameterizing the transmitter angle as a function of the receiver polar angle. This is

$$t = \sqrt{r^2 + R_{xmtr}{}^2 - 2rR_{xmtr}\cos(\phi - f(\theta_{rcvrr}))} + \sqrt{r^2 + R_{rcvr}{}^2 - 2rR_{rcvr}\cos(\phi - \theta_{rcvr})} \quad (4\text{-}18)$$

Two such cases are presented for illustration. In the first example, shown in Figure 4.14, the transmitter angle rate is 2 times that of the receiver with both moving over circular trajectories with the same radius. The aperture duration is such that the receiver completes 2π radians of motion while the bisector sweeps out 3π, starting from an initial bistatic angle of 45 deg. As earlier the wavelength used for the unmodulated carrier is 0.705 m (400 MHz).

The second example is configured such that the bisector sweeps out the full 2π radians of the two dimensional collection aperture. The PSF response is shown as a surface in Figure 4.14a and as a surface projection (contour) in Figure 4.14b. The normalized response is clipped at -40 dB to highlight image features. We observe that the resolution is largely unchanged and the circular sidelobe symmetry has decomposed with a finer sidelobe structure resulting. Additionally the and the peak sidelobe levels are slightly degraded, relative to a constant β geometry. This case is compared to a second example,

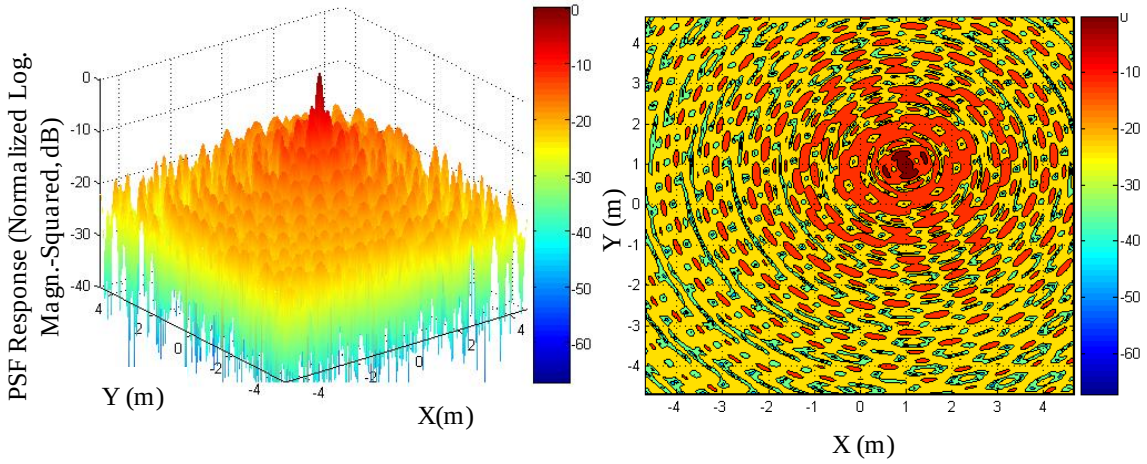

(a) Response Surface (b) Response Contour

Figure 4.14. 2D Bistatic Example, Transmitter Angle Rate Twice Receiver Angle Rate

Figure 4.15, where the bistatic bisector only traverses 2π radians of angle, and to one of the earlier constant β examples, in Table 4.2. In this Table image metrics are summarized, including an estimate of the integrated sidelobe ratio (ISLR).

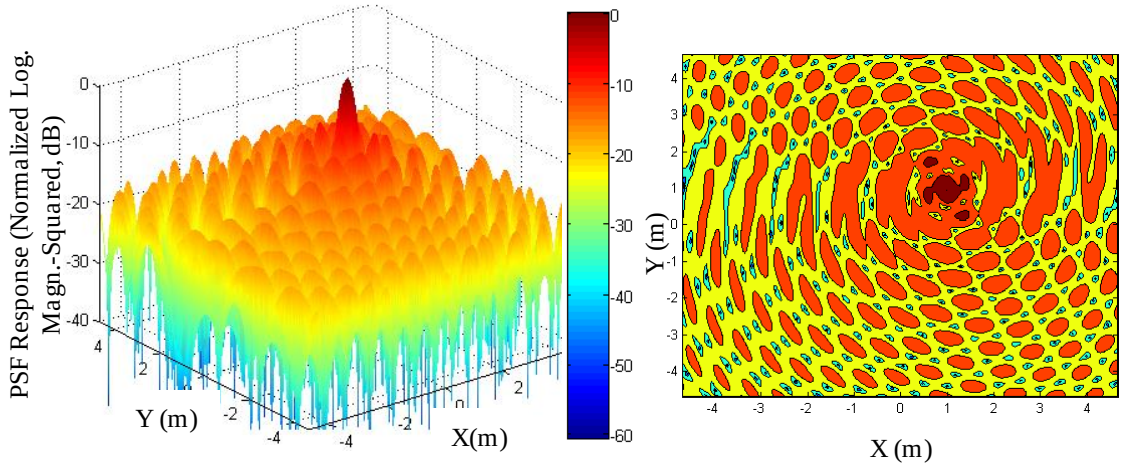

(a) Response Surface (b) Response Contour

Figure 4.15. 2D Bistatic Example - Bisector Sweeps 2π radians

In the cases examined up to this point there was always a net angle rate associated with the bistatic bisector vector as the platforms propagate over the tomographic aperture. Platforms in motion moved in the same direction. The third example of decoupled motions appears in Figure 4.16. In this case, the transmit and receive platforms have equal and opposite motions and consequently the bisector vector is fixed over the aperture ($d\beta/dt$=0). The PSF exhibits the expected resolution only along a single axis. None of the

Aperture	Resolution (m)		ISLR (dB)	Peak SLL (dB)	Average SLL (dB)
	X	Y			
Synchronous β=45°	0.14	0.14	-15.0	-7.8	-21.2
Xmtr 1.33X Rcvr (2π)	0.22	0.43	-9.25	-8.4	-19.1
Xmtr 2X Rcvr (β=3π)	0.168	0.17	-12	-6.9	-21.4

Table 4.2. Image Metrics Comparison for Example Decoupled Bistatic Apertures

trajectories or apertures examined here exhibit any spatial dispersion, i.e., there is no change in the radius of motion of either transmit or receive platforms (range sum is constant). This will not be the case as we expand to three dimensional apertures.

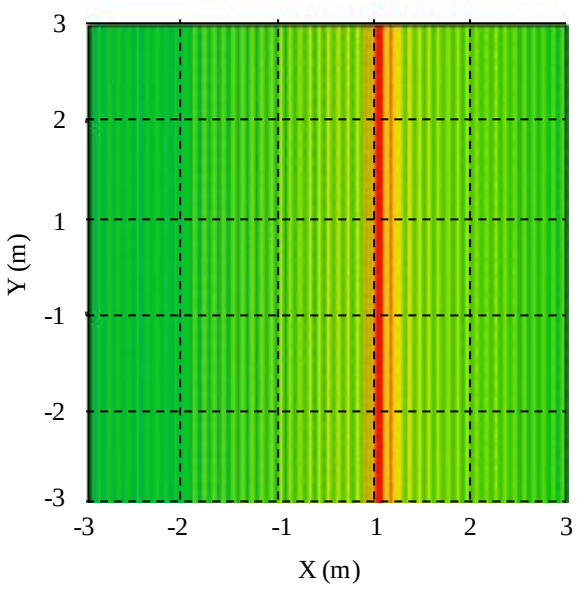

Figure 4.16. IPR When Transmitter and Receiver Motions are Equal and Opposite

4.3 Three Dimensional Apertures.

The extension to three dimensions closely follows that of two dimensions. We begin with monostatic collection apertures, followed by the bistatic case.

4.3.1 Monostatic geometry. We expand the two dimensional monostatic geometry to three dimensions, as depicted in Figure 4.17, by redefining the angle variables used in the two dimensional case in Section 4.2. The initial method is an extension of the two dimensional case following the approach in [92]. The back projection filtering extension

to three dimensions, again based on plane wave propagation, begins with the inverse Fourier transform of the forward transformed, sampled projections comprising the object response. Starting from (4-12), extended to three Cartesian dimensions with coordinates defined in Figure 4.17 we have

$$g(x,y,z)=\int_{-\infty}^{\infty}\int_{-\infty}^{\infty}\int_{-\infty}^{\infty}G(\rho,\phi,\theta)e^{j2\pi(xf_x+yf_y+zf_z)}df_x df_y df_z. \tag{4-19}$$

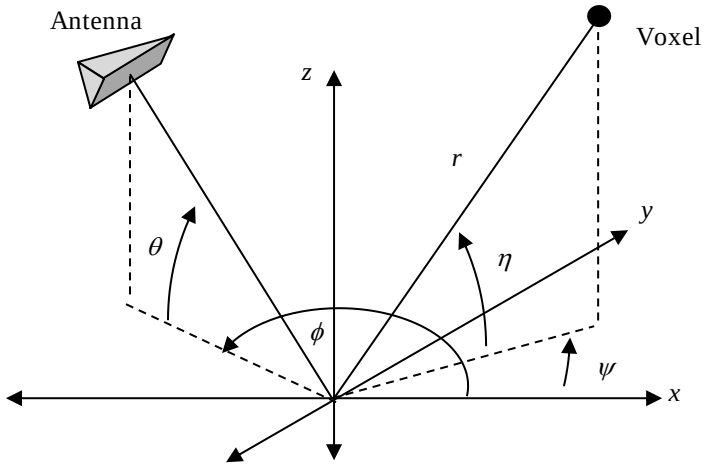

Figure 4.17. Definition of Tomographic, Three-Dimensional Monostatic Geometry

Let $f_x = 2\cos(\phi)\cos(\theta)/\lambda$, $f_y = 2\sin(\phi)\cos(\theta)/\lambda$ and $f_z = 2\sin(\theta)/\lambda$ and $r=\sqrt{x^2+x^2+z^2}$, η = arctan(*z, r'*), $r'=\sqrt{x^2+y^2}$) and ψ = arctan(*y, x*). Note from Figure 4.17 that θ is measured in increasing positive sense relative to the *x-y* plane toward the positive *z* axis, not relative to the *z* axis. Also *arctan* is the principal value function. Making the substitution and evaluating the Jacobian for the change of variable yields

$$g(r,\psi,\eta)=\int_0^{2\pi}\int_0^{\frac{\pi}{2}}\int_{-\infty}^{\infty}\cos(\theta)\rho^2 G(\rho,\phi,\theta)e^{j\pi\rho r\kappa}d\rho d\theta d\phi \tag{4-20}$$

where κ = $\cos(\theta)\cos(\eta)\cos(\psi-\phi)+\sin(\eta)\sin(\theta)$ and $\rho = 2/\lambda$. Again, using the generally defined backprojection operator $Q_\phi(t)$, eqn. 4-7, we start with

$$Q_\phi(t)=\int_{-\infty}^{\infty}G(\rho,\phi,\theta)\rho^2 e^{jkt}d\rho \quad \text{such that} \quad g(r,\psi,\eta)=\int_0^{2\pi}\int_0^{\frac{\pi}{2}}\cos(\theta)Q_{\phi,\theta}(t)d\theta d\phi \tag{4-21}$$

where $t = r(\cos(\theta)\cos(\eta)\cos(\phi-\psi)+\sin(\eta)\sin(\theta))$.

Extending to non-plane wave propagation, consider the geometry in Figure 4.18. A spherical wavefront propagating outwards from a monostatic radar at (x_0, y_0, z_0) that follows a trajectory around the object/scene at constant radius (R_{radar}), scattering and propagating back to the radar as a spherical wavefront. The path of the line integral described by the transmitted wavefront, that is the locus of points of constant one-way delay, is

$$t = \sqrt{(x - x_0)^2 + (y - y_0)^2 + (z - z_0)^2} \tag{4-22}$$

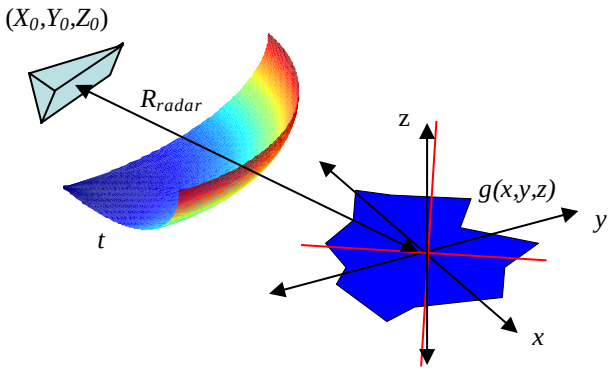

Figure 4.18. Tomographic Monostatic Geometry – Spherical Wavefront

Defining the scatterer and radar positions in the object-centered polar coordinates with

$$(x, y, z) = \begin{pmatrix} r\cos(\psi)\cos(\eta) \\ r\sin(\psi)\cos(\eta) \\ r\sin(\eta) \end{pmatrix} \qquad \text{and} \qquad (x_0, y_0, z_0) = \begin{pmatrix} R_{radar}\cos(\phi)\cos(\theta) \\ R_{radar}\sin(\phi)\cos(\theta) \\ R_{radar}\sin(\theta) \end{pmatrix}$$

and expanding the squares, invoking the trigonometry difference angle identity, and substituting into (4-22) gives

$$t = \sqrt{r^2 + {R_{radar}}^2 - 2rR_{radar}(\cos(\theta)\cos(\eta)\cos(\phi - \psi) + \sin(\eta)\sin(\theta))} \tag{4-23}$$

This is substituted into (4-20) and results in the exact expression for 3D monostatic backprojection.

4.3.2 Bistatic geometry. And finally, the extension of the two dimensional bistatic geometry to three dimensional is straightforward and follows two dimensional development. As in Section 4.2, the propagation path is composed of two terms, emitter-

to-scatterer and scatterer-to-receiver. The geometry is shown in Figure 4.19. Thus for a 3D geometry the individual range terms are combined as $t=t_{xmtr}+t_{rcvr}$, or

$$t=\frac{\sqrt{(x-x_{xmtr})^2+(y-y_{xmtr})^2+(z-z_{xmtr})^2}}{\sqrt{(x-x_{rcvr})^2+(y-y_{rcvr})^2+(z-z_{rcvr})^2}}+. \tag{4-24}$$

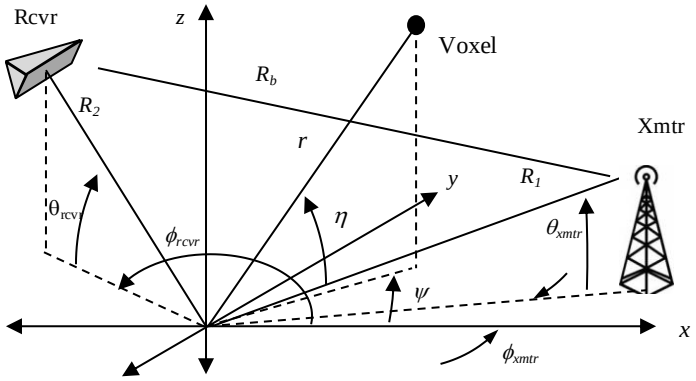

Figure 4.19. Three Dimensional Bistatic Geometry Definition

Making the same polar substitutions as the monostatic case (expanded with the receiver term) and maintaining arbitrary position versus time along the tomographic aperture (e.g., removing/avoiding the coupling enforced through a constant bistatic angle which supports dissimilar angle rates as well as orbital radii) results in

$$t=\sqrt{r^2+R_{xmtr}{}^2-2rR_{xmtr}\kappa_{xmtr}}+\sqrt{r^2+R_{rcvr}{}^2-2rR_{rcvr}\kappa_{rcvr})} \tag{4-25}$$

with, analogous to (4-23), $\kappa_{xmtr}=\cos(\theta_{xmtr})\cos(\eta)\cos(\psi-\phi_{xmtr})+\sin(\eta)\sin(\theta_{xmtr})$, and for κ_{rcvr} with θ_{xmtr} and ϕ_{xmtr} being replaced by the equivalent receiver angles. Finally, insertion of (4-25) into (4-21) yields the expression for bistatic, three dimensional reconstruction.

4.4 Tomographic Imaging Dependence on Waveform.

Tomographic performance was briefly addressed in Section 4.1 as part of the motivation for studying tomographic apertures. This was accompanied with a cursory assessment of the value of bandwidth in tomographic imaging. Using Fourier techniques we demonstrated that as the spatial frequency spectrum became fuller, for a given operating

frequency, the Point Spread Function (PSF) was improved through the reduction/suppression of the response sidelobes. This was realized without affecting the resolution (this is in marked contrast to Synthetic Aperture Radar where along-range resolution is a function of waveform bandwidth). We assumed a rectangular spectrum in the frequency domain and numerical Fourier techniques to illustrate the behavior. In this section we expand on the impulse response performance using commonly applied radar waveforms with tomographic reconstruction.

For the determination of the PSF, and associated properties, of the aperture-waveform combination an idealized, isotropic scatterer is utilized; represented as a Dirac delta function. This scatterer reflectivity is spatially invariant, and is manifested only through the phase response as a function of frequency with radar cross section constant over angle. This permits development of the PSF, also called the impulse response, for a specific geometric aperture/waveform without consideration of the complex scattering from real objects or shapes. This gives, as will be shown, the imaging performance upper bound (together with error-free position knowledge for reconstruction). The single scatterer enables the assessment of imaging performance in terms of conventional image metrics (resolution, peak, and average sidelobe levels).

An analytic representation of the forward transformed projection $G(k,\theta)$ is necessary for the calculation of the PSF. It is generally given by

$$G(k,\theta) = \int_{-\infty}^{\infty} \left(g(r,\theta) \otimes S(r-r') \right) e^{-jkr} dr \tag{4-26}$$

where $\otimes$ indicates convolution, S the waveform (temporal dependence expressed as range), and $k=2\pi/\lambda$. Because the forward transform of a convolution is equivalent to the product of the forward transform of the constituent terms, (4-26) can also be written

$$G(k,\theta) = S_{waveform}(k) S_{\theta}(k) \tag{4-27}$$

where $S_{waveform}$ is the wavenumber spectrum of the waveform and S_θ the spatial frequency spectrum of the object projection at angle θ.

Instead of a continuum of scatterers, let the object be represented by a Dirac delta function at range r_0. The second term in (4-27) is then given by

$$S_\theta(k) = \int_{-\infty}^{\infty} \delta(r - r_0) e^{-ikr} dr. \tag{4-28}$$

The filtering function (sifting property) of the integral of the Dirac delta makes evaluation of (4-28) very direct, or

$$S_\theta(k) = e^{-ikr_0}. \tag{4-29}$$

We next evaluate a limited set of waveforms, each commonly employed. These are continuous wave (CW), simple envelope modulated carrier (i.e., pulsed) waveform, and pulsed linear frequency modulated (LFM). Table 4.3 presents the waveforms evaluated and relevant attributes. The expressions in Table 4.2 include the RF carrier, and also assumes complex sampling for the frequency domain representation.

An arbitrary amplitude of A is shown (set at 1 for evaluation), while T represents pulse length, α is the LFM chirp (frequency) rate, ω_0 the carrier and B the bandwidth.

Waveform	Time Domain	Spatial Frequency Domain
Continuous Wave	$A\cos(\omega t + \vartheta)$ or $\mathrm{Re}\left(e^{j(\omega t+\vartheta)}\right)$	$\delta(k - k_0)$
Pulsed (envelope only)	$rect(\frac{t}{T})A\cos(\omega_0 t + \vartheta)$ $rect = \begin{cases} 1; \lvert t\rvert < T/2 \\ 0; otherwise \end{cases}$	$\frac{\sin\left(\frac{k-k_0}{2} R_{pulse}\right)}{\frac{k-k_0}{2} R_{pulse}}$ $k_0 = \frac{2\pi f_0}{c}$
Pulsed LFM	$rect(\frac{t}{T})\,\mathrm{Re}\left(Ae^{j(\omega_0 t + \alpha\vartheta^2)}\right)$ $rect = \begin{cases} 1; \lvert t\rvert < T/2 \\ 0; otherwise \end{cases}$	$\frac{1}{\sqrt{2B}} e^{-\left(j\pi\frac{f^2}{\alpha}\right)} (Z(x_1) - Z(x_2))$ $Z(x) = \int_0^x e^{j\pi\gamma^2} d\gamma$ $x_{1,2} = -2f\sqrt{\frac{T}{2B}} \pm \sqrt{\frac{TB}{2}}$
Sinc pulse	$\frac{\sin(2\pi(t - t_0)B)}{2\pi(t - t_0)B}$	$rect\left(\frac{f}{B}\right) = \begin{cases} 1; \lvert f\rvert < B/2 \\ 0; otherwise \end{cases}$

Table 4.3. Waveforms Evaluated

Filtered back projection includes the $|k/\pi|$ or $|\rho|$ filter function in two dimensions (eqn. 4-31 as example) and ρ^2 in three dimensions (eqn. 4-20). This has the effect of multiplying noise, resulting in poorer image quality [87]. Consequently several tapers have been developed for image reconstruction [86]. The filters are applied as

$$\hat{G}(k,\theta) = T(|k|)F(k)G(k,\theta) \tag{4-30}$$

where $T(|k|)$ represents the taper and $F(k)$ any receiver filtering, including pulse envelope matched filtering. Tapering is applied over the inner integral of the BPF reconstruction, over wavenumber. Additional discussion is presented in Section 6.

Moving to aperture/waveform evaluation we mostly address monostatic configurations. With the exception of different trajectories with dissimilar speeds/trajectories (using kinematics to fill *k*-space) and such we have seen that bistatic results differ from monostatic only in resolution, again under the assumption of the ideal scatterer.

4.4.1 ***2D and 3D monostatic apertures, CW waveform***. The reconstruction of a two dimensional aperture using filtered backprojection is realized using equation 4-30. $G(\rho,\theta)$ defines the set of forward transformed projections which includes the reflectivity function, the illuminating waveform, and any receiver processing, such as matched filtering, that affects the waveform and $\rho=2/\lambda$.

$$g(r,\phi) = \int_0^{2\pi}\int_{-\infty}^{\infty} |\rho| G(\rho,\theta) e^{j2\pi(\rho r\cos(\theta-\phi)} d\rho d\theta \tag{4-31}$$

In that which follows we employ the standard radar definition of resolution: the full width, half maximum width of the point spread function along the image coordinate frame cardinal axes. We also employ the normalized, magnitude-squared response when describing impulse response properties such as mean and peak sidelobe levels.

Five cases are examined for the 2D monostatic aperture point spread function following those listed in Table 4.2. Cases 4) and 5) represent a rectangular spectrum, corresponding

to a sinc(*x)* waveform in the time domain, with and without amplitude tapering. As noted elsewhere, and which will be discussed more completely in Section 4.6, the azimuth sampling is 1 degree in that which follows. This is set for reasons of computational expediency only. In elevation sampling for the 3D geometries, an increment of 1 degree is also used.

The unmodulated CW waveform is given by $e^{j\omega t}$, with forward, temporal frequency, transform $\delta(\omega-\omega_0)$. The spatial transform, substituting $\omega t=2\pi r/\lambda$, or equivalently $\omega t=\pi\rho r$ ($\rho=2/\lambda$), is $\delta(\rho-\rho_0)$. As shown in (4-6), the two dimensional aperture and CW signal with isotropic scatterer has a closed form solution, with sample PSF depicted in Figure 4.5. Resolution at the FWHM points is 0.2λ with sidelobes rolling off at a rate of $1/r$. This is a demonstration of achieving high resolution without bandwidth. We next examine the effects of adding bandwidth to the signal.

Extending to three dimensions we insert (4-23) into (4-21) with the result shown in Figure 4.20. There are several potential apertures which will be discussed in detail in later sections. For this evaluation we assume a spherical aperture wherein the monostatic system illuminates and receives from discrete points, equally spaced, over 2π steradians; the upper hemisphere over a ground-located scatterer. A 400 MHz frequency CW was assumed with spatial samples every 1 degree over the upper half-space (in general contrast to the 1 degree azimuth sample increment used for the two dimensional apertures). We note that extending the aperture into three dimensions results in reduction of the first sidelobe level to -13 dB with a faster sidelobe roll off rate. Elevation resolution and sidelobe spacing are indicative of the shorter projected aperture than in the horizontal plane.

A note regarding the distance reference in (4-31) and (4-23). Referencing the pixel position relative to the scene origin, as in (4-31), requires that the range to scatterer be

normalized against the range to scene center, given the radar position. When the projection integral form in (4-23) is employed then the true range is employed in simulating the scattered phenomenology.

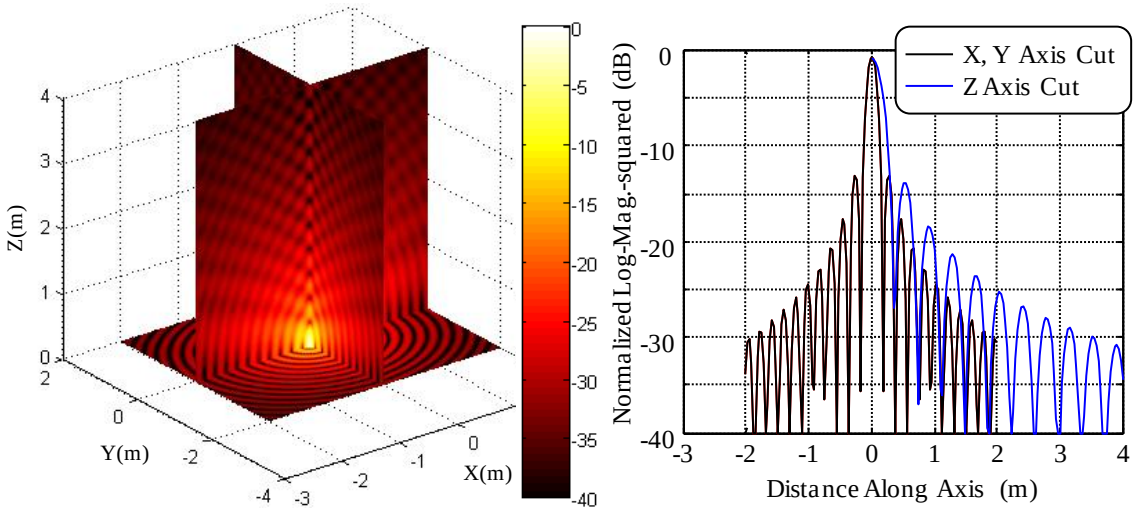

a) Principle Plane Image Results b) Log-magnitude Cardinal Axis Cut

Figure 4.20. Three Dimensional Point Spread Function for CW Waveform

4.4.2 Pulsed waveforms. The wave number spectrum for a rectangular envelope (rect) modulated sinusoid is given by (for a real sampled signal)

$$S(\rho,\rho_0)=\frac{\sin(\pi(\rho-\rho_0)R_{pulse})}{\pi(\rho-\rho_0)R_{pulse}}+\frac{\sin(\pi(\rho+\rho_0)R_{pulse})}{\pi(\rho+\rho_0)R_{pulse}} \tag{4-32}$$

where R_{pulse} is the two-way length of the radiated pulse (duration converted to length). The underlying assumption is that the radar receiver performs wideband filtering so that the rect waveform is sampled without alteration and formats the signal in complex form via Hilbert Transform, or equivalent. In two dimensions the reconstruction is, evaluated with pulse length (spatial extent or bandwidth) as a parameter

$$g(r,\phi)=2\int_0^{2\pi}\int_0^{\infty}|\rho|\left(\frac{\sin(\pi(\rho-\rho_0)R_{pulse})}{\pi(\rho-\rho_0)R_{pulse}}\right)e^{-j\pi\rho r_0(\theta)}e^{j2\pi(\rho r\cos(\theta-\phi)}d\rho d\theta \tag{4-33}$$

In (4-33) the product of the spectrum of the waveform and the isotropic scatterer represents the forward transform of the convolution in the time domain. Equation 4-33 was evaluated for waveform bandwidths from 100 kHz up through an instantaneous

bandwidth of 25%, or 100 MHz, technically ultrawideband given the 400 MHz carrier (fractional bandwidth defined as $(f_u - f_l)/f_{mid}$). The purpose was to gradually increase bandwidth and confirm that low bandwidth pulsed waveforms essentially matched the CW case, as a validation (out to the physical limit of the pulse length), while demonstrating the improved contrast of the PSF through the more spatially confined response. It also demonstrates that the resolution is a weak function of bandwidth. Weak as there is only slight improvement in resolution with increasing bandwidth. The results are shown for the full response in Figure 4.21a and a cardinal axis cut (X axis), with the scale expanded around the scatterer position, in 4.21b. In this example the scatterer was positioned at (1,0). The immediate observation is the sharp delimiting of the spatial extent of the PSF response with the increase in bandwidth (100 MHz bandwidth yields 1.5 m of pulse envelope range resolution while a matched filter output to a rectangular pulse would be of extent $2T_{pulse}$).

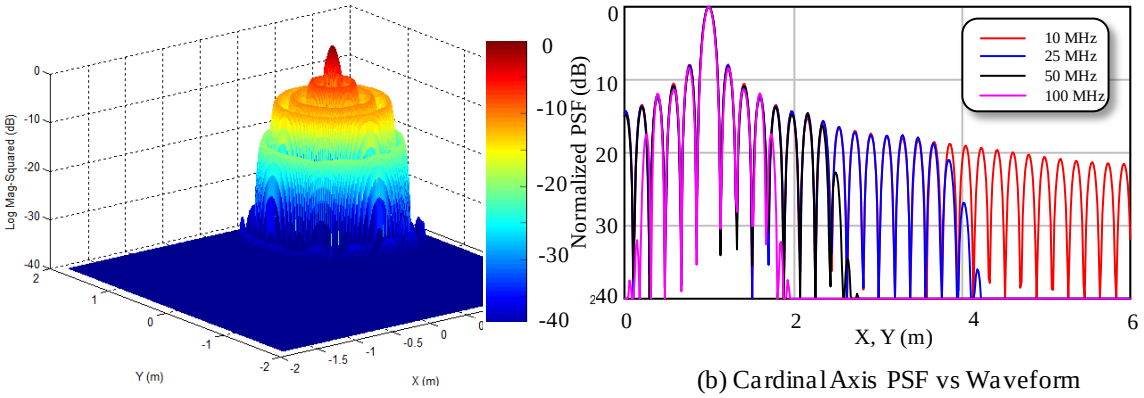

(a) PSF 100 MHz Bandwidth (scatterer at (0,0))

(b) Cardinal Axis PSF vs Waveform Bandwidth

Figure 4.21. Point Spread Function – 400 MHz Center Freq., Rectangular Pulsed Waveform (a) and Cardinal Axis Response with Bandwidth as a Parameter (b)

The rectangular-envelope modulated carrier result assumes that the receiver passband exceeds the pulse bandwidth, resulting in no modification of the waveform envelope (or spectrum). We next consider the use of a matched filter, one implemented at the signal carrier (in order to preserve the waveform carrier and associated resolution). From eqn. 4-32, the matched filter response will be $S(\rho)^* S(\rho)$ (where * indicates the complex conjugate

and $S(\rho)$ the signal complex spectrum). Repeating the evaluation of eqn. 4-33 with matched filter processing of the received waveform gives the results presented in Figure 4.22. In this Figure the matched filtered result is plotted against the wideband receiver result (Figure 4.21b). The waveform bandwidth is the same in both cases (100 MHz) with a scatterer located at (1,1). As in Figure 4.21 the PSF is symmetric about the scatterer position so only the X axis cut is shown. The effect of the matched filter is akin to a taper that is centered on the carrier frequency: the sinc response roll off is increased in the frequency domain. The close-in sidelobes are reduced along but the farther out sidelobes are increased.

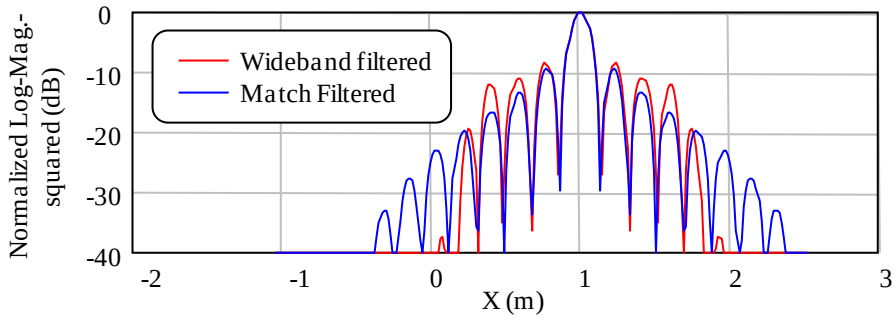

Figure 4.22. PSF Cardinal Axis – 400 MHz *rect* Waveform, Match Filtered

In filtered back projection (FPB) there is discussion regarding the effect of the multiplication (the filtering aspect) by $|\rho|$ (e.g., eqn. 4-33). The argument is that the filtering enhances high frequency noise [86]. We test this without injected noise through examining spectrum distortion by evaluating a waveform with rectangular spectrum. This corresponds to an amplitude modulated signal in the time domain. This is also the case we evaluated in Figure 4.7 using Fourier-based reconstruction. Here FBP is used which alleviates sampling/quantization issues and which should illustrate any additive noise effects with results shown in Figure 4.21. The time domain *sinc* waveform (blue curve in Figure 4.23) does produce higher outer sidelobes which are suppressed with a frequency domain taper (black curve) which has the effect of slightly increasing the close in sidelobes which suppressing more radially distant ones. But the effects are small. A series

of cases, which are not presented, applied a Hamming taper in the frequency domain produced similar results to that of the matched filter(on the time domain rectangular pulse) but again with little effect. There will be more discussion on tapers in Section 5.5.

The collection aperture evaluated for the monostatic three dimensional studies is a hemisphere that is centered relative to the image coordinate frame. This represents the upper bound for sampling above a ground plane. The constant radius hemisphere, eliminating any considerations of motion compensation or actual realization, is sampled at 1 degree increments in azimuth and elevation. A single monostatic example is shown for the simple pulsed waveform at 400 MHz with 100 MHz of bandwidth and the three

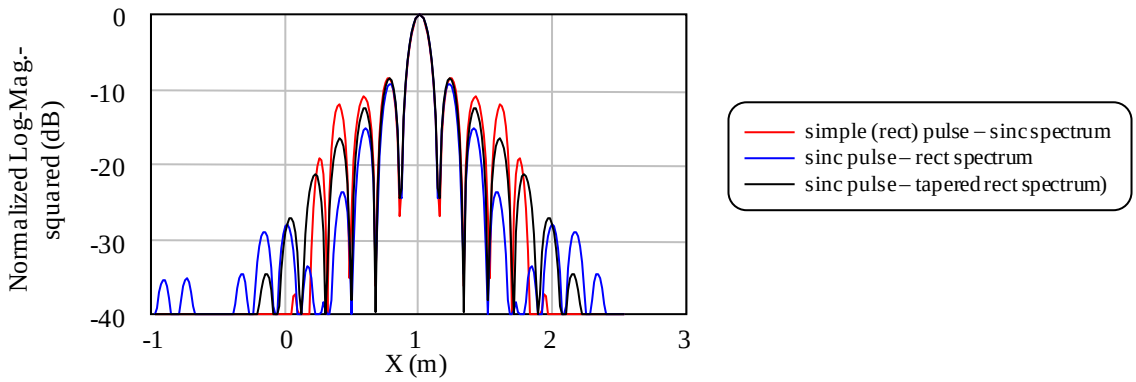

Figure 4.23. Cardinal Axis Cuts - *Rect* Pulse, *Rect* Spectrum (Time Domain sinc), and Tapered *Rect* Spectrum

dimensional hemispherical aperture in Figure 4.24. The first Figure (4.24a) contains the cardinal plane cuts against a point scatterer at (1, 1, 1). The sidelobe structure in the X-Y plane resembles that of the 2D case, extending to twice the pulse length and with similar levels (Figure 4.24b with bandwidth as a parameter). Figure 4.24c presents the PSF structure, also with bandwidth as a parameter, for the reconstruction Z axis. It is interesting to observe the smoothing of the Z axis response as the frequency content of the waveform increases.

A taper example in 3D reconstruction is shown in Figure 4.25. The cardinal axes results for the hemispherical aperture with the 100 MHz simple pulse waveform are shown,

contrasting tapered versus non-tapered PSF. AS in the 2D case there is slight improvement only. Note that in Figure 4.25a the untapered PSF was reconstructed only over half the axis extent of the tapered case.

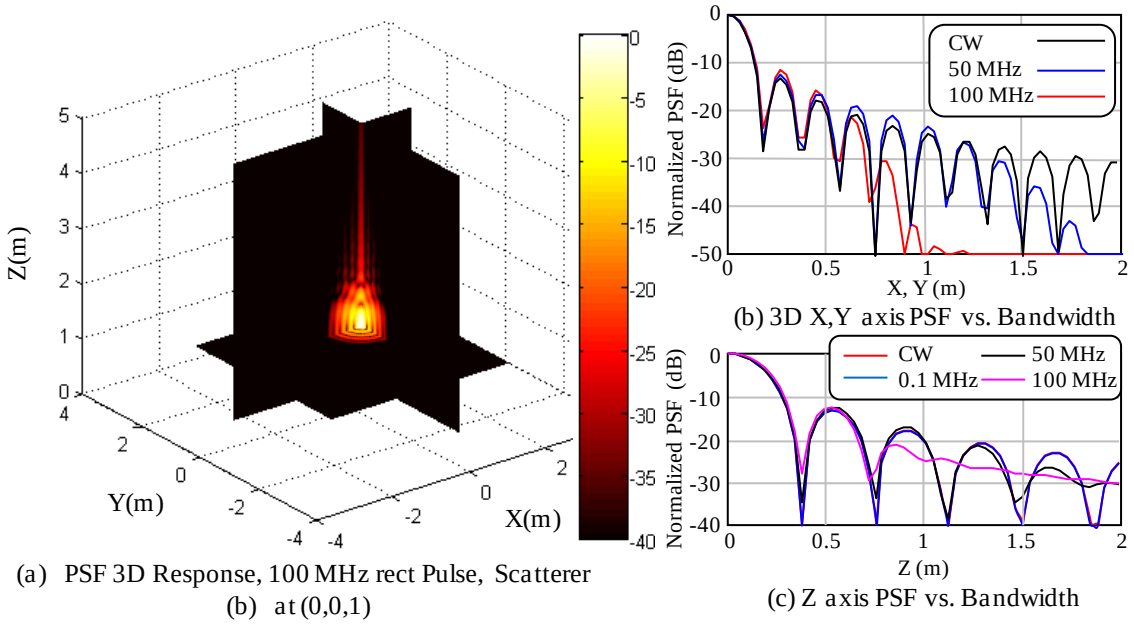

(a) PSF 3D Response, 100 MHz rect Pulse, Scatterer (b) at (0,0,1)

(b) 3D X,Y axis PSF vs. Bandwidth

(c) Z axis PSF vs. Bandwidth

Figure 4.24. Cardinal Plane Perspective View – Pulsed Waveform with 100 MHz Bandwidth (a), and Cardinal Axis Cuts: X-Y (b) and Z (c)

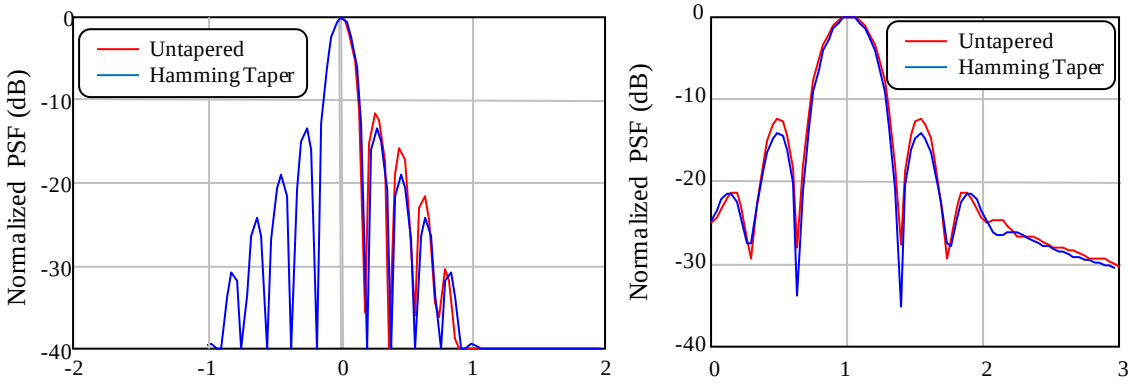

a) X,Y Axis PSF

b) Z Axis PSF

Figure 4.25. Effects of Taper on 3D Reconstruction - Pulsed Waveform

4.4.3 Linear frequency modulated waveforms. The use of coherent modulation allows longer pulses for increased energy while meeting bandwidth/resolution requirements to be met via pulse compression. The use of an LFM waveform in a monostatic geometry with the same bandwidth as the simple pulse. Monostatic operation is examined in this section. The LFM waveform is described in Table 4.3. An isotropic scatterer positioned at (0.7, 0,

0) with a waveform of 140 MHz chirp bandwidth centered at 1.3 GHz resulted in the 3D reconstruction cardinal axes cuts shown in Figure 4.26. The LFM was match filtered prior to reconstruction. The point spread function demonstrated the resolution expected for the frequency used.

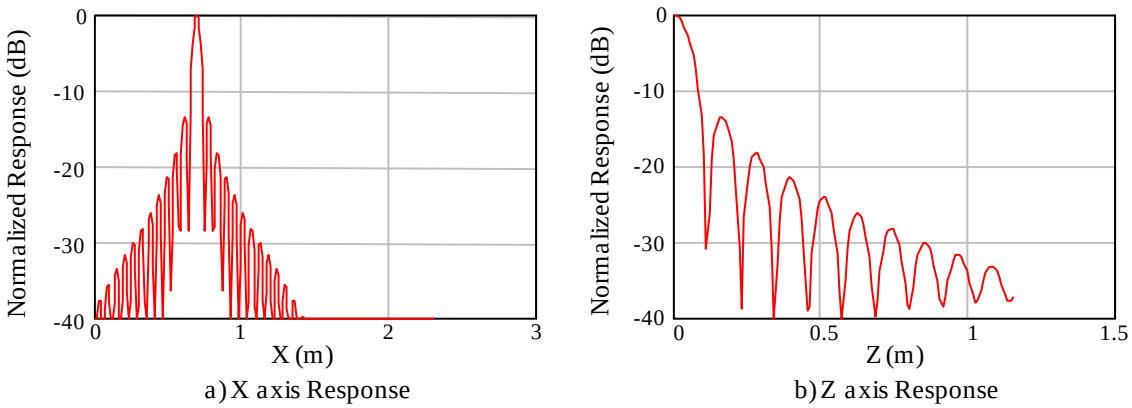

Figure 4.26. Point Spread Function for LFM with Matched Filtering

The effects of bandwidth can be seen in Figure 4.27 where the bandwidth is varied from 1 MHz to 140 MHz, keening the expanded pulse duration constant. As was demonstrated in Figure 4.8 the effect of increased bandwidth was the increased rate of sidelobe level roll off with distance.

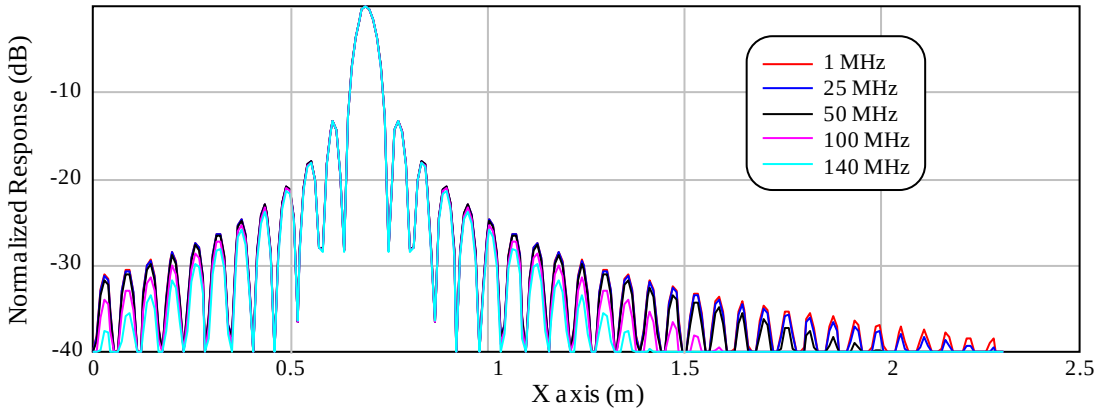

Figure 4.27. PSF of Match Filtered LFM and Dependence on Bandwidth

This is consistent in that the LFM spectrum is much more nearly rectangular than the sinc spectrum for the rectangular pulse. It is also noted that the Z axis response, while at a frequency 3 times higher and only extending slightly over 1 m of sampled distance, does not demonstrate the dispersive-like sidelobe behavior in Figure 4.25b. Evaluated, but not

presented, were comparative cases for the LFM waveform without matched filtering. The results were similar in form to those of Figure 4.22, with the PSF sidelobe peaks lower with matched filtering.

4.4.4 Bistatic CW waveforms. Using the three dimensional bistatic geometry in Figure 4.19 we move to the bistatic point spread function for CW waveforms. Simple variations on the monostatic three dimensional case(s) is made. In all examples, as in the monostatic case, the platforms are not constrained kinematically as a "real" vehicle would be.

The first case uses a single fixed transmitter while the receiver trajectory is sampled identically to the 3D monostatic hemispheric aperture. Figure 4.28 presents the point spread function, Figure 4.28a the cardinal plane slices and Figure 4.28b the principal axis result. Also, as for the monostatic results, the dynamic range of the plotted result is limited to 40 dB for readability. The resolution for the 3D aperture (termed here bistatic Case 0) is exactly one-half that of the monostatic case, with a similar sidelobe structure, also scaled by a factor of 2 (spatially). The images from this geometry are independent of the location of the transmitter.

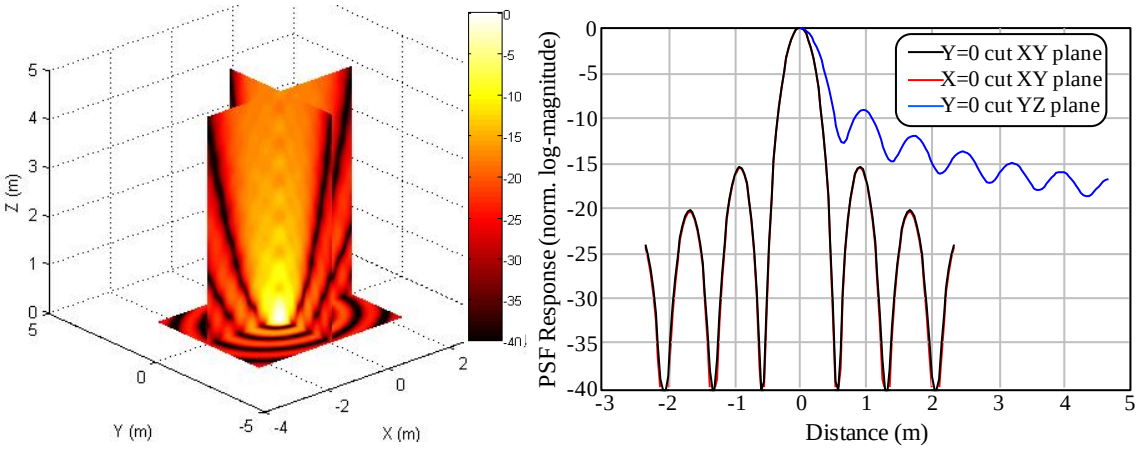

a) PSF Response Along Cardinal Planes

b) PSF Response Along Cardinal Axes

Figure 4.28. PSF for 3D Bistatic Case 0

A second trajectory (Case 1) placed the transmitter in a circular orbit at a fixed elevation angle relative to the image coordinate frame. The receiver executed a hemispherical trajectory. The transmitter motion was synchronous with the receiver (e.g., β=0^o)

regardless of the receiver elevation angle about the hemisphere, i.e., the transmitter and receiver were always on the same "longitude" of the hemisphere (the bistatic angle projected onto the X-Y plane). A series of runs were made varying the transmitter elevation angle from 0 degrees to 70 in 15 degree increments and the results are summarized in Table 4.4. Calculated full-width, half-maximum resolution, peak and average sidelobe levels are presented. A single example point spread function is

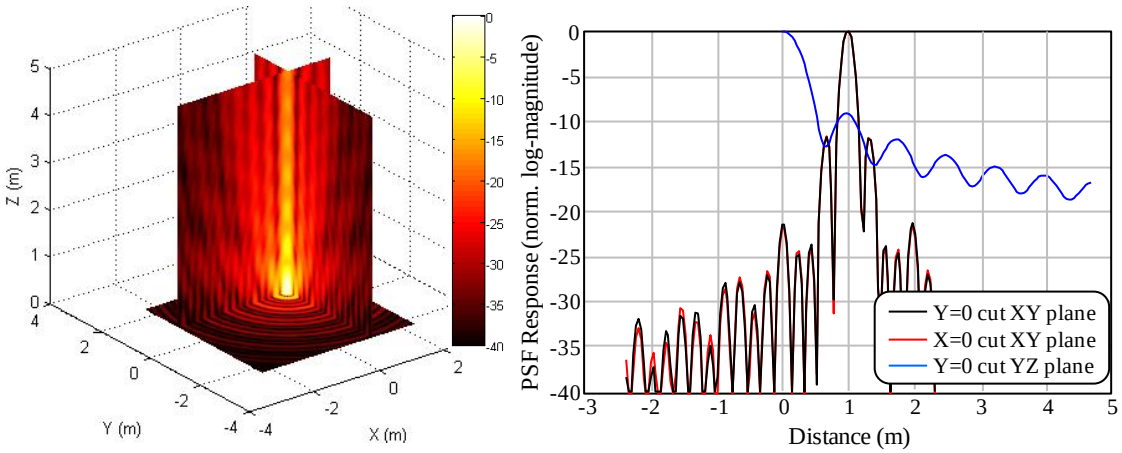

a) PSF Response Along Cardinal Planes b) PSF Response Along Cardinal Axes

Figure 4.29. PSF for 3D Bistatic Case 1: Transmitter Elevation Angle 45 Degrees, Single Orbit with Receiver Executing Hemispherical Aperture

presented in Figure 4.29 for a transmitter elevation angle of 45 degrees. The format is the same as Figure 4.28. A quick look at the dependency on the bistatic angle was made by executing a single case where β was set to 45 degrees. The bistatic angle (β) used was defined by the projection of the transmitter and receiver vectors at the start of the aperture onto the X-Y plane.

The results in Table 4.4 indicate that the transmitter position exerts no influence on the vertical resolution. This is not the case in the horizontal plane. A degradation in X-Y plane resolution as the elevation angle of the transmitter is increased is seen, which is well described by an inverse-root-cosine dependency. The average sidelobe levels reflect the use of 250 data points along the X-Y axes, instead of the 125 values used earlier. To

yield equal axis lengths 125 elevation points are used. It is interesting to note that the peak sidelobe level in the X-Y plane was positively impacted by increasing the transmitter elevation angle while the X-Z and Y-Z cardinal plane results were unaffected.

The final example might be considered the bistatic equivalent of circular SAR (bistatic Case 2). In this geometry both platforms move in a simple circular orbits that are offset in elevation. This example places the transmitter at 60 degrees elevation and the receiver at 15. degrees. Both platforms maintain a constant range relative to the origin. In Figure 4.30a the platforms are in synchronous motion with a bistatic angle of 0 (which is constant through the aperture). In the second example (Figure 4.30b) the transmitter is moving in the opposite direction from the receiver, but in the same initial geometry. As is the case for low resolution circular SAR there is no resolving power in elevation.

Transmitter Orbit Elevation	Resolution (FWHM, m)			Average SLL (dB)			Peak SLL (dB)		
	X	Y	Z	XY	XZ	YZ	XY	XZ	YZ
0 deg	0.058	0.058	0.26	-32.9	-26.6	-26.6	-10.2	-9.1	-9.1
15 deg	0.06	0.06	0.26	-32.9	-26.6	-26.6	-10.4	-9.1	-9.1
30 deg	0.065	0.065	0.26	-32.8	-26.3	-26.3	-10.7	-9.1	-9.1
45 deg	0.072	0.072	0.26	-32.7	-25.8	-25.9	-13.4	-9.1	-9.1
60 deg	0.09	0.09	0.26	-32.7	-25.1	-25.1	-13.4	-9.1	-9.1
75 deg	0.11	0.11	0.26	-32.3	-23.8	-23.8	-17.7	-9.1	-9.1
45 deg (β 45°)	0.08	0.08	0.26	-32	-25.5	-25.5	-11.3	-9.1	-9.1

Table 4.4. Bistatic Case 1 Image Metric Compilation

4.5 Reflection Tomography Image Properties.

In this section we examine the dependencies of resolution for both full and partially-executed apertures. A derivation is presented for an expression for the two dimensional case which is augmented with repeated operation of tomographic simulations.

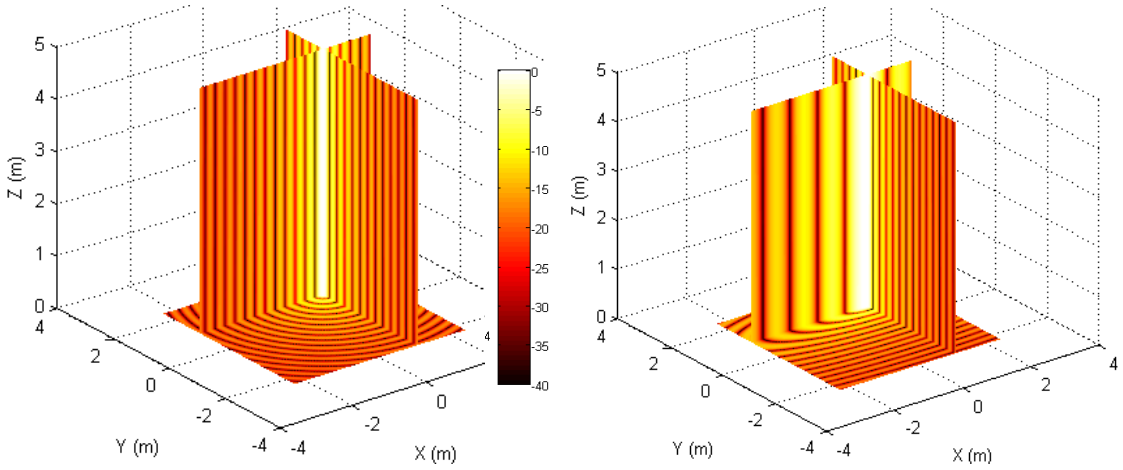

a) 60° Transmitter, 15° Receiver Orbits Parallel b) 60° Transmitter, 15° Receiver Orbits Antiparallel

Figure 4.30. Bistatic Case 2, Offset Orbit Geometry

4.5.1 Resolution. Mensa [93] offers a resolution relation derived from Doppler principles for the 2D tomographic geometry, given as $\delta x = \lambda/4\pi$. The collection aperture transformed to the Fourier domain (*k*-space), for a CW waveform and isotropic scatterer at the origin, has radius $4\pi/\lambda$ (or $2k$) [100] and [87]. Thus the spatial resolution of the reconstructed image can be expressed in terms of the inverse of the collection aperture radius in *k*-space.

This is tested below. Two-dimensional backprojection filtering using a Riemann sum integral approximation and the closed form expression of the PSF for a scatterer at the origin in target/object coordinates (eqn. 4-7) were used to generate PSF response as a function of radial distance and the half-width, half-maximum point found by interpolation. This was done as a function of frequency. The resolution metric that is commonly encountered in the tomographic literature is based on the first PSF null. We use the HWHM (half-width, half-maximum), or the full-width, half-maximum (FWHM) as the customary practice of the radar community. Figure 4.31 gives the result compared with the Mensa result. The Figure shows a (nearly) linear relation between resolution and wavelength over the range 200-600 MHz. This result yields an error in the resolution prediction of about 12% as indicated in the Figure.

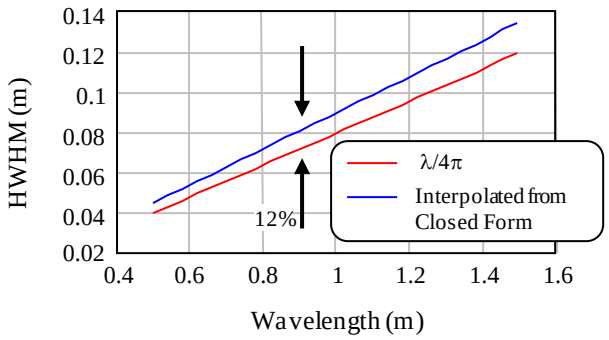

Figure 4.31. Calculated Resolution (HWHM) vs. Frequency

An improved estimate of resolution is found using the closed form solution, solved for the radial distance that produces the normalized response of 0.5 (the HWHM point). The Bessel function can be alternatively expressed as [94]

$$J_n(z) = \sum_{m=0}^{\infty} \frac{(-1)^m}{2^{2m+n} m!(m+n)!} z^{2m+n} \tag{4-34}$$

Beginning with the interpolated HWHM result and setting an error bound of 1%, (4-34), for order 0, is inserted into eqn. 4-35 and the number of terms required to meet the error tolerance found (three). Since $J_0(0)=1$ the $4\pi/\lambda$ term in (4-34) normalizes out, leaving the algebraic expression for the normalized, magnitude-squared PSF as

$$0.5 = \left[1 - \frac{1}{4}\left(\frac{4\pi}{\lambda} r\right)^2 + \frac{1}{2^6}\left(\frac{4\pi}{\lambda} r\right)^2 \right]^2 \tag{4-35}$$

The solution to (4-35) is straightforward. Setting $r = \delta x$, yields

$$\delta x = \frac{\lambda}{3.545\pi} \tag{4-36}$$

The comparison of the value derived in equation 4-36 to the calculated resolution yields a match within 0.2%. The full-width, half maximum result (resolution) is twice that of (4-36).

To test the robustness of this result, the pixel location was increasingly displaced from the origin, out to the sampling ambiguity limit (Section 4.6). The PSF mainlobe dimensions were determined for pixels on radials at from 0 to 90 degrees in 15 degree increments.

Cardinal axis dimensions of the response mainlobe were estimated at each position. The result demonstrated a response insensitive to radial distance.

Three dimensional resolution was investigated in a similar fashion, as reported in [95]. The cardinal axis PSF responses were calculated along the X, Y, and Z axes and the HWHM estimated using a table look-up and linear interpolation routine. Unlike the 2D result, the 3D were calculated over the frequency range 300-800 MHz, in 5 MHz steps and are based on a CW waveform. The resolution result is seen in Figure 4.32. Overlaid on the 3D result is the 2D result from Figure 4.31 with the ordinate rescaled from wavelength to frequency. It is noted that for the 3D comparative cases (monostatic) where waveform bandwidth was treated parametrically, the resolution realized is a weak function of bandwidth (Figure 4.24) slightly improving along the Z dimension but no real differences in the X-Y plane. This was not evaluated more critically. The X and Y curves overlay and are intentionally slightly offset in the Figure.

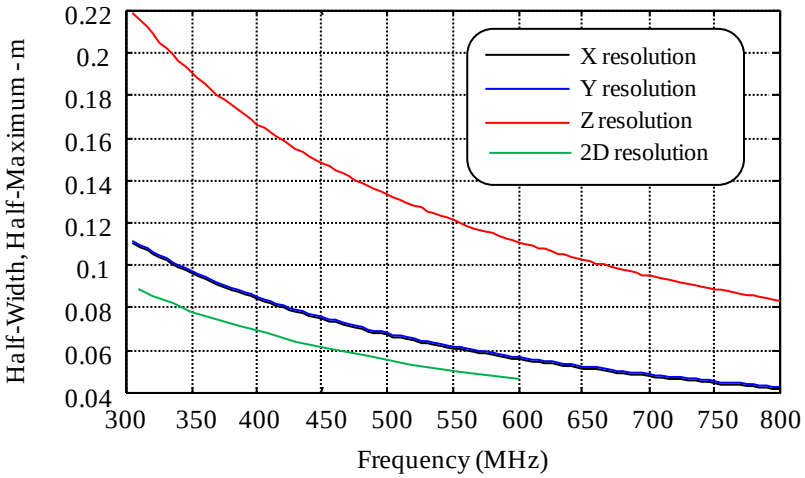

Figure 4.32. Three Dimensional Aperture - Resolution versus Frequency with Comparison to the Two-Dimensional Result

4.6 Partial Apertures.

In complex target geometries/environments where, in spite of the selection of low operating frequencies, full aperture visibility of constituent scatterers may be compromised, we evaluate the resolution properties of partial apertures to emulate such a

condition. We define "partially sampled" to be the collection over a solid angle region smaller than the limiting hemispherical aperture (or the two dimensional equivalent). This is investigated for both two and three dimensional apertures, monostatic and bistatic geometries. We seek to extend the full aperture resolution approximations to partial apertures. This is a straightforward exercise for the monostatic aperture but is more complex for bistatic case due to the added degrees of freedom, examples of which have also been presented earlier. The approach is straight-forward: the integration limits for image reconstruction are hard-limited. This introduces a binary "access" to the idealized scatterer, without any amplitude (radar cross section) modulations as might be evidenced by a real scatterer. A significant effort was expended, without success, to develop an analytic expression for the two dimensional monostatic aperture resolution with arbitrary integration angles. This led to the technique used here.

4.6.1 Monostatic apertures. Monostatic partial apertures are divided into three classes for this exploration. The first consists of a full aperture azimuth (2π radians subtended by the radar, the polar angle in the X-Y plane of the scene coordinate frame) with a contiguous elevation aperture of variable angular extent and elevation position(s). The second is a full elevation aperture ($\pi/2$ radians, in the half-space above the X-Y plane) and partial azimuth aperture of variable extent. The third variation simultaneously combines both azimuth and elevation partial apertures. In all cases the aperture sampled is a subset of the hemispherical collection surface. Though not specifically partitioned, two dimensional geometries are placed into the second class. The partial aperture assessment was conducted for CW waveforms only. We begin with the two-dimensional monostatic case. As discussed in Section 4.6, there is a closed form solution for this geometry. However it only is valid for apertures that span 2π radians: several months' effort was spent attempting to derive a closed form result for partial apertures, without success. Replacing the limits in eqn. 4-7 with the start and stop angles (relative to the X-axis) as variables in

the numerical integration, we develop curves that define the cross range (along Y) and down range (along X) resolutions, as defined from the geometry in Figure 4.33. The cross range resolution for the aperture, as a function of aperture angle, in 5

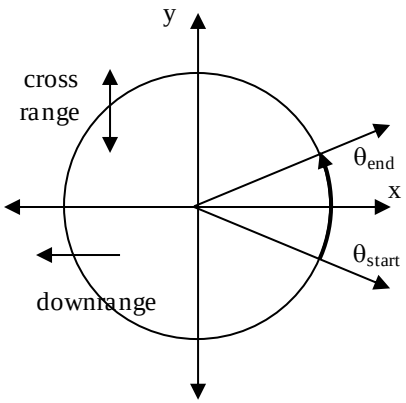

Figure 4.33. Geometry for Partial Aperture Response Calculations

degree increments (5-360 deg.), is shown in Figure 4.34a for CW signals with wavelengths 0.5 m, 1 m, and 2 m. Figure 4.34b is the calculated down range resolution using the same aperture angles. In both cases three frequencies were used. As expected, as the aperture angle decreases the locus of points at matched phase quickly increases to the point where the resolution becomes essentially undefined in range, consistent with the CW waveform. The degradation of cross range resolution occurs more slowly, in terms of the rate of change of resolution versus aperture angle because of the projected aperture length, the basis of traditional SAR. We see that the cross range resolution is largely unchanged until the angle subtended by the aperture becomes less than 180 degrees.

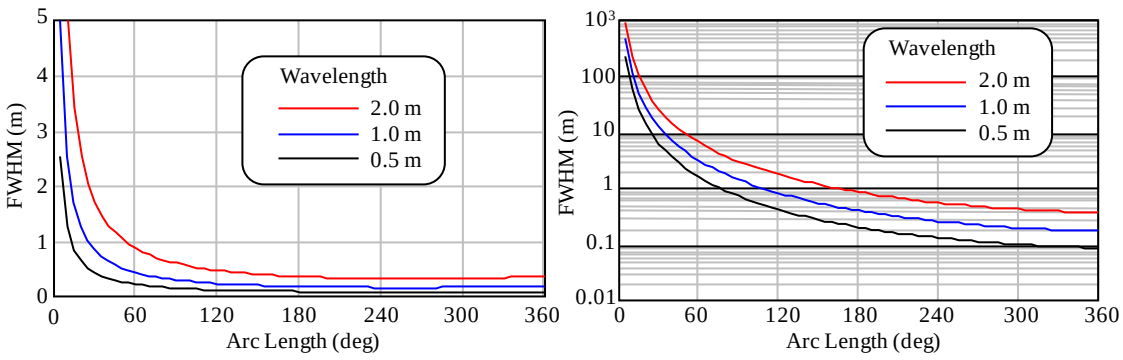

(a) Cross Range Resolution vs. Aperture Length (b) Down Range Resolution vs. Aperture Length

Figure 4.34. 2D Monostatic Resolution for Partial Apertures

A comparison of the calculated cross range resolution for a partial tomographic aperture is compared to a rule-of-thumb for SAR in Figure 4.35a for the cross range dimension. The SAR integration angle range was more restricted than the tomographic result. Also included is an approximation for the tomographic cross range resolution based on the aperture radius in *k*-space. The functional forms of the approximation (cross range) and coarse fit (down range) are where θ is the total aperture angle subtended. These

$$\delta_{cross\_range} = \begin{cases} \dfrac{\lambda}{2\pi \sin(\theta/2)} & \theta < \pi \\ \dfrac{\lambda}{2\pi} & otherwise \end{cases} \quad \text{and} \quad \delta_{down\_range} \approx \frac{\lambda}{2\pi \tan(0.16\theta)^{2.1}} \quad (4\text{-}37)$$

approximations, derived for the 1 m wavelength case in Figure 4.34, are intended only to loosely convey the resolution achievable in a given aperture configuration. Down range results are shown in Figure 4.35b.

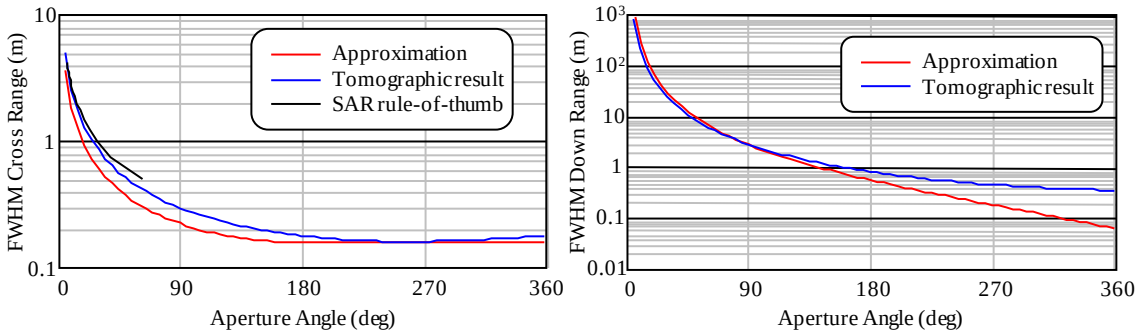

a) Cross Range Result and Aperture Approx..

b) Down Range Result and Aperture Approx.

Figure 4.35. Cross Range and Down Range Resolution and Approximations

Moving to three dimensional apertures, Figure 4.36 presents the X, Y and Z (principal) axis resolutions when a variable sector of angular extent ϕ (azimuth) in the image *x-y* plane is collected, together with full sampling in elevation (θ=90 deg), using a 400 MHz waveform. This is the first case referred to at the top of this section. As in the 2D case this is a highly idealized geometry and was examined to evaluate the degree of interdependency between the azimuth and elevation sampling apertures under the likely scattering effects of actual targets. The azimuth window was maintained symmetrically around the image X axis which affects the instantaneous X or Y resolutions over angle,

though the voxel area in the X-Y plane is independent of the angle origin. As ϕ goes below 90 deg., the *Y* axis resolution begins to dilute; an artifact of the ultra-narrowband waveform. With the *Z* axis fully instrumented (sampled) there is no change in vertical resolution with decreasing azimuth sample extent. Further there is a layover effect on the X axis resolution where the vertical aperture extent projected along the X axis determines the X axis resolution (Figure 4.36a).

Figure 4.36a suggests that the horizontal and vertical resolutions are independent. This was tested by evaluating the second case identified above; the full azimuth with a limited elevation aperture. Results appear in Figure 4.36b. In developing this result a fixed elevation window of 10 degrees was sampled while a full azimuth aperture was collected. The elevation window was positioned in increasing elevation increments from 5 to 85 degrees, the PSF calculated and resolution (HWHM) determined for each position in elevation. As the elevation angle to the window midpoint increased toward zenith, the projected *k*-space radius of the aperture onto the k_x-k_y plane decreases. This dilution is equivalent to sampling the azimuth aperture at lower elevation angles using a lower frequency (longer wavelength). The right-hand axis of 4.36b is the HWHM resolution calculated along the *Z* axis as the elevation angle to the 10 degree window increases. Visualizing the projection of the vertical extent of the elevation window, as the center angle is increased, as nonlinearly collapsing matches the degradation in vertical resolution observed.

This suggests an area relationship for resolution based on the collection aperture in *k*-space. For the CW waveform the aperture radius is $4\pi/\lambda$. In producing the results in Figure 4.36c, the full azimuth aperture was sampled with three elevation sampling strategies; he angle extent of the elevation aperture varied from 5 degrees to 90, the sequentially positioned 10 degree elevation window, or a 50 degree, sequentially positioned elevation window. Resolution is presented as a function of the fraction of the

area of the collection surface in *k*-space. A value of 1.0 represents the complete hemisphere over the object. As the elevation aperture decreases there is a corresponding degradation in resolution. All sample curves fall onto the same curve. As the angle to the center of the window increases the *k*-space surface area decreases with corresponding reduction in resolution along the *Z* axis. This observation was tested using a 20 deg elevation window with similar results; horizontal plane resolution was increased and linearly tracked the positioning elevation of the collection aperture. Finally Figure 4.36d compares the *z* axis resolution with an approximation based on the projection of the height of the *Z* aperture onto the *Z* axis ($Z_{approx} \approx \lambda/4.4a \sin(A_{ratio})$).

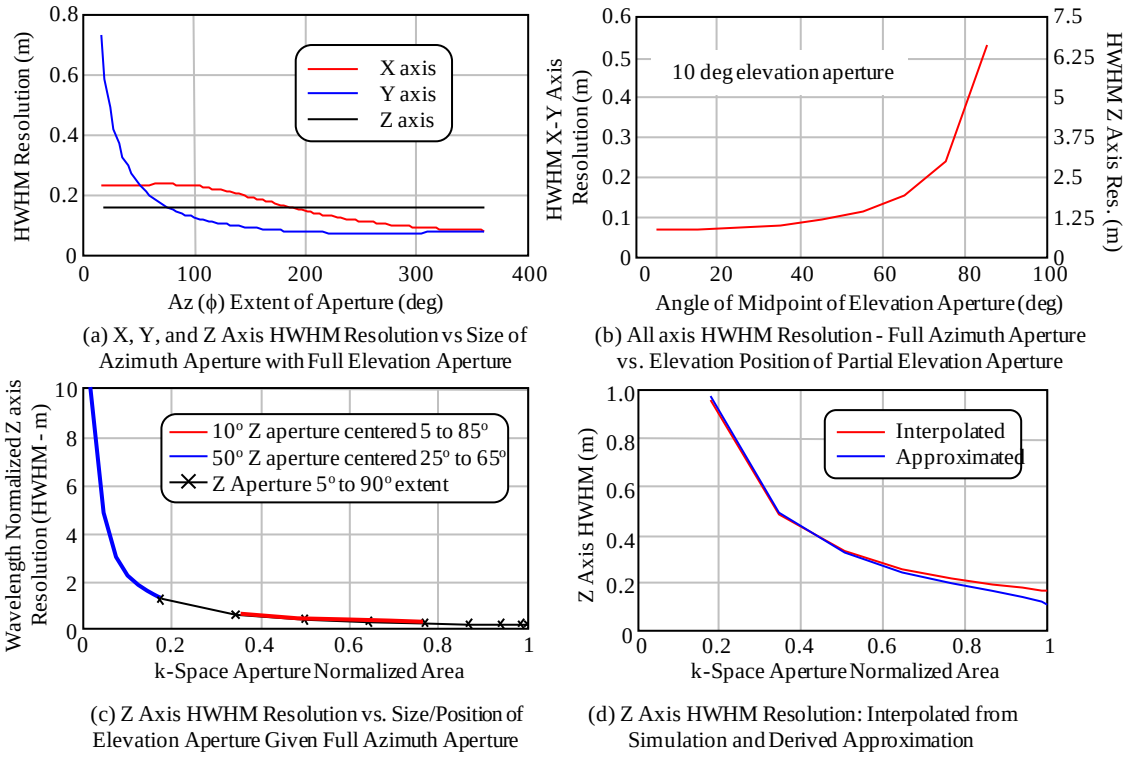

(a) X, Y, and Z Axis HWHM Resolution vs Size of Azimuth Aperture with Full Elevation Aperture

(b) All axis HWHM Resolution - Full Azimuth Aperture vs. Elevation Position of Partial Elevation Aperture

(c) Z Axis HWHM Resolution vs. Size/Position of Elevation Aperture Given Full Azimuth Aperture

(d) Z Axis HWHM Resolution: Interpolated from Simulation and Derived Approximation

Figure 4.36. Resolution Dependencies (a) Partial Azimuth, Full Elevation Aperture, (b) Horizontal Plane Resolution of Partial Elevation Aperture, (c) Vertical Axis for Partial Elevation Aperture, and d) Elevation Aperture Resolution Approximation

4.6.2 Bistatic apertures. Section 4.4 explored the 2D bistatic aperture for CW waveforms and for synchronous transmitter and receiver motions with the key finding that the resolution was a function of the bistatic angle between transmitter and receiver, while the

sidelobe structure was equal in level but diluted (fewer sidelobe peaks per unit radial distance) by this same dependency. Here we examine partial apertures, as in the 2D monostatic case, testing the effect on resolution through the angle subtended by the bistatic bisector vector. Only apertures with synchronous motion of transmitter and receiver are considered.

The results are summarized in Figure 4.37. Three bistatic angles (45, 90 and 135 deg.) were assessed over apertures of varying length from 5 to 360 degrees (as defined by the arc swept by the bisector). Results are given for the down range (*i.e.*, along X, see Figure 4.33) and cross range axes, as in the 2D monostatic case, calculated for a 400 MHz tone. Figures 4.37 a) through c) depict resolution along each axis for the specific bistatic angle. Figure 4.37d takes the cross range result from each bistatic angle and scales it, over aperture, by $\cos(\beta/2)$, again highlighting the dependency on the bistatic angle.

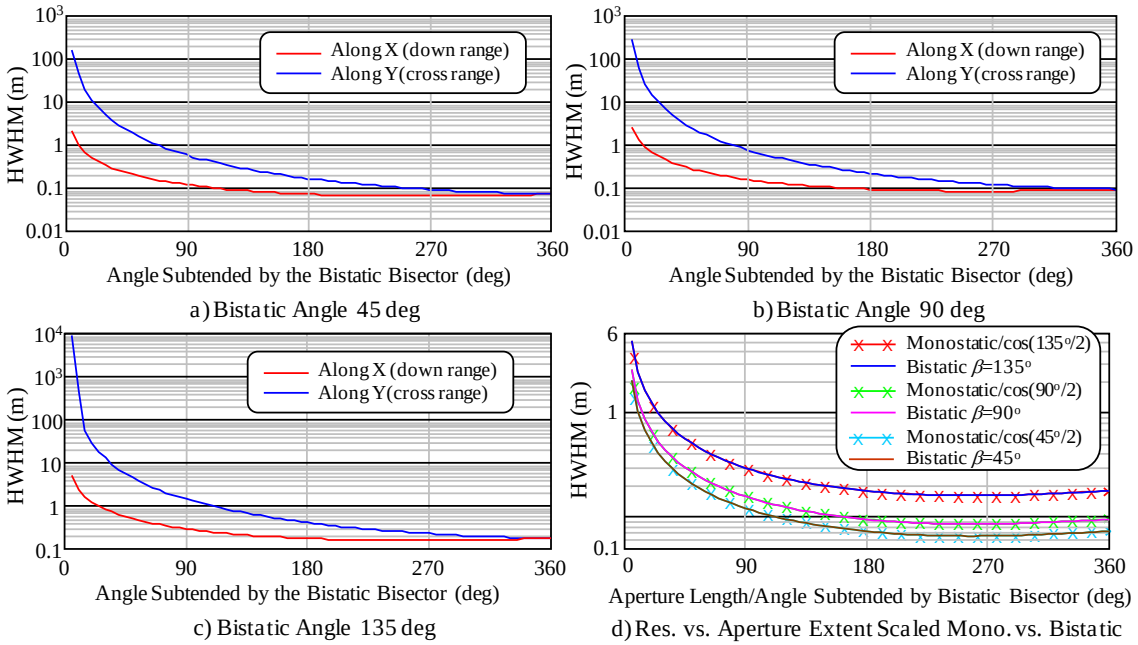

Figure 4.37. Summarized Results for Partial 2D Bistatic Apertures

The results in Figure 4.37 should collapse to the monostatic result when β=0. The comparison appears in Figure 4.38 for a 1m wavelength waveform, demonstrating that

this is indeed the case. The downrange resolution comparison in Figure 4.38a with the cross range resolution vs. aperture angle in Figure 4.38b.

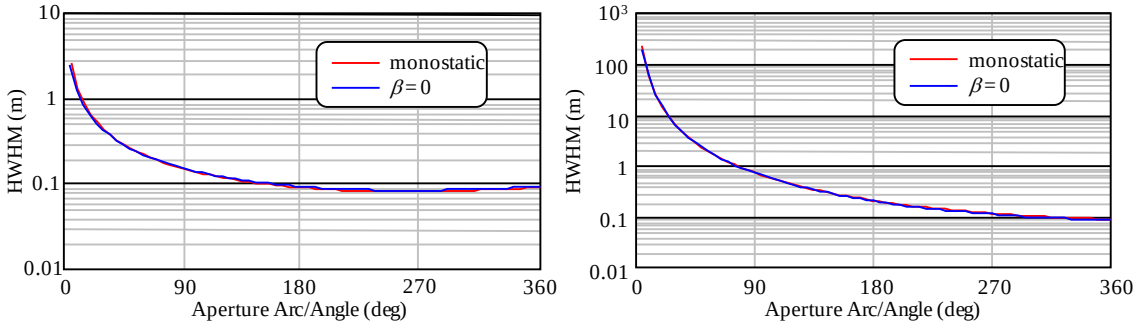

a) Cross Range b) Down Range

Figure 4.38. Comparison of 2D Monostatic Resolution to Bistatic with β=0°

4.7 Spatial Sampling Requirements.

In [93] Mensa defines the angular sample spacing for 2D imaging of rotating objects based on Nyquist arguments. The result is given based on Doppler arguments and has been widely cited. In this section the result is developed using spatial arguments and the derivation extended to the elevation dimension for three dimensional reconstruction.

4.7.1 Two-dimensional monostatic geometry. Consider the geometry in Figure 4.39 with the antenna in uniform circular motion of radius R_{radar} about the origin with position defined in object/scene coordinates. Let a scatterer be positioned at radius r and angle ψ delimiting the maximum extent of the object or scene to be imaged. Analogous to array beamforming we require sample spacing such that there are no phase ambiguities (grating structures) in the area to be imaged. In the array problem we require that the element spacing/scan angle combination be such that the path length difference between adjacent elements be less than 2π radians (a wavelength). Here the radar problem requires that the two way range difference meet that constraint. That is

$$\Delta R_\theta \frac{4\pi}{\lambda} \le 2\pi \qquad \text{or} \qquad \Delta R_\theta \le \frac{\lambda}{2} \tag{4-38}$$

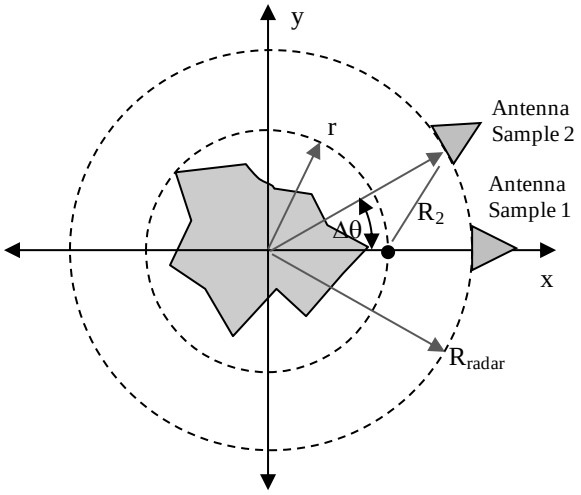

Figure 4.39. Imaging Geometry for X-Y Plane and Phase Ambiguity Derivation

The absolute phase is derived from the two-way path from radar-to-scatterer. However it is the relative phase which is the observable exploited in image formation. Given the geometry, the instantaneous phase vs. rotation angle is, for a given scatterer position

$$\zeta(\theta) = \frac{4\pi}{\lambda} R(\theta, r, \psi) \quad \text{or} \qquad \Delta\zeta(\theta) = \frac{4\pi}{\lambda} \Delta R(\theta, r, \psi) \tag{4-39}$$

where

$$R(\theta, r, \psi) = \sqrt{{R_{radar}}^2 + r^2 - 2rR_{radar}\cos(\theta - \psi)} \tag{4-40}$$

Defining a change in range as $\Delta R_\theta = R_1 - R_2$ we can define the range (and hence the phase) difference in terms of the angle change, $\Delta\theta$ between the two positions as

$$\Delta R(\theta) = \sqrt{{R_{radar}}^2 + r^2 - 2rR_{radar}\cos(\theta_1 - \psi)} - \sqrt{{R_{radar}}^2 + r^2 - 2rR_{radar}\cos(\theta_2 - \psi)} \tag{4-41}$$

considering Figure 4.39, the radar position with respect to a scatterer which produces the largest change in range is (θ-ψ) ~ 90 degrees. Letting ψ=0 and defining two radar positions at $\theta = \pi/2$ +/- $\Delta\theta/2$, then, with factoring R_{radar} out of the radical and with the assumption that $R_{radar} >> r$, (4-41) becomes

$$\Delta R(\theta) = R_{radar}\sqrt{1 - \frac{2r}{R_{radar}}\cos(\frac{\pi}{2} + \frac{\Delta\theta}{2})} - R_{radar}\sqrt{1 - \frac{2r}{R_{radar}}\cos(\frac{\pi}{2} - \frac{\Delta\theta}{2})} \tag{4-42}$$

Making the substitution

$$x = \frac{2r}{R_{radar}} \cos\left(\frac{\pi}{2} \pm \frac{\Delta\theta}{2}\right) \tag{4-43}$$

and since the cosine argument is bound to the interval [0, 2π], and $r << R_{radar}$ then $|x|<1$ and the Taylor expansion for the square root can be invoked. The first three terms are retained due to diminishing magnitude of higher order terms. The first term in (4-42) is

$$\sqrt{1-x} = 1 + \frac{1}{2}\frac{2r}{R_{radar}} \cos\left(\frac{\pi}{2} + \frac{\Delta\theta}{2}\right) - \frac{1}{8}\left(\frac{2r}{R_{radar}} \cos\left(\frac{\pi}{2} + \frac{\Delta\theta}{2}\right)\right)^2 \cdots \tag{4-44}$$

Some manipulation (cosine sum angle substitution and invoking the small angle approximation for the sine term resulting) gives

$$\Delta R(\theta) = \left(R_{radar} + r\frac{\Delta\theta}{2} - \frac{1}{2}\frac{r^2}{R_{radar}}\left(\frac{\Delta\theta}{2}\right)^2\right) - \left(R_{radar} - r\frac{\Delta\theta}{2} - \frac{1}{2}\frac{r^2}{R_{radar}}\left(\frac{\Delta\theta}{2}\right)^2\right) \tag{4-45}$$

Equation 4-45 reduces to $\Delta R(\theta) = r\Delta\theta$. Returning to equation 4.38

$$2\pi \geq \frac{4\pi}{\lambda} r\Delta\theta \qquad \text{or} \qquad \Delta\theta \leq \frac{\lambda}{D} \tag{4-46}$$

An example of the magnitude of the ambiguous phase is shown in the point spread function in Figure 4.40. In this example sample angle spacing is parametric at 1, 2 and 4 degrees. In each case the point spread function is found at pixel positions that straddle the calculated unambiguous response limit. The single scatterer is located at (2,0), λ = 0.75 m

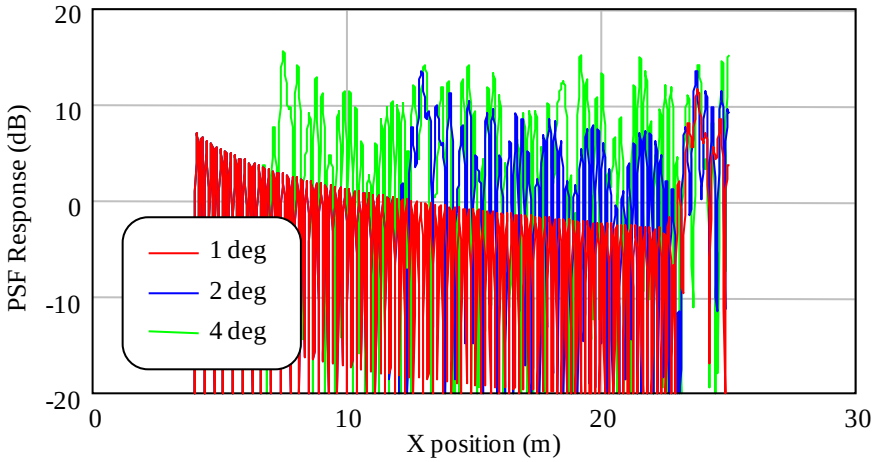

Figure 4.40. PSF Response for X-Y Plane Demonstrating Phase Ambiguous Responses vs. Sample Spacing

(400 MHz) with a sample spacing of $\lambda/50$. The predicted image/scene diameter for these three angle increments is, respectively, 21.5 m, 10.7 m and 5.4 m. The calculated/sampled positions of the peak response of the first ambiguity are 24 m, 13.2 m and 7.6 m (from Figure 4.40).

In three dimensions a scatterer in the X-Y plane in object coordinates has the response versus radial position and azimuth sample spacing, with the elevation spacing used throughout (1 deg.) that is shown in Figure 4.41. Though the form of the impulse response is slightly altered relative to that in Figure 4.40 (both Figures 4.40 and 4.41 are not normalized), the location of the onset of phase ambiguous responses is nearly the same as the 2D case.

4.7.2 Elevation sampling requirements. The expression for monostatic filtered back projection in three dimensions is (eqn. 4-21 using eqn. 4-23)

$$g(r,\psi,\eta) = \int_0^{2\pi}\int_0^{\pi/2} \cos(\theta) \int_{-\infty}^{\infty} G_{\theta,\phi}(\rho)\rho^2 e^{-j2\pi\rho(\sqrt{R_{radar}{}^2+r^2-2rR_{radar}\kappa})} d\rho d\phi d\theta \qquad (4\text{-}47)$$

where $\kappa = \cos(\theta)\cos(\eta)\cos(\phi-\psi)+\sin(\eta)\sin(\theta)$ and recalling that there was a change of variable definition in transitioning from the 2D to the 3D geometry. In the elevation

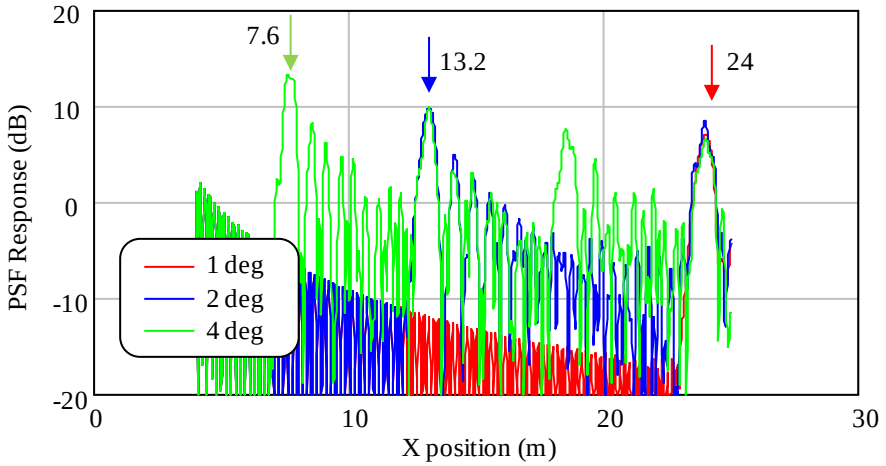

Figure 4.41. PSF Response in X-Y plane with 3D Aperture, Sample Spacing in Azimuth as Parameter

dimension we constrain the target to the Z axis and again determine the angular step size that results in the path length difference exceeding a wavelength (two-way).

Again we are interested in determining the spacing in elevation sample points before the image is perturbed by phase ambiguous responses. From a usage perspective this is a slightly softer dimension since, in a remote sensing context, the elevation extent of the scene is expected to be generally much less than the horizontal extent. Using the range term from the exponent in (4-47) and with the Dirac delta point scatterer, as used throughout, we define

$$R_2 = \sqrt{{R_{radar}}^2 + r^2 - 2rR_{radar}(\cos(\theta_2)\cos(\eta)\cos(\phi-\psi) + \sin(\eta)\sin(\theta_2))} \quad (4\text{-}48)$$

with R_1 similarly defined. By confining the scatterer (or test voxel) to the Z axis $r=z$, $\eta=\pi/2$, and $\psi=0$ and the range difference again by $\Delta R_\theta = R_2 - R_1$. With this R_2 becomes

$$R_2 = \sqrt{{R_{radar}}^2 + z^2 - 2zR_{radar}\sin(\theta_2)}. \quad (4\text{-}49)$$

Factoring the R_{radar} term and making the assumption that $z<R_{radar}$ then gives

$$R_2 = R_{radar}\sqrt{1 - \frac{2z}{R_{radar}}\sin(\theta_2)}. \quad (4\text{-}50)$$

Making the same substitution and using the series expansion as in eqn. 4-44 and letting $\theta_1=0$, $\theta_2=\Delta\theta$ (a difference from the azimuthal or 2D case because of the physical limits on the aperture) then gives

$$R_1 - R_2 = R_{radar} - R_{radar} + z\Delta\theta. \quad (4\text{-}51)$$

produces, using equation 4.38, the same result as in the 2D portion $z_{max}=\lambda/(2\Delta\theta)$. Exercising eqn. 4-47 over a range of z with a point scatterer located at (0, 0, 2) gives the result shown in Figure 4.42. The peak responses (7.85 m/4 deg, 13.2 m/2 deg, 24m/1 deg) closely match the 2D result.

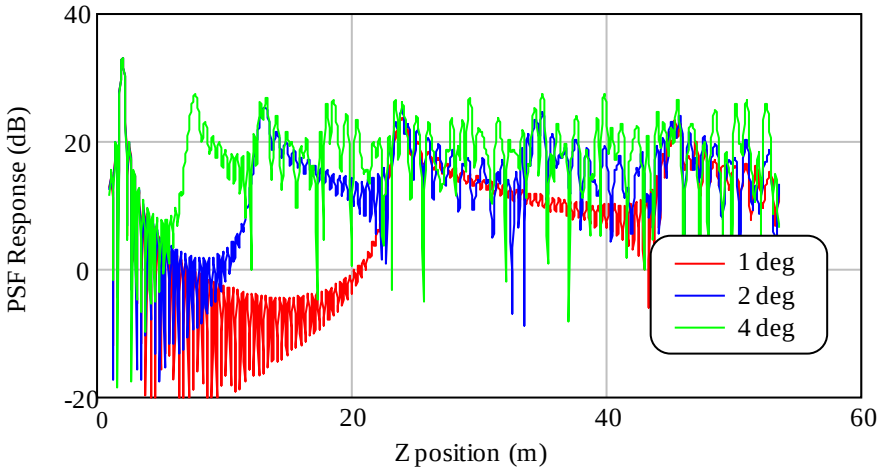

Figure 4.42. PSF Response Along Z axis as a Function of Sample Spacing in Elevation

4.8 Combining Space (Aperture Shape) and Waveform.

We have demonstrated that the resolution of the tomographic aperture is largely established by the illuminating frequency with no significant contribution resulting from bandwidth over the range explored. We have also demonstrated the effect of increasing bandwidth on the properties of the point spread function; specifically the spatial extent of the sidelobe structure (in the case of simple pulsed waveforms, Figures 4.21 and 4.24) and/or the rate of roll off of the sidelobe peaks (LFM waveform, Figure 4.27). The truncation of the spatial extent of the envelope-modulated sinusoid is a consequence of the physical length of the pulse, while the sidelobe roll-off is the result of the complex interference of a greater number of frequency terms in the inverse transform integral in back projection.

Reflection tomography is generally characterized by the torus-shaped spatial spectrum, centered at DC in two dimensional monostatic tomography, with the obvious extension to three dimensions. This indicates bandlimited operation when constrained by hardware, environmental and regulatory realities. Mapping a scene to a partial aperture then to full aperture is conceptually shown in Figure 4.43, with a notional scene in Figure 4.43a, a SAR or partial tomographic aperture in the second panel with the full, tomographic

spectrum illustrated in Figure 4.43c. We observed similar behavior to that depicted in Figure 4.43c for bistatic two-dimensional apertures with the center of the receive aperture in a pseudomonostatic relationship with the illuminating plane wave and with the physical receive aperture at the beginning of this section.

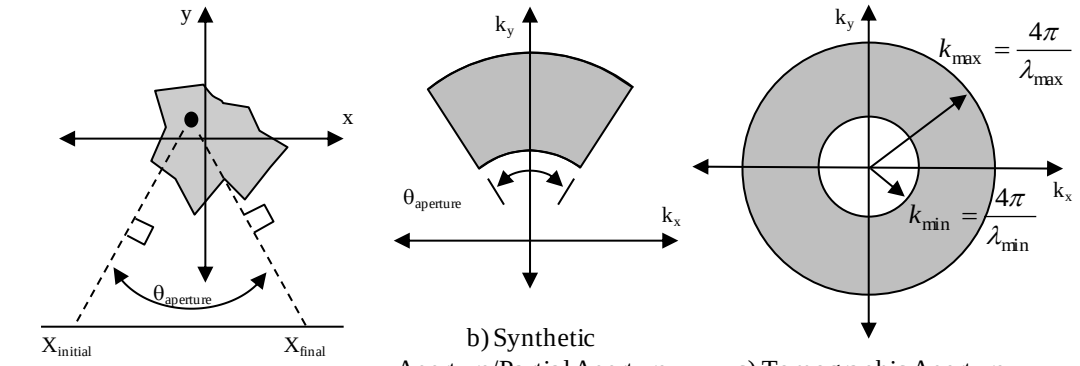

a) Synthetic Aperture – Object Space

b) Synthetic Aperture/Partial Aperture – Fourier (k-) Space

c) Tomographic Aperture – Fourier (k-) Space

Figure 4.43. Spatial Frequency Representation of Two Dimensional Apertures

We briefly explore the limiting case where the spatial spectrum is filled; the general case for transmission tomography that is not realized in bandlimited, reflection tomography. In doing so we ignore realities on ultrawideband (including DC) signal radiation (and reception). Conceptualizing an impulse-like waveform, yielding a uniform spectrum, spanning $f_{min} = 0$ to f_{max}, and sampling over a two dimensional monostatic aperture creates a disk-shaped spatial spectrum representing an isotropic scatterer located at the scene origin which we assume is of unity magnitude. We define the point spread function as in Section 3.2, starting with equation 3-43;

$$g(x,y) = \int_{-\infty}^{\infty}\int_{-\infty}^{\infty} G(f_x, f_y) e^{j\left(2\pi f_x x + 2\pi f_y y\right)} df_x df_y. \tag{4-52}$$

With change of variable to polar coordinates $x=r\cos(\phi)$ and $y=r\sin(\phi)$ gives

$$g(r,\phi) = \int_{-\infty}^{\infty}\int_{-\infty}^{\infty} G(f_x, f_y) e^{j\left(2\pi r\cos(\phi) f_x + 2\pi r\sin(\phi) f_y\right)} df_x df_y \tag{4-53}$$

A second change of the integrand variables $f_x=\rho\cos(\theta)$ and $f_y=\rho\sin(\theta)$,$\rho=2/\lambda$, and with Jacobian $|\rho| d\kappa d\theta$ results in

$$g(r,\phi) = \int_0^{2\pi\rho_m}\int_0 G(\rho\cos(\theta),\rho\sin(\theta))e^{j(2\pi r\cos(\phi)k\cos(\theta)+2\pi r\sin(\phi)k\sin(\theta))}|\rho|d\rho d\theta \qquad (4\text{-}54)$$

and where the integral limits reflect the radius of the disk (maximum frequency, ρ_m) and full angular range integration. Since ρ is by definition positive the absolute value is ignored for the remainder of the derivation. Also since we are assuming a disk of constant amplitude $G(\rho cos(\theta),\rho sin(\theta)) = 1$. The cosine angle difference identity gives the final form

$$g(r,\phi) = \int_0^{2\pi\rho_m}\int_0 e^{j(2\pi\rho r\cos(\theta-\phi))}\rho dk d\theta \qquad (4\text{-}55)$$

Evaluating the inner integral results in

$$g(r,\phi) = \int_0^{2\pi}\left\{\frac{e^{\alpha\rho_m}(\rho_m\alpha-1)+1}{\alpha^2}\right\}d\theta \qquad (4\text{-}56)$$

in which the substitution $\alpha = jr^2cos^2(\theta-\phi)$ was made. Following the approach suggested[2] taking the derivative of the integrand with respect to ρ_m and with simplification

$$\frac{d(g(r,\phi))}{d\rho_m} = \rho_m\int_0^{2\pi}\left\{e^{jrk_m\cos(\psi)}\right\}d\psi = 2\pi\rho_m J_0(2\pi r\rho_m) \qquad (4\text{-}57)$$

where the change of variable $\psi=\phi-\theta$, $d\psi=d\theta$ was made. This result derives from the integral form of the Bessel function (Bessel's first integral) of order 0. The solution is given for the derivative of the scene function. If we let $z = 2\pi r\rho_m$ and define a chain rule differentiator as

$$\frac{d}{d\rho} = \frac{d}{dz}\frac{dz}{d\rho} = 2\pi r\frac{d}{dz} \quad \text{so that} \quad 2\pi r\frac{dg(r,\phi)}{dz} = \frac{z}{r}J_0(z) \qquad (4\text{-}58)$$

Using the identity

$$\frac{d}{dz}(zJ_1(z)) = zJ_0(z) \qquad (4\text{-}59)$$

resulting in

[2] https://adriftjustoffthecoast.wordpress.com/2013/06/06/2d-fourier-transform-of-the-unit-disk/

$$g(r,\phi) = \frac{\rho_m}{r} J_1(2\pi\rho_m r) \tag{4-60}$$

Equation 4-60 is evaluated and compared to the reconstruction for a CW signal of the same upper frequency (ρ_m = 15, λ =0.419m) with unanticipated results, depicted in Figure 4.44. It was expected that sidelobe levels would taper off more rapidly (without the incorporation of a taper, the literature associates window functions with this class of spatial spectra, *cf* [86] and [96] as examples). What was not expected was the slight reduction in resolution in the IPR mainlobe given the frequency range. Also, evaluated, but not presented, is the conventional application of a window function, resulting in the expected impulse response sidelobe levels, another benefit.

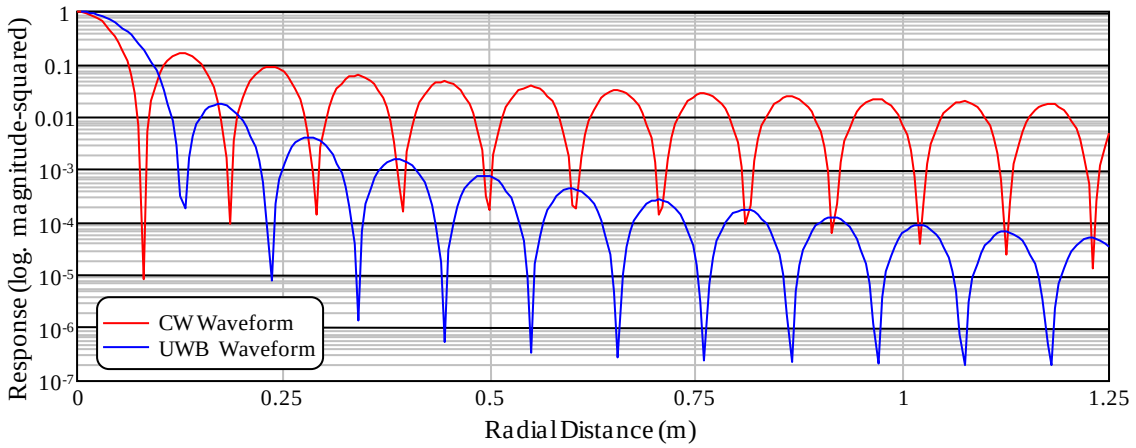

Figure 4.44. Radial Cuts, Monostatic Fully-filled Spatial Spectrum and CW Spectrum

Image quality is the rationale behind this examination of the "limiting case" spatial spectrum. The value of filling k-space in this manner is clearly evident in the improved sidelobe structure which translates into higher contrast images. However the waveforms which would provide such ultra wideband capabilities are problematic for the reasons noted: regulatory, RF hardware and antennas (physical size and efficiency), not to mention sensitivity. One can generate monocycle L-band waveforms with 100% bandwidth [97] but with concomitantly low energy.

In Section 4.1 we employed a method of mapping geometry/sampling aperture into spatial spectrum ([57]) which suggests another alternative: the combination of waveform

and collection aperture, a form of space-frequency trajectory, to fill *k*-space in like manner to the disk spectrum. In the general case spatial frequency is given by

$$K(\vec{R}_{xmtr}, \vec{R}_{rcvr}, \lambda) = \frac{4\pi}{\lambda} \cos\left(\frac{\beta}{2}\right) \vec{U}_b \tag{4-61}$$

where R represents position vectors, β the bistatic bisector angle and U_b the bistatic bisector vector. In the monostatic case this simplifies to

$$K(\vec{R}, \lambda) = \begin{bmatrix} K_x \\ K_y \\ K_z \end{bmatrix} = \frac{4\pi}{\lambda} \begin{bmatrix} \cos(\phi)\cos(\theta) \\ \sin(\phi)\cos(\theta) \\ \sin(\theta) \end{bmatrix} \tag{4-62}$$

where ϕ and θ describe the radar position. An example mapping is shown in Figure 4.45 for a CW waveform. Whereas in the 2D case, the monostatic spectrum was an infinitesimally thin ring, the three dimensional spherical spiral produces a hemispherical shell of the same thickness. Evaluating (4-62) in two dimensions over all frequencies in a waveform would produce the result shown in Figure 4.43c, weighted by the waveform spectrum and assuming an isotropic scatterer.

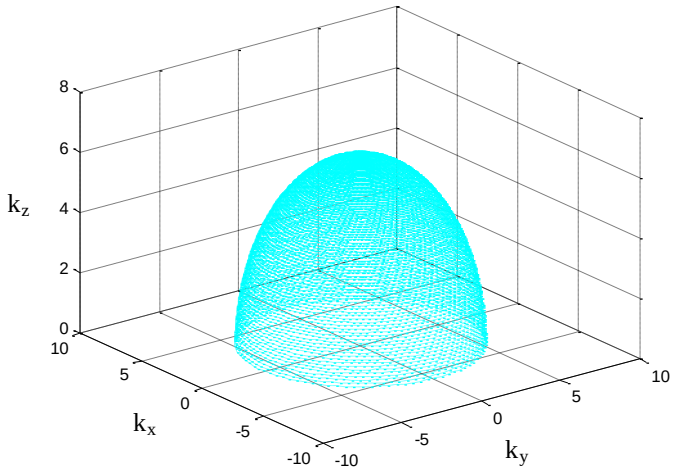

Figure 4.45. Three-Dimensional, Monostatic CW Aperture in *k*-space

The addition of the second (or more) platforms in (4-61) incorporates new degree(s) of freedom. If the two platforms move such that the β is constant over the aperture (and the scene origin is also the center of motion), then the radius in *k*-space is reduced by cos(β/2) with an attendant (equivalent) reduction in resolution (Section 4.2.2). The

bistatic *k*-space mapping for a CW waveform with β constant produces a spectrum centered on the origin in *k*-space with radius ("equivalent" frequency) decreased in proportion to the bistatic angle . This is shown in Figure 4.46a for $\beta = 45^{o}$ and 90^{o}.

If β is not constant, for example because one platform is stationary, then the aperture mapping is displaced from the origin. The orientation of the offset (angle to the center of the mapped aperture) is a function of the initial position of the stationary platform or the initial bistatic angle. Spectrum diameter is one-half, reflecting that one platform is non-moving, and the origin offset is $2\pi/\lambda$. Three examples are shown in Figure 4.46b. It is easy to visualize how increasing the number of combinations of transmitters, receivers, and frequencies will begin to fill *k*-space. This illustrates the approach of Lo Monte, *et al.* [59]. Incorporating multiple frequencies and simultaneous monostatic and bistatic operation, with only one moving platform creates the 2D spatial spectrum in Figure 4.46c, where no effort was made to isolate the individual platform-mode-frequency contributions. As can be seen, very low spatial frequencies result, even DC (k = 0), simply from geometry. Figure 4.46d illustrates the impact on the aperture form when transmitter and receiver rates are unequal, and non-zero. Two curves are shown for the case where the transmitter angle rate is 1.5 times the receiver with initial β of 45^{o} and 90^{o}.

These results suggest potential strategies to improve image quality while minimizing the spectral footprint of the collection waveform. We consider waveform trajectories in *k*-space that have reduced instantaneous bandwidths while in some manner either simultaneously or sequentially subtending a larger bandwidth cumulatively (e.g., over the aperture duration). This includes varying the geometry/collection aperture using a constant waveform (spatially invariant) and coupling waveform and position in some deterministic or random manner (spatially variant).

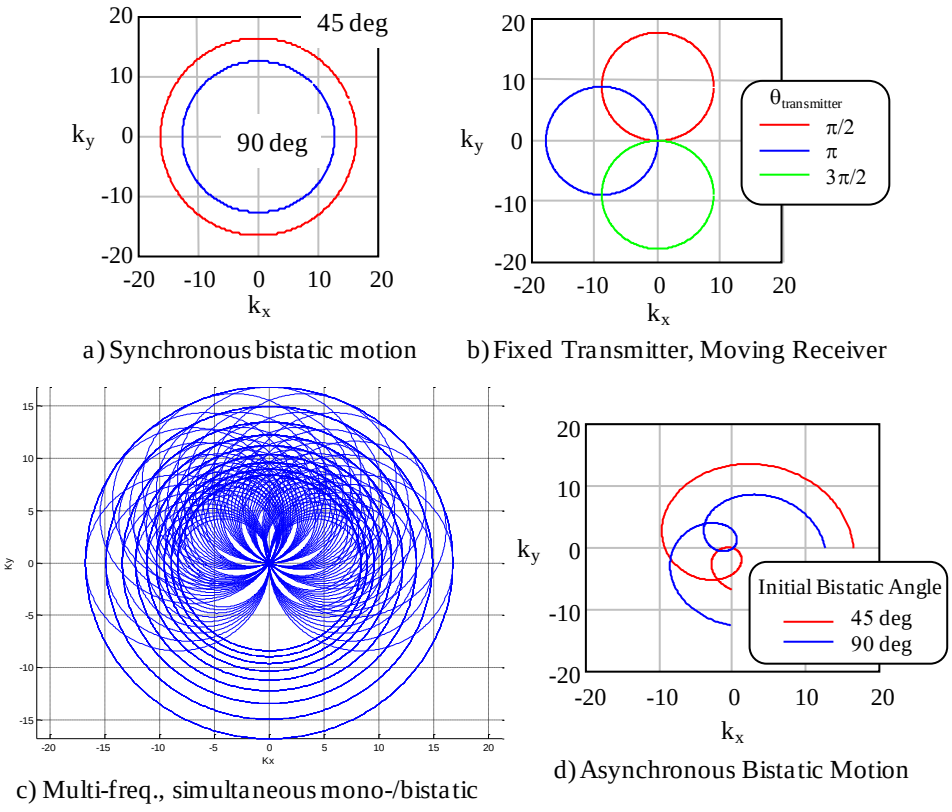

Figure 4.46. Example 2D Bistatic Apertures Mapped to *k*-space

4.8.1 Spatially invariant narrowband waveforms. In [17] the authors made a limited exploration, over two dimensional monostatic apertures, of the effects of combining images generated using multiple, orthogonal, CW waveforms collected over a full spatial aperture. The purpose was to cancel image sidelobes at one frequency using nulls generated at a second frequency, reducing sidelobe levels. The selection of tones was *ad hoc*, and the results shown against a numeric scale. The *k*-space representation for this aperture concept resembles Figure 4.46a, in two dimensions, with wavelength replacing bistatic angle as the determining factor on the aperture radius. The approach is visualized in three dimensions, using Figure 4.45, where the lower frequencies "nest" within the Fourier aperture of higher frequencies. In using CW waveforms image construction over frequency is equivalent to the coherent addition of images constructed at each frequency individually. For two dimensions and two ultra narrowband, offset frequency waveforms, and using the idealized impulse scatterer, then equation 4-3 can be written

$$\int_0^{2\pi}\int_{-\infty}^{\infty}(\delta(\rho-\rho_0)+\delta(\rho-\rho_1))|\rho|e^{\alpha\rho}\,d\rho d\theta=\int_0^{2\pi}\int_{-\infty}^{\infty}(\delta(\rho-\rho_0)|\rho|e^{\alpha\rho}\,d\rho d\theta+\int_0^{2\pi}\int_{-\infty}^{\infty}(\delta(\rho-\rho_1)|\rho|e^{\alpha\rho}\,d\rho d\theta \tag{4-62}$$

where $\rho=2/\lambda$ and $\alpha=j2\pi r(cos(\theta-\phi))$. In this approach each tone is constant over the aperture.

We extended this approach into three dimensions and over a more general frequency set to assess the image improvement using a limited set of tones. This was done by generating images over a 2:1 frequency band (400-800 MHz) in 5 MHz steps and then examining coherent combinations of 2, 3 and, in a single instance, 4 tones. The collection apertures were full (1 deg sample spacing in azimuth and elevation) monostatic hemispheres. The 2:1 frequency band was judged a sufficiently stressing upper bound for the system antenna. Image quality parameters of resolution, peak and average sidelobe level were determined. The goal was to identify the "best" combination using minimum entropy as the metric from the 4950 (2-at-a-time), 161700 (3-at-a-time), and 3.92E+06 (all cases) combinations. To facilitate the evaluations the PSF responses were computed only for cardinal axis. The work here was reported in greater detail in [95] and [98].

The results are presented in Table 4.5. The baseline, single frequency aperture image metrics are given along with the improvements realized for the best combination of frequencies from the 100 frequencies employed. These results demonstrate that a sparsely populated *k*-space does offer improved image quality relative to a single tone. Resolution most obviously benefits, dominated by the higher frequency contribution. It was hoped that a greater improvement in the elevation sidelobes might have been realized. A brief effort was made to apply a taper to the elevation integral in an effort to improve the performance, without any measureable success.

It should be noted that during this process the citation in [91] was found which was a more rigorous, two dimensional evaluation of this approach. Using the closed form 2D

Aperture	Resolution (FWHM, m)			Average SLL (dB)			Peak SLL (dB)		
	X	Y	Z	X	Y	Z	X	Y	Z
Baseline	0.156	0.156	0.306	-26	-26	-26	-13	-13	-13
Two Frequency	0.065	0.065	0.123	-33.9	-33.9	-30.6	-18.1	-18.1	-14.7
Three Frequency	0.069	0.069	0.133	-35.9	-35.9	-30.2	---	---	---

Table 4.5. 3D Monostatic Image Quality Improvement Using Multiple Narrowband Tones

solution (see eqn. 4-6) permitted the use of more tones and allowed several tone selection strategies to be evaluated. The results show significant reduction in sidelobe level. However, the spatial extent of the sidelobe response may remain problematic when imaging scenes with high dynamic range.

4.8.2 Spatially variant waveforms. Several examples are considered here; the first two are adapted from research into improving the collection time of Magnetic Resonance Imaging (MRI) images: the rosette and the spiral trajectory [67]. The technique is adapted to RF by modulation of the carrier waveform as a function of time/angle over the collection aperture. The potential for these methods is explored over a 2D monostatic-only aperture with the operating bandwidth constrained to a 2:1 wavelength band. The rosette trajectory in two dimensions is given by

$$f(\phi) = f_{\min} + 0.5(f_{\max} - f_{\min})(\cos(2\pi N_p \phi) + 1) \tag{4-63}$$

where N_p defines the number of cycles (periods) over which the full frequency range varies over the aperture, and f_{max} and f_{min} define the frequency extrema, bounding the aperture area in *k*-space (Figure 4.47a shows a 16 period rosette), and ϕ the instantaneous aperture angle which is coupled to the frequency switching. The aperture is sampled at 1 degree increments.

Unlike the MRI, the monostatic tomographic aperture with finite wavelength cannot produce the null wave number (k=0) so the RF rosette oscillates between λ_{min} and λ_{max}.

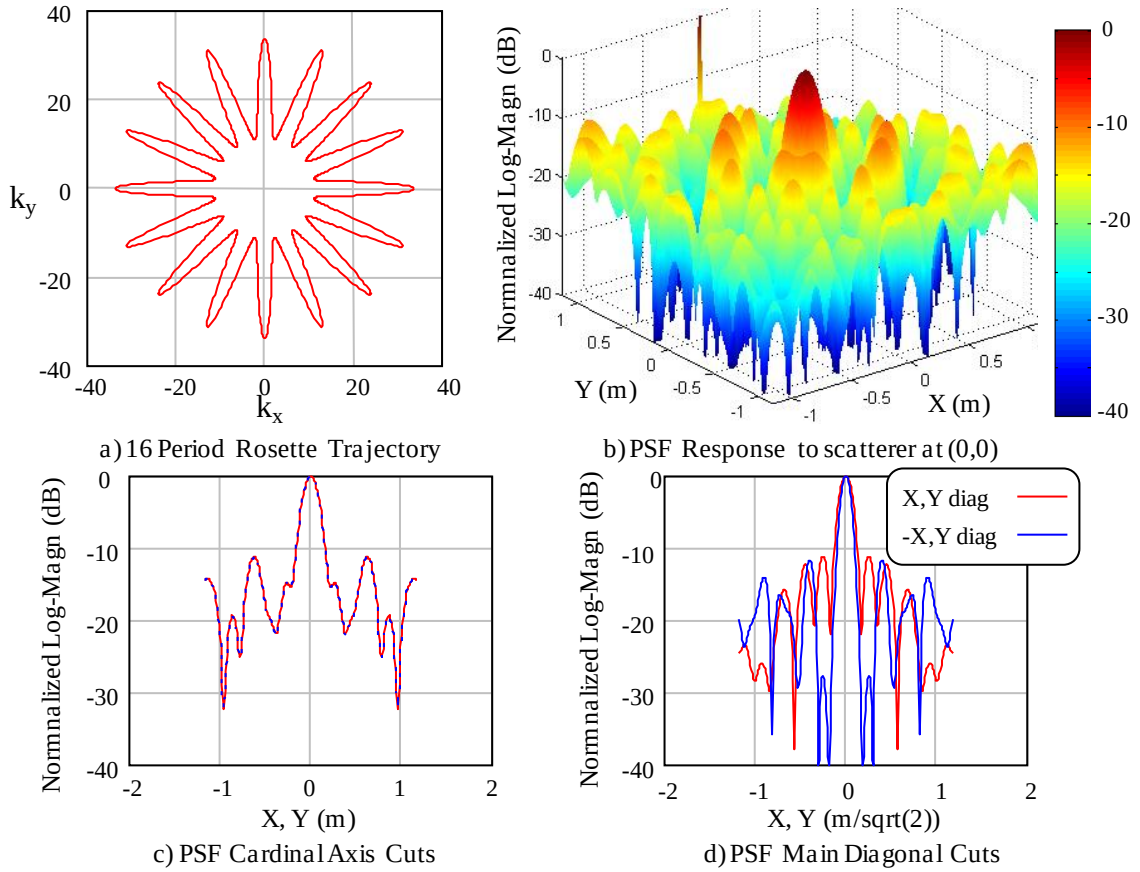

Figure 4.47. Rosette Trajectory and 2D PSF

With this waveform the instantaneous bandwidth is CW but the cumulative bandwidth over the aperture is ultrawide. The resulting PSF is shown in Figure 4.47b. Cases run with a few periods, but not shown, had quadrant-like regions of high and low sidelobes. As the number of periods increased the sidelobe level becomes more uniform, though this is a limited observation as the greatest number of periods examined was 16. Figure 4.47c and d are cuts of the PSF along cardinal and main diagonal cuts. Image metrics are listed in Table 4.6.

The relative performance of the rosette, compared to the CW waveform can be seen in Figure 4.48. Here we contrast CW with three rosette periods (4, 8, and 16 periods per orbit) in three dimensions. The left half of each plot is on an expanded horizontal linear scale to depict image artifacts resulting from the waveform while the right half gives finer detail close-in to the main response lobe. The space-frequency trajectories are constructed by repeating the number of rosette periods each elevation position, where an idealized,

hemispherical collection aperture is defined which uniformly samples in azimuth and elevation relative to the scene coordinate frame. The phasing of the rosettes is constant at each elevation position, though this is another degree of freedom for potential future study. The resolution achieved with the rosette trajectory in three dimensions relative to the CW case was degraded, as were the X-Y plane sidelobes. However, the rosette did yield an improved peak and average sidelobe level along the Z dimension. Results are summarized in 2D in Table 4.6 and in three dimensions in Table 4.7.

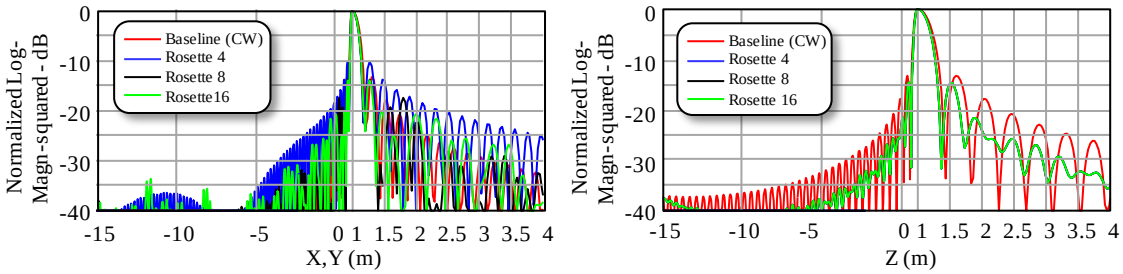

a) X,Y Axis Rosette Waveform Response b) Z Axis Rosette Waveform Response

Figure 4.48. Cardinal Axis Cuts of Rosette Space-Frequency Trajectory in Three Dimensions

The second example of space-frequency trajectory is the spiral trajectory, also from [67]. Here a series of tones, or spectral components, are continuously tuned, in parallel - representing turns around the spiral - as a function of angle. The number of simultaneous components is the degree-of-freedom. The spiral trajectory is constructed by radiating at each spatial sampling position a single pulse envelope of multiple, offset carriers. The trajectory is defined by an Archimedean spiral ($r=a+b\phi$). The spiral separation given the number of spirals (N_s) is

$$b = \frac{k_{up} - k_{low}}{2\pi N_s} \tag{4-64}$$

with $k_{up}=/cF_{max}$ and $k_{low}=c/F_{min}$. With this the k-space trajectory is, in two dimensions and i_{sp} the spiral index

$$k(\phi, i_{sp}) = k_{low} + b(2\pi i_{sp} + \phi). \tag{4-65}$$

For this investigation the waveform was not a CW, but rather a 1 MHz bandwidth (1 μsec duration), simple pulse envelope on a carrier. This is essentially a number pulses simultaneously transmitted with center frequencies a progressive value of angle. With multiple frequency offset narrowband pulses the spectrum is

$$S'_{\phi,\theta}(k,k_0)=\sum_{N_{sp}}\frac{\sin\left(\left(k-k(\phi,i_{sp})\right)R_p\right)}{(k-k(\phi,i_{sp}))R_p} \tag{4-66}$$

The return from a point scatterer at range r_0 is given, in the spatial frequency domain, by

$$S_{\phi,\theta}(k,k_0)=S'_{\phi,\theta}(k,k_0)e^{-ikr_0}. \tag{4-67}$$

Figure 4.49 is presented in the same format as for the rosette case; a) presents the trajectory in *k*- space for the lowest frequency component (of the five) and, b) the PSF presented as a surface plot. The spiral demonstrates a very nice, symmetrical PSF with sidelobe structure improved substantially over the CW case. Figure 4.49c is a radial cut, while Figure 4.49d is an extended cut along the *Y*=0 PSF axis. Here the effects of the

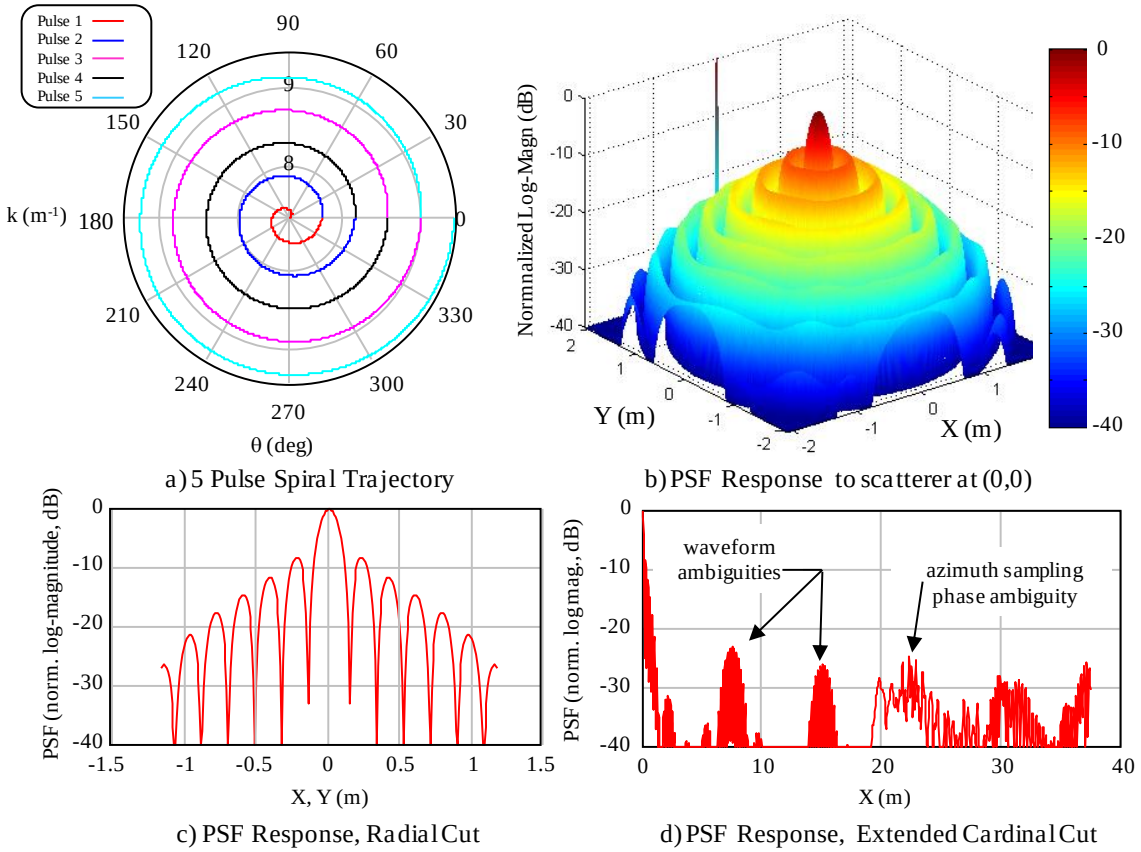

Figure 4.49. 2D Spiral Trajectory in *k*-Space and Reconstruction Results

sparse frequency aperture can be seen through the presence of the regular sidelobes. Also noted is the ambiguous phase response limit (Section 4.7). Image quality metrics are summarized in Table 4.6.

We define a third space-frequency trajectory, this of a random frequency, envelope modulated carrier. A uniform random draw is carried out at each spatial sample position. The frequency extent (total bandwidth) of the waveform set is common to the examples above. The random frequency waveform was pulsed with 1 MHz bandwidth using frequencies defined by

$$S_{\phi,\theta}(f, BW) = BWrnd(0,1) + F_{\min}. \tag{4-68}$$

The *k*-space mapping for such an aperture, in two dimensions is exemplified in Figure 4.50. This space-frequency trajectory was evaluated in three dimensions.

Aperture	Resolution (m)		ISLR (dB)	Peak SLL (dB)	Average SLL (dB)
	X	Y			
400 MHz CW	0.129	0.129	-8.4	-7.9	-15.4
Rosette (2:1 BW)	0.181	0.181	-4.0	-9.3	-17.6
Spiral (5 cycles)	0.133	0.133	-5.73	-8.1	-19.3

Table 4.6. Image Properties of Example Rosette and Spiral Apertures in Two Dimensions

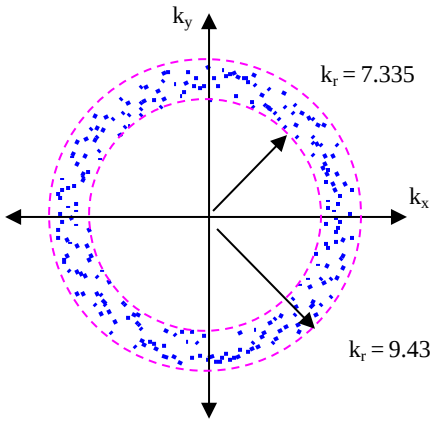

Figure 4.50. Two Dimensional Example – Random Frequency vs. Position

The random waveform and the spiral results are graphically depicted in Figure 4.51 in the same format as Figure 4.48, with the X and Y axis response plotted in Figure 4.51a and

the Z response in Figure 4.51b. These results show a much more rapid decrease in sidelobe level relative to the baseline CW waveform. This would produce a better image as the contract would improve with lower sidelobes. It was a surprising result that both the spiral and random waveform responses virtually overlay one another. As in Figure 4.48, the simulated scatterer was positioned at (1, 1, 1). Both waveforms were further explored in which the spatial analysis extent was expanded, looking at both waveform and sampling artifacts when there is no harmonic or periodic waveform dependencies.

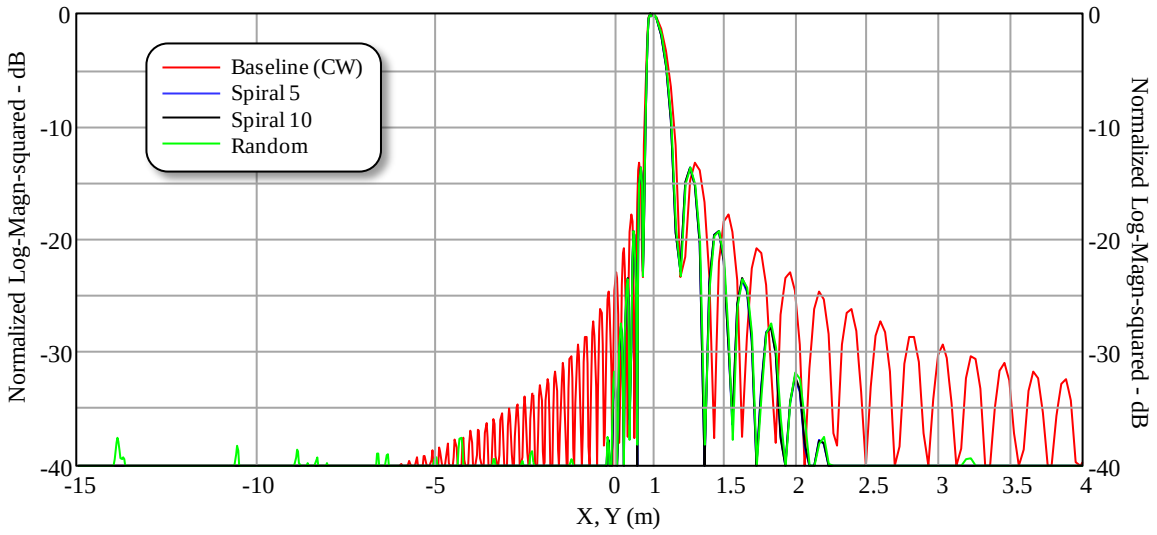

a) X, Y Principal Axis Response

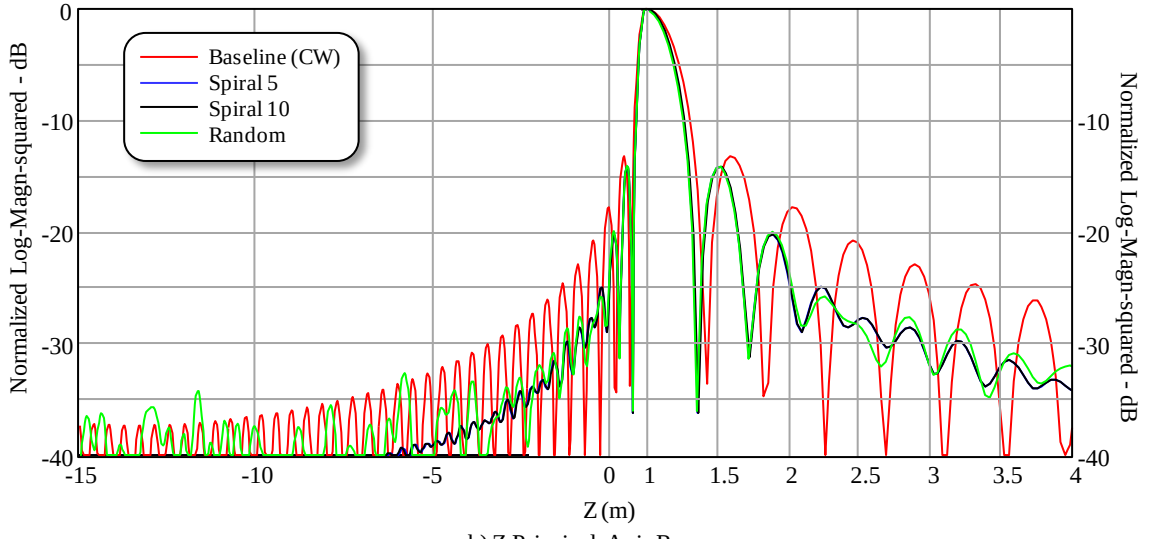

b) Z Principal Axis Response

Figure 4.51. 3D Principal Axis Cuts of Spiral and Random Space-Frequency Trajectory

The results are shown in Figure 4.52. The random space-frequency trajectory results are in Figures 4.52a and b with the spiral waveform (5 pulse frequencies) in Figures 4.52c

and d. Interestingly, the sampling phase artifact is not observed in the X-Y results for either waveform with the 1 degree sample spacing in elevation visible. Numeric results for all three space-frequency trajectory types are summarized in Table 4.7. These results were calculated from the first null out to 6 meters for the close-in sidelobe summary, and from 6 meters out to 15 meters for the far out sidelobe summary. Resolution, as can be seen in Figures 4.48 and 4.51 is largely unaffected. *Z* axis results are all very similar and, on average 2.5 to 3 dB better than the CW baseline and also similar in form to the

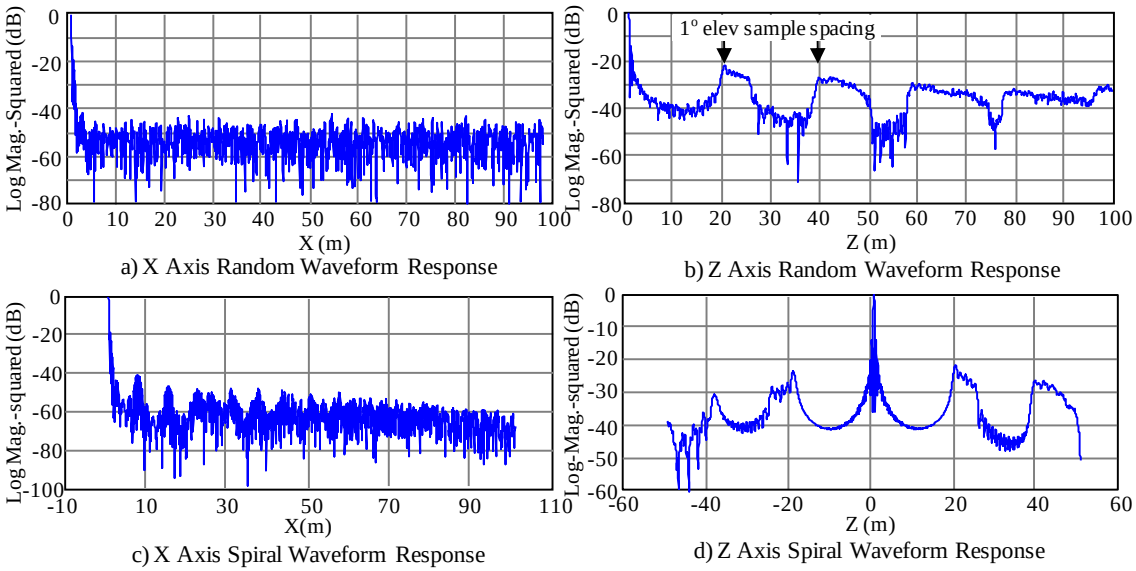

Figure 4.52. Random and Spiral Waveforms – Responses over Expanded Spatial Range

pulsed results shown in Section 4.4. The greater frequency content of the wideband pulsed waveform contributing to a smoother response with *Z* position (e.g., Figure 4.38) than the sparse waveform results in Figure 4.51. The far out sidelobes are biased high

Trajectory	X,Y Ave. SLL	Z Axis Near SLL	Z Far out SLL
Baseline (CW)	-26.68 dB	-23.85 dB	-37.58 dB
Rosette 4 Periods	-22.29 dB	-26.31 dB	-39.51 dB
Rosette 8 Periods	-27.07 dB	-26.31 dB	-39.51 dB
Rosette 16 Periods	-26.95 dB	-26.31 dB	-39.51 dB
Spiral 5 Freqs.	-28.75 dB	-26.02 dB	-39.51 dB
Spiral 10 Freqs.	-28.73 dB	-26.02 dB	-39.51 dB
Random Freq.	-28.71 dB	-25.93 dB	-38.10 dB

Table 4.7. PSF Metrics Summary of Space-Frequency Waveforms- 3D

because the calculated results were clipped at -40 dB (relative to the peak response) prior to the metric calculation. The uniformity of the *Z* axis results was unexpected, with all cases nearly overlaying.

Finally we present three dimensional views of the reconstructed point spread functions for the three space-frequency trajectories presented here. Figure 4.53 presents contour plots from the principal planes.

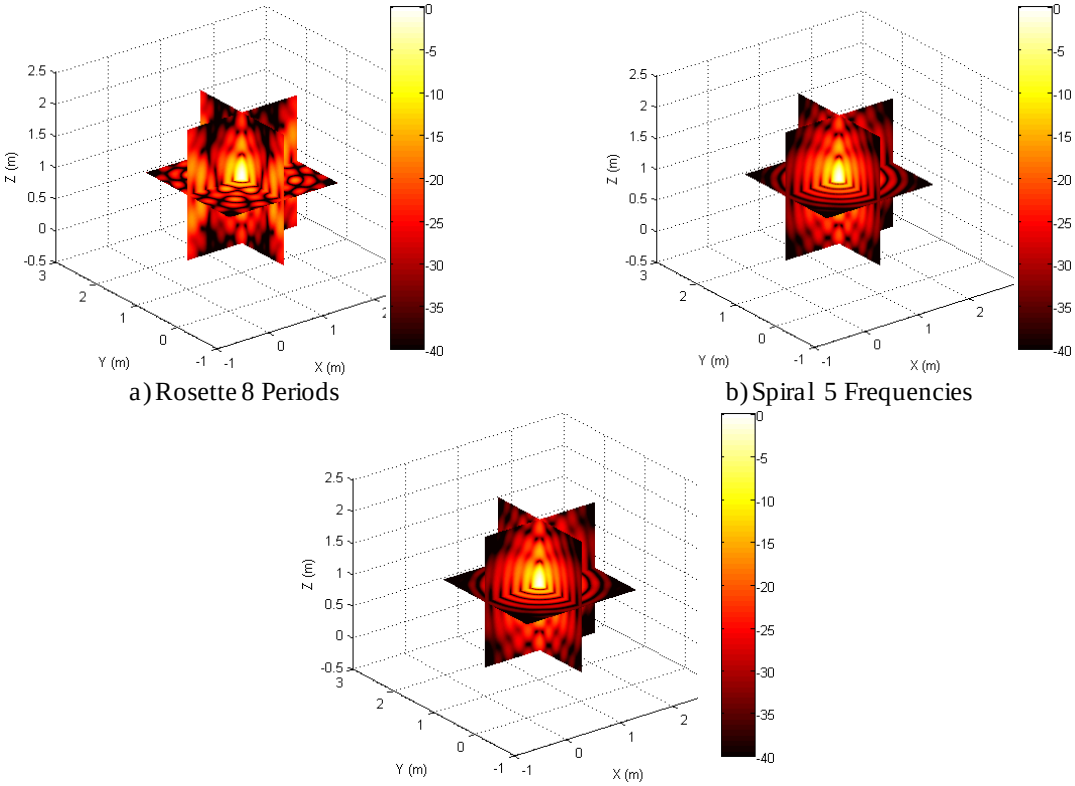

a) Rosette 8 Periods

b) Spiral 5 Frequencies

b) Random Frequency

Figure 4.53. Principal Plane Contour Visualization of Reconstructed IPR

4.9 Doppler-based Projections and Reconstruction.

Sensor configuration, probing modality and phenomenology all contribute to the form of the measured projections and hence tomographic reconstruction. In prior sections we have detailed plane wave, spherical (circular) and ellipsoidal (elliptical) projections. Others exist as well, for example fan beam projections in real beam, scanning applications [87]. In Section 4.1 we described an array technique wherein a linear array of elements which was sequentially positioned around a collection aperture. Combination of simultaneous

measurements, in this pseudo-monostatic geometry, from all elements formed the basis for back projection reconstruction. In this section we examine a variation of this method but one in which we use sequential measurements to create a synthetic aperture based on Doppler-principles.

For an elevated radar system moving relative to and illuminating the ground there is a well known relationship between the Doppler frequency of a the return from a fixed scatterer and its geometry relative to the velocity vector of the platform [99]. The clutter Doppler shift of a point scatterer, is given by

$$f_{dop} = 2\frac{V_{plat}}{\lambda}\sin\left(\phi_{squint}\right)\cos\left(\theta_{depr}\right) \tag{4-69}$$

where the squint angle (ϕ_{squint}) is measured from the normal to the velocity vector and θ_{depr} the depression angle from the local horizontal at the platform (level flight).

It is common to represent the mapping of the lines of constant Doppler (isodops) as hyperbolas [99] on a plane parallel to (for level flight) and below the moving platform. For the development of the integral (projection) contours we need to express the dependency in spatial terms: test pixel and platform positions relative to a scene-based coordinate frame. The development of Doppler-based projections is based on the geometry in Figure 4.54. The geometry is presented in two dimensions and is readily

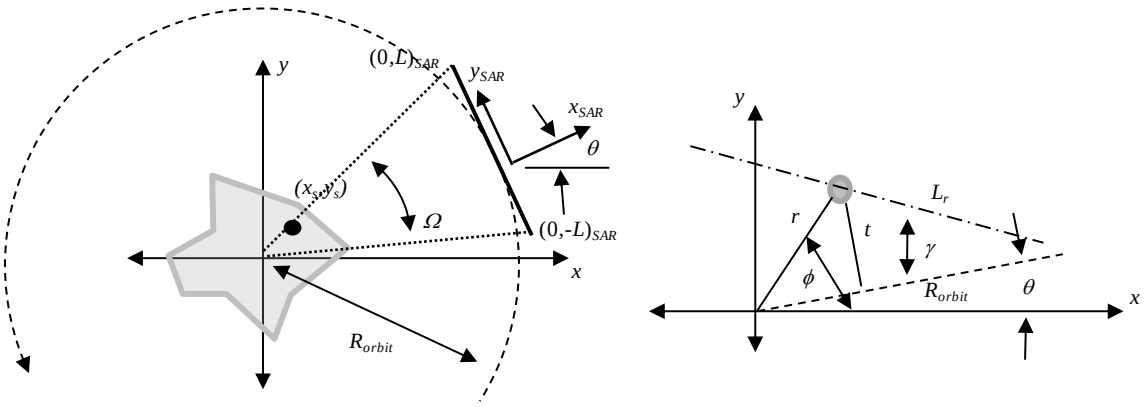

a) Tomographic and Subaperture Geometry b) SAR Fan Beam Equivalent Geometry

Figure 4.54. Analysis Geometry for Doppler-based Projections

extensible to three dimensions. Both scene-based and platform centered coordinate systems are shown with elements identified by subscript. In the left hand drawing (Figure 4.54a) both the scene geometry and SAR geometry are shown. The SAR geometry is rotated by angle θ with respect to x, representing the angle to the midpoint of the synthetic aperture. The synthetic aperture angle is denoted Ω: as distinct from the tomographic aperture angle of 2π. Figure 4.54b defines the tomographic variables: L_r is the distance from radar to point (x_s, y_s) which is defined by (r, ϕ) in scene-based polar coordinates, and γ the angle between the synthetic aperture boresight and (x_s, y_s). The variable t represents the normal from the normal to the synthetic aperture, passing through scene center. The tomographic aperture therefore contains a series of measurements representing the outputs from SAR-based subapertures.

Beginning with the two-dimensional case ($\phi_{el} = 0$), we require the projection to be expressed in terms of the scene coordinate frame. Writing the azimuth angle in SAR coordinates gives.

$$f_{dop} = 2\frac{V_{plat}}{\lambda}\sin\left(\tan^{-1}\left(\frac{y_{SAR}}{x_{SAR}}\right)\right) \tag{4-69}$$

If the position of the center point to a specific synthetic subaperture in scene coordinates is (x_0, y_0) then we can find the SAR frame coordinates (x_{SAR}, y_{SAR}) of a point in the scene (x_s, y_s) by

$$\begin{pmatrix} x_{SAR} \\ y_{SAR} \end{pmatrix} = R(\theta)\left[\begin{pmatrix} x_s \\ y_s \end{pmatrix} - \begin{pmatrix} x_0 \\ y_0 \end{pmatrix}\right] \tag{4-70}$$

where $R(\theta)$ is a rotation matrix, with as θ defined in Figure 4.54. Consistent with back projection filtering (4-70) is converted to polar coordinates with the substitutions (x_0,y_0)=($R_{orbit}\cos(\theta)$, $R_{orbit}\sin(\theta)$) and (x_s, y_s)=(r$\cos(\phi)$, $rsin(\phi)$). With these substitutions and some algebra (4-70) becomes

$$\begin{pmatrix} x_{SAR} \\ y_{SAR} \end{pmatrix} = \begin{bmatrix} r\cos(\phi-\theta) - R_{orbit} \\ r\sin(\phi-\theta) \end{bmatrix} \tag{4-71}$$

With (4-71) then (4-69) becomes

$$f_{dop} = 2\frac{V_{plat}}{\lambda}\sin(\gamma) \tag{4-72}$$

where γ = atan($r$sin(ϕ–θ)/($r$cos(ϕ–θ)-R_{orbit}). Figure 4.55 was created from (4-72) and demonstrates that the points of constant Doppler are, in two dimensions, linear, radiating as spokes relative to the platform over the scene. Each color represents a different cross range resolution cell based on the coherent dwell. When performing Doppler processing, the essence of SAR processing, spatially unresolved points of constant Doppler combine in a single cross range response. The ensemble of filters for a subaperture produces the Doppler-based projection. This is indicated by the single, unweighted filter response overlaid on Figure 4.55.

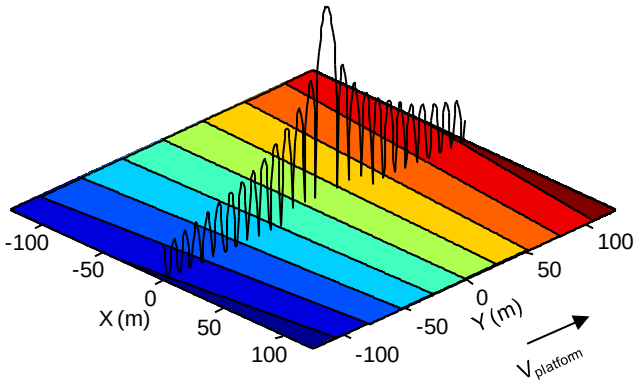

Figure 4.55. Line Integral/Projection Shape for Doppler-based Sampling

The equation for the integration contour that describes the locus of points of constant Doppler is realized directly from (4-72), or

$$t = L_r\sin(\gamma) \tag{4-73}$$

where L_r is defined as in Figure 4.54 and γ from (4-72). Because the loci of constant Doppler are dependent on angle relative to the SAR subaperture midpoint, the rays are divergent. Thus this reflection geometry also parallels that of the fan beam reconstruction problem [87].

The signal model follows from Soumekh [100]. Referring to Figure 4.54a we have defined a local, Cartesian, SAR coordinate frame relative to the scene coordinate frame. The SAR frame has origin located on the collection aperture with y_{SAR} tangent to the circular path, positively oriented, as shown. We define K uniformly spaced (equiangular relative to scene coordinates) sample points along the circular motion segment which are grouped in sets of n corresponding to a specific subaperture. The total angle subtended by the SAR aperture is Ω. The local SAR frame origin is at angle θ with respect to the scene coordinate frame and represents the midpoint of the subaperture midpoint.

The range as a function of time to a specific scatterer at (x_s, y_s) in scene coordinates, after rotation into SAR coordinates (x_{SAR}, y_{SAR}) and motion compensation to the line representing the linear SAR subaperture (Figure 4.54a) is

$$R_n = \sqrt{(x_{SAR})^2 + (y_{SAR} - u_n)^2} \tag{4-74}$$

where u_n is the radar position along the subaperture ($-0.5L \leq u_n \leq 0.5L$). The geometry is defined such that the scatterer position is at constant x_{SAR} position over the synthetic aperture. Equiangular sampling projects onto the linear aperture in this geometry with a maximum difference of 0.18 μrad; receive data is resampled to uniform along track spacing, consistent with [100]. The scattered signal is then

$$s_n{}^{\theta}(t,\omega) = \exp(-j\omega_0 t)\sigma \exp\left(-j2k_0\left(\sqrt{(x_{SAR})^2 + (y_{SAR} - u_n)^2}\right)\right) \tag{4-75}$$

where σ is the scatterer cross section (dropped in what follows for convenience), ω_0 the carrier frequency and k_0 the associated wave number. Taking the forward transform with respect to the along track dimension of (4-75) after down conversion to baseband gives

$$S_n{}^{\theta}(\omega, k_u) = \int_{-L}^{L} s_n{}^{\theta}(\omega, k_u) e^{-jk_u u} du \tag{4-76}$$

with $2L$ the length of the subaperture. This yields [100 page 68]

$$S_n^{\theta}(\omega, k_u) = \frac{e^{-j\pi/4}}{\sqrt{4k_0{}^2 - k_u{}^2}} e^{-j\left(\sqrt{4k_0{}^2 - k_u{}^2}\, x_{SAR} - k_u y_{SAR}\right)} \tag{4-77}$$

The nonzero range of k_u for a specific point scatterer in (4-77) is

$$k_u \in \left[2k_0 \sin\left(\tan^{-1}\left(\frac{y_{SAR} - u_0}{x_{SAR}} \right) \right), 2k_0 \sin\left(\tan^{-1}\left(\frac{y_{SAR} - u_n}{x_{SAR}} \right) \right) \right] \tag{4-78}$$

whereas the range of k_u is defined by the scene size (here a 100 m radial distance is applied) so that $\min(k_u) = 2k_0 \sin(\tan^{-1}(R_{scene}/R_{orbit}))$.

Focusing occurs relative to scene center. The signal model contains an along line of sight from subaperture center to scene center term (independent of position along the linear subaperture) wherein the projections reconstruct along *t*, normal to the radial. This term is the projection of x_{SAR} onto the radial and is a function of subaperture angle (θ).

$$R_{\theta}(k_u) = e^{-j\left(\sqrt{4k_0{}^2 - k_u{}^2}\, x_p\right)} \tag{4-79}$$

In equation 4-79 the term x_p represents the *x* position in SAR subaperture coordinates of the pixel under reconstruction. Reconstruction is performed using (4-7) with the integral contour *t* from (4-73). For each subaperture the complex conjugate of (4-79) is multiplied with (4-77) before the back projecting (inner integral) is evaluated.

The specific case evaluated employed an orbit radius of 1000 m and platform speed of 25 m/sec. The 2 m cross range resolution required an aperture time of 7.45 sec (a single orbit would require ~253 seconds) at the 400 MHz frequency used. The sample rate was 266.845 Hz resulting in 2000 along track sample points, corresponding to an aperture length of 187.375 m. Subapertures were formed at 1 degree intervals; an equivalent arc length of 159.155 m, so a slight overlap of samples between adjacent subarrays was employed. The wavenumber range used was based on a scene size of $\pm$ 100 m with the

isotropic scatterer located at (25, 1) in scene coordinates. Sample points were spaced $\lambda/20$ for a smoothly reconstructed profile.

Doppler-based reconstructions along the scene cardinal axes, passing through the scatterer position are shown in Figure 4.56. Overlaid on the X and Y axis cuts is the closed form result for the 2D CW aperture. We see good agreement, with a slight offset of the sidelobe peaks relative to the Bessel function result.

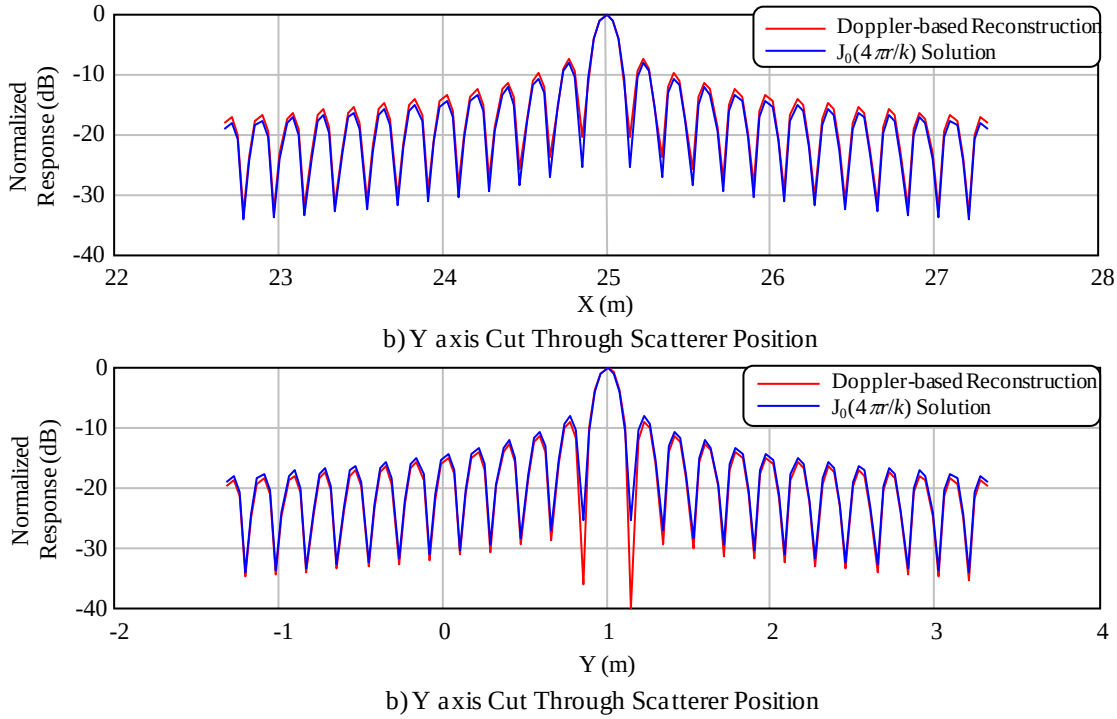

Figure 4.56. 2D Aperture Reconstruction using Doppler-based Projections

Note that the derivation and results shown in this section correct an error that was included in the paper presented in [101]. The error used an incorrect expression for the forward transformed phase history; significantly under-predicting the resolution.

Chapter 5

Digital Broadcast Signals as Bistatic Illuminators for Tomography

5.0 Introduction.

In the tomography development in earlier sections the analysis specifically addressed operation with radar waveforms known *a priori*; whether monostatic or bistatic. These "for-purpose" waveforms were pulsed and continuous wave, and with or without the additional modulations commonly used to increase waveform energy (via pulse duration) without sacrificing bandwidth. In Section 4 we demonstrated the use of ensembles of discrete tones, Doppler-based projections, and coupling of waveform with aperture geometry to fill in *k*-space such that an improved point spread function, *e.g.*, lower, spatially-constrained sidelobe levels, could result while maintaining resolution as the main figure-of-merit. Here we extend the tomography application from controlled waveforms to exploiting emitters-of-opportunity which generate modulated, continuous wave signals which are not known *a priori* (except for class descriptions) and the additional considerations associated therein.

Significant active research into bistatic radar applications has demonstrated the exploitability of high power commercial transmitters (digital television and digital broadcast radio) for surveillance. Transmitters are available in quantity, are relatively widely dispersed, use stable clocks for generating the signal(s), and exhibit high ERP.

These features allow radar research with affordable, receive-only electronics such as the software-defined radio/radar (SDR). The preponderance of the work has been performed against moving targets from stationary receivers using terrestrial sources. *e.g.*, [23]-[25] and [27]-[29]. However, imaging has been demonstrated using airborne receiver and ground based transmitter in [64] and spaceborne emitters in a synthetic aperture context with a stationary receiver [102], [103] and [104]. ISAR imaging research has also been conducted; fixed transmitter and receiver as described in [105]. Example programs which employed an airborne (moving) receiver are [62] where clutter measurements based on digital broadcast radio were obtained, and [106] where detection of moving targets from an airborne platform was investigated with a multi-channel receive system. SAR imaging using an airborne receiver and ground based digital television was reported in [64] and [65].

A key attribute of this type of bistatic radar, and in distinct contrast to the prior chapters where a known, pulsed waveform was employed, is the necessity of creating a template of the transmitted waveform (which is not known *a priori*), measured along the bistatic baseline via a reference or auxiliary antenna. The signal from the direct path is cross correlated with the signal(s) received from the scattered or bistatic path via the main antenna in order to develop a measure of scatterer delay: the range difference. This process, often referred to as ambiguity function processing, explored in detail in a later section, is analogous to a pulse compression process as the waveform bandwidth is realized in a resolution sense, there is coherent processing gain, and the effects of platform motion during the "pulse" necessitate consideration and the narrowband assumption can begin to weaken.

This chapter covers the specifics of the digital television waveform used in the United States as applied to bistatic radar in general and bistatic three-dimensional tomography specifically. Because of the random nature of the terrestrial digital television signal, the

random nature a combination of program encoding and the channel format/modulation; an analytic waveform model is first described which is used for the development of processing algorithms and image reconstruction evaluations to assess performance potential. The chapter then applies the narrowband approximation and the move-stop-move model to develop a signal model which is reconstructed using filtered back projection. We follow this with the exact solution taking into account platform motion to allow longer waveforms or higher platform speeds which violate the narrowband assumption. We finish with the design, development, test, and analysis of the experimental radar used in flight test that demonstrates the principles developed herein.

5.1 DVB-T US Domestic Protocols (HDTV).

The standard modulation for digital television in the United States (HDTV – High Definition Television) is termed 8VSB which was defined by the Advanced Television Systems Committee (ATSC). 8VSB is an amplitude modulation scheme using 8-level vestigial sideband, digital modulation [107], [108], and [109]. The total modulation scheme consists of a base transport packet of 187 bytes which are randomized using a pseudo-random bit stream to produce a noise-like spectrum and reduce interference to NTSC channels. This step is followed by forward error correction and application of Reed-Solomon encoding. This produces a 20 byte data block that is appended to the end of the 187 data bytes. Trellis encoding (8 states) follows then the segment synch and frame synch multiplexing; segment synch replaces the original MPEG-2 synch byte which is removed after the synchronizer. The pilot tone is inserted by adding a fixed offset to the Trellis encoder states, followed by vestigial sideband modulation (partial suppression of one sideband), up conversion, power amplification and filtering. There is a closed loop feedback function which can monitor the radiated signal. This allows developing pre-corrections to compensate for the transmission process. The 8VSB modulation carries a symbol rate of 10.76 Mbaud, a gross bit rate of 32 Mb/s, and a net

bit rate of 19.39 Mb/s of usable data. The use of forward error correction codes enable the lower net bit rate and results in the nominal spectrum with a data bandwidth of 5.38 MHz.

The structure of the waveform (magnitude) spectrum is depicted in Figure 5.1a, on a linear scale. Key features are the flat response over the central 4.76 MHz of the 6 MHz channel allocation and the presence of the pilot tone at 2.691 MHz below the center of the channel allocation, 0.309441 MHz from the channel lower (allocation) bound. There are three variations of the waveform spectrum dictated by an emissions mask: a primary commercial version (full service transmission emitter limits), intended for application to high power commercial operators. The second (stringent emission limits) and third (simple emission limits) have identical shape in the passband, differing only in the out-of-band sidelobe levels and shape, and are applied to low power repeaters which complement the full service transmitters to overcome line-of-sight masking. The structure of the full emission mask is shown in Figure 5.1b [109], with the sideband emissions masks, stringent and simple, overlaid (less restrictive sidebands). Emission amplitudes are referenced to a 500 kHz bandwidth and must be less than the emission levels indicated. The regulatory metric for signal level is dB relative to total allocated channel power or dB_{DTV}. The work herein is concerned exclusively with the full service mask.

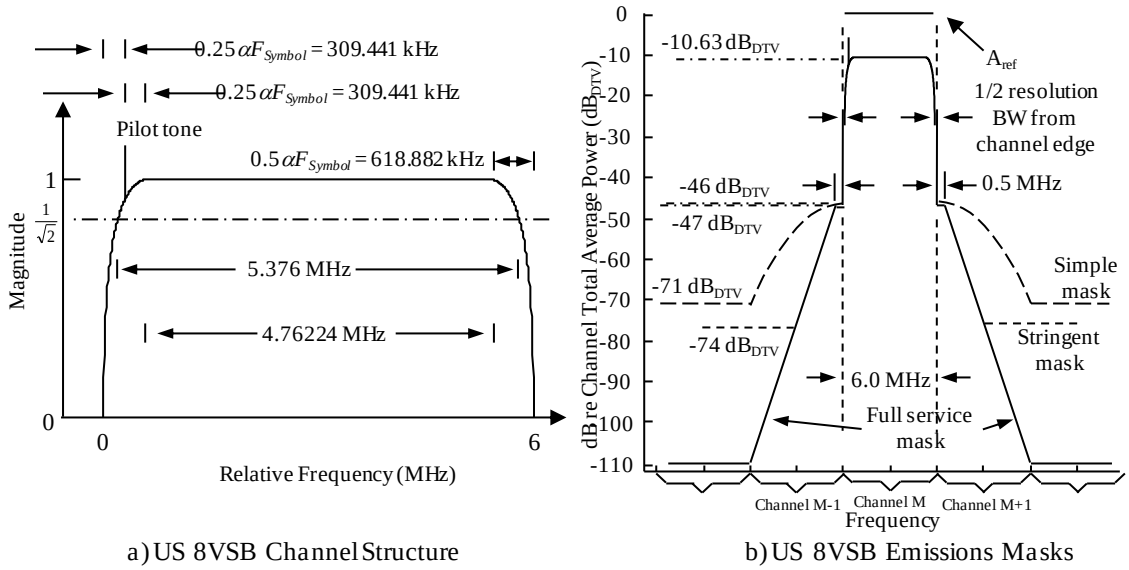

a) US 8VSB Channel Structure b) US 8VSB Emissions Masks

Figure 5.1. U. S. 8VSB (HDTV) Waveform Spectrum and Mask

An example HDTV data set is presented in Figure 5.2. Figure 5.2a is a single power spectrum for an 80 μsec aperture time (12.5 kHz resolution); while a waterfall spectrum representing a 0.5 second data segment composed of 50,000 contiguous sample windows, each also 80 μsec long, is shown in Figure 5.2b. The signal examples demonstrate a temporally uniform, as well as spectrally white, signal (excepting the presence of the pilot tone). The time interval was selected randomly.

In the time domain the complex voltage signal has clear Gaussian tendencies as indicated by the amplitude and phase histograms in Figure 5.3. The data set, burst duration and

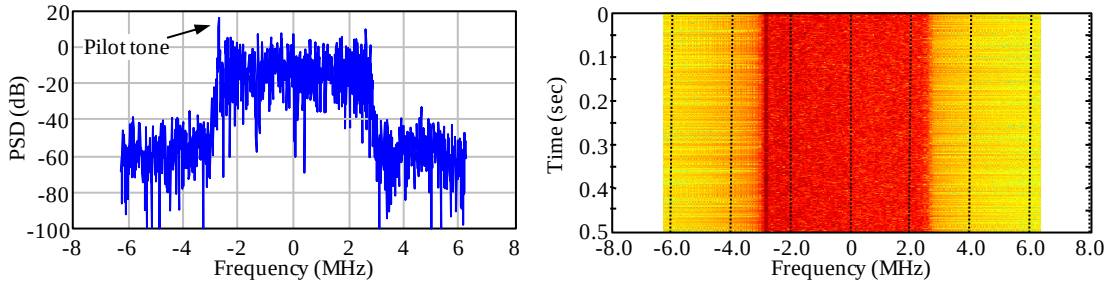

a) VSB8 Single Window Spectrum b) VSB8 Spectrum Waterfall Plot

Figure 5.2. Spectral and Temporal Properties of HDTV Signal

broadcast channel (frequency) used for Figure 5.3 being different than that of Figure 5.2. The complex components of the signal exhibit distinctly zero-mean, Gaussian-like amplitude and phase statistics, thus the magnitude distribution would tend toward exponential. Likewise the phase is zero mean with a near-uniform distribution over the range $\pm \pi$; a low amplitude, periodic phase ripple and specific phase value excursions is evident. This particular sample is based on 50E+07 digital samples and was measured from a low grazing angle location with a long slant path through heavy coniferous foliage. The horizontal scale is relative to this one-way measurement, only.

Figure 5.4 is a single autocorrelation for a sampled HDTV waveform. The autocorrelation is performed after the pilot tone is removed (otherwise, a periodic response around the zero-delay lobe and higher time sidelobe levels result). Pilot tone removal is performed in the frequency domain in which 21 filters (pilot tone peak $\pm$ ($N_{filters}$-1)/2) are replaced with

noise. To define the edited filter extent around the pilot tone the filter count was increased until no noticeable contribution to the response around zero delay was observed (a lesser filter extent produced autocorrelation residuals which perturbed the shape of the near zero delay response) and the close in sidelobes of the autocorrelation were equivalent to the expected level for a noise-like waveform. The mean close-in sidelobe level in Figure 5.4 is -35.3 dB. The equivalent number of chips, derived from the waveform bandwidth and burst duration) for this sample is 4664 or 36.68 dB. Processing a longer sample set (10000 bursts, different collection run) yields an average sidelobe level of -36.07 dB (again after pilot tone removal).

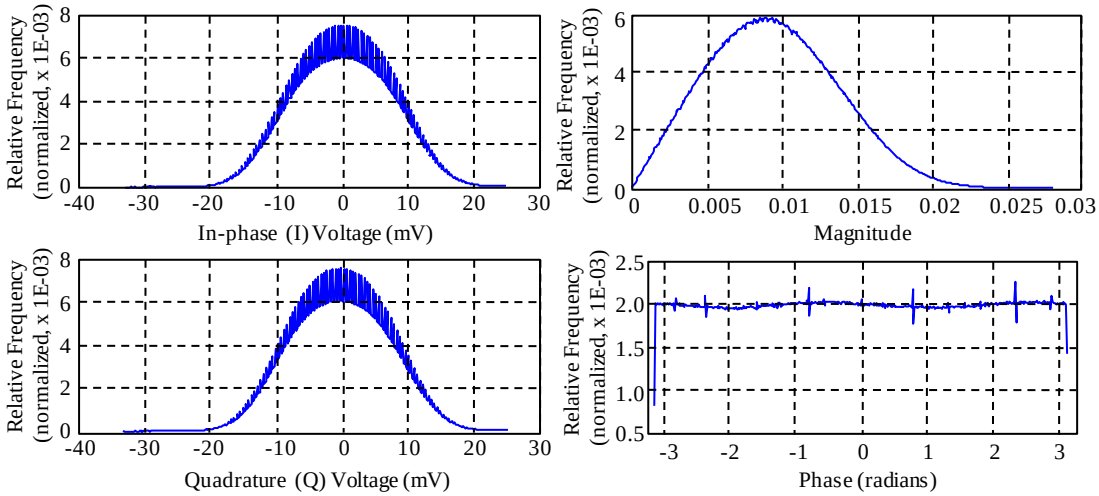

Figure 5.3. Sample HDTV Signal Statistics in the Time Domain (including phase)

As was shown by Griffiths, *et al*. [110], the bandwidth of broadcast entertainment signals, including digitally-modulated ones, is a function of the content/format. We observe a variable resolution for the 8VSB (HDTV) signal which may reflect this. The zero delay magnitude response illustrates the subtle bandwidth changes from sample burst-to-burst. Figure 5.5 illustrates the variation in the width of the zero delay response of the autocorrelation for a set of aliasing of adjacent channels (slightly modifying the actual channel spectrum). Figure 5.5a illustrates the general shape of the auto ambiguity response at zero delay. The data are sampled above the Nyquist rate (sample resolution 29.979 m or 10 MCSPS). Samples from two different receiver chains and randomly

selected in time are included for illustration. The second Figure (5.5b) contains estimates of the resolution based on the full width, half maximum width of the magnitude-squared of the autocorrelation. The nominal 3 dB bandwidth suggests a resolution on the order of 55.7 m. However the sample mean of the results in Figure 5.5b (estimation error less than 0.3 m at SNR=40 dB) yields a value of 49.78 m.

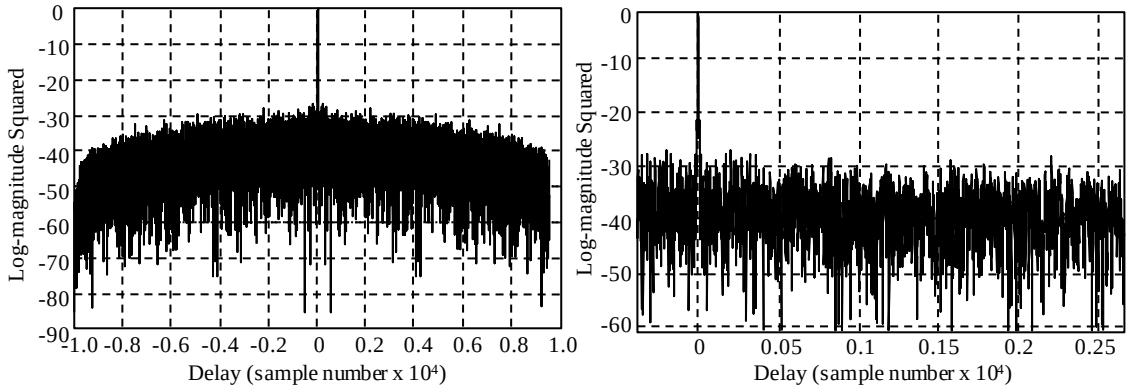

a) Sample HDTV Autocorrelation b) Zoomed View

Figure 5.4. HDTV Autocorrelation Example

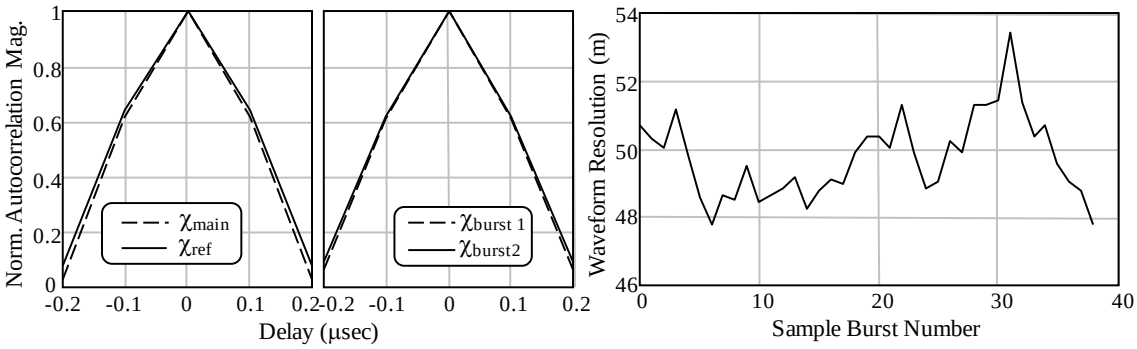

a) Random Selection of Mainlobe Responses b) Sample Full-width, Half-max.(power) Resolution

Figure 5.5. Demonstration of Time/Waveform Dependent Resolution

5.2 Simulating the HDTV Waveform.

As we saw in Section 4, the filtered backprojection-based, reconstructed IPR resulting from purpose-designed waveforms depended both on the operating frequency and the waveform modulation. CW waveforms yielded nearly the same resolution as finite (large fractional) bandwidth waveforms (taking into consideration the highest frequency in the waveform, not necessarily the carrier), while the spatial extent of the sidelobe structure and the rate of sidelobe roll-off with radial distance from the steered (focus) pixel/voxel

depended on the waveform modulation and bandwidth (*cf* section 6.1.3.2). In analysis and simulation, it was convenient that these waveforms could be expressed as relatively simple mathematical functions, even though, with the exception of the circular, two dimensional, monostatic aperture with CW waveform, the generation of the tomographic IPR with arbitrary collection cannot be accomplished in closed form (though solutions for several specific geometries are found in [19]).

The pulse compressed/match filtered HDTV waveform exhibits properties strongly reflective of noise waveforms. This includes a sharp, unambiguous, correlation peak and (relatively) uniform, but random, time sidelobe levels. This assertion is also borne out by the statistics of the signal as shown in Figure 5.3. In this section we develop a functional approximation of the HDTV waveform after compression. We then use the move-stop-move approximation to reconstruct the point spread function from an isotropic scatterer (as in Section 4). Suitability of the approximation is demonstrated by comparing the IPR from high fidelity waveform simulation to the approximation. The purpose of the functional approximation is to support the analytic development of the exact solution incorporating the effects of platform motion during pulse compression and reconstruction. A key difference from Section 4 will be the generalization of the bistatic collection geometry. There we evaluated bistatic geometries with transmitter and receivers in uniform circular or spherical motion (if moving) and that the image scene was at the center of motion. We now broaden the synthetic aperture to arbitrary bistatic geometries. The specific geometry evaluated relates to the flight test program described in Section 6.

5.2.1 ***Without platform motion (the move-stop-move approximation)***. Figure 5.6 illustrates the general bistatic geometry. The bistatic receiver executes a three dimensional path around the scene to be imaged (Figure 5.6a). A wide elevation beamwidth pattern is notionally projected in the geometry, and the stationary bistatic illuminator is at some distance outside the collection orbit. The projections thus formed are elliptical in two

dimensions (with foci at the transmitter and receiver), and ellipsoidal in three dimensions, as shown in Figures 5.6b and c, respectively. Image reconstruction in three dimensions is executed using filtered back projection given by

$$\hat{f}(r,\psi,\eta) = \hat{f}(x,y,z) = \int_0^{2\pi}\int_0^{\pi/2} \cos(\theta) \int_{-\infty}^{\infty} S_{\phi,\theta}(k) k^2 e^{-jkt(\phi,\theta)} dk d\theta d\phi \tag{5-1}$$

where $S_{\phi,\theta}(k)$ is the forward Fourier transform of the projections over the reflectivity spatial distribution which includes the waveform influence, k^2 is considered a window function and k the spatial frequency, x, y, and z are the voxel positions in scene-referenced Cartesian coordinates and r, ψ, η in spherical coordinates, as shown in Figure 5.6c. The general bistatic projection contour, $t(\phi,\theta)$, is given in (5-2) where the distinction between two- and three dimensional apertures is, in addition to the elevation integral, the functional form of κ [114]

$$t = \sqrt{r^2 + {R_r}^2 - 2rR_r\kappa_r} + \sqrt{r^2 + {R_x}^2 - 2rR_x\kappa_x}\,. \tag{5-2}$$

In (5-2) R_r and R_x are the radii of the receiver and transmitter orbits (relative to scene-based reference), respectively, and κ is given by $\kappa = \cos(\theta_i)\cos(\eta)\cos(\psi - \phi_i) + \sin(\eta)\sin(\theta_i)$, where the subscript i represents transmitter or receiver as appropriate. The received signal or imaging path (emitter-to-scatterer-to-receiver), or $R_1 + R_2$ is the range sum (R_s) and the direct path is the bistatic baseline (R_b). The move-stop-move approximation [100] assumes that the platform/radar executing a synthetic aperture is motionless during intervals of transmission and reception. The platform is positioned at successive sampling points, stops, and then resumes motion. Thus there are no waveform dispersion or distortion due to Doppler effects experienced.

5.2.2 ***Continuous random waveforms***. Passive radar based on 100% duty factor, opportunistic signals creates a template of the signal, received via a reference channel, which is correlated against the signal received in the main/surveillance/imaging antenna to

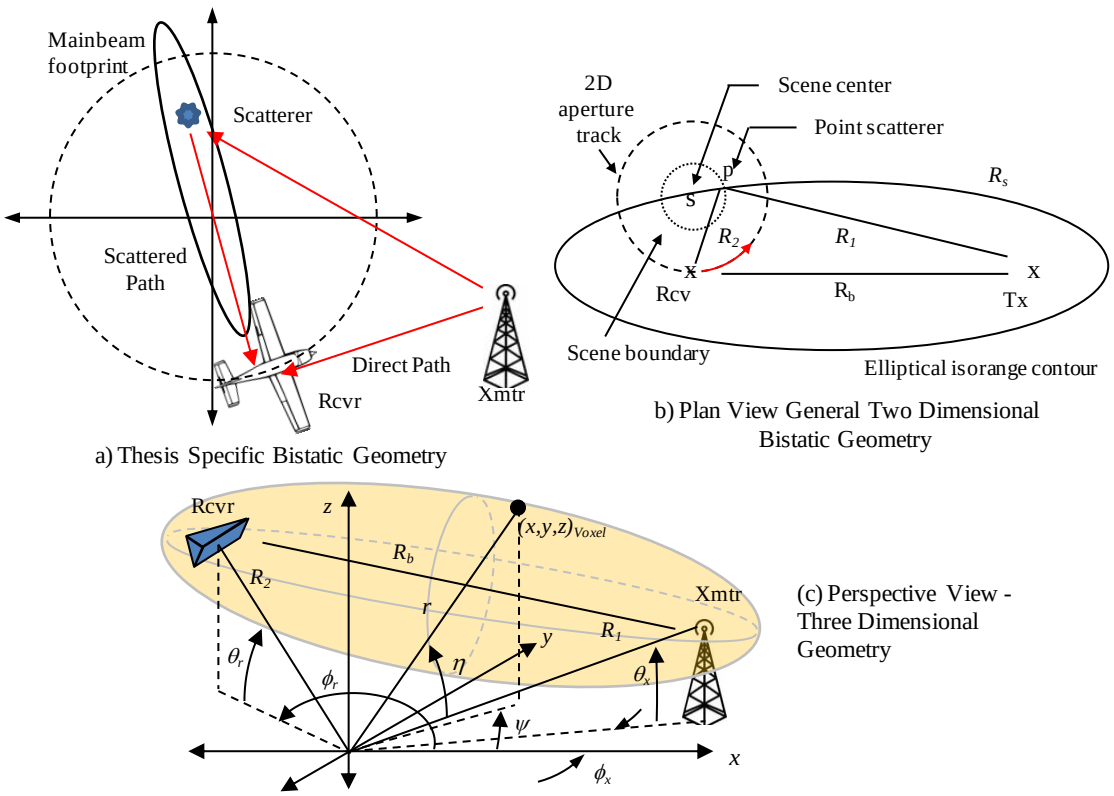

Figure 5.6. General Bistatic Imaging Geometry

extract delay information along the bistatic path. This correlation is, in effect, a pulse compression operation and is given in (5-3) from [105], among many.

$$\chi(\tau) = \int_0^T X_s(t) X_r^*(t-\tau) dt. \tag{5-3}$$

The waveform coherent processing interval is T, and X_s represents the main channel signal and X_r the reference channel. We can generally write both the transmitted and received waveforms as

$$x_T(t) = CA(t)e^{j(\omega_0 t)} \quad \text{and} \quad x_R(t-\Delta_\tau) = C'A(t-\Delta_\tau)e^{j\omega_0(t-\Delta_\tau)} \tag{5-4}$$

where $A(t)$ is the envelope of the signal modulated onto the carrier of frequency ω_0, C is a system transmission voltage scalar with C' incorporating propagation and reception gains, and Δ_τ is the time delay equivalent to range r. We can equivalently write $\omega_0\Delta_\tau = k_0 r$. After down conversion to baseband and substituting the baseline range for the reference channel (direct path with no scene energy) and the main channel (without direct path contribution) are

$$X_s = C_s A\left(t - \frac{R_s}{c}\right)e^{-jk_0 R_s} \quad and \quad X_r = C_r A\left(t - \frac{R_b}{c}\right)e^{-jk_0 R_b}. \tag{5-5}$$

In (5-5) C_s has absorbed the complex scatterer response and space loss for the main channel while C_r represents the direct path term. Substituting into (5-3) yields

$$\chi(\tau) = C_s C_r e^{-jk_0(R_s - R_b)} \int_0^T A\left(t - \frac{R_s}{c}\right) A^*\left(t - \frac{R_b}{c} - \tau\right) dt. \tag{5-6}$$

Making the change of variable $t'=t-R_s/c$ and substituting $\tau'=\Delta_r/c-t$ gives

$$\chi(\tau') = C_s C_r e^{-jk_0(R_s - R_b)} \int_0^T A(t') A^*(t' - \tau') dt' \tag{5-7}$$

or

$$\chi(\tau') = C_s C_r e^{-jk_0 \Delta_r} \Gamma(\tau') \tag{5-8}$$

with $\Gamma(\tau')$ the autocorrelation of the waveform envelope with delay referenced to the range difference $\Delta R=R_s - R_b$.

The autocorrelation is also equivalent to the Fourier transform of the auto-power spectrum of the waveform complex envelope.

$$\Gamma(\tau') = \int_{-\infty}^{\infty} S(f') S^*(f') e^{j2\pi f t} df'. \tag{5-9}$$

Reabsorbing the constants in (5-7) into (5-9)

$$S_s(f') = C_s S(f) e^{j(k+k_0)R_s} \quad \text{and} \quad S_r(f') = C_r S(f) e^{j(k+k_0)R_b} \tag{5-10}$$

with k as wave number and $k_0=\omega_0/c$.

Considering equations (5-6) and (5-10) there are two approaches to model the HDTV waveform used opportunistically: in the time domain or the frequency domain. In the first, there are two sub-options: 1) replicate the signal modulation process using MPEG formatted content segments as inputs and as described in Section 5.1, or 2) simply emulate the statistical behavior in the time domain with spectral shaping as mandated by regulation. In the frequency domain there are also two options: 1) emulate the statistical

variation over frequency (versus sample-to-sample as in the time domain), or use the ensemble average of the voltage spectrum. An advantage in the frequency domain approach is that the projection forward transform is not needed as a conditioning step that would be necessary if the data were time domain. In the search for a mathematically simple way to describe the underlying waveform, we look at both frequency domain approaches.

We initiate the analysis using the frequency domain, statistical representation. Because the amplitude statistics are Gaussian-like in the time domain, a Gaussian model is appropriate in the frequency domain. The number of burst points may exceed the modulation bandwidth (in terms of independent sampling) but the spectrum envelope constrains the content. The voltage mask (magnitude) of the HDTV waveform is given by [108], and is altered to produce a baseband spectrum centered at 0 Hz as given by

$$S(f)=\begin{cases} 0 & f > F_p+\frac{F_{sym}}{2}\left(1+\frac{\alpha}{2}\right)-\frac{BW}{2} \\ \sin\left(\frac{\pi\left(\frac{F_{sym}}{4}(2+\alpha)-\left(f+\frac{BW}{2}\right)+F_p\right)}{\alpha F_{sym}}\right) & f > F_p+\frac{F_{sym}}{2}\left(1-\frac{\alpha}{2}\right)-\frac{BW}{2} \quad f \le F_p+\frac{F_{sym}}{2}\left(1+\frac{\alpha}{2}\right)-\frac{BW}{2} \\ 1 & f \ge F_p+\frac{\alpha F_{sym}}{4}-\frac{BW}{2} \quad f \le F_p+\frac{F_{sym}}{2}\left(1-\frac{\alpha}{2}\right)-\frac{BW}{2} \\ \sin\left(\frac{\pi\left(\left(f+\frac{BW}{2}\right)-F_p+\frac{F_{sym}\alpha}{4}\right)}{\alpha F_{sym}}\right) & f > F_p-\frac{\alpha F_{sym}}{4}-\frac{BW}{2} \quad f < F_p+\frac{\alpha F_{sym}}{4}-\frac{BW}{2} \\ 0 & f < F_p-\frac{\alpha F_{sym}}{4}-\frac{BW}{2} \end{cases} \tag{5-11}$$

where F_{sym} = 10.762238E+06, F_p = 309.441E+03, $\alpha = 2BW/F_{sym}$-1 and BW=6.0E+06. A baseband spectrum is constructed spanning $\pm F_{sample}/2$ centered at 0 Hz. The number of frequency points, with uniform spacing, is based on the sample duration. At each point (frequency value) a Gaussian random amplitude is draw from $N(0, 1)$ and a uniformly distributed phase is drawn from the range $[-\pi, \pi]$; intrinsic MATLAB functions are used. The burst process is repeated for each spatial sample position.

The synthetic tomographic aperture phenomenology was generated using the cylindrical spiral trajectory (Section 6.3 Flight Test Design) sampled at 1 degree increments (recalling the angular sampling dependence of the reconstruction ring-phase artifact, also from Section 4). The collection aperture spanned 200-1250 m in elevation at an orbit radius of 1.25 km. The scattered bistatic signal (587 MHz) is created with the idealizing assumptions of perfect isolation of the direct path from the signal path and that the point scatterer is isotropic. The sample rate used was 10E+06 complex samples/sec and an equivalent burst duration of 0.8 msec, intentionally selected to be less than the interval between successive spatial points such that no overlap of processed bursts results. This also limits the coherent gain realized via correlation and fixes the burst time sidelobe noise floor. Figure 5.7 depicts the impulse response (IPR) for a point scatterer located at (20, 20, 0) in both contour and perspective. The principal axis cuts for Figure 5.7 are shown in Figure 5.8 and illustrate the achievable resolution. Using the full-width, half maximum metric, the resolutions in each axis are: X and Y axes 0.12 m (about 0.2λ midband) and Z axis 0.46 m. Sidelobe levels match expectations for the bistatic geometry with only one platform moving (8 dB in X-Y and 13 dB along Z). We also assume for the initial image performance evaluation that there is perfect isolation between the illuminator and the main receiving antenna such that there is no Direct Signal Breakthrough (DSB). The implications of DSB (and impacts on sensitivity) and method for mitigation are addressed in Section 5.4.

Figure 5.8 was initially an unexpected result given the random waveform nature. It is contrasted with the CW waveform at 587 MHz center frequency in the same collection geometry and sample interval in Figure 5.9, and is virtually identical (note: the CW case was truncated at – 40 dB and -30 dB for X and Z axes, respectively). No resolution differences were expected as the difference between the CW frequency and the HDTV channel upper edge is very small, but some effect was expected due to the random

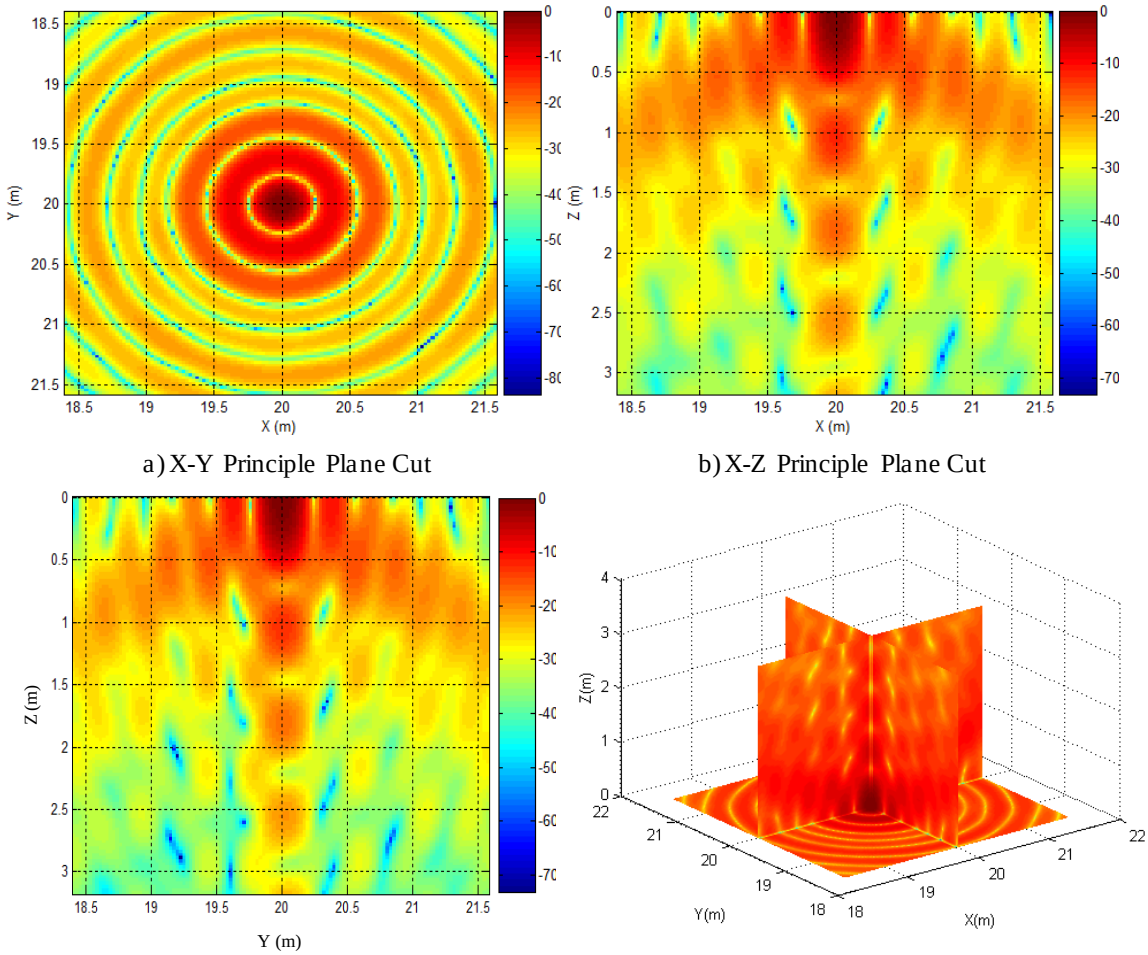

a) X-Y Principle Plane Cut

b) X-Z Principle Plane Cut

c) Y-Z Principle Plane Cut

d) Intersecting Principle Plane Perspective View

Figure 5.7. IPR for Randomly Drawn HDTV Simulation

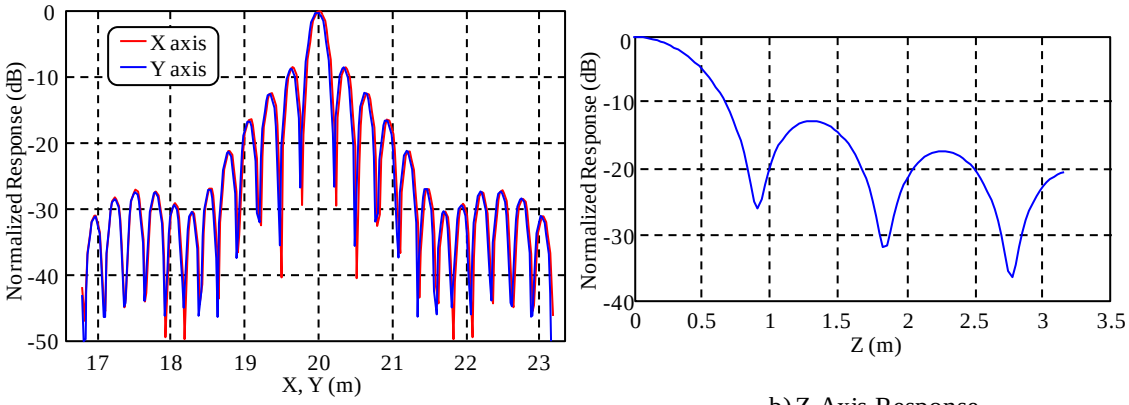

a) X and Y Axis Response

b) Z Axis Response

Figure 5.8. Principal Axis Results for Randomly Drawn HDTV Simulation

waveforms. However, considering the extent of the processed spatial window for reconstruction against the resolution of the waveform (roughly a 1:10 ratio) we are only integrating via back projection over the smoothly varying mainlobe region. We would expect to see the random sidelobe structure once the reconstruction extends outside the

compressed mainlobe. This is explored in Figure 5.10 where the X axis was reconstructed out to over 100 m from the target pixel position. All parameters are the same as Figure 5.8. Sidelobe levels roll off until the radius equivalent to the phase ambiguity radius is reached (at approximately 46 m). However no judgment can be made that the sidelobe shape is due to the random waveform. Indeed it is likely not when previous results are considered (*e.g.*, Figure 4-40).

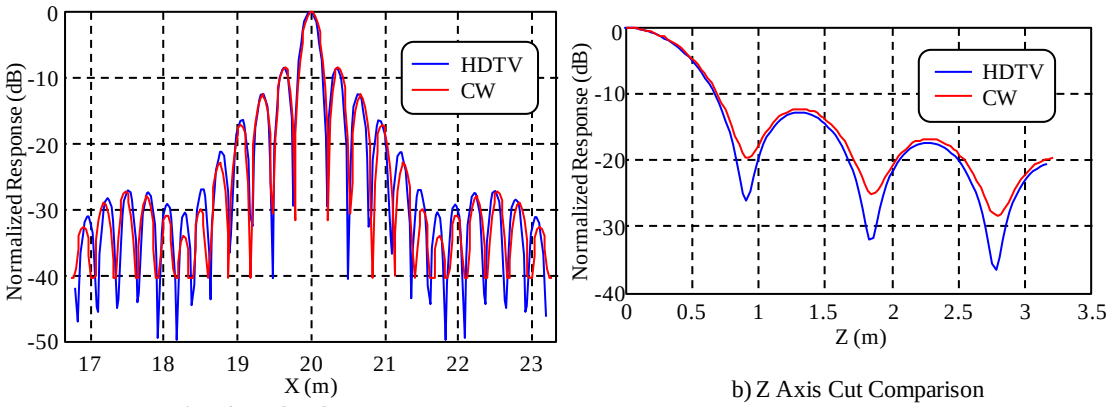

a) X Axis Cut Comparison

b) Z Axis Cut Comparison

Figure 5.9. Reconstruction Comparison: HDTV Simulation to CW

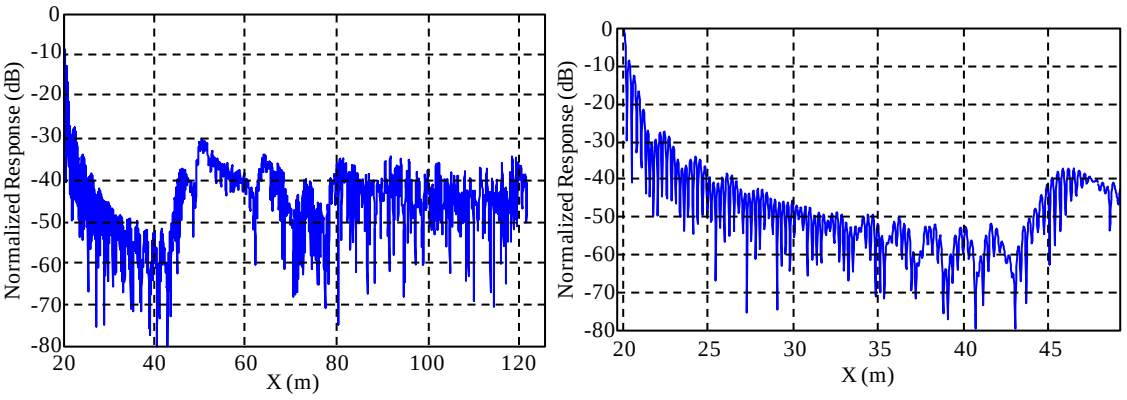

a) Reconstruction Full Extent

b) X Axis Zoomed View

Figure 5.10. Extended X-Axis Reconstruction

Kulpa [31] suggests using the ensemble average of the waveform power spectrum, allowing calculation of the general autocorrelation (the matched filter response) via the inverse Fourier transform. In [31] he demonstrates this for the Gaussian noise waveform; noting that in the limit of an infinite sample size there are no range sidelobes but the finite burst duration produces a sidelobe structure such as that seen in Figure 5.4. The averaging yields the Gaussian power-shaped, zero-phase spectrum; the inverse Fourier transform of

which is a pure Gaussian autocorrelation response. This also eliminates the slight variations in the response width from burst-to-burst.

Using (5-11) we compute the autocorrelation analytically, starting from

$$R(\tau) = \int_{-\infty}^{\infty} S(f)^2 e^{j2\pi f\tau} df \tag{5-12}$$

where we use *R* to distinguish from the pulse compression response (χ). The spectrum is effectively 0 outside the channel boundaries ($|S(f)| > 3$ MHz) and we can decompose the integral into three discrete terms

$$R(\tau) = \int_{f_0}^{f_1} S_1(f)^2 e^{j2\pi f\tau} df + \int_{f_1}^{f_2} S_2(f)^2 e^{j2\pi f\tau} df + \int_{f_2}^{f_3} S_3(f)^2 e^{j2\pi f\tau} df \tag{5-13}$$

where S_1, S_2 and S_3 are the three nonzero regions in (5-11), with the limits

$$\begin{aligned} f_0 &= F_p - \frac{\alpha F_{sym}}{4} - \frac{BW}{2} & f_1 &= F_p + \frac{\alpha F_{sym}}{4} - \frac{BW}{2} \\ f_2 &= F_p + \frac{F_{sym}}{2}\left(1-\frac{\alpha}{2}\right) - \frac{BW}{2} & f_3 &= F_p + \frac{F_{sym}}{2}\left(1+\frac{\alpha}{2}\right) - \frac{BW}{2}. \end{aligned} \tag{5-14}$$

The first and third terms of (5-12) yield expressions of the form

$$R(\tau) = \int_{f_0}^{f_1} \sin^2(x) e^{j\frac{2\pi}{\kappa}(x-\beta)\tau} dx \tag{5-15}$$

with a change of variable and *k* and *b* constants. We use the double angle trigonometric identity

$$\cos(2x) = 1 - 2\sin^2(x) \tag{5-16}$$

to arrive at a form found in integral tables

$$\int e^{bx}\cos(ax)dx = \frac{e^{bx}}{a^2+b^2}\left(a\sin(ax) + b\cos(ax)\right). \tag{5-17}$$

The second term is more straight-forward since at the peak to the channel response the magnitude is 1, resulting in

$$R_2(\tau) = \int_{f_1}^{f_2} e^{j2\pi f\tau} df \tag{5-18}$$

The form of the third term is nearly the same as the first term. Full derivation of the autocorrelation function can be found in Appendix A. The function resulting can be seen in Figure 5.11. The time sidelobes are seen, like the Gaussian case from Kulpa [31], to be much less than the limited sample duration HDTV signals (Figure 5.4).

The bistatic tomography simulation from Figure 5.7 was modified by eliminating the random amplitude and phase draw, using only the spatial frequency weighted voltage spectrum as in (5-10). The results along the cardinal axes, compared to the Monte Carlo

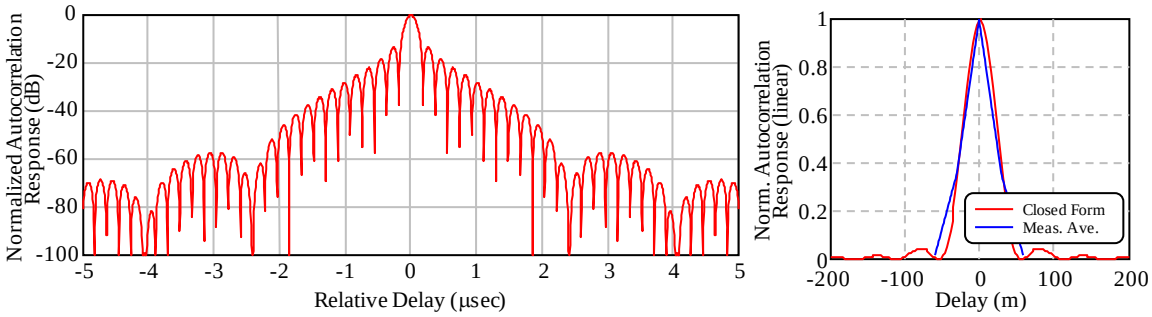

a) Closed Form HDTV Autocorrelation

b) Closed Form Compared to Fig 5.1-5

Figure 5.11. Autocorrelation of the HDTV Power Spectrum – Closed Form Derivation

results in Figure 5.8, are shown in Figure 5.12. The ensemble averaged spectrum results are offset in order to visualize the match. The Figure demonstrates that the reconstructed IPR may be accomplished without need to consider the random waveform nature (sidelobes from finite duration random signal do not contribute). The simulation uses the equivalent burst duration (frequency resolution) as the random waveform simulation and the same collection aperture.

The closed form for the power spectrum (5-11) or autocorrelation (Appendix D) are both very unwieldy. Simulation of digital broadcast video using PN codes to represent digital broadcast signals was suggested in [111] and [112]. Specifically, Kouemou [112] indicates that as replication for white noise signal, in terms of correlation at the receiver, is, or can be, difficult to achieve, PN sequences can be used instead. Such sequences are deterministic waveforms which yield noise-like behavior and which are easily generated.

PN waveforms have good autocorrelation properties and high spectrum efficiency. We next examine ideal phase codes to emulate the HDTV waveform thereby allowing development more convenient closed form expressions for correlation in either the time or frequency domain.

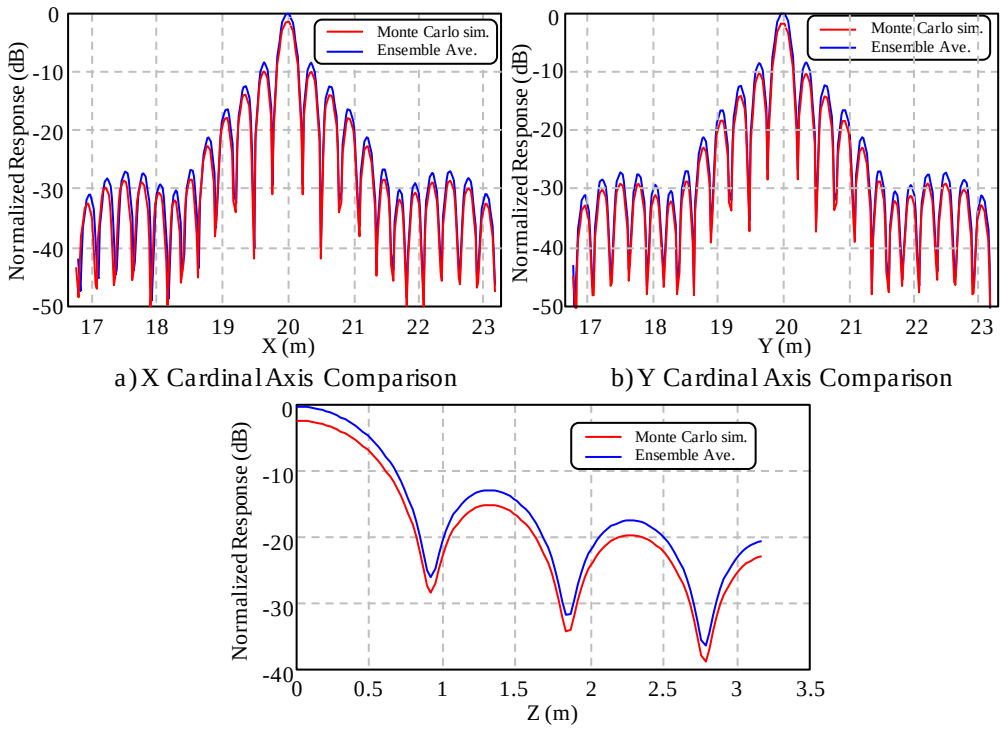

a) X Cardinal Axis Comparison

b) Y Cardinal Axis Comparison

c) Z Cardinal Axis Comparison

Figure 5.12. Reconstruction Using the Ensemble Average Method Compared to Monte Carlo Simulation

5.2.3 ***Alternate waveform representations***. The similarity of the cross correlated (pulse compressed) PN code to that of HDTV signal similarly processed allows a functional equivalence. We recognize that the perfectly rectangular chip, as the constituent building block of the PN code sequence, is unrealizable because the infinitesimal rise time would require infinite bandwidth. We defined an equivalent chip rate, based on the channel bandwidth and, given the burst duration, calculated a number of equivalent chips in the burst as a means to tie the PN code to the HDTV global characteristics.

The baseband PN code is defined by [113]

$$A(t) = \sum_{m=1}^{N} rect\left(\frac{t-(m-1)t_p}{t_p}\right) e^{j\varphi_m} \tag{5-19}$$

where t represents time, t_p is the code chip duration, and φ_m has two states $\{0,\pi\}$ in the work here, but may represent an arbitrary number of code bits. Implicit in the use of (5-19) as the modulation is that the pilot tone has been filtered. The phase code produces a white (uniform, random) spectrum, in which individual filter voltages are Gaussian distributed, while the overall spectrum is modulated by the spectrum of the envelope of the code chip, a sin(x)/x response.

Equation 5-19 is an idealized representation which assumed that sampling is perfectly synchronous with respect to the code chip. A more general representation from [38] is

$$A(t) = \sum_{n=1}^{N} e^{j\varphi_m}\left[u(t-nt_p) - u(t-(n+1)t_p)\right] \tag{5-20}$$

where $u(t)$ is the unit step function. Example spectra are shown in Figure 5.13 for both binary (5.13b) and hex bit (16-state, 5.13a) phase codes of length 1000. The codes are pseudo randomly drawn using MathCAD built in functions. The sample rate used was 50 million complex samples/sec (MCS/s).

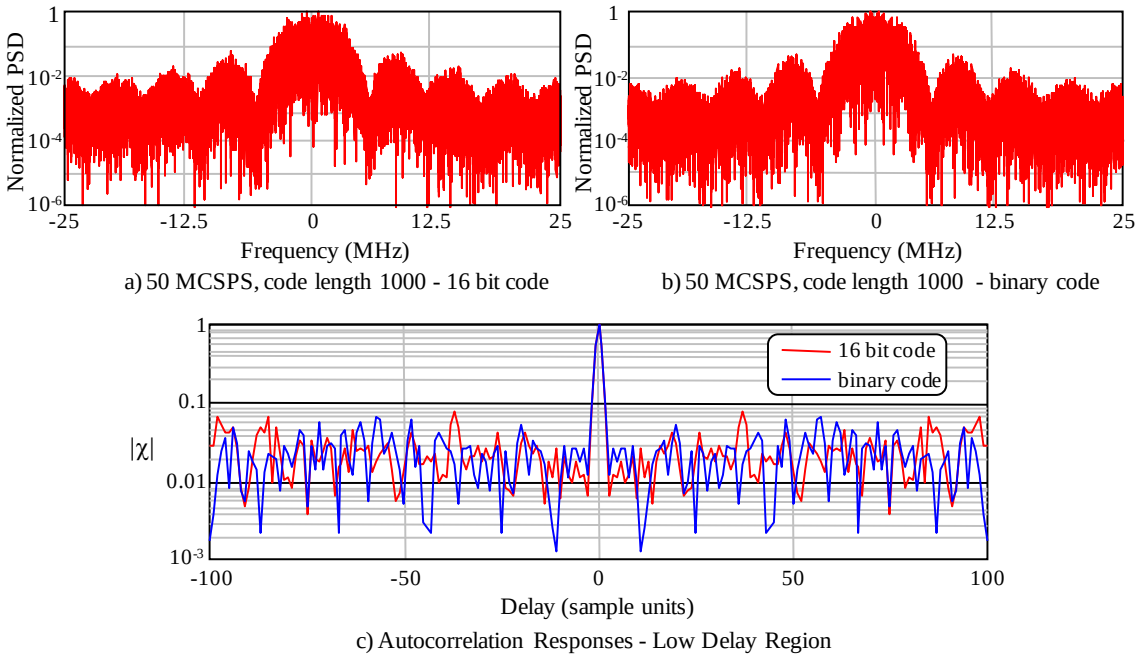

Figure 5.13. Example Spectra and Compressed Pulses for PN Codes

Interestingly, Doerry in [111] has evaluated spectrum shaping of PN codes, as purpose-designed radar waveforms, to achieve range sidelobes that emulate those of pulse compressed LFM signals. Though not applicable the paper represents an interesting approach to improve the application of phase-only codes.

We start with the forms in (5-4) and (5-5) and substitute (5-15) to get

$$\chi(\tau) = C_s C_r e^{-jk_0(R_s-R_b)} \int_0^T \sum_{m=0}^{N-1} rect\left(\frac{t - \frac{R_s}{c} - mt_p}{t_p} \right) e^{j\phi_m} \left[\sum_{n=0}^{N-1} rect\left(\frac{t - \frac{R_b}{c} - nt_p - \tau}{t_p} \right) e^{j\phi_n} \right]^* dt \qquad (5\text{-}21)$$

where * indicates complex conjugation and τ is delay. Making the change of variable

$$t_b = t - \frac{R_s}{c} - mt_p \quad t = t_b + \frac{R_s}{c} + mt_p \quad dt_b = dt \qquad (5\text{-}22)$$

giving

$$\chi(\tau) = C_s C_r e^{-jk_0(R_s-R_b)} \int_0^T \sum_{m=0}^{N-1} rect\left(\frac{t_b}{t_p} \right) e^{j\phi_m} \left[\sum_{n=0}^{N-1} rect\left(\frac{t_b + (m-n)t_p - \tau}{t_p} \right) e^{j\phi_n} \right]^* dt_b. \qquad (5\text{-}23)$$

A second substitution introduces a modified delay variable $t_{prime}=(n-m)t_p-\tau$ together with taking the complex conjugate and reversing the order of integration and summation

$$\chi(\tau') = C_s C_r e^{-jk_0\Delta R} \sum_{m=0}^{N-1} \sum_{n=0}^{N-1} e^{j\phi_m} e^{-j\phi_n} \int_0^T rect\left(\frac{t_b}{t_p} \right) rect\left(\frac{t_b - \tau'}{t_p} \right) dt_b \qquad (5\text{-}24)$$

where $\Delta R= R_s-R_b$. Now the limits of the integral are changed from the full burst duration to reflect the code chip duration with the interchange integral-summation interchange. The products of the rect functions are nonzero when the ranges of the two functions intersect. This is shown in Figure 5.14.

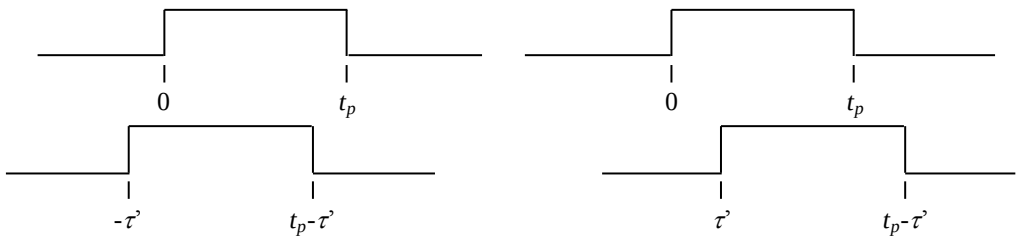

a) Case 1 - $\tau' > 0$ b) Case 2 - $\tau' < 0$

Figure 5.14. Rect Function Evaluation and Integral Limits

The two halves of the solution are

$$\chi(\tau' \geq 0) = C_s C_r e^{-jk_0 \Delta R} \sum_{m=0}^{N-1} \sum_{n=0}^{N-1} e^{j\phi_m} e^{-j\phi_n} \int_0^{t_p - \tau'} 1 dt_b$$
$$\chi(\tau' < 0) = C_s C_r e^{-jk_0 \Delta R} \sum_{m=0}^{N-1} \sum_{n=0}^{N-1} e^{j\phi_m} e^{-j\phi_n} \int_{-\tau'}^{t_p} 1 dt_b . \quad (5\text{-}25)$$

Evaluating the integrals yields

$$\chi(\tau' \geq 0) = C_s C_r e^{-jk_0 \Delta R} \sum_{m=0}^{N-1} \sum_{n=0}^{N-1} e^{j\phi_m} e^{-j\phi_n} \left(t_p - \tau' \right)$$
$$\chi(\tau' < 0) = C_s C_r e^{-jk_0 \Delta R} \sum_{m=0}^{N-1} \sum_{n=0}^{N-1} e^{j\phi_m} e^{-j\phi_n} \left(t_p - \tau' \right). \quad (5\text{-}26)$$

Reverse substituting for τ' and with some manipulation yields the final expression

$$\chi(\tau) = C_s C_r e^{-jk_0 \Delta R} \sum_{m=0}^{N-1} \sum_{n=0}^{N-1} e^{j\varphi_m} \left(e^{j\varphi_n} \right)^* \times \begin{cases} \left(t_p - \left| \tau - (n-m) t_p \right| \right) & \left| \tau - (n-m) t_p \right| < t_p \\ 0 & \left| \tau - (n-m) t_p \right| > t_p . \end{cases} \quad (5\text{-}27)$$

The absolute value is used as the result is symmetrical with respect to the delay reference. The cross correlation in (5-27) is evaluated by performing a random draw on a uniform random number generator and performing the double summation with delay as the independent variable.

Sample autocorrelations for the two code cases are also included in Figure 5.13c corresponding to the specific codes (when normalized) regardless of the phase code resolution, at zero delay. drawn for the power spectra in the same Figure. The mean sidelobe levels for these cases are -30.53 dB (16 bits) and -30.83 dB (binary) relative to peak. The rule-of-thumb is that the mean sidelobe level (magnitude-squared, relative to the peak response) is 1/*N* (1000 chips ~ -30 dB). We observe that the code phase resolution is not a dependent factor on the portion of the autocorrelation response of primary interest, only the chip duration.

Equation 5-27 is used with the cylindrical spiral aperture (spiral vertical extent 200-1250 m, 120 kts/63 m/sec with sample interval of 1 degree along-orbit and 1000 chip sample

burst duration) to evaluate the PN code as a surrogate for the HDTV signal. The cross correlation is evaluated using a unique code sequence for each burst and 100 lag terms retained (equivalent range greater than scatterer range over the full aperture) and forward transformed to the frequency domain using a DFT. The results are shown in Figure 5.15. The Figure compares the PN code substitution for the HDTV signal with, again, excellent results. As with Figures 5.13, the results are offset vertically to visualize both sets of curves.

For reconstruction we generally need only be concerned with the mainlobe portion of the correlation result. The distance over which we perform reconstructions are less than the resolution distance of the compressed waveform. Thus the steered positions in the back projection operation are all to positions where the range response is functionally well behaved (*e.g.*, not random as in the time sidelobe region). Consider only the region between the mainlobe response first nulls.

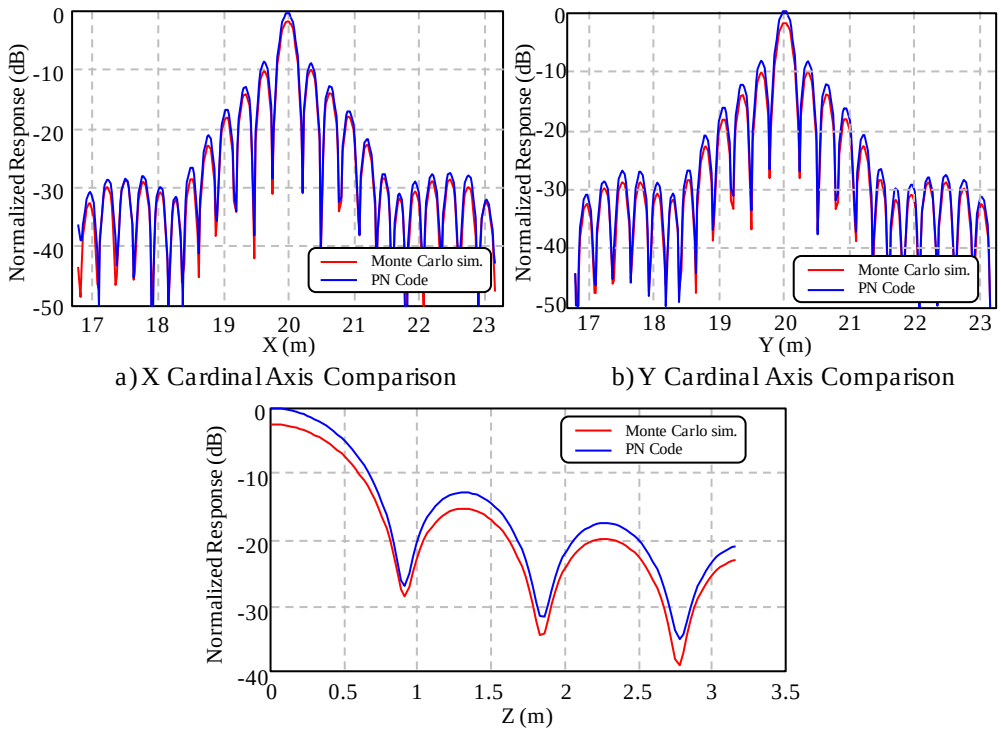

Figure 5.15. Reconstructed Cardinal Axes using PN Code Compared to HDTV Random Waveform Results (vertical offset is intentional)

This expression is exactly known, except for voltage scaling, mainlobe response ($-t_p<\Delta R/c<t_p$)

$$A(r,\Delta R) = 1 - \left|\Delta R - \frac{\tau}{c}\right| / \frac{t}{c} \qquad \text{for} \qquad \left|\Delta R - \frac{\tau}{c}\right| < \frac{t_p}{c}. \tag{5-28}$$

centered on the range difference defined by the scatterer position. This defines a triangular waveform which approximates the full code correlation. The derivation of the forward transform, representing the frequency domain form of the projections for a point target, can be found in Appendix B. The result, to simulate the scattering phenomenology, is

$$S_{\phi,\theta}(k) = N_c t_p C_s C_r e^{-j(k_0+k)\Delta R} \frac{\sin\left(\frac{r_p}{2}k\right)^2}{r_p k^2} \tag{5-29}$$

where r_p is the pulse length (one way). The details of the development of (5-29) can be found in Appendix B. We see from Figure 5.13 and (5-29) that the spectrum derived from the zero delay response lobe is equivalent to the ensemble average of the PN code performed in the frequency domain (as was done for the Gaussian noise waveform and the HDTV channel mask earlier in Section 5.2). This is also referred to as the Triangle response approximation.

Using the same collection aperture we evaluate (5-29) in simulate the bistatic scattering phenomenology, again without the presence of the direct path signal, via reconstructing the IPR. The number of frequency points used in the initial evaluation (and published in [114]) was low (only 100) and resulted in higher than expected image sidelobes, and filled nulls, starting at about the 8th sidelobe . That effort was repeated using a higher count of 1000 frequency points, with the results shown in Figure 5.16. This Figure compares the PN code, triangle approximation to the HDTV Monte Carlo simulation of Figure 5.7. As in Figure 5.12 the curves are slightly offset along the response axis for comparison.

In terms of the structure of the responses compared in Figure 5.16, we see virtually no difference. The two waveforms have subtly different spectral envelopes, which translate into slightly different mainlobe responses in the time domain. As a final test for the suitability of this approximation, we perform a reconstruction to parallel the range extended one in Figure 5.10. The results are presented in Figure 5.17.

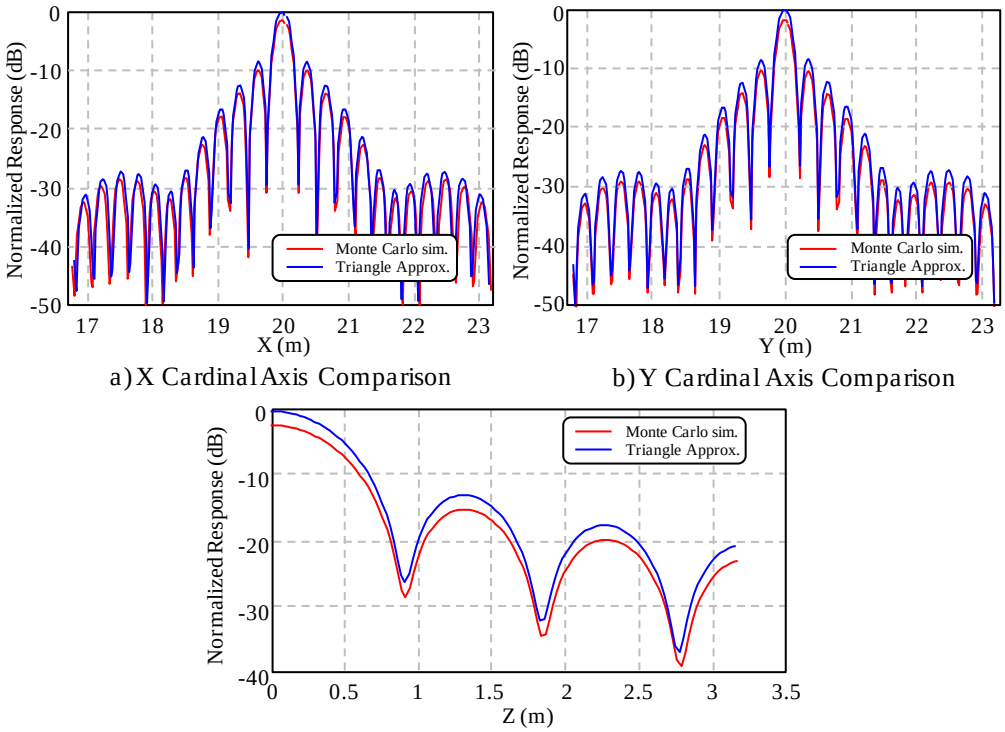

a) X Cardinal Axis Comparison

b) Y Cardinal Axis Comparison

c) Z Cardinal Axis Comparison

Figure 5.16. PN Triangle Approx. Compared to HDTV Random Waveform Results

Qualitatively mainlobe and sidelobe reconstruction within the radius of the phase ambiguity artifact are equivalent (the radius is increased with respect to the monostatic case because the transmitter is stationary). Extending to the sidelobe region beyond the anomaly radius the sidelobe level is slightly lower using the analytic approximation. This comparison indicates that the Triangle approximation is well suited as a proxy for the random waveform. We apply it, and the time domain representation using the PN code, to the effects of motion on the bistatic imaging process that follow.

The results presented in this section indicate that subtle differences is the shape of the spectrum derived from the compressed/correlated continuous wave random noise

waveform result in subtle differences in the impulse response of point target reconstructions based on these waveforms. Again, as shown earlier, bandwidth is the dominant contribution.

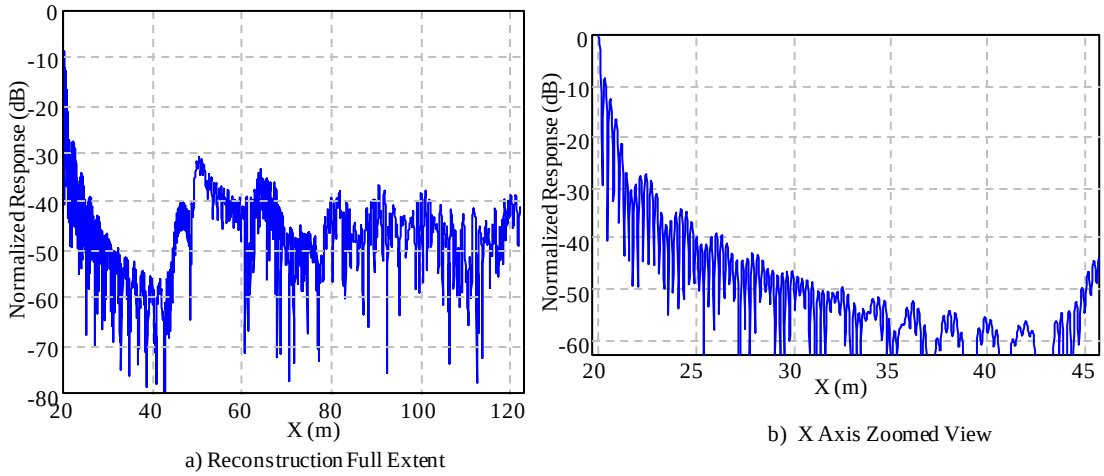

Figure 5.17. Extended X-Axis Reconstruction with Triangle Approximation

5.3 Reconstruction with Full Platform Motion Incorporated.

The move-stop-move approximation assumed that any platform motion is arrested while transmission and/or reception (or both) are exercised, followed by translation to the next spatial sample point. However, longer coherent processing intervals may be necessary to yield the sensitivity level necessary for image formation against small scatterers. As the burst duration increases, the possibility that the effects of platform motion can no longer be neglected arises and a (more) exact formulation is necessary for reconstruction without Doppler introduced distortions.

5.3.1 ***Introducing platform motion dependence***. In this section we include the effects of platform motion over the period of reception of the signal corresponding to a single spatial sample. We do not consider bursts which may overlap in time, *e.g.*, each burst is uniquely processed at only one spatial sample point. Also we do not address the presence of the direct signal in the main channel (Section 5.4). The exact expressions for motion are developed first in the time domain using the PN code substitution for the HDTV

signal with the formulation in both the time and frequency domain developed in Section 5.2 and Appendix B. We begin again with the general form of the transmitted waveform and the received signal when the motion of the platform modifies the received signal.

$$x_T(t) = CA(t)e^{j\omega_0 t} \quad \text{and} \quad x_R(t-\Delta_\tau) = C'A(t-\Delta_\tau)e^{j\omega_0(t-\Delta_\tau)} \tag{5-30}$$

The change in platform position between signal radiation and reception, or changes due to motion between the leading and trailing portions of the waveform are captured with the recursive delay function

$$\Delta_\tau = \frac{1}{c}R(t-\Delta_\tau). \tag{5-31}$$

The bistatic form of the delay function, which addresses one-way propagation, is given in (5-31). Rihaczek [32] and Skolnik [115] both follow the approach of Wishner and Kelly [116] in developing a non-recursive solution to (5-31) by expanding Δ_τ as a Taylor series, evaluated at an arbitrary but consistently applied point on the received waveform, and keeping the nonzero terms under the assumption of constant speed over the waveform duration. This implies all higher time derivatives are equal to zero. The result of the truncated expansion is that (5.31) becomes

$$\Delta_\tau \approx \frac{r_0}{c} - \frac{\dot{R}}{c}t \tag{5-32}$$

where r_0 is the initial range and $\dot{R}$ the range rate: delay is a monotonic function of initial range and range rate.

There is a second effect of motion and that is the distortion of the waveform complex envelope when employing matched filtering and the reference function does not include motion effects. Setting an acceptable phase error over the waveform duration at $\pi/2$, Rihaczek [32] then defines that the effect on the waveform envelope of platform motion is negligible when the time-bandwidth of the waveform satisfies the inequality

$$TB <\sim 0.1\frac{c}{V} \tag{5-33}$$

where T is the waveform duration, B the waveform bandwidth and V the platform (or scatterer) velocity. The implication of (5-33) for the digital television signal is the coherent processing interval associated with the pulse compression process. This is shown in Figure 5.18 using a constant bandwidth with a variable coherent processing time increasing the time-bandwidth product. The coherent processing time for the imaging application is in tension between the time sidelobe levels, absent considerations on the leakage of the direct path signal into the signal channel (Section 5.4): levels are reduced – along with increasing sensitivity - as T increases, and the angular separation of spatial samples, which affects reconstruction phase ambiguity artifacts, is constant or decreases. The range of interest of the planned flight test (Section 6) is indicated in Figure 5.18 by the black oval. Rihaczek's Rule (5-33) holds for those points which lie below the plotted dashed contour. For those points platform motion can be ignored.

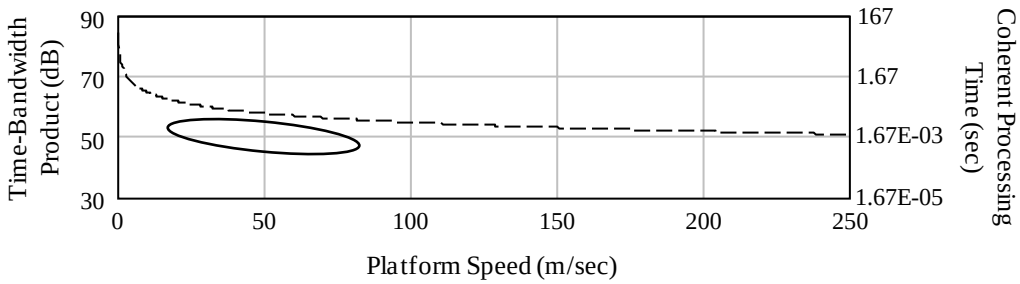

Figure 5.18. Time-Bandwidth and Platform Velocity Considerations for HDTV Signal

The combination of (5-30) and (5-32), when satisfied, let us write the received signal envelope

$$A(t-\Delta_\tau) \approx A(t-t_0). \tag{5-34}$$

Here t_0 is the arbitrary point on the received waveform (assumption noted above) and is typically assigned to the leading edge of the received signal. With (5-34) we can rewrite the received signal in (5-33), before down conversion, as

$$x_R(t-\Delta_\tau) =\sim x_R(t-t_0) = C'A(t-t_0)e^{j\omega_0\left(t-\frac{r_0}{c}+\frac{\dot{R}}{c}t\right)} \tag{5-35}$$

The development of the exact solution follows the approach used earlier but incorporating

(5-35). We form the signals in the main (imaging) antenna channel and the reference channel using the single scatterer model present only in the main channel and without reference signal leakage (Section 5.4). After down conversion and making the substitutions $\omega_0 r_0/c = k_0 r_0$ and $\omega_0 \dot{R}/c = \omega_{dop}$ (5-35) becomes

$$x_R(t,t_0) = C'A(t-t_0)e^{j\left(-k_0 r_0 + \omega_{dop} t\right)}. \tag{5-36}$$

The signals received in the reference channel and the imaging channel are each given by

$$\begin{aligned} x_{ref}(t,t_0) &= C_r A\left(t - \frac{R_b}{c}\right)e^{j\left(-k_0 R_b + \omega_{ref} t\right)} \\ x_S(t,t_0) &= C_s A\left(t - \frac{R_1 + R_2}{c}\right)e^{j\left(-k_0 (R_1+R_2) + \omega_{scat} t\right)} \end{aligned} \tag{5-37}$$

where the range terms and constants are as defined in Section 5.2. In (5-37) the Doppler terms ω_{ref} and ω_{scat} represent the frequency shift impressed on the received signals from platform motion, the temporal axis compression replaced by a simple shift. Note: equation 5-37 assumes that the two antennas share a common phase center. The magnitude of the Doppler is given by the projection of the velocity vector in the direction of the emitter

$$\omega = \frac{V_p}{\lambda}\cos(\phi_{az\_xmtr})\cos(\theta_{el\_xmtr}) \tag{5-38}$$

and, since the transmitter is fixed only the platform motion contributes. The angles in (5-38) are defined in a velocity-vector referenced coordinate system centered at the receiver: the velocity vector defines the X axis. Y is defined in the plane of the local horizontal (orthogonal to the earth radial through the center of the vehicle). The Z axis is X crossed into Y, nominally the left wing. Translation about the collection aperture makes (5-37) and the main channel Doppler, functions of position.

When the cross correlation is formed for compression using (5-3) with (5-37)

$$\chi(\tau) = C_r C_s \int_0^T A\left(t_b - \frac{R_s}{c}\right)e^{j\left(-k_0 R_s + \omega_{scat} t\right)} A\left(t_b - \frac{R_b}{c} - \tau\right)^* e^{j\left(k_0 R_b - \omega_{ref}(t-\tau)\right)} dt. \tag{5-39}$$

The signal channel (5-39) contains the cross-Doppler terms with time dependency

$$\chi(\tau) = C_r C_s e^{-jk_0 R_s} e^{jk_0 R_b} e^{j\omega_{ref}\tau} \int_0^T A\left(t_b - \frac{R_s}{c}\right) e^{j(\omega_{scat}-\omega_{ref})t} A\left(t_b - \frac{R_b}{c} - \tau\right)^* dt \tag{5-40}$$

which, when letting R_s-R_b=ΔR, can be simplified to

$$\chi(\tau) = C_r C_s e^{-jk_0 \Delta R} \int_0^T A\left(t_b - \frac{R_s}{c}\right) e^{j\omega_{scat}t} e^{-j\omega_{ref}(t-\tau)} A\left(t_b - \frac{R_b}{c} - \tau\right)^* dt \tag{5-41}$$

The expressions for the code sequence are substituted for the general complex envelope term before proceeding. Also, for notational convenience, the constants leading the integral are briefly omitted, yielding

$$\chi(\tau) = \int_0^T \sum_{m=0}^{N-1} e^{j\omega_{scat}t} rect\left(\frac{t - \frac{R_s}{c} - mt_p}{t_p}\right) e^{j\phi_m} \left(\sum_{n=0}^{N-1} e^{-j\omega_{ref}(t-\tau)} rect\left(\frac{t - \frac{R_b}{c} - nt_p - \tau}{t_p}\right) e^{j\phi_n} \right)^* dt. \tag{5-42}$$

As in Appendix A, the following substitutions are made. Let $t'=t-R_s/c-mt_p$ or $t=t'+R_s/c+mt_p$ and $dt'=dt$. At the same time, define $-\tau' = R_s/c + (m-n)t_p - R_b/c - \tau$. Then (5-42) becomes

$$\chi(\tau) = \int_0^T \left[\sum_{m=0}^{N-1} e^{j\omega_{scat}(t'+\frac{R_s}{c}+mt_p)} rect\left(\frac{t'}{t_p}\right) e^{j\phi_m} \cdot \left(\sum_{n=0}^{N-1} e^{-j\omega_{ref}(t'+\frac{R_s}{c}+mt_p-\tau)} rect\left(\frac{t'-\tau'}{t_p}\right) e^{j\phi_n} \right)^* \right] dt \tag{5-43}$$

Eliminating τ so that only the primed time (t') or delay (τ') remain, taking the complex conjugate of the expression in the second (rightmost bracket), and rearranging the order of summation and integration gives

$$\chi(\tau) = \sum_{m=0}^{N-1} \sum_{n=0}^{N-1} e^{-j\phi_n} e^{j\phi_m} \int_0^T e^{j\omega_{scat}(t'+\frac{R_s}{c}+mt_p)} e^{-j\omega_{ref}(t'+\frac{R_b}{c}+nt_p-\tau')} rect\left(\frac{t'}{t_p}\right) rect\left(\frac{t'-\tau'}{t_p}\right) dt. \tag{5-44}$$

Factoring constants from the integral

$$\chi(\tau) = e^{j\omega_{scat}\frac{R_s}{c}} e^{-j\omega_{ref}\frac{R_b}{c}} \sum_{m=0}^{N-1} \sum_{n=0}^{N-1} e^{-j\phi_n} e^{j\phi_m} \int_0^T e^{j\omega_{scat}(t'+mt_p)} e^{-j\omega_{ref}(t'+nt_p-\tau')} rect\left(\frac{t'}{t_p}\right) rect\left(\frac{t'-\tau'}{t_p}\right) dt' \tag{5-45}$$

which will be included with the other constants (Z_c) briefly dropped for notational convenience.

Removing non-*t'* dependent terms from within the integral and after some simplification we arrive at a form similar to (5-24)

$$\sum_{m=0}^{N-1}\sum_{n=0}^{N-1} e^{-j\phi_n} e^{j\phi_m} e^{j(\omega_{scat} m t_p - \omega_{ref} n t_p - \omega_{ref}\tau')} \int_0^T e^{j(\omega_{scat}-\omega_{ref})t'} rect\left(\frac{t'}{t_p}\right) rect\left(\frac{t'-\tau'}{t_p}\right) dt'. \quad (5\text{-}46)$$

The limits of the integral under the definition of the *rect* function range over the nonzero convolution of the two integrand terms. The limits 0 and T become $-t_p$ to t_p as we constrain the solution to the nonzero correlation range of the delayed rect functions. Using

$$rect\left(\frac{t'}{t_p}\right) = 1 \quad \text{if} \quad |t'| < t_p \quad \text{and 0 otherwise.} \quad (5\text{-}47)$$

The nonzero convolution regime, as previously shown in Figure 5-14, has two cases based on the sign of τ'. With this, as in Section 5.2, (5-46) is broken into two solutions ($\tau' < 0$) and ($\tau' \geq 0$)

$$\sum_{m=0}^{N-1}\sum_{n=0}^{N-1} e^{-j\phi_n} e^{j\phi_m} e^{j(\omega_{scat} m t_p - \omega_{ref} n t_p - \omega_{ref}\tau')} \int_{\tau'}^{t_p} e^{j(\omega_{scat}-\omega_{ref})t'} dt' \text{ for } \tau' < 0 \quad (5\text{-}48)$$

and

$$\sum_{m=0}^{N-1}\sum_{n=0}^{N-1} e^{-j\phi_n} e^{j\phi_m} e^{j(\omega_{scat} m t_p - \omega_{ref} n t_p - \omega_{ref}\tau')} \int_0^{t_p-\tau'} e^{j(\omega_{scat}-\omega_{ref})t'} dt' \text{ for } \tau' \geq 0 \quad (5\text{-}49)$$

In both cases it is required that $|\tau'| < t_p$. Evaluating the definite integral in (5-49) first

$$\int_0^{t_p-\tau'} e^{j(\omega_{scat}-\omega_{ref})t'} dt' = \frac{1}{j(\omega_{scat}-\omega_{ref})}\left(e^{j(\omega_{scat}-\omega_{ref})(t_p-\tau')} - 1\right). \quad (5\text{-}50)$$

which becomes

$$\int_0^{t_p-\tau'} e^{j(\omega_{scat}-\omega_{ref})t'} dt' = e^{j\frac{(\omega_{scat}-\omega_{ref})(t_p-\tau')}{2}} \frac{\sin\left(\frac{(\omega_{scat}-\omega_{ref})(t_p-\tau')}{2}\right)}{\frac{(\omega_{scat}-\omega_{ref})}{2}}. \quad (5\text{-}51)$$

Substituting (5-51) back into (5-49)

$$\sum_{m=0}^{N-1}\sum_{n=0}^{N-1} e^{-j\phi_n} e^{j\phi_m} e^{j(\omega_{scat} m t_p - \omega_{ref} n t_p - \omega_{ref}\tau')} e^{j\frac{(\omega_{scat}-\omega_{ref})(t_p-\tau')}{2}} \frac{\sin\left(\frac{(\omega_{scat}-\omega_{ref})(t_p-\tau')}{2}\right)}{\frac{(\omega_{scat}-\omega_{ref})}{2}} \quad (5\text{-}52)$$

The exponential terms not related to the PN code sequence (index) are expanded, then simplified, giving

$$\begin{aligned} &e^{j(\omega_{scat} m t_p - \omega_{ref} n t_p - \omega_{ref}\tau')} e^{j\frac{(\omega_{scat}-\omega_{ref})(t_p-\tau')}{2}} = \\ &e^{j\omega_{scat}(1/2+m)t_p} e^{-j\omega_{ref}(1/2+n)t_p} e^{j(1/2)(3\omega_{ref}-\omega_{scat})\tau'}. \end{aligned} \quad (5\text{-}53)$$

With (5-53) inserted into (5-52) and defining

$$K_4 = \frac{\sin\left(\frac{(\omega_{scat}-\omega_{ref})(t_p-\tau')}{2}\right)}{\frac{(\omega_{scat}-\omega_{ref})}{2}} e^{j\omega_{scat}(1/2+m)t_p} e^{-j\omega_{ref}(1/2+n)t_p} e^{j(1/2)(3\omega_{ref}-\omega_{scat})\tau'} \quad (5\text{-}54)$$

the solution is given (for τ'>0) then has the same form as (5-27), or

$$\chi(\tau) = Z_c \sum_{m=1}^{N_c}\sum_{n=1}^{N_c} K_4 \left[u_m u_n^*\right] \quad (5\text{-}55)$$

With $|\tau'| < t_p$ (as earlier) or

$$K4(\tau'>0) = \begin{cases} \frac{\sin\left(\frac{(\omega_{scat}-\omega_{ref})(t_p-\tau')}{2}\right)}{\frac{(\omega_{scat}-\omega_{ref})}{2}} e^{j\alpha}, |\tau'| < t_p \\ 0, otherwise \end{cases} \quad (5\text{-}56)$$

with

$$\begin{aligned} \alpha &= \omega_{scat}(1/2+m)t_p - \omega_{ref}(1/2+n)t_p + (1/2)(3\omega_{ref} - \omega_{scat})\tau' \\ Z &= C_r C_s e^{-jk_0\Delta R} e^{j\omega_{scat}\frac{R_s}{c}} e^{-j\omega_{ref}\frac{R_b}{c}}. \end{aligned}$$

As indicated in (5-56) the Doppler-derived phase contribution is a function of delay and will be present in the combined, pulse compressed signal result.

Returning to (5-48) (τ'<0) and following the same series of steps as above we get the solution of the same form as (5-25) with the constant in (5-26) slightly modified as

$$K4(\tau'<0)=\begin{cases}\dfrac{\sin\left(\dfrac{(\omega_{scat}-\omega_{ref})(t_p+\tau')}{2}\right)}{\dfrac{(\omega_{scat}-\omega_{ref})}{2}}e^{j\alpha}, |\tau'|<t_p\\ 0, otherwise\end{cases} \tag{5-57}$$

with α as defined in (5-56).

Equations 5-55, 5-56 and 5-57 represent the time domain solution using the PN code as a surrogate for the HDTV signal. We complete the analytic development in this section by constraining the temporal response to the interval plus and minus one code chip duration about the matched delay and develop the frequency domain Triangular approximation, which incorporates the effects of platform motion. In the time domain this expression is of the form (Appendix C equation C-10)

$$\begin{aligned}\chi(\tau>0)&=\alpha N_c\left(t_p-\left(\tau-\frac{\Delta R}{c}\right)\right)C_rC_se^{-jk_0\Delta R}e^{j\omega_{scat}\frac{R_s}{c}}e^{-j\omega_{ref}\frac{R_b}{c}}\\ \chi(\tau<0)&=\alpha N_c\left(t_p+\left(\tau-\frac{\Delta R}{c}\right)\right)C_rC_se^{-jk_0\Delta R}e^{j\omega_{scat}\frac{R_s}{c}}e^{-j\omega_{ref}\frac{R_b}{c}}\\ \alpha&=e^{j\left(\frac{1}{2}(3\omega_{ref}-\omega_{scat})\left(\tau-\frac{\Delta R}{c}\right)\right)}e^{j\frac{N_c}{2}(\omega_{scat}-\omega_{ref})t_p}\end{aligned} \tag{5-58}$$

The derivation of the spectrum function with Doppler contributions can be found in Appendix C. The results in (5-55) to (5-58) are subjected to the same assumption as the move-stop-move case: only the dominant response is considered. The range response is delimited to ΔR-t_p to ΔR+t_p, eliminating the time sidelobe region or concentrating on the main response lobe. The spectrum for the signal component including motion is

$$S_{\phi,\theta}(k)=2C_sC_rN_ct_pe^{-j(k+k_0)\Delta R}e^{j\omega_{scat}(R_s/c)}e^{-j\omega_{ref}(R_b/c)}e^{j(N_c/2)(\omega_{scat}-\omega_{ref})t_p}\frac{\sin\left(\frac{r_p}{2}(\beta-k)\right)^2}{\frac{r_p}{2}(\beta-k)^2} \tag{5-59}$$

where β=1/(2c)(3ω_{ref}-ω_{scat}). As a final step, if we rewrite the sinc-squared term as the product of two sinc terms, factor a (-1) from the denominator -1(k-β) and argument of the numerator and use the identity sin(-x)=-sin(x). The negatives cancel and we are left with

$$S_{\phi,\theta}(k) = 2C_s C_r N_c t_p e^{-j(k+k_0)\Delta R} e^{j\omega_{scat}(R_s/c)} e^{-j\omega_{ref}(R_b/c)} e^{j(N_c/2)(\omega_{scat}-\omega_{ref})t_p} \frac{\sin\left(\frac{r_p}{2}(\beta+k)\right)^2}{\frac{r_p}{2}(\beta+k)^2} \tag{5-60}$$

with β=1/(2c)(ω_{scat} -3ω_{ref}).

We see from the development above a dependence on both the Doppler impressed on the reference channel, which is necessarily different from the Doppler on scatterers within the intended image scene, and the main channel. The signal in the main channel contains the contributions from the myriad of scatterers in that channel while the reference channel contains, preferably, only the transmitted waveform (absent multipath). The Doppler contribution in the reference channel could be compensated prior to pulse compression. The derivation of the pulse compression product in this condition was found in Appendix D and in the time domain is

$$\begin{aligned}
\chi(\tau' > 0) &= Z_{cc} N_c t_p \left(1 - \left(\frac{r-\Delta R}{r_p}\right)\right) e^{-j\frac{\omega_{scat}}{2c}(r-\Delta R)} e^{j\frac{N}{2}\omega_{scat}t_p} \\
\chi(\tau' < 0) &= Z_{cc} N_c t_p \left(1 + \left(\frac{r-\Delta R}{r_p}\right)\right) e^{-j\frac{\omega_{scat}}{2c}(r-\Delta R)} e^{j\frac{N}{2}\omega_{scat}t_p}
\end{aligned} \tag{5-61}$$

In the frequency domain the equivalent result is given by

$$S_{\phi,\theta}(k) = 2C_r C_s N_c t_p e^{-j(k_0+k)\Delta R} e^{j\omega_{scat}\left(\frac{R_s}{c}+\frac{N_c t_p}{2}\right)} \frac{\sin^2\left(\left(\frac{\omega_{scat}}{2c}+k\right)\frac{r_p}{2}\right)}{\frac{r_p}{2}\left(\frac{\omega_{scat}}{2c}+k\right)^2}. \tag{5-62}$$

We see in (5-60) two perturbation sources to tomographic reconstruction. Both are spatially varying, one a phase term. The first error source is a phase contribution which results in mismatch during reconstruction. This phase term has two components: one a function of position and the other related to burst time bandwidth. Equation 5-58 is

consistent with the move-stop-move result from earlier: when the platform speed goes to 0 then (5-60) reduces to (5-59). The second distortion source is the envelope term which is very slightly shifted under the Doppler influence (the value of β is very, very small with the speed of light in the denominator). This is in contrast to the result in the time domain (5-56) where the Doppler contribution is a function of the code index and thus a function of time.

The magnitude of the effect on image reconstruction in the presence of uncompensated platform motion can now be assessed. We have two approaches to model the impact which are relevant to the remainder of Section 5. We first illustrate the degree of image degradation resulting from platform motion while holding the time-bandwidth (TB product) constant. Spatial variations in the distortion are briefly surveyed with platform speed and constant TB product. Finally, the contribution due to TB product with constant speed is covered.

Figure 5.19 presents the calculated point spread function realized based on using (5.58) without compensation and for the kinematic regime represented by the planned flight collection. A small, low speed, civil aircraft (Cessna 170) executing a cylindrical spiral trajectory with a time-bandwidth product representative of the planned collection. Three different airspeeds are run; 120, 240 and 360 knots (62, 124, and 185 m/sec). In order to keep the number of spatial sample constant (for run time considerations, only) the rates of climb were increased as a function of speed; 100, 200 and 300 fpm (0.51, 1.02 and 1.52 m/sec) producing essentially identical sampling apertures (and the angle between spatial samples held constant at 1 degree). Maintaining a constant sample count also means that the density of vertical samples is approximately equal: the number of spiral orbits completed in the elevation aperture of 200-2000 m. The burst duration is 1.67 msec or TB= 10,000. With increasing speed the X-Y plane sidelobes are seen to degrade, relative to the peak response and the peak response shifts off the simulated scatterer position.

Slightly asymmetric sidelobes occur along the X cardinal axis with a more severe lobe-splitting seen along the Y axis. The Z axis is largely unaffected but does show effects as the vertical component of platform speed increases. It should be noted that the simulation geometry used a test location different from that flown so geometry discussions here are relevant only to this analysis geometry.

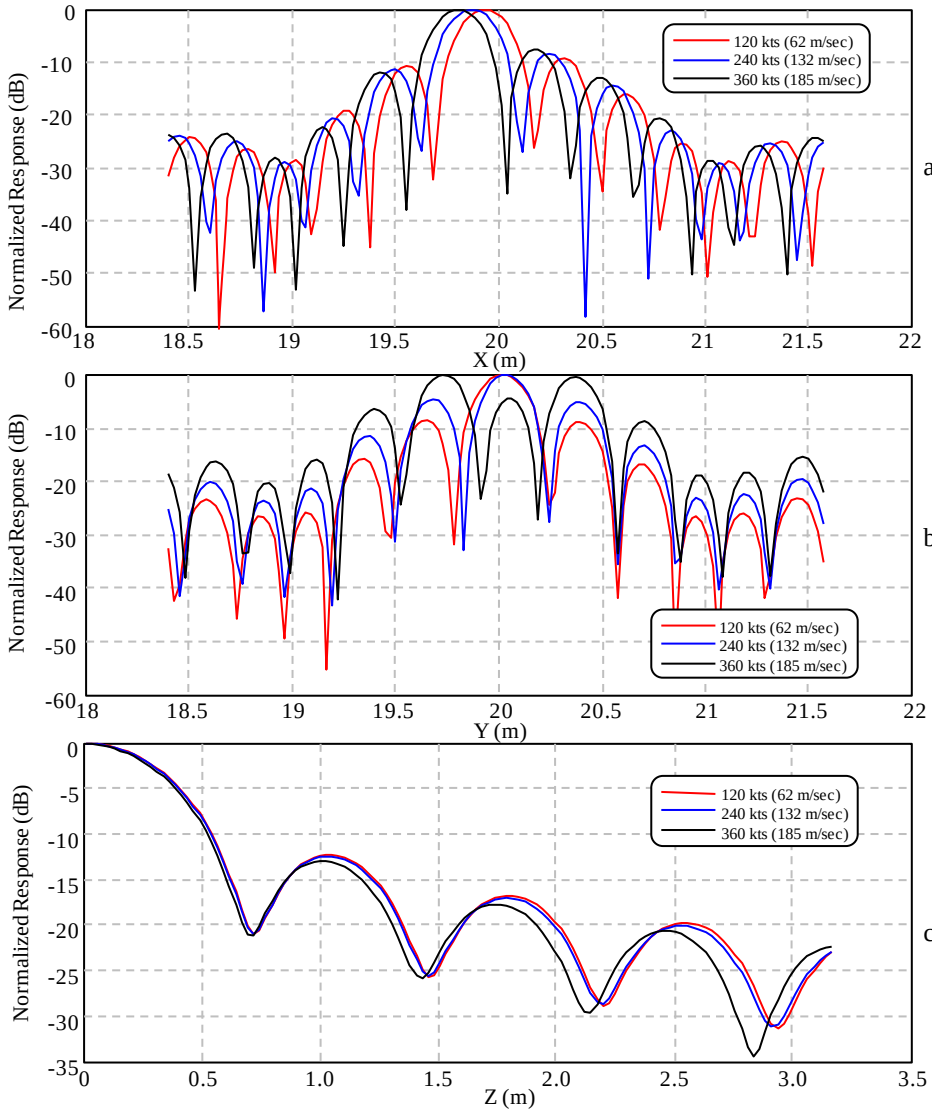

Figure 5.19. Reconstruction w/out Doppler Comp. – Dependence on Platform Speed

Spatial variance in the reconstruction is seen in the next two Figures. In Figure 5.20 the points on the corners of a square are defined (constant radial distance from scene origin) and reconstructed without compensation. In this example the highest platform speed from Figure 5.19 was used (185 m/sec) with the same TB product (10^4). The responses along the X and Y axes nearly overlay, matching the corresponding results in Figure 5.19.

However we experience a slight degradation in the sidelobe levels and resolution of the Z response for those voxels located at X < 0 relative to those (two points) in the plane positive half-space. Only the Z axis responses are shown.

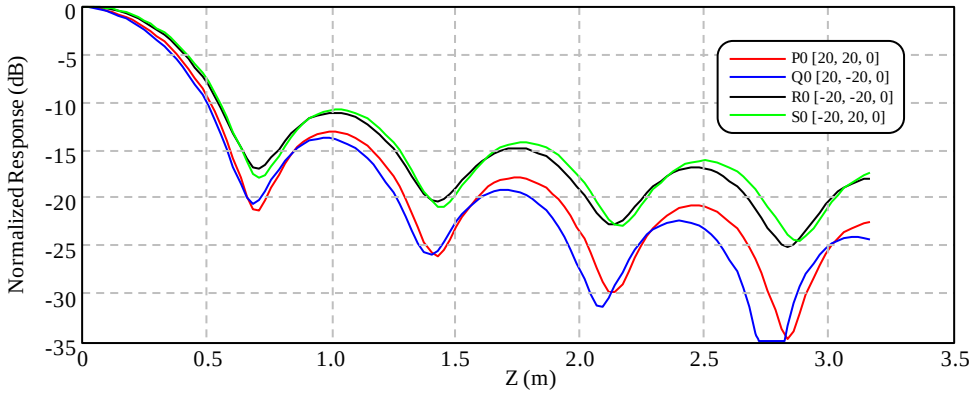

Figure 5.20. Reconstruction without Doppler Compensation, Z axis Only

Figure 5.21 also examines spatial variation, this case we vary the radial distance from the origin along a line of constant polar angle. The flight condition and collection aperture used matches the two previous cases. Again the X and Y axis results are predominately unchanged (a slight increase in the Y axis lobe at the position of the simulated scatterer with increasing radial distance) but the lobe splitting is equally pronounced. Again the Z axis results show the most variation where sidelobe level decreases with increasing radial distance.

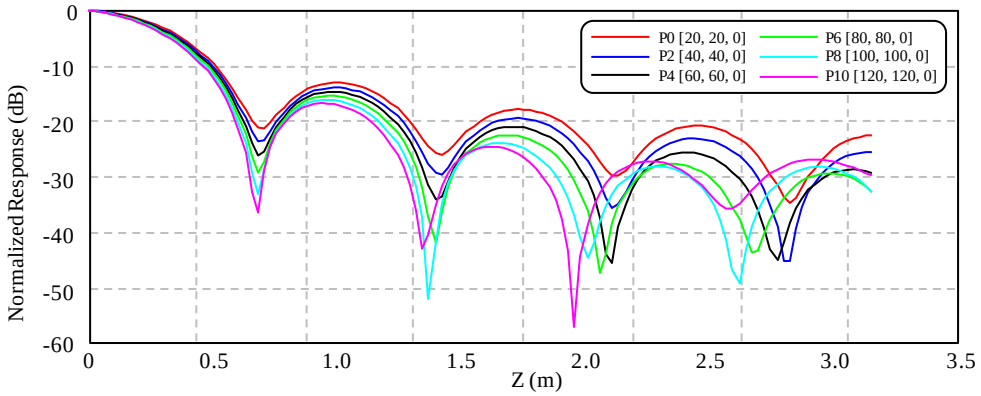

Figure 5.21. Reconstruction without Doppler Compensation – Spatial Variation with Fixed Speed (185 m/sec) and Time-Bandwidth (10^4) Z axis Only

Finally, the effects of the coherent integration time are seen in Figure 5.22. Figure 5.22a and 5.22b are X axis and Y axis comparisons of the effect of TB product at a constant

speed: three burst durations, incrementing by a factor of 10, were chosen to illustrate the effect. Processing runtimes were again the only consideration in depicting cardinal axis performance. The results in the Figure are based on the same geometry as the preceding graphs and a platform speed of 120 knots. The simulated isotropic scatterer was positioned at (20, 20, 0). Increasing the burst duration introduces the same effect as platform speed. Comparing Figure 5.22 to the X-Y plots in Figures 5.19 and 5.20 show the same trend. The increasing phase error introduced by motion results in peak response shifting with degradation in sidelobes along the X axis. Along Y we see the mainlobe response split into two lobes as TB increased. The generation of Figure 5.22 is different than the previous three cases in that direct signal leakage into the main channel was enabled. A fixed, low side/backlobe level was used over the full aperture. More on this in the next Section.

The differences between the X and Y axis results in the presence of uncompensated Doppler were unexpected. The Doppler contribution to the phase mismatch is dominated by the direct path contribution in the reference channel (again this section has assumed

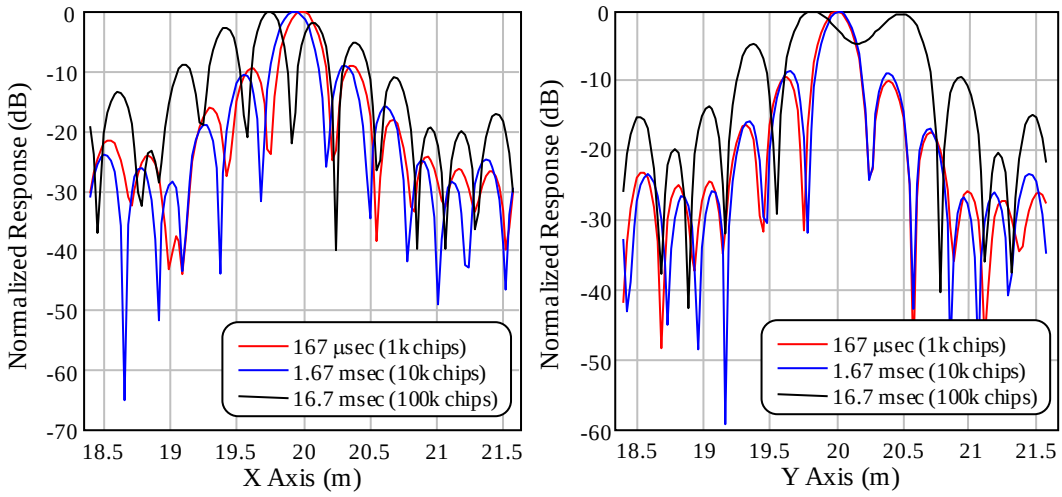

Figure 5.22. Reconstruction without Doppler Compensation – Dependence on Coherent Integration Time/TB Product

perfect isolation between main and reference signals). This is unsurprising given that the main antenna is oriented at 90 degrees to the flight vector. We make a cursory

examination to the root cause or dependency of the mechanism for the different responses experienced along X and along Y before proceeding to compensation. Figure 5.23 is composed of several plots which represent the underlying processes as calculated for a single orbit of the multiple orbit cylindrical spiral. Figure 5.23a shows scatterer and direct path Doppler versus angle, demonstrating the observation above. Two speeds are shown for both the direct path (solid curves) and the scattered path (dashed curves), referenced against a single point in the scene (20, 20, 0). The Doppler-induced phase distortion, for this same point, which is the real argument of the second exponential term in (5-59), as a function of both platform speed (for fixed TB product) and TB for fixed speed, is shown in Figure 5.23b. The change in total phase due to position over the aperture is much greater than Doppler, though both increase with radial distance from scene origin. It should also be noted that the degree of reconstruction mismatch is less evident when the individual runs, along each axis, are self-normalized then displayed on the same scale. Examples which illustrate the phase error in X and Y are shown in Figure 5.23c.

In Figure 5.23, four points are symmetrically defined, along the cardinal axes, with respect to the scatterer. The phase error due to the spatial-only mismatch between each position and the scatterer position is given by the solid curves. This mismatch in the no-Doppler case is anti-symmetric along both axes (sign). When Doppler is introduced the response along +X has increased magnitude while –X is compressed and the error along Y shifts in angle in opposite directions depending on the half-plane that the point lies in, producing the shifted peak response upon reconstruction Figure 5.23d illustrates the locus of the minimum total phase error, the value along X corresponds to the reconstruction peak in Figure 5.19a. The phase error is larger along Y but nearly symmetric.

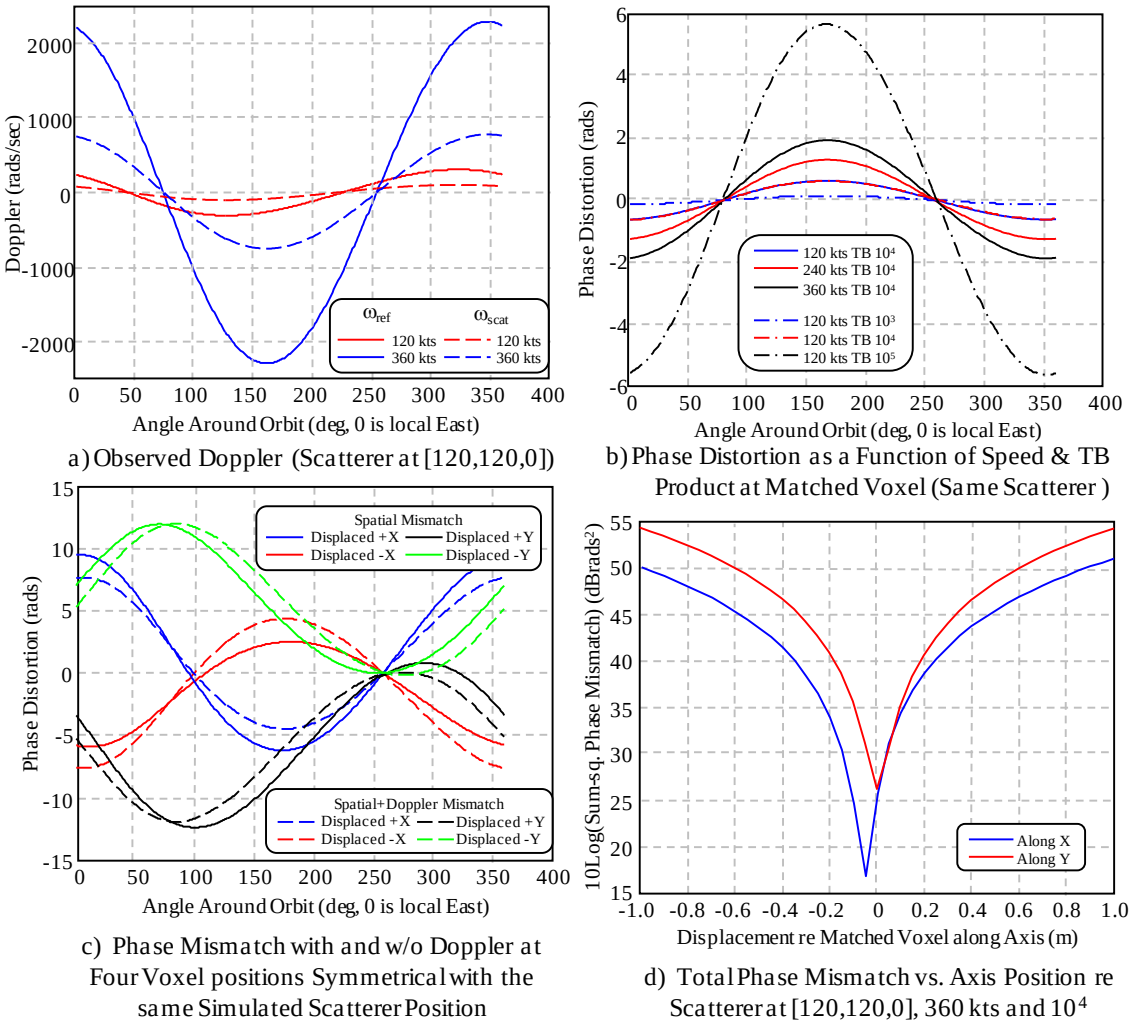

a) Observed Doppler (Scatterer at [120,120,0])

b) Phase Distortion as a Function of Speed & TB Product at Matched Voxel (Same Scatterer)

c) Phase Mismatch with and w/o Doppler at Four Voxel positions Symmetrical with the same Simulated Scatterer Position

d) Total Phase Mismatch vs. Axis Position re Scatterer at [120,120,0], 360 kts and 10^4

Figure 5.23. Phase Mismatch due to Platform Motion

We examine the Z contribution separately. This is motivated by the near independence if the aperture vertical extent contribution from the overall resolution. The form of the point spread function has been shown to be, in the X-Y plane, virtually unaffected by the vertical aperture extent, and that the Z response resembles that of an antenna-like aperture. The (limited) results presented in this section, in the presence of platform motion, show a dependence on voxel location with +X half space realizing a degree of sidelobe reduction, as though a taper or window was applied, while those in the –X half space experience degraded sidelobe levels. The behavior between Figures 5.19, 5.20, and 5.21 is as though, at some positions, the phase error virtually extends the vertical aperture (decreased mainlobe width as well as sidelobe nulls at decreasing separation) while at others the phase mismatch degrades the sidelobe peak level.

It is interesting to note that examining the Doppler generated phase error over elevation and at the same azimuth position demonstrates that the total phase error at each azimuth position is small and is periodically modulated. Figure 5.24 depicts the total spread of Doppler phase at each azimuth increment. This Figure displays the results for the four points in Figure 5.20 with the same geometry and attributes. It is interesting that a (sometimes) positive artifact is introduced along Z while simultaneously the PSF degradation is experienced in the X-Y plane. Note that the slight discontinuity at 310 degrees is the result of the total number of points in the aperture not being an integer multiple of 360. When binning points in elevation, 310-360 degrees only occupied 27 orbits instead of 28. The lower altitude for these angles yields a smaller depression angle and correspondingly altered the Doppler error. This range, not the actual values, is solely due to scene scatterers (only a single scatterer shown). The phase function in elevation is cubic with a general slope that is a function of the azimuth sample position; slope the highest at the angles with the largest extent.

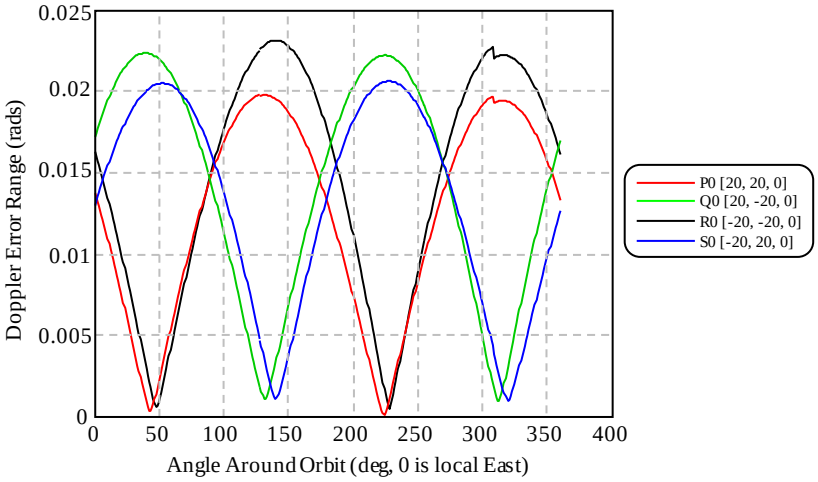

Figure 5.24. Periodic Modulation of Phase Error Extent over Elevation vs. Polar Angle

5.3.2 ***Compensating for the effects of platform motion***. Equations 5-55, 5-56 and 5-57 represent the time domain compressed pulse solution using the PN code as a surrogate for the HDTV signal, and which contains Doppler time dependencies relating to the code

index in the compressed response. Equations 5-59 and 5-60 contain the same for the representation in the frequency domain. The frequency domain result contains a clear contribution due to platform motion that is easily separable in the sense that it, though complex, is a simple multiplicative term which is dependent on the spatial position and platform kinematic state. The phase term solely contains Doppler and TB product dependencies and is spatially variant. A single correction can be applied during reconstruction using the conjugate of the phasor based on the location of the voxel-under-test and the kinematic state of the receiving platform at the sample burst time. This latter is provided by the radar navigation (motion solution) function.

The simulated phenomenology used to create all the results including platform motion was generated in the frequency domain using (5-58). This represents the forward transformed projections. As the collection spatial aperture is exactly simulated, it was a simple matter to apply the conjugate phase expression during reconstruction. Without system errors the compensation is perfect (the product of the error and correction phasors is unity) and the IPR reconstruction is compensated. Two examples are shown in Figure 5.25. On the left (Figure 5.25a) the slower, but larger TB product (10^5) case (Figure 5.22) while on the right (Figure 5.25b) the faster scenario from Figure 5.19.

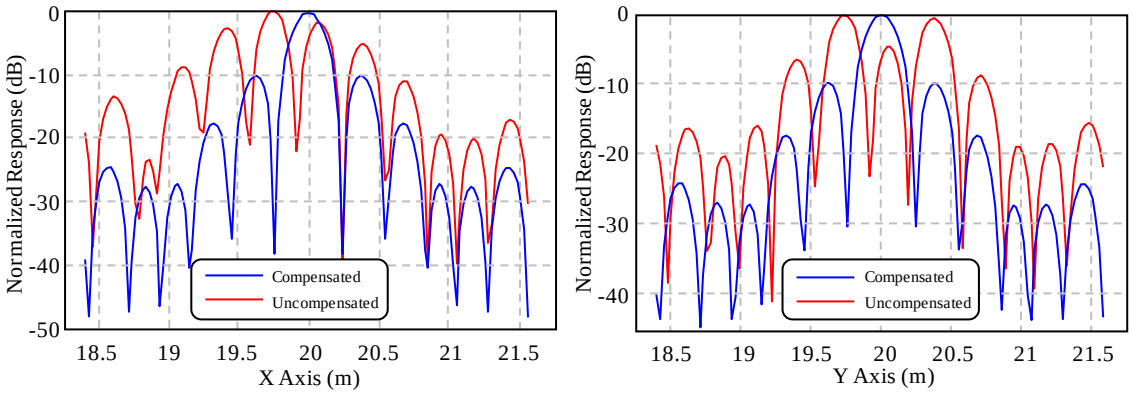

a) TB = 10^5, V = 120 kts b) TB = 10^4, V = 360 kts

Figure 5.25. Reconstructed Response after Doppler Compensation

The need to implement Doppler compensation was primarily driven by the motion effects superimposed on the reference channel which are then mixed into the compressed burst

through correlation processing. We saw that when the motion-Time-Bandwidth product was low that little to no degradation was observed. By compensating the reference channel ahead of the pulse compression operation we are left with the result in (5-62) where only the scatterer contribution to Doppler remains. The magnitude of this term is much smaller with a side oriented antenna with the scene Doppler being filtered through the receive antenna pattern. There remains dependence on the coherent integration time associated with the cross correlation. As we saw from Figure 5.22 though the Time-Bandwidth component easily dominates over the range of Doppler evaluated.

5.4 Direct Path Signal Influence.

Several sources illustrate the problems associated with the imperfect isolation between the main and reference channels that unless the direct signal breakthrough is managed a usable radar product is unlikely to result: the leakage signal time sidelobes mask returns of interest. Continuing our reliance on the single scatterer model [117], we codify the impact due to direct path energy entering through the finite sidelobes of the main channel and implement mitigation as also suggested in [118].

The signal at the imaging antenna is the linear combination of signal from the scattered (bistatic) path with a component of the direct path received through the sidelobes of the imaging antenna. Following (5-5)

$$X_s(t) = C_s A\left(t - \frac{R_s}{c}\right)e^{-jk_0R_s} + C_{rl}A\left(t - \frac{R_b}{c}\right)e^{-jk_0R_b} \tag{5-63}$$

where C_s is a voltage scalar which includes gain in the direction of the scatterer, scatterer bistatic radar cross section, bistatic range sum, and any systematic contributions. C_{rl} is the main antenna gain in the direction of the transmitter (sidelobe gain) and includes the baseline range and other system scaling factors. The direct path signal received in the reference antenna with voltage scalar (C_r) including the antenna gain in the direction of the

transmitter and has the same form as the second expression in (5-5). We assume that no scene energy enters the reference channel, though direct path multipath may be present. Inserting into (5-63) and the reference antenna term from (5-5) permits the derivation of the compressed pulse containing both contributions using (5-3)

$$\chi(\tau) = \int_0^T \left[\begin{array}{l} C_s A\left(t - \frac{R_s}{c}\right) e^{-jk_0 R_s} \\ + C_{rl} A\left(t - \frac{R_b}{c}\right) e^{-jk_0 R_b} \end{array} \right] C_r A\left(t - \frac{R_b}{c} - \tau\right)^* e^{jk_0 R_b}\, dt. \tag{5-64}$$

As earlier, R_s is the range sum (R_1+R_2), R_b the baseline range.

Equation 5-64 can be factored into two integrals which are evaluated independently.

$$\chi(\tau) = \chi_1(\tau) + \chi_2(\tau). \tag{5-65}$$

The second ($\chi_2(\tau)$ is the scattered path signal which has been addressed in Sections 5.2 and 5.3 (as the term $\chi(\tau)$). The first term represents the leakage of the direct path signal in the reference channel correlated with the direct path signal (direct signal breakthrough) in the main channel

$$\chi_1(\tau) = C_{rl} C_r \int_0^T A\left(t - \frac{R_b}{c}\right) A\left(t - \frac{R_b}{c} - \tau\right)^* dt. \tag{5-66}$$

Substituting the surrogate PN code (ϕ_m represents the m^{th} code bit)

$$\chi_1(\tau) = C_{rl} C_r \int_0^T \sum_{m=0}^{N-1} rect\left(\frac{t - \frac{R_b}{c} - mt_p}{t_p}\right) e^{j\phi_m} \left[\sum_{n=0}^{N-1} rect\left(\frac{t - \frac{R_b}{c} - nt_p - \tau}{t_p}\right) e^{j\phi_n} \right]^* dt. \tag{5-67}$$

Making a substitution for time

$$t_b = t - \frac{R_b}{c} - mt_p \quad t = t_b + \frac{R_b}{c} + mt_p \quad dt_b = dt \tag{5-68}$$

giving

$$\chi_1(\tau) = C_{rl} C_r \int_0^T \sum_{m=0}^{N-1} rect\left(\frac{t_b}{t_p}\right) e^{j\phi_m} \left[\sum_{n=0}^{N-1} rect\left(\frac{t_b + (m-n)t_p - \tau}{t_p}\right) e^{j\phi_n} \right]^* dt_b. \tag{5-69}$$

A second substitution introduces a modified delay variable $t_{prime}=(n-m)t_p-\tau$ reduces to the well known form for phase codes (taking the complex conjugate and reversing the order of integration and summation (as earlier), we get

$$\chi_1(\tau') = C_{rl}C_r \sum_{m=0}^{N-1}\sum_{n=0}^{N-1} e^{j\phi_m} e^{-j\phi_n} \int_0^T rect\left(\frac{t_b}{t_p}\right) rect\left(\frac{t_b-\tau'}{t_p}\right) dt_b. \tag{5-70}$$

The evaluation of the integral proceeds as shown in Figure 5.19 for $\tau'<0$ and $\tau'\geq 0$

$$\begin{aligned} \chi_1(\tau' \geq 0) &= C_{rl}C_r \sum_{m=0}^{N-1}\sum_{n=0}^{N-1} e^{j\phi_m} e^{-j\phi_n} \int_0^{t_p-\tau'} 1 dt_b \\ \chi_1(\tau' < 0) &= C_{rl}C_r \sum_{m=0}^{N-1}\sum_{n=0}^{N-1} e^{j\phi_m} e^{-j\phi_n} \int_{-\tau'}^{t_p} 1 dt_b \end{aligned} \tag{5-71}$$

The solution to (5-66) is the autoambiguity function for the waveform modulation $A(t)$. The solution to (5-71) is

$$\chi_1(\tau) = C_{rl}C_r \sum_{m=1}^{N_c}\sum_{n=1}^{N_c} K_1\left[u_m u_n^*\right] \tag{5-72}$$

where K_1 is defined as (after reversing the substitution for τ')

$$K_1 = \begin{cases} t_p - \left|\tau-(n-m)t_p\right|, \left|\tau-(n-m)t_p\right| < t_p \\ 0, otherwise \end{cases} \tag{5-73}$$

t_p the code chip duration, $u_m=exp(j\phi_m)$; $\phi=(0,\pi)$, and N_c remains the number of code chips in the coherent processing interval. In the direct path response there is no geometry dependency (the baseline range delay terms cancel). The delay reference (τ=0) corresponds a range difference of 0 (we could have developed and carried a delay term, $\Delta_r=R_b-R_b$, in equation 5-70, analogous to the derivation for the χ_2 in Section 5.2). Thus the peak response of the directly leaking signal occurs at 0 delay reference and is only scaled by an R^2 (one-way propagation) dependency.

We can use the results derived for the individual channel contributions in (5-72) and (5-57) in (5-65) which gives the solution depicted notionally in Figure 5.26, to address the single

burst sensitivity of the random waveform. Note that in this development we have assumed that no other signals are present, such as multipath scattering in the reference channel.

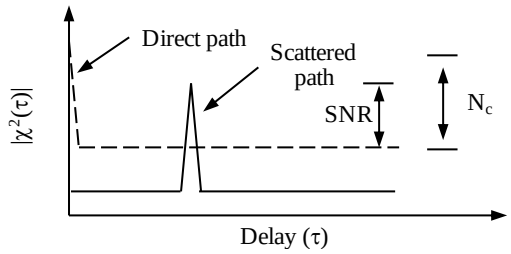

Figure 5.26. Graphical Illustration Direct Path Imposed Noise Floor

Scaling of the results in (5-73) and (5-57) are realized by evaluating both at peak (autocorrelation) response; the cross correlation in (5-57) yields an impulse of magnitude at $\tau - \Delta R/c = 0$ (or $t = (R_s - R_b)/c$) of

$$\left| \chi_2 (\tau - \frac{\Delta R}{c} = 0) \right| = C_s C_r N_c t_p \tag{5-74}$$

where N_c is the number of chips (PN code or effective equivalent) in the coherent integration time T ($=N_c t_p$). For nonzero delays the response from (5-74) is a nominally uniform time sidelobe [113] with level $|\chi_2(\tau - \Delta R/c)|/N_c^{1/2}$, if the magnitude is taken, and $\chi_2(\tau - \Delta R/c)/N_c$ if the magnitude-squared is employed. Likewise evaluating (5-73)

$$\left| \chi_1 (\tau = 0) \right| = C_r C_{rl} N_c t_p \tag{5-75}$$

with the same sidelobe structure resulting from the same code (in a single burst). The scaling voltage constant for the signal channel is given by

$$C_s = \sqrt{G_s(\phi) \frac{P G_{xmtr} \lambda^2}{(4\pi)^2 L_s R_1^2 R_2^2} \frac{\sigma}{(4\pi)}}. \tag{5-76}$$

The reference channel scalar (C_r) does not include a scatterer cross section (σ) and the range terms are replaced by the baseline range. The time sidelobes of $\chi_1(\tau)$ create an effective noise floor, as shown in Figure 5.26. As the platform executes the collection aperture the response will be a function of position as the (installed) antenna gains in the direction of the transmitter vary during sampling.

Simulating the combined system response using (5-65) resulted in the image shown in Figure 5.27. In the example the isotropic scatterer RCS was 1 m^2, baseline range 29 km with a 1000 chip PN code employed. The direct signal breakthrough clearly masks the underlying scatterer, the image is the result of essentially averaging over 3240 noise like samples. The measurement system represented the initial design configuration of the bistatic collection system described in Section 6 in terms of the antenna gains and expected sidelobe levels. Figure 5.27 was generated based on the cylindrical spiral aperture used earlier, with vertical aperture extending from 200-2000 m and platform speed of 62 m/sec.

5.4.1 ***Direct signal breakthrough mitigation***. This can be realized in several ways: the approach used in this work is that of using the reference antenna as the auxiliary antenna for an adaptive sidelobe canceller prior to pulse compression. The configuration of the adaptive sidelobe canceller is of a low gain, wide angular coverage antenna that is co-located with the sensing antenna, in this case the imaging antenna. A notional configuration is shown in Figure 5.28, along with antenna patterns specific to the sidelobe cancellation application. The antenna patterns were derived from initial analytic pattern derivations (three element main antenna with binomial weights and turnstile). The goal of the adaptive process is to maximize the signal to noise ratio in the main channel. We define the signal measurement vector $\boldsymbol{x}(t)$ as

$$\boldsymbol{x}(t) = \boldsymbol{s}(t) + \boldsymbol{n}(t) \tag{5-77}$$

where $\boldsymbol{s}(t)$ is the desired signal and $\boldsymbol{n}(t)$ is the unwanted or noise component. The derivation of the optimum weights for the two channel canceller requires knowledge of the second moment statistics of the interfering signal. With the covariance $\boldsymbol{R}$ the optimum weights are given by

$$\boldsymbol{w}_{opt} = \boldsymbol{R}^{-1}\boldsymbol{s} \tag{5-78}$$

In (5-78) there is a constant of proportionality which we have set to 1.

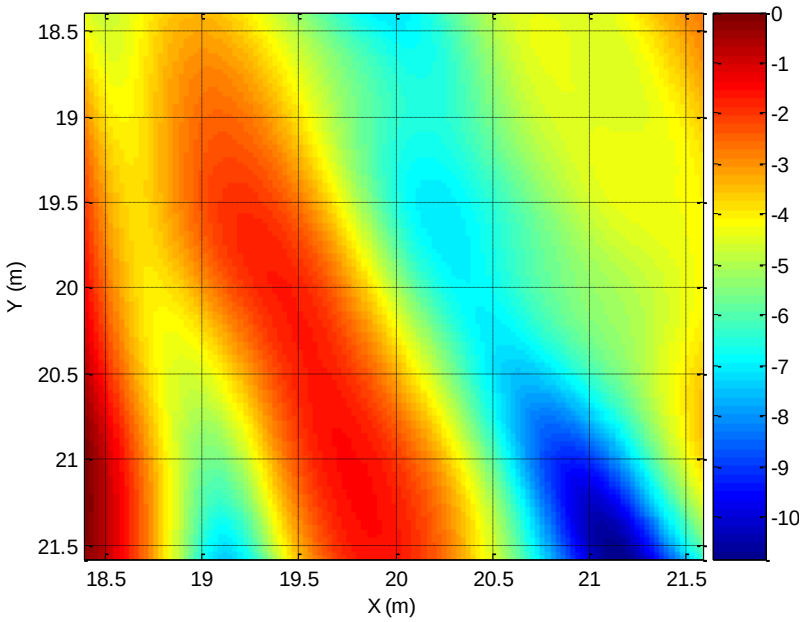

Figure 5.27. Image Formed with DSB Present

This result is obtained through maximization of the output signal-to-noise ratio [119, among many]. Other methodologies which might be selected are Mean Squared Error (MSE), Maximum Likelihood (ML) and Minimum Noise Variance (MV). All yield essentially the same formulation for the realization of the optimum antenna weights [119].

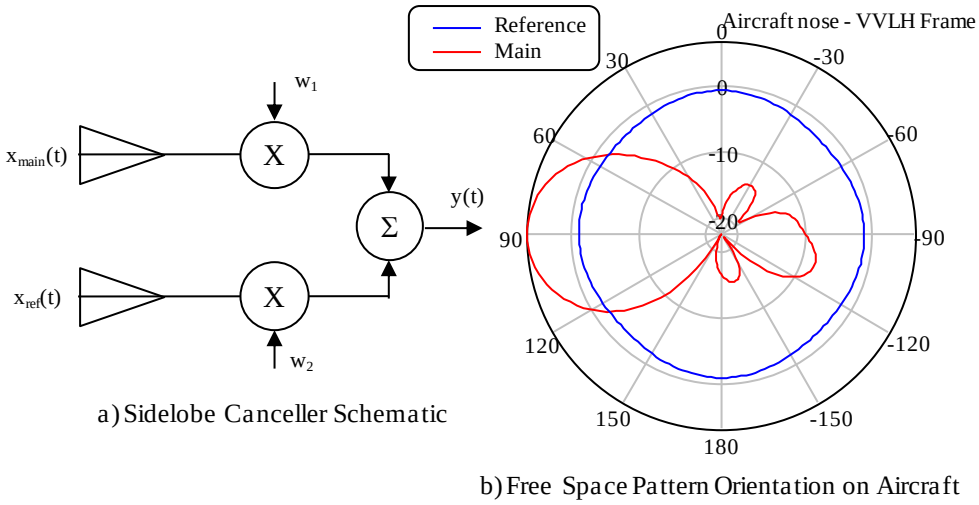

a) Sidelobe Canceller Schematic

b) Free Space Pattern Orientation on Aircraft

Figure 5.28. Adaptive Beamformer Schematic and Antenna Patterns

As the waveforms and statistics are not known *a priori* the covariance must be estimated. As we are dealing with a narrowband signal (1%) there are no bandwidth considerations [119] and we use Sample Matrix Inversion (SMI) [120] to estimate the degree of

correlation between signals in the main channel and the reference channel. A requirement that the interfering signal be the most strongly correlated avoids cancellation of the signal of interest in the main channel. The implication is that the antenna gain in the reference channel in the direction of the interfering source be greater than the main channel, hence the gain configuration in Figure 5.28b. If this is not met then the adaptive beamformer trains on signal of interest resulting in self nulling. The SMT estimated covariance is

$$\hat{\mathbf{R}} = \frac{1}{N}\sum_{i=0}^{N-1}\mathbf{x}_i\mathbf{x}_i^{*} \tag{5-79}$$

where $\boldsymbol{x}$ is a 2×1 vector formed from stacked synchronous samples of the antenna channels and * represents conjugate transpose. The row vector $\boldsymbol{s}$ in (5-78) is the steering vector. For the discrete antenna case here (as opposed to an array application) this vector selects the channel to be maximized. With the formation of **x** as

$$\mathbf{x} = \begin{bmatrix} \mathbf{x}_{main} \\ \mathbf{x}_{ref} \end{bmatrix} \qquad \text{then } \boldsymbol{s} \text{ is given by} \qquad \mathbf{s} = \begin{bmatrix} 1 \\ 0 \end{bmatrix} \tag{5-80}$$

The cancelled output is then given by

$$y(t) = \mathbf{w}_{opt}^{*}\mathbf{x}(t) \tag{5-81}$$

where the weights have been normalized to unity magnitude. Equation 5-81 is evaluated using the PN code surrogate for the HDTV signal with two examples shown in Figure 5.29. The first case (Figure 5.29a) is specifically intended to illustrate a scenario where the point target return is at the level of the time sidelobes due to direct path signal leakage (10^3 code chips) prior to cancellation while the second case (Figure 5.29b) with the target visible before the canceller is applied (10^4 code chips). In both cases the effective noise floor ($1/N_c$) can be observed. The geometry used in the generation of Figure 5.29 is from preliminary flight test planning, and are based on the antenna patterns in Figure 5.28 which represent uninstalled estimates.

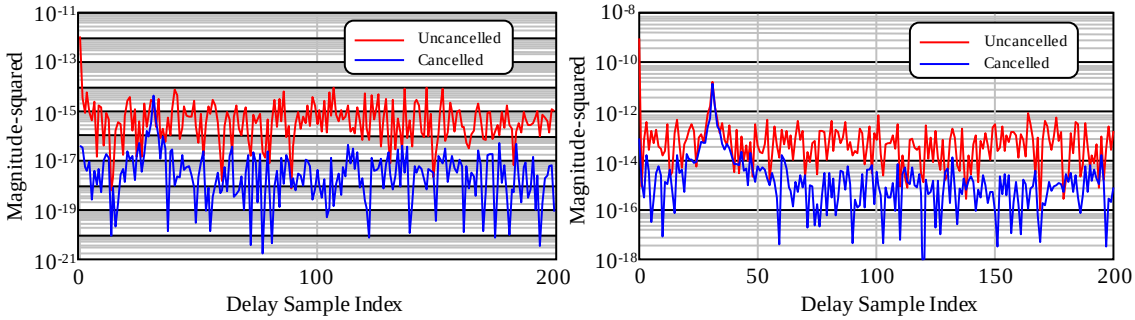

a) Target Masked by Time Sidelobes due to DSB b) Case with Increased Coherent Gain

Figure 5.29. Sample Sidelobe Canceller Results

The antenna separation must be such that the interference signal is correlated between the two channels. The 5.83 MHz HDTV bandwidth equates to approximately 50 m of delay to the first null. Consequently antennas mounted in the cockpit of a small aircraft with a maximum separation of 1-2 m will easily meet the spatial constraint. Unlike the typical radar application, where the interference term is assumed to be a noise-like signal with the same (or similar) bandwidth but different in form to the signal of interest, in this bistatic application the signal of interest is a delayed version of the signal-as-interference. Because the waveform has a 100 percent duty factor there are no intervals for sampling in the absence of signal. Delay more than one inverse bandwidth effectively decorrelates the scene scattered signal from the direct path component in both measurement channels. This is shown by examining the covariance matrix.

$$\mathbf{R} = E\left[\mathbf{x}\mathbf{x}^{*}\right] \qquad \mathbf{R} = E\begin{bmatrix} x_{main}x_{main}^{c} & x_{main}x_{ref}^{c} \\ x_{ref}x_{main}^{c} & x_{ref}x_{ref}^{c} \end{bmatrix} \tag{5-82}$$

where the superscript '*c*' indicates conjugate and *E* denotes expected value. As earlier we expand the main channel as the sum of signal and leaking direct path component

$$\mathbf{R} = \begin{bmatrix} E\left(\left(x_{scat} + x_{ref\_l}\right)\left(x_{scat} + x_{ref\_l}\right)^{c}\right) & E\left(\left(x_{scat} + x_{ref\_l}\right)x_{ref}^{c}\right) \\ E\left(x_{ref}\left(x_{scat} + x_{ref\_l}\right)^{c}\right) & E\left(x_{ref}x_{ref}^{c}\right) \end{bmatrix} \tag{5-83}$$

where the subscript *ref_l* refers direct path term leaking into the main channel. Taking the expected value of the covariance matrix term wise after completing the multiplications

then using the sum identity for the expected value we have (after absorbing the exponential into the gain ratio constant)

$$\mathbf{R}=\begin{bmatrix} E\left(x_{scat}x_{scat}^{\,c}\right)+E\left(x_{scat}x_{ref\_l}^{\,c}\right)+E\left(x_{ref\_l}x_{scat}^{\,c}\right)+E\left(x_{ref\_l}x_{ref\_l}^{\,c}\right) & E\left(x_{scat}x_{ref}^{\,c}\right)+E\left(x_{ref\_l}x_{ref}^{\,c}\right) \\ E\left(x_{ref}x_{scat}^{\,c}\right)+E\left(x_{ref}x_{ref\_l}^{\,c}\right) & E\left(x_{ref}x_{ref}^{\,c}\right) \end{bmatrix} \tag{5-84}$$

Now we interpret the expected value as the time average of the sampled process. The expected value then for a random process and a delayed version of that same random signal is zero, the delayed form being indistinguishable from a separate random signal and under the condition that the delay exceeds any signal correlation time. With this (5-84) reduces to

$$\mathbf{R}=\begin{bmatrix} E\left(x_{scat}x_{scat}^{\,c}\right)+E\left(x_{ref\_l}x_{ref\_l}^{\,c}\right) & E\left(x_{ref\_l}x_{ref}^{\,c}\right) \\ E\left(x_{ref}x_{ref\_l}^{\,c}\right) & E\left(x_{ref}x_{ref}^{\,c}\right) \end{bmatrix} \tag{5-85}$$

The signal x_{ref} differs from x_{ref_l} only through a complex scalar; the ratio of the antenna gains in the direction of the transmitter and the separation projected onto the line of sight (with the assumption that the receive chains are exactly matched). With this

$$E\left(x_{ref}x_{ref\_l}^{\,c}\right)=E(x_{ref}\alpha^{c}x_{ref}^{\,c}) \text{ or } E\left(x_{ref}x_{ref\_l}^{\,c}\right)=\alpha^{c}P_{ref}. \tag{5-86}$$

With this (5-85) becomes

$$\mathbf{R}=\begin{bmatrix} P_{scat}+\alpha\alpha^{c}P_{ref} & \alpha P_{ref} \\ \alpha^{c}P_{ref} & P_{ref} \end{bmatrix} \tag{5-87}$$

In (5-87) P_{scat} and P_{ref} are power terms from the scene, direct path and leakage, respectively. Taking the matrix inverse gives, with some simplification

$$\mathbf{R}^{-1}=\frac{1}{P_{scat}P_{ref}}\begin{bmatrix} P_{ref} & -\alpha P_{ref} \\ -\alpha^{c}P_{ref} & P_{scat}+\alpha\alpha^{c}P_{ref} \end{bmatrix}. \tag{5-88}$$

Using the steering vector from (5-80) the optimum weights are given by (5-78)

$$\mathbf{w}_{opt}=\frac{1}{P_{scat}}\begin{pmatrix} 1 \\ -\alpha^{c} \end{pmatrix} \tag{5-89}$$

Then forming the product for the canceller output

$$y(t) = \mathbf{w}_{opt}^{*} \begin{bmatrix} \mathbf{x}_{main} \\ \mathbf{x}_{ref} \end{bmatrix} \qquad \text{with} \qquad \begin{bmatrix} \mathbf{x}_{main} \\ \mathbf{x}_{ref} \end{bmatrix} = \begin{bmatrix} \left(x_{scat} + x_{ref\_l}\right) \\ x_{ref} \end{bmatrix}. \tag{5-90}$$

Finally

$$y(t) = \frac{1}{P_{scal}} \begin{bmatrix} 1 & -\alpha \end{bmatrix} \begin{bmatrix} \left(x_{scat} + x_{ref\_l}\right) \\ x_{ref} \end{bmatrix} = \frac{x_{scat}}{P_{scat}} + \frac{x_{ref\_l}}{P_{scat}} - \frac{\alpha x_{ref}}{P_{scat}} \tag{5-91}$$

and the second two terms are equal and the signal of interest passes the canceller.

An example of such a canceller with weights defined for a specific geometry (hence constant) then applied as the geometry rotates is shown in Figure 5.30. This example uses the antenna patterns from Figure 5.28b over the range 90-180 degrees (relative to peak mainbeam directivity), sampled at 1 degree increments, with the weights determined with the transmitter held constant at 150 degrees. Total power is plotted versus angle, the matched angle representing the signal power clearly evident. An antenna separation of 1.2 m was used in the calculation with maximum projected antenna separation at 180 deg (the projected separation is 0 at 90 deg).

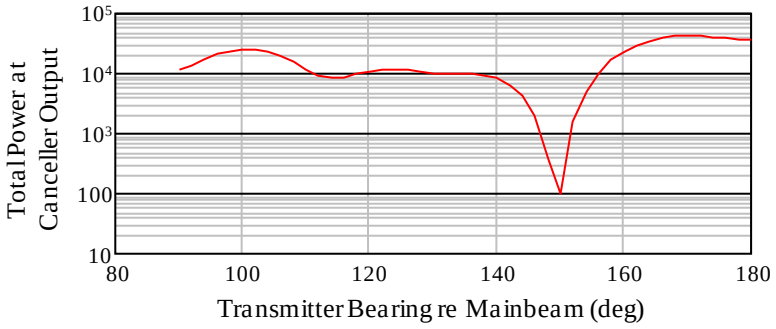

Figure 5.30. Canceller Response over Angle – Response with Antennas Displaced

We applied the adaptive sidelobe canceller to the reconstruction example shown in Figure 5.27 with all other parameters maintained. The reconstructed results are presented in Figure 5.31 and Figure 5.32. The first shows the principal plane reconstruction individually. One can observe interaction or influence from the adaptive canceller as the X-Y plane results (see Figure 5.7 for comparison) in the slight departure from circular of the interim sidelobe rings (resembling the gain pattern of the reference antenna). In Figure

5.29, as well as the generation of the phenomenology used for the images reconstructed in Figures 5.27 and 5.31 it was assumed that the main and reference antennas shared a common phase center. In the results shown in Figure 5.30, and the derivation leading up to the Figure, this assumption was not made, the spatial phase change as the antenna doublet rotated with respect to the weights generated at a single angle giving rise to the mismatch at angles away from the matched geometry. The relative antenna patterns in the direction of the interference are a lesser consideration as long as the reference (also called auxiliary) gain is greater than the main antenna gain.

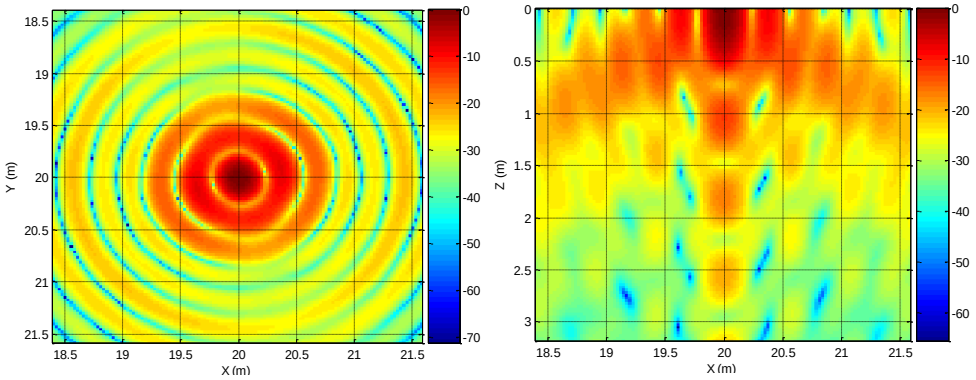

a) XY Principle Plane b) XZ Principle Plane

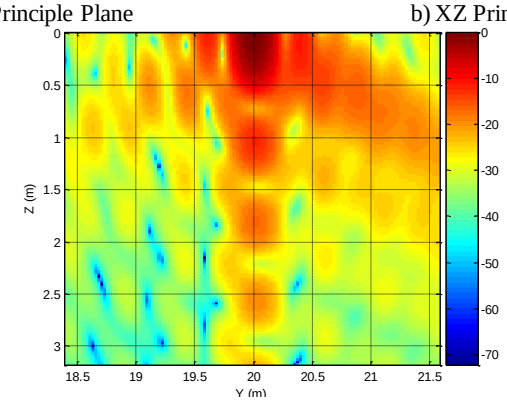

c) YZ Principle Plane

5.31. Reconstruction with Adaptive Canceller – Principal Plane IPR Contour View

5.5 Apodization.

The use of apodization (also called tapering or windowing) to control/improve the sidelobes of the point spread function is a common imaging practice [121], [122] and [89]. Window functions overcome the effects of the finite sampling window in time, frequency or space; by smoothing the response to the sampling window edges, reducing

the peak sidelobe level from -13 dB to some lesser value, depending on the specific function. This positive effect occurs as the expense of a slight coarsening of the resolution as the sample aperture is effectively shortened. In application the taper is applied in one data domain before transform into the conjugate domain where the effects of the sampling sidelobes are to be mitigated. In SAR applications, the taper can be applied in the frequency domain to both range and cross range, as orthogonal functions (along k_x and k_y) for joint reduction of image sidelobes (for example in polar format processing, [121]). Likewise, the tapers can be applied radially and circumferentially, along k_r and k_θ. A one dimensional taper along k_θ was applied to the 2D apertures focused in Section 6, with a positive result of sidelobe reduction in two spatial dimensions.

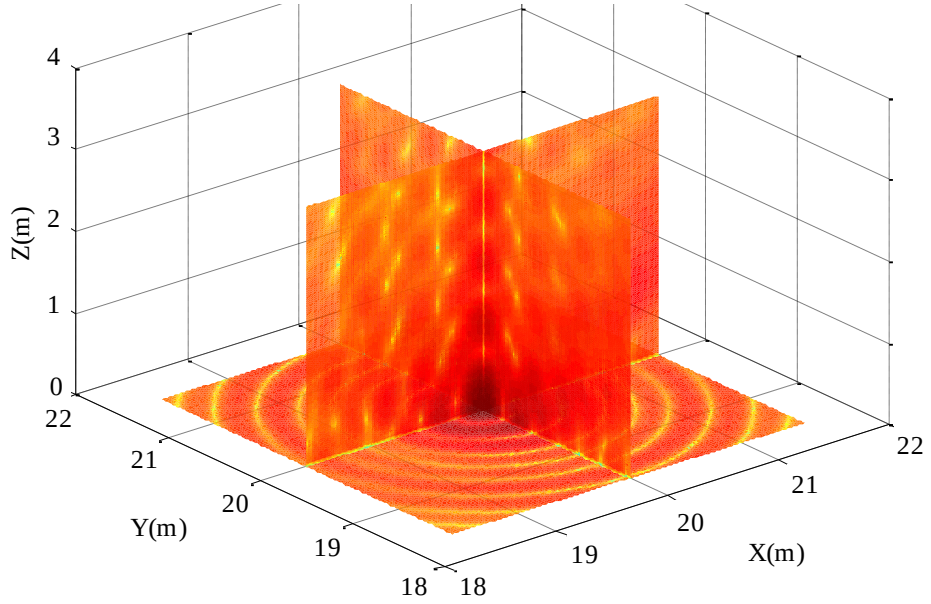

Figure 5.32. Reconstruction w/ Adaptive Canceller –IPR Slice Projection View

Applying the taper as an element-wise multiplication before the Fourier transform is equivalent to convolving the taper function in the image (or conjugate) domain. For taper function t and image domain functional representation f with $\Im$ representing the forward transform

$$\Im^{-1}\left(\Im(t)\cdot\Im(f)\right)\equiv t\otimes f \tag{5-92}$$

where the dimensionality is arbitrary.

Apodization in tomographic reconstruction when the collection aperture spans 2π radians is much less obvious (which is also reflected through the sparsity in the literature). This is most easily visualized in Figure 5.33a where the frequency domain mapping of an isotropic scatterer being illuminated by a waveform of bandwidth k_{min} - k_{max} in a two-dimensional aperture. The isotropic response insures a uniform response over angle and frequency (modeled as a rectangular spectrum), hence the toroidal response. In light of the previous paragraph one might taper radially, as might also be suggested by examining (5-1), *e.g*. a window on the transformed projection ($S_{\theta,\phi}(k)$), as shown in Figure 5.33b. However has the only effect of reducing the effective bandwidth while having no impact on the sidelobes of the IPR (whereas higher bandwidth was shown to increase the rate of sidelobe roll off in Section 3). With the radial taper could be combined a circumferential one (along k_θ). However, with the continuous aperture this has dubious effect, as suggested by Figure 5.33c. If orthogonal tapers were applied along k_x and k_y they combine to yield a radially symmetric circular taper. When applied a weighted frequency response is produced, resembling Figure 5.33b without the lower frequency (inner) edge smoothing. These approaches were all attempted in simulated tomographic images with the results described and are not shown. In [123] it is suggested that range tapering be performed prior to the forward transform. For the phase coded waveform this contributes little to the realizable range sidelobe level [124] because of the large waveform discontinuities; shift invariant tapers as opposed to mismatch filtering (pulsed, repeated code sequence). It is also noted that mismatched filtering was evaluated for the cross correlation-based pulse compression of the CW phase coded waveform with very limited results [114].

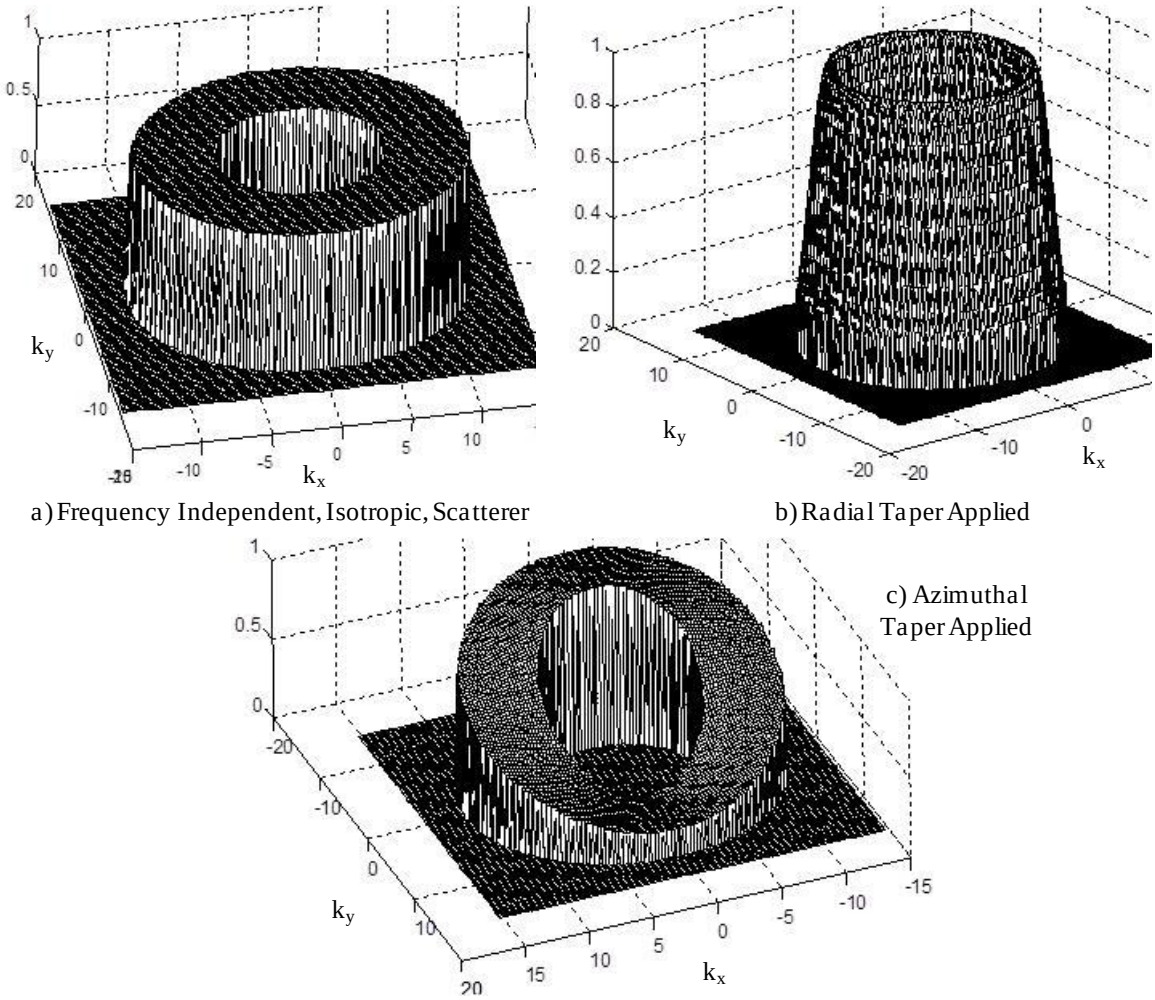

Figure 5.33. Window Functions Applied in the Frequency Domain

A complex image, reconstructed from a simulated HDTV signal, is processed with a two-dimensional taper, a 35 dB Taylor, following (5.92) with results shown in Figure 5.34. The forward transformed image appears in Figure 5.34a with the weighting function in Figure 5.34b. The frequency domain depicts the isotropic scatterer spatial spectrum offset from the origin, a property of the bistatic aperture and transmitter position relative to the scene. The y=0 cuts of the input image and the weighted image appear in Figure 5.34c. Clearly there are no effects from the taper. The small sample spacing means that the transformed frequency range is large (the $\lambda/20$ sample intervals corresponds to a spatial frequency of ~240 rads/m) so that the modeled aperture only subtends 12 of the FFT-derived frequency bins. Thus the taper effectively only imposes a constant weight where the spectrum has significant content. Consideration was given to compress the taper

function and resample more closely matched to the aperture spectrum. But the spectrum offset DC in X and Y would only result in something resembling Figure 5.33c.

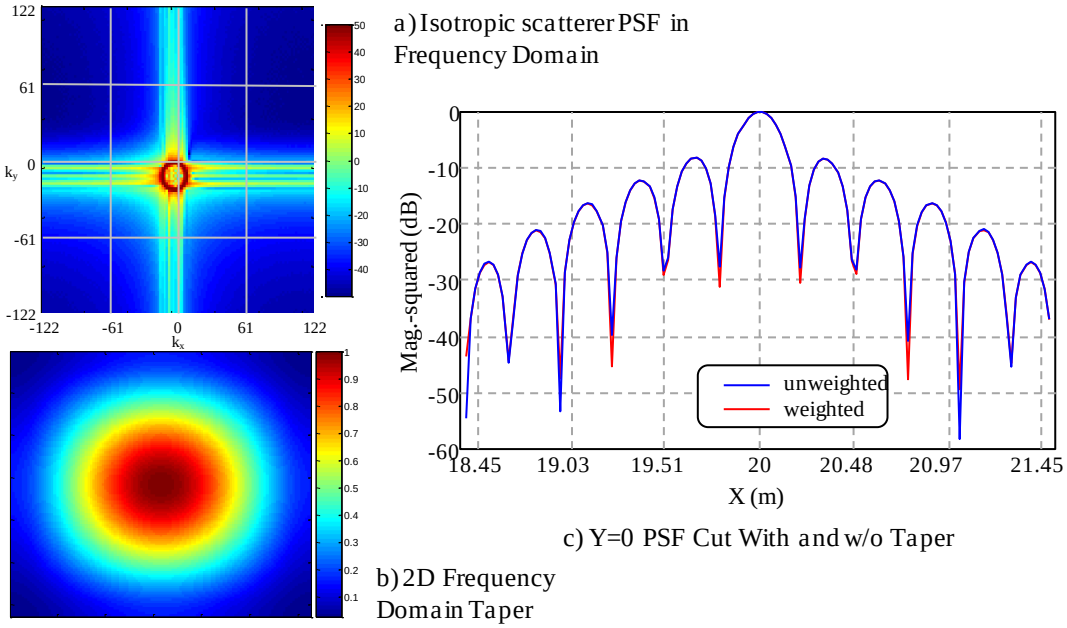

Figure 5.34. Window Functions Applied to HDVT Waveform-based Reconstruction

Centering the 2D taper only on those bins which contain the significant spectral energy, instead of more broadly across the full spectrum produces the same result. As noted in Section 5.4, the virtually separable vertical aperture might be suitable for a taper applied vertically, as a function of Z and independent of the polar angle.

One technique that is potentially applicable to improve the image sidelobes in the tomographic reconstruction is a nonlinear technique called Spatially Variant Apodization (SVA). SVA relies on nonuniform frequency domain weighting of the image data [125], doing so using a weighting function which is dependent upon the location within the image. This technique reduces image sidelobe levels, doing so without degrading the resolution. Developed in 1994 [126] the technique is now widely employed in imaging, super-resolution, and bandwidth extrapolation [127]. SVA is based on the cosine-on-a-pedestal weighting functions

$$W(n) = 1 + 2\alpha \cos(2\pi n / N), 0 \le \alpha \le 0.5. \quad (5\text{-}93)$$

Taking the length-N Fourier transform of (5-93) yields the Nyquist sampled impulse response

$$w(m) = \alpha\delta_{m,-1} + \delta_{m,0} + \delta_{m,1} \quad \delta_{m,n} = \begin{cases} 1 & m = n \\ 0 & otherwise \end{cases} \tag{5-94}$$

Equation 5-94 demonstrates that the IPR in the image domain only has three nonzero points. Application of the taper is a three point convolution using (5-94). The term Nyquist-sampled refers to one image sample per resolution cell (complex). Next consider an image *g* defined in the image domain as composed of (*m*, *n*) complex values at the Nyquist sample spacing. The convolution (5-94) defines an apodized image point

$$g'(m,n) = \alpha(m)g(m-1,n) + g(m,n) + \alpha(m)g(m+1,n) \tag{5-95}$$

The weighting coefficients are obtained by solving for the $\alpha(m)$ which minimizes $|g'(m,n)|^2$ given the underlying constraint of the cosine-on-a-pedestal taper; $0 \leq \alpha(m) \leq 0.5$. If $\alpha(m)$ is unconstrained the weight obtained is

$$\alpha_u(m) = -\frac{g(m,n)}{g(m-1,n) + g(m+1,n)} \tag{5-96}$$

which results in $g'(m,n)=0$. When $0 \leq \alpha_u(m) \leq 0.5$ then

$$g'(m,n) = \begin{cases} g(m,n), & \alpha_u(m,n) < 0 \\ 0, & 0 \leq \alpha_u(m,n) < 0.5 \\ g(m,n) + 0.5\big(g(m-1,n) + g(m+1,n)\big), & \alpha_u(m,n) > 0.5. \end{cases} \tag{5-97}$$

In (5-97) we used a two dimensional notation but performed the convolution in one dimension. The may be serially applied, first along the row dimension followed by columns to extend this technique to two dimensions [128]. Arguing by analogy, this could further be extended to serial application three dimensions. The convolution is extended to two dimensions via simultaneous operation in [127] and [128] using the same principles. The convolution kernel in two dimensions contains nine nonzero points given by

$$\begin{bmatrix} \alpha_m\alpha_n & \alpha_n & \alpha_m\alpha_n \\ \alpha_m & 1 & \alpha_m \\ \alpha_m\alpha_n & \alpha_n & \alpha_m\alpha_n \end{bmatrix}. \tag{5-98}$$

Defining three input scene-derived quantities

$$\begin{aligned} Q_m &= g(m-1,n) + g(m+1,n) \quad Q_n = g(m,n-1) + g(m,n+1) \\ P &= g(m-1,n-1) + g(m+1,n+1) + g(m-1,n+1) + g(m+1,n-1) \end{aligned} \tag{5-99}$$

the output image is given by

$$g'(m,n) = g(m,n) + \alpha_m\alpha_n P + \alpha_m Q_m + \alpha_n Q_n \tag{5-100}$$

The procedure again is based on minimizing $|g'(m,n)|^2$ with the dual constraint $0 \leq \{\alpha_m, \alpha_n\} \leq 0.5$. For any α_m or α_n, (5-100) is a linear function of the other. Therefore, for any pair (α_m, α_n) inside the interval [0, 0.5] × [0, 0.5], the value of the pair (α_m, 0)(α_m, 0.5) will be less than or equal to (α_m, α_n). Extending the argument leads to evaluation of the (5-100) at the four corners (0, 0), (0, 0.5), (0.5, 0) and (0.5, 0.5) which will yield both maximum and minimum. As $g'(m,n)$ is a monotonic function it passes through zero only if there is a sign change within the interval. This leads to the SVA algorithm of [127]: 1) calculate $g'(m,n)$ for (α_m, α_n) = (0, 0.5), (0.5, 0) and (0.5, 0.5), 2) if the sign of any of the three values are opposite set $g'(m,n)$=0, otherwise $g'(m,n)$=min($|g(m,n)|$, $|g'(m,n)_{(0,\ 0.5)}|$, $|g'(m,n)_{(0.5,\ 0)}|$, $|g'(m,n)_{(0.5,\ 0.5)}|$). Reference [129] offers a slightly different algorithm: 1) calculate $g'(m,n)$ at the four pairs of weights at the interval bounds ($g_{corner}(i)$, i=1:4), 2) if any are opposite sign (pair-wise comparison of 4 elements, 6 combinations) then $g'(m,n)$=0, otherwise $g'(m,n)$=min($|g_{corner}|$).

The algorithms above are specifically for Nyquist samples images. Algorithms also exist for non-integer sampled images [125]. Variants are available that process complex-sampled images jointly or by serially processing the in-phase and quadrature images. Also, the weights in 2D processing may be uncoupled, as above, or coupled. [128] presents a summary of the four algorithm cases.

In [129] the authors are specifically operating against a sampled sinc function: characteristic of the sinc is that the null positions are harmonically related. Nyquist sampling and SVA produces excellent sidelobes (though a linear scale is used). The tomographic IPR does not exhibit that null position behavior. We test SVA against a two-dimensional tomographic reconstruction using the exact solution. This choice allows easy spatial sampling for the test reconstruction (though it is real-valued-only) on a square grid. The sample interval was set to the distance from peak response to the first null, as projected along the X or Y axis. Three algorithm cases were evaluated: the two dimensional algorithms from [127] and [129] and the serial 1D case from [128]. Figure 5.35 summarizes the principal axis (Figure 5.35a) and 45 degree inter-axis results (Figure 5.35b). Performance along the X and Y axes was identical. For each case the overall reduction in sidelobe level reduction is computed by summing the total sidelobe power and normalizing by the input image total sidelobe power. Each of the three algorithms produced nearly identical sidelobe reduction with the serial 1D algorithm slightly under performing the other two -7.68 dB to -8.18 dB and -8.18 dB. The greatest sidelobe reduction occurs along the cardinal axis directions. The 45 degree inter-axis cut shows the least improvement.

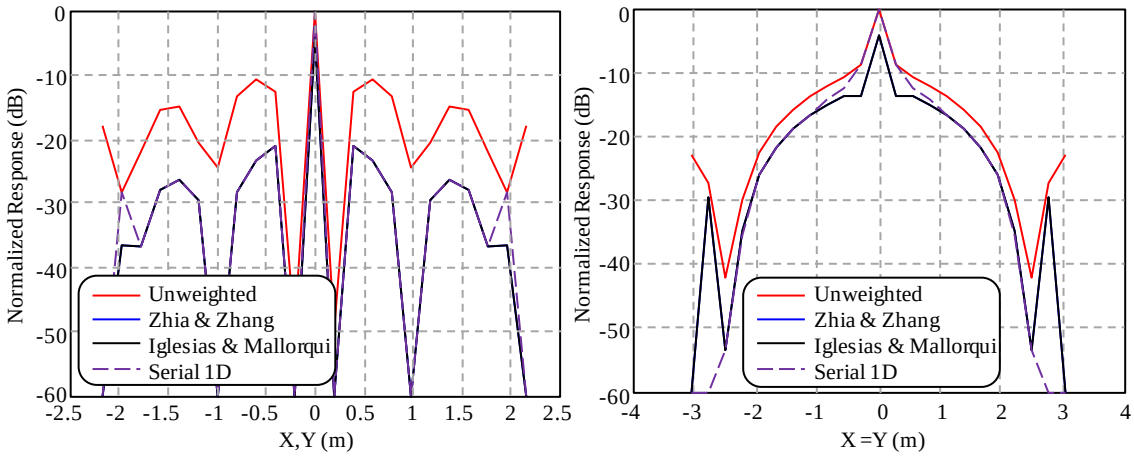

a) Image Levels along X,Y Axes b) Image Levels along 45 deg Axes Cut

Figure 5.35. SVA Assessment Against 2D Tomographic Reconstructions

Chapter 6

Bistatic Tomography Flight Test and Results

This final section details the analysis, design, planning, radar instrumentation, calibration, signal and data processing and, reconstruction which tests the HDTV-based bistatic tomography developed in Section 5.0. Included are high resolution images formed for the region of the test target for each orbit of the three-dimensional aperture as well as reconstructed three dimensional images of the same target. Point spread functions for the processed flight data are compared to simulated responses because of unknowns in the target scene and lack of controlled targets, and to evaluate error contributions within the limits of the instrumentation.

6.1 Bistatic Instrumentation Radar System.

This section presents the analysis, design, and test of the two channel, bistatic radar system. Receivers are addressed in the first section, followed by the development of the flight antennas. The third section specifically addresses band pass filters, including alternatives sought when purchase of filters with necessary attributes looked to be unlikely. The final section addresses the position measurement and navigation devices as well as the explorations and fabrication of calibrated target(s).

6.1.1 ***Flight test radar – bistatic receivers***. We have described at the top level the receive instrumentation associated with a bistatic imaging system. This section describes the tradeoffs, design, assembly and test of the analog and digital portions of the system used

in the flight test. The geometry which evolves from the use of terrestrial transmitters at stand-off collection distances imposes challenging requirements on the receive system: dynamic range against high ERP emitters (the imaging mainbeam oriented at the transmitter), spectrum occupancy in the commercial broadcast bands (contiguous channels, spatially distributed), and the need to cohere and synchronize multiple receive channels when constrained by prime power available in civil aircraft.

In this section the constraints are outlined and requirements are defined, allocated and discussed, leading to a electrical description of the two channel receiver assembled for the test campaign.

• **6.1.1.1** ***Requirements***. The planned test geometry emerged from the theoretical developments in Section 5.0; a regular orbit offset some distance from the elevated illuminator. The receiver would be required to support the UHF frequency range allocated to broadcast high-definition television operation with digital conversion which supports the allocated channel bandwidth (6 MHz), at a minimum. Two tightly synchronized receive channels are also required, at a minimum. Sample rates and analog filtering must be sufficient to avoid aliasing of adjacent channel signals with a dynamic range that would permit collection without loss of sensitivity as the antennas sweep past the illuminator in the collection aperture. Digital transfer bandwidth must be compatible with available commercial laptop (battery powered) capabilities (240 Mbps, minimum over burst duration). Total power must be supported, including conversion losses, by the limited capacity of civil aircraft of the type envisioned for the flight test (typically a 10 ampere auxiliary circuit for the cigarette lighter).

To establish system sensitivity requirements the test geometry was modeled. This was performed at the initial planned test location (Section 6.3.3), a location, generally rural, with orbit center 24.74 km from the transmitter, generally flat with a transmitter grazing

angle of 1.4 degrees at scene center. The system model included a constant gamma, geometric mean clutter model [30]

$$\sigma_0 = 10^{\gamma/10}\left[\sin\left(\theta_{graz\_xmtr}\right)\sin\left(\theta_{graz\_rcvr}\right)\right]^{\frac{1}{2}} \tag{6-1}$$

where θ_i, i=xmtr, rcvr is the grazing angle due to transmitter or receiver, with three reflectivity values, γ = -15, -14, and -13 dB. The clutter integrator was exercised at the lowest collection altitudes to estimate mean received clutter power and results were weakly dependent on reflectivity. The clutter model divided a large area, including the scene, into 5 m square pixels on a spherical earth (eliminating flat earth approximations though, on the scale analyzed, the differences would have been small). A range profile is created by integrating along the ellipsoidal isorange contour with range delay as the parameter. The pixel power level is given by

$$P_{pixel_{x,y}} = \frac{ERP_{xmtr}G_{rcvr}G(\phi)G(\theta)\lambda^2\sigma_c}{(4\pi)^3 L_{rcvr}R1^2R2^2} \tag{6-2}$$

with $\sigma_c = \delta x \delta y \sigma_0$, δx and δy the edge lengths of the clutter cell, *R1* the range from transmitter-to-cell, *R2* the range from cell-to-receiver, L_{rcvr} the receiver losses and $G(\phi)$ and $G(\theta)$ the relative gains, referenced to the peak receive gain G_{rcvr}, in azimuth (ϕ) and elevation (θ). The range difference profile is generated by the integration of those pixels that lie along an isorange contour with physical origin within the resolution width defined by a 12.5 MSPS sample interval. This is given by

$$P_{i\delta} = \sum_{ix=X_{\min}}^{X_{\max}} \sum_{iy=Y_{\min}}^{Y_{\max}} P_{pixel_{ix,iy}} \; if \; round\left(\left|\frac{\frac{1}{c}\left(\left|X_{rcvr} - C_{ix,iy}\right| + \left|X_{xmtr} - C_{ix,iy}\right| - \left|X_{xmtr} - X_{rcvr}\right|\right)}{\Delta T}\right|\right) = i\delta$$
$$0; \quad otherwise \tag{6-3}$$

In equation 6-3 C represents the clutter cell (pixel) location vector and ΔT is the sample interval and c the speed of light. The position vectors of transmitter and receiver are X_i, i = *rcvr, xmtr*.

The simulation covered a 10 km by 10 km region centered on the scene origin with the point geometry the receiver orbit 1 km offset to the east (bistatic angle at scene center ~74 deg). In this sample geometry the domain of clutter integration spans an angle greater than the main antenna null-to-null angular extent. Clutter power versus range delay relative to the receiver is shown in Figure 6.1a for a reflection coefficient of -15 dB. To give an indication of the potential dynamic range, the estimated direct path signal strength in the main and reference antennas is shown in Figure 6.1b. The range of the projection of the scene over the collection geometry is approximately indicated in Figure 6.1a, showing the region of interest.

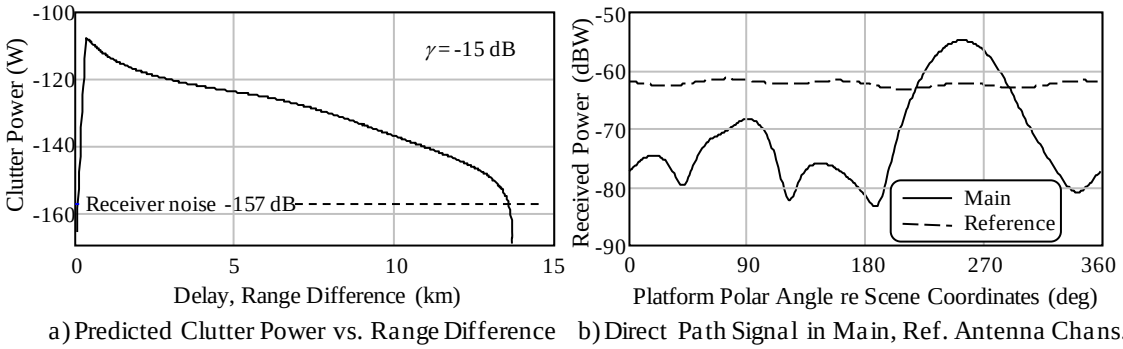

a) Predicted Clutter Power vs. Range Difference b) Direct Path Signal in Main, Ref. Antenna Chans.

Figure 6.1. Clutter Power vs. Range Difference, Simulated Geometry

Dynamic range overall can be inferred from Figure 6.1. Mean clutter-to-noise is of the order of 50 dB and direct path leakage-to-clutter is, outside the main beam, in the range 35-50 dB. Since, as was demonstrated in Section 5, performance limiting, in terms of sensitivity, is primarily due to the compressed time sidelobes, noise level considerations on dynamic range are not driving receiver requirements.

• **6.1.1.2** ***Bistatic system architecture***. Two options were considered, a multi-channel, direct sampling system from the University of Washington (Dr. John Sahr) or a commercial software defined radio. The first option required more power than could be supplied for envisioned experiment duration (minimum 90 minutes). An array of heavy-duty marine batteries was considered but was heavy and offered flight safety concerns.

Likewise, backup power supplies of reasonable cost/weight could not supply sufficient power for the planned test duration.

The software defined radio choice was relatively straight forward because Boeing Research and Technology (BR&T, Dr. Gary Ray) had acquired an Ettus Research N200 for evaluation. Ettus (http://www.ettus.com/) offers complete system solutions that were very affordable and which operated within the tight power constraints. In addition to several classes of digital chassis spanning a range of capabilities, there were several analog tuners (termed RF daughterboards). An integrated GPS disciplined oscillator (GPSDO) card was also available. In particular the WBX analog assembly provided a wideband (though without preselection filter) tuner covering 50-2200 MHz with both receive and transmit capabilities. The Ettus units also included enclosures. A formal loan was arranged to University College London for the BR&T unit and a second, matching unit was purchased, including the GPSDO (approximately $4000 US total). The Ettus architecture also facilitated two chassis synchronization with a special purpose "MIMO cable". Two units share a single GPSDO with the slave unit locked to the master and digital data transfer controlled by the master. The top level receiver system is shown in the block diagram in Figure 6.2.

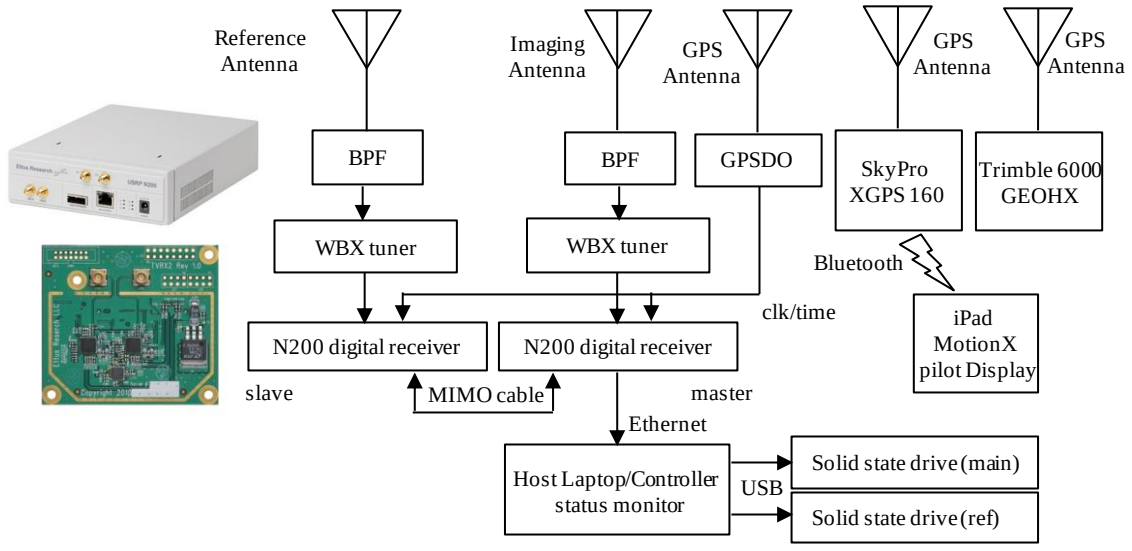

Figure 6.2. Top Level Two-channel Bistatic Instrumentation System Block Diagram

The UHD (Universal Software Radio Peripheral (USRP) Hardware Driver) driver library supports a variety of platforms, operating systems ranging and programming and control languages including Gnuradio, C++, Python and others. An IBM ThinkPad operating under Windows 7 was configured as the controller using Windows C++ Development Environment. A more powerful, Windows 8 machine was configured but was too unreliable as no Windows 8 UHD drivers had been released and applying backward compatibility through Windows proved to be too unstable. A key component of the digital chassis is the Spartan FPGA which provides real time signal processing under user control. Table 6.1 provides a tabulation of the Ettus N200, WBS and GPSDO features and parameters.

USRP WBX RF Daughterboard	
Power dissipation – 6V @ 1A	Noise Figure – 5 dB (nominal)
Independently operable Tx and Rcv. channels	31.5 dB tunable gain range
40 MHz instantaneous bandwidth	Tunable 50-220 MHz in 1 kHz steps
Maximum input power 0 dBm	IIP3 – 0 dBm
N200 Digital Receiver	
Power dissipation – 6V @ 1.3A	Spartan 3A DPS 1800 FPGA
ADC Sample rate – 100 MSPS @ 14 bits	SSB/LO Suppression - >35/50 dB
ADC SDFR < -88 dBc	phase noise 80 dBc/Hz @ 10 kHz (internal
Stability 2.5 ppm (internal clock)	Direct digital tuning, quadrature demodulation
Up to 50 Ms/s streaming	Weight – 1.2 kg
GPS Disciplined Oscillator (GPSDO)	
10 MHz stable clock	Freq. stability over temp +/- 2.5E-08
Power dissipation < 1.8W (max), 1.35 W (typ.)	Phase noise @ 10 MHz
1 Hz, 10 Hz, 100 Hz, 1 kHz: -80 dBc/Hz, -110 dBc/Hz, -135 dBc/Hz, -145 dBc/Hz	

Table 6.1. Ettus Research N200 Unit Attributes

Additionally, precise navigation data are required for reconstruction. Leasing an instrument capable of decimetric-level accuracy, which was battery operated (as was the control laptop and two channel receiver) consumed the available aircraft power (provided via a 150 W inverter). These are detailed in Section 6.1.3.

Not shown in Figure 6.2 is prime power conversion (conditioning). The Cessna 170 aircraft provided only 10A at 12V via a cigarette lighter. A Cobra CPI-150 BK inverter (DC to 110V AC at greater than 78 % efficiency) was used to provide AC power which

was converted back to conditioned DC for the digital receivers (80.6% efficiency based on vendor AC-DC convertor specifications). With the circuit rating and the specified converter efficiency, only ~93.6 Watts remained for instrumentation. The power budget is rolled up in Table 6.2. The N200 power does not include the efficiency of the unit power supply. Using the vendor value (80.6%) the power dissipation for the receivers in Table 6.2 is increased by 3.45W (each) for a total of 6.9 W.

Component	Power	Component	Power
N200	21.3 W (each), 42.6 W	Trimble GEOHX	battery
GPSDO	1.35 W	GPS X160	battery
Laptop	Battery	iPad map display	battery

Table 6.2. Total Power Budget – Flight Experiment

• **6.1.1.3** ***WBX analog receiver***. Top level attributes of the WBX tuner were outlined in Table 6.1. Additional detail is provided in this section. A block diagram of the tuner card can be found in Figure 6.3. Table 6.2 contains specifics on the RF cascade used to develop noise figure estimates and to aid in gain setting. Under external control the RF daughterboard can be tuned from 50 to 2200 MHz in 1 kHz steps (integer tuning is recommended with the UHD drivers). There is no provision for dynamic tuning in the UHD driver library so gain settings had to serve all points along the collection aperture, including those times when the mainbeam was oriented at the transmitter. No transmit functionality was needed/employed so that capability is not discussed. Note in Figure 6.3 the tuner has no preselection filter. Given the dense RF environment in the broadcast spectrum such filtering was necessary to avoid serious aliasing. The filter requirement development is covered in Section 6.3.4 with the design exploration in Section 6.1.3.

The parameters for the components in the receiver, with the exception of the filters and the ADC were extracted from part datasheets. The filter insertion losses were calculated using the ABCD method with specific inductance and capacitance values from the detailed WBX schematics (without consideration of parts tolerances). The ADC (TI

ADS62P4X) is actually contained in the digital chassis (next section) but is included here for the purposes of noise figure calculation.

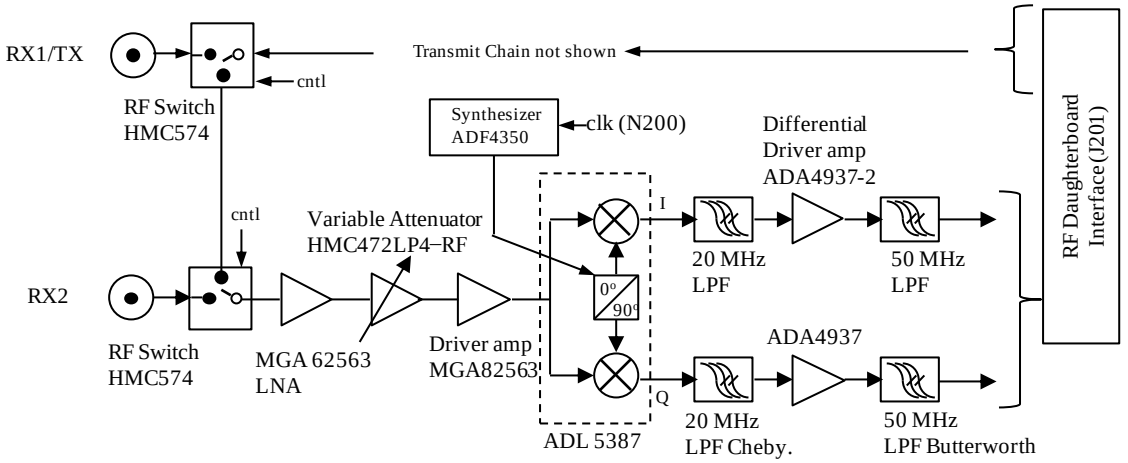

Figure 6.3. RF Daughterboard Block Diagram

Component	F_n	P1dB	P_{max}	Gain	Insertion Loss	Comments
RF Switch	0.3 dB	38 dBm	39 dBm	n/a	0.3 dB	30 dB isolation
LNA	0.9 dB	17.8 dBm	21 dBm	22 dB	n/a	Pin absolute max
Variable Attenuator	1.5 dB (min)	20 dBm	27 dBm	-30 to 0 dB	1.5 dB (min)	0.5 dB steps
Driver Amp	2.2 dB	17.4 dBm	13 dBm	14.7 dB	n/a	VSWR 1.8:1
Low Pass Filter One	6.0 dB	--	--	n/a	6.0 dB	20 MHz BW Chebychev 0.1 dB ripple
Quadrature Demodulator	13.5 dB	12.7 dBm	15 dBm	4.4 dB	n/a	
Low Pass Filter Two	6.19 dB	--	--	n/a	6.19	50 MHz BW Butterworth
Differential Amplifier	13.5 dB	--	10 dBm	0 dB	n/a	
ADC	33 dB		< 3V p-p	n/a	n/a	

Table 6.3. Detail Tuner/Analog Receiver Daughterboard

The ADC noise figure was calculated using a method outlined in http://www.maximintegrated.com/en/app-notes/index.mvp/id/1197. The noise figure is given by

$$F = \frac{V_{noise\_RMS}{}^2}{k_B TRB} = \frac{V_{FS}{}^2}{R}\frac{1}{k_B T}10^{-0.1SNR}\frac{1}{B} \tag{6-4}$$

where B is the bandwidth, R the input resistance, k_B Boltzmann's constant, and T is 290 K. The full scale voltage rating of the ADC is V_{FS}. The total noise figure then calculated with the cascade equation

$$F = F_1 + \frac{F_2 - 1}{G_1} + \frac{F_3 - 1}{G_1 G_2} + \frac{F_4 - 1}{G_1 G_2 G_3} + \ldots \quad (6\text{-}5)$$

where the subscript indicates the cascade stage and F is the stage noise figure and G the stage gain and is a function of the attenuator setting. For a gain value of 25 dB (attenuator setting for a loss of 6.5 dB), and using the values in Table 6.2, a noise figure of 7.87 dB results. In this calculation the passive losses of the RF switches are booked with the cabling losses. These are, in each channel, 1.82 dB (measured). The GaAs RF switches yield 0.3 dB loss each and the band pass filter employed added an additional 3.95 dB for a total of 6.37 dB in each channel. To this is added the 3:1 combiner loss in the main channel (2.1 dB).

The cascade analysis was used to fix the receive gain which was verified by ground measurement. Maximum signal levels were complied for each stage of the cascade, then reduced using recommended de-rating values (from datasheets or the community postings on the USRP listserve). The levels are shown in Figure 6.4. The signal power for the transmitter at the initially planned test condition (27 km from the transmitter) as a function of stage of the receiver is shown for both main and reference channels with a user gain of 25 dB (set attenuation of 6.5 dB) the value later used in flight (and which was confirmed to not saturate based on ground testing). This setting places the transmitter power at approximately 1 bit below maximum power level for the receiver, at ADC saturation, when peak mainbeam gain is directed to the illuminator. Also shown on Figure 6.4 is the mean clutter power from Figure 6.1a for the 1.5-2.5 km swath region (~-83 dBm), together with the noise floor represented by the effective number of A/D bits. This demonstrates sufficient dynamic range for the planned experiment.

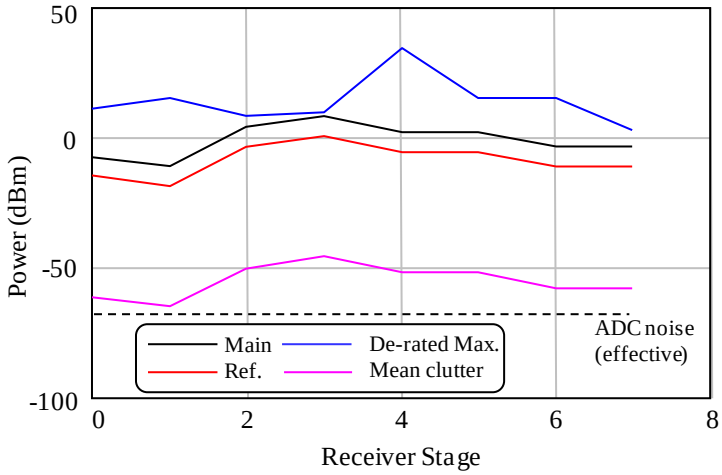

Figure 6.4. Peak Signal Power through Receive Cascade

• **6.1.1.4** ***N200 digital receiver***. The digital receiver, as indicated, was a pair of Ettus Research N200s. Provisions are available to mount the RF daughterboards within the chassis case, as well as for the internal GPSDO (in the master unit). The digital receiver accepts conditioned baseband (single stage down conversion by the analog card) with dual 100 MSPS analog to digital converters. A general block diagram of the digital assembly appears in Figure 6.5.

The ADCs continuously operate at a 100 MSPS rate with 14 bits of resolution (11.8 bits effective). UHD instructions from the control laptop set the sample rate in the DDC/decimate stage of the FPGA processor. User selectable sample rates are strictly-limited to an integer ratio of the sample rate to the requested sample rate. There are further constraints on the selectable sample rate. If the required decimation or interpolation exceeds 128, then the resulting decimation must be evenly divisible sample rate. There are further constraints on the selectable sample rate. If the required decimation or interpolation exceeds 128, then the resulting decimation must be evenly divisible by 2. Likewise, if the required decimation exceeds 256, the resulting decimation must be evenly divisible by 4. The digital data transfer rate (streaming) is 50 MSPS (for 16 bit data words, double if 8 bits are used). For a single unit this is 25 MSPS I and Q. The

streaming capacity has to be shared between two units in the MIMO configuration or 12.5 MSPS I and Q, each.

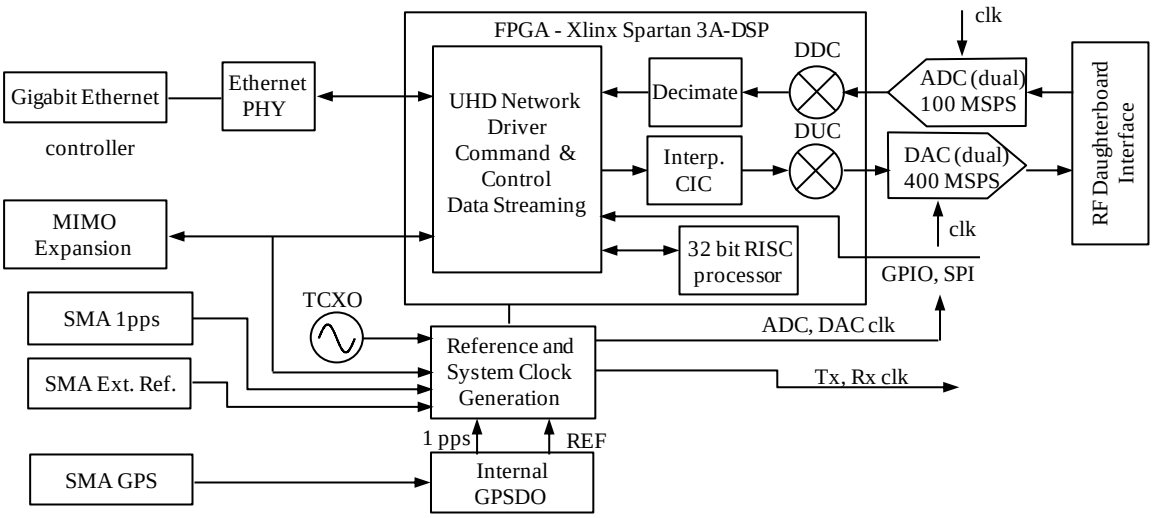

Figure 6.5. N200 Digital Receiver Block Diagram

Data are transferred in packets of 363 samples. Sampling may be interrupted or operated in a burst manner. However Ettus recommends that continuous sampling be performed (to avoid start transients which commonly occur, resulting in tainted data). Control software development (in C++) was initially performed on a Lenovo laptop (IdeaPad U530, ACPI x64-based motherboard) operating under Windows 8 in the Microsoft development environment with a Realtek PCIe GBE Family Controller. The control laptop could receive and push the full streaming rate with high packet reliability. However the code itself (executable) with the pre-Window 8 UHD drivers was very unreliable in Windows 8. Therefore an earlier model IBM ThinkPad operating under Windows 7 and in the same development environment was configured. This laptop had an older generation of Ethernet-controller which did not operate at the same level of packet delivery reliability. Consequently the sampling rate was decreased from 12.5 MCSPS to 10 MCSPS with acceptable performance. The breakdown on the data rate and storage requirements are: the numbers of bits per sample burst (0.8 msec duration) is 0.256 Mb. The sustained data rate into the control PC is 560 Mb/sec. This was down sampled to a 20 Hz along-track

sample rate resulting in 5.12 Mb/s transfer rates to an external solid state drive. The total collection (1 hour spatial aperture plus channel calibration) requires 27.648 Gb/channel.

The various components were attached to a plywood pallet for easier handling and cable management when in the back seat of the aircraft. The pallet is pictured in Figure 6.6.

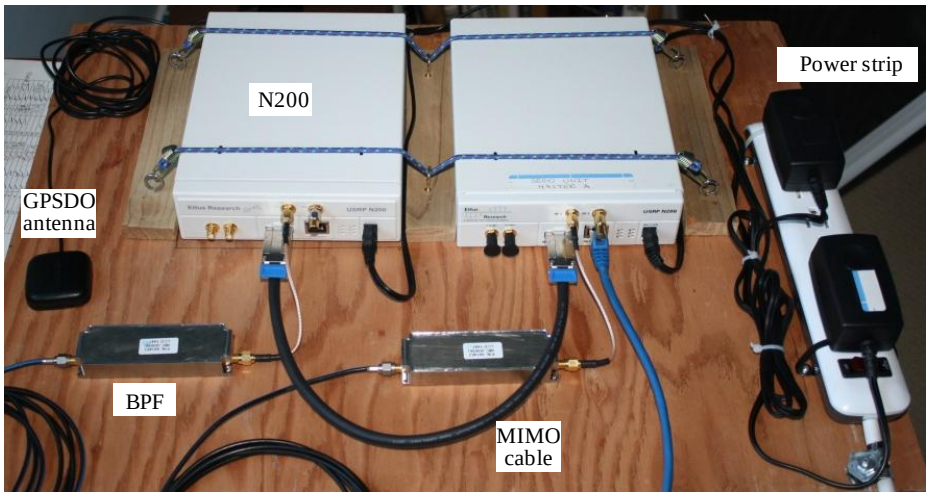

Figure 6.6. Bistatic Instrumentation System Pallet

6.1.2 ***Antenna design, analysis and fabrication***. Antennas for the flight collection have been described variously within this thesis. In this section the idealized antennas are converted to practice. We begin with a collection of the antenna requirements as derived from the analytic developments, undertake a physical design and analysis using FEKO [130], and compare modeled results with measured using local broadcast transmitters and the bistatic receiver described in Section 6.1.1. This section is composed of two main subsections: reference antenna and the main antenna.

• **6.1.2.1** ***Reference antenna***. As has been described, the bistatic imaging radar is comprised of two dissimilar antennas: the imaging or main antenna and the reference antenna. Antenna requirements are driven by the tomographic collection aperture and issues that are unique to the HDTV transmitter, while being constrained by the installation in a small civil aircraft (the Cessna 170 – class civil aircraft).

The reference antenna serves two purposes; the first is the reception of the reference signal which is used as the waveform template for the cross correlation, or ambiguity function, processing; a process which is equivalent to pulse compression. The reference antenna also serves as an auxiliary antenna for adaptively cancelling the direct path signal component in the main antenna. There are two main considerations: bandwidth and channel matching to produce a high fidelity replica of the waveform, and gain over angle. The difference in instantaneous antenna gains only affects the magnitude of the response but not the SNR. Effects of pattern modulation, which will certainly result once installed in the aircraft, would be indistinguishable from scatterer RCS variation over angle, changing the instantaneous magnitude but not the SNR. As the image reconstruction employs back projection, as opposed to Doppler-based techniques, is was expected to be immune to magnitude variations. Therefore, from the waveform and imaging perspective, the degree of uniformity of the azimuth response of the reference antenna is a goal.

The SNR invariance is demonstrated in Figure 6.7 where a PN code of length 1000 was used, in the flight test geometry (Section 6.3) and based on the ideal response of a 3×1, binomially-weighted, linear array and an omni-directional reference antenna with three gain values varying in 10 dB steps. The specific geometry had the TV illuminator located in the vicinity of the 90 degree (end fire) null of the main antenna pattern (receiver at ϕ=0 degrees relative to test scene geometry) so that SNR could be observed without the necessity of invoking the sidelobe canceller. The plot includes a 10 dBsm isotropic scatterer with an SNR of ~22 dB. The SNR can be seen to be independent of reference antenna gain.

The use of the reference antenna as an auxiliary antenna in a sidelobe canceller configuration places more stringent requirements on the antenna gain pattern. To provide the correct canceller weights, the gain of the reference antenna in the direction of the interfering signal must exceed the primary (main) antenna gain [131] over that angular

region where cancellation is required, while having gain less than the main antenna in the direction of signals of interest (the mainbeam region). When the illuminator is in the mainbeam the sidelobe canceller causes cancellation of the signal of interest, or when main channel gain exceeds the auxiliary channel in the direction of the interfering signal. The receiver gain settings for the flight experiment were set such that the ADC would be at saturation in the main channel when the transmitter was at the peak of the mainbeam (note: no saturation was observed in the data).

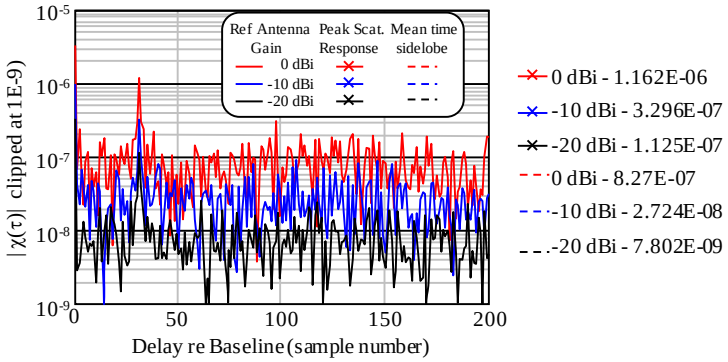

Figure 6.7. Example Ambiguity Function with Reference Antenna Gain as a Parameter

The antenna design, analysis and evaluation of the complete radar were performed using free space assumptions. The potential for limited reconstructed regions were absolutely expected due to the anticipated negative impacts of the air vehicle on the radiation pattern, particularly with the antenna housed within the aircraft cabin (with passengers).

The requirements for the reference antenna are summarized in Table 6.4. Not listed, but a strong driver nonetheless, are ease of fabrication and cost.

Parameter	Value	Comments
Polarization	Horizontal	Matched to Source
Center Frequency	587 MHz	UHF Chan. 33 KWPX
VSWR 2:1 Bandwidth	>2% of Matched Channel Carrier	Support multiple TV channels for c/o
Gain	0 dBi	Min. in azimuth principal cut at $\theta=90^o$
Azimuthal Coverage	Omni-directional	Gain variation < 3 dB over 2π radians @ $\theta=90^o$
Elevation Coverage	> 90^o beam width	Near constant directivity over vertical extent of collection aperture
Size/Volume	$\leq \lambda/2^3$	Located within aircraft cabin (4 passenger)
Interface	50 ohm coax/SMA	Matched to USRP (receiver) input

Table 6.4. Reference Antenna Requirements

Three antenna types were considered that had potential to simultaneously meet the polarization and azimuthal pattern constraints: an electrically small loop (radius <~ 0.1λ), a slot antenna (folded or half wavelength resonant slot) in a cylinder, and a turnstile, crossed dipole (coplanar crossed dipoles configured for circular polarization). The antennas are depicted in Figure 6.8. A single, vertical dipole was not considered because, while easier to fabricate and to install on/in an aircraft window, of the effective gain with polarization mismatch would have been insufficient to cover the main antenna sidelobes. While receiver gain might be considered to offset this (with the resulting noise imbalance) the gain settings of the receiver did not have sufficient range from the sensitivity-derived settings to offset the cross polarization mismatch.

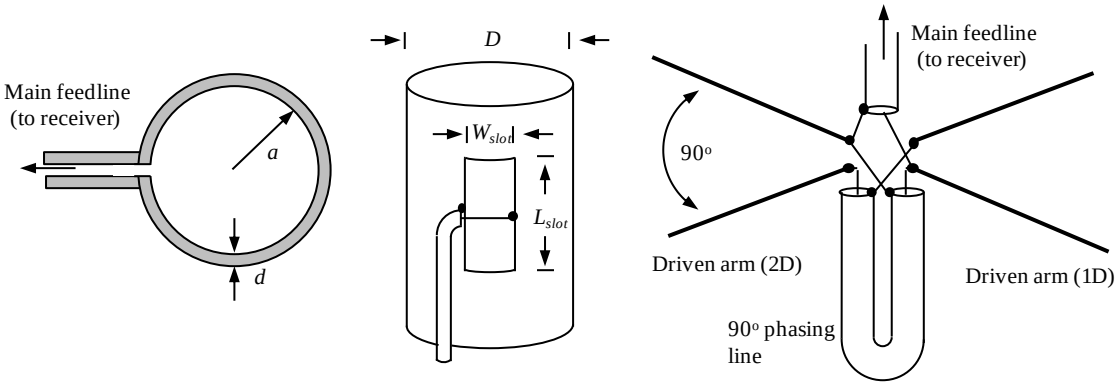

a) Electrically Small Loop b) Cylindrical Slot c) Crossed Dipoles (Turnstile)

Figure 6.8. Candidate Reference Antennas Evaluated

• **6.1.2.1.1** ***Electrically small loop***. The electrically small antenna, total conductor length (circumference) <~ 0.1λ, is characterized by a nearly constant current distribution over the antenna. The loop satisfied the dual requirements of horizontal polarization (plane of the loop aligned horizontally) with an omni-directional gain pattern aligned with the polarization. The far field electric field is given by

$$E_{\phi}(r) = \frac{120\pi^2[I]A}{r\lambda^2}\sin(\theta). \qquad (6\text{-}6)$$

In (6-6) θ is the angle from the Z axis (the axis of symmetry, loop in the X-Y plane), A is the loop area, and [I] is the retarded current. Azimuthal symmetry is observed by the

absence of ϕ dependency. As the circumference increases the pattern becomes less "doughnut-like" with the appearance of narrower elevation lobes while retaining the azimuthally uniform response [132].

The directivity of a loop antenna with uniform current is given by

$$D = \frac{2C_\lambda \left(J_1^2\left(C_\lambda \sin(\theta)\right)\right)_{\max}}{\int_0^{2C_\lambda} J_2(y)dy}. \tag{6-7}$$

The angle θ is the value at which the maximum field strength occurs (for the loop it is 90 deg.). Equation 6-7 evaluated for the small loop (C_λ <1/3) yields D=3/2. Directivity is converted to gain through the efficiency of the antenna. The efficiency combines radiation resistance (R_r) and resistive losses (R_L) which is given by

$$\eta = \frac{R_r}{R_r + R_L}. \tag{6-8}$$

The issue with the loop antenna is that the impedance is dominated by a large reactive component which requires a matching network to compensate. The radiation resistance for a small loop (C_λ < 1/3, radius a) is given by [132]

$$R_r \cong 32000\left(\frac{\pi a^2}{\lambda^2}\right)^2 \cong 197C_\lambda^4. \tag{6-9}$$

The resistive loss of solid conductor (wire) of diameter d, conductivity σ, frequency f, and length L (= C, C_λ=C/λ) is

$$R_L = \frac{L}{d}\sqrt{\frac{f\mu_0}{\pi\sigma}} \tag{6-10}$$

From (6-8), (6-9) and (6-10) the antenna gain can be expressed as

$$G = kD = 1.5\frac{1}{1+\frac{R_L}{R_r}} = 1.5\frac{1}{1+\frac{\frac{L}{d}\sqrt{\frac{f\mu_0}{\pi\sigma}}}{197C_\lambda^4}} \tag{6-11}$$

For 12 gauge copper wire d=2.05 mm. The loop circumference is 0.161 m (a=0.05λ, meeting the condition the C_λ<1/3 for the uniform current distribution assumption). At 587 MHz the resistive loss is 0.306 Ω and the radiation resistance is 1.919 Ω, yielding a gain of 1.294.

The antenna impedance is the sum of the internal and external impedance contributions

$$Z_{Loop} = (R_r + R_L) + j\omega(L_L + L_e) \tag{6-12}$$

using L_e as the external inductance and L_L the internal contribution (subscript L matching the resistive loss – internal wire – component). The external inductance [133] is

$$L_e = \mu_0 d\left(\ln\left(8\frac{d}{a}\right) - 2\right) \tag{6-13}$$

Straight wire impedance is used to approximate the internal component, from [134].

$$L_L = 0.002C\left(\ln\left(4\frac{C}{d}\right) - 1.0 + \frac{d}{2C} + \frac{\mu d T(x)}{8}\right) \tag{6-14}$$

with

$$x = \pi d\sqrt{\frac{2\mu f}{\sigma}} \quad T(x) = \sqrt{\frac{0.873011 + 0.00186128\ x}{1.0 - 0.278381\ x + 0.127964\ x^2}}. \tag{6-15}$$

Combining (6-9), (6-10), (6-13), and (6-14) into (6-12) gives the antenna impedance of 2.225+j1.929E+04.

The bandwidth is estimated using the Q-factor of the antenna. Following Kraus [132], as modified for a single wire loop and without ferrite core or similar, Q and the bandwidth are given by

$$Q = \frac{2\pi f_0 L_e}{R_r + R_L} \quad BW = \frac{f_0}{Q}. \tag{6-16}$$

Yielding 67 kHz at midband, insufficient for the HDTV signal.

• **6.1.2.1.2** ***Cylindrical slot***. A second antenna that offers omni-directional coverage in the same plane as the incident polarization is the cylindrical slot (Figure 6.8b). Also known as

the Alford antenna, the antenna is basically a slot cut into a ground plane which is then formed into a cylinder. The antenna is fed across the slot using a coaxial cable [135]. According to Kraus [132], if the diameter of the cylinder is a sufficiently small fraction of a wavelength, and $D< \lambda/8$ is offered to define this condition, a vertically oriented slotted cylinder generates a horizontally polarized field which is nearly omni-circular. The slot dimensions are established to be at resonance, length slightly longer than the corresponding planar slot or dipole (a loading effect of the cylinder). Rule-of-thumb dimensions for the resonance condition are D=0.125λ, L_{slot}=0.75λ with W_{slot}=0.02λ. The Alford slot may employ a longer slot (1.2λ to 2λ) for higher directivity and a narrower elevation beamwidth [136]. For a 587 MHz resonant slot design center frequency these dimensions are diameter=0.069 m, slot length 0.413 m and slot width 0.011 m.

The impedance from a resonant $\lambda/2$ slot is 530 Ω. The longer cylindrical slot for resonance has impedance on the order of 200 W [137]. A 4:1 coaxial balun would be needed to operate efficiently with the 50 Ω receiver load. The advantage of the cylinder is that feed cables can be integrated internal to the cylinder, including balun.

The antenna sized for the target transmitter was modeled in FEKO (FEKO LITE student version 6.3), as shown in Figure 6.9, unfortunately there were insufficient number of degrees of freedom enabled in the student version to evaluate the configuration. Consequently this antenna option was not taken forward.

An example of the performance of the antenna, more generally, was found in [138] having been evaluated using 4NEC2. The dimensions modeled were specific to VHF frequencies (diameter 0.15 m, more appropriate for 250 MHz) and the results demonstrated the desired pattern and gain performance, together with a very wide 2:1 VSWR bandwidth. Interestingly, from this example, the resonant frequency was 620 MHz (zero reactance) with an antenna resistance of 500 ohms though the front to back

ratio was of the order of 3:1 at that frequency.

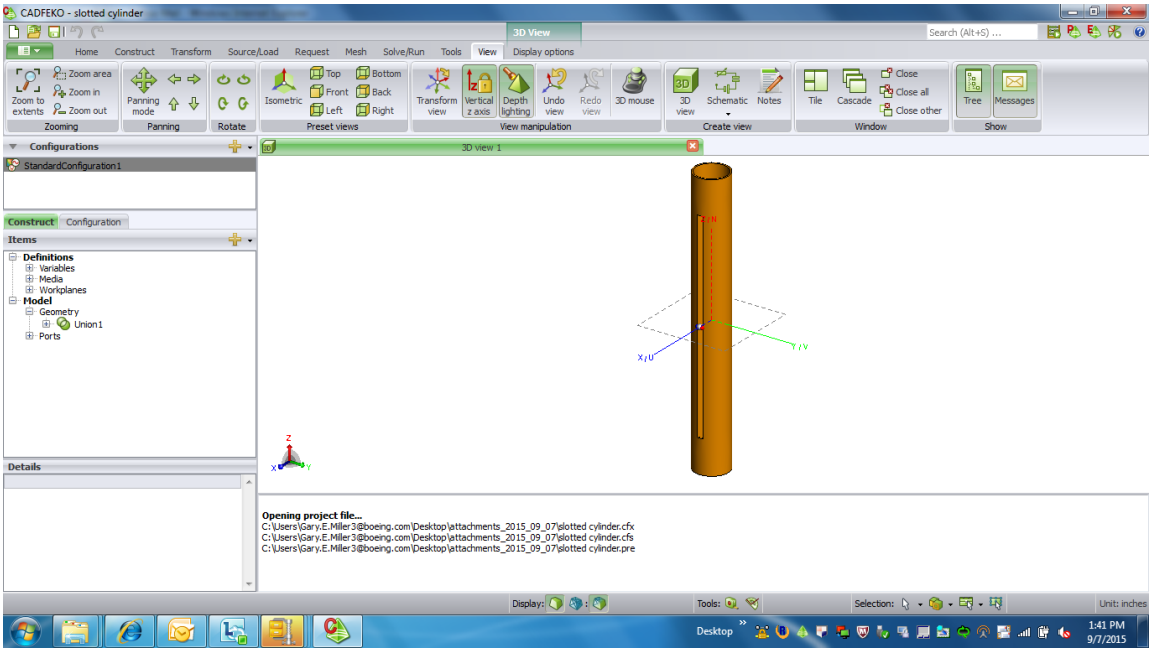

Figure 6.9. FEKO Model Cylindrical Slot Element

• **6.1.2.1.3** ***Turnstile antenna***. The crossed dipole antenna in its simplest form is pictured in Figure 6.8c [139] and [140]. The antenna consists of two resonant dipoles (antenna impedance – 77 Ohms – has no reactive component, length ~0.48λ) and that may be offset slightly in the Z direction (the plane represented by the dipoles is the X-Y plane). A 90 degree phasing line, a short segment of impedance matched, semi-rigid, coaxial waveguide connects the two driven dipole arms via the center conductor. The length of the phasing line must take account of the group velocity in the coax to realize the 90 degree delay (placing the two driven arms into quadrature). When fused the antenna exhibits an impedance of one-half the individual dipole (35.5 ohms). The antenna is oriented with the effective plane of the crossed dipoles co-linear with the incident polarization (horizontal and the antenna X-Y plane). The combination of dipole responses result in a near omni-directional response in azimuth through the phasing across the driven arms. The electric field (ϕ the polar angle) is a function of angle and time [132];

$$E(\phi,t)=\frac{\cos\left(\frac{\pi}{2}\cos(\phi)\right)}{\sin(\phi)}\cos(\omega t)+\frac{\cos\left(\frac{\pi}{2}\sin(\phi)\right)}{\cos(\phi)}\sin(\omega t) \qquad (6\text{-}17)$$

As the angular width of the main lobe of the antenna pattern of a single dipole is slightly less than 90 degrees, at the 45 degree inter-arm angles the combined response is sufficient to nearly circularize the gain. The George Brown turnstile using resonant dipoles should be circularized to within ±5% [139]. Reference [140] indicates that gain should be at a maximum when either dipole is parallel with the incoming wave and slightly reduced at 45 degrees (centered between the dipole arms). Equation 6-17 confirms this assertion.

Turnstile performance was evaluated using FEKO. The antenna is constructed of wire segments that have a feed gap defined by the intrinsic FEKO function ”wire port”. The dipole cruciform forming the coordinate basis with the arms of one dipole pair located at Z=±2.5 mm along the Y=0 axis, each with length 12.2 cm and the other at Z=±2.5 mm aligned on the X=0 axis with the same length. This corresponds to a 5mm feed gap on both dipoles. FEKO requires the generation of a network to represent the electrical connection of the phasing line (defined as a transmission line) to the driven arms and the outer shield to the non-driven arms. The physical geometry is shown in Figure 6.10a with the inset representing the transmission line model used to emulate the phasing line. The calculated gain pattern is shown in Figure 6.10b as a polar plot with a 10 dB scale; the nearly uniform azimuthal pattern easily evident and compares nicely with Figure 16-15a in [132].

The turnstile was selected for use. Design details are shown in Figure 6.11a. Fabrication was straight forward, performed in a home workshop. Material used for the dipole arms was 12 gauge solid copper wire. Semi-rigid RG-59 was employed for the phasing line because of the radius of curvature, as it would hold shape during assembly. It was also selected because the impedance (73 Ohms) was a relatively good match to the dipole impedance (77 Ohms). The dipole arms were bonded to a low dielectric foam block to make handling and assembly easier (Figure 6.11b). After bonding, which set the feed gap, the dipole arms were trimmed to length. The phasing line was formed over a mandrel to

avoid kinking the inner dielectric insulator (then reshaped to fit the tube opening). The phasing line inner conductor was soldered between both driven arms (labeled 1A and 2A) with the non-driven arms soldered to ground as shown in Figure 6.11c. A rigid polyvinyl tube was bonded through an opening in the foam block to sheathe cabling and provide a convenient means of handling and mounting the antenna.

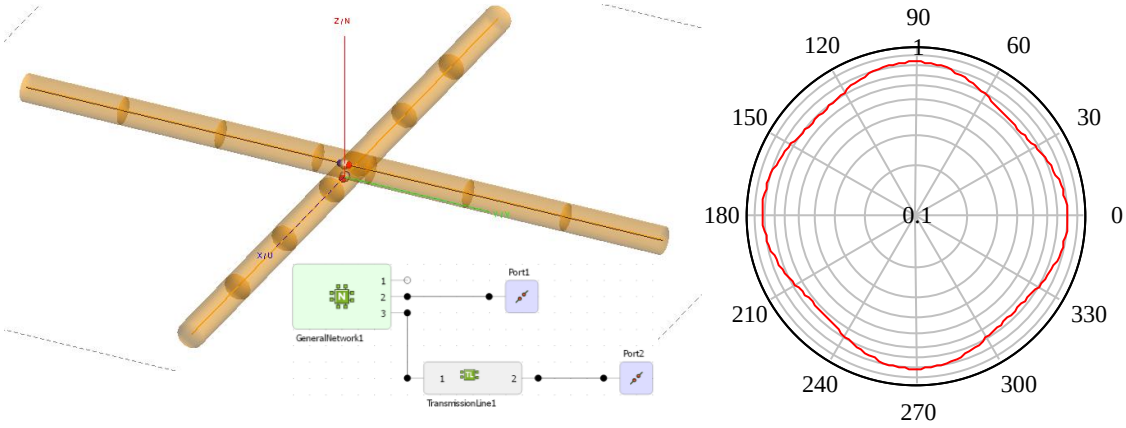

a) FEKO Geometry and Phasing Line Model

b) Calculated Pattern (Linear Scale)

Figure 6.10. FEKO Calculated Reference Antenna Gain Pattern

The 37 Ohm antenna is coupled to an impedance transformer which consisted of a parallel 1/4 wave transmission line using RG6U, 93 Ohms, as the best commercially available match (design value of 85.44 Ohms would have been optimal). The transformer appears in Figure 6.11d. Field test measured patterns from this antenna for two different trials at two different sample resolutions are shown in Figure 6.11d. Measurements taken in an anechoic chamber can be found in the calibration Section 6.2, Figure 6.33.

• **6.1.2.2** ***Main antenna***. The window opening on the test aircraft, both front and front and rear combined, set the outer bound on the main antenna length. Further, per FAA rules, the antenna had to be mounted internally (to avoid the complexities associated with structural and outer mold line modifications. Further, for safety reasons the aircraft door

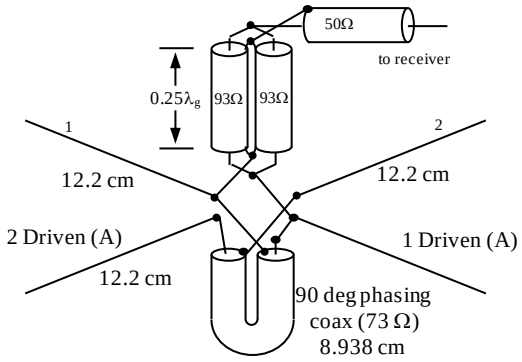

a) Reference Antenna Schematic

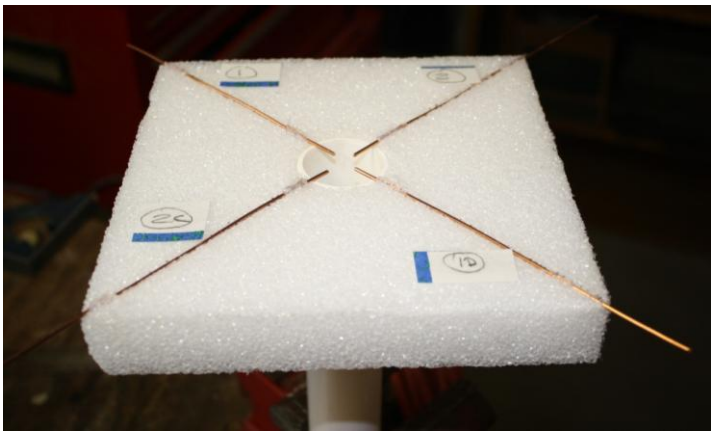

b) Dipole Arms (untrimmed), Foam Block and Tube

c) Phasing Coaxial Line Installed

d) 1/4 Wave Impedance Transformer

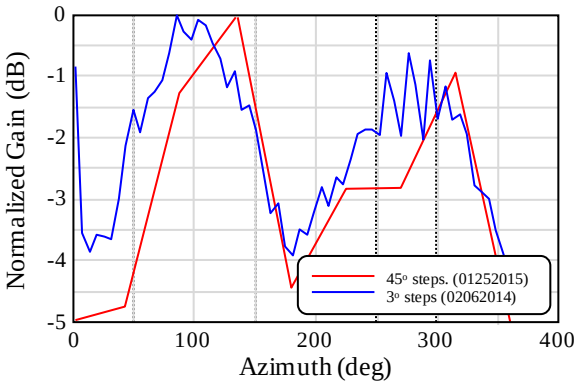

e) Measured Normalized Gain Patterns

Figure 6.11. Turnstile Antenna Design, Assembly and Test

had to operate when the antenna was installed. This effectively limited the antenna length to that of the window opening. Finally the antenna could not completely cover the window opening (visibility). The antenna pattern would be constrained by the window opening, but required a gain/sidelobe pattern that did not exceed the reference antenna at angles outside the mainbeam region. The main antenna requirements are summarized in Table 6.5. Unable to drill holes for mounting, the antenna support brackets would have to clamp to the inside of the window opening.

Installation limitations virtually mandated a planar antenna design. Two variations of a 3 × 1 linear array were designed and evaluated. Both used variations on a patch element. The first an edge shorted, air dielectric patch and the second a dielectric loaded patch using fiberglass FR4. At a nominal half-lambda spacing this size would fill the aircraft forward cockpit window. This activity had begun before the specific test aircraft had been

identified. However all Cessna aircraft in the 17X model series have windows that are of similar size.

Parameter	Value	Comments
Polarization	Horizontal	Matched to Source
Center Frequency	587 MHz	UHF Chan. 33 KWPX (λ = 0.511m)
VSWR 2:1 Bandwidth	>2% of Matched Channel Carrier	Support multiple TV channels for c/o testing
Gain	10 dBi	Limited by opening
Azimuthal Coverage	~20 degree beamwidth	Also limited by window opening
Elevation Coverage	> 90^o beam width	Maximum collection altitude
Size/Volume	$\leq$ 0.78 m by $\leq$ 0.254 m by $\leq$ 0.025m	Limited by window opening with thickness limited by proximity to passengers seat position
Mounting	No structural modifications	Brackets affix (clamp) to window frame
Weight	< 3 kg	Support brackets and ease of installation
Interface	50 ohm coax/SMA	Matched to USRP (receiver) input

Table 6.5. Main Antenna Requirements

• **6.1.2.2.1** ***Dielectrically loaded patch array***. Patch elements were sized using standard rules of thumb for microstrip patch antennas. Beginning with the choice of FR4 (FR for flame retardant) as the loading dielectric: FR4 glass epoxy is a high-pressure thermoset plastic laminate with near zero water absorption [141]. The two electrical/mechanical properties of interest are the density (1850 g/cm^3), the relative dielectric constant (4.70 max., 4.35 @ 500 MHz, 4.34 @ 1 GHz), and the loss tangent (0.008 for frequency range 100 MHz to 3.0 GHz).

The patch thickness (substrate height, h) is taken from the rule of thumb; $0.003\lambda_0 < h < 0.05\lambda_0$ where λ_0 is the free space wavelength [142]. Alternatively, the height can be calculated from [143]

$$h \leq \frac{0.3c}{2\pi f\sqrt{\varepsilon_r}}. \tag{6-18}$$

From (6-18) for 587 MHZ resonant (radiating) frequency we get $h \leq$ 0.0119 m (0.023λ or 0.468 in). The initial patch dimensions are given by

$$W = \frac{c}{2f\sqrt{\frac{\varepsilon_r + 1}{2}}} \qquad \varepsilon_{eff} = \frac{\varepsilon_r + 1}{2} + \frac{\varepsilon_r - 1}{2}\left(1 + 12\frac{h}{W}\right)^{-0.5} \tag{6-19}$$

$$L_{eff} = \frac{c}{2f\sqrt{\varepsilon_r}} \qquad \Delta L = 0.42h\frac{\left(\varepsilon_{eff} + 0.3\right)\left(\frac{W}{h} + 0.264\right)}{\left(\varepsilon_{eff} + 0.258\right)\left(\frac{W}{h} + 0.8\right)} \tag{6-20}$$

and finally the patch length is found from

$$L = L_{eff} - 2\Delta L. \tag{6-21}$$

These expressions for FR4 combine to give the dimensions in Figure 6.12. Single element patch size (copper) was calculated to be (L, W) = (0.121 m, 0.158 m). These result in a width to length ratio of 1.312 (1.5 is a typical value). The width is defined as the y coordinate and the length the x coordinate. The dimensions of the dielectric slab were calculated as (L_{FR4}, W_{FR4}) = (19.2 cm, 22.98 cm). The width supports half-lambda spacing for a 3 × 1 element array. The E-plane for the TM10 mode is coincident with the x axis. The original placement of the feed probe, along the patch width bisector, the y=0 axis, was based on the calculated edge resistance of 208.04 Ω. Per standard practice the feed would be positioned on the y=0 axis. Using

$$R(x) = R_0 \cos^2\left(\frac{\pi x}{L}\right) \tag{6-22}$$

and solving for x with $R(x)$ set to 50 Ω for the receiver load, the calculated feed position is 4.1 cm from the x=0 axis. This is also indicated in Figure 6.12. The calculated radiation efficiency and bandwidth, based on the Pozar enhanced CAD equations from [144] were 67% and 2.98%, respectively. The element was defined in FEKO as shown in Figure 6.12c.

Commercially available FR4 occurs in 1.113 and 1.27 cm thickness with slabs cut to length. For sizing calculations the thicker size was selected to preserve the estimated bandwidth. FR4 density is 1.850 g/cm^3 [141] so if individual dielectric slabs were cut, the weight would be 0.45 kg, and three would be 1.35 kg. To support the dielectric, 18 gauge rolled steel was selected for both structure and ground plane. The total weight of a three

element antenna, without cabling, connectors, brackets, and the 3:1 combiner would have been 3.04 kg and was judged too heavy for a safe window mount.

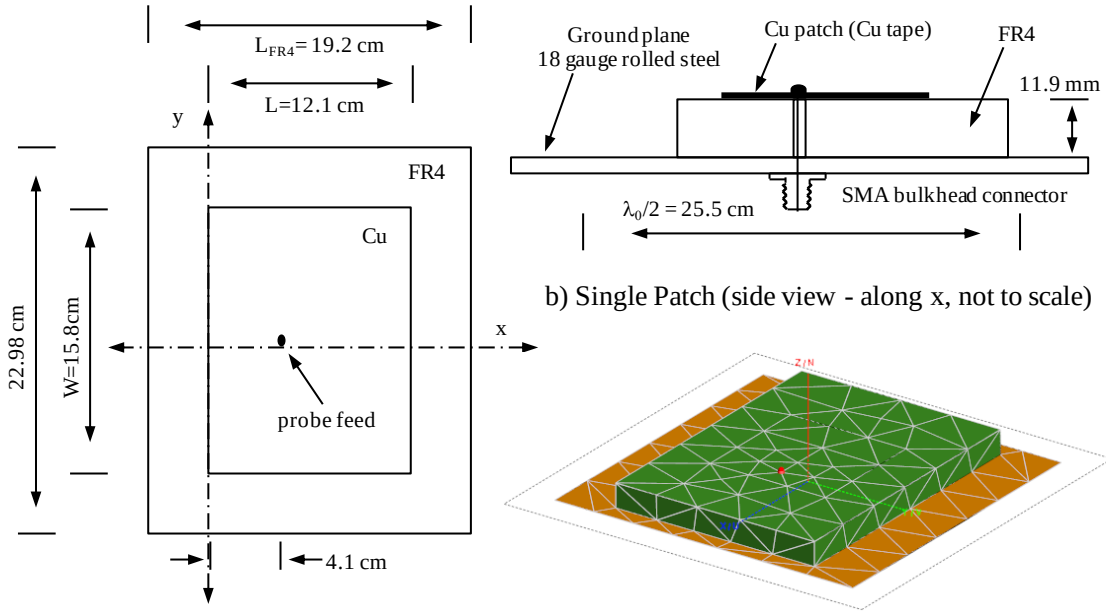

a) Single Patch (top view)

b) Single Patch (side view - along x, not to scale)

c) FEKO Physical Model

Figure 6.12. Horizontally Polarized Dielectrically-loaded Rectangular Patch

• **6.1.2.2.2** ***Edge-shorted patch array***. As a more lightweight option to the patch array with elements dielectrically loaded with FR4, an array of edge-shorted, air dielectric, one quarter wavelength patch elements was evaluated. Suggested by Dr. Gary E. Miller, this version has approximately the same ground plane area with slightly increased element depth with the air dielectric. The use of the shorting wall is a common technique and allows the patch size to be reduced from the half-lambda size to one quarter-lambda [145]. The increased air dielectric thickness was needed to provide sufficient bandwidth. The single element and full array designs are shown in Figure 6.13. The location of the feed point on the three elements was determined by trial and error, the condition of success defined by the best match of mutual coupling impedance. The initial position is indicated in Figure 6.13a. Detail of the individual patch is shown in Figure 6.13b. The design was implemented in FEKO, as shown in Figure 6.13c.

Mutual impedances were minimized through the location of the feed point. Iterations using FEKO with minimized return loss mismatch amongst the three elements as the

metric resulted in shifting the feed 0.275 in (6.5 mm) away from the shorting wall relative to the dimensions identified in Figure 6.13a. The results of the FEKO evaluation are given in Figure 6.14. The original intention was to employ a binomial taper (0.5, 1.0, 0.5) across the three elements to effectively eliminate the first sidelobe. The taper was implemented using 3 dB pads on the outer elements. This configuration was carried for a while but was dropped: the 4.26 dB taper loss was excessive and the sidelobe control not needed. However the results in Figure 6.14 all include the weighting. The final return loss versus frequency results are shown in Figure 6.14a. The feed position, as indicated, slightly offset from the initial position. Gain versus angle in the cardinal azimuth (in Figure 6.13c the red axis and blue axis define the azimuth plane) and elevation (red and green) cardinal planes. Polar plots of gain are presented in Figures 6.14c (azimuth) and 6.14d (elevation). Predicted peak gain is 6.6 dB, again with the taper. As expected due to the small ground plane size, a modest front-to-back ratio was realized (a consideration related to direct path breakthrough).

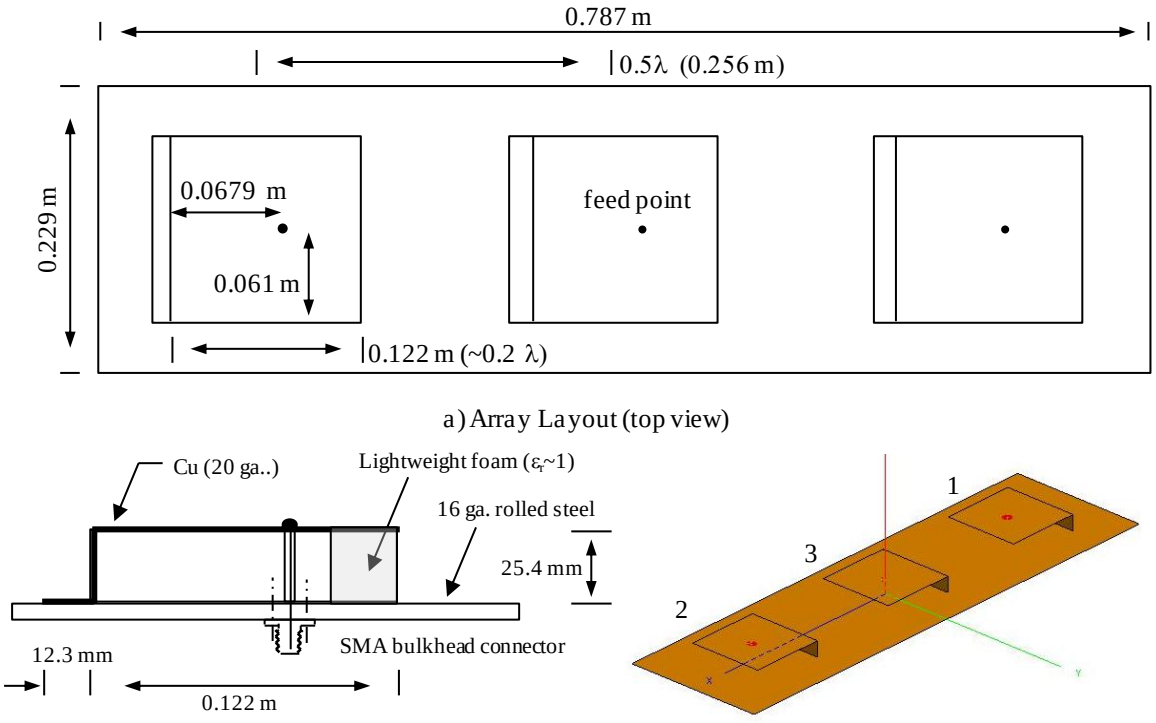

Figure 6.13. Edge-shorted Patch Array Design

This configuration had acceptable performance and would be straight forward to build with the materials and tools available. The patches were fabricated from 20 gauge copper sheets from a hobby store using a printed paper pattern for the cuts and bend lines. The patch is center-fed using an SMA bulkhead connector mounted from the ground plane back side (bottom), slightly protruding through a hole drilled in the patch, secured with four attach screws and soldered. The ground plane initially was composed of 16 gauge rolled steel (cut to size by the metal vendor) and was assembled 6 months prior to testing. This was replaced after corrosion was observed at the bulkhead connector attach points to the ground plane. The replacement was thinner brass which required an aluminum frame for stiffness. The center patch was soldered to the ground plane along the shorting wall fold with less than ideal results (large heat sink) so all were clamped with bolt-washer-

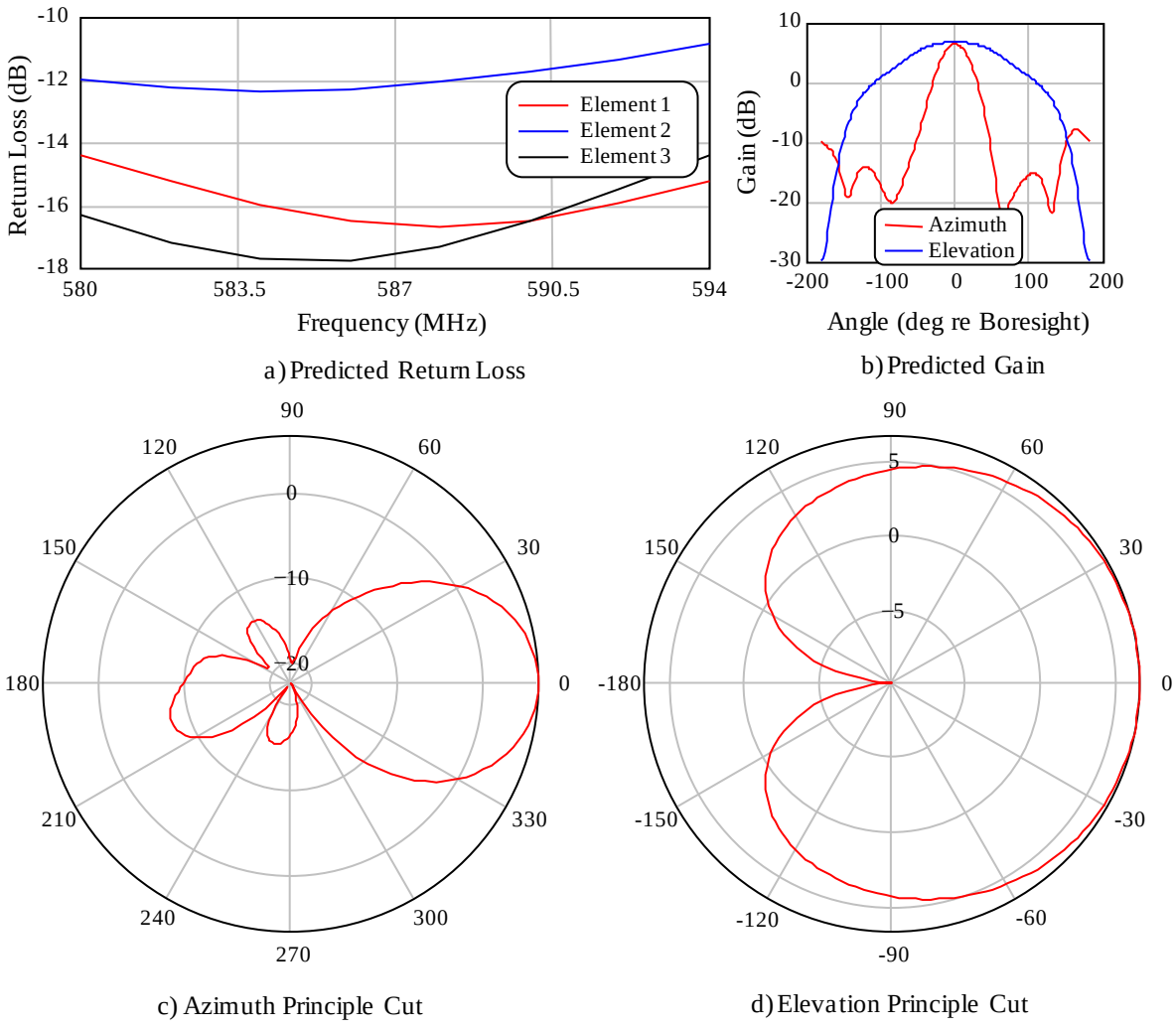

Figure 6.14. Horizontally Polarized, Dielectrically-loaded, Rectangular Patch Results

nuts and taped with copper tape to insure grounding. To support the open end a small block of very lightweight, open pore foam was bonded between the patch edge and the ground plane. The initial antenna build (on rolled steel) appears in Figure 6.15, in several perspectives. An enlargement of the center patch is shown in Figure 6.15b with rear and edge views in Figures 6.15c and d, respectively. Figure 6.16 is a photo series of the antenna with the replacement (brass) ground plane.

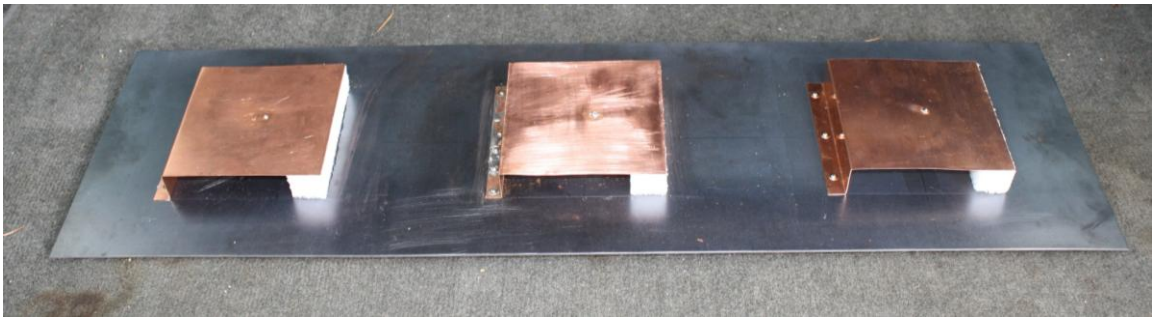

a) Front Perspective View

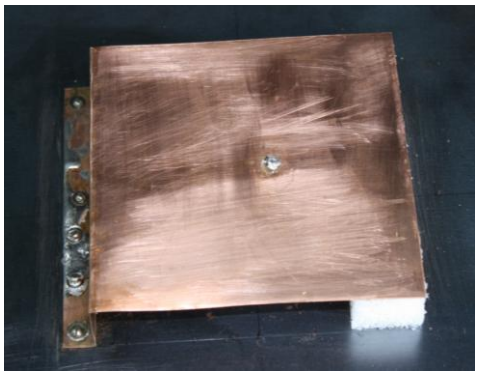

b) Center Element (Enlarged)

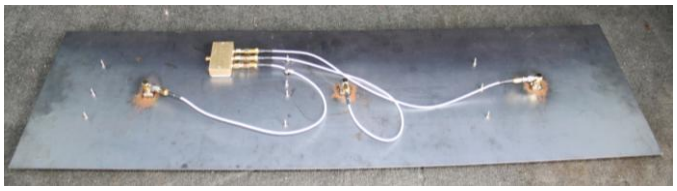

c) Rear View

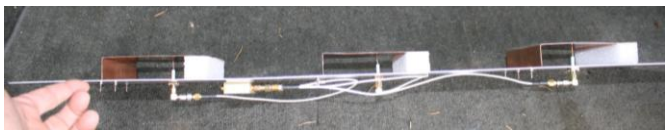

d) Edge View

Figure 6.15. Fabricated Main Antenna

The three elements were manifolded with a surplus 3:1 combiner (I. F. Engineering PD-3003-S) and matched length coaxial cables (visible in Figure 6.15c) which exhibited an insertion loss per unit length of 0.669 dB/m (midband). The combiner was specified only up to 500 MHz. However the measured insertion loss at 587 MHz was less than 0.5 dB above the specified value (2.1 dB measured): so the part was deemed acceptable.

Measured pattern attempts outside of an anechoic chamber produced unacceptable results in spite of several attempts at different locations. A comparison of the FEKO model results (with binomial weights) against the calibration measurement from the anechoic

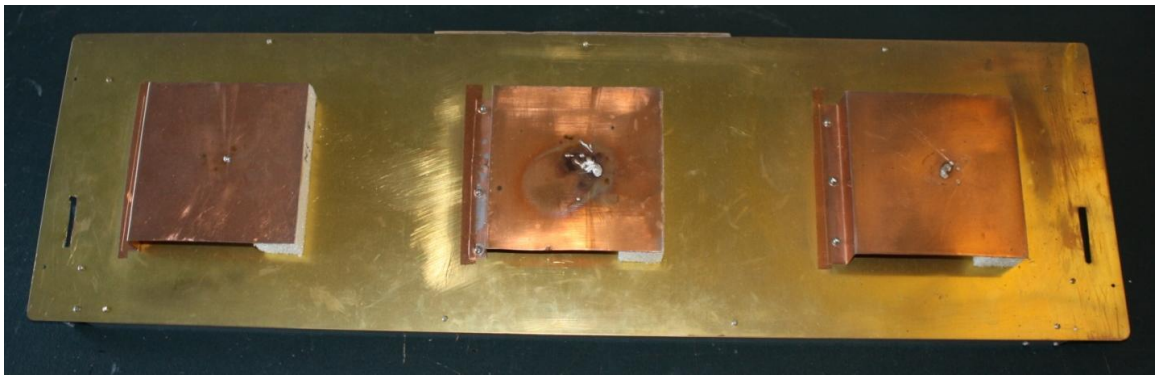

a) Front View

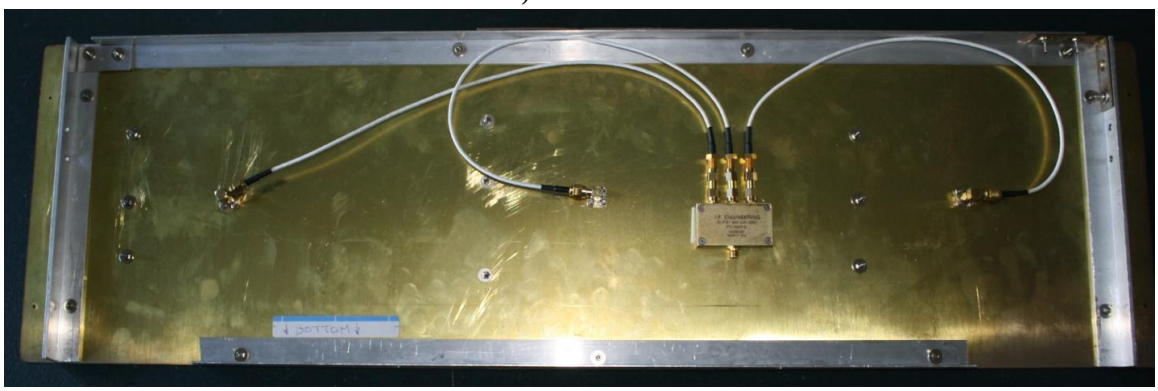

b) Reverse Side View

Figure 6.16. Main Antenna with Brass Ground Plane

chamber (detailed in Section 6.2) is made in Figure 6.17a. To facilitate the comparison the FEKO result is normalized to the calculated peak gain. Figure 6.17b is a comparison of a non-anechoic lab measurement using a Vector Network Analyzer (VNA) and compared to field measurements using a single channel of the bistatic receiver described in Section 6.1.1.

6.1.3 ***Support instrumentation***. Support instrumentation is briefly described in this section. Support instrumentation includes the GPS instrumentation and designed and partially and completely fabricated calibrated targets. These latter were intended for use at the original test location to the south and east of the target transmitter where permission to access the test location had been obtained, and for a test wherein the receiver was to be automobile-mounted. This ground two-dimensional aperture test was planned as a precursor to the flight collection but which ultimately was not conducted because of inability to obtain permission to access test locations with emitter visibility.

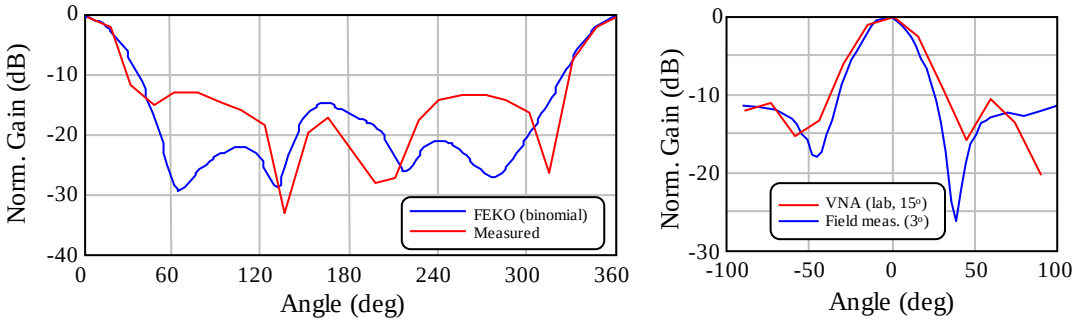

a) Simulated Compared to Measured b) Lab and Field Measured

Figure 6.17. Pattern Comparison - Flight Configuration to FEKO Model

• **6.1.3.1** ***Navigation instrumentation***. The GPS test components were shown in the block diagram in Figure 6.2. These consisted of the Trimble GEOXH hand-held, survey-quality receiver, the SkyPro XGPS160 GPS WAAS (Wide Area Augmentation System) receiver, and the 3V Garmin GA25 MCX antenna used with the GPSDO integral to the N200.

The Trimble GEOXH is shown in Figure 6.18. The unit measures 234 mm by 99 mm by 56 mm, weighing 0.925 kg (2.0 lbs). The receiver has 220 channels and services the GPS, GLONASS and SBAS (Space Based Augmentation Systems; the latter including WAAS (Wide Area Augmentation System), EGNOS (European Geostationary Overlay System) and MTSAT Satellite-based Augmentation System (MSAS), with an integrated L1/L2 antenna. The Trimble update rate is only 1 Hz but provides decimetric-level accuracy. The Trimble also includes Wi-Fi and cellular capability for real-time corrections to this level of accuracy (10 cm plus 1 ppm) or the data can be stored for off-line processing (as was done in this experiment). Horizontal RMS error with the real time WAAS is better than 1m. The single unit height error with SBAS/WAAS is less than 2m. With post processing the height error can equal the horizontal error (decimetric). Horizontal decimeter accuracy is obtained via post processing. Battery lifetime is 10 hours. The Trimble was rented from GeoPlane Services (A Division of Universal Ensco Inc., 4848 Loop Central Drive Houston, Texas 77081). Also delivered with the hand unit was Trimble GPS Pathfinder Office. The software package facilitated data transfer and post

processing using atmospheric corrections obtained from the Washington State Reference Network (WSRN), Continuously Operating Reference Stations (CORS). As described in Section 6.4.3, GPS Pathfinder provided turnkey implementation of the multisite corrections.

The XGPS160 is also pictured in Figure 6.18. The unit also supports both GLONASS and GPS constellations with SBAS (WAAS/MSAS/EGNOS/GAGAN) and can operate as high as 10 Hz data rate with a 99 channel receiver. GPS L1 (1575.42 MHz) and GLONASS L1 (1598.0625~1605.375 MHz) are supported. Published accuracy is +/- 2.5 m CEP. A rule- of-thumb is that the vertical error is 1.5× to 4× the horizontal error[3]. However, data are not stored in format which is suitable for post processing as was the

a) Trimble 6000 Series GEOXH b) XGPS160

Figure 6.18. GPS Instruments (not to same scale)

Trimble. The flexible, no skid rubber base allows the unit to sit on the aircraft glare shield and transmit position data via Blue Tooth 2.4 GHz wireless link to an iPad or similar viewing device. On the display device the data is integrated with map or navigation software. Collected position data are stored on the WGPS160 unit and downloaded via Wi-Fi to the vendor who, in turn, transmits the data as a text file attachment to email. The

[3] https://groups.google.com/forum/#!topic/giscolorado/TMfGmFAePxA

unit size is 55 mm by 70 mm by 22 mm (H x W x D). 10 hours of battery life are available with Blue Tooth functionality enabled.

All the GPS antennas were positioned in the glare shield in order to maximize the view of the sky (satellite access). This position worked quite well with greater than 10 satellites, GPS and GLONASS, visible to both GPS units. Installation is described in Section 6.3.2.

• **6.1.3.2** ***Calibrated targets***. Early studies had a monostatic focus and the inclusion of target(s) with a known response under three-dimensional imaging aperture was planned. Simulated response would provide a known benchmark against which flight test reconstruction results could be compared. An L-band monostatic radar was a flight test candidate and access to the image scene for placement of known targets for both spatial and radiometric effects was coordinated. Most simulation activity utilized the hypothetical isotropic (angle and frequency invariant) scatterer and realizable targets which would support wide aperture scattering were sought. The conducting sphere, a right circular cylinder with length/circumference ratio of approximately one, the spherical trihedral (three circular planes intersecting at 90 degrees), and the tophat were all considered. As the focus of study shifted to bistatic tomography using HDTV the list of potential targets was modified, the trihedral being dropped. This section presents scattering analysis results and the associated reconstructions.

Scattering from the PEC (perfectly electrically conducting) sphere is exactly known. The well known normalized response (radar cross section) derived from the Mie Series [146] is shown in Figure 6.19a. In Figure 6.19b the scattered spectrum from a simple, envelope-only modulated pulse of 223 MHz bandwidth and after reception by a frequency independent antenna and match filtering, is shown. A 1.5 m radius sphere is assumed and the spectrum is centered at 587 MHz.

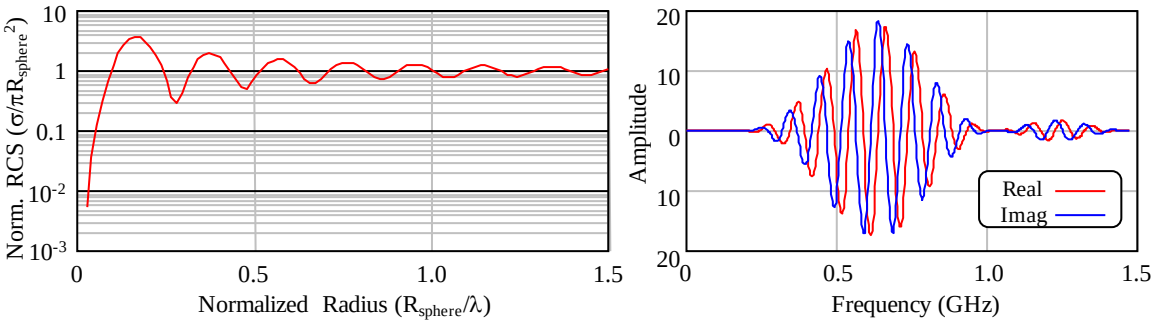

a) Normalized RCS versus Normalized Radius, λ = 1m

b) Complex Scattered Field after Match Filtering

Figure 6.19. Monostatic RCS and Example Scattered Field

The broadband monostatic response in the time domain appears in Figure 6.20. Range is relative to the sphere centroid. The dominant response (-1.5 m) is the specular return. The secondary response is that of the creeping wave. Delay (two-way) of the creeping wave, relative to the specular, is one radius plus one quarter the circumference. With the sphere symmetry, this response is invariant to aspect angle.

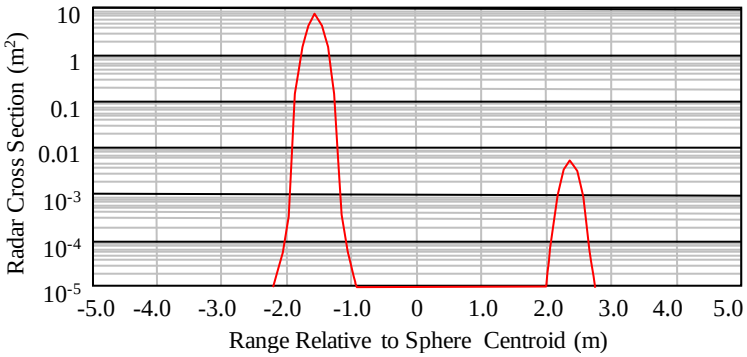

Figure 6.20. Sphere Time Domain Response (from Fig. 6.19b)

The scattered field in Figure 6.19b was then computed over two pi radians, and applied to a two dimensional aperture reconstruction. The results are shown in Figure 6.21. There are two results, the first a linear scaled contour view (which illustrates only the specular return), in Figure 6.21a and a cut along the X=0 axis (Figure 6.21b).

To test the reconstruction, the bandwidth of the illuminating rect pulse was reduced to 6 MHz and the scattered field recomputed. The results are shown in Figure 6.22. The narrowband reconstruction does not resolve any features, collapsing to a point. Effectively this is the same result as the isotropic scatterer.

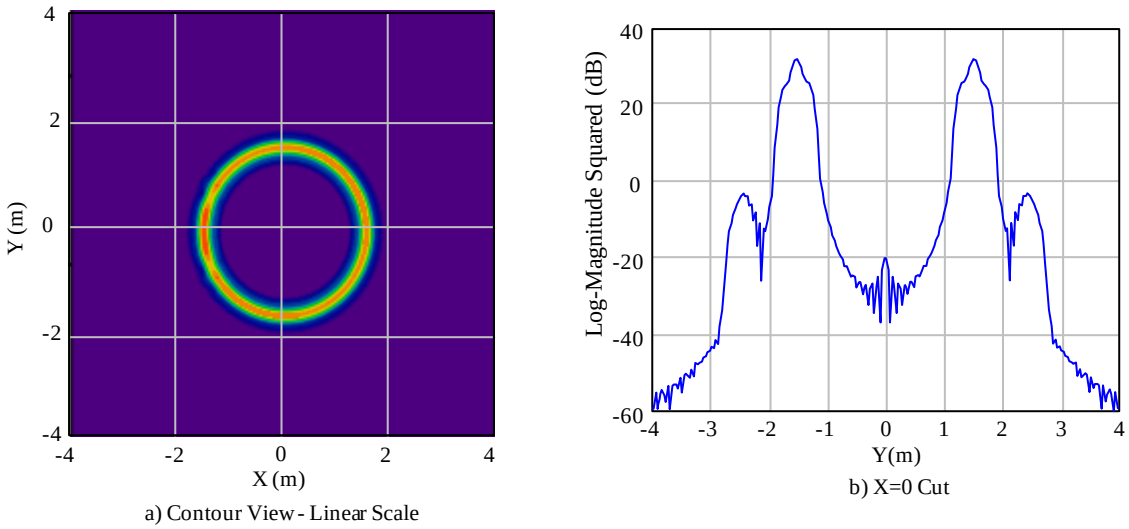

a) Contour View - Linear Scale

b) X=0 Cut

Figure 6.21. Two Dimensional Aperture, Monostatic Reconstruction (Wideband)

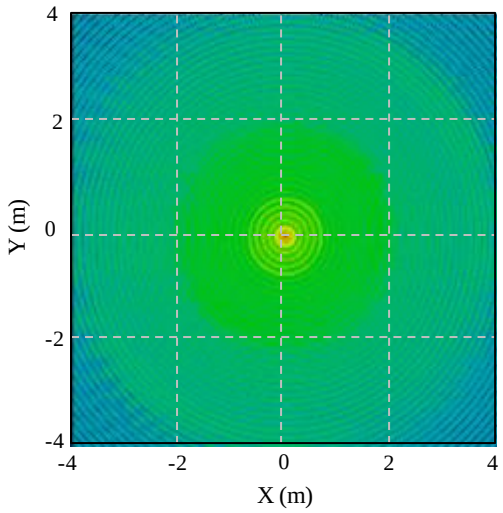

Figure 6.22. Two Dimensional Aperture, Monostatic Reconstruction (Narrowband)

The bistatic scattered fields from a PEC sphere no longer exhibit aspect independent symmetry. Defining the bistatic angle as the angle between incident and scattered directions, in the plane defined by those directions with the Mie series [146], the RCS of a sphere as a function of bistatic angle, when observed along an equatorial cut, is presented in Figure 6.23a. A single sphere radius (1.5 m) and 1 m wavelength were used for this calculation.

Bistatic angle (beta) varies from 0 to π radians. The response strongly resembles the monostatic (normalized radius 1.0 in Figure 6.19) in the region out to around 50 degrees (the pseudo-monostatic region). Between 50 deg and 150 degrees the RCS oscillated in

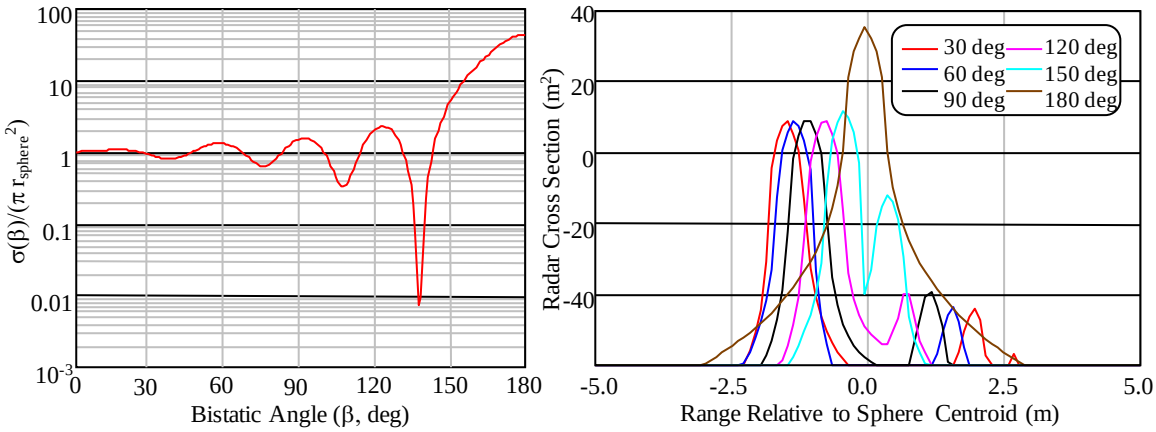

a) RCS vs. Bistatic Angle (β, deg) b) RCS vs. Range, β as parameter)

Figure 6.23. Bistatic Response of a PEC Sphere

the bistatic region and beyond 150 degrees we see the RCS bloom in the forward scatter regime. Figure 6.23b depicts the range response of the sphere when observed bistatically with the same wideband waveform as the monostatic case. At β=0 deg we have the monostatic response (Figure 6.20). As β increases the apparent range of the specular point reflects the migration of this point around the sphere and the angle at which the creeping wave is observed, foreshortening separation relative to the specular. Thus we have an angle dependent response that will introduce distortion during image formation. For the bistatic case three cases are considered for the two-dimensional aperture: wideband (223 MHz), narrowband (6 MHz) and CW, this latter to verify the reconstruction code. Figure 6.24 contains cuts of the reconstruction of a 2D aperture along the Y=0 axis (Figure 6.24a), the X=0 axis (Figure 6.24b) and a contour plot (Figure 6.24c). The transmitter location is along the Y=0 axis at X=1000. The radius of the collection aperture was also 1000 m with the origin of the sphere coincident with the scene origin. In both cases the direct (unscattered) path contribution is neglected.

The 6 MHz waveform result is shown in the same format in Figure 6.25 and also exhibits the reconstruction distortion relative to the monostatic case. To test the reconstruction, a single tone from the scattered spectrum was used as input. The result, which is not shown, resembled Figure 6.22, as expected, with the mainlobe resolution twice the monostatic

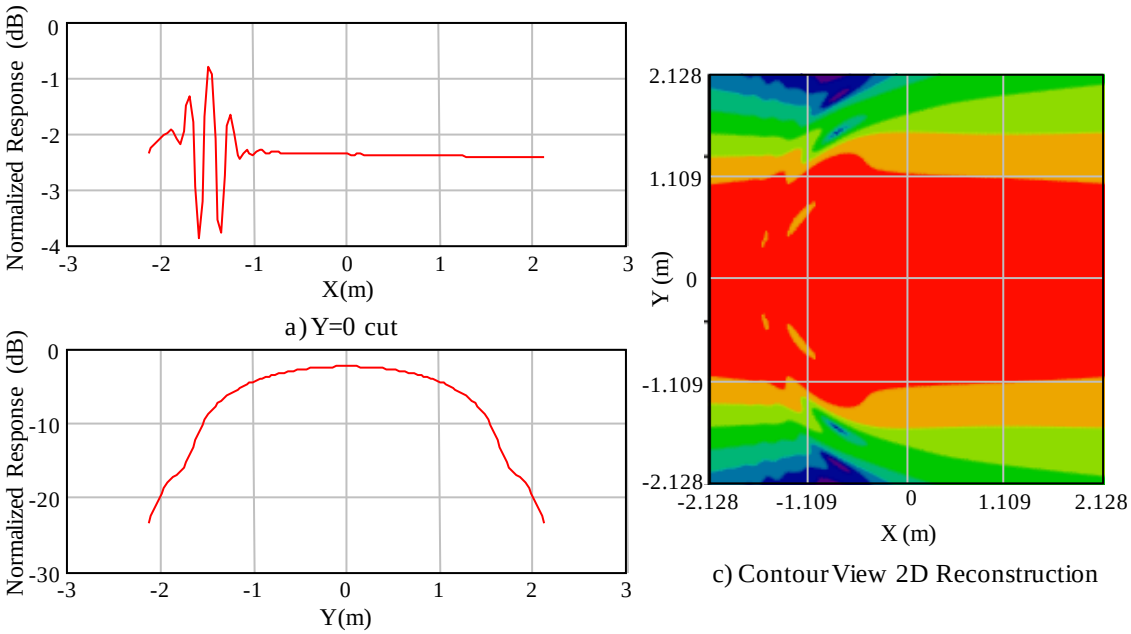

Figure 6.24. 2D Bistatic Reconstruction of Perfectly Conducting Sphere (Wideband)

case. This gave confidence that the reconstruction code was operating correctly, but does not explain the distortion in Figures 6.24 and 6.25.

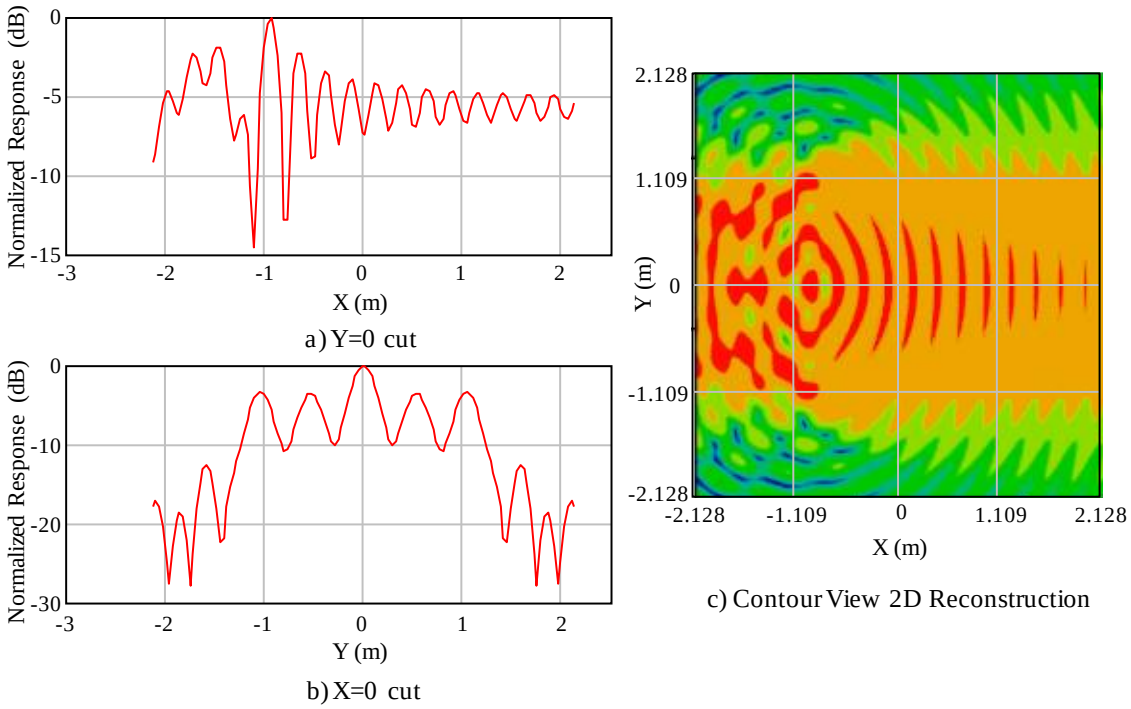

Figure 6.25. 2D Bistatic Reconstruction of Perfectly Conducting Sphere (Narrowband)

The use of the sphere illustrates the variation of the target point spread function when the aperture is extended to 2π radians as in the tomographic reconstruction, and as the bandwidth is varied. With respect to known targets for flight test, the first observation is

that the bistatic geometry which might give rise to forward scatter blooming will not be experienced. And, though speculars from large objects might be encountered, they are unlikely from man-made structures as buildings have vertical walls, the illuminating signal is arriving only 1.4 degrees from tangential to a smooth Earth (grazing angle), and flat and shallowly pitched roofs (particularly metal) would be expected to scatter above the altitude of the highest operating altitude of the test aircraft. A sphere was purchased (3 m diameter, inflatable weather balloon) but was too difficult to "conductorize". Silver-based paint was too expensive and application of aluminum foil with copper tape too unwieldy.

The vertical cylinder was evaluated using FEKO specifically for an automobile-based ground test. A 1.5 m (high), 0.56 m diameter aluminum foil-covered test was built for vertical orientation against the horizontally polarized illuminator. Estimated RCS was 5.8 m^2 (*ka*=3.142). The short range and 90 degree aperture would have largely been a pseudo-monostatic test. However access permission for the test location was not obtained and this was not performed. The cylinder is pictured in Figure 6.26a.

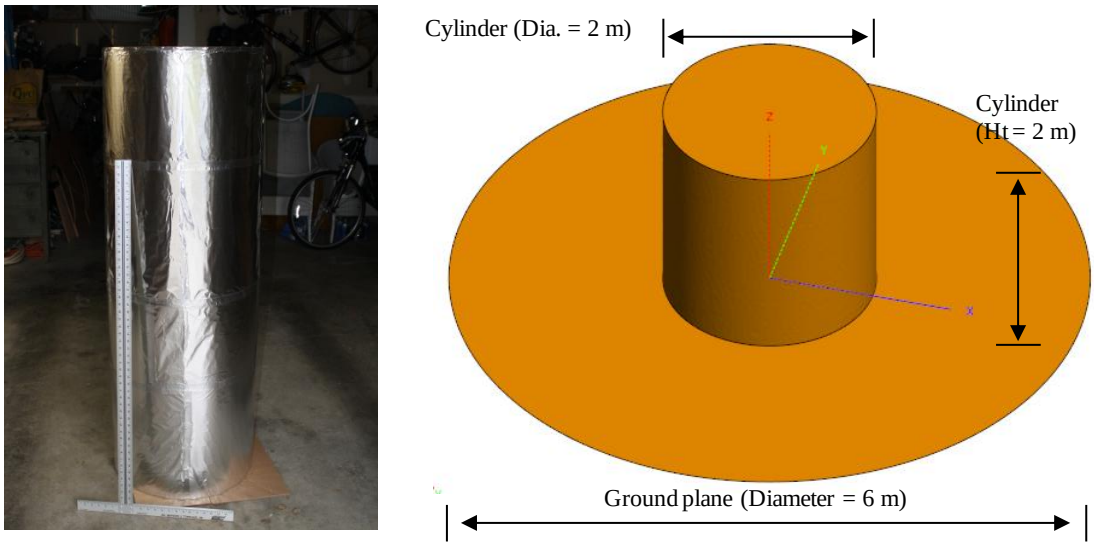

a) Foil-covered Cylinder (Ground Test)

b) Tophat (wooden frame and foil-covered)

Figure 6.26. Candidate Test Targets

The tophat target in Figure 6.26b was also constructed, but never (fully) assembled. The tophat was sized using monostatic arguments (it was intended for the originally planned monostatic flight test and carried over into the bistatic work with access to the initial test location). Sizing was done based on [147] presented from a monostatic SAR perspective: RCS at 587 MHz for a 6 m ground plane, 2 m high, 2 m diameter cylinder exceeds 10 m^2 between 10 and 85 degrees elevation aspect angle. To develop bistatic scattered phenomenology the tophat was modeled in FEKO and weighted by the voltage spectrum of the forward transformed waveform (see Section 5.0 and Appendix B, (B-9)). Symmetry is exploited to reduce the run times. Several elevation cuts of the predicted RCS at midband are presented in Figure 6-27. As in the case of the sphere, complex scattered fields were calculated in 14, 0.5 MHz steps symmetric with the channel center frequency.

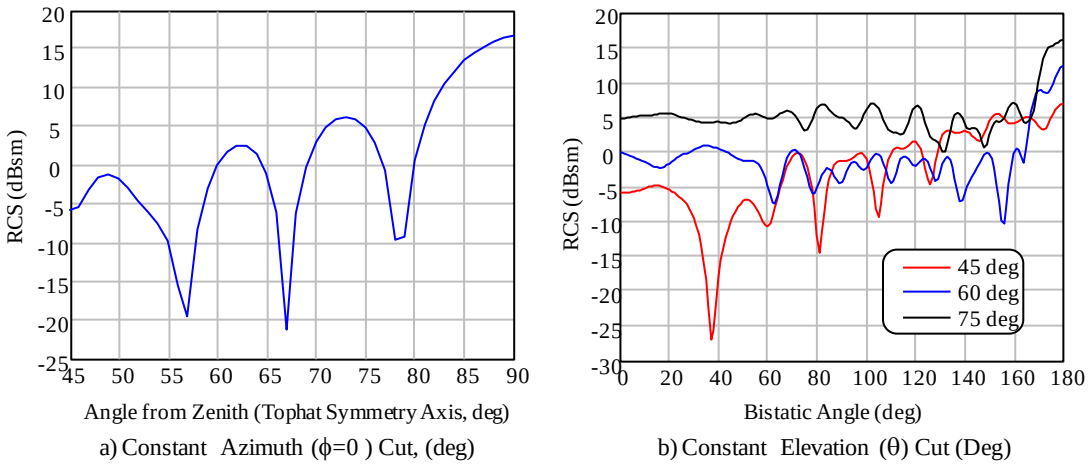

Figure 6.27. Bistatic RCS at 587 MHz – Select Aspect Cuts

6.2 Calibration.

Calibration serves twofold purpose: 1) compensating for the effects of nonlinearities and additive delay, resulting in a linear system of known electrical length to derive measured delay as referenced to the main antenna phase center, and 2) to force the transfer function response of the two channels into alignment (*e.g.*, channel matching) in order to obtain the highest cancellation ratio from the adaptive sidelobe canceller. Implementing 2)

results in the highest system sensitivity by suppressing the direct signal breakthrough [113], maximizing the effective SNR. These two requirements are not necessarily realized in a single operation. This section describes the approach and static (ground or laboratory) measurements made, as well as flight test data collected and processed to correct for systematic errors or deviations in the receiver hardware

The original approach was for a completely deterministic calibration and compensation. Channel matching, and spatial corrections would be applied to project the displaced reference antenna onto the main antenna to realize a phase stable range difference profile for each equivalent pulse repetition interval. As will be seen (Section 6.4) this was not (completely) the case.

The receiver system is a cascade of active electronics components, which exhibit temperature-dependent characteristics, and passive components which tend to be more stable. The responses of quiescent (passive) components, external to the receiver, are characterized in the laboratory, under controlled conditions while active components require the sampling of some probing signal(s) with processing required prior to application (and with the unit at operating temperature). In receiver calibration, particularly multiple receivers which must operate coherently, a controlled, known signal is injected at some point in the receive chain, normally after the antenna elements (which are stable and can thus be statically measured), and the receiver output sampled. The SNR of the probing signal is high so that the estimation error of amplitude and phase are controllably small, especially when combined with averaging or similar means to smooth random errors.

Also in the multichannel receiver, particularly when each channel employs an independent, though phase locked, master oscillator, the initial phases of the oscillators are a consideration. While the phase locked channels are coherent in that the time rate of

relative phase change is made small through the action of phased locked loops, the initial phases are random. The absolute phase difference is a consideration in that range/delay errors might result in the cross correlation process.

Several approaches were considered for channel-to-channel calibration before ultimately electing to use of the illuminating HDTV signal. These are briefly discussed before moving to the calibration details. The first method is the most obvious, the incorporation of a calibrated source, combined with a suitable means to couple the calibration signals into the receive channels after the antennas. The second is to exploit an external or environmental signal. Before proceeding we have a brief discussion on the use of the N200 as the digital receiver. The N200 is controlled via an operating program on the control processor. Any sampling change, gain, tuning or sample rate changes, or transmit or receive operation requires a restart. Calibration application would be run and terminated, followed by the collection application. Each restart results in different initial phases in the oscillators and thus one reason for calibrating would be defeated. There is no automatic gain control. Thus it is preferential to perform calibration with the unit continuously operating in the sampling mode.

As described in 6.1.1.2, the receiver system consumes about one-half the available prime power (10 amp circuit at 12 VDC with inverter conversion efficiency of the order of 78%, or 93.6 W). During experiment planning and design, 15 W overhead was reserved should the addition of low noise amplifiers ahead of the bandpass filter be necessary. With this insufficient power remained for a dedicated signal source, such as a laboratory generator. Signal could be injected to each receiver via 2:1 couplers or use of manual coaxial switches. The both would increase the system noise figure and require an additional set of static measurements to calibrate as part of the cascade. But the former, with the gains set for collection, would have external TV signals combined with the calibration signal. The calibration signal could not use a significantly higher SNR as the receive gains are gains

are balanced to just bring the ADC into saturation when the main antenna is facing the target illuminator. The use of A-B coaxial switch, one per channel, would overcome this. The switch locations, however, would have to be in the rear seat of the aircraft and would be difficult to actuate simply because of the cramped cockpit.

The WBX daughterboards of the N200 have an independent transmit channel that could be used to generate signals that could be coupled into the receive chain. LFM/swept tone, OFDM or noise signal at high SNR are all supported. Configuring the channels then launching a separate calibration routine (after the hardware had thermally stabilized) was a possibility. The WBX can also be configured to simultaneously transmit while receiving and the GbE and MIMO interfaces could handle the necessary bandwidth (12.5 MHz). However this would require a separate routine and was discarded for the reasons above

Examination of the temporal and statistical properties of the HDTV waveform suggested another alternative, that of using the illuminating waveform. As described in Section 5.0, the HDTV waveform, with temporally changing channel content in addition to the spreading code PN employed is essentially a random waveform. Figure 5.3 demonstrated that the voltage distribution is zero mean Gaussian (by inspection) and that phase is effectively uniformly distributed. Figure 5.3 is based on a sample size of 50E+07. Since this could be accommodated with the sampling application and since we are not concerned with radiometric calibration, only channel matching, it was made the baseline.

In Section 6.2.1 the calibration methodology is broadly described. This primarily relates to developing transfer functions for the receiver channels and includes details on the passive channel components. Section 6.2.2 specifically describes the development of the spatially varying transfer functions for the two flight antennas. Section 6.2.3 covers the use of the broadcast signal to derive the relative responses of the active electronics in flight. This is done in the context of the generalized, adaptive sidelobe canceller

necessary for mitigation of direct signal interference (DSI). Section 6.2.4 addresses the several corrections to reference zero range to the phase center of the main antenna. This includes reference-to-main phase center physical (range) offset due to geometry and residual corrections.

6.2.1 ***Passive component calibration***. The bistatic receiver system design was presented in Figure 6.2 with a detailed block diagram shown in Figure 6.3. The system block diagram is presented in a calibration-centric perspective in Figure 6.28. The system consists of two different antennas (main or imaging antenna directed at the scene and the near-omni directional reference), each instrumented with the same model software-defined radio (SDR) analog tuner and digital receiver. Each channel also includes a custom designed, steep rejection band, bandpass filter (see Section 6.3.4, RFI Analysis) ahead of the somewhat limited anti-aliasing filters found in the WBX tuner. Both channels employ slightly different coaxial cable lengths between antenna and bandpass filter.

Each channel is represented in the frequency domain by cascaded transfer functions representing contributions of antenna, filters, amplifiers coaxial cabling, etc. We write the total transfer function in the frequency domain as

$$H_{m,r}(\omega) = \Pi_{i=1}^{K} H_i(\omega) \tag{6-23}$$

where $H_i(\omega)$) represents the i^{th} stage of the receiver, up to the analog-to-digital convertor, and the subscript *m*, *r* indicates the main or reference channel.

The principal method for component compensation/channel matching/equalization is the Zero Forcing technique [149] or Zero Forcing Equalizer (ZFE). The basic concept of ZFE is shown in Figure 6.28, implemented in the frequency domain. In the taxonomy of [149] ZFE is a linear equalizer. Linear phase response of a component is equivalent to a constant delay between the terminals of that component, group delay τ_{group}=-(dϕ(ω)/dω),

whereas nonlinear phase results in dispersion as some frequencies propagate at different speeds between the terminals. The implication of employing ZFE is that delay, as evidenced by group delay, is eliminated (to within the measurement and other systematic tolerances). This allows the establishment of the range/delay reference at the antenna phase center, matching physical position with electrical position. Gain corrections are based on normalized, averaged spectra to capture only relative changes. The inverse dependency in the equalizer can act to amplify system noise so care is taken to only operate in the portion of the allocated channel spectrum above the 6 dB roll-off points. Likewise, in generating the estimate of the transfer function avoiding zeros is necessary.

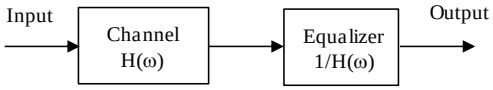

Figure 6.28. Zero Forcing Equalizer Operation

The calibration cascade is decomposed in Figure 6.29. This includes serial application as well as the cross channel operations necessary for channel matching: ZFE is employed stage-to-stage as described in Section 6.4.

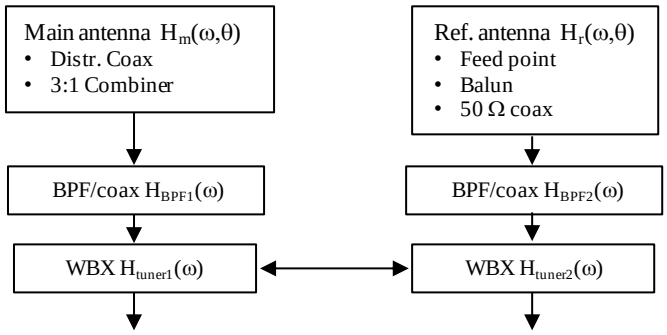

Figure 6.29. Calibration Perspective Block Diagram

Instrumental calibration of the passive components was performed using a vector network analyzer. Analog components (filters and cabling) were measured on the lab bench using an Agilent 5818A, providing S21 measurements over frequency. Figure 6.30 is the magnitude and phase response for the channel bandpass filters and coaxial cable over a 50 MHz measurement range. The cable-filter pairs, once assigned, were not mixed

throughout testing. Figure 6.31 presents a zoomed response, limited to the 10 MHz band of the flight test data.

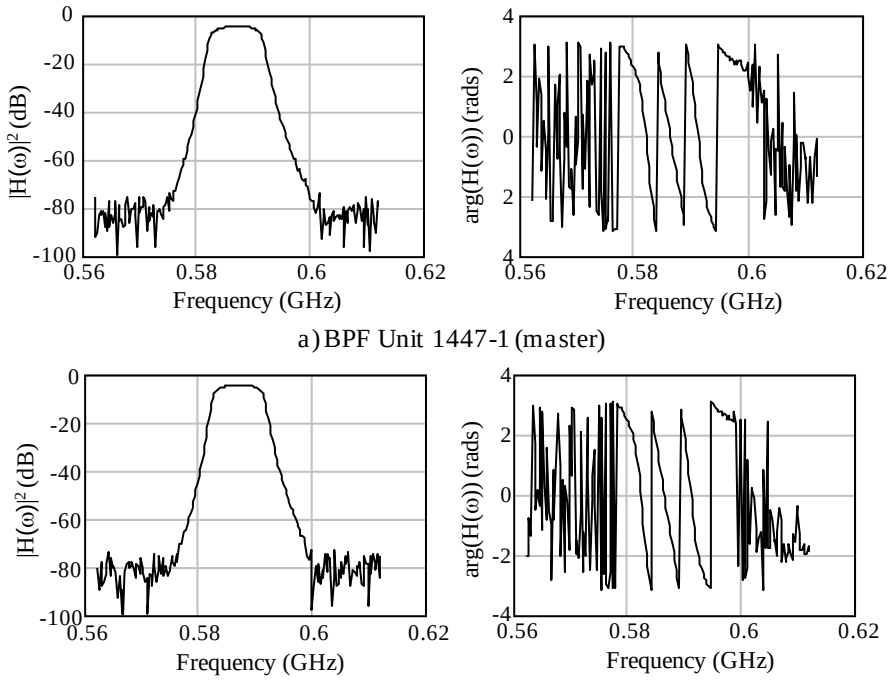

Figure 6.30. Bandpass Filter Characterization

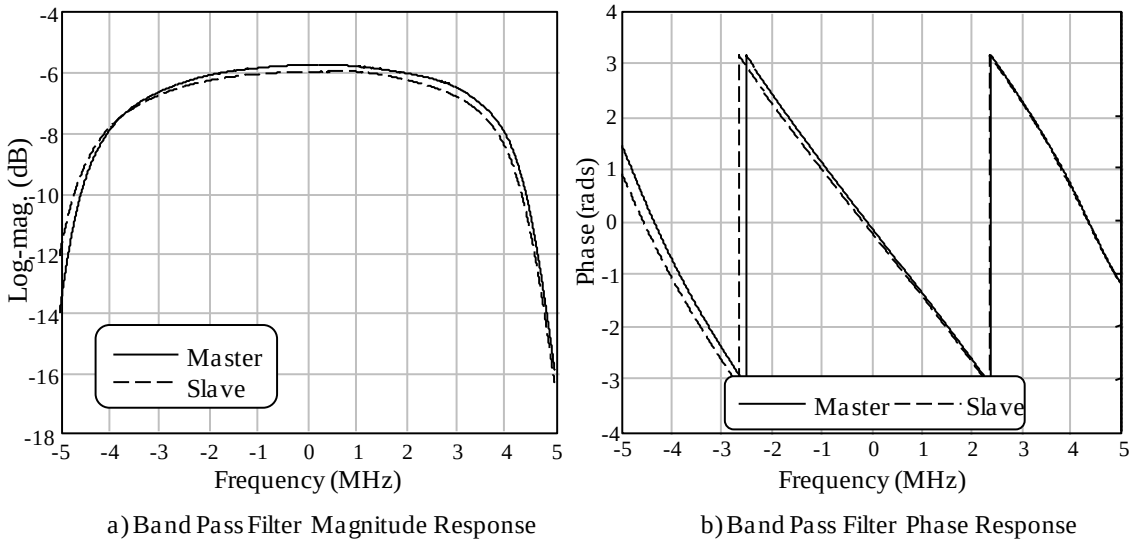

Figure 6.31. Zoomed Plots - Bandpass Response

The responses in both Figures 6.30 and 6.31 include the assigned coaxial cable. Nominal mean insertion loss (averaged over the 50 MHz range) is 3.8 dB, reducing the minimum insertion loss of the filters to slightly more than 2 dB. The insertion phase was linear over the 6 MHz center portion of the response spectrum with slope 0.161 rad/MHz.

6.2.2 ***Antenna calibration***. The static transfer functions of both antennas also include contributions from spatial dependencies as well as responses in the frequency domain. Spatial dependencies arise from phase center variation (essentially an angle dependent group delay) and fabrication errors. This is most notable in the reference turnstile antenna where the 90 degree phase delay between driven arms of the crossed dipole introduces a $\pi/2$ phase advance from 90 degree sector-to-sector. Channel-to-channel phase errors will introduce phase errors in the cross correlation/pulse compression process, resulting in a nonzero, potentially spatially variant initial phase at zero delay (Section 6.2.4).

Antenna calibration was more complex than the bench top measurements of passive components. The general procedure involved making measurements using two identical log periodic dipole (LPDA) antennas in an anechoic chamber, solving for the transfer function of the LPDA under a strict reciprocity argument, then replacing one antenna with the antenna-under-test (either the main or the reference antenna. This is shown in Figure 6.32. A vector network analyzer generates a frequency swept signal which is coupled to the transmit antenna through a coaxial cable with a known (measured) transfer function,

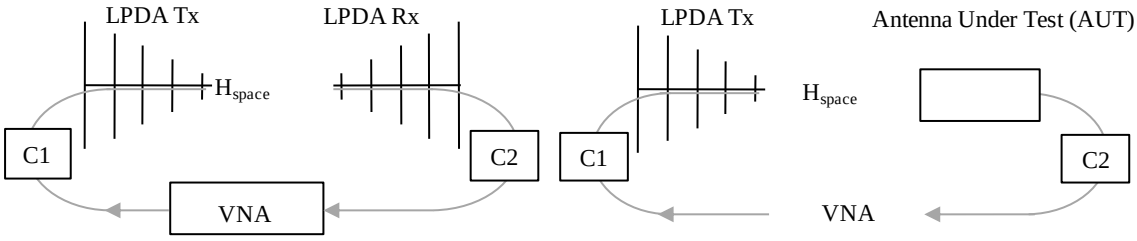

a) Developing Single Antenna Transfer Function

b) Only Unknown is the Antenna Under Test

Figure 6.32. Antenna Calibration Schematic

radiated toward the receive antenna a known distance away (taking into consideration any phase center frequency dependency), received and sampled by the VNA via a second cable of known properties. The forward scattering parameter S21 is given by

$$S21(\omega) = H_{C1}(\omega)H_{LPDA\_TX}(\omega)H_{space}(\omega)H_{LPDA\_RX}(\omega)H_{C2}(\omega) \qquad (6\text{-}24)$$

With the identical antenna/reciprocity assumption we can solve for the antenna transfer function, giving

$$H_{LPDA}(\omega) = \sqrt{\frac{S21(\omega)}{H_{C1}(\omega)H_{space}(\omega)H_{C2}(\omega)}} \tag{6-25}$$

Then when substituting the receive LPDA with the antenna under test (AUT), the transfer function of that antenna is given by

$$H_{AUT}(\omega) = \frac{S21(\omega)}{H_{LPDA}(\omega)H_{C1}(\omega)H_{space}(\omega)H_{C2}(\omega)} \tag{6-26}$$

The experimental test setup is shown in Figure 6.33 in two perspectives. Antennas were set several wavelengths from the chamber walls (as only a portion of the room was utilized). Distances were measured carefully to account for the spatial/propagation term in Equation 6-26. Included in the spatial distance are estimates of the radiating phase center over the narrow band of frequencies tested.

The log periodic antennas were the Ettus LP0410 [150] variant on the WA5VJB, bandwidth 400 to 1000 MHz. The log periodic radiates at the resonant distance along the antenna (the active region) so that the phase center location is estimated as the distance from the feed where the effective half-lambda element would be located. This antenna has a spread half-angle (α) of 22.5 degrees with 10 alternating dipole arms and an overall length of 9.1 inches (23.1 cm). The active region was estimated at 7.5 in (19.1 cm) from the leading (feed) edge, and termed L_{pc}. Twice this distance is added to the leading edge-to-leading edge to define the H_{space} term in (6-26), expanded in (6-27) to incorporate ΔR

$$H_{space}(\omega) = \frac{e^{-jk\Delta R}}{2\sqrt{\pi}\Delta R} \qquad \Delta R = R_{ant} + 2L_{pc} \tag{6.27}$$

One half the value of L_{pc} is used with the antenna under test with the distance reference either the ground plane (main antenna) or the feed location/dipole crossover (reference antenna).

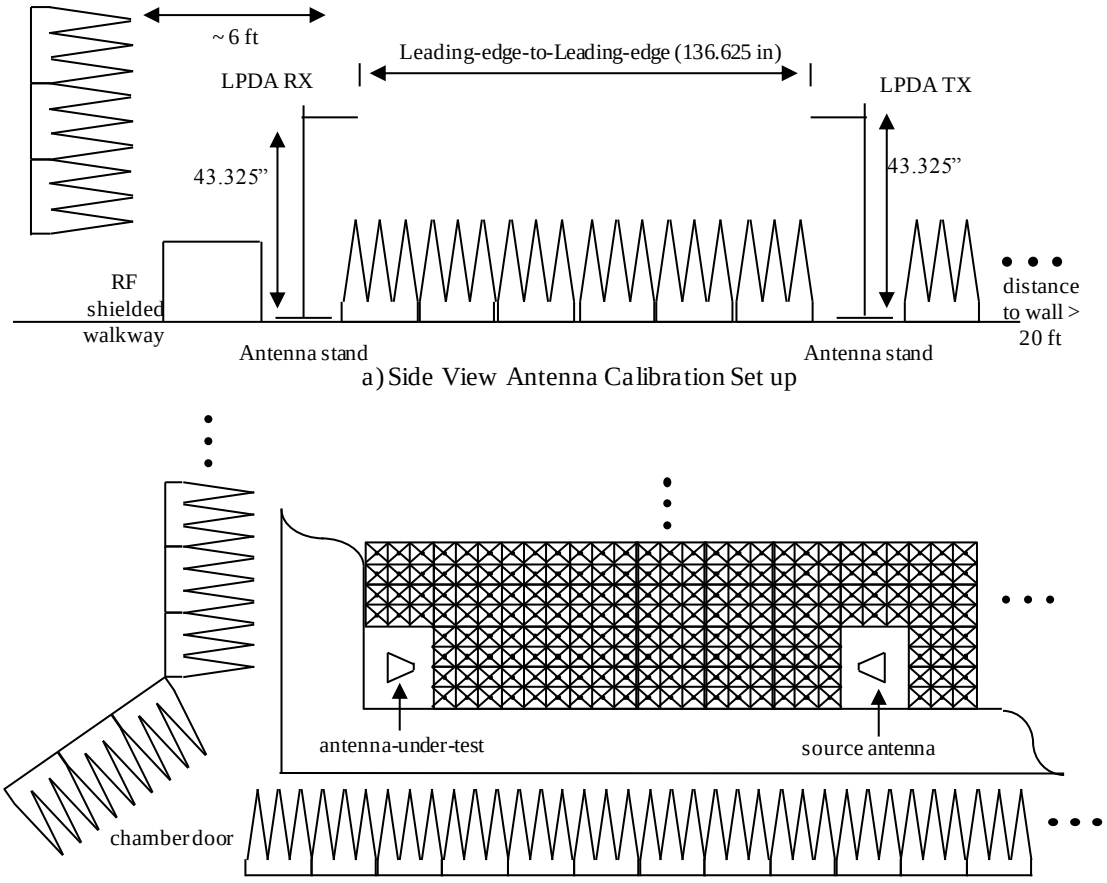

Figure 6.33. Antenna Calibration – Anechoic Chamber Setup

Instrumentation was located outside the chamber with the operator exiting and closing the chamber door for each measurement. Several S21 sweeps were made in the event that any measurement averaging was necessary. The bistatic radar antennas were mounted on the stand nearer the door for ease of access, to minimize time between measurements and the amount of walking over treated surfaces. S21 was measured in 15 degree increments for both antennas. Results shown are truncated to 10 MHz bandwidth to match the sample rate actually employed in the flight collection. The zero degree reference for the main antenna is the normal to the ground plane representing the location of the mainbeam peak response. The zero degree reference for the reference antenna is the midpoint between the driven arm and the grounded crossed dipole arm. This was chosen so that the antenna square side was flush with the aircraft window when installed. Which of the four faces selected was arbitrary, but consistently applied throughout testing. Additionally the sense

of angle employed is opposite for the two antennas. This was an accident during calibration but was maintained throughout application. Azimuth angle for the main antenna was measured clockwise from boresight which it was measured counter clockwise for the reference antenna.

Reference antenna phase and magnitude results over frequency and angle appear in Figures 6.34 and 6.35, respectively. To avoid perturbing the channel-to-channel gain (and possible impact to the adaptive sidelobe canceller) the gain curves are normalized to the value at the channel center frequency. The magnitude plots illustrate the gain ripple across the channel bandwidth.

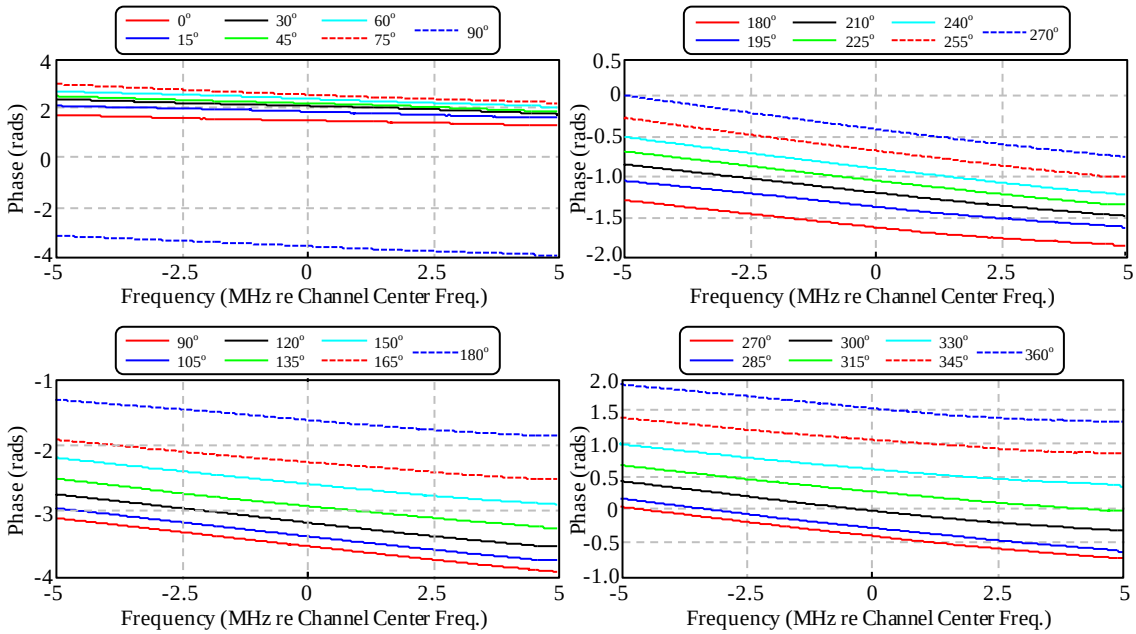

Figure 6.34. Phase Response over Angle - Reference Antenna

The calibration data for the main antenna appear in Figures 6.36 and 6.37, phase and magnitude, respectively. The main antenna data were generally well behaved with the exception of the 135 degree dataset and the 315 degree data from the main antenna (both points 180 degrees apart. Only the 135 degree phase response failed to match the broad trend of the surrounding angular values, while both angles were out of the ordinary when the magnitude was considered.

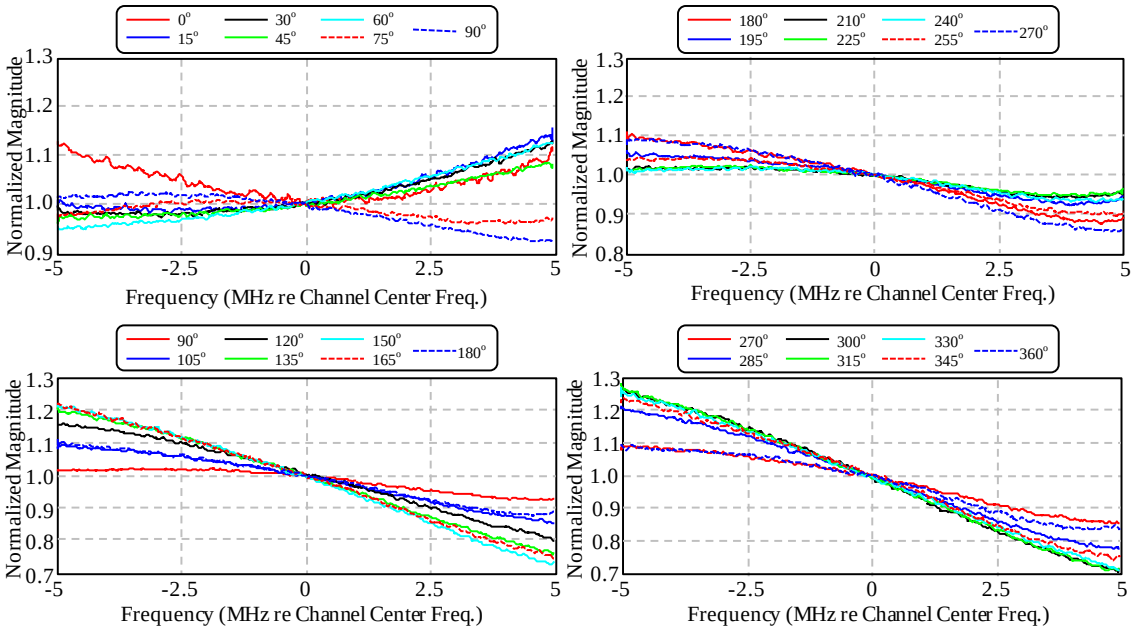

Figure 6.35. Magnitude Response over Angle - Reference Antenna

The group delays of both antennas, at a single angle, are illustrated in Figure 6.38 with the main antenna response in Figure 6.38a, the reference in 6.38b. Both sets of curves are found from the negative of the first difference phase as a function of frequency.

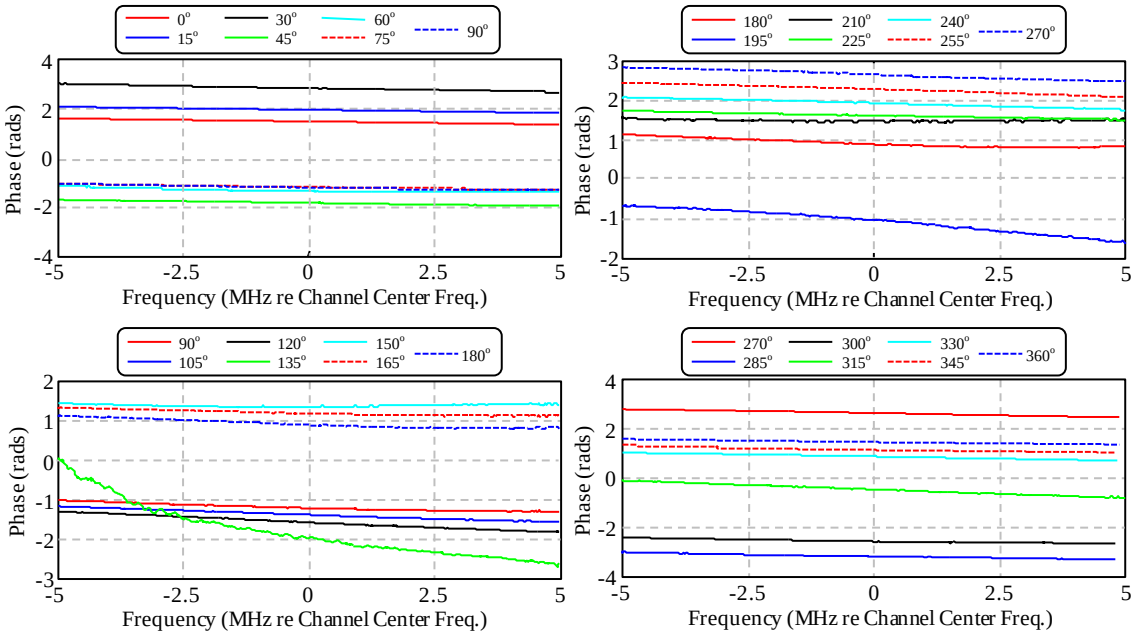

Figure 6.36. Phase Response over Angle - Main Antenna

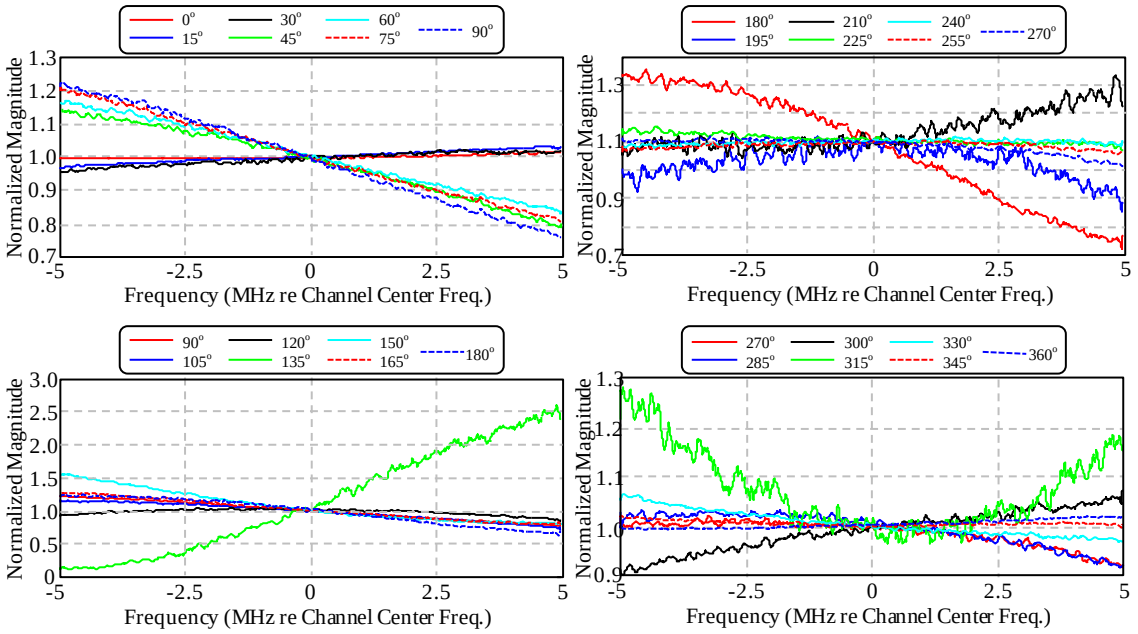

Figure 6.37. Magnitude Response over Angle - Main Antenna

For the main antenna this represents to the output terminal of the 3:1 combiner while for the reference antenna this includes the RG-59 coaxial cable (64 inches long, 1.626 m including SMA gender adapter) which was intrinsically part of the antenna feed. The mean value of the group delay for the main antenna was 4.559 nsec or a free-space equivalent delay of 1.367 m. The reference antenna mean value was 11.121 nsec (equivalent delay of 3.36 m). Applying the calibration functions normalizes the group delay to the physical phase center of the antenna in preparation for the projection of the reference antenna onto the main antenna, including relative positions (installed).

Relative gain patterns were produced for both test antennas. Two patterns are re-created from the measurements; the main antenna at midband (587 MHz) in Figure 6.39a, and the reference antenna at two frequencies, both below mid-channel (6.39b).

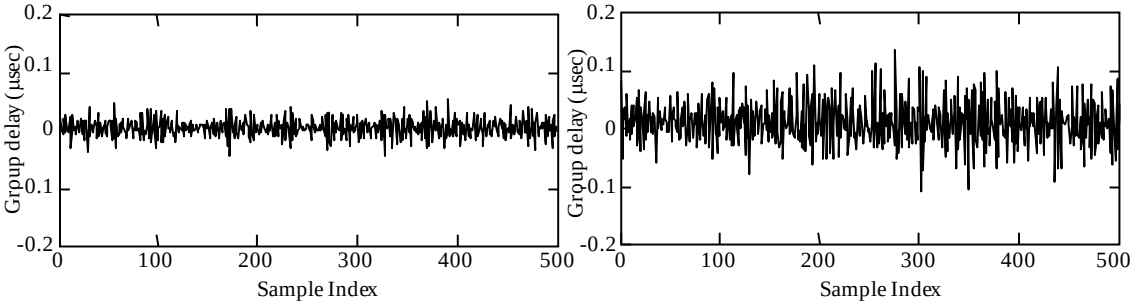

a) Main Antenna Group Delay - 0 deg b) Reference Antenna Group Delay - 0 deg

Figure 6.38. System Antennas Group Delay

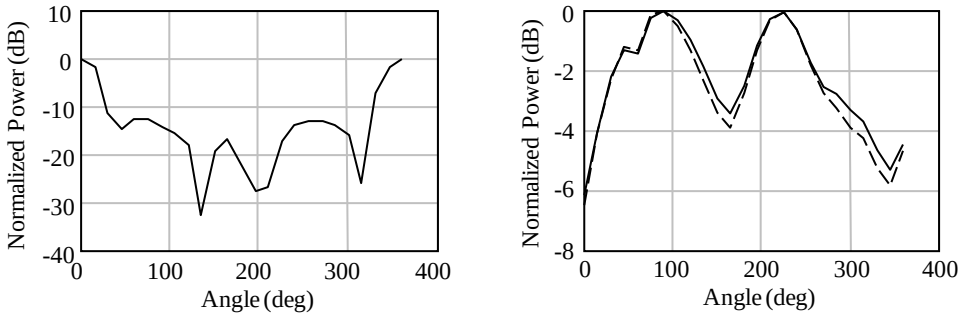

a) Main Antenna (Mid-channel Freq.) b) Reference Antenna (582.5 and 585.4 MHz)

Figure 6.39. Anechoic Chamber Measured Antenna Patterns

The reference pattern as simulated showed (Figure 6.10) four broad, but discernible, peaks; one at each dipole normal, or every 90 degrees. While not representing the design as simulated, the gain pattern is sufficient, less air vehicle installation effects, to cover the main antenna side and backlobes.

6.2.3 ***Channel matching***. To this point we have considered the calibration of passive components which are expected to have static, stable responses (except for the effects of the air vehicle on the antennas when installed). As discussed at the beginning of Section 6.2 we elected to make use of the illuminating signal as the means to make simultaneous measurements of both channels against an external probing signal because of limitations on space or power. Section 5.0 demonstrated the random nature of the HDTV signal in the time domain and presented examples of the signal spectral showing the flat response across the channel bandwidth. The need for matching the transfer functions of the two channels derives from the need to remove the direct signal breakthrough in the main channel, as discussed in Section 5.1. A secondary consideration is to minimize the introduction of resolution errors in the pulse compression process.

The adaptive canceller configuration is depicted in Figure 6.40. Two channels with nominally equal receiver gain and phase responses, with the requirement that auxiliary antenna gain in the direction of the interference source must be greater than the main

antenna gain (maximizing the gain in the direction of the interference and minimizing in the direction of signal would the optimum).

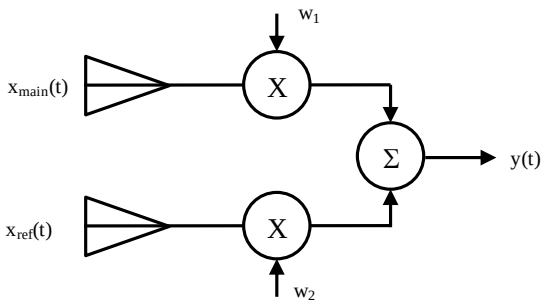

Figure 6.40. Adaptive Sidelobe Canceller Geometry

In the discussion that follows we assume sampled data, processed offline, with LO and antenna offset corrections implemented (this latter implements the spatial phase offset between channels), that the pilot tone has been removed, and that the static component ZFE corrections have been applied. An adaptive weight is calculated by estimating the covariance between channels using sample matrix inversion (SMI) and steering vector *t* as defined by

$$w = \begin{bmatrix} w_1 \\ w_2 \end{bmatrix} = \hat{R}^{-1}\vec{t}; \quad \hat{R} = \frac{1}{N}\sum_{n=0}^{N-1} X_n X_n{}^H \tag{6-28}$$

$$X_n = \begin{bmatrix} x_{main}(n) \\ x_{ref}(n) \end{bmatrix} \qquad \text{with} \quad \vec{t} = \begin{bmatrix} 1 \\ 0 \end{bmatrix} \tag{6-29}$$

where *H* indicates conjugate transpose. The filtered output in the time domain is then

$$y_n = w^T X_n = w_1\left(h_{main} * s_n\right) + w_2\left(h_{ref} * s_n\right) \tag{6-30}$$

where * indicates convolution, superscript *T* for transpose, and s_n is the sampled signal. The frequency domain form of (6-30) is

$$Y(\omega) = w_1 H_{main}(\omega) S(\omega) + w_2 H_{ref}(\omega) S(\omega) \tag{6-31}$$

To minimize the output power of the interference signal requires that w_2=-w_1 and H_{main}=H_{ref}.

$$Y(\omega) = wS(\omega)\left(H_{main}(\omega) - H_{ref}(\omega)\right). \tag{6-32}$$

Equation 6-32 illustrates the canceller dependency on the degree of similarity of the channel transfer functions.

The canceller performance is defined in terms of a cancellation ratio (CR), P_o/P_n, where P_o is the canceller output power and P_n the channel noise power. In [119] cancellation ratio is defined as a function of amplitude and phase mismatch for a simple two-channel, narrowband canceller with identical antennas. For the case of magnitude-only errors a channel mismatch of 0.5 dB ($10\log(P_{chan1}/P_{chan2})=0.5$dB) limits the CR to -25 dB while in the phase only case the same level of performance is met at 2.8 degrees of phase error. Performance versus mismatch for each quantity individually is shown in Figure 6.41.

The quantities in Figure 6.41 are defined in the time domain with the amplitude mismatch defined as $10\log(G_1/G_2)$, G_1 and G_2 the channel gains (G_2 assumed to be 1). Likewise the phase mismatch is given as $\Delta\varphi=\varphi_1-\varphi_2$. As we are operating over the channel bandwidth we need a representation of the mismatch over frequency. Define the mismatch between two channels as

$$D(j\omega)=\frac{H_{main}(j\omega)}{H_{ref}(j\omega)}=d(\omega)e^{j\varphi(\omega)} \tag{6-33}$$

where d is the magnitude mismatch and φ the phase mismatch. The mean and root mean

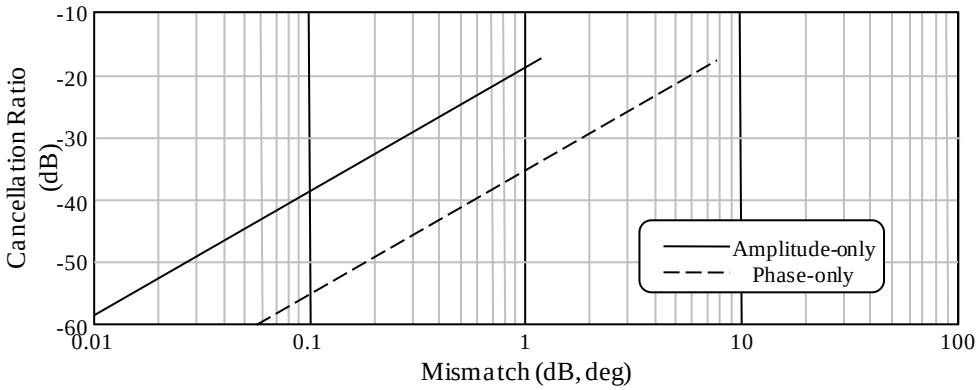

Figure 6.41. Cancellation Ratio versus Magnitude and Phase Mismatch (after [119])

square amplitude and phase mismatch over frequency, since the channels have to match over the pass band of the operating signal, are given as [119]

$$\bar{d} = \frac{1}{2\pi B}\int_{-\pi B}^{\pi B} d(\omega)d\omega \quad d_{rms} = \left[\frac{1}{2\pi B}\int_{-\pi B}^{\pi B}(d(\omega)-\bar{d})^2 d\omega\right]$$
$$\bar{\varphi} = \frac{1}{2\pi B}\int_{-\pi B}^{\pi B} \varphi(\omega)d\omega \quad \varphi_{rms} = \left[\frac{1}{2\pi B}\int_{-\pi B}^{\pi B}(\varphi(\omega)-\bar{\varphi})^2 d\omega\right] \tag{6-34}$$

This representation supports both linear and higher order error functional descriptions.

Equalization approaches for multichannel radar systems, such as [151], [152] and [157] use estimates of the individual channels, with one of the channels designated a reference, to normalize all responses to the reference channel, as shown in (6-35) for relative calibration and (6-36) for absolute calibration [152]. For *K* parallel channels (*k*=1: *K*-1)

$$\tilde{H}_k(\omega) = H_k(\omega)E_k(\omega); E_k(\omega) = \hat{H}_{ref}(\omega)/\hat{H}_k(\omega)\text{ ; channel K = ref} \tag{6-35}$$

$$\tilde{H}_k(\omega) = M(\omega) - H_k(\omega)/\hat{H}_k(\omega) \tag{6-36}$$

where the tilde indicates a calibrated channel response and the caret indicates the estimate of the transfer function of the channel. In (6-36) *M(ω)* is a specific, desired response. Our approach for the two channel system is based on eqn. (6-35). We do not want to perturb the gain relationships between the two antennas so the magnitude is normalized to unity at the channel center frequency. In this manner relative magnitude variations are equalized between channels.

During test design a goal cancellation ratio of 35 dB was established, based on expected signal levels from mean clutter using vegetated farmland-level clutter reflectivity in conjunction with the planned test geometry. This requires amplitude matching of 0.1 dB and phase matching to 0.8 deg (or some similar combination). The matching metrics are realized after the application of the zero forcing equalizer using the estimated transfer function of each channel. The time domain matching requirements are decomposed to the individual filter. The time domain mismatch errors can be flowed directly to the individual filters (to all filters equally). This can be seen by exercising mean value expressions from eqn. 6-34. We equate the mismatch error as the estimation uncertainty

in measuring the channel parameters. Otherwise stated, the amplitude mismatch equals the amplitude estimation error. The same is true with the phase.

Using the illuminator as the calibration probing signal requires that the data be sampled, converted to the frequency domain where it is averaged to improve the estimate of the magnitude and phase at each filter in the passband. In the time domain, as shown in Section 5.0, the HDTV signal is Gaussian distributed in amplitude and uniform [0, 2π] in phase. When transformed into the frequency domain, the voltage statistics in each filter remain Gaussian in amplitude, though with a change in scale, and we have an ensemble of parallel estimates of magnitude and phase of a noise signal. On average, as required by the channel mask, the mean signal power in any filter is constant. The signal/information content adds a random component. Thus we effectively have the problem of estimating a constant amplitude and phase signal embedded in noise. We use the signal power as the proxy for relative channel gain.

The instantaneous error in estimating the magnitude and phase of a signal (HDTV signal competing with receiver noise) in the presence of additive Gaussian noise are, respectively, given by

$$\sigma_{ampl} = \frac{1}{\sqrt{SNR}} \quad \sigma_{\varphi} = \frac{2\pi}{\sqrt{SNR}} \tag{6-37}$$

where SNR is the signal to noise ratio in the individual filter. We see from ground test examples (Section 5.0) that the SNR for the 0.8 msec burst is > 40 dB (for flight test examples see Section 6.3.4). Using these as typical (ground based measurement trials returned similar results) we can estimate the single observation accuracy of magnitude at 0.01 and phase at 0.063 deg.

While the individual estimates are themselves very accurate, the measurements reflect the underlying statistics where we need to estimate the mean amplitude and the mean phase of a random process. To improve the accuracy of the estimate a sufficiently large number

of samples must be collected and averaged so that the sampling error (difference between true mean and estimated mean magnitude and phase) meets an allocated accuracy. Define A and φ as the amplitude and phase estimates. We set the sample size based on the variance of the estimator (also called the error of the mean). This is given by

$$\text{var}(\overline{A}) = \frac{\sigma(A)^2}{N}; \quad \text{var}(\overline{\varphi}) = \frac{\sigma(\varphi)^2}{N}. \tag{6-38}$$

where $\overline{A}$ and $\overline{\varphi}$ indicate mean values. To get an estimate of the variance of the amplitude and phase, ground measurements were made with an antenna with similar gain to both the main and reference antennas and analyzed to produce $\sigma(A)$ and $\sigma(\varphi)$. With these in hand we can develop a sample size requirement for the flight test. 1.6E+06 samples were processed, yielding var(A)=60.068 and var(φ)=3.2837 (rads). Setting the mean variance to be equal to 0.1 of the channel mismatch (either amplitude or phase) and solving for N yields 587 samples (amplitude) and 2352 samples (phase, 0.08 deg).

Dedicated test geometry was designed for the estimate of the channel transfer functions that held the antenna gains in the direction of the transmitter, and the range constant. The flight path was an arc centered on the transmitter with radius equal to the range from the transmitter to the test scene. The arc ground track can clearly be seen in Figure 6.53. The duration of the calibration leg was 408 seconds, allowing the collection and processing of 8028 bursts for smoothing the channel gain and phase estimates. The condition was started after the receivers had been powered up for 20 minutes at altitude (4000 ft/1219 m initially, climbing to 5500 ft/1676 m due to airspace limitations). The duration was longer than required to provide ample sample margin.

Estimates of the relative magnitude responses for both channels are shown in Figure 6.42 with the main channel in Figure 6.42a and the Reference (slave) channel in 6.42b. After

averaging 8028 bursts the magnitude is normalized to the band center frequency. Further, filter-wise, the data were further smoothed using a 5 filter sliding window. Two curves

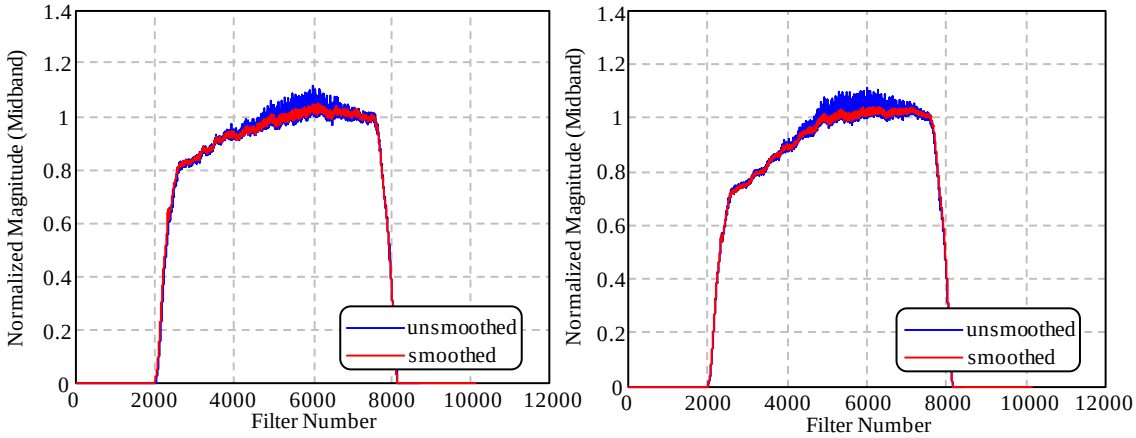

Figure 6.42. Individual Channel Response Estimates – Magnitude

are thus shown for each receiver smoothed (red) and unsmoothed (blue). The phase responses are presented in Figure 6.43. For phase, four figures are presented because of the more random nature, for readability.

There is a noticeable difference in the channel gain characteristic, less so in the phase. We judge the level of channel similarity by dividing the main channel complex response by

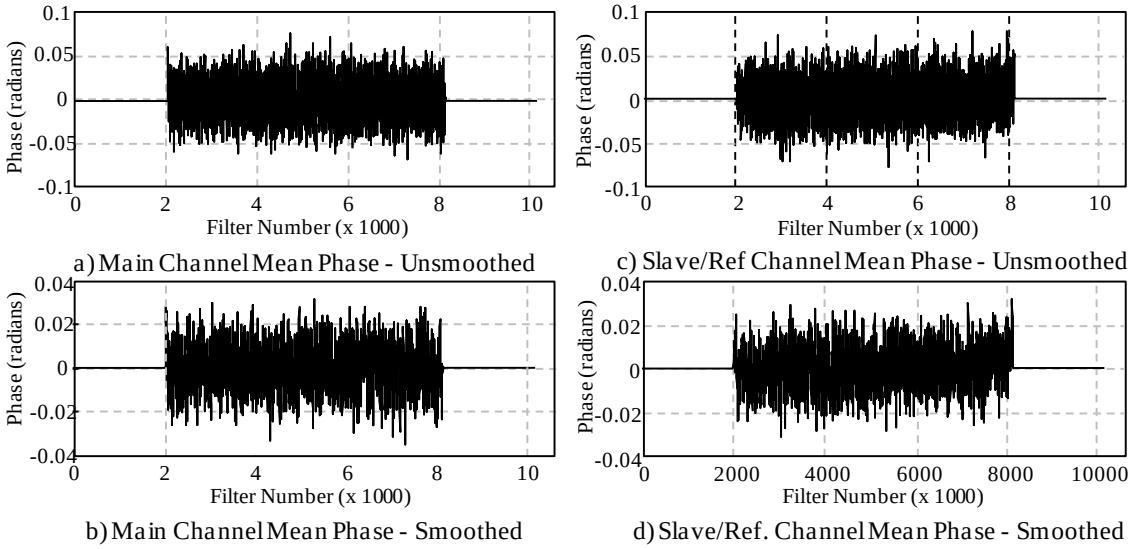

Figure 6.43. Individual Channel Response Estimates – Phase

the reference channel, then form the magnitude and phase of that result and calculate the overall magnitude and mismatch after equation 6-36. The degree of channel similarity can

be seen in Figure 6.44. Numerical evaluations of eqn. 6-34 are found in Table 6.6 which summarizes the channel degree of similarity.

Parameter	Mean Value	RMS Value
Magnitude	1.0227 (0.97 dB)	0.047 (-13.28 dB)
Phase	3.9293E-04 (0.023 deg)	0.0296 (1.696 deg)

Table 6.6. Channel Matching Results Summary

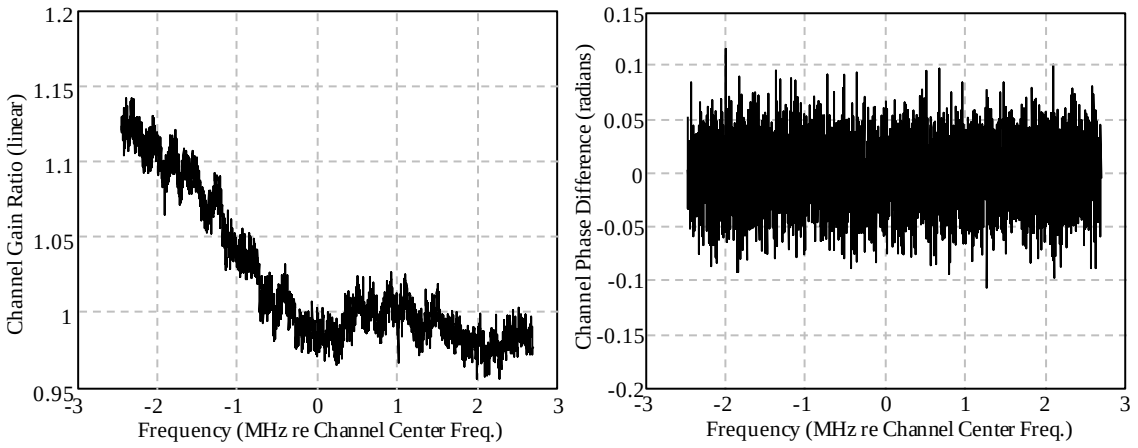

a) Channel Gain Mismatch b) Channel Phase Mismatch

Figure 6.44. Channel Response Similarity – Amplitude and Phase

The calibration run-derived amplitude and phase matching met the matching requirement goal. The effectiveness of the canceller can be seen in Section 6.4 (Figures 6.72 and 6.73) where only static calibration corrections were performed. Removal of the direct path signal was expected to lower the overall compressed pulse sidelobes. This expectation was based on a limited number of point scatterers simulated. Reviewing of the noise radar literature [36] and [37], the noncoherent combination of the all ground returns (which have compressed responses that are scaled and shifted version of the autocorrelation response) defines the actual range sidelobe noise level.

6.2.4 ***Offset corrections***. A series of offset corrections were identified as part of the calibration process. These include the random start up phase of the local oscillators of the two receive channels (LO offset), the range offset of the two antennas (separated by the cabin width), and differential delay between the two (ostensibly identical) receivers. These corrections are detailed in this section.

• **6.2.4.1** ***LO offset***. The receiver system consists of two local oscillators that are individually slaved to the stable clock provided by a GPS disciplined oscillator (GPSDO, installed internally in the main channel, or master, N200). A phase locked loop in each unit locks against the local oscillator (LO). After tuning the RF front-ends, each local oscillator may have a random phase offset due to the dividers in the VCO/PLL chains [154]. This offset will remain constant after the device has been initialized, and will remain constant until the device is closed or re-tuned. In this section the impact of the phase offset on the pulse compression process is defined and a method which exploits features in the HDTV signal to determine the LO offset is described. This process results in a correction factor which is incorporated prior to cross correlation.

As was shown in Section 5, pulse compression via cross correlation, for the PN code signal model and a point scatterer there are two components to the compressed pulse response. One component the Direct Signal breakthrough, the other the range profile of the received scene scattered energy. Solutions to the two components are (given that the phase centers are coincident)

$$\chi_1(\tau) = C_1 C_2 \chi(\tau) \quad \chi_2(\tau) = C_s C_r e^{-jk_0(R_s - R_b)} \chi(\tau) \tag{6-39}$$

where C_1, C_2, C_s and C_r are systems constants that primarily account for antenna gains and range along the direct path main antenna (C_1) or reference antenna (C_2) or the scattered path main antenna (C_s) or reference (C_r). The code autocorrelation is given by $\chi(\tau)$.

If there is a phase difference between the two exactly tuned and phase-locked oscillators then, after down conversion (and absorbing the phase difference into a single term on one channel), and repeating the derivation, we are left with

$$\chi_1(\tau) = C_1 C_2 e^{j\Delta\varphi} \chi(\tau) \quad \chi_2(\tau) = C_s C_r e^{-j(k_0 \Delta R - \Delta\varphi)} \chi(\tau) \tag{6-40}$$

In (6-40) ΔR refers to the point scatterer range sum (R_s) minus the baseline range (R_b). This result shows that the unknown phase shift adds a phase error, potentially shifting the range response by up to a wavelength. For the planned illuminator this is up to 0.511 m and will be on the order of the image resolution. Though constant, without correction this will add errors in back projection, potentially resulting in image defocusing.

To compensate the pilot tone was evaluated as a stable calibration source, the phase difference between the two antennas could be found for each burst. The tone itself is ultra stable, per FCC regulation and confirmed with the KPWX station chief engineer ("absolute stability of 1 Hz"). If all other factors were constant, antenna separation and platform attitude relative to the illuminator, and the presence of the pilot and radar operator in the small cockpit did not perturb the propagation, then we could estimate the phase difference, averaged over bursts, and apply a fixed correction before cross correlation. This was a secondary requirement of the calibration leg. However the radar crashed after the calibration leg completed. The restart resulted in a new, unknown phase offset. This was ultimately accommodated via the adaptive channel matching described in Section 6.4 (after adaptive sidelobe cancelling).

• **6.2.4.2** ***Antenna phase center offset***. The aircraft antenna installation (Figure 6.48) and variable geometry over the planned three dimensional collection aperture (Figure 6.67) means that the two-antenna baseline is a function of position along the aperture. The separation means that the phase center location for pulse compression is, absent other factors, at some point between the reference and the main antenna. Starting from equations 5-63 through 5-65 where, as in the preceding developments, we assumed that main and reference antennas have coincident phase centers we expand the range difference (ΔR) term, first for coincident phase centers.

$$\Delta R = R_s - R_b \quad or \quad \Delta R = \left(\left|X_m - X_p\right| + \left|X_p - X_x\right|\right) - \left|X_r - X_x\right|. \tag{6-41}$$

In (6-41) X is a position vector, the subscript m represents the main antenna phase center, p a point scatterer, r the reference antenna phase center and x the transmitter. Explicitly, $X_r = X_m$ and we obtain the result that is presented in equation 5-8. In the more general case, when $X_m \neq X_r$, the correlation establishes the range difference reference relative to the reference antenna phase center. The expression for $\chi_1(\tau)$ (*e.g.*, 5-72) now exhibits a range offset of the peak response equal to the range difference between main and reference antennas projected onto the line of sight to the transmitter (δ_r). A longer range to main than reference gives a positive delay, shorter range yields a negative delay.

This also means that the range difference (ΔR) tracks the reference antenna position, whereas we want to use the main antenna phase center as the delay reference for reconstruction. The range sum (R_s) to the same fixed scattering point is still defined relative to the main antenna position but the baseline is now changed ($R_{b'}$). The range difference becomes $\Delta R = R_s - R_{b'}$. With $R_{b'}$ less than R_b the apparent range difference is increased, resulting in a range error. The converse is also true: in both cases the range error would result in defocusing.

The correction for the phase center offset is a spatially variant shift that projects the reference antenna range relative to the transmitter onto the main channel, the correction which must occur prior to the cross correlation. We shift the baseline to zero offset by using the known relative positions of the GPS receiver and main and reference phase centers. From the positions in the aircraft coordinate frame the antenna range separation was calculated as a function of time, including vehicle attitude/yaw (Figure 6.69). The reference channel burst was transformed to the frequency domain, multiplied by $e^{-jk\Delta R}$, before inverse transform and pulse compression. The worst case offset is of the order of a meter (Table 6.7). The antenna positions relative the aircraft firewall position reference are given in Table 6.7. These combine to give the radial separation of the antennas when

projected onto the line of sight with respect to the transmitter. After static correction the data were adaptively corrected using the post canceller residual signal.

• **6.2.4.3** ***Mismatched delay in digital electronics***. The N200 receiver digital stages also introduce group delay. This results from analog bandpass filtering prior to the ADC, digital filtering following the ADC and FPGA operations including digital down conversion (DDC) and down sampling to the requested complex sample rate (in MIMO operation this is hard limited to 25 MSPS, 12.5 from each device). A member of the user community has calculated this for the N210[4] (the number of 100 MHz, 10 nsec clock cycles). The result is of the order of a microsecond, but no similar work has been done for the N200. As two identical units were used which were identically configured and both clocked off an external, common reference, and because the cross correlation output produces the range difference, it was expected that this factor could be ignored in terms of adding a channel-to-channel correction.

However, bench top testing against a surrogate HDTV transmitter revealed a slight channel misalignment. If all delays are properly matched between both channels then a symmetrical zero delay response, similar to that shown in Figure 6.45 would be expected. Identical log periodic antennas, aligned at the same range, with cabling matched to the receiver from VNA testing were used to collect multiple bursts from a station at 575 MHz

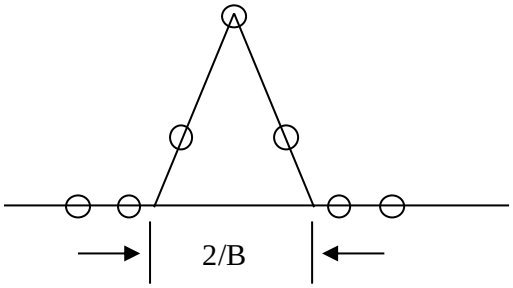

Figure 6.45. Ideally Matched Channels After Pulse Compression

[4] USRP-users [mailto:usrp-users-bounces@lists.ettus.com] On Behalf Of Ian Buckley via USRP-users, N210 DSP Group delay, 6 Dec 2014.

(KONG-TV Capitol Hill, Seattle). The cross correlation shows a bias in the resulting delay (without pilot tone editing) in Figure 6.46a. The compressed pulse response is not exactly centered but is slightly skewed to negative delay. The figure displays five successive 10164 sample bursts after pulse compression.

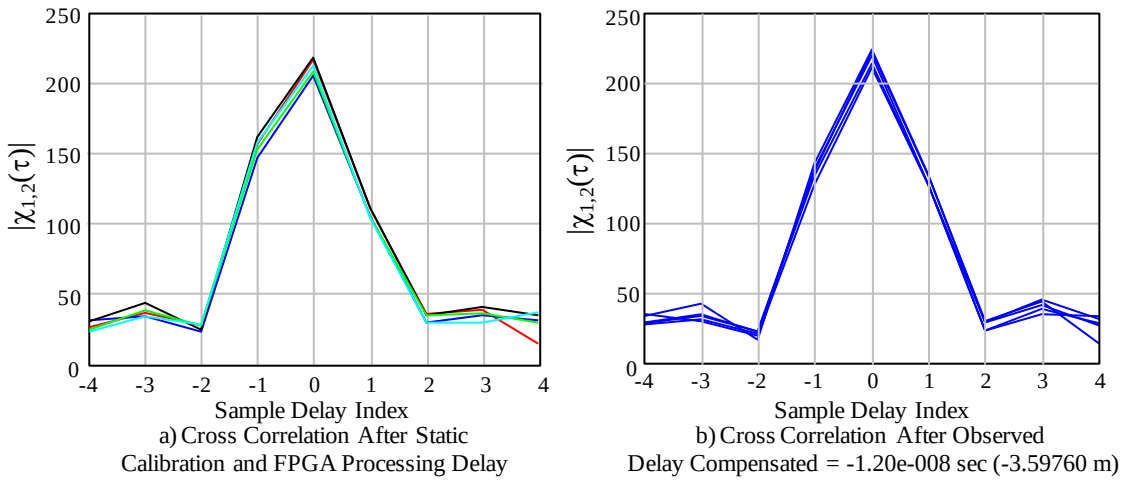

Figure 6.46. Channel Alignment with and without Final Correction

Using a bandwidth of 5.83MHz (slightly higher that the calculated 3dB bandwidth of the 8VSB spectral envelope, FCC exact expression is 5.595MHz) a minimum mean-squared error estimate of the residual delay offset was made. The mean magnitude response of 5 successive samples was taken and upsampled and the delay calculated given as the mean of the MSE. The value estimated was -1.20e-08 sec (-3.59760 m). Correlation prior to compensation is shown in Figure 6.46a. Application of the delay, using the same technique as described in the previous section for ΔR, appears in Figure 6.46b.

6.2.5 ***Pilot tone editing***. This is not a calibration function but is addressed here as an essential step to realizing the time sidelobes related to the code and processed time-bandwidth product for the HDTV waveform. The pilot tone is clearly evident in the signal spectrum (Figure 6.61, for example). If the pilot tone is present in the data then the time sidelobe level is very high and signal returns are masked. Pilot tone editing occurs in the frequency domain, as one of several processing steps that occur prior to pulse compression. The approach is straight forward; the 13 filters centered on the pilot tone

frequency (f_{pilot} +/- 6 filters) are replaced with random voltages based on the mean I, Q voltage magnitudes and a uniform random phase.

6.3 Flight Test Design (Collection Aperture, Aircraft and Installation).

6.3.1 ***Aircraft***. The flight test aircraft was a 1950 Cessna model 170. The four seat vintage aircraft is pictured in Figure 6.47. The pilot flew the collection route from the right-hand seat and was aided by the iPad map and GPS overlay (Section 6.1.3). The main antenna was installed in the forward port window and the reference antenna in a starboard rear window location. Both are described in greater detail in Section 6.3.2. Control laptop was operated in the passenger lap (forward starboard seat) with the radar instrumentation on a wooden pallet and secured in the rear seat. Prime power (12 V at 10 Amps DC) was available from the cigarette lighter with a 150 W (max) inverter providing 120 V AC power for the N200 receivers via a standard power strip.

Nominal airspeed of this model is in the 90-100 knot range (46-62 m/sec). Maximum (design) elevation was fixed by predominately by the proximity of class C airspace associated with Seattle-Tacoma International airport. Permission was received to operate in the lower ranges of the airspace given the traffic because of the approach-departure flow on the specific test day. The initial elevation angle (50 degrees), relative to scene center was designed also with elevation beamshape and dilution of geometry for the cylindrical spiral (Section 6.3.3). A 100 ft/min (30.48 m/min) rate of climb (descent) was chosen to sample the three dimensional aperture. Practice runs demonstrated that it was easier for the pilot to hand-fly a descending orbit than an ascending one.

6.3.2 ***Antenna installation***. As has been indicated, main and reference antenna sizing was performed explicitly for the window mounting in a four-place civil aircraft. The Cessna 172 was used as a model to establish an upper size limit with the intent of using mounting brackets to adapt to a specific aircraft model (antenna design and build began before the

Figure 6.47. Cessna 170 Flight Test Aircraft

specific aircraft was identified). Antenna installation is depicted in the Figure 6.48 (graphics aided by [161]), showing the location of all five test antennas (two radar and three GPS) in two perspectives. After installation the positions of the geometric centers of the antennas were measured (a challenging proposition in the small cockpit). The reference point selected was the planar portion of the instrument panel which was orthogonal to the longitudinal waterline. The point was selected at the same offset from the left/right symmetry plane as the GPS navigation antenna (Figure 6.48a), or y=0. Antenna positions relative to this point are listed in Table6.7. Note that precise positions were not required for either the XGPS 160 (flight navigation/visualization aid) or the GPSDO which was only used to provide the 1 pps signal for the master clock.

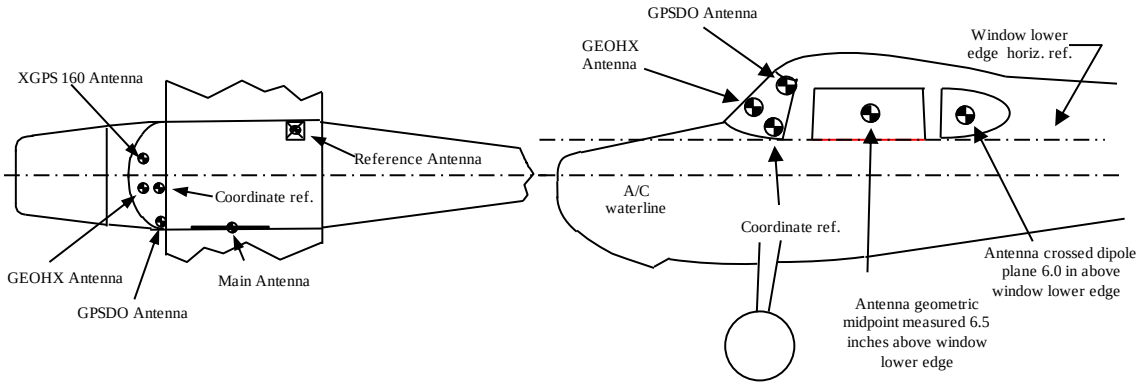

a) Aircraft Top View

b) Aircraft Port Side Perspective

Figure 6.48. Antenna Installation Positions

Figures 6.49 and 6.50 are photographs of, respectively, the main and reference antennas as installed. Orientation of the reference antenna was made so that the angular reference

Antenna	Position x, y, z (cm) ACLS
Main	-81.915, 37.084, 0
Reference	-153.035, -53.918, -1.27
GPS Nav (GEOXH)	8.89, 0, 5.715
GPS Visualization	8.89, 21.844, 2.54
GPSDO	N/A

Table 6.7. Measured Antenna Positions in Aircraft Coordinates

a) View with Starboard Door Open b) View with Starboard Door Closed

Figure 6.49. Main Antenna Installed

from the calibration measurements was opposite of the main antenna (Section 6.2).

Measurement of the location of the main and reference antenna phase centers as installed in the aircraft was with an estimated accuracy of ± 0.3 cm. The GEOXH was placed on the glare shield (near centerline) and secured with bungee cords. This position resulted in excellent visibility of the sky (satellite access) but made establishment of the antenna phase center difficult. It is estimated that the GPS phase center is known within ± 0.635 cm (developed using a replica of the handset).

a) Interior View Installed b) Exterior View Installed

Figure 6.50. Reference Antenna Installed

6.3.3 ***Flight test location and collection aperture.*** Initial flight test planning involved a location to the south-southwest of the transmitter at a private airfield. Selection was made based on visibility to the illuminator, access for the installation of calibrated targets (a large top hat reflector was planned, sized and materials testing was performed), and lacked large stands of tall, mature trees between illuminator and scene location. However in final flight planning with the test pilot it emerged that the location, while suitable in all other regards, was positioned too close to Seattle-Tacoma International Class B airspace (a Federal Aviation Administration designation given to those airports with the heaviest traffic loads) such that the access ceiling was too low to support the planned vertical aperture. The location is highlighted in Figure 6.51[5]. This position mandates a ceiling of 10000 ft with floors of 3000, 5000 or 7000 ft depending on the aircraft position in the collection aperture (3040 m and 914/1524/2134 m), depending on location, and below the planned maximum altitude of greater than 4500 ft (1372 m). This location also had higher levels of civil aviation traffic.

The test pilot suggested an alternative to the north of the illuminator position which was outside of the class B controlled volume. The Snoqualmie valley had line of sight (though more heavily forested in places) and it was possible to negotiate a single transit of the

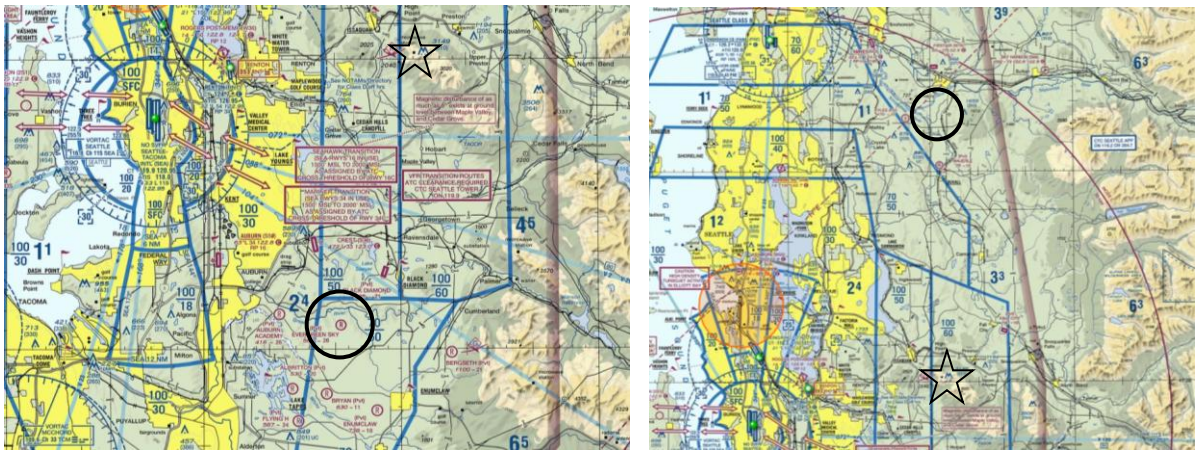

a) Initial Flight Test Orbit Location b) Flight Test Orbit Location - as Flown

Figure 6.51. Aeronautical Navigation Charts with Test Locations

[5] https://skyvector.com/?ll=47.449888889,-122.311777778&chart=128&zoom=3

Class B airspace for the calibration leg. It also offered to possibility of a ground test, placing the test antennas on automobile roof top fixtures and the collection of training apertures with calibrated targets over a wide angle, coplanar (two-dimensional) aperture. Targets and fixtures were built but permission was not received from the county authorities to operate at the ground test location (Evergreen State fairgrounds). However the northern location did not afford any locations to place the large top hat target (6 m ground plane, 2 m tall, and 2 m diameter cylinder) so the test site was based on the alternative target of a grain silo as shown in Figure 6.52. The silo was cylindrical with segmented concrete walls and topped with a segmented metallic hemisphere. There is external structure, such as ladders. The silo also has the advantage in that it projects above the lines of trees between the scene area and the transmitter, and the very low grazing angle at scene center. No modeling of the specific geometry was performed prior to flight, though prior modeling of monostatic spheres demonstrated that such shapes collapse to a point when narrowband and ultra-narrowband waveforms are employed (Section 6.1.3.2).

Figure 6.52. Google Earth Scene Center Image

The planned versus executed flight trajectory appears in Figure 6.53, generated by kml overlay on Google Earth. The test aircraft departed Paine Field (KPAE) to the south and

climbed out to 2500 ft. GPS was enabled during climb out (1). Temporarily orbiting at (2) while waiting for clearance to transit the lower portion of the Class B airspace (daily flow was southbound). The initial point for the calibration leg is indicated by (3). Constant bearing relative to the transmitter was held at a slight rate of climb to position the aircraft for the descending cylindrical spiral at (4). The only radar (soft) fail was experienced slightly before (4) and about two thirds of the first orbit was spend bringing the system back online.

Three collection apertures had been evaluated for possible monostatic operation and nine for bistatic operation as detailed in [155]. With a fixed transmitter the three monostatic apertures; spherical spiral, cylindrical spiral and the planar spiral were considered for the bistatic receiver.

A series of constraints were established or existed: maximum altitude for the laboratory-quality N200 digital receivers (6000 ft/1829 m, 5000 ft set for margin), maximum safe bank angle for the 65 year old airplane (30 deg), and a subjective criterion on relative ease to hand-fly. A planned orbital radius of 1250 m for the cylindrical and spherical

Figure 6.53. Planned (white) vs. Executed (black) Flight Trajectory

spirals was established with a minimum height above terrain at scene center of 200 m (this to set a minimum elevation angle which translated into the initial range for the planar spiral). The apertures are shown in Figure 6.54 in both physical and *k*-space

(frequency domain) forms for a narrowband signal source. For each of the three apertures there are two renderings: the first (Figures 6.54a, c, and e) are the spatial apertures. The second (Figures 6.54b, d, and f) are the frequency domain representation of the sampling. Two colors are used in the frequency domain to indicate the bandwidth of the probing waveform with red the band upper edge and blue the lower. All the apertures are distributed essentially the same in *k*-space, meaning that there is no difference in resolution. The apertures in the frequency domain are all thin shells. Both the planar

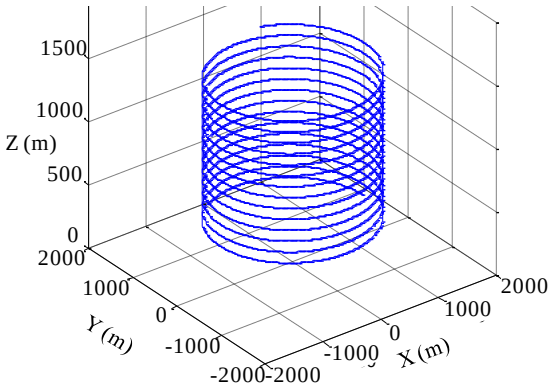

a) Cylindrical Spiral Spatial Aperture

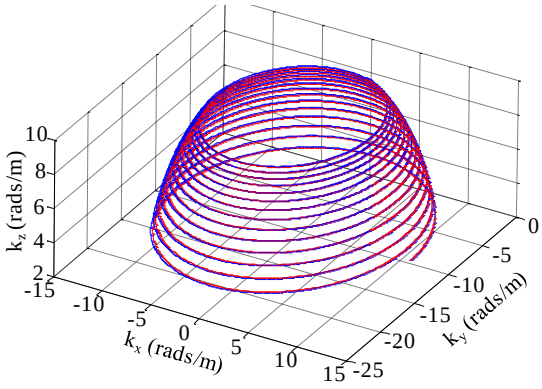

b) Cylindrical Spiral Fourier Aperture

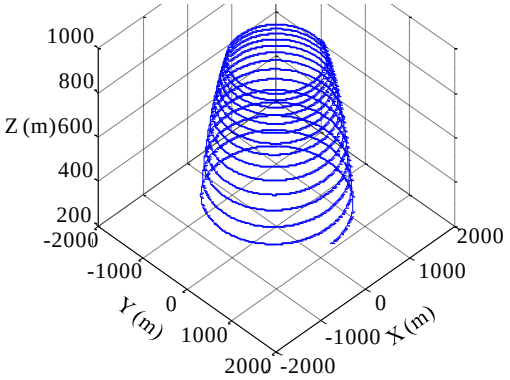

c) Spherical Spiral Spatial Aperture

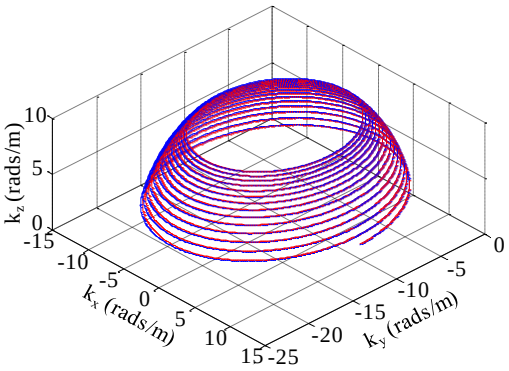

d) Spherical Spiral Fourier Aperture

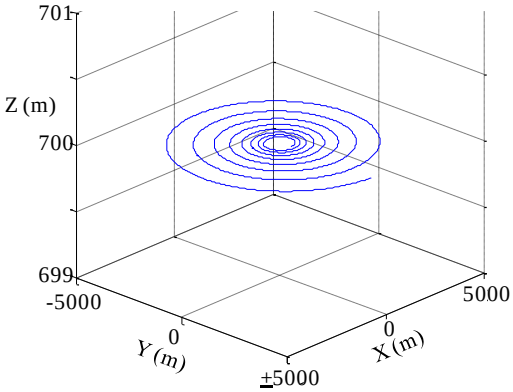

e) Planar Spiral Spatial Aperture

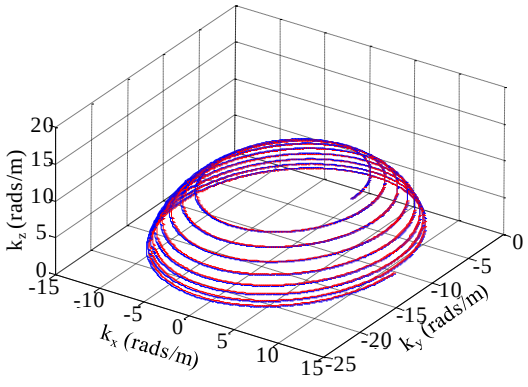

f) Planar Spiral Fourier Aperture

Figure 6.54. Collection Aperture Options

spiral and the spherical spiral require roll up turns (of increasing bank) with position, making collection more difficult. Also the planar spiral has substantially more range dependence (>4000 m versus a 1500 m maximum for the cylindrical spiral).The spherical spiral maintained a constant range with time. Ultimately the cylindrical spiral was selected for ease of collection.

6.3.4 ***RFI analysis*****.** To insure that image quality is not affected or degraded by interfering RF signals mitigation steps are necessary in the bistatic receiver. The degradation is realized by the inclusion of non-target signals (defined as those emissions from the target transmitter) in the pulse compression. The composite spectrum at the receiver(s) in the frequency domain can be expressed as the sum of the spectra of *N* commercial broadcast emitter signals as

$$S_{main}(\omega) = \sum_{i=0}^{N-1} A_i S_i(\omega) \tag{6-42}$$

where A_i is the voltage scaling of the i^{th} transmitter due to receiver frequency response, range, transmit gain in the direction of the receiver, power level and receive gain in the direction of the transmitter. The channel spectrum is S_i including coding and programming. A similar expression is generated for the reference antenna. The pulse compression process (cross correlation) can be written as

$$s(\tau) = \Im^{-1}\left(S_{main}(\omega) S_{ref}(\omega)^*\right) \tag{6-43}$$

where τ represents delay, * complex conjugation and $\Im^{-1}$ the inverse Fourier transform. Also in (6-43) we have not included the adaptive sidelobe canceller stage because the number of signals (emitters) is much greater than 1 (the single reference antenna acting as a single auxiliary element or a single loop canceller) thereby significantly diluting the nuisance signal rejection [131]. The rule of thumb for adaptive cancellation is one narrowband jammer per spatial degree-of-freedom [156]. In principle, the spectrum in (6-42), assuming no aliasing, could be channelized (given adequate sampling) and each 6

MHz segment relating to a specific source, in both channels, could be extracted and individually processed as a frequency dependent single-loop canceller The product in (6-43) can be expanded as

$$S_{main}(\omega)S_{ref}(\omega)^* = \left(S_{m1}(\omega)+\ldots+S_{mN}(\omega)\right)\left(S_{r1}(\omega)+\ldots+S_{rN}(\omega)\right)^*. \qquad (6\text{-}44)$$

Taking advantage of the orthogonality realized through regulatory control and spectrum shaping (and for the moment ignoring aliasing), the product $S_iS_j^*$, $i \neq j$ is 0. The expression in eqn. 6-44 reduces to the sum of the auto-spectrum products for each emitter. This assumes that both channels are identically matched, etc. The inverse transform can be taken term wise. This produces a final compressed pulse which is the sum of the emitter pair wise cross correlations

$$\chi(\tau) = s_1(\tau)+s_2(\tau)+\ldots+s_N(\tau) \qquad (6\text{-}45)$$

If the emitters were all received with equal strength this would result, on average, in degradation in SNR by N–1 through the elevated time sidelobes of the summed autocorrelations, with the image scene only illuminated by the target emitter, since each autocorrelation peak response is, by definition, at 0 delay with the range sidelobes combining to increase the effective noise floor [113]. This is a particular consideration for the elevated receiver while allocation of television coverage is based on ground-based receivers.

The URSP unit (N200) chosen employs the model WBX tuner which provides a 40 MHz instantaneous bandwidth (Section 6.1.1), with a tuning range of 50-2200 MHz. The tuner does not employ any band-limiting (preselection) filtering prior to the single stage (direct) down conversion/quadrature demodulation to complex baseband; the 40 MHz bandwidth is realized through an analog filter after the down conversion mixer, prior to analog-to-digital conversion. The N200 ADC samples at 100 MS/s and can stream 25 MS/s in 16 bit complex mode. However when operated via the MIMO cable this reduces to 25 MS/s for both receivers, or 12.5 MS/s each. This was ultimately derated to 10 MS/s (complex)

because of laptop controller issues (incompatibility of hardware drivers with Windows 8.1 forcing use of a slightly slower laptop operating under Windows 7 and resulting in elevated occurrences of dropped packets). Consequently an additional analog filter was necessary minimize aliasing and to preserve the effectiveness of the single loop adaptive canceller to maintain sensitivity.

In addition to signal-to-noise ratio degradation from undesired signals, the receiver gain settings were set such that when the main antenna is directed at the target emitter during the repeated orbits constituting the aperture, the signal level would be at ADC saturation. The N200 has a single gain control stage and no provisions to dynamically manage receive gain; the driving code/program must be restarted for a new gain setting. The design gain settings are based on the targeted transmitter (station ID/call sign KPWX) and the system gain cascade, including the main antenna. Other transmitters in the field of view have the potential to saturate the ADC if unmitigated, thus potentially denying large angles of collection aperture.

In this section the RF environment and RFI analysis leading to the specification, design and fabrication of a narrowband analog prefilter is described. Note: this portion of analysis was performed on a preliminary test location to the southwest of the transmitter location, not the location ultimately tested (to the north). However, the requirements for the filter performance are independent of location because of the density of transmitters and the action of the airborne receiver effectively rastering the mainbeam to all bearings about the test scene.

• **6.3.4.1** ***Spectrum allocation and emitter density***. As described in Section 5.0, television spectrum is rigorously allocated with analog and digital channels in a common spectrum block, with digital channels exhibiting a nominal 5.83 MHz bandwidth on 6 MHz channel centers. The US UHF allocation is defined in contiguous 6 MHz bands from 470 MHz

(channel 14) to 890 MHz (channel 83). The VHF High band is composed of 7 channels spanning 174-216 MHz. Figure 6.55 is the total allocation from the NTIA (National Telecommunications and Information Administration [157]). Within this allocation we are interested in large Effective Radiated Power (ERP) signals which may cause imaging degradation. This includes radar systems and broadcast television. A lower bound of 100 MHz is chosen under the rationale that any mitigation that addresses the megawatt-class television signals will address lower power, lower frequency emitters (*e.g.*, audio broadcast) that are farther out-of-band. Using a commercially available web tool [158] a listing of TV channels with potentially usable signal, as defined from a television receiver perspective and which includes line-of-sight, single and double edge diffraction, or a tropospheric path, is obtained at an antenna height 500 ft (152.4 m) above ground level (AGL), at the coordinate representing the test scene origin (that altitude being a limit of the online tool). The listing (Table 6.8) was used to populate a database with frequency, antenna type and height, average power and gain in the direction of the

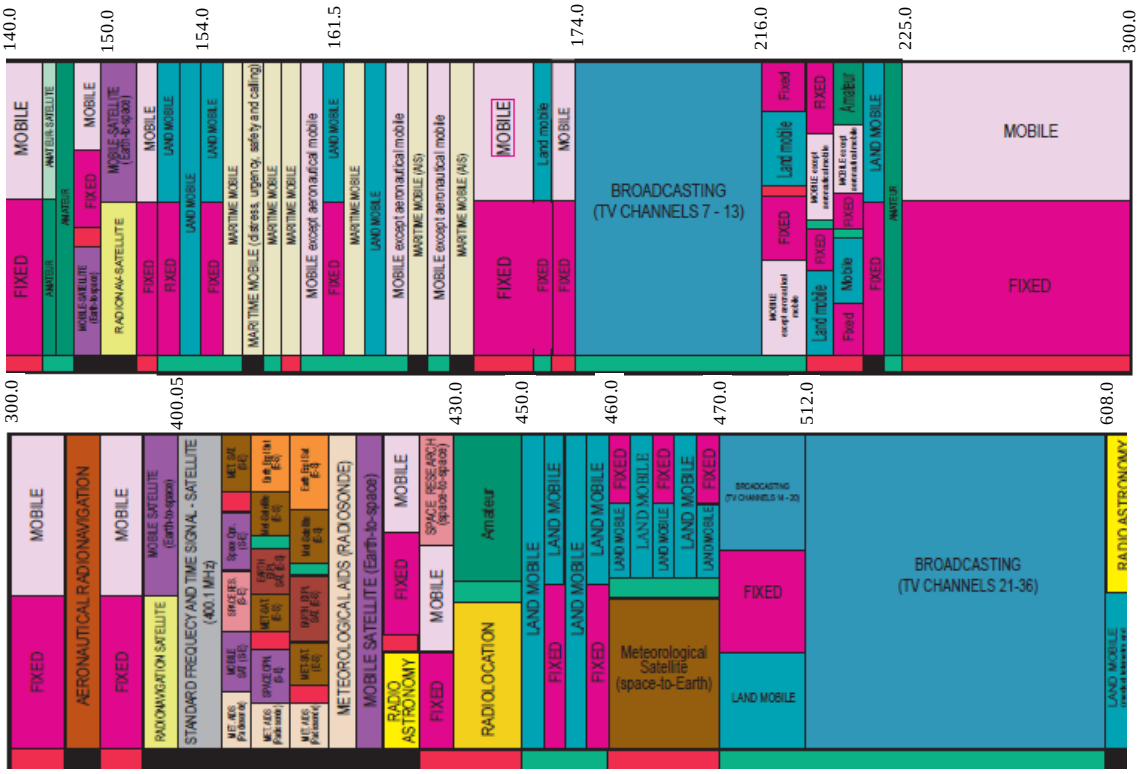

Figure 6.55. U. S. Radio Frequency Spectrum Allocation 100-608 MHz

test scene, derived from FCC (Federal Communications Commission) filings (Table 6.8). The spatial distribution of TV transmitters in Table 6.8, which may contribute non-negligible energy to an airborne receiver at the test scene location. is given in Figure 6.56.

As of June 2008, only full-power transmission of digital TV was permitted in the US with more relaxed transition of low power stations/translators. There are three spectrum masks that are assigned to manage out-of-band emissions of digital television transmissions. The mask assigned to a particular transmitter depends on whether the unit is full service, or low-power digital TV (LPTV) transmitters, Class A digital transmitters and digital TV translators. One mask is termed "Simple", another "Stringent", and yet a third "Full Service" [159]. The individual channel masks are shown in Figure 6.57 [113], a more detailed representation than initially given in Figure 5.1. As seen, the masks define the adjacent channel signal spill-over levels. The Full Service mask refers to full power HDTV operators wherein the Stringent and Simple masks were authorized for low power transmitters [160]. As seen from Table 6.8, low power stations exhibit ERP values that are 20 dB or more below the full power, megawatt-class stations resulting in beyond-second-adjacent (channel) levels that are comparable to the full power stations in the

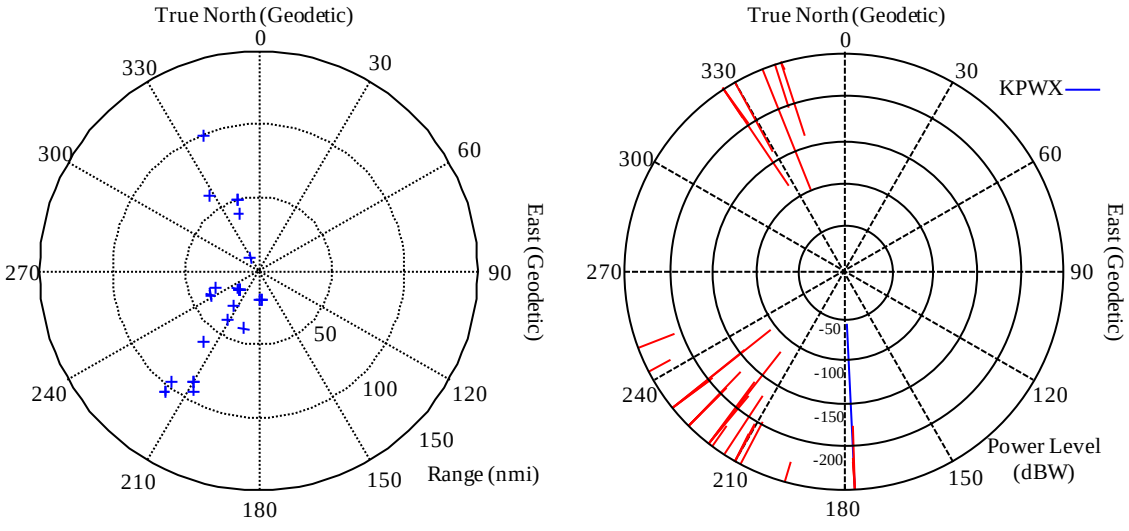

a) Emitter Polar Plot - Bearing/Range re Scene b) Highest Power Emitters - Power Level at Scene

Figure 6.56. Distribution of TV Transmitters Relative to Test Location

Call Sign	Freq (MHz)/ Channel	Antenna Type/Pattern/Manufacturer	ERP (kW)/Gain	Location/ Altitude	Altitude (m,MSL)
KZJO	536-542 chan. 25	Directional 0.75° Elec. Beam Tilt; Dielectric TFU-20GTH O4	1000/1	47° 36' 56.8" N -122° 18' 30.2" E	325
KWPX[1]	584-590 chan. 33	Directional DIE, TFU-31ETT-R CTSP Major lobes - N/A, Beam Tilt 1° (elec.) 1° (mech., 270°T)	400/1	47° 30' 17" N -121° 58' 06" E	948.2
KIRO	620-626 chan. 39	Directional DIE, TFU-32DSC C164 Major lobes 25, 155°, Beam Tilt 0.5°	1000/0.971	48° 38' 1" N -122° 21' 20" E	297.7
KUNS	686-692 chan. 50	Directional 0.75° Elec Beam Tilt; ERI ATW28H3-ESC1-50H	1000/0.963	47° 37' 55" N -122° 21' 09" E	285
KING	674-680 chan. 48	Directional DIE, ODD980227KF Major lobes 0, 180° Beam Tilt 0.5°	960/0.597	47° 37' 55" N -122° 20' 59" E	279
KONG	572-578 chan. 31	Directional DIE TFU-24DSB-I Major lobes 30, 190° Beam Tilt 1°	700/1.0	47° 37' 55" N -122° 20' 59" E	258
KOMO	614-620 chan. 31	Non-Directional ERI ATW28H3-ETO-38H Major lobes - N/A Beam Tilt 0.65°	1000/0.996	47° 37' 55" N -122° 21' 09" E	300.2
KWDK	638-644 chan. 42	1° Elec. Beam Tilt Systems With Reliability SWED16OI	144/1.0	47° 30' 17" N -121° 58' 06" E	926.6
KSTW	198-204 chan. 11	1° Elec. Beam Tilt Dielectric TUV-24GTH/8HV-R 4BP250/P220	100/0.76	47° 36' 56.00" N -122° 18' 29.00" E	311.3
KBTC	548-554 chan. 27	1.25° Elec. Beam Tilt ERI AL-12O-27	100/1.0	47° 16' 44.00" N -122° 30 '42.00" E	258
KBTC	482-488 chan. 16	1.75° Elec. Beam Tilt ERI AL8-16-OC	1/0.88	47° 36' 57.0" N -122° 18'30.4" E	225
KCTS	186-192 chan. 9	0.8° Elec. Beam Tilt Dielectric TW7B9-R(S)	21.7/1.0	47° 36' 58.00" N -122° 18 '32.00" E	284.7
KCPQ	210-216 chan. 13	1° Elec. Beam Tilt Andrew ATW13V4-ETO1-13	30/1.0	47° 32' 53.00" N -122° 48 '22.00" E	718
KCPQ	518-524 chan. 22	0.75° Elec. Beam Tilt; Dielectric TFU30-EBT/VP-R SP155)	15/1.0	47° 36' 57.00" N -122° 18 '30.4" E	284.7
KTBW	470-476 chan. 14	0.75° Elec. Beam Tilt Andrew ATW18H3-HSC-14S	90/0.94	47° 32' 50.00" N -122° 47 '40.00" E	581
KRUM	530-536 chan. 24	1° Elec. Beam Tilt Propagation Systems PSILP12RUM-24-CP	4/0.95	47° 36' 55.6" N -122° 18 '28.5" E	293
KIRO	692-698 chan. 51	unknown or 0 deg tilt ERI ALP4L1-HSP	0.95/0.728	48° 38' 1" N -122° 21' 20" E	934
KIRO	590-596 chan. 34	unknown or 0 deg tilt Kathrein 1X2KBBU	0.5/0.9	47° 0' 57" N -122° 54' 59" E	168
KIRO	554-596 chan. 28	unknown or 0 deg tilt Kathrein 1X2KBBU	0.5/0.05	48° 29' 1" N -122° 19' 24" E	282
KFFV	650-656 chan. 44	0.5° Elec Beam Tilt; Bogner B16UG	169/0.4	47° 36' 56" N -122° 18' 29" E	244.7
KUSE-LD	662-668 chan. 46	0.75° Elec. Beam Tilt Systems With Reliability SWLP8EC	0.5/0.94	47° 30' 17.00" N -121° 58' 10.00" E	934.2
KUSE-APP	494-500 chan. 18	unknown or 0° tilt Dielectric DLP-8H	10/0.94	47° 30' 17.00" N -121° 58' 10.00" E	934.2
K47LG-D	668-674 chan. 47	unknown or 0 deg tilt Kathrein 4DR-16-2HW	1.1/0.983	47° 25' 43.0" N -122° 26' 16.0" E	91.7
K26IC-D	542-548 chan. 26	unknown or 0 deg tilt Kathrein 4DR-16S	0.9/0.08	47° 38' 27.0" N -122° 43' 28.0" E	189
KVOS	596-602 chan. 35	1° beam tilt Dielectric TFU-31JTH-R O4SP	580/1.0	48° 40' 50.0" N -122° 50' 22.0" E	834
KBCB	500-506 chan. 19	0.75° beam tilt RF Systems R032UA16	165/0.77	48° 40' 46.0" N -122° 50' 31.0" E	792.5
K24IC-D	530-536 chan. 24	unknown or 0° tilt RF Systems RD32UA16	15/0.77	48° 40' 46.0" N -122° 50' 31.0" E	792.5
KCKA	500-506 chan. 19	1° Elec. beam tilt Dielectric TLP-24H	187/0.51	46° 33' 16.0" N -123° 03' 30.0" E	499.8
K49IX-D	680-686 chan. 49	unknown or 0° tilt Kathrein 4DR-16S	2.2/0.813	47° 10' 25.0" N -122° 15' 51.0" E	499.8
CIVT-TV	578-584 chan. 32	Non-directional no rotation	33/1.0	49° 21' 29.0" N -122° 57' 9.0" E	740.3

[1] Target Emitter for Tomographic Experiment

Table 6.8. Emitter Listing for RFI Analysis

sidelobe level allocation. Since individual channel emission masks were not available with station licensing (where RF specifics are listed), this permits the use of a single mask

for the RFI analysis (1000 kW station with -110 dB mask roughly equates to 1 kW ERP with -76 dB mask. Original system design indicated a higher digital sampling rate than was ultimately realized. This would have permitted a combination of analog and digital filtering to isolate the single channel of interest. Wider passband, steep roll-off analog filter would have yielded a reduced insertion loss. It also would have permitted channel-to-channel adaptive cancelling for the adjacent channel signals.

From Figure 6.55, while we are concerned with all potential interfering signals, we focus on high power-aperture, CW HDTV signals (analog operation is effectively ended) in the UHF band. Station KPWX is roughly in the middle of the broadcast TV allocation. Addressing these adjacent interference sources will then cover low power communications, industrial and scientific emitters. Some of the allocations in frequencies adjacent to broadcast television include civil and military radar systems. Of most concern would be ground based systems with mechanically scanning antennas and 10-12 second revisit times.

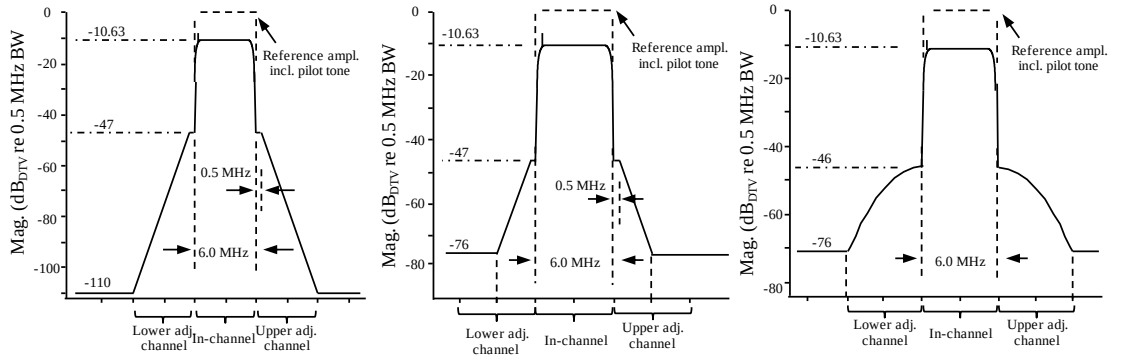

a) Full Service Mask b) Stringent Service Emissions Mask c) Simple Service Emissions Mask

Figure 6.57. Emissions Masks U. S. Digital TV

An initial analysis was performed to establish analog filter requirements. We proceeded by generating a single orbit of the tomographic collection aperture (300 m AGL). This permits the dynamics of the gain in the direction of each source in both main and reference channels to be included over the measurement geometry. This is mostly driven by the main antenna with approximately 20 dB of front-to-back ratio (the gain variation in

the reference channel based on FEKO modeling is essentially flat – Figure 6.11). In this analysis the individual channel signals are simply modeled as rectangular spectra with a uniform power spectral density over the 6 MHz channel allocation. At each spatial position the unambiguous spectrum was calculated, including gain and range contributions, weighted by the analog bandpass filter (BPF) response (magnitude only). Two example calculated spectra, main and reference channel, are shown in Figure 6.58. The spectra operate span both UHF and VHF ranges to illustrate the filter suppression.

The analog bandpass filter (BPF) was parametrically represented by

$$H(\omega)=\frac{1}{\sqrt{1+\varepsilon^2\left(\frac{\omega_0}{B}\left(\frac{\omega}{\omega_0}-\frac{\omega_0}{\omega}\right)\right)^{2n}}} \tag{6-46}$$

with ε the filter gain at midband, B the bandwidth (angular frequency), n the filter order and ω_0 the filter center frequency. Figure 6.58 illustrates analysis results for a 5th order BPF using the emitters listed in Table 6.8 with the receiver positioned 1250 m East of the scene origin and a heading of 0°. Several order and bandwidth combinations were

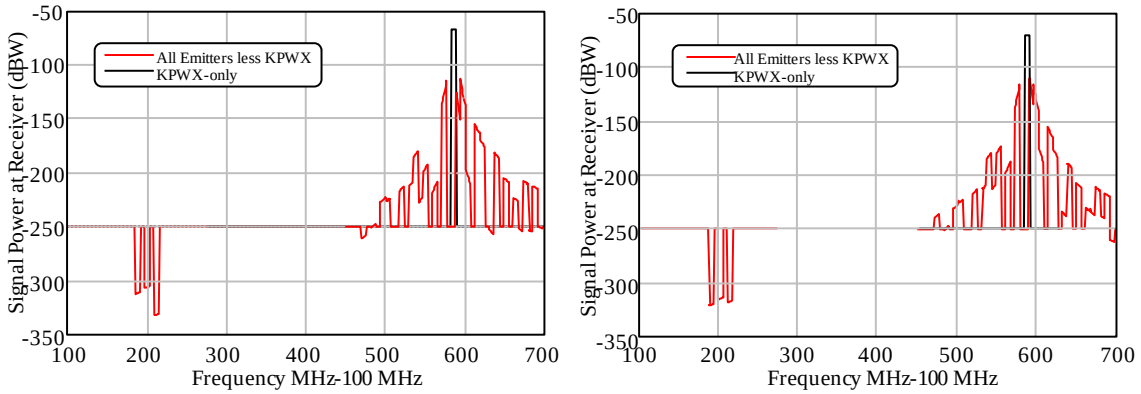

Figure 6.58. Snapshot Calculated UHF/VHF Spectra with Analog Filtering

evaluated in deriving the filter requirements. Figure 6.59 shows two examples, 4th order and 5th order filters using a 587 MHz center frequency and 8 MHz 3 dB bandwidth. Figure 6.59a spans the frequency range of VHF and UHF emitters while Figure 6.59b

zooms around the design center frequency. The calculated spectra are then aliased based on the (then) planned sample rate (25 MCSPS), discretely evaluated in 1 MHz frequency intervals. For convenience the spectrum is referenced to 0 Hz representing down conversion of the target channel center frequency. Also, the frequency range of the target

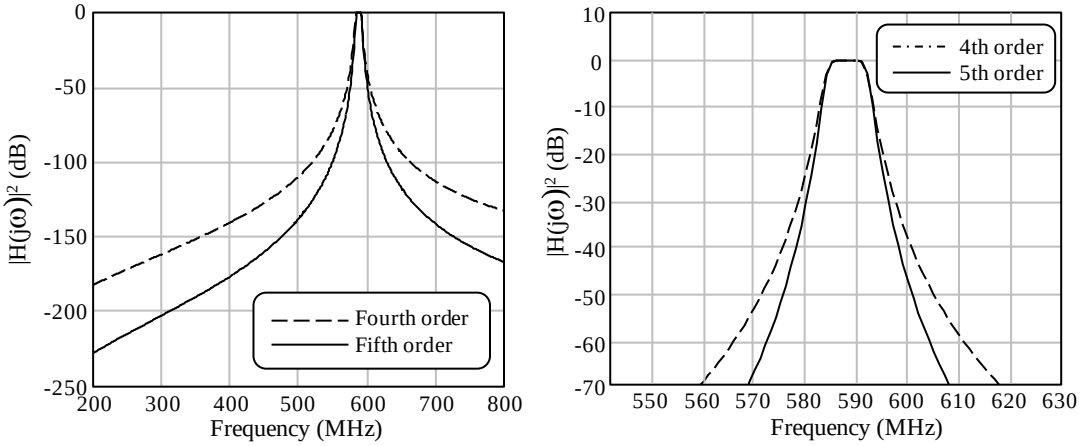

a) Ideal Magnitude Response vs. Frequency b) Zoomed Magnitude Response

Figure 6.59. 4th and 5th order Band Pass Filter Magnitude-squared Responses

station is shown (with received power as indicated in Figure 6.58) in the aliased spectra in Figure 6.60. This result indicated that the 5th order filter was adequate for adjacent channel filtering. The determination that the actual sampling rate would be one-half the value used in the analysis above occurred prior to bandpass filter purchase. At that time the 3 dB passband was reduced to 6 MHz, introducing a slight signal loss.

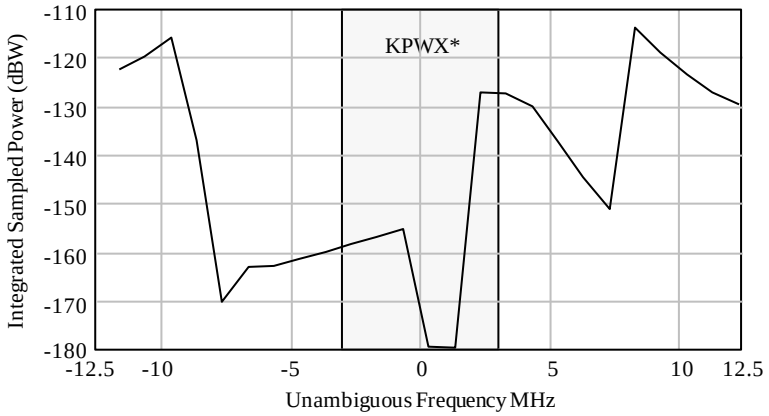

Figure 6.60. Aliased Spectrum after 8 MHz 5th order BPF

The emitter database included Canadian stations, due to the relative proximity of the test location to the Canadian border. After the analysis of US stations was complete, the

Canadian channels (which use the same allocation as the US channels) were inspected for any allocations on the target channel (none) or adjacent channels (one, relatively low power).

Figure 6.61 contains examples of an adjacent channel signal in the measured flight data, from two different times. In Table 6.8 a Canadian station and another lower power US station are listed as adjacent channels. Both were to the north of the scene and were only visible in the antenna mainlobe during the portions of the collection aperture when the main antenna was oriented to the north, and only at the higher elevation, early in the aperture. The attenuation of the channel spectrum from the bandpass filter can be seen. The actual sample rate and channel spacing results in the pilot tone for the adjacent lower channel to alias to the same frequency as the pilot tone in the adjacent upper channel. Both cases are noted in Figure 6.61. The actual location of the channel can be inferred from the shape of the spectrum portion above +3 or below -3 MHz.

As noted earlier, during signal conditioning, prior to cross correlation/pulse compression, a rectangular mask was applied in the frequency domain (matched to the target emitter spectrum) to remove out-of-band signals, after static calibration and before recovery of the time signal.

6.4 Signal and Data Processing.

This section covers the signal conditioning necessary to prepare the two-channel, digitally recorded flight data for reconstruction. This is broken into three main portions: preprocessing (initial data assessment, time alignment, and estimation of unmeasured flight parameters), navigation data conditioning, and signal processing resulting in forward transformed range strobes written to data file(s) formatted for image reconstruction.

6.4.1 ***Preprocessing*****.** Flight data were stored as binary formatted files. Four flight data files were collected: a data overflow caused the laptop radar controller to crash, resulting in four files instead of two. This occurred, fortuitously, between the calibration leg and the imaging leg. The main effort here was the alignment of sample burst receiver time

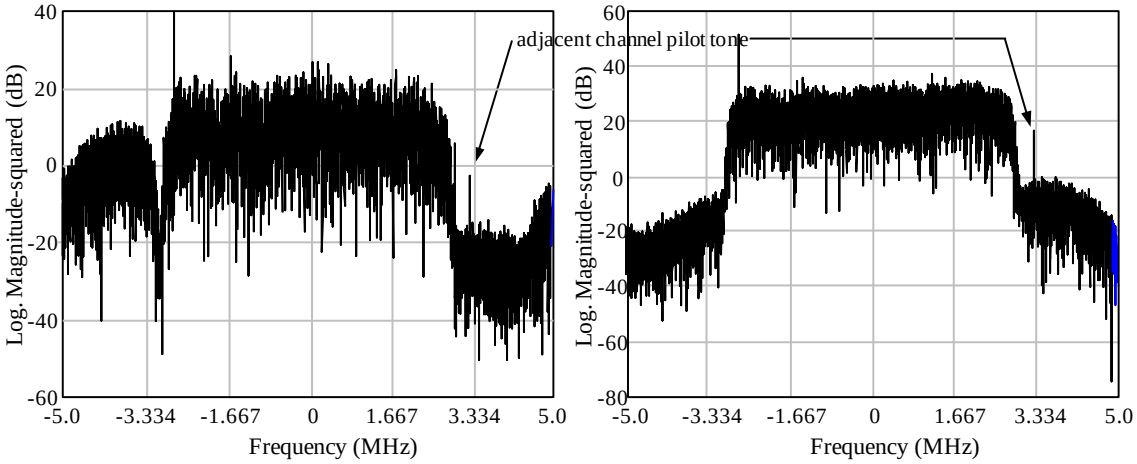

a) 157215.279 sec Adjacent Channel Below F0 b) 157215.279 sec; Adjacent Channel Above F0

Figure 6.61. Examples Adjacent Channel Signal Spectrum

with GPS time. The former was derived from the GPS disciplined oscillator (GPSDO), clock cycles converted to time (seconds) after receiver initialization, and recorded at the start of each sample burst for both channels. GPS time was available only at the 1pps rate (integer GPS seconds in UNIX format) through the GPSDO. Using an available hardware call set_time_next_pps() to set the master clock was followed by a five successive calls to get_gps_time which were saved at the top of the data file. The first A/D sample occurred 7.28000025 seconds after receiver clock initialization as an absolutely repeatable delay. Elapsed receiver time from the GPS pps used to initialize the receiver clock (master clock was distributed to slave receiver via the MIMO interface cable) to first sample was 5.2800025 sec allowing the GPS time of the first sample burst to be set at 156980 sec for the imaging leg (156138 calibration leg). In other words, the set_clock_next_pps time was one second before the first GPS time call. This aligned the radar data to the 1Hz navigation GPS data. From the measured data the actual burst rate was confirmed at

19.67729240456513 bursts/second; equivalent to an interburst interval (first-sample-to-first-sample) of 0.0508200 second.

Table 6.9 outlines the preprocessing steps, largely unrelated (*e.g.*, stand alone), which assessed the flight data quality and supported troubleshooting early data analysis problems. The various preprocessing tasks were largely mutually independent.

Preprocessing Step	Description
Out of band power	Received in adjacent channels in sampled range
Installed Effects	Antenna patterns for main and reference antennas in-flight
Missing/dropped packets	Time gaps to correct file pointer function (data read pointer positioning) - bursts
Missing/dropped packets	Serial correlations within burst, searching for dropped packet/alignment (intraburst)
I, Q Balance	Sampled data quality
Multipath	In the reference channel

Table 6.9. Data Preprocessing Listing

Three preprocessing assessments of note include the amount of out-of-band power from adjacent channels that was received and the quick look installed antenna patterns. Sampling at 10 MCSPS (instead of the 12.5 MCSPS planned) means that portions of the adjacent channel (2 MHz worth on either side of the design channel) can alias into the desired signal region. The bandpass filter attenuates the edge aliased frequencies ($f_0 \pm 5$ MHz) by 33 dB so the impact was expected to be minimal. The two potentially "offending" transmitters were both to the north and both at longer ranges (Section 6.4.3). Figure 6.62 illustrates the received power integrated from design band edge to the sampling limit (a 4 MHz span, -5 to -3 and 3 to 5 MHz) as a function of time (aircraft altitude) and antenna pointing. After the first orbit (25 second sample duration from Orbit 1 is shown) out-of-band power was inconsequential;. levels are 20-30 dB down.

The (I, Q) balance assessment sampled the received data and estimated the mean value of the square of both terms, along with the product (I × Q). The measures of merit are a zero mean to the in-phase and quadrature voltages and an I-Q product of 0 (a measure of orthogonality). As covered in the Calibration section the (I, Q) balance for the single

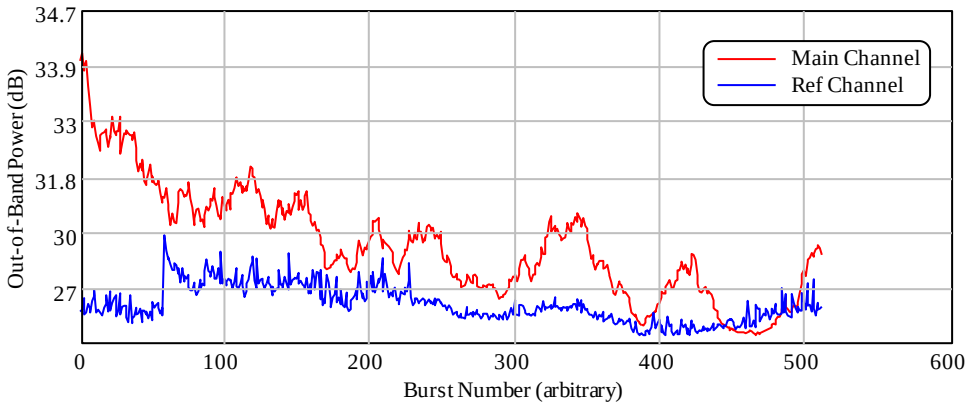

Figure 6.62. Adjacent Transmit Channel Power Level

stage, down converting receiver is a UHD function. The results of the I, Q assessment are listed in Table 6.10. Master channels are significantly greater than slave/reference.

Channel	Mean I^2/Mean Q^2	IQ product
Master	0.0008899 (-30.51 dB) / 0.0008911	0.0000001
Slave	0.0000087 (-50.6 dB) / 0.0000087	0.0 (precision limit)

Table 6.10. In-phase and Quadrature Channel Balance Results

Several measurement attempts were made of the (uninstalled) antenna patterns of both antennas with limited success. Patterns derived from the calibration measurements in the anechoic chamber were not radiometrically calibrated but showed expected trends with the peak magnitude of the chamber/VNA measurements suggesting a higher peak gain in the reference channel than from the main channel, as well as similarity to simulated patterns. It was expected that the antenna radiation patterns would be significantly impacted by the presence of the metal airframe and the pilot and operator. To examine this each burst over the full one hour aperture (some 55155 bursts in total – 2600 seconds of data) was forward transformed and masked to the allocated channel bandwidth and the total power calculated by summing over frequency. Results are presented in Figure 6.63.

There are a couple of notable observations in Figure 6.63. First is that the elevation pattern of the HDTV transmitter can be seen as the aircraft descends, in both the main and reference channels, through the envelope of power versus time. The periodicity of the orbit is clearly seen, though the patterns are quite unexpected. Main channel power when

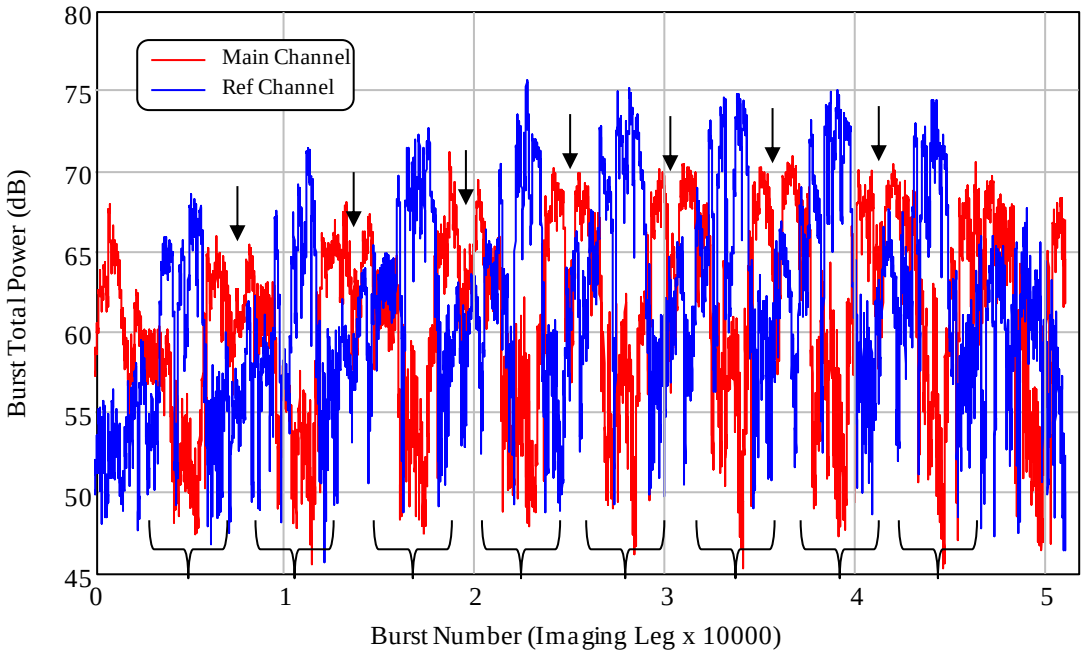

Figure 6.63. Quick-look Installed Antenna Patterns

mainbeam is oriented toward the transmitter is less than the reference channel (no absolute gain references were developed during calibration with predicted main antenna gain, less combiner losses, of 6 dBi and less than 0 dBi for the reference antenna). The gain responses of both installed antennas are strangely rectangular, and roughly constant for both antennas, with a nominal 10-15 dB front-to-back ratio exhibited. This was as expected for the main antenna and more than expected for the reference antenna. The longer duration of mainbeam oriented toward the transmitter (in red) is due to the winds aloft with upwind flight in this portion of the geometry (aircraft speed 20 knots slower), while the downwind leg had the transmitter in the back half-space of the main antenna (20 knots faster). The angular extent of nearly constant received power is broader than the azimuth mainbeam (not shown but determined by overlaying gain vs. time with power vs. time). Finally, there is a repeatable ~5 dB dropout in the main pattern as indicated the vertical arrows in Figure 6.63.

Of main importance are those regions, illustrated by a downward half-bracket, where the gain of the reference channel exceeds the gain in the main channel (as evidenced through the signal power). This defines the region over which the adaptive canceller can be

applied without negative effect on the signal channel. These intervals are used to guide orbit arc selection for image reconstruction.

The multipath check was motivated by the conditions in the valley that ran from nearly the base of the mountain the transmitter was located on to the scene, where winter flooding had occurred. Unlike an airborne transmitter, multipath scattering potentially begins at the tower base (and tower structure) to the nadir point of the aircraft. Sample bursts were randomly selected and the reference channel return was autocorrelated, checking for delay peaks ground bounce that might necessitate filtering. Two such, representative examples, appear in Figure 6.64. Appearance of secondary correlation peaks was common, derived from programming content, AM/PM code, as they are symmetric with respect to zero delay. Both plots exhibit a slight skew at the first delay increment but are otherwise symmetric. Tower height (82 m AGL) should set the first delay, unless scattering was occurring from the tower itself.

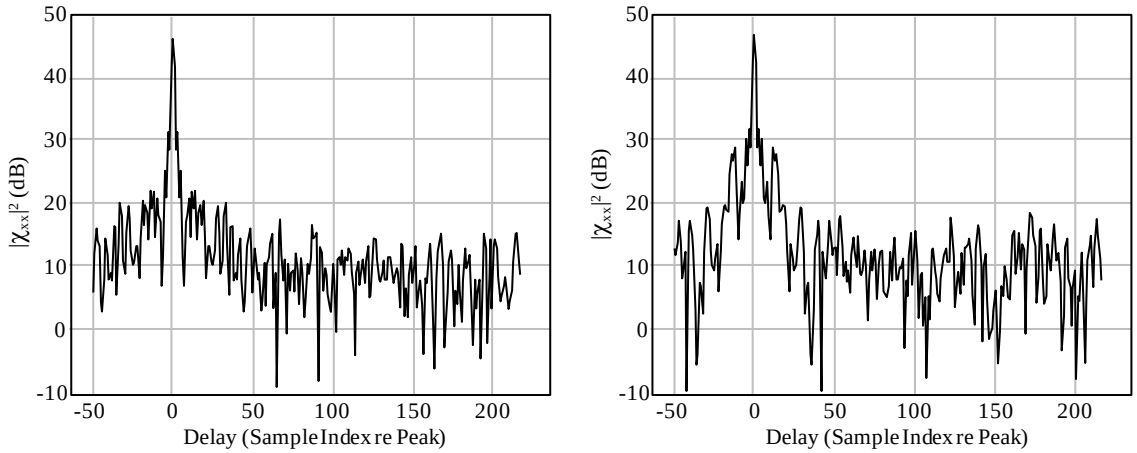

Figure 6.64. Example Reference Channel Autocorrelation (Multipath Check)

6.4.2 ***Coordinate systems***. Several coordinate frames were used in this effort. These are briefly defined before details on navigation data processing are covered (Figure 6.65). Position data from GPS devices was provided as defined with respect to the WGS84 datum. Position date were defined in an Earth-centered, Earth-fixed (ECEF) coordinate system: latitude, longitude and altitude. The working coordinate frames were Cartesian:

first an ECEF Cartesian with the X axis defined as the axis originating at Earth center which intersected with the geoid at 0 degrees latitude (φ) and 0 degrees longitude (θ) as seen in Figure 6.65a. The Y axis intersects the geoid at 90 degrees east longitude and the

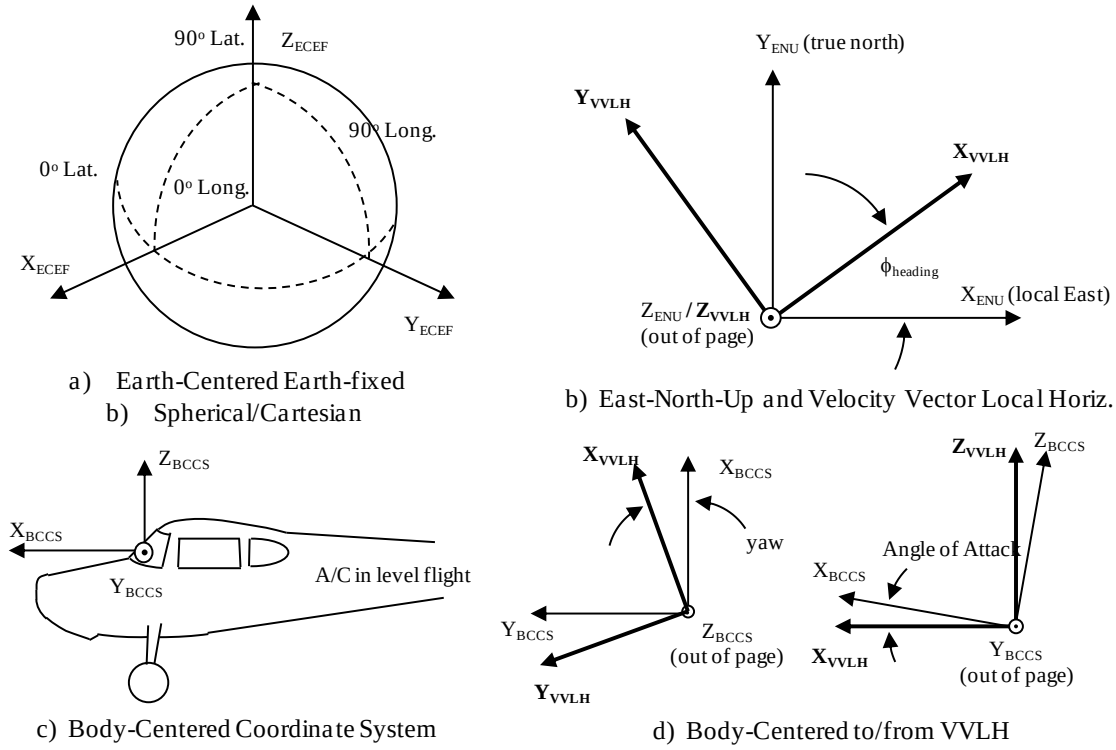

Figure 6.65. Coordinate Frame Definitions

Z axis is (X x Y), intersecting the geoid at the point defined by 90 degrees latitude. Translation from ECEF spherical to ECEF Cartesian made use of a WGS84 earth radius model. Scene coordinates are defined by an East-North-Up (ENU) Cartesian system where X_{ENU} is aligned to due east at the reference point, Y_{ENU} is aligned with local north and Z_{ENU} is oriented normal to the geoid surface at the reference point, outward from the Earth center. For reference point defined by (latitude, longitude, altitude) = (φ, θ, h), rotation to-from Cartesian ECEF to ENU are given by

$$Rot_{ECEF\_ENU} = \begin{bmatrix} \cos\left(\frac{\pi}{2}-\varphi\right) & \sin\left(\frac{\pi}{2}-\varphi\right) & 0 \\ -\sin\left(\frac{\pi}{2}-\varphi\right) & \cos\left(\frac{\pi}{2}-\varphi\right) & 0 \\ 0 & 0 & 1 \end{bmatrix} \begin{bmatrix} 1 & 0 & 0 \\ 0 & \cos\left(\theta+\frac{\pi}{2}\right) & \sin\left(\theta+\frac{\pi}{2}\right) \\ 0 & -\sin\left(\theta+\frac{\pi}{2}\right) & \cos\left(\theta+\frac{\pi}{2}\right) \end{bmatrix} \tag{6.47a}$$

$$Rot_{ENU\_ECEF} = \begin{bmatrix} 1 & 0 & 0 \\ 0 & \cos\left(-\frac{\pi}{2}-\theta\right) & \cos\left(-\frac{\pi}{2}-\theta\right) \\ 0 & \cos\left(-\frac{\pi}{2}-\theta\right) & \cos\left(-\frac{\pi}{2}-\theta\right) \end{bmatrix} \begin{bmatrix} \cos\left(\varphi-\frac{\pi}{2}\right) & \sin\left(\varphi-\frac{\pi}{2}\right) & 0 \\ -\sin\left(\varphi-\frac{\pi}{2}\right) & \cos\left(\varphi-\frac{\pi}{2}\right) & 0 \\ 0 & 0 & 1 \end{bmatrix}. \quad \text{(6-47b)}$$

The dynamic coordinate systems relating to the aircraft are a velocity-vector local horizontal (VVLH) Cartesian frame where X_{VVLH} is aligned with the velocity vector of the aircraft. Z_{VVLH} is parallel to the earth radial vector at the platform position (velocity vector defined level flight). Y_{VVLH} is then defined as (Z_{VVLH} x X_{VVLH}). For the case of no crab this is the aircraft left wing. The rotation to/from VVLH from/to an ENU system centered at the aircraft is a single rotation given by the heading angle (Figure 6.65b) defined against X_{ENU} in the classical polar sense and is given by

$$Rot_{ENU\_VVLH} = \begin{bmatrix} \cos(\phi_{heading}) & \sin(\phi_{heading}) & 0 \\ -\sin(\phi_{heading}) & \cos(\phi_{heading}) & 0 \\ 0 & 0 & 1 \end{bmatrix} \quad Rot_{VVLH\_ENU} = \begin{bmatrix} \cos(-\phi_{heading}) & \sin(-\phi_{heading}) & 0 \\ -\sin(-\phi_{heading}) & \cos(-\phi_{heading}) & 0 \\ 0 & 0 & 1 \end{bmatrix}$$

(6-48)

Antenna positions are defined in a Body-Centered Coordinate System (BCCS) Cartesian frame which defines X_{BCCS} as the aircraft longitudinal axis, YBCCS as the left wing, and ZBCCS the normal to the X_{BCCS}-Y_{BCCS} plane. This is shown in Figure 6.65c where the origin of this frame is shown at the position of the GEOHX unit. The translation between VVLH and BCCS is through the aircraft attitude rotation; pitch, yaw and roll. Roll was not instrumented and is not needed as all motions were small combined with large elevation beamwidths and the fact that reconstruction is not dependent on attitude (roll could be indirectly calculated through the angular turn rate and ground speed). Yaw was estimated (as described below) as part of the static compensation scheme, projecting the reference antenna phase center onto the main antenna phase center such that 0 degree phase/zero range were referenced to the main antenna. A static pitch angle was assumed,

based on pilot's experience with this aircraft and the rate of descent (100 ft/min, 0.508 m/sec). Rotation matrices to/from BCCS and VVLH are

$$Rot_{VVLH\_BCCS} = \begin{bmatrix} \cos(pitch) & 0 & -\sin(pitch) \\ 0 & 1 & 0 \\ \sin(pitch) & 0 & \cos(pitch) \end{bmatrix} \begin{bmatrix} \cos(yaw) & \sin(yaw) & 0 \\ -\sin(yaw) & \cos(yaw) & 0 \\ 0 & 0 & 1 \end{bmatrix}$$
$$Rot_{BCCS\_VVLH} = \begin{bmatrix} \cos(-yaw) & \sin(-yaw) & 0 \\ -\sin(-yaw) & \cos(-yaw) & 0 \\ 0 & 0 & 1 \end{bmatrix} \begin{bmatrix} \cos(-pitch) & 0 & -\sin(-pitch) \\ 0 & 1 & 0 \\ \sin(-pitch) & 0 & \cos(-pitch) \end{bmatrix}. \quad \text{(6-49)}$$

Antenna coordinates were covered in the calibration section (Section 6.2) but are revisited here briefly. The main antenna, placed in the forward port window, boresight was defined as the Y_{MAIN} axis with X_{MAIN} facing forward. Positive azimuth angle was defined from Y_{MAIN} into X_{MAIN} in the increasing positive sense (*e.g.* toward the aircraft nose). Hence the main antenna coordinate system is the same as BCCS and the no rotation is necessary (only care in computing azimuth). The reference antenna coordinate frame was arbitrarily defined using driven arm 1 of the crossed dipole as the X_{REF} axis with Y_{REF} aligned with the fuselage and azimuth angle defined X_{REF} into Y_{REF}. This is the opposite sense as the main antenna and results in 90 degrees for the main antenna and 270 degrees for the reference antenna defining the same physical direction with respect to the BCCS frame. Likewise 0 degrees main is equivalent to 180 degrees for the reference antenna.

6.4.3 ***Navigation data and data processing***. Navigation data were available from two sources, the Trimble GEOXH unit mounted on the aircraft glare shield (so located to maximize the view of the satellite constellations) and the XGPS160 which interfaced via Blue Tooth to an iPad to overlay measured position with the planned flight route. The XGPS160 was also positioned on the glare shield. Data were stored on both units and offloaded following the flight. The GEOXH via Cat-5/Ethernet cable and the XGPS160 via a somewhat roundabout means via email through the vendor and delivered via email. The XGPS160 data were translated into standard .kml format. The overall processing flow for the navigation data is shown in Figure 6.66.

The GEOXH data in native format were post processed using the Trimble GPS Pathfinder Office suite which was included in the lease package. This primarily consisted of turnkey operation of the differential correction. Three Washington State Reference Network (WSRN, http: http://www.wsrn3.org/About.aspx) Continuously Operated Reference Stations (CORS) ground locations were identified as part of test site selection, forming a rough equilateral triangle around the scene origin. The WSRN sites are listed in Table 6.11. Bearing is relative to East in the scene centered East-North-Up (ENU) frame. Static correction data was delivered and processed to produce very precise aircraft position estimates (code correction and carrier phase). The Trimble GPS Pathfinder tool assessment was that 99.07% of the data points from the imaging leg were within 5-15 cm absolute position accuracy (endpoints being those points which exceeded the accuracy

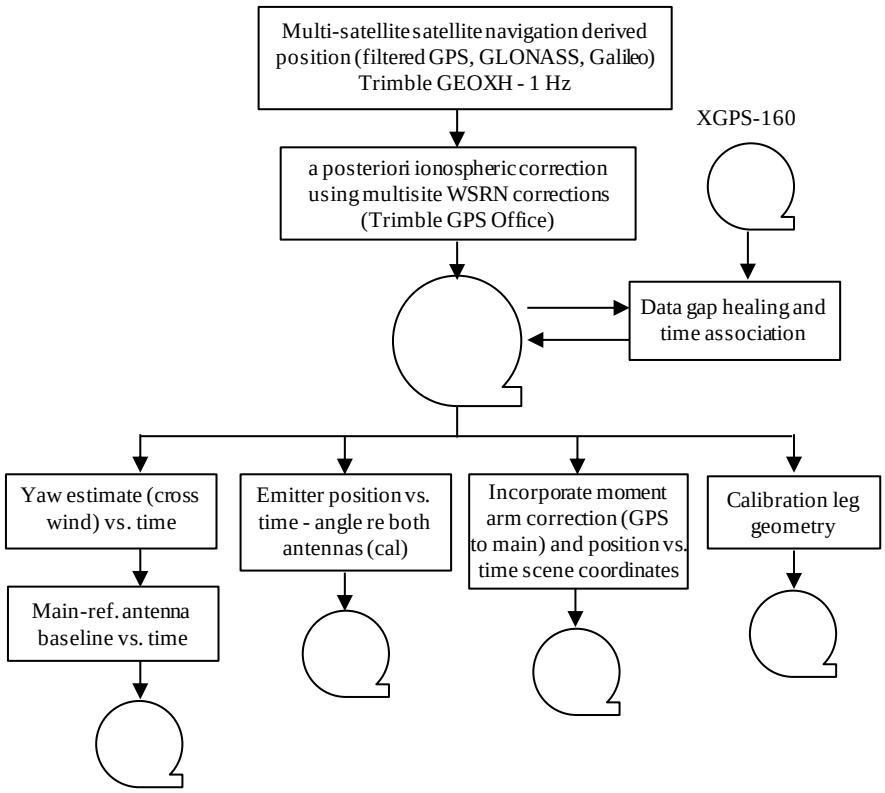

Figure 6.66. Navigation Data Processing

band). Again, these accuracies are specified in the horizontal plane. GEOXH data were exported to working text files but a problem was experienced getting time so the start time was derived by overlaying with the XGPS160 data. Also, as noted, there was a 4.6

second data gap in the GEOXH data which was filled using the XGPS160 data with the altitude adjusted to match the ionosphere-corrected result on both sides of the missing window. Ultimately this time period did not correspond to a reconstructed interval.

Station ID	Lat. (deg)	Long (deg)	Bearing	Range (km)
PFLD	47.898503	-122.282165	159.764	23.028
SSHO	47.682295	-122.315148	-146.393	29.024
LSIG	47.695197	-121.689826	-32.728	27.076

Table 6.11. Washington State Reference Network Sites

Specifics of the imaging collection aperture, as flown, are given in Figure 6.67. The full three dimensional aperture is depicted in Figure 6.67a, as flown as the descending cylindrical spiral. Range to scene center versus time is seen in Figure 6.67b with the ramp up after 2500 seconds occurring when the aircraft as exited the spiral pattern. The elevation extent of the aperture can be seen in Figure 6.67c. In total the aperture

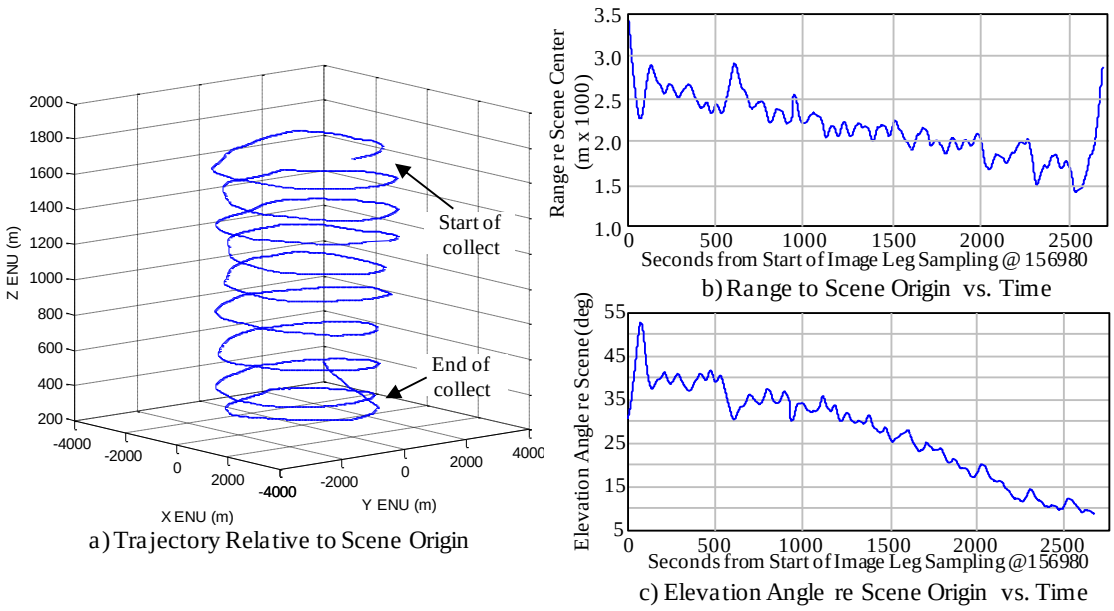

Figure 6.67. Collection Aperture Details

subtended 30 degrees relative to the scene origin. No IMU was available (again power limits) and both units provided GPS position at 1 Hz rates. The winds aloft (forecast and experienced) were high and introduced a significant yaw as a function of position. GPS unit velocity was derived by differentiating the position data. This yielded a velocity vector and speed estimate, the latter shown in Figure 6.68a as a function of time. The points on each orbit which produced maximum and minimum speed align with flight

directly upwind and maximum directly downwind (zero yaw case), giving the wind bearing (Figure 6.68b). The assumption of a uniform wind velocity field over the intervals between minimum and maximum, and using the average speed over the orbit, then allowed estimation of the wind speed as a function of altitude (Figure 6.68c). The vector difference between GPS-derived velocity and the vector wind field gave the yaw estimate and is shown in Figure 6.69.

In Figure 6.69a the heading derived from the velocity vector, after unwrapping, is plotted along with the estimated heading of the aircraft body (the angle between X_{BCCS} and X_{scene} against time during the imaging leg. The scale does not adequately highlight the differences so Figure 6.69b is that difference, again plotted versus time.

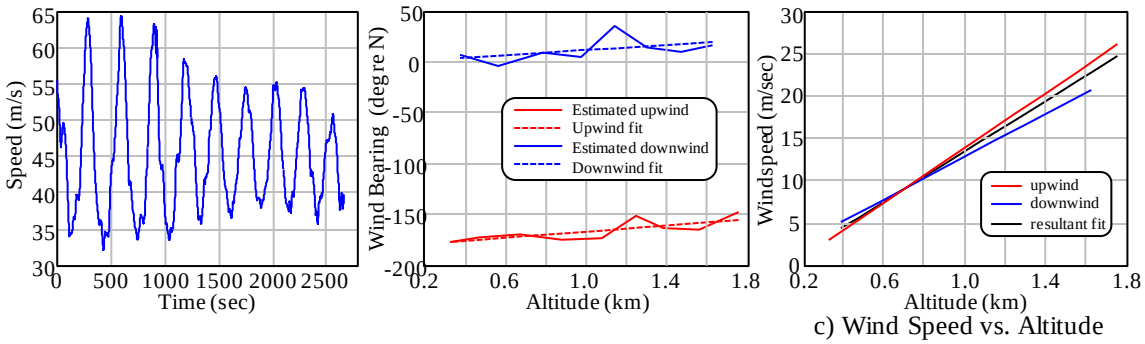

c) Wind Speed vs. Altitude

Figure 6.68. Wind Vector Estimation for Imaging Leg

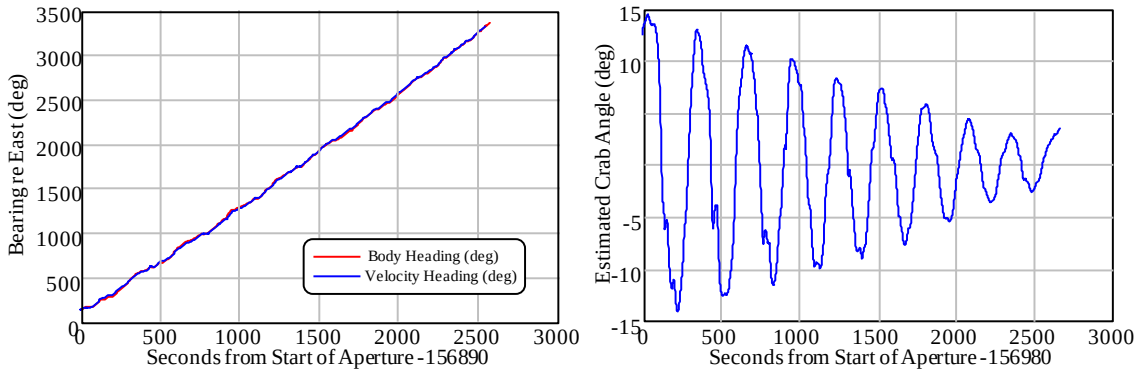

a) Unwrapped Heading vs. Time (deg)

b) Estimated Crab Angle vs. Time (deg)

Figure 6.69. Final Wind Vector Estimation for Imaging Leg

This function is used as a correction for the projection of the reference antenna onto the man antenna as part of the calibration process (delta range). The derived wind field was also tested against the calibration leg which flew a constant radius arc to allow estimation

of any channel to channel mismatches in the receiver active electronics. The derived antenna separation as projected onto the transmitter radial through the main antenna is shown in Figure 6.70. The horizontal axis is seconds from the start of GPS recording (155220 sec) and includes the calibration leg; the approximately 550 second interval ending at 1500 seconds. Positive range indicated the main antenna is farther downrange, relative to the transmitter, than the reference antenna.

6.4.4 *Signal processing*. This section describes preparation of the recorder flight data for reconstruction. The overall flow of processing steps is shown in Figure 6.71, followed by detailed description of each step. The dual N200 receive system supplied sampled complex voltages. The received signals in both channels were output from the FPGA as32 bit complex words (16 I and 16 Q), decimated to an equivalent sample rate of 10 million complex samples per second. The synchronously sampled data were stored in a continuous file in binary format. Sample time of the first sample of the first packet (363 samples) was stored with each burst.

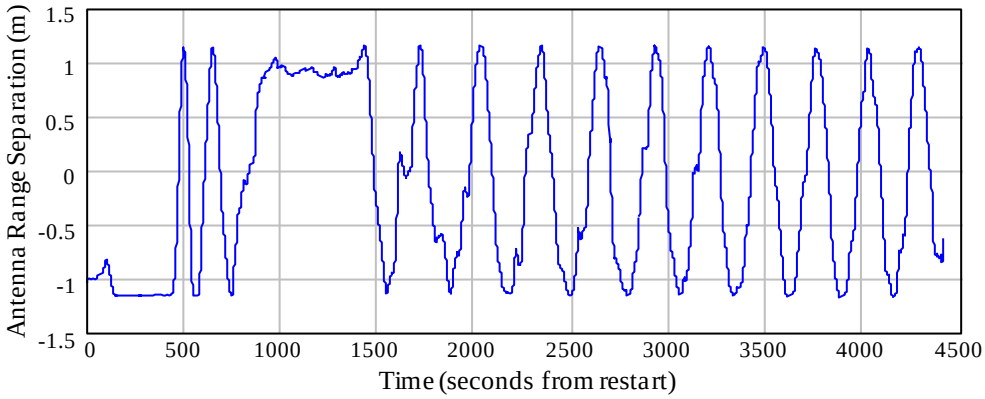

Figure 6.70. Main-Reference Antenna Projected Separation vs. Time

All processing was performed in MATLAB release 7.0.4 and the majority of the signal processing accomplished within a single script file. The overall strategy was the application of static corrections, electrical and spatial, to produce a compressed range (delay) profile that was referenced to the phase center of the main antenna. With this and

navigation/position data also reference to the main antenna reconstruction would be facilitated.

As shown in Figure 6.70, the processing is performed burst-to-burst over specific time intervals within the overall data set, and is predominately in the frequency domain. Input data are converted from binary to complex format and forward transformed. To eliminate the out-of-band power a binary, rectangular mask filter is applied (a filter-wise multiply); defined as 1 over the spectral extent to the transmit channel and zero elsewhere. The measured transfer functions of the individual channel analog RF cables and band-pass filters are then used on the zero forcing sense to normalize out insertion loss and phase, as was described in section 6.2. Transmitter position as a function of time, quantized to the sampling resolution of the indoor range measurements (15 degrees) was then used to load

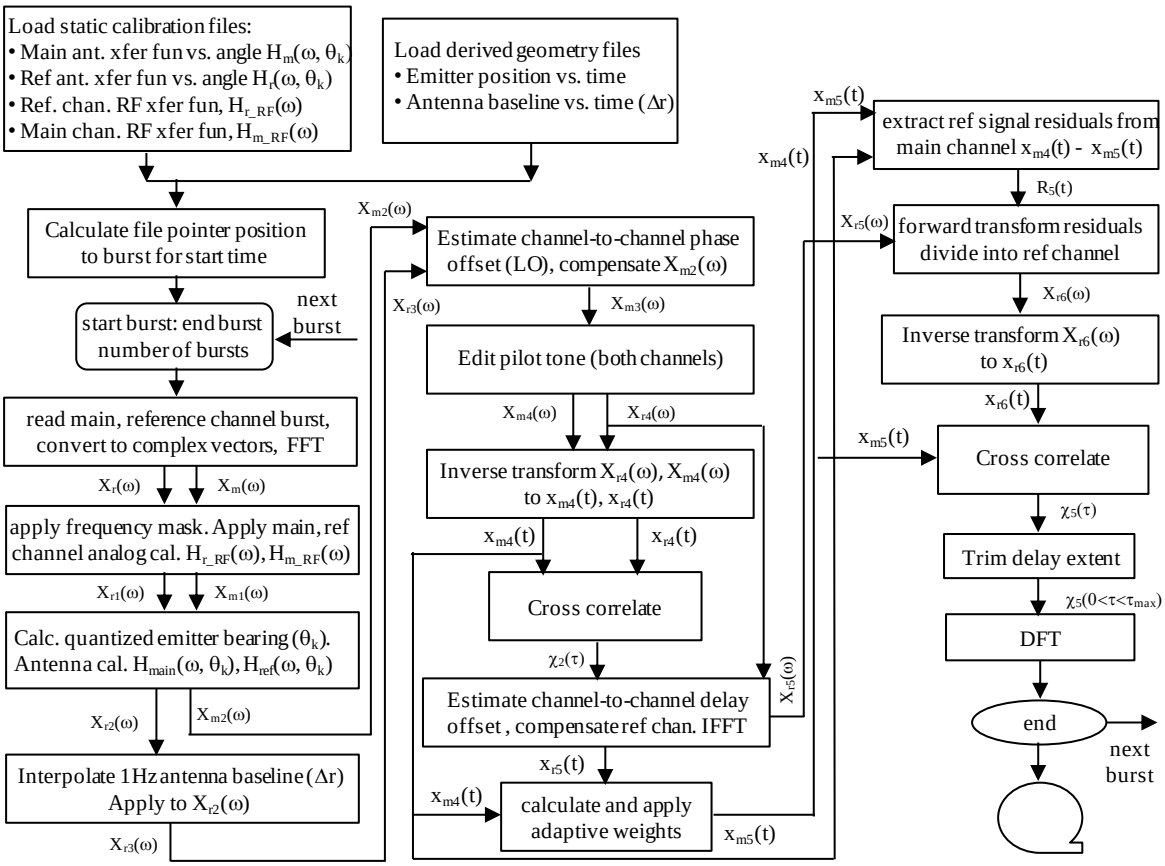

Figure 6.71. Signal Processing Flow Diagram

the proper antenna transfer functions which were also applied to the sample spectra. Sample HDTV spectra where given in Figure 5.2.

$$X_{m2}(\omega) = \frac{X_m(\omega)}{H_{m\_RF}(\omega) H_{main}(\omega, \theta_k)} \quad \text{and} \quad X_{r2}(\omega) = \frac{X_r(\omega)}{H_{r\_RF}(\omega) H_{ref}(\omega, \theta_k)} \tag{6-50}$$

At this point the signals were (or should have been) referenced to the phase centers of the respective antennas. With identical digital receivers and with identical software loads, the group delay from A/D to decimated data samples should have been identical as well. The calibration section results showing no relative contribution (group delay), confirming the expectation, and only a slight difference in channel-to-channel amplitude match. This left the compensation of the (dynamic) spatial separation of the antennas. Using the measured moment arms relative to the GPS unit location (a challenge to measure manually and in the small cockpit) the separation was calculated off line at the GPS sample times then interpolated using the MATLAB *interp1* function to the sample burst time. The reference antenna was projected onto the main antenna as in equation 6-51.

$$X_{r3}(\omega) = X_{r2}(\omega) e^{-j\omega\Delta r} \tag{6-51}$$

The RF reference is coherent across the two channels, implemented via the MIMO cable, but the tuners in each receiver initialize to a random phase relative to each other when the collection program is run. Coherency is maintained through the master clock/oscillator resulting in a constant phase offset for the duration of the collection run. To compensate for this, which could result in a deterministic range error, the phase offset was estimated as the mean difference between the phases of both spectra and applied to the main channel spectrum in manner analogous to equation 6-51.

The pilot tone can clearly be seen in the burst spectrum, typically some 15-20 dB above the mean signal level (*e.g.*, Figure 5.2). If the pilot tone is not removed then close-in, periodic correlation sidelobes might result. The pilot tone location is exactly known per the regulatory signal definition. The approach taken to edit (filter) the pilot tone was to zero 21 filters, centered on the tone frequency, were set to 0 and replaced with a complex random value. In each filter the magnitude was Gaussian drawn using a mean magnitude

estimated over the 1 dB defined (regulatory) bandwidth (some 6000 points) and using a uniformly distributed in phase.

Pilot tone editing was followed by inverse transforming both channels to the time domain and performing the cross correlation (MATLAB function xcorr). Though this could have been done in the frequency domain directly, because fftshift was used to order the spectrum naturally around zero frequency the (perhaps) more roundabout method was used for bookkeeping. Examination of the immediate region around zero delay indicated that a residual delay remained between the two channels after calibration. An adaptive estimator was developed that exploited the triangular response of the points in the immediate region of 0 delay (the combined amplitude and phase modulated 8VSB was not as well behaved as the PN code, as discussed in Section 5.0, but $\pm$ 2 samples were reasonable well represented). On each burst the range offset of the peak response from the 0 range sample index was estimated and applied to the reference channel spectrum, $X_{r4}(\omega)$, in the same manner as equation 6.51, with the delay estimate replacing Δr. This result was again forward transformed (after reversing the fftshift).

In Section 5.1 the problem of the direct path leakage and the impact associated with the time sidelobes masking small signal returns was addressed. The use of an adaptive sidelobe canceller was identified as a means to cancel the reference signal received in the backlobes of the main antenna. A Generalized Sidelobe Canceller (GSC) was developed for this purpose. As the data was processed, and there were no computational restrictions, the entire sample segment of the reference channel burst was used for training using Sample Matrix Inversion (SMI). The covariance matrix estimate being given by

$$\hat{R} = \frac{1}{N}\sum_{n=0}^{N-1}\begin{bmatrix} x_{m4}(n) \\ x_{r5}(n) \end{bmatrix}\begin{bmatrix} x_{m4}(n) & x_{r5}(n) \end{bmatrix}^{*} \tag{6-52}$$

where the subscripts are referenced to Figure 6.70, N is the number of samples in the burst (=10164) and * represents complex conjugation. $\hat{R}$ is a 2 × 2 matrix. The adaptive weights are determined using

$$W_{un} = \hat{R}^{-1}\begin{bmatrix}1\\0\end{bmatrix} \qquad \text{followed by} \qquad W_n = \frac{1}{\sqrt{W_{un}{}^H W_{un}}}. \tag{6-53}$$

In (6-53) the subscript '*un*' indicated un-normalized. The adaptively cancelled main channel is then the vector product of the row vector with the input data and the column vector containing the weights

$$x_{m5}(t) = \left[x_{m4}(n) \quad x_{r5}(n)\right] W_n \tag{6-54}$$

Taking the cross correlation of the fifth stage main and reference channels produces the compressed pulse range profile. Figure 6.72 is an example over the full range of the cross correlation. Each delay increment is approximately 30 m so the total range extent is equivalent to ~300 km. Ground returns are clearly seen at positive delays.

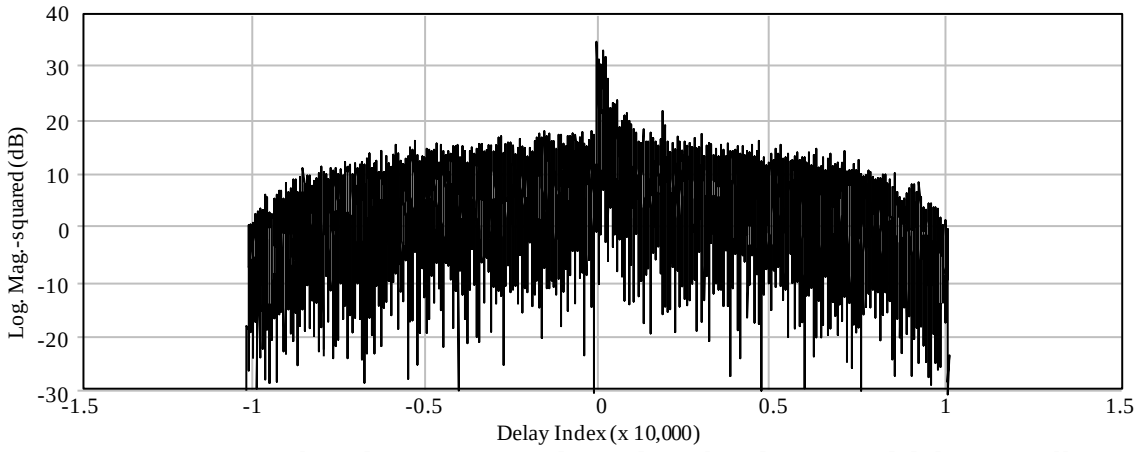

Figure 6.72. Example Pulse Compressed Result with Adaptive Sidelobe Canceller

Two bursts from the highest orbit were randomly selected to illustrate the effects of the adaptive canceller on the compressed data. Both magnitude and phase effects are shown. Burst 115 from the 157230 (GPS time) segment is shown as Figure 6.73a contrasting the uncancelled result (red trace) to cancelled (blue). A second burst some 18.6 seconds later appears as Figure 6.73b. The delay axis is truncated to an equivalent bistatic range delay of 6500 meters. The degree of channel amplitude and phase matching that was achieved

was sufficient to provide a cancellation ratio on the order of 30 dB, as observed by the ratio of the cross correlation at 0 delay between the two cases. Calculating the average

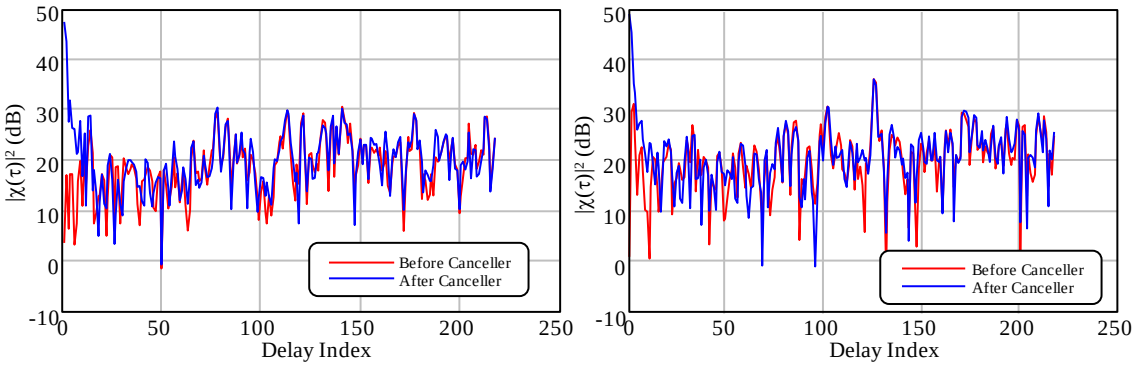

a) 157230 25 sec (burst 115) b) 157230 25 sec (burst 487)

Figure 6.73. Comparison of Compressed Result with and without Canceller – Magnitude

cancellation ratio over the approximately 12,000 bursts used for the three dimensional aperture yielded 24.86 dB. 1160 bursts from orbit 1 (the highest altitude orbit) were processed to estimate the average time sidelobe level for the 8VSB waveform fragments sampled. 1500 negative delay (no ground return), compressed values were extracted, for each burst, starting 150 samples from the zero delay index using the non-adaptively processed compressed burst. The mean sidelobe level, referenced to the cross correlation peak, was calculated to be nearly -33 dB. The ground returns in the examples in Figure 6.73 are in the approximate range 12-17 dB above the mean interference floor derived from the sidelobe cancelled (compressed) results. The mean sidelobe level of the cancelled bursts was only slightly reduced at -32.3 dB relative to the peak of the uncancelled cross correlation product.

The phase responses over the same delay interval are shown in Figure 6.74, for the same bursts. In these examples the effect of the removal of the direct path leakage contribution can be seen prevalently at short delays with the effect decreasing with delay. The mechanism is believed to be the high, close-in time sidelobes without the canceller

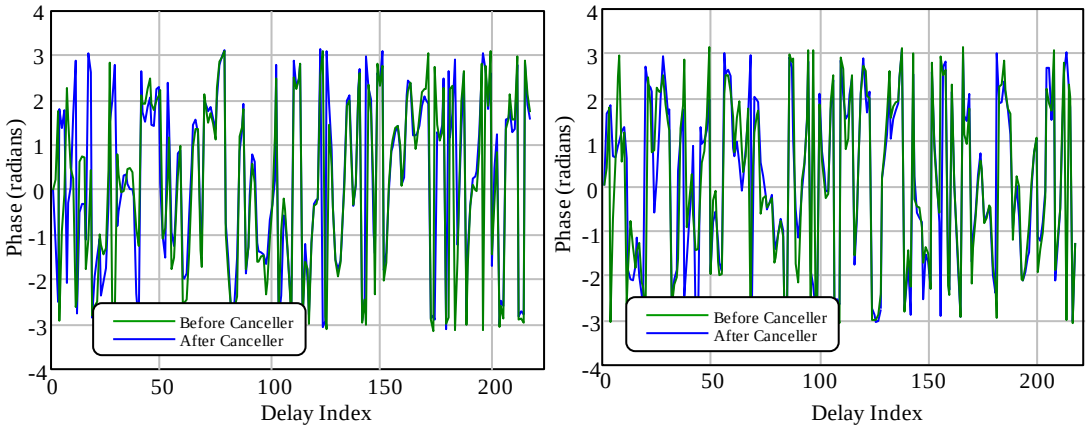

a) 157230 25 sec (burst 115) b) 157230 25 sec (burst 487)

Figure 6.74. Comparison of Compressed Result with and without Canceller - Phase

Initial attempts at image reconstruction using the compressed pulse result were failures. The images were essentially noise-like, indicating incoherent input data. Returning to Section 5.1, the analytic development of the compressed pulse result using the HDTV waveform indicates that the compressed pulse phase at zero delay should be 0 (equation 5-8), which can be seen by letting the range difference term go to zero representing both antennas at a common phase center with no group delay mismatch. Evaluation of the phase of the uncancelled compressed bursts at zero delay found a nonzero initial value and what could be described as a random phase from burst-to-burst (note that the examples in Figure 6.73 had the adaptive correction applied and so do not exhibit this behavior). The analysis devolved into an evaluation of the system coherency and search for potential unknown modulations that might have introduced a channel-to-channel non-stationarity, or temporally variant mismatch.

As has been noted there was a significant leakage of the transmitter signal into the main channel. This contribution was effectively removed by the adaptive canceller, as demonstrated. The reference signal component in the main antenna signal exhibits the antenna offset and cabin propagation environment and main channel and receiver response. It is possible to isolate this component by subtracting the post-cancelled result, $x_{m5}(t)$, from the pre-cancelled signal $x_{m4}(t)$, the difference being the leakage signal

weighted by the main channel response. This residual was then forward transformed and divided by the reference channel spectrum at that stage of processing ($X_{r5}(\omega)$). The phase as a function of frequency over the channel spectrum was calculated and applied to the reference channel spectrum, followed by inverse transformation, or

$$x_{r6}(t) = \Im^{-1}\left(X_{r5}(\omega)e^{j\phi_{residuals}(\omega)}\right) \text{ where } \phi_{residuals}(\omega) = angle\left(\frac{\Im(x_{m4}(t) - x_{m5}(t))}{X_{r5}(\omega)}\right)^{-1} \quad (6\text{-}55)$$

This process aligned the reference signal with the main channel. The final cross correlation was performed, the delay extent was trimmed from 20328 to 218 points (0 to 6500 meters range difference) for the adaptively cancelled case ($\chi_5(\tau)$) and 224 points for the nonadaptive case (5 negative delay points were retained around the zero delay peak). In preparation for reconstruction the truncated range strobes were forward transformed using a DFT and the results written to disk file with GPS time on a burst-to-burst basis.

The results for zero range delay phase angle are presented for all 9 orbits over the azimuth windows selected for processing in Figure 6.75. The phase errors after pulse compression at the zero delay range are listed in Table 6.12. These values are influenced on each orbit

Orbit Number	RMS phase error	Orbit Number	RMS phase error
1	0.0020842 rads	6	0.0010135 rads
2	0.00085015 rads	7	0.0017481 rads
3	0.0020417 rads	8	0.0014198 rads
4	0.0016919 rads	9	0.0019071 rads
5	0.0024804 rads		

Table 6.12. RMS Zero Delay Phase Error Summary by Orbit

by a relatively short duration (in the angular sense) somewhat repeatable. This can be seen from the plot sequence in Figure 6.75, representing the zero delay phases for each burst, over the processed duration of the orbit segment. The results all show a residual phase error burst which is approximately an order of magnitude more severe than the majority of the processed interval. Reploting the zero delay phase against aircraft heading indicates that the burst occurs when the heading is between 30-40 degrees south of east;

around 30 degrees on the higher orbits (which exhibit a higher crab angle) increasing to 40 degrees SE (-40 deg re the scene ENU) in the lower orbits (Figure 6.69). Under the hypothesis that the aircraft was contributing or the source of the effect the position of the transmitter was considered with respect to the antennas at these heading angles. The peak effect occurs in the region 40-50 degrees to the right of the aircraft nose (Figure 6.76b). The line of sight to the transmitter does not pass through the propeller (Figure 6.76a); however some scattering may be occurring due to the propeller shape/angles toward the tips. The phase difference may result from scattering only into a single channel.

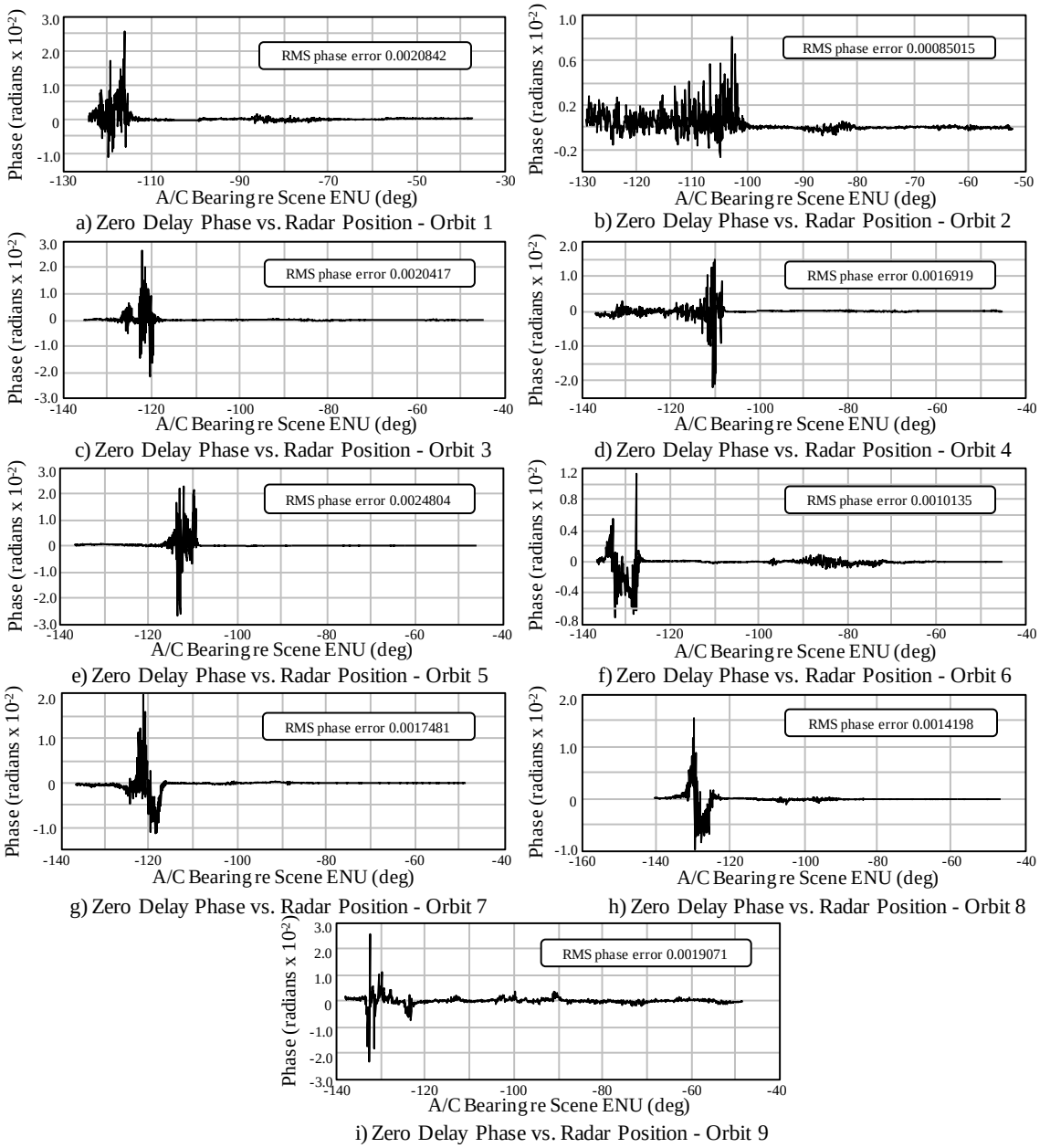

Figure 6.75. Zero Delay Phase vs. Orbit/Position

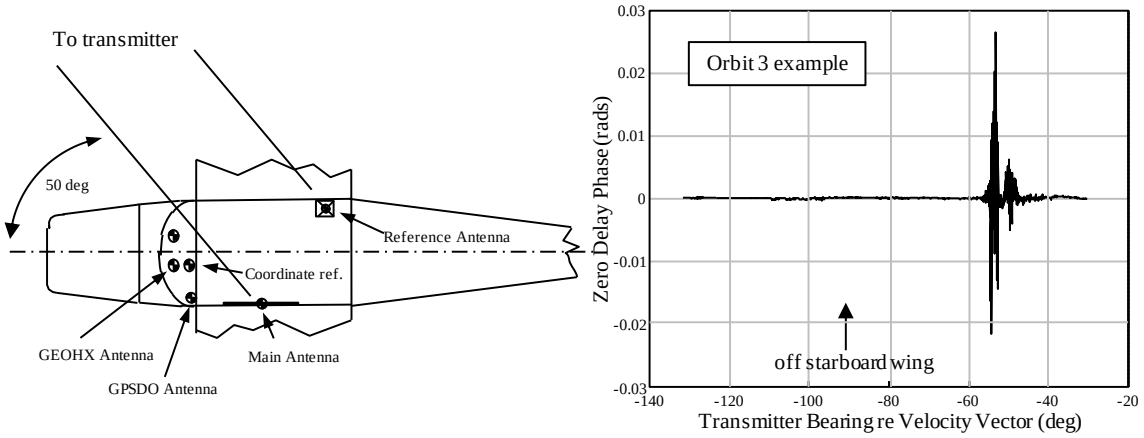

a) Antenna-Transmitter Geometry b) Phase Noise vs. Transmitter Bearing

Figure 6.76. Geometry of the Phase Artifact

6.5 Image Reconstruction.

The bistatic tomography simulation functions in MATLAB were adapted for reconstruction with only minor changes. Most notable was the interpolation (via cubic spline) of the 1 Hz GPS position-time data to match the sample time of the first ADC sample of each burst. Pulse compression processing was performed over an angular segment of each orbit, as detailed in the last section. The segment was defined semi-symmetrically around the transmitter-scene center vector; each segment is approximately 90 deg in extent when measured in the "plane" of the orbit (*e.g.*, polar angle ignoring the height component). The processed segments are shown graphically in Figure 6.77 with three views, and in tabular form in Table 6.13. In the table degrees are rounded to the nearest 0.01 deg and GPS time to the nearest millisecond. The azimuth values are relative the scene-based ENU coordinate frame.

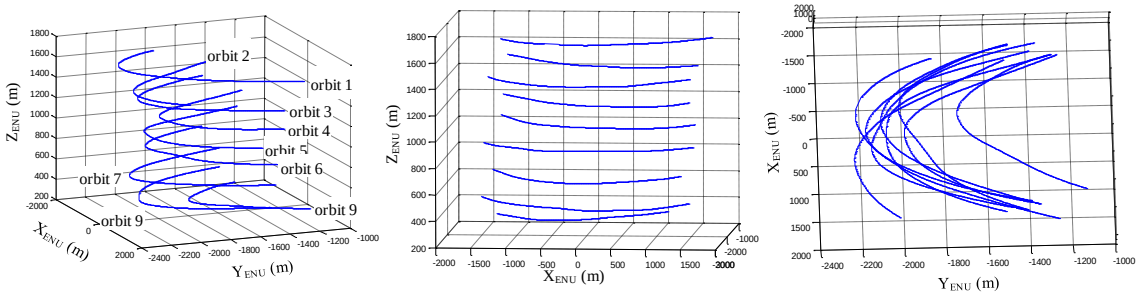

Figure 6.77. Processed Segments of Full Aperture

The azimuth regions, portions of each orbit, where the reference antenna pattern covers the sidelobes and backlobes of the main antenna (the adaptive sidelobe canceller condition), as seen in Figure 6.63, are identified in Table 6.14. The shorter aperture segments were further motivated by processing speed limits and image formation time (a

Orbit Number	Start Az. (deg)	Start El. (deg)	Start Time (sec)	End Az. (deg)	End Az. (deg)	End Time (sec)
1	-124.3	36.72	157200.785	-33.33	38.052	157263.299
2	-129.13	38.05	157495.029	-51.99	30.278	157557.045
3	-135.42	32.5	157806.210	-44.91	34.544	157871.205
4	-136.83	29.19	158095.904	-45.18	30.978	158158.921
5	-136.66	21.41	158364.455	-46.14	25.361	158433.471
6	-136.59	21.41	158647.247	-44.88	22.18	158718.245
7	-136.52	17.51	158925.773	-48.49	17.644	158994.791
8	-140-11	11.43	159192.545	-46.82	11.187	159263.601
9	-138.03	8.64	159459267	-48.36	11.152	159518.267

Table 6.13. Processed Orbit Segment Details

126 by 126 by 100 voxel aperture at 0.3048 m spacing required a 9 day continuous run time in MATLAB). An examination of the arc segments in terms of the height change over the processed portion indicates that 20-40 m of elevation change was occurring (Figure 6.78), with the exception of the last, which would serve to sample the vertical

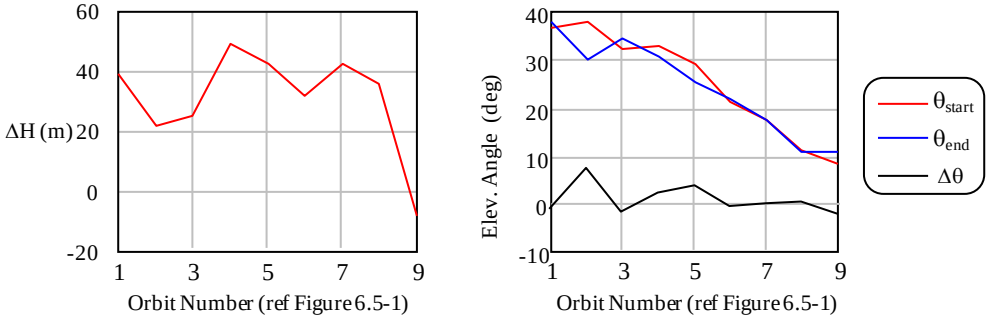

a) Aircraft Alt. Δ over Aperture Seg. b) Elev. Angle Δ over Aperture Seg.

Figure 6.78. Elevation Angle Subtended for each Orbit Segment

aperture along the slant descending path. However, when the actual trajectory is converted to elevation angle the change with respect to scene center, the angle subtended during the processed portion, diminishes. This is the result of the platform horizontal

position changing over the orbit segment.

Orbit Number	Start Az. (deg)	Start El. (deg)	Start Time (sec)	End Az. (deg)	End El. (deg)	End Time (sec)
1	-166.362	37.615	157160	10.339	35.774	157292
2	-157.187	36.842	157470	-6.492	29.1	157592
3	171.805	33.692	157755	19.141	29.945	157908
4	178.77	30.15	158055	4.81	29.003	158188
5	-165.853	27.459	158340	15.388	24.909	158473
6	-160.074	22.674	158625	-8.572	21.632	158742
7	178.355	17.864	158885	8.47	18.121	159027
8	-159.57	12.427	159175	-17.05	12.687	159282
9	-143.277	8.776	159455	13.049	9.847	159552

Table 6.14. Times and A/C Position where ASC Condition Met

6.5.1 ***Two dimensional reconstruction***. To test the input data and reconstruction a shorter aperture was processed to a two-dimensional image. Using a 25 second segment of orbit 1 which was approximately centered about the scene-transmitter baseline a two dimensional image was reconstructed at the focus height equal to that of the center of the scene (steering is done in scene coordinates which are connected to WGS 84 through the scene origin coordinate). The scene center is the estimated center of the target grain silo as depicted in Figure 6.52. This geometry represents an aperture angle of 42.645 deg (polar angle subtended projected into X-Y plane) while the vector difference of the starting and ending positions yields a total angle of 33.67 deg. The reconstructed image is shown in Figure 6.79b. The elongation was expected due to the low resolution waveform. To confirm the result, the flight GPS data was used as truth and a simulated signal generated (as in Section 5) and reconstructed. The simulated point spread function appears in Figure 6.79a. Both Figures 6.79a and –b are intensity plots with a linear scale and normalized to the largest scene pixel. Principal cuts taken along the image X- and Y-axes for the real and simulated image are shown in Figures 6.79b (along Y) and 6.79d (along X). The overlay was manually generated and is shown in Figure 6.79c.

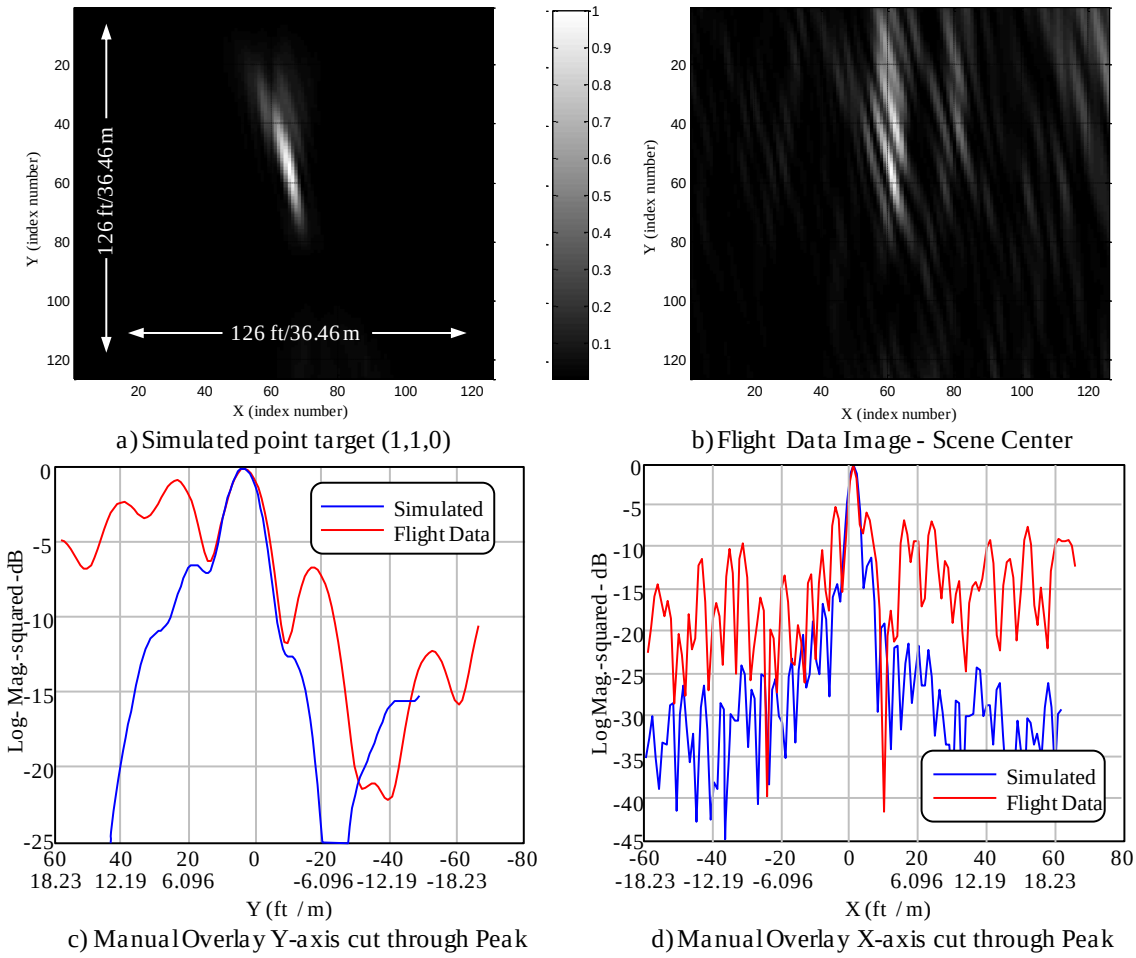

a) Simulated point target (1,1,0)

b) Flight Data Image - Scene Center

c) Manual Overlay Y-axis cut through Peak

d) Manual Overlay X-axis cut through Peak

Figure 6.79. Test Image 25 Second Test Aperture Orbit 1

Resulting resolution was estimated along the cardinal axes in image coordinates, not in the along-range direction suggested by the 14 degree rotation of the primary response (this angle graphically estimated. Though resembling bistatic SAR imaging modeled by Soumekh (with a stationary transmitter and wideband, CW, noise waveform) in [162], this apparent rotation is a combination of the fact that the transmitter is slightly offset from scene Y as well as descending. A linear fit to the synthetic aperture X-Y trajectory yielded a value of 12.75 deg between the synthetic aperture and the scene coordinate frame. The slight aperture asymmetry with respect to the transmitter position at -87.4 degree polar angle in scene coordinates also contributes to the rotation. The resolution projection along Y_{scene} (more downrange) is 3.679 m/12.069 ft while the projection along X_{scene} is 0.793 m/2.602 ft (more cross range). In Section 4.7 (eqn. 4-38) monostatic resolution approximations were suggested for partial apertures in two dimensions (based

on a CW waveform). Degrading by a factor of 0.5 for the stationary transmitter suggest a cross range resolution of the order of 0.6 m. Alternatively, [163] offers the (monostatic) expression

$$\delta_{xr} = \frac{\lambda}{4\sin\left(\Delta\theta/2\right)} \tag{6-56}$$

where $\Delta\theta$ is the angle at the target subtended by the aperture. Dividing (6-56) by 2 for the stationary transmitter yields a cross range value of 0.71 m for the 25 second test aperture.

The expected form of the IPR is an "hourglass" shaped response with the constriction at the point of peak response along the response axis representing the longest projection of the sampling aperture (*cf* [165]). For monostatic SAR and the bistatic case where the collection aperture is symmetric with respect to the transmitter line of sight the long axis of the IPR is parallel to the aperture bisector or, in the bistatic case, the line of sight from the transmitter to the scene. As the bistatic aperture departs from the symmetric case, the IPR exhibits a rotation (noted above) with the direction and angle reflecting the degree of asymmetry. Further, the shape of the IPR is a function of position within the scene. Model results, which are not presented, demonstrate a positive rotation (in the scene polar angle sense) when the pixel is located at x>0 and a negative rotation for the converse. With a large scene, and short range to scene center from the receiver, we experience a spatially variant resolution over the scene; the projected aperture angle is greater for pixels at shorter range (y<0) and reduced for pixels at y>0. Finally, receiver descent over the collection aperture induces additional rotation of the IPR.

This result in Figure 6.79 gave confidence that the images were coherently focusing and that the upsampled navigation data were of sufficiently low error. To further build confidence, we then continued by processing the full angular extent of each of the 9 orbits to a set of two dimensional images. The scene size was small (+/- 19 m in both dimensions) centered on the silo position from Figure 6.52. The same approach was used

as Figure 6.79; a simulated image was generated using the actual (upsampled GPS) flight trajectory, to create an expected point spread function, followed by the flight data reconstructed image. Each orbit processed result is represented by 4 plots: the simulated point spread function on both linear and logarithmic magnitude scales, followed by the images derived from flight data, also plotted using both linear and logarithmic scales. All the runs (the individual orbit segment processed) were over the same geometry but there was a slight mismatch in the height of the focus plane. The simulated target was placed in the scene at (1, 1, 0) but the focus height was 14 m. The selected focus height was an error, discovered after the fact. The terrain elevation at scene center is 14 m but all the focus height (and trajectory data) is referenced to the scene origin, removing this contribution.

The results are presented in 9 sequential Figures, Figures 6.80 through 6.88 on the following pages, representing orbits 1 through 9. The use of trajectory as-flown (and as interpolated) incorporates the exact trajectory into the phenomenology simulation, removing position/navigation as an error source in the reconstructed point spread function. The differences then, between the simulated as-flown and the actual flight data include any aircraft parasitic scattering effects, errors in pulse compression and phase errors resulting therein (Section 6.4), and other environmental effects. The low contrast of the back projection algorithm, and aperture contributions, can be seen in the logarithmically scaled images.

To check the IPR for the focus height correctly set at the scene ground level; all 9 2D images were rerun, both the simulated data and the flight data, though over a smaller area. A scene size 31 pixels on a side, samples at 0.3048 m spacing were rerun with the focus height (Z) set to 0. Each of the 18 image chips is approximately 9.5 meters on a side and appear as pairs in Figure 6.89 with a) corresponding to orbit 1 (the highest) and i) orbit 9. The full-width, half-maximum of the simulated point target responses for each orbit was

then estimated. Because the image was normalized to unity peak magnitude, and because the simulated target was not placed at a location that would not straddle when sampled spatially, the results are approximations. In addition, the IPR resolution (FWHM) was estimated from the focused flight data image chips in Figure 6.89. The results are summarized in Table 6.15. It is clear that the images are focusing from both the IPR responses and the calculated resolutions.

The images presented in Figures 6.80 through 6.88 were, to a degree, unexpected, exhibiting no resemblance to that from the Google Earth overhead image of the test scene (Figure 6.52). The metal-walled, and roofed, buildings can be expected to scatter specularly. The very low grazing angle of the illuminator at vertical wall and the lowest orbit altitude means that the receiver avoids the flat plate responses, though a large return is seen at the lower orbits may be the larger metal barn in that location. Heavily rusted, corrugated metal comprises the exterior of the older structure to the west, anticipated to further diffuse the return. It was thought that the horizontally polarization and (thin wire equivalent) horizontal roof edges might provide a visible return but none is observed. The silo was expected to focus somewhat to a point given the symmetry (though it is segmented), and there are such observed at/near scene center, and that the silo cap would exhibit the ~24 m height in the 3D imagery. Finally, substantial shadowed areas were also expected, again because of the low grazing angle of the incident energy. The poor contrast (IPR sidelobes) resulting from using back projection may be masking such. The logarithmic scale simulated IPR results clearly exhibit the hourglass response noted earlier. However the as-flown simulations, which reflect the measured trajectory, indicate an imbalance. First the near range and far range nulls are unequally distant from the peak response (more than a factor of 2) and that the intensity (sidelobe levels) are asymmetric. The asymmetry can be seen, or appears to be more evident, in Figures 6.80a-6.88a than Figure 6.89, but where it is still observable. This will be explored in more detail later.

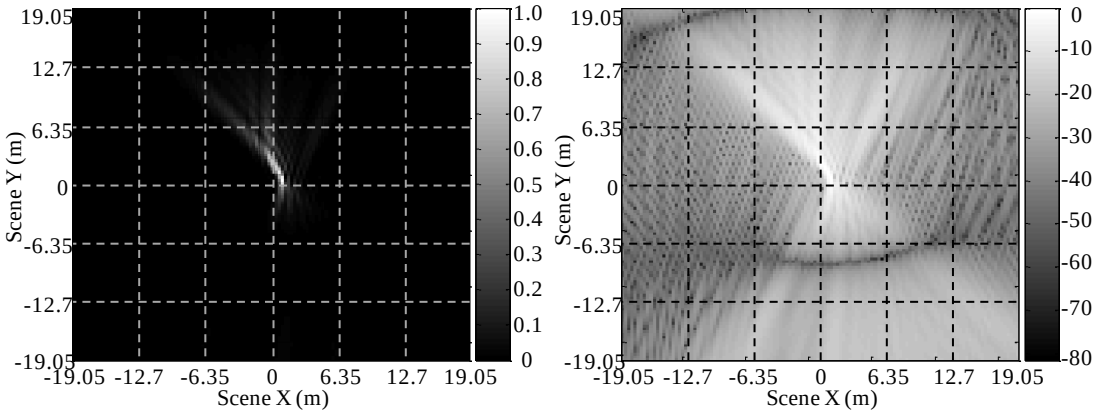

a) Orbit 1 Simulated PSF - Linear

b) Orbit 1 Simulated PSF - Log-Magnitude

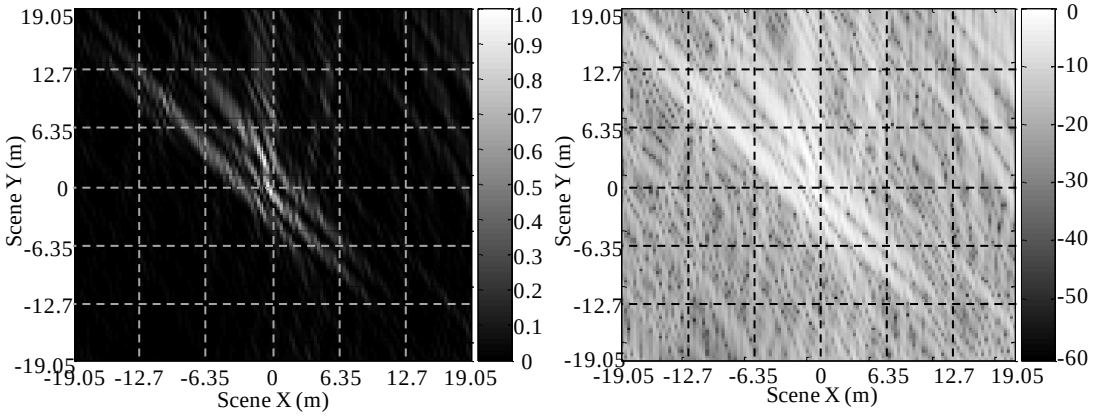

c) Orbit 1 Flight Image- Linear

d) Orbit 1 Flight Image - Log-Magnitude

Figure 6.80. Orbit 1 2D Reconstruction: Simulated As-Flown and Flight Data

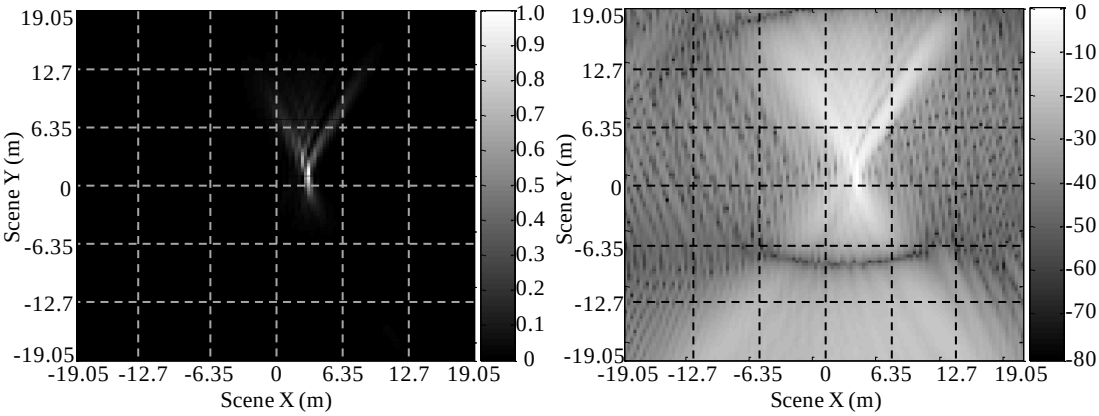

a) Orbit 2 Simulated PSF - Linear

b) Orbit 2 Simulated PSF - Log-Magnitude

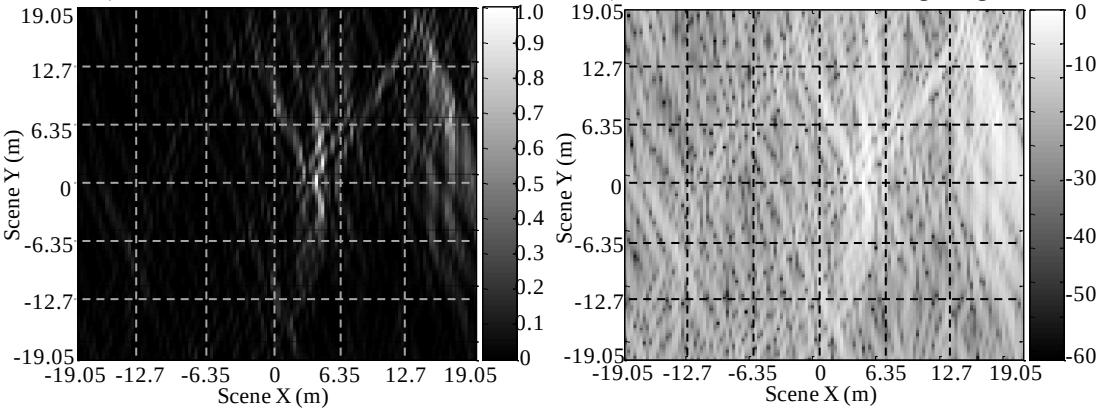

c) Orbit 2 Flight Image- Linear

d) Orbit 2 Flight Image - Log-Magnitude

Figure 6.81. Orbit 2 2D Reconstruction: Simulated As-Flown and Flight Data

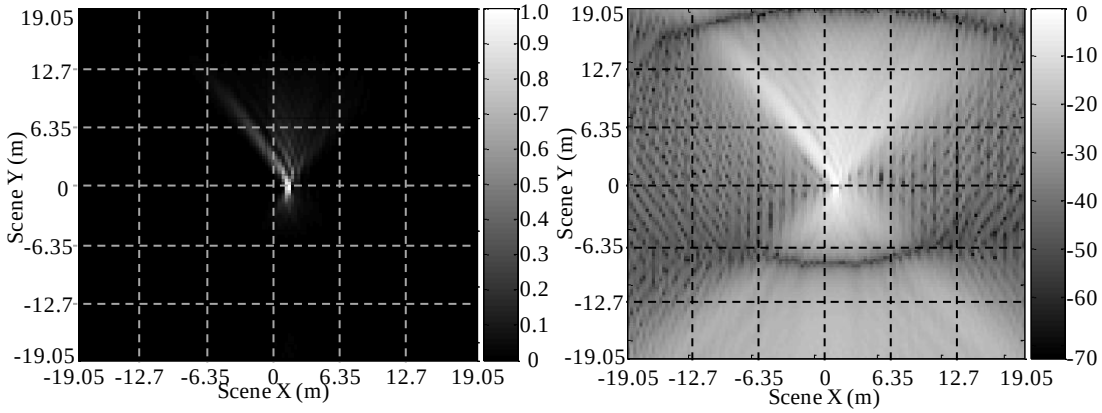

a) Orbit 3 Simulated PSF - Linear

b) Orbit 3 Simulated PSF - Log-Magnitude

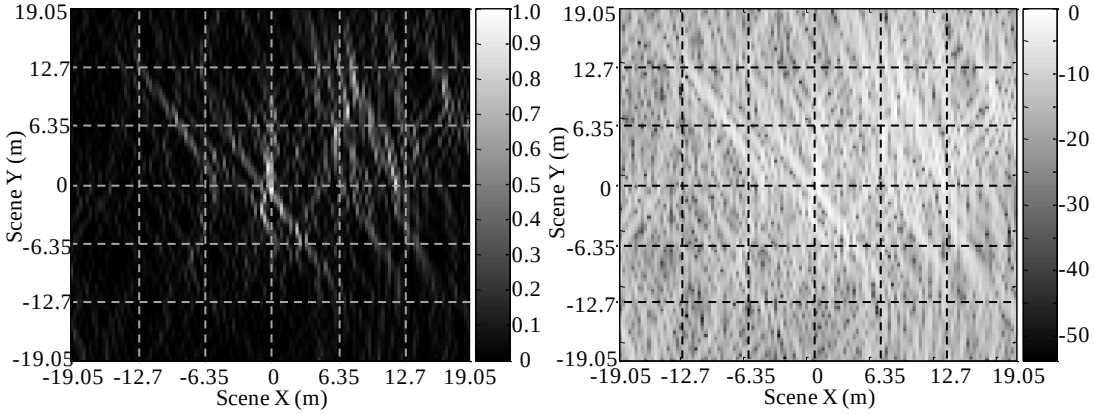

c) Orbit 3 Flight Image- Linear

d) Orbit 3 Flight Image - Log-Magnitude

Figure 6.82. Orbit 3 2D Reconstruction: Simulated As-Flown and Flight Data

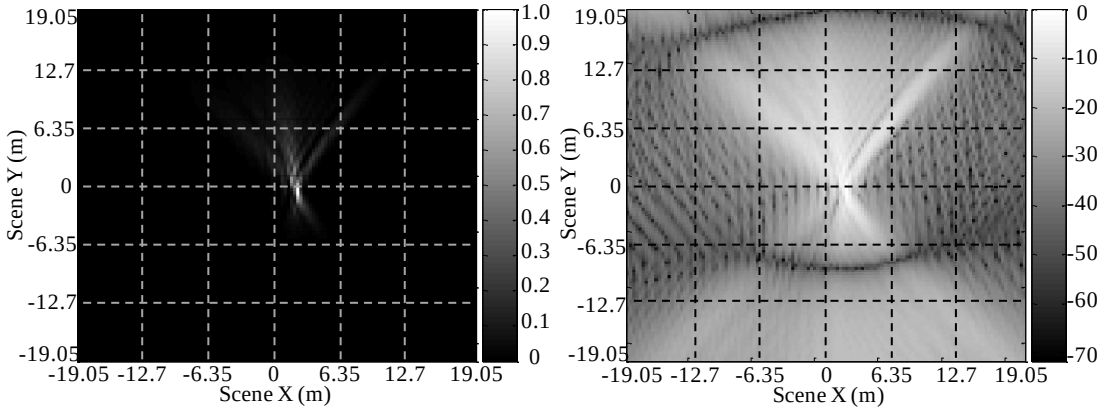

a) Orbit 4 Simulated PSF - Linear

b) Orbit 4 Simulated PSF - Log-Magnitude

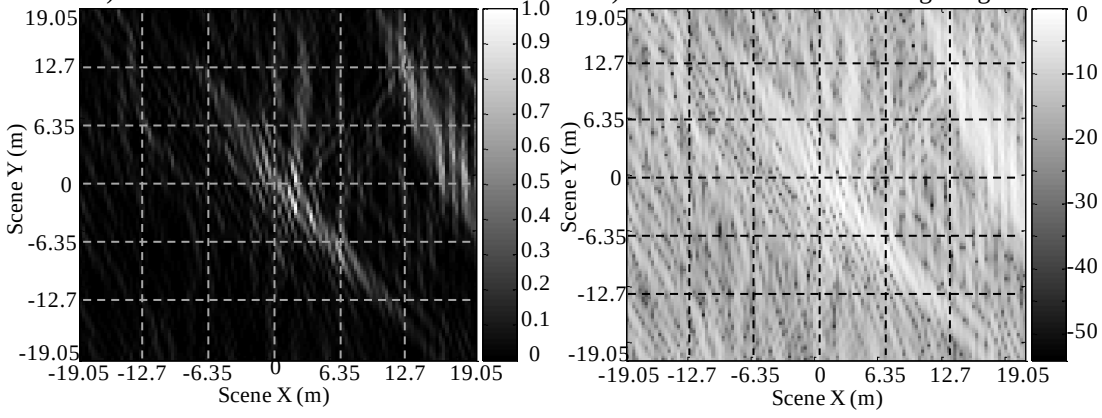

c) Orbit 4 Flight Image- Linear

d) Orbit 4 Flight Image - Log-Magnitude

Figure 6.83. Orbit 4 2D Reconstruction: Simulated As-Flown and Flight Data

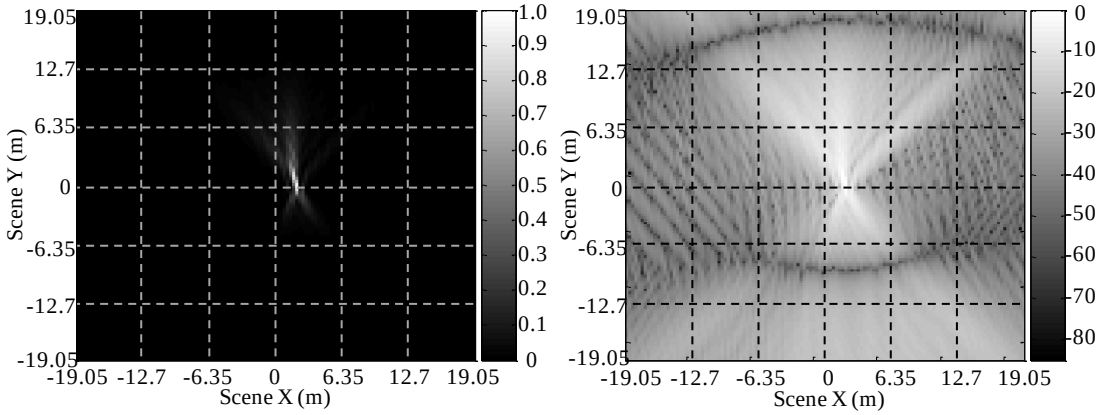

a) Orbit 5 Simulated PSF - Linear

b) Orbit 5 Simulated PSF - Log-Magnitude

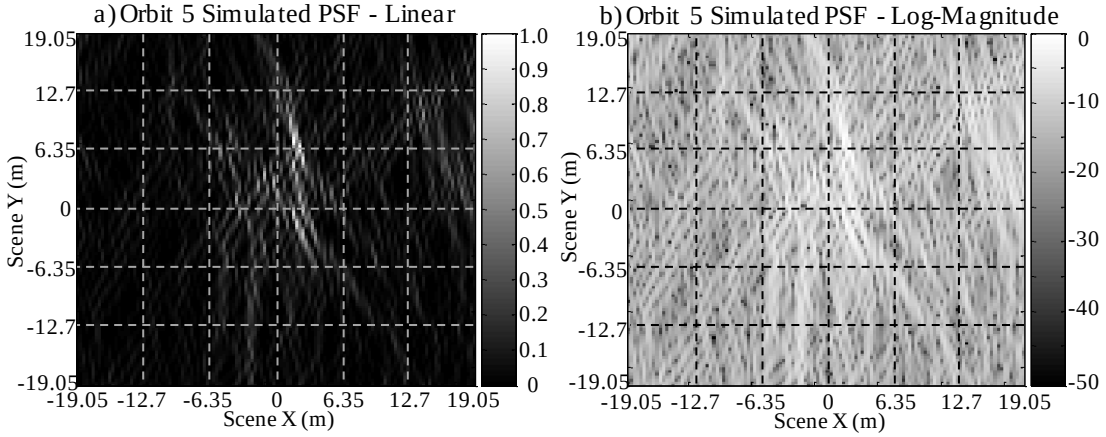

c) Orbit 5 Flight Image- Linear

d) Orbit 5 Flight Image - Log-Magnitude

Figure 6.84. Orbit 5 2D Reconstruction: Simulated As-Flown and Flight Data

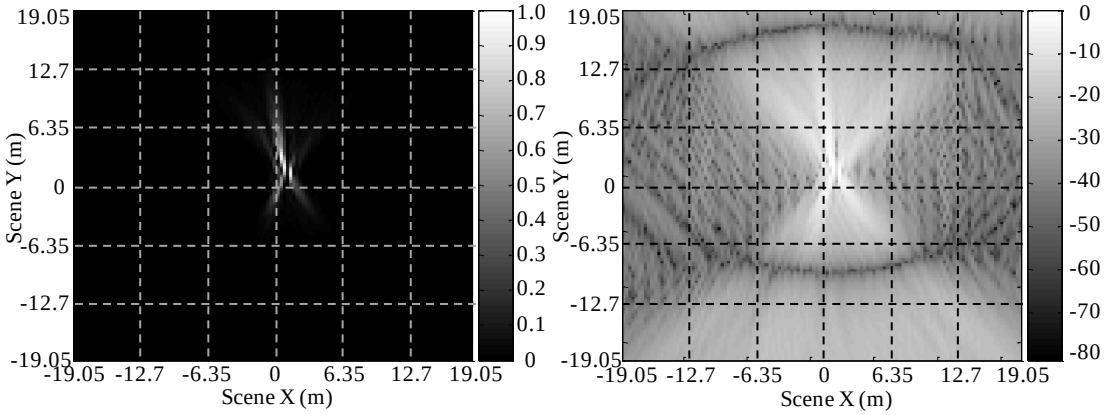

a) Orbit 6 Simulated PSF - Linear

b) Orbit 6 Simulated PSF - Log-Magnitude

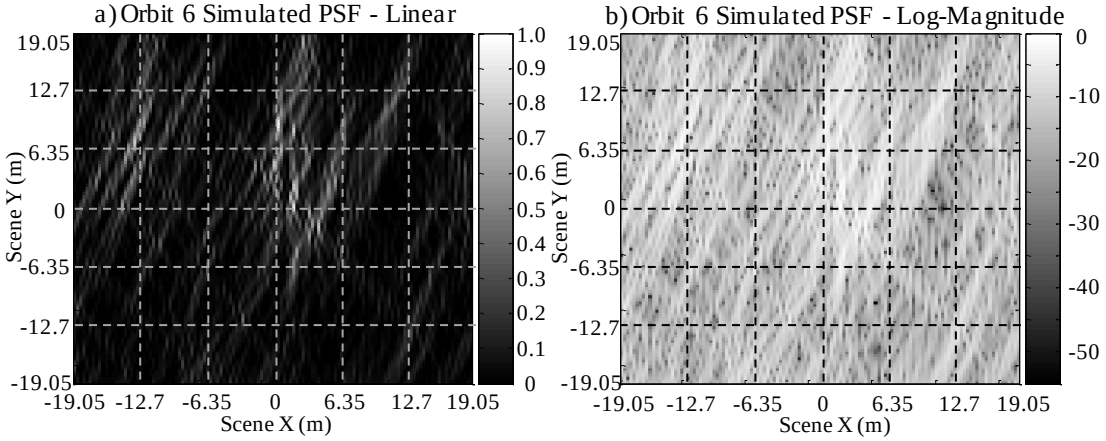

c) Orbit 6 Flight Image- Linear

d) Orbit 6 Flight Image - Log-Magnitude

Figure 6.85. Orbit 6 2D Reconstruction: Simulated As-Flown and Flight Data

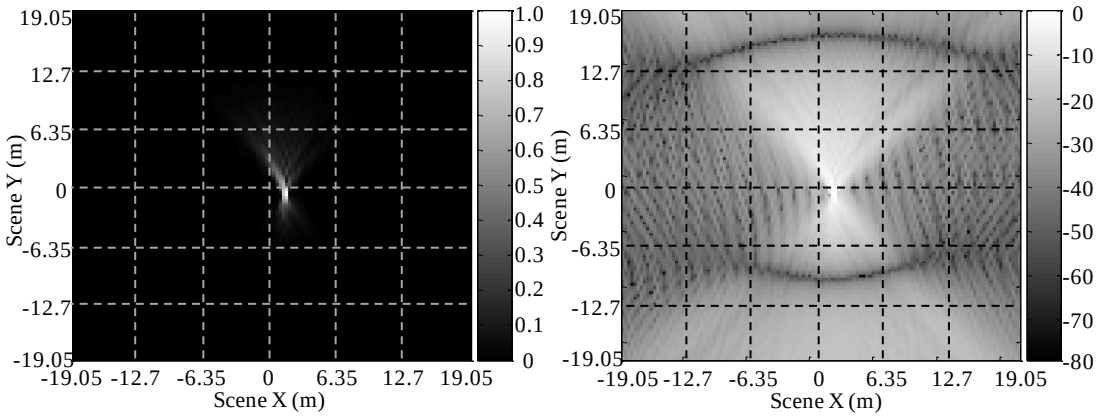

a) Orbit 7 Simulated PSF - Linear

b) Orbit 7 Simulated PSF - Log-Magnitude

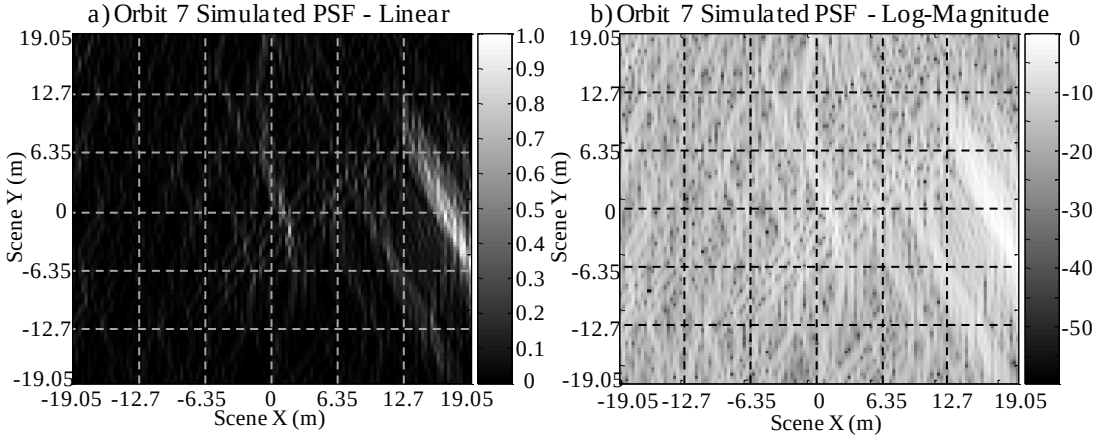

c) Orbit 7 Flight Image- Linear

d) Orbit 7 Flight Image - Log-Magnitude

Figure 6.86. Orbit 7 2D Reconstruction: Simulated As-Flown and Flight Data

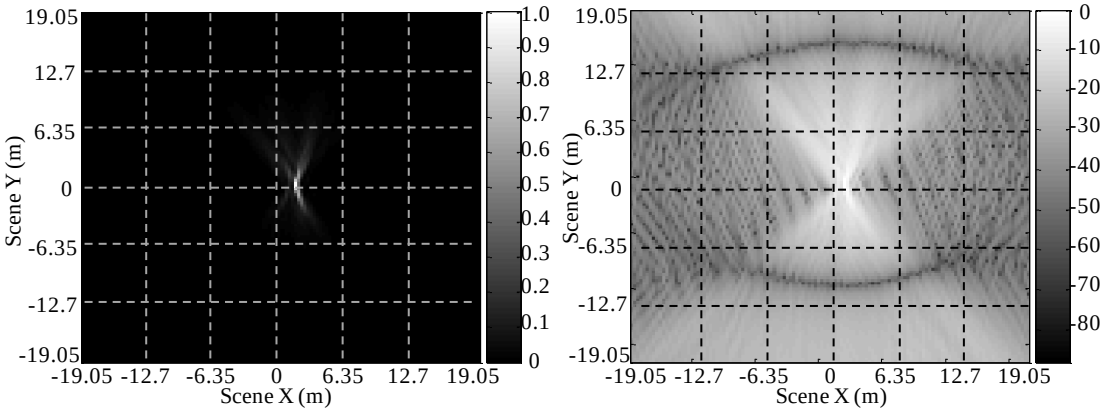

a) Orbit 8 Simulated PSF - Linear

b) Orbit 8 Simulated PSF - Log-Magnitude

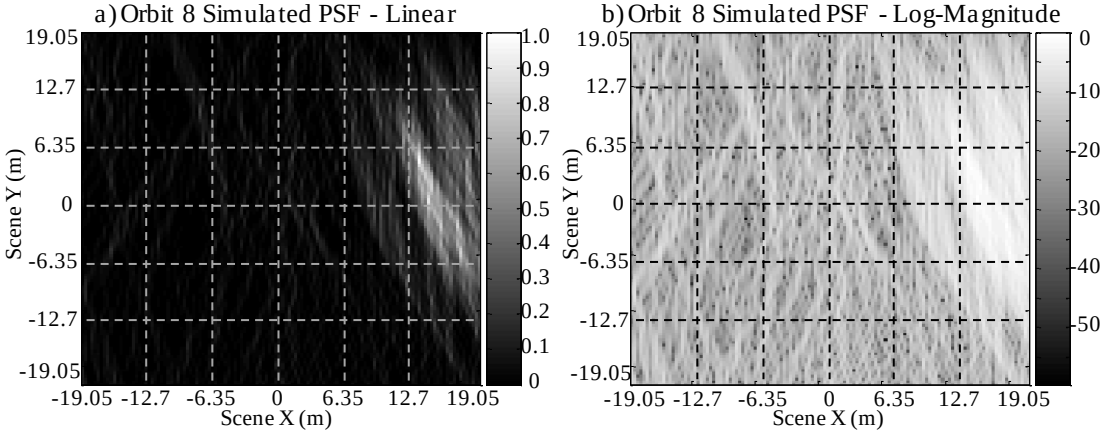

c) Orbit 8 Flight Image- Linear

d) Orbit 8 Flight Image - Log-Magnitude

Figure 6.87. Orbit 8 2D Reconstruction: Simulated As-Flown and Flight Data

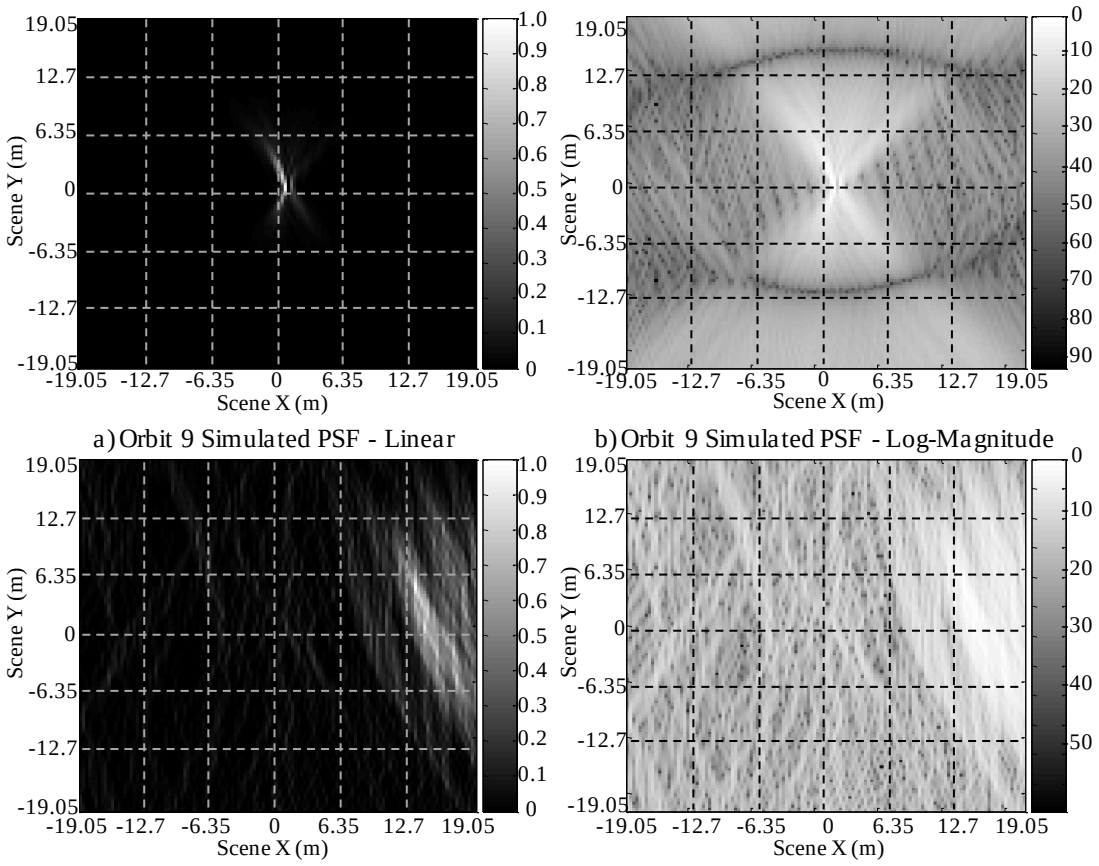

a) Orbit 9 Simulated PSF - Linear

b) Orbit 9 Simulated PSF - Log-Magnitude

c) Orbit 9 Flight Image- Linear

d) Orbit 9 Flight Image - Log-Magnitude

Figure 6.88. Orbit 9 2D Reconstruction: Simulated As-Flown and Flight Data

A single, shorter aperture (40 degrees) was focused over a 1.25 km by 1.25 km area [164] and appears in Appendix E, Figure E.1. Each orbit was also focused over a larger region than shown in Figure 6.89, 240 m by 240 m by sampling the scene at the Nyquist resolution for the particular orbit. Each image was convolved with a two-dimensional -35 dB Taylor taper, followed by clipping the dynamic range 20 dB below the scene peak response. Orbits 1 through 9 results appear in Figure E-2 through E-10, respectively. The images in Appendix E show clear correlation and registration between geographic and reconstruction features. The most obvious being clusters of large trees.

Finally, two additional steps were taken to confirm that the reconstruction was functioning correctly (*e.g.*, that measured PSF matches simulated). In the first, two idealized orbit sets were generated which were perfect in the trajectory sense (ideal cylindrical spiral segments) and with the same radius as flown and using a rate of climb

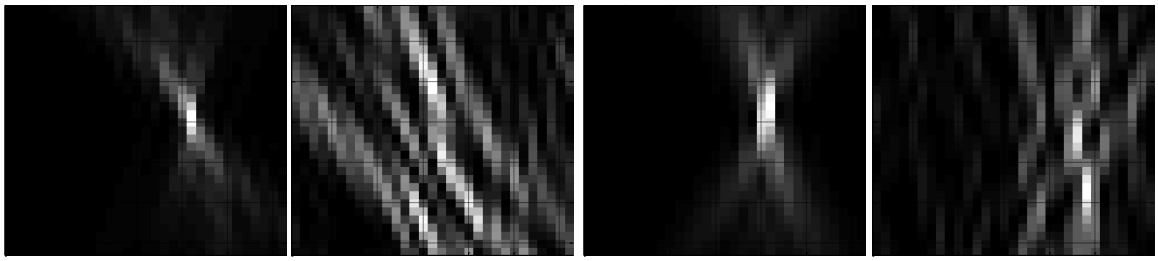

a) Orbit 1 simulated (left) and Flight Data (right)Z=0

c) Orbit 2 simulated (left) and Flight Data (right)Z=0

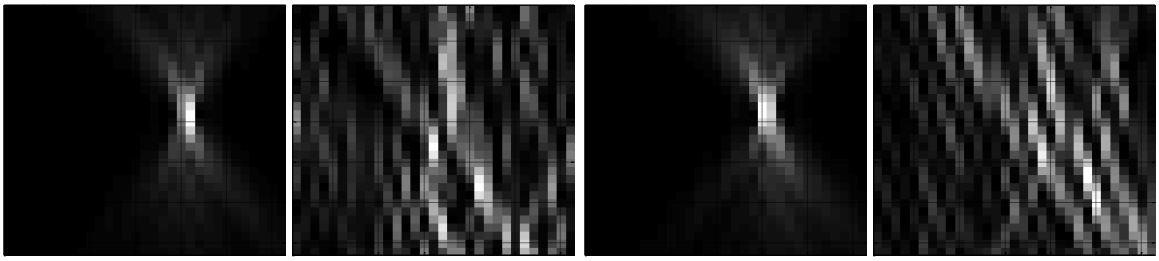

c) Orbit 3 simulated (left) and Flight Data (right)Z=0

d) Orbit 4 simulated (left) and Flight Data (right)Z=0

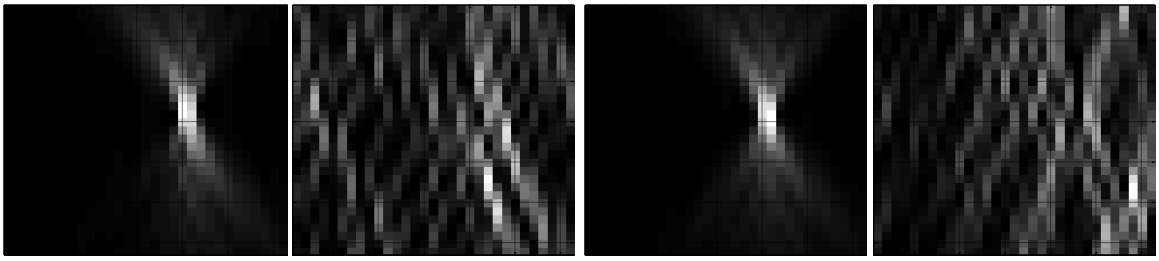

e) Orbit 5 simulated (left) and Flight Data (right)Z=0

f) Orbit 6 simulated (left) and Flight Data (right)Z=0

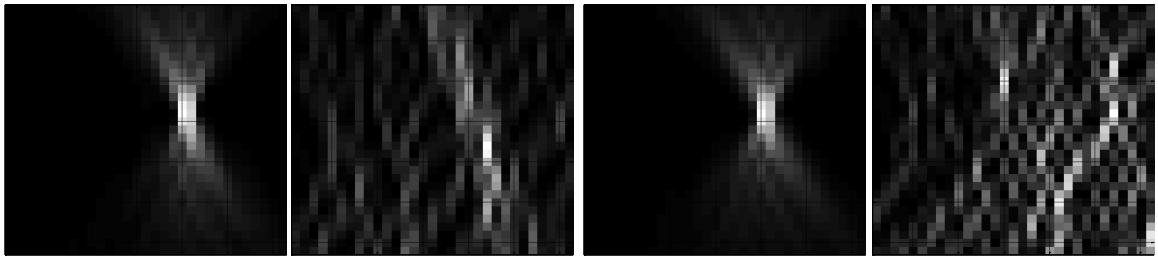

g) Orbit 7 simulated (left) and Flight Data (right)Z=0

h) Orbit 8 simulated (left) and Flight Data (right)Z=0

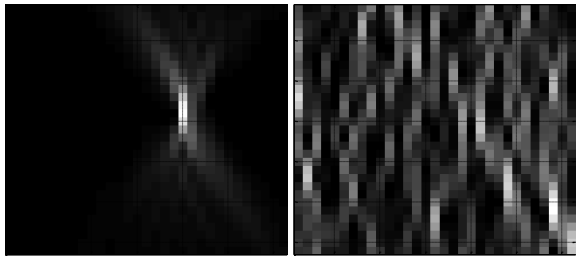

i) Orbit 9 simulated (left) and Flight Data (right)Z=0

Figure 6.89. 2D Reconstructions: Simulated As-Flown & Flight Data Focused to Z=0

(actually descent) derived from the flight data. The first was a single orbit segment, emulating orbit 1, and spanning 90 degrees of arc in the X_{scene}–Y_{scene} plane at a mean altitude of 1020 m with 40 m of altitude change over the aperture. The second orbit set was the idealized three dimensional collection aperture (used later). The second method

was based on constructing the as-flown sampling aperture in Fourier Space and generating the PSF via the inverse two-dimensional Fourier Transform.

The isotropic target for the ideal orbit simulation was located at (10, 10, 0) in scene coordinates. Figure 6.90 presents two contour plots of the two dimensional point spread function in the scene X-Y plane. The first (Figure 6.90a) was generated using a sample spacing of 0.3048 m (1 ft.) and the second (Figure 6.90b) at 10 cm spacing (4 inches). Resemblances to the results from Figure 6.89 are clearly evident, particularly in Figure 6.90b. Likewise, though not shown completely, the first nulls are not symmetric in range.

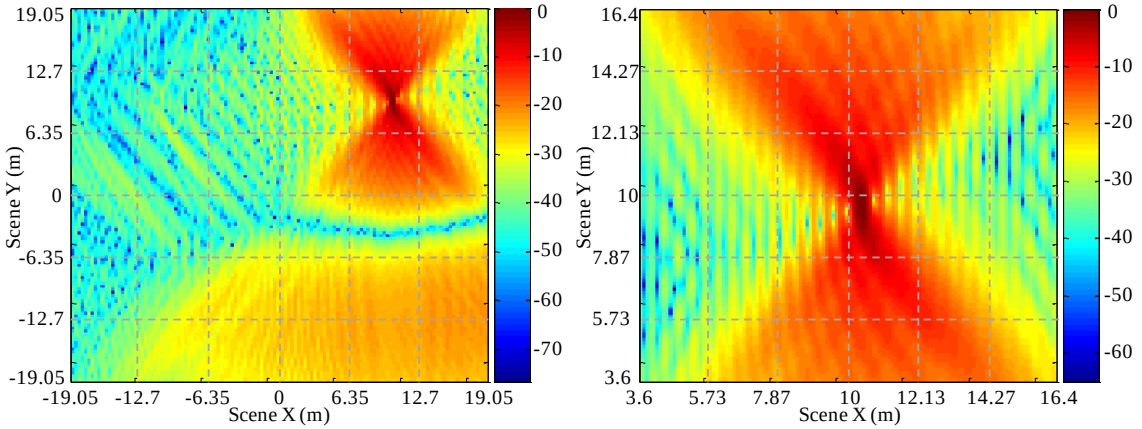

a) Sample Spacing 0.305 m (1 ft.) b) Sample Spacing 0.1 m (4 in.)

Figure 6.90. Ideal Orbit Segment Point Spread Function (2-D Contours)

The Orbit 1 trajectory was converted to the equivalent frequency domain representation, as was portrayed for the candidate orbits in the test design section (Figure 6.54) as shown in Figure 6.91a. The two colors represent the channel band edges. A square matrix with wave number resolution of 0.1 and spanning $-25 \leq k_x \leq 25$ and $-25 \leq k_y \leq 25$ was defined and the trajectory was down sampled into the frequency domain matrix, as shown in Figure 6.91b, the quantization clearly visible. The inverse two dimensional FFT was taken and FFT shifted to place the peak response at the center of the PSF. That result appears in Figure 6.91c. The X and Y axis resolutions were graphically estimated yielding 0.5 m in X and 0.9 m along Y. The scene size in Figure 6.91 is approximately 62 m square.

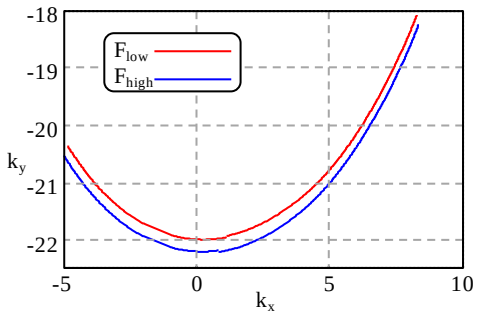

a) Orbit 1 - Frequency Domain

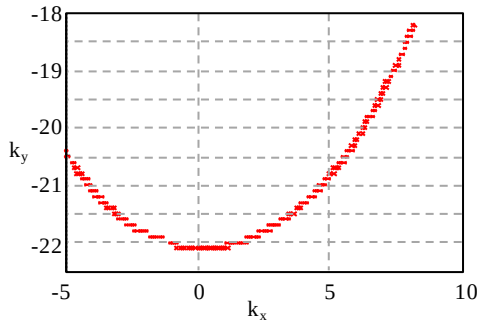

b) Orbit 1 Quantized

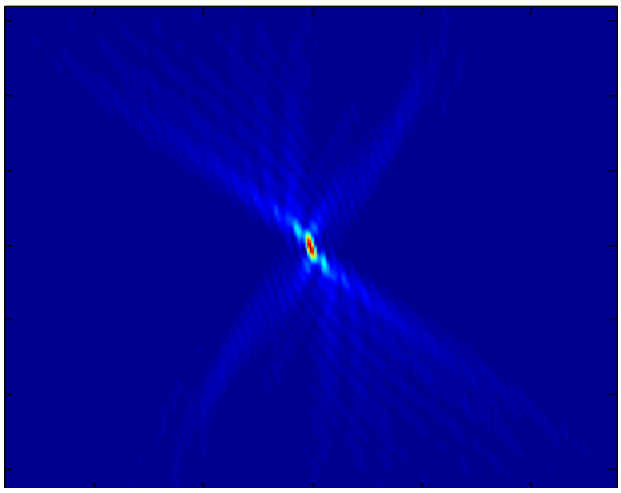

c) Point Spread Function (mag.-squared, linear scale)

Figure 6.91. Point Spread Function Reconstructed from 2D Fourier Aperture

All the derivations of the two dimensional response agree with the measured result, both qualitatively and quantitatively, so that we can reasonably assert that the measured data are suitable, the aperture(s) are focusing, and the results reflect the scene bistatic reflectivity (albeit with poor contrast). However there are some results in Figure 6.89 and 6.90 which were unanticipated. The response peaks demonstrate a slight offset from the simulated target position. The displacement is 0.35 m along Y (peak response at 9.65 m) and X (peak response at 10.35 m) in Figure 6.90. This was also observed when the 9 orbit segments were simulated with the as-flown trajectory, with the peak response shifting from orbit-to-orbit. As previously stated, the simulated scatterer was not positioned to avoid straddle. The mean cross range resolution resulting from the 9 apertures (orbits) based on (6.56) is 0.37 m with an average (in-plane) aperture angle of 88 degrees, with some dilution because of the sample lattice was not aligned with the aperture, as noted for the 25 second aperture. The actual shape of the collection aperture may be the cause. As noted in Figure 6.78 the receiver elevation change over the aperture create a slight rotation when projected into the scene focus plane, resulting in the observed shift.

Additional details on the response are seen in Figures 6.92 and 6.93. In Figure 6.92 the contours of Figure 6.90b are presented as a surface, with the response (Z) axis on a linear scale. Cuts along the X and Y cardinal axes, as well as along the peak intercardinal axis, defined as the locus of points with the maximum response away from the peak pixel, are presented in Figure 6.92. Using the cuts along the X and Y (Figure 6.93a) axes the resolution is estimated at the full-width, half-maximum points. Using a cubic spline interpolation resulted in the calculated lobe width along X of 0.3831 m. The calculation

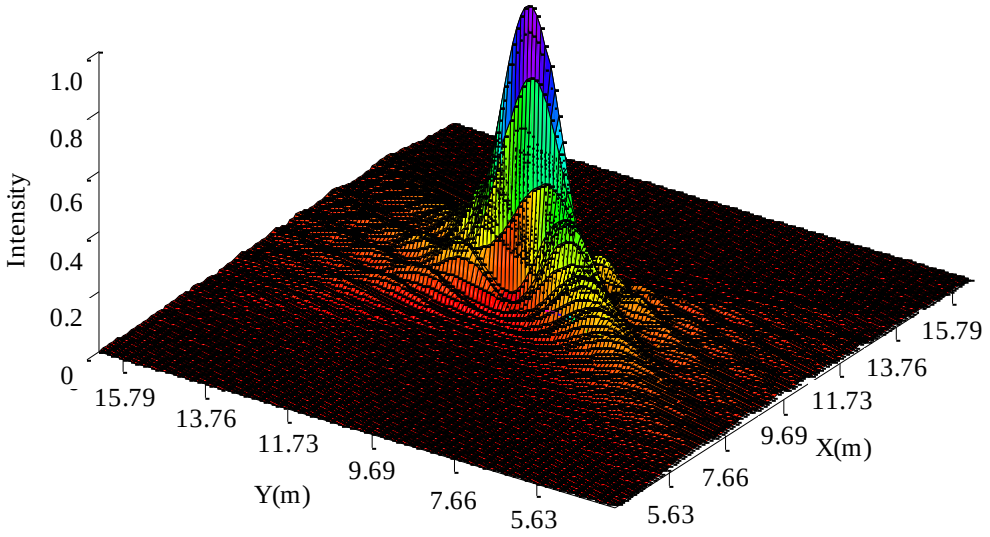

Figure 6.92. Ideal Orbit Segment Point Spread Function Surface

along Y yielded 1.7483 m. The intercardinal cut, which is identifiable visually in Figure 6.89b, runs at an angle of approximately 60 degrees to the X axis. The horizontal axis is the row/column index number of the reconstructed response (Figure 6.93b).

The same calculations (resolution estimates) were made for the 2D reconstructions in Figure 6.89 and are summarized, along with the ideal single orbit above, in Table 6.15. The rerun cases corrected for the focus height error so that matched estimates could be formed. The measured results were based on selecting the brightest pixel and then X and Y cuts were extracted around this peak magnitude pixel.

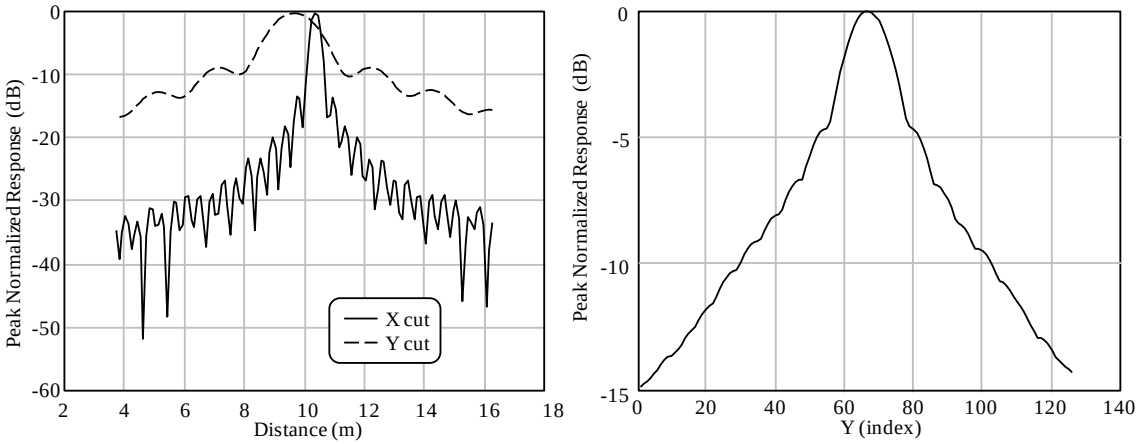

a) Y, X Principle Axis (0.1 m sample spacing) b) Intercardinal Axis (peak response over Y)

Figure 6.93. PSF Cuts along Cardinal and Intercardinal Axes

The reconstructions based on an ideal aperture with wide aperture angles are symmetric with respect to range and cross range [165] and as evaluated herein when the aperture is symmetric with respect to the transmitter line-of-sight. The scatterer modeled height and reconstruction plane mismatch in Figures 6.80-6.88 result in the breaking of that symmetry with respect to pseudo cross range (that direction parallel to the longest aperture projection with respect to the scene and with the highest resolution). This also creates a layover effect and results in a displacement of the peak response in the pseudo range dimension. These errors are eliminated in the results in Figure 6.89 but we still observe, in some cases, only a two-fold, mirror-like, symmetry (6.89a, and slightly e and g) and which in clearly evident in Figure 6.91c (matching 6.89a). Being guided by [89] we examined the aperture in the frequency domain (following 6.91) and found that the effect was most pronounced for the most asymmetrical spectra. The endpoints differ by >2 rads/m along k_y and >3 along k_x for orbit 1 (6.89a). This was the most pronounced asymmetry. Orbit 5 (6.89e) differed by >1 rads/m along k_x and ~1 along k_y.

We conclude from the agreement between theoretical, simulated, and measured resolutions that the data are correctly focusing, even though the images produced do not obviously resemble the optical images of the scene (likely an unrealistic expectation, particularly considering the carrier frequency). All ranges used to steer the back

projection algorithm are derived from WGS-84 referenced coordinates (scene center and GPS-based position measurements), range errors mapping the compressed data into range, and into scene/pixel coordinates, would degrade the images, producing a more randomized scene.

Orbit Number	X Res. Sim. Data	Y Res. Sim. Data	X Res. Flight	Y Res. Flight
Ideal Orbit	0.3831 m	1.7483 m	N/A	N/A
Fourier Reconst. Orbit	0.5 m	0.9 m	N/A	N/A
1	0.41 m	1.582 m	0.67 m	1.714 m
2	0.63 m	2.505 m	0.41 m	2.26 m
3	0.45 m	1.63 m	0.63 m	1.85 m
4	0.66 m	1.85 m	0.50 m	1.43 m
5	0.66 m	1.96 m	0.45 m	1.41 m
6	0.66 m	1.96 m	0.4 m	1.63 m
7	0.66 m	1.96 m	0.4 m	1.63 m
8	0.66 m	1.82 m	0.4 m	0.99* m
9	0.42 m	1.67 m	0.45 m	1.87 m
Average	0.579 m	1.882 m	0.479 m	1.643 m

* Two closely spaced, nearly equally sized scatterers at same X position

Table 6.15. Resolution Estimates Derived from 2D Reconstructions

6.5.2 ***Three dimensional reconstruction*****.** The approach used to validate that the two dimensional result was focusing properly (covering both the reconstruction algorithms as well as the data) was then applied to three dimensional image formation. We start with the three dimensional ideal collection aperture mentioned earlier; idealization of all 9 orbit segments individually 2D focused. Again an isotropic point scatterer is placed at (10, 10, 0) and the bistatic phenomenology simulated. The idealized orbits are depicted in Figure 6.94. Note that in the lowest orbit, the trajectory was clipped by the minimum altitude limit applied. Reconstruction was performed over three dimensions, but only along the cardinal planes centered at the simulated target position (to reduce computation time) producing the sampled point spread function in Figure 6.95, with point spread function response plotted as logarithmic log-magnitude.

The features observed in the two dimensional reconstruction are seen to carry over to the three dimensional case; most notably the elongation of the along-Y response due to the

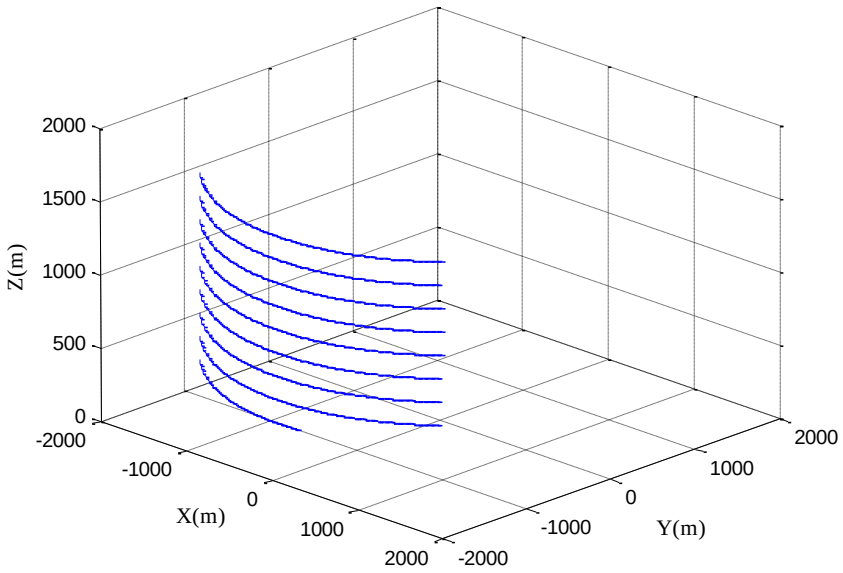

Figure 6.94. Ideal Orbit Simulation - Spatial Aperture

shorter aperture projection onto that axis. With the exactly repeated orbit height separation along Z is it unsurprising to see grating lobe-like responses at +/- 8.01 m and a weaker response at +/- 15.4 m. The orbits were defined symmetrically with respect to the

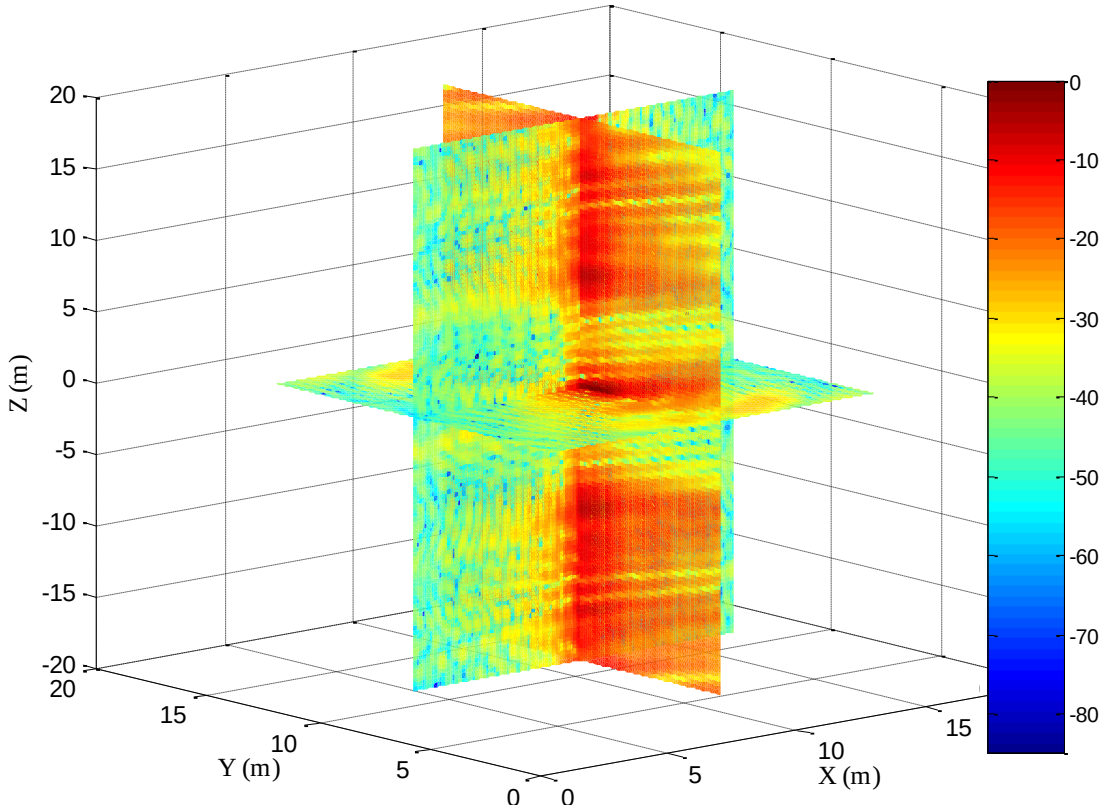

Figure 6.95. Ideal Orbit Simulation PSF - Principal Plane Reconstruction

scene Y axis over a 90 degree arc as defined in the X-Y plane. Sloping away from the receiver (toward +Y). We observe a slight rotation in the X-Y plane, with respect to the

X=0, Z=0 axes of 2-3 degrees (by examination). This corresponds to the angle of the transmitter away from the Y axis. Full slices were calculated over a range of Z from -18 to +18 meters in 0.1 m (4 inch) increments (126 total), with the same voxel spacing in the X and Y planes (126 by 126). The individual cardinal plane responses, plotted on a linear magnitude scale are shown in Figure 6.96. In Figure 6.96a the light rotation of the PSF, reflecting the transmitter offset, can be seen.

The responses are generally higher along the Z axis. The resolution in the vertical direction is misleading because of the mismatched plot axes (only Figure 6.97a uses the same scaling on both). Principal cuts for this result, from which the three dimensional resolution values are calculated, appear in Figure 6.97. The X-Y plane sample spacing was 0.1 m, while samples were spaced 0.3048 m in Z. The resolution values scaled from these cuts, similar to the 2D cases are found in Table 6.16.

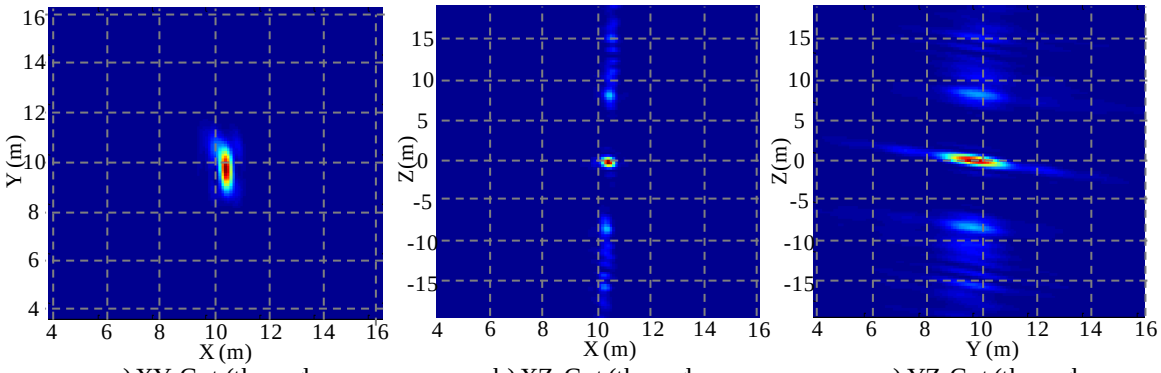

a) XY Cut (through scatterer Z position) b) XZ Cut (through scatterer Y position) c) YZ Cut (through scatterer X position)

Figure 6.96. Ideal Orbit Simulation PSF - Principal Plane Cuts

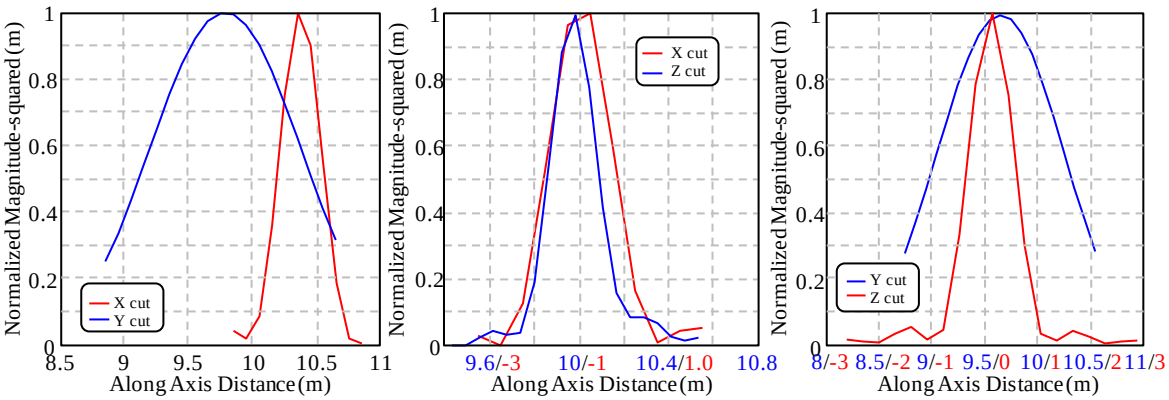

a) X-Y Cut along Z=0 plane b) X-Z Cut along Y=10 plane c) Y-Z Cut along X=10 plane

Figure 6.97. Ideal Orbit Simulation - Principal Axis Cuts and Resolution

Next the actual trajectories were simulated and a full reconstruction over the volume measuring -18 to +18 meters in 0.305 m (1 ft) voxel sample increments in the X-Y plane (126 total each axis). In the Z direction voxel spacing was also 0.3048 m with 100 voxels between -10 m and 20.18 m. Results are presented in the same manner as the ideal orbits in Figure 6.98. The full volume reconstruction was performed in segments because of run times with the full volume response reconstructed from the run segments. Results are very similar to the ideal orbit case with the high response levels in the vertical dimension and

Case	Data Source	X-Y Plane at Peak Z	X-Z at Peak Y	Y-Z at Peak X
Ideal Orbit	Simulated	X_{res}=0.38m, Y_{res}=1.35m	X_{res}=0.38m, Z_{res}=1.17m	Y_{res}=1.35m, Z_{res}=1.17m
As-Flown	Simulated	X_{res}=0.34m, Y_{res}=1.36m	X_{res}=0.34m, Z_{res}=0.85m	Y_{res}=1.33m, Z_{res}=0.85m
As-flown	Flight data (1)	X_{res}=0.32m, Y_{res}=1.24m	X_{res}=0.32m, Z_{res}=1.08m	Y_{res}=1.24m, Z_{res}=1.08m
As-flown	Flight data (2)	X_{res}=0.27m, Y_{res}=1.83m	X_{res}=0.27m, Z_{res}=0.95m	Y_{res}=1.83m, Z_{res}=0.95m
As-flown	Flight data (3)	X_{res}=0.35m, Y_{res}=1.01m	X_{res}=0.35m, Z_{res}=0.92m	Y_{res}=1.01m, Z_{res}=0.92m

Table 6.16. Three Dimensional Reconstruction Resolution Values

the response slope negative in the positive Y direction. The actual flight trajectory does not exhibit the idealized shape so that the ambiguity/grating structure is less evident. This is more clearly seen in Figure 6.99, particularly Figure 6.99b. In this simulation the point

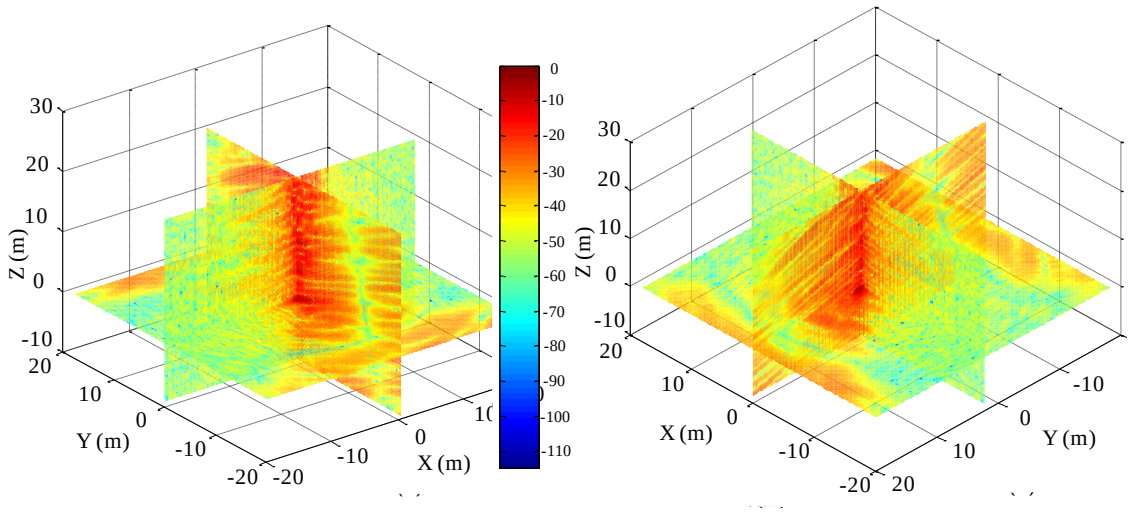

a) View azimuth = –37.5° (re -Y), elev. = 30° b) View azimuth = –135° (re -Y), elev. = 45°

Figure 6.98. As-Flown Simulated PSF - Principal Plane Reconstruction

scatterer was positioned at (1, 1, 0) and also exhibits the slight peak response offset on upon reconstruction (Figure 6.99a). In Section 5 we demonstrated that the effects of Doppler during the sample duration pulse compression could result in image distortion, but for full azimuth-processed images, not partial orbits as performed here. Further move-stop-move was implemented in the simulations. A geometric effect due to the partial aperture is still suspected. Interestingly, clear grating lobes observed at +/- 8 m in Figures 6.97c and 6.99c, there is an additional coherent phase ambiguity, albeit weaker, at +/- 5 m. Normalized principal cuts along the cardinal axes are plotted in Figure 6.100. Each axis from within the principal plane that passed through the peak response voxel is plotted. Resolution values for the as-flown simulated point scatterer are given in Table 6.16, listed As-flown, simulated. As this case represents the first full volume attempt to generate meaningful imagery, separately and in combination. The first was to

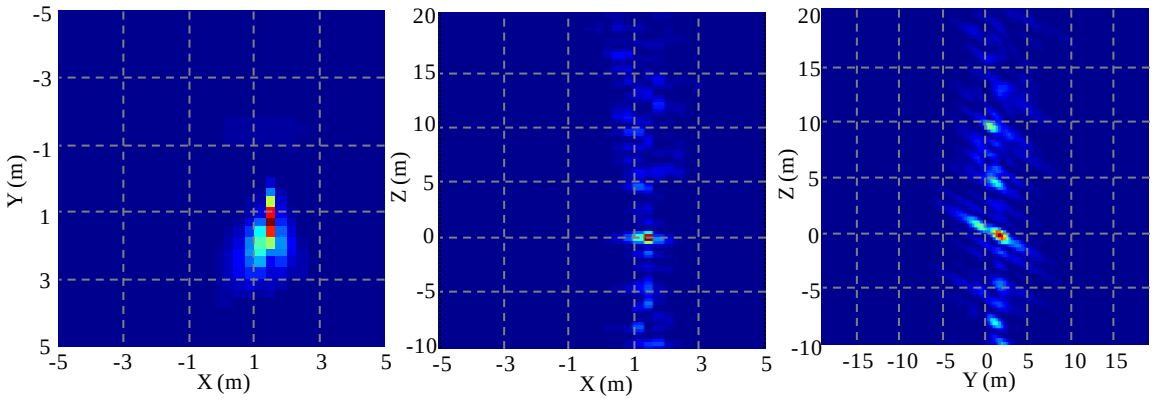

a) X-Y Cut through target Z pos. b) X-Z Cut through target Y pos. c) Y-Z Cut through target X pos.

Figure 6.99. As-Flown Simulated PSF - Principal Plane Cuts

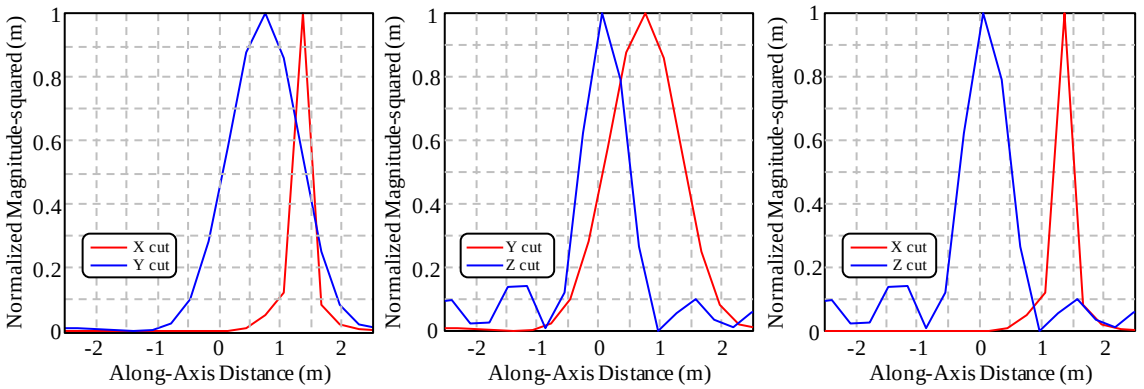

a) X-Y plane cuts through peak Z response

b) Y-Z plane through peak X response

c) X-Z plane cuts through peak Y response

Figure 6.100. As-Flown Simulation - Principal Axis Cuts and Resolution

reconstructed case (the only other being the flight data), the response is displayed in three dimensions using a point cloud representation. Each voxel is represented by a cube that with edge length that is 25% of the voxel spacing. Various techniques were used in an limit the total dynamic range of the scene. For example, with 20 dB dynamic range, all voxels with response less than 0.01 (after normalization) were set to 0. Our second approach was based on the transparency option supported by the MATLAB function 'patch'. Transparency (alpha) was set based on a functional dependence on the voxel response (magnitude-squared). In some cases, for improved visibility of internal voxels, as outer voxels occlude interior ones with some measure of control, the transparency was an exponential function of the response ($T \propto |m|^4$. where m is the voxel magnitude). Figure 6.101 is the response in Figures 6.98 and 6.99 represented as a point cloud. The viewing geometry is (45, 45), which in MATLAB is 45 degrees from the negative Y axis, measured in the polar sense, and 45 degrees above the X-Y plane. The plot is slightly trimmed in X-Y to $\pm$10 m in size. The total dynamic range is 20 dB and the plot spans the full reconstructed volume. The transparency is linearly related to the voxel magnitude-squared and linear magnitude scaling is applied.

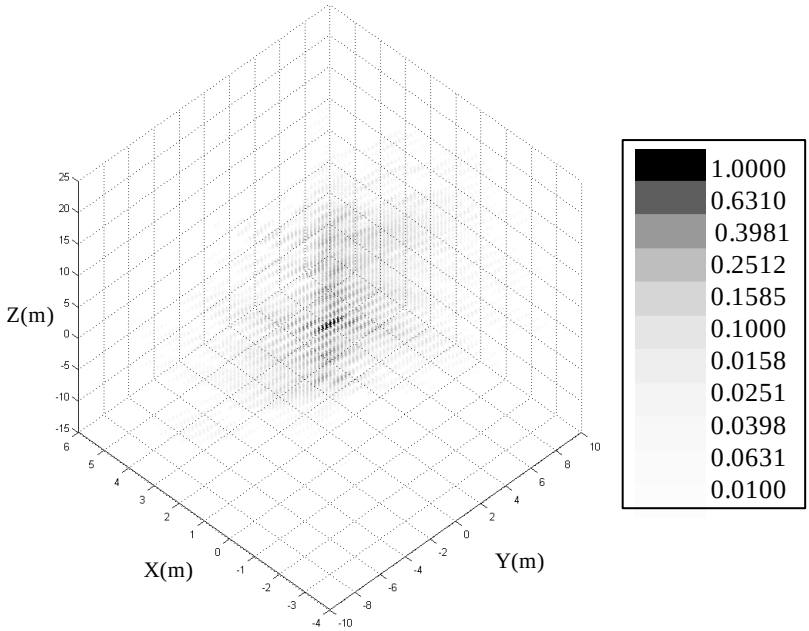

Figure 6.101. Point Cloud PSF Representation – As-Flown Simulation

Two zoomed views of the main response are shown in Figure 6.102. In this depiction the transparency coefficient is still linear and proportional to the normalized magnitude-squared (*e.g.*, value of the voxel magnitude sets the transparency directly on the scale 0 to 1). The Zoomed views span 10 meters in X and Y, centered on the simulated target position with the range of the vertical axis reduced to match. The dynamic range is hard limited to 30 dB in the zoomed images.

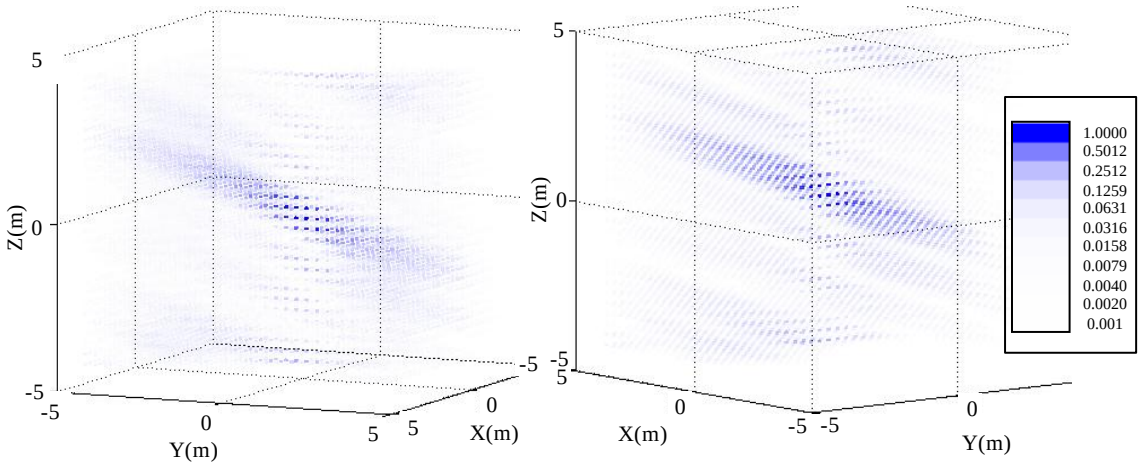

Figure 6.102. Point Cloud PSF Representation - As Flown Simulation

The flight data were focused over the same area as the 2D images shown earlier (Figures 6.80 through 6.88), in a scene containing the two metal buildings and the silo (Figure 6.52). Because of uncertainty of the height of the terrain (Google Earth indicating 13.4 m relative to the geoid and on-site, non-ionospheric corrected, differential GPS measurements suggesting 4.87 m) the vertical range of reconstruction was -10 m relative to the scene reference to a height greater than the silo height. The average difference (over 1000 seconds) in altitude from the simultaneously recorded GPS sources during flight, one corrected for ionospheric delay, is 16.77 m, with the non-corrected GPS signal registering the higher altitude. The on-site measurements were on different days and with the expectation that the ionosphere is highly dynamic, no conclusions can be drawn except to observe a rather significant difference and that the uncertainty is encompassed by the voxel vertical range.

The first flight data volumetric reconstruction is presented in Figure 6.103. The data are presented in point cloud format. The viewing perspective is 41 deg relative to –Y and 41 deg above the scene X-Y plane. The total magnitude-squared dynamic range is limited to 20 dB. In this image, the transparency factor is proportional to the fourth power of the absolute value of the voxel voltage (magnitude-squared, squared). The dark mass of in the image is coincident with the silo location at the center of the X-Y plane and extending vertically (by design). Voxel spacing in Figure 6.103 is 0.3048 m (1 ft, 0.028 m^3) along all axes.

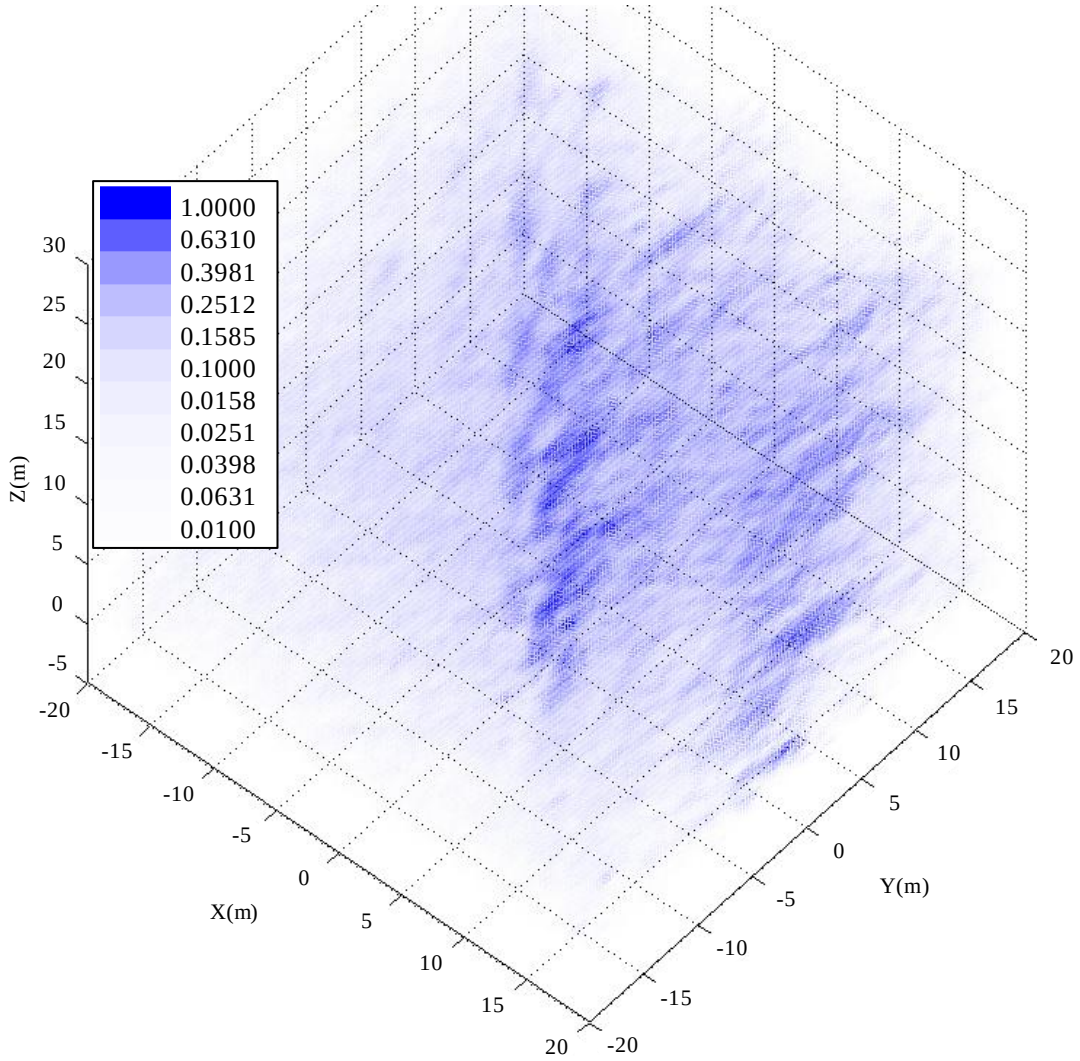

Figure 6.103. Flight Data Reconstruction – Volume 50540 m^3, Linear Scale

A second perspective appears in Figure 6.104, this one from 120 deg relative to –Y and 25 degrees up from the X-Y plane. From this angle the point spread elongation along Y

with the tilt relative to the local horizontal as seen in Figures 6.98, 6.99 and6.102. The darkest voxels in the point cloud represent the strongest responses. Dynamic range and scaling are the same as Figure 6.103.

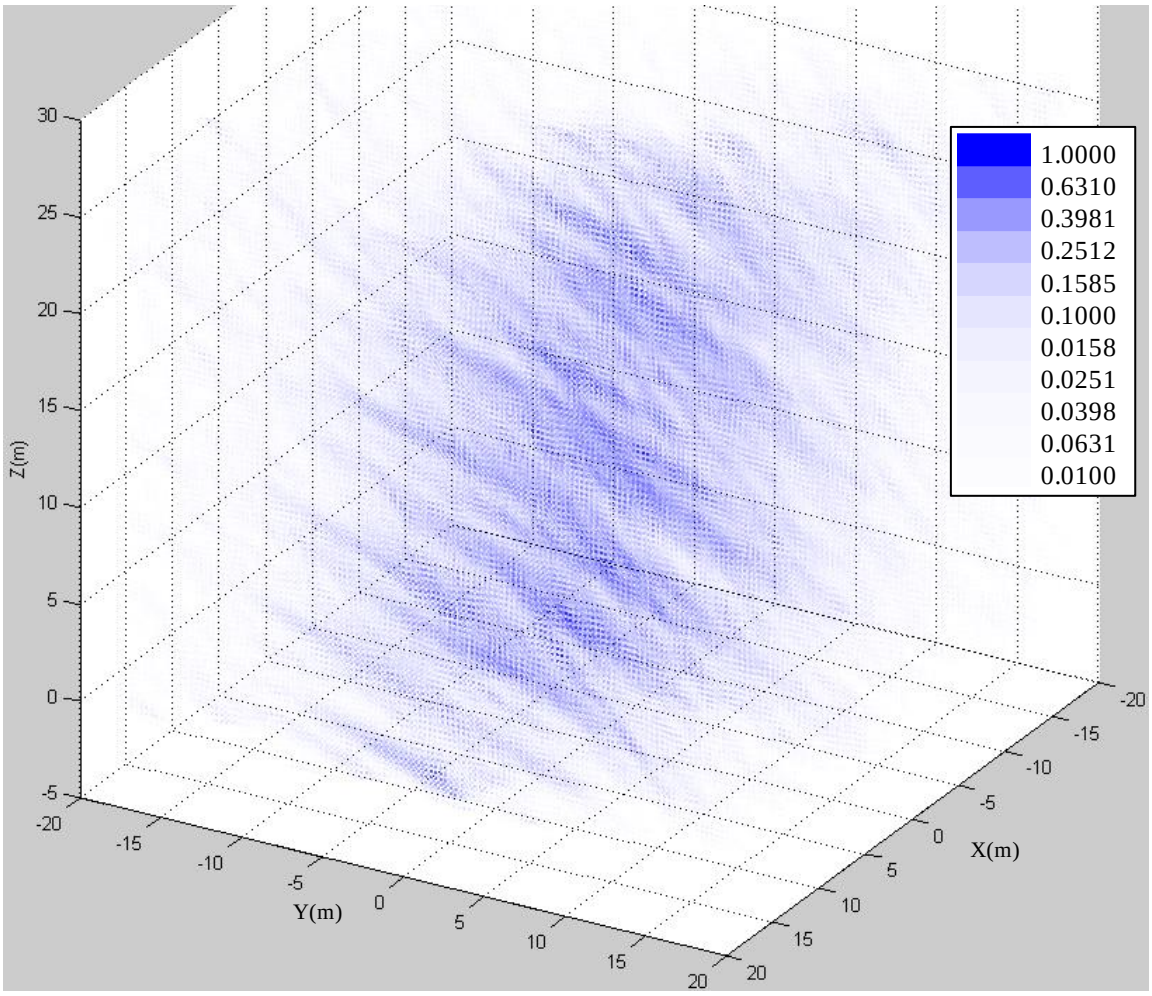

Figure 6.104. Flight Data Reconstruction – Perspective from Northeast of Scene

As in the two dimensional image cases presented earlier, this response is not obviously recognizable visually. There is a locus of brighter voxels which are distributed vertically and coincident with the silo position. This is seen more clearly in Figures 6.105 and 6.107 through 6.109 where line drawings of the structures are overlaid on the reconstruction. The structure corners were sampled from Google Earth and include some layover. Wall and roof heights were scaled from photos of the test scene (Figure 6.52) from the silo height identified by a local landowner. Additionally, to aid in selecting a voxel from which the resolution can be estimated to confirm the reconstruction efficacy, as shown

earlier. Further we reduce the dynamic range in the image to only 3 dB so that the brightest voxels are shown. The first image (Figure 6.105) is presented from a location southeast of the scene origin.

We test the quality of the reconstruction again through the resolution achieved the scene was examined for voxels which appeared to correspond to a point scatterer, or which collapse to a point, and extract resolution along the three axes. The results are graphically depicted in Figure 6.106 for three scatterers selected from different portions of the image. The estimated FWHM values are listed in Table 6.16 as Flight Data (1) through (3). The scatterer positions which were selected were Point 1 (14.478, 17.831, 19.261), Point 2 (14.478, -1.067, -1.161), and Point 3 (-1.067, -1.676, 0.058). Note that in the 9 cases in Figure 6.106 the axis scale varies from plot-to- plot. As in the two-dimensional case, the three dimensional resolution results compare very favorably with the simulated results, indicating that the three dimensional aperture is focusing. Clustering of response around the silo position and extending vertically is also strongly suggestive that the coordinate frames are aligned.

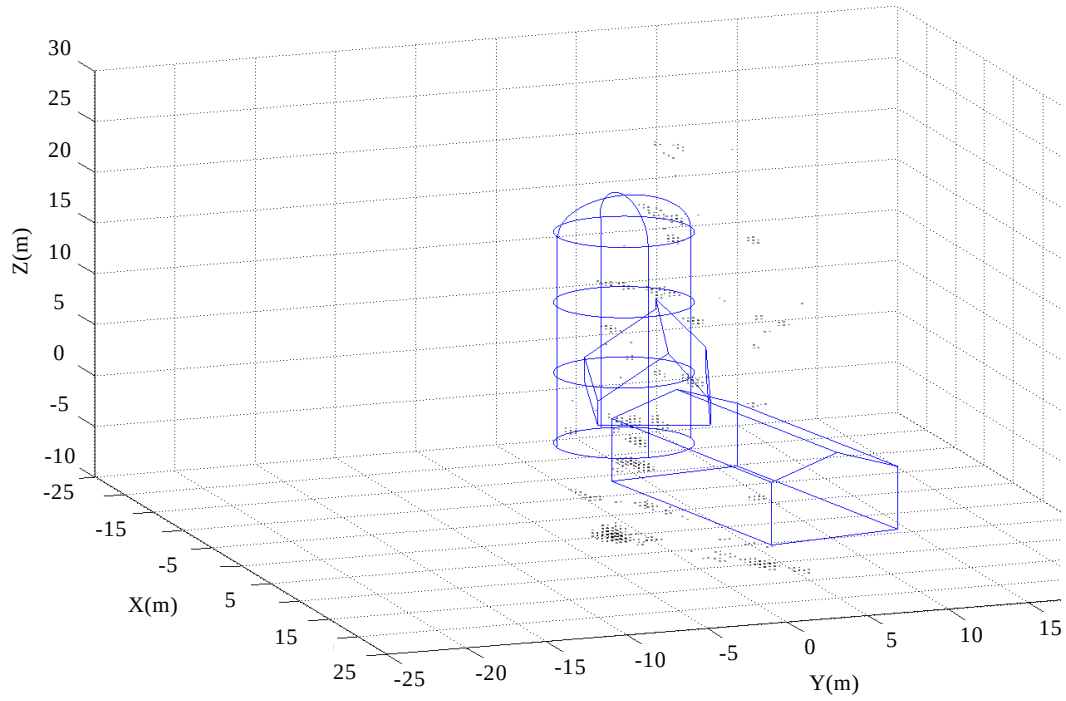

Figure 6.105. 3D Point Cloud Scene Buildings Overlain - 3 dB dynamic range

However there is a large volume of returns that are “underground” when referenced to the scene origin height. The image in Figure 6.107 is an enlargement of the central portion of Figure 6.105, highlighting this region, viewed from the nearly diametrically opposite position (northwest of scene origin). Also an insert figure is a perspective from ground level illustrating the focus height question.

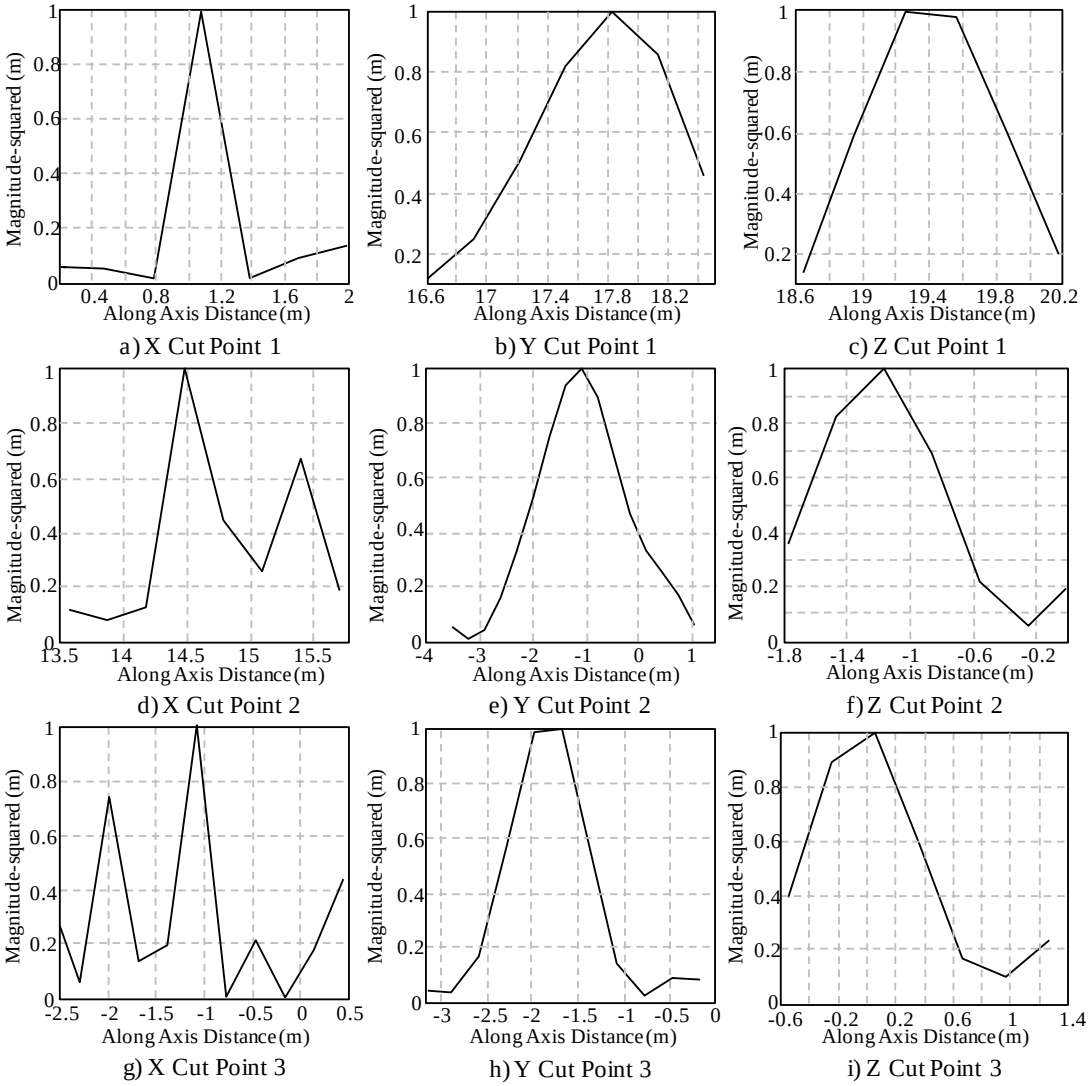

Figure 6.106. Point Spread Function Resolution - Principal Plane Cuts 3 Points in Scene

The final plot (Figure 6.110) is an overlay of the 3 dB clipped point cloud and the line drawing contours of the silo with a photograph of the scene origin, and from the best rendered, manual perspective. The silo drawing and reconstructed image points were scaled until dimensions matched the silo photograph. The ground plane reference altitude

with respect to the geoid was adjusted downwards by 5 meters based on error estimated from the GPS measurements from the road passing next to the property.

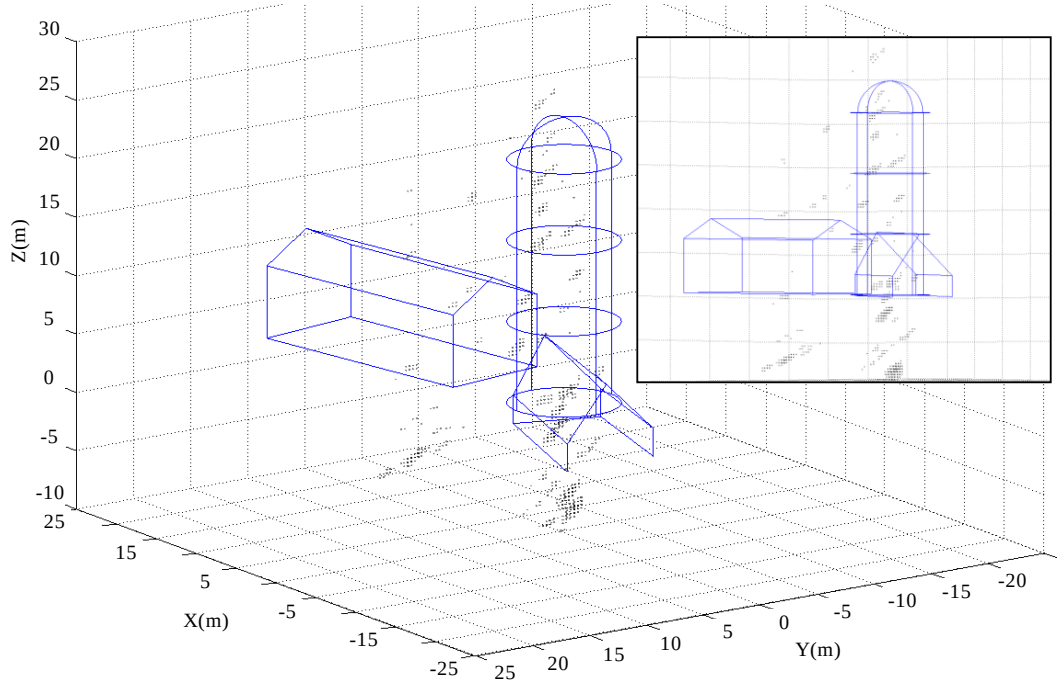

Figure 6.107. Scene with Buildings - 3 dB dyn. Range and Ground Perspective (Insert)

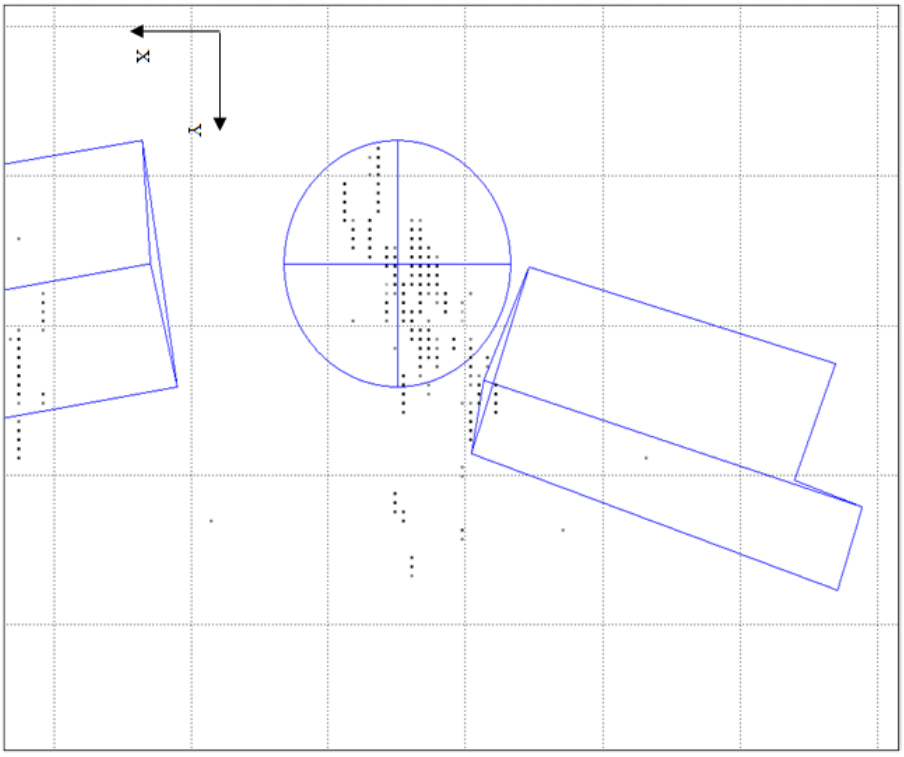

Figure 6.108. Scene from Zenith Perspective - 3 dB dynamic range

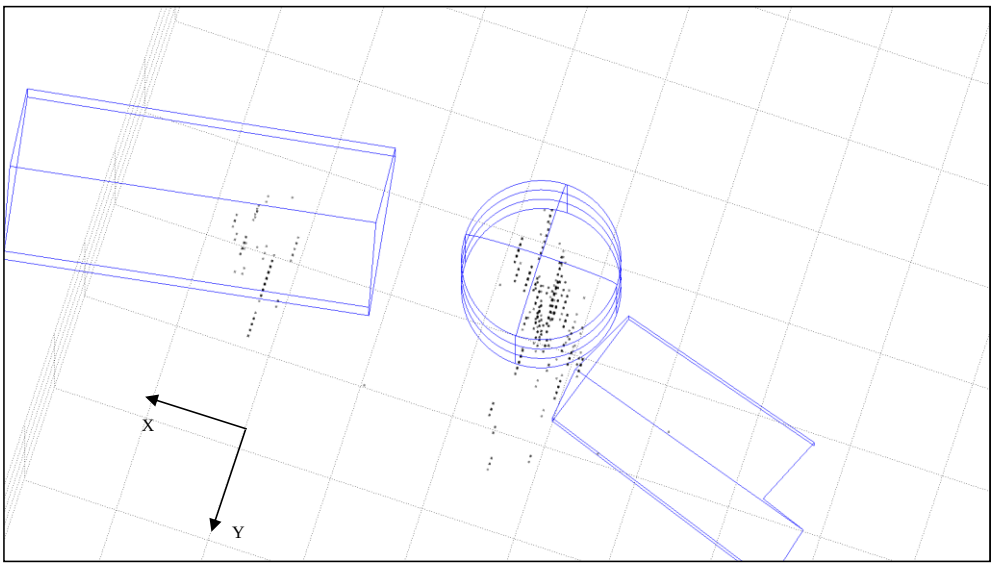

Figure 6.109. Scene North View near Zenith

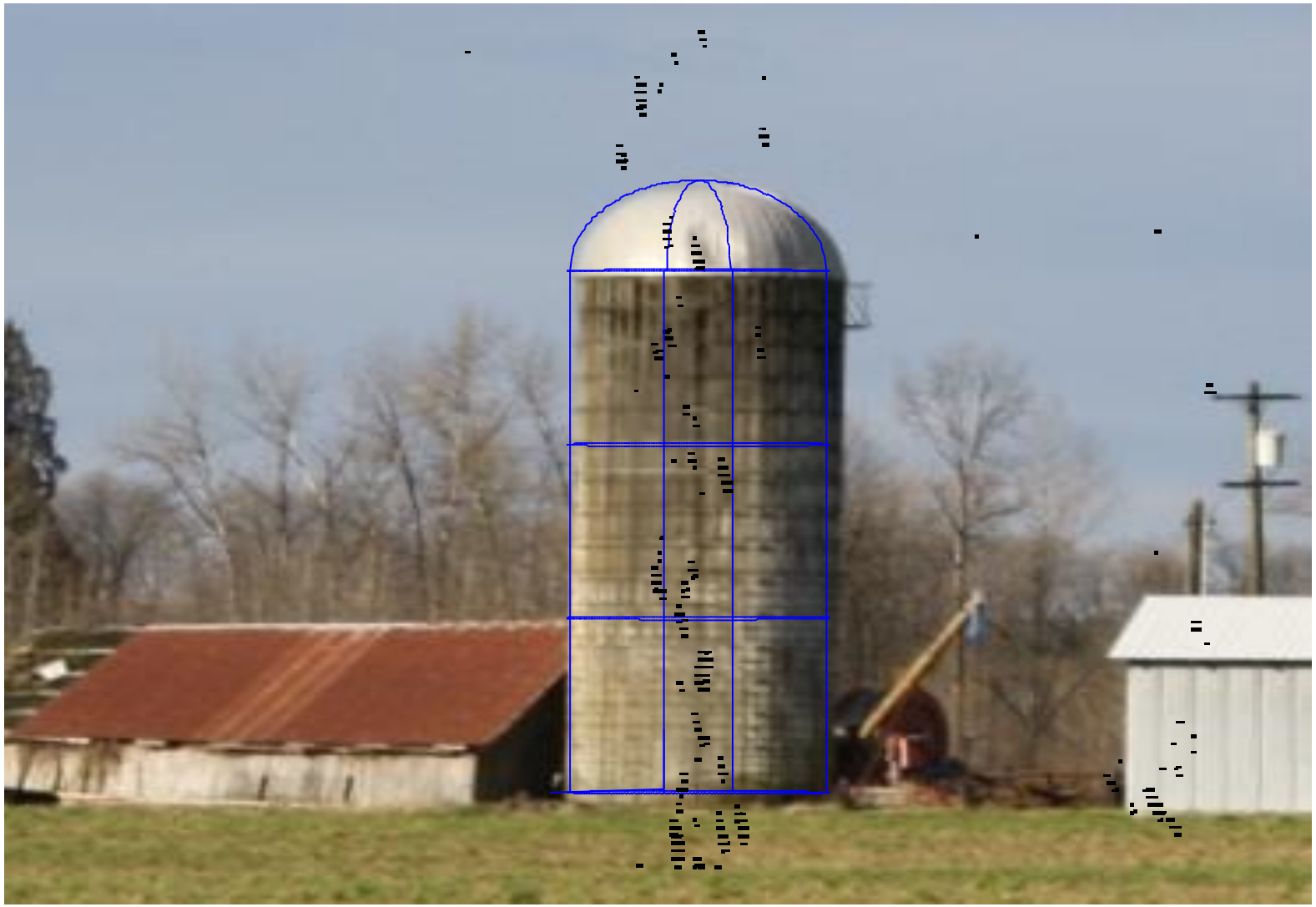

Figure 6.110. Image Results and Silo Overlain on Photograph at Best Rendered Perspective

Chapter 7.0

Discussion, Conclusions and Future Work

We have examined the potential for tomographic imaging to produce high resolution radio frequency images while consuming, or occupying, a reduced portion of the microwave spectrum. This was done from the perspective of a congested and/or constrained RF environment where traditional SAR may be challenged to find sufficiently unoccupied spectrum. The basic approach in Space-Frequency tomography trades off the occupied spectrum against the collection time/aperture (Section 4). But high resolution imagery is not sufficient: usable images must exhibit suitable contrast. To this end we evaluated methods to fill *k*-space using Space-Frequency apertures which would employ monostatic, bistatic, or both, apertures. The greater spatial frequency spectrum content, the more rapid the roll-off in point spread function sidelobes producing increased image contrast.

This exploration was abetted through the use of the hypothetical isotropic scatterer. Electromagnetic scattering is dependent on the scatterer shape and material composition, imaging geometry (including scatterer orientation), frequency, bandwidth, and polarization. Extending to bistatic geometries further complicates the geometry. As imaging scheme evaluation relies on matched filtering to a phase history (a non-closed form process), adding multiple degrees of freedom to reflect scattering reality is conceptually prohibitive, excepting only in the most narrowly defined conditions. It is essential to recognize that the isotropic scatterer results in the most optimistic calculated

performance. The factors affecting scattering combine to limit the performance of imaging schemes by restricting visibility over wide aperture angles [165], the response to which was noncoherent combination of subapertures. This sensitivity is demonstrated through a brief assessment of scatterer and imaging geometry which made use of the conducting sphere. An isotropic scatterer the monostatic case, the enhanced resolution resulting from tomographic (wide aperture angle in the limiting sense) yielded a focused but distorted image of concentric circles in the wideband case and collapsed to a point in the narrowband example. Extending to the bistatic geometry resulted in failure to focus when bandwidth was other than ultra-narrowband; the failure attributed to spatially migrating scatterer location and possibly the dynamic range of the returns in the forward scatterer region. Testing with a non-migrating phase center, a three wavelength flat plate, produced IPR with resolution essentially matched by the mainlobe response as the receiver passed through the specular lobe. More discussion appears in Appendix E. However, it must be noted that actual imagery generated a substantial number of pixels which, though randomly selected, exhibited full aperture resolution in both axes in the magnitude response.

Starting from a baseline of radar-specific waveforms we extended the analysis to limited combinations of CW tones which operated simultaneously throughout the aperture: exploiting mutual coherent cancellation of single frequency IPR sidelobes. The breadth of frequencies employed was an order of magnitude larger than previous two-dimensional efforts, and the addition of bistatic apertures had not been found in reporting of previous efforts. This also represented the first extension of the concept into three dimensional apertures. Improvement realized was modest. Greater success was obtained from sampling more frequencies representing swept or tuned CW signals over a deterministic pattern or discrete, unmodulated pulses with random carrier frequency over some fixed

frequency band. These latter approaches were adapted from the MRI research community.

The effects of motion on large time-bandwidth waveforms is known. Here we examined the susceptibility of tomographic image formation when employing cross correlation to platform motion from the perspective of integration time for sample (single burst) sensitivity. Image degradation was demonstrated, varying speed and Time-Bandwidth. We then developed a closed form method to compensate for platform motion, based on narrowband radar principles, which permitted recovery of image quality (resolution and sidelobe structure).

Further, while we demonstrated limited potential for sidelobe suppression using apodization against simple narrowband apertures/narrow ring-shaped spatial frequency spectra, we demonstrated Space-Frequency aperture concepts which fill *k*-space to the point of approaching the disk-shaped spatial spectrum of transmission tomography. This would enabling window functions regularly applied in that operating modality for image quality improvement.

Against a rich research background of bistatic research into radar functionality using nontraditional emitters and waveforms we have demonstrated the potential for high resolution image formation in both two and three dimensions (this latter we believe represents the world's first such application) exploiting commercial digital television transmissions as part of a bistatic imaging radar. To do so we took advantage of the proliferation of low cost software-defined radios/radars to construct our two-channel, coherent, instrumentation radar.

Substantial effort was put into analysis and system design to support direct path breakthrough mitigation in order to maximize the dynamic range and receiver sensitivity. The adaptive sidelobe canceller functioned well to reduce the zero delay magnitude due

to the direct path but did not contribute much to the reduction of time sidelobes post-pulse compression. That result was confirmed in examining published research into noise radar. The angular constraints of the adaptive canceller (main/aux ratio) limited the regions over the collection aperture against which reconstruction was performed to about 90 degrees on each of the nine flight test orbits.

However, the adaptive canceller proved essential in achieving burst-to-burst phase coherency (zero delay phase) which was more difficult than expected. Exploitation of the pilot tone, along with deterministic corrections, was either incorrectly implemented or the signals were too perturbed by aircraft structure and/or occupants to meaningfully deconstruct. Using the residuals of the adaptive sidelobe cancelling process, the direct path signal component could be isolated from the combined signal in the main channel and used as a zero forcing equalizer applied to the reference channel to force both channels to a common phase center. In spite of this, increased phase noise was experienced in approximately the same position, aircraft relative to the transmitter, on each orbit.

Two dimensional apertures, evaluated as an interim validation to three dimensional reconstruction, clearly focused, exhibiting mainlobe IPRs (shape and width/resolution) which matched theoretical predictions. These predictions were based on both ideal apertures and Fourier reconstruction, and error-free signal simulation using the as-flown orbits (from measured GPS). This demonstrated that the deterministic motion solution from the survey-grade, handheld GPS was at least minimally acceptable. Imagery clearly showed clusters of scatterers in the correct relative positions in the scenes processed but were somewhat disappointing in that many manmade (metallic) structures, with the exception of those selected to be the scene reference, were not readily observed. The silo is clearly evident (by position, Appendix E, Figure E.1) but immediately adjacent structures were not observable, yet a wooden structure (a house) nearby did appear at the

correct position in the imagery. Also the dark band representing the Snohomish River within the scene (also Figure E.1) is observed as well as regions corresponding to wooded areas are seen. A combination of factors could contribute to the lack of observing the metal structures. The first is that the vertical walls/shallow sloped roofs and very low incident transmitter grazing angle will only produce relatively far-out sidelobe scattering over the angular region the receiver sampled; all specular scattering is directed well away from the sampling aperture positions. Further that the sidelobe levels will roll off quickly below any surface diffuse scattering. Finally, integration over angles where specific object returns are below clutter will tend to raise the overall pixel power and mask the structure. Yet another consideration is that, as in the case of the sphere, the response of planar reflectors may collapse to a point representing the apparent phase center of the reflector. We do observe multiple returns in the immediate vicinity of the silo at image center which may be such.

Returns from trees are visible throughout the reconstructed scene (highlighted in Figure E.1 from the accompanying overhead image). It can be inferred that the low frequency, horizontally polarized signal (the HDTV standard) scatters from the trunks over a wider angle, integrating up to be visible in the images.

IPR sidelobes were such that images appeared most identifiable using a linear magnitude scale. Using reduced dynamic range logarithmic scales (for example total scene dynamic range of 20 dB) did not result in visually more satisfying images. Examples of this for each orbit processed can be found in Appendix E. In Chapter 5 we addressed apodization from the perspective of the circularly symmetric, tomographic aperture. This is a different consideration than the partial aperture. We address wide angle, partial aperture, two dimensional apodization in Appendix E where apodization was applied in both the spatial frequency domain (on forward transformed reconstructed images) and during reconstruction as a one dimensional taper applied along the collection aperture. It is noted

that the latter was a more efficient application, jointly in terms of pseudo-cross range sidelobe level and resolution and loss of resolution and degraded sidelobes along the pseudo range axis.

Data were sampled at 20 Hz and with backprojection (which does not employ Doppler processing) we have no concerns with sample aliasing in cross range (the data are range unambiguous out to beyond the horizon from the airborne receiver). The receive antenna sidelobes were those of a linear array in conjunction with widely uniform transmitter illumination. In assessing the IPR of the individual orbits (only Orbit 1 was presented in Figure 6.91) we evaluated the sidelobe levels for all nine. In the pseudo-cross range the sidelobes are on the order of 30 dB below peak response at and beyond 15 resolution cells (~5 m) from the peak response. Likewise along pseudo-range (along scene Y axis) the sidelobes recede below -20 dB at 20 m from the peak response. However these axes do not align with the IPR "cardinal" axes as shown in Figure 6.91 and 6.92 which, it is suggested, contribute to the longer diagonal regions observed. Out-of-scene contributions will be modulated by the receive antenna gain and the scatterer distance from the scene. With the IPR sidelobes extending indefinitely it is possible for out-of-scene energy to degrade image contrast. This also applies to the backprojection phase ambiguity (sample angular spacing), evaluated in Section 4.7, and which all persistent scatterers will exhibit.

We approached the 3D reconstruction with the same approach as the two dimensional case. As the orbit angular extents realized by maintaining the main/aux ratio were reduced from the complete orbits used in the aperture modeling and analysis from Section 5, we first wanted to develop the expected impulse response to have a standard for comparison to the flight data results. Both the ideal trajectory with inverse Fourier reconstruction and error-free, as-flown trajectory with backprojection agreed well: resolutions and qualitative evaluation of the PSF. Both exhibited phase ambiguous responses (grating lobes) along the image Z-direction from the sparse elevation sampling from the truncated orbits. The

flight data three dimensional reconstruction resolutions results from scatterers chipped out of the final image also agreed well with the simulated results, suggesting a wide angle scattering response. Presentation of the volumetric image in a meaningful manner proved to be challenging. The magnitude-clipped point cloud with line drawing of the scene structures (extracted from Google Earth photographic images, with layover) as an overlay showed very well the scene large responses physically coincident with the silo position. This supports the assertion that image reconstruction and registration are consistent, though less than fully satisfying. As discussed, a better value for the height above the geoid representing the scene origin would have been helpful. However, manually overlaying the point cloud results onto a photograph, and from the same perspective, shows the alignment of the brightest voxels with the target silo.

The use of a 3 dB scene dynamic range facilitated image interpretability. A large number of voxels exceeded the threshold. It is possible that the segmentation of the silo resulted in a large number of nearly equally sized scatterers which were observed. Each scatterer would generate grating lobes in Z which were only -5 to -10 dB relative to peak response, noncoherent combinations from multiple scatterers may be contributing to the observed voxel count in the 3 dB image dynamic range.

Future Work

With the recorded flight data in hand several follow-on activities suggest themselves. Initially we propose to explore the image quality improvement obtainable through autofocus. The particle swarm approach suggested by Parker and Norgard[6] would be the first considered, initially seeded by the carrier and code-phase corrected GPS measurements. Done for a single orbit initially then extending to all 9 would then provide the swarm optimized, motion solution for the three dimensional aperture.

[6] Parker, J. T. and Norgard, J., 'Autofocusing for RF tomography using particle swarm optimization', *IEEE Radar Conference 2008*, Rome IT, pp1-6, May 2008.

A second effort would be focusing the aperture over a full 360 degree. This raises the challenge of burst-to-burst phase coherency when the adaptive canceller may not be usable to extract a good estimate of the direct path signal at the main channel receiver. In both this effort and the one suggested above an improved sidelobe suppression algorithm would be applied. Several citations, derived from noise radar research, suggest means to improve time sidelobe suppression, such as Rigling [37].

The truncated orbits introduced grating lobes into the point spread function as was demonstrated in determining point spread function. The regular periodicity was broken in the actual trajectory but still grating lobes were observed. It would be very interesting to apply the CLEAN algorithm to 3D image focused three dimensional image

Finally, the bistatic, tomographic collection aperture intrinsically samples the out-of-plane response of ground clutter. Though the receiver was not radiometrically calibrated it may be possible to make an estimate of the radiometric sensitivity and translate the pulse compressed returns into reflectivity. Though the transmitter grazing angle is fixed throughout the collection, a wide range of out-of-plane clutter samples in a rural, farmland environment might be obtained.

Chapter 8.0

References

[1] Bloom, R. G. and Comer, D. C, 'Detection and identification of archaeological sites using radar data', http://www.serdp.org/Program-Areas/Resource-Conservation-and-Climate-Change/Cultural-Resources/RC-1260, April, 2006.

[2] Bloom, R. G. and Comer, D. C., 'Detection and identification of archeological sites and features using radar data', Final Report SERDP SI-1260, 2006.

[3] 'CBP Awards $45 million maritime radar award to Raytheon' web citation, http://www.gsnmagazine.com/ article/23673/cbp_awards_45_million_maritime_radar_award_raytheon.

[4] Davenport, Clark G., 'Remote sensing applications in forensic investigations', *Historical Archaeology*, Vol. 35, No. 1, pp 87-100, Spring 2001.

[5] Inggs, M. R. and Lord, R. T., 'Applications of satellite imaging radar', web citation, http://www. slidefinder.net /a/applications_satellite_imaging/radar/669351.

[6] Eguchi, R. T., Huyck, C., Beverley, J. R., Babak, M., Houshmand, M. and Shinozuka, M., 'Resilient disaster response: using remote sensing technologies for post-earthquake damage detection', web citation: http://mceer.buffalo.edu/publications/resaccom/03-SP01/09eguchi.pdf.

[7] Baranowski, E. J., 'VisiBuilding: sensing through walls', *4th IEEE Workshop on Sensor Array and Multichannel Processing*, Waltham MA, pp1-22, 12-14 July 2006.

[8] Davis, M. E., ***Foliage Penetration Radar: Detection and Characterization of Objects under Trees***, SciTech Publishing, Inc, Rayleigh NC, 2011.

[9] Attachment 1 to FCC Public Notice DA 11-47. Resolution 806 (Rev. WRC-12), 'Agenda for the 2015/16 World Radio Communication Conference', http://transition.fcc.gov/Daily_Releases/Daily_Business/ 2011/db0310/DA-11-447A2.pdf

[10] Higgins, T., Webster, T., and Shackleford, A. K., 'Mitigating interference via spatial and spectral nulling', *IET Radar, Sonar and Navigation, Special Issue: Bistatic and MIMO Radars and their Applications in Surveillance and Remote Sensing*, Vol. 8, Issue 2, pp84-93, Feb. 2014.

[11] Miller, T., Potter, L. and McCorkle, J., 'RFI suppression for ultra wideband radar', *IEEE Trans. on Aerospace and Electronic Systems*, Vol. 33, No. 4, pp1142-1156, Oct 1997.

[12] Committee on a Survey of the Active Sensing Uses of the Radio Frequency Spectrum. Board of Physics and Astronomy. *A Strategy for Active Remote Sensing amid Increased Demands for Radio Spectrum*, The National Academy Press, http://www.nap.edu/read/21729/chapter/10#172, /chapter/11#190.

[13] De Maio, A., 'Cognitive radar signal processing', *2014 Workshop on Mathematical Issues in Information Sciences*, http://meeting.xidian.edu.cn/workshop/miis2014/uploads/files/July-7th-1400pm_Antonio De Maio Cognitive Radar signal processing.pdf, July, 2014.

[14] Willis N. J., Griffiths, H. D. (ed.), ***Advances in Bistatic Radar***, SciTech Publishing, Inc, Rayleigh NC, Dec, 2007.

[15] Negishi, T., Farzami, F. Picco, V., Erricolo, D., Gennarelli, G., Soldovieri, F., Lo Monte, L., Wicks, M. C. and Ansari. F., 'Detection and imaging of cracks in reinforced concrete structures using RF tomography: quadratic forward model approach', *IEEE International Geoscience and Remote Sensing IGARSS 2015*, Milan, IT, pp3552-3555, 26-31 July 2015.

[16] Norgard, J., Musselman, R., and Drozd, A., 'Three dimensional microwave tomography: waveform diversity and distributed sensors for detecting and imaging buried objects with suppressed electromagnetic interference', *Asia Pacific Symposium on Electromagnetic Compatibility 2008 & 19th International Zurich Symposium on Electromagnetic Compatibility*, Singapore, pp371-374, 19-22 May 2008.

[17] Mensa, D. and Heidbreder, G., 'Bistatic synthetic aperture radar imaging of rotating objects', *IEEE Trans. on Aerospace and Electronic Systems*, Vol. AES-18, No. 4, pp423-431, July 1982.
[18] Munson, D. C., O'Brien, J. D. and Jenkins, W. K., 'A tomographic formulation of spotlight-mode synthetic aperture radar', *Proceedings of the IEEE*, Vol. 71, No. 8, pp917-925, August 1983.
[19] Norton, S. J. and Linzer, M., 'Ultrasonic reflectivity imaging in three dimensions: exact inverse scattering solutions for plane, cylindrical and spherical apertures', *IEEE Trans. on Biomedical Engineering*, Vol. BM-28, No. 2, pp 202-220, Feb. 1981.
[20] Norton, S. J. and Linzer, M., 'Ultrasonic reflectivity tomography: reconstruction with circular transducer arrays', *Ultrasonic Imaging*, Vol. 1, No. 2, pp154-184, April 1979.
[21] Mensa, D. L., Halevy, S., and Wade, G., 'Coherent Doppler tomography for microwave imaging', *Proc of the IEEE*, Vol. 71, No. 2, pp254-261, Feb 1983.
[22] Griffiths, H. D. and Long, N., 'Television-based bistatic radar', *IEE Proceedings Part F*, Vol. 133, No. 7, pp649-657. Dec. 1986
[23] Nordwall B.D., 'Silent Sentry a new type of radar', *Aviation Week & Space Technology*, No. 30, pp70–71, Nov. 1998.
[24] Coleman, C. J., Watson, R. A. and Yardley, H., 'A practical bistatic passive radar system for use with DAB and DRM ', *IEEE Radar Conference 2008*, Rome IT, pp1514-1519, May 2008.
[25] Poullin, D., 'Passive 3D tracking of low altitude targets using DBV (SFN broadcasters)', *IEEE AESS Magazine*, Vol. 27, No. 11, pp36-41, Nov 2012.
[26] Palmer, J., Palumbo, S., Van Cao, T-T. and Howard, S., 'A new illuminator of opportunity: bistatic radar research project at DSTO', *DSTO-TR-2269*, May 2009.
[27] O'Hagan, D. W., Capria, A., Petri, D., Kubica, V., Greco M., Berizzi F. and Stove, A. G., 'Passive bistatic radar (PBR) for harbour protection applications', *2012 IEEE Radar Conference Proceedings*, Atlanta GA,. pp446-450, 7-11 May 2012.
[28] Colone, F., Bongioanni, C. and Lombardo, P., 'Multifrequency integration in FM radio-based passive bistatic radar. Part I: target detection'. *IEEE AES Magazine*, Vol. 28, No. 14, pp28-39, April 2013.
[29] Krysik, P., Samczynski, P., Malanowski, M., Maslikowski, L. and Kulpa, K. S., 'Velocity measurement and traffic monitoring using a GSM passive radar demonstrator', *IEEE AES Magazine*, Vol. 27, No. 10, pp43-51, Sept 2012.
[30] Willis, N., ***Bistatic Radar*** (ed.), Artech House, Dedham MA, 1991.
[31] Malanowski, M. and Kulpa, K., 'Detection of moving targets with continuous-wave noise radar: theory and measurements', *IEEE Trans Geoscience and Remote Sensing*, Vol. 50, No 9, pp3502-3509, Sept 2012.
[32] Rihaczek, A. W., ***Principles of High Resolution Radar***, Artech House, Dedham MA, 1969.
[33] Falcone, P., Colone, F. and Lombardo, P., 'Potentialities and challenges of WiFi-based passive radar', *IEEE AESS Magazine*, Vol. 27, No. 11, pp36-41, Nov 2012.
[34] Guner, A., Temple, M. A. and Claypoole, R. L., 'Direct path filtering of DAB waveform from PCL receiver target channel', *Electronics Letters*, Vol. 39, No. 1, pp118-119, Jan 2003.
[35] Kulpa, K. S. and Czekala, Z., 'Masking effect and its removal in PCL radar', *IEE Proc. on Radar Sonar Navig.*, Vol. 152, No. 3, pp174-178, June 2005.
[36] Rigling, B. D., 'Intrinsic processing gain in noise radar', *Proceedings 2nd International Waveform Diversity and Design Conference*, Orlando FL, pp 579-583, 22-27 Jan 2006 (paper provided by author).
[37] Callahan, M. J., Rigling, B. D. and Rangaswamy, M., 'Impact of processing approach on SNR performance for passive bistatic noise radar', *IEEE International Radar Conference 2015*, Arlington VA, pp808-810, 10-15 May 2015.
[38] Blunt, S. D., Cook, M. R. and Stiles, J., 'Embedding information into radar emissions via waveform implementation', *Proceedings International Waveform Design and Diversity Conference WDD10*, Niagara Falls, CA, pp195-199, 8-13 Aug, 2010.
[39] Fry, R. D. and Gray, D. A., 'CLEAN deconvolution for sidelobe suppression in random noise radar', *Proceedings of the 2008 International Conference on Radar*, pp209-212, Adelaide AS, 2-5 Sept 2008.
[40] Poullin, D., Flecheux, M. and Mathieu, K., 'Elevation angle estimation for low-altitude targets using DBV (SFN broadcasters)', *IEEE AESS Magazine*, Vol. 27, No. 11, pp27-35, Nov 2012.

[41] Colone, F., O'Hagan, D. W., Lombardo, P. and Baker, C. J., 'A multistage processing algorithm for disturbance removal and target detection in passive bistatic radar', *IEEE Transactions on Aerospace and Electronic Systems*, Vol. 45, No. 2, pp698-722, April 2009.

[42] Cardinelli, R., Colone, F., Lombardo, P., Crognale, O., Cosmi, A. and Lauri, A., 'Multipath cancellation on reference antenna for passive radar which exploits FM transmission', *Proceedings 2007 IET Conference on Radar Systems*, Edinburgh, UK, pp1-5, 15-18 Oct 2007.

[43] Kulpa, K., Samczynski, P., Malanowski, M., Gromek, A., Gromek, D., Gewarek, W., Salski, B. and Tanski, G., 'An advanced SAR simulator of three-dimensional structures combining geometrical optics and full-wave electromagnetic methods', *IEEE Trans. on Geoscience and Remote Sensing*, Vol. 52, No. 1, pp776-784, Jan 2014.

[44] Walker J. L., 'Range-Doppler imaging of rotating objects', *IEEE Trans Aerospace and Electronic Systems*, Vol. AES-16, No. 1, pp23-52, Jan 1980.

[45] Wu, Y. and Munson, D. C., 'Wide-angle ISAR passive imaging using smoothed wigner-ville distribution', *Proceedings IEEE Radar Conference 2001*, Atlanta GA, pp363-368, 1-3 May 2001.

[46] Suwa K., Nakamura, S., Morita, S., Wakayama, T. and Maniwa, H., 'ISAR imaging of an aircraft target using ISDB-T digital TV based passive bistatic radar', *IEEE Geoscience and Remote Sensing Symposium 2010*, pp 4103-4105, Honolulu HI, 25-30 July 2010.

[47] Baczyk, M. K., Samczynski, P. and Kulpa, K., 'Passive ISAR imaging of an air targets using DVB-T signals', *IEEE Radar Conference 2014*, Cincinnati OH, pp502-506, 19-23 May 2014.

[48] Lu, K., Yang, Y., Qi, X. and Zhang, L., 'Passive ISAR imaging using multichannel DBV-T signals', *Sensors and Transducers*, Vol. 166, Issue 3, pp203-212, March 2014.

[49] Olivadese D., Giusti E., Petri, D., Martorella, M., Capria, A., Berizzi, F. and Soleti, R., 'Passive ISAR imaging of ships using DBV-T signals', *IET International Conference on Radar Systems 2012*, Glasgow UK, pp64-68, 25-27 Oct 2012.

[50] Pastina D., Sedehi, M. and Cristallini, D., 'Passive bistatic ISAR based on geostationary satellite for coastal surveillance', *IEEE Radar Conference 2010*, Washington D. C., pp865-871, 10-14 May 2010.

[51] Turin F. and Pastina D., 'Multistatic passive ISAR based on geostationary satellites for coastal surveillance', *IEEE Radar Conference 2013*, Ottawa CA, 29 April-3 May 2013.

[52] Norton, S. J. and Linzer, M., 'Ultrasonic reflection tomography: reconstruction with circular transducer arrays', ***Journal of Ultrasonic Imaging***, Vol. 1, Issue 2, pp154-184, April 1979.

[53] Lam, K., Yedlin, M. and Farquharson, C. G., 'Two dimensional radio frequency tomography', *IEEE Trans on Microwave Theory and Techniques*, Vol. 55, No. 4, pp801-808, April 2007.

[54] Wilson, J. and Patwari, N., 'Radio tomographic imaging with wireless networks', web citation Univ. of Utah, http://www.eng.utah.edu/~jwilson/files/RTI.pdf.

[55] Lo Monte, L., Erricolo, D., Soldovieri, F. and Wicks, M.C., 'Radio frequency tomography for tunnel detection', *IEEE Trans. Geoscience and Remote Sensing*, Vol. 48, No. 3, pp1128-1137, March 2010.

[56] Wicks, M.C., 'RF tomography with application to ground penetrating radar', *Conference Record of the Forty-First Asilomar Conference on Signals, Systems and Computers*, Pacific Grove CA, pp2017–2022, 4-7 Nov 2007.

[57] Bracken, L. J. E., Bacsom, H., Clancey, J., Himed, B. and Wicks, M. C., 'Ultra narrow band adaptive tomography', *1st IEEE Intl Workshop on Computational Advances in Multi-Sensor Adaptive Processing*, Puerto Vallarta MX, pp36-39, 13-15 Dec 2005.

[58] Li, Y., Rizos, C., Donski, E., Homer, J. and Mojarrabi, B., '3D multistatic SAR system for terrain imaging based in indirect GPS signals', *Journal of Global Positioning Systems*, Vol. 1, No. 1, pp34-39, 2002.

[59] Cherniakov, M., Saini, R., Zuo, R. and Antoniou, M., 'Space surface bistatic SAR with spaceborne noncooperative transmitters', *European Radar Conference 2005 (EURAD 2005)*, Paris FR, pp 9-12, 6-7 Oct 2005.

[60] Kubica, V., Neyt, X. and Griffiths, H. D., 'Improved cross-range resolution in TOPSAR imaging using Sentinel-1A in bistatic operation', *IEEE International Radar Conference 2015*, Arlington VA, pp 117-122, 10-15 May 2015.

[61] Zeng, Z., 'SS BSAR with GNSS and a stationary antenna - experimental results', *Progress in Electromagnetics Research B*, Vol. 48, pp271-287, 2013.

[62] Brown, J., Woodbridge, K. and Griffiths, H. D., 'Passive bistatic radar experiments from an airborne platform', *IEEE Aerospace and Electronic Systems Magazine*, Vol. 27, No. 11, pp50-55, Nov 2012.

[63] Brown, J., Woodbridge, K., Stove, A. and Watts, S., 'VHF airborne passive bistatic radar ground clutter investigation', *IET Radar Conference 2012*, Glasgow UK, pp53-58, 25-27 Oct. 2012.

[64] Ulander, L. M. H., Frolind, P., Gustavsson, A., Ragnarsson, R. and Stenstrom, G., 'VHF/UHF bistatic and passive ground imaging', *IEEE International Radar Conference 2015*, Washington, D. C., pp669-673, May 2015.

[65] Gromek, D., Samczynski, P., Kulpa, K., Krysik, K. and Malanowski, M., 'Initial results of passive SAR imaging using a DVB-T based airborne radar receiver', *Proceedings of the 11th European Radar Conference*, Rome, IT, pp137-140, 8-10 October 2014.

[66] Prati, C., Rocca, F., Giancola, D. and Monti Guarnieri, A., 'Passive geosynchronous SAR system reusing backscattered digital audio broadcasting signals', *IEEE Trans on Geoscience and Remote Sensing*, Vol. 36, Issue 6, pp1973-1976, Nov 1998.

[67] Pruessmann, K. P., Weiger, M., Börnert, P. and Boesiger, P., 'Advances in sensitivity encoding with arbitrary *k*-space trajectories', *Magnetic Resonance in Medicine*, Vol. 46, Issue 4, pp638-651, Oct 2001.

[68] Cetin, M. and Lanterman, A. D, 'Region-enhanced imaging for sparse-aperture passive radar', *Proc. SPIE 5427, Algorithms for Synthetic Aperture Radar Imagery XI*, pp176-187, Sept 2004.

[69] Parker, J. T., Ferrara, M., Bracken, J. and Himed, B., 'Preliminary experimental results for RF tomography using distributed sensing', *International Conference on Electromagnetics in Advanced Applications*, Sydney AS, pp549-552, Sept 2010.

[70] US Patent 9176226, 'Tomography using Doppler-based projections', granted 3 Nov, 2015 assignee The Boeing Company, Inventor Daniel; J. Sego.

[71] Ishimaru, A, ***Electromagnetic Wave Propagation, Radiation and Scattering*,** Prentice Hall, 1991.

[72] Daveney, A.J., 'Introduction to inverse scattering theory', Stanford Lecture Series, Part 1 web citation: www.ece.neu.edu/faculty/devaney/ppt/stanford.ppt.

[73] Norton, S. J. and Linzer, M., 'Ultrasonic reflectivity imaging in three dimensions: Exact inverse scattering solutions for plane, cylindrical and spherical apertures', *IEEE Trans. on Biomedical Engineering*, Vol. BME-28, No. 2, pp202-220, Feb. 1981.

[74] Semenov, S. Y., Svenson, R. H., Bulyshev, A. E., Souvorov, A. E., Nazarov, A. G., Sizov, A. N., Pavlovsky, A. V., Borisoz, V. Y., Voinov, B. A., Simonova, G. I., Starostin, A. N., Posukh, V. G., Tatsis, G. P. and Baranov, V, Y., 'Three-dimensional microwave tomography: Experimental prototype of the system and vector Born reconstruction method', *IEEE Trans on Biomedical Engineering*, Vol. 46, No. 8, pp937-946, Aug. 1999.

[75] Cheney, M. and Borden, B., 'Problems in synthetic-aperture radar imaging', *Inverse Problems*, Vol. 25, No. 12, pp1-18**,** Nov. 2009.

[76] Soliman, N. A. and Boerher, W. M., 'The depolarization term in vector (polarization) diffraction tomography and its importance in microwave imaging', *IEEE International Symposium on Electromagnetic Compatibility*, Nagoya Japan, pp 941-946(Vol. 2), Sept. 1989.

[77] Stakgold, I., ***Green's Functions and Boundary Value Problems** (2nd Ed)***.,*** New York, NT Wiley Intersciences, 1997.

[78] Kak, A. C. and Slaney, M.., ***Principles of Computerized Tomographic Imaging***, IEEE Press, The Institute of Electrical and Electronics Engineers Inc., New York. 1987.

[79] Jaramillo, H., 'The scattering theory approximations', http://s3.amazonaws.com/elasticbeanstalk-us-east-1-200981706290/wufu/57326b7013610.

[80] Web citation Duhamel's Principle, http://en.wikipedia.org/Duhamel's_principle/.

[81] University of Maryland Institute for Advanced Computer Studies eBook, ***Introduction to the Helmholtz Equation***, web citation http://www.umiacs.umd.edu/~ramani/FMM_HELMHOLTZ/Introduction.pdf

[82] Morse, P. M. and Feshbach, H., ***Methods of Theoretical Physics***, New York, NY, McGraw-Hill, 1953.

[83] Daveney, A. J., 'A filtered backpropagation algorithm for diffraction tomography', *Ultrasonic Imaging*, Vol. 4, issue 4, pp 336-350, Oct. 1982.

[84] Pan, S. X., Kak, A. C., 'A computational study of reconstruction algorithms for diffraction tomography: Interpolation vs. filtered-backprojection', *IEEE Trans. on Acoustics and Speech Signal Processing*, Vol. ASSP-31, pp. 1262-1275, Oct. 1983.

[85] Radon, Johann (1917), 'Über die bestimmung von funktionen durch ihre integralwerte längs gewisser mannigfaltigkeiten", *Berichte über die Verhandlungen der Sächsische Akademie der Wissenschaften (Reports on the proceedings of the Saxony Academy of Science)* (69): 262-277; *Translation:* Radon, J.; Parks, P.C. (translator) (1986), "On the determination of functions from their integral values along certain manifolds", *IEEE Transactions on Medical Imaging*, Vol. 5, No. 4, pp170-176, 1986.

[86] Jain, A.K., ***Fundamentals of Digital Image Processing***, Prentice Hall Information and Science Systems, Englewood Cliffs, NJ. 1989.

[87] Kak, A. C., Slaney, M.., ***Principles of Computerized Tomographic Imaging***, IEEE Press, The Institute of Electrical and Electronics Engineers Inc., New York. 1987

[88] Herman, G. T., ***Fundamentals of Tomography: Image Reconstruction from Projections***, Academic, New York, NY, 1980.

[89] Doerry, A. W., 'Anatomy of a SAR Impulse Response', *Sandia National Laboratories Technical Report SAND2007-5042*, Aug 2007.

[90] Moon, S. and Heo, J., 'Inversion of the elliptical Radon transform arising in migration imaging using the regular Radon transform', http://arxiv.org/pdf/1507.06031v2.pdf

[91] McCoy, J., Magotra, N., and Chang, B.: 'Coherent Doppler tomography; A technique for narrowband SAR', *IEEE AES Magazine*, pp19-22, Feb 1991.

[92] Knaell, K. K. and Cardillo, G. P., 'Radar tomography for the generation of three dimensional images', *IEE Proc., Radar, Sonar, Navig.*, Vol. 142, No. 2, April 1995.

[93] Mensa, D. L., Heidbreder, G. and Wade, G., 'Aperture synthesis by object rotation in coherent imaging', *IEEE Trans on Nuclear Science*, Vol. NS-27, No. 2. pp989-997, April 1980.

[94] web citation, Wolfram Mathematics, Bessel Functions, www.//mathworld.wolfram.com/Bessel FunctionoftheFirstKind.html

[95] Sego, D. J., Griffiths H. D., and Wicks, M. C: 'Waveform design for low frequency tomography", *IEEE 2010 Conference on Waveform Design and Diversity*, Niagara Falls CA, pp230-237, May 2010.

[96] You, J, 'Image Reconstruction from Projections – *math and C++ implementation*', http://citeseerx.ist.psu.edu/viewdoc/summary?doi=10.1.1.88.312 ,2/27/2005.

[97] Phase II SBIR Report, 'A Long life, High Voltage, Shortpulse Generator Based on Optically Activated Bulk Avalanche Semiconductor Switch. Phase 2', ADA 206078, ONR Contract Number N00014-88-C-0024, 27 Jan. 1989.

[98] Sego, D. J., Griffiths H. D., and Wicks, M. C: 'Waveform and aperture design for low frequency RF tomography', *IET Radar, Sonar & Navigation*, Vol. 5, issue 6, pp686-696, July 2011.

[99] Carrera W. G., Goodman R. S. and Majewski R. M., ***Spotlight Synthetic Aperture Radar Signal Processing Algorithms***, Artech House, Boston, 1995.

[100] Soumekh, M., ***Synthetic Aperture Radar Signal Processing with MATLAB Algorithms***, John Wiley and Sons, New York, 1999.

[101] Sego, D. J., Griffiths, H. D. and Wicks, M. C., 'Tomography using Doppler-based projections', *IEEE Radar Conference 2010 RadarCon '10*, Kansas City MO, pp403-407, May 2010.

[102] Griffiths, H. D., Baker, C. J., Baubert, J., Kitchen, N. and Treagust, M., 'Bistatic radar using satellite-borne illuminators of opportunity', *Proc. International Conference RADAR 2002*, pp 1–5, Oct 2002.

[103] Sanz-Marcos , J., Mallorqui, J. J. and Aguasca, A., 'First ENVISAT and ERS-2 parasitic bistatic fixed receiver SAR images processed with the subaperture range-Doppler algorithm', *IEEE International Geoscience & Remote Sensing Symposium, IGARSS 2006*, pp 1840-1843, Denver, Co, July 31-Aug 4, 2006.

[104] Duque, S., Lopez-Dekker, P., Merlano, J. C., and Mallorqui, J. J., 'Bistatic SAR tomography: processing and experimental results', *IEEE International Geoscience & Remote Sensing Symposium 2010 (IGARSS 2010)*, Honolulu HI, pp154-157, July 2010.

[105] Olivadese, D., Martorella, M., Guisti, E., Petri, D. and Berizzi, F., "Passive ISAR with DVB-T", *Ninth European Conference on Synthetic Aperture Radar, EUSAR 2012*, Nuremberg, Germany, pp 287-290, April 23-26 2012.

[106] Dawidowicz, B., Samcyzynski, P., Malanowski, L. Misiurewicz, J., and Kulpa, K. S., 'Detection of moving targets with multichannel airborne passive radar', *IEEE Aerospace and Electronics Systems Magazine*, Vol. 27, No. 11, pp 42-49, Nov 2012.

[107] Tektronix Application Note, 'Fundamentals of 8VSB', http://www1.tek.com/ Measurement/ App_Notes/ 25_15787/eng/25W_15787_0.pdf.

[108] ATSC A53 Specification http://www.atsc.org/cms/standards/a53/a_53-Part-1-6-2007.pdf.

[109] DTV Spectrum Mask, http://broadcastengineersnotebook.files.wordpress. com/2009/03/8-vsb-mask-dtvemissions.pdf , IEEE P1631™/D3 - Draft Recommended Practice for Measurement of 8-VSB

Digital Television Mask Transmission Compliance for the USA, Feb 2008 (The ideal frequency response of an 8-VSB transmitter is shown in Figure 2 [B2] [FCC 7CFR§73.682(a)1]).
[110] Griffiths, H.D. and Baker, C.J., "Measurement and analysis of ambiguity functions of passive radar transmissions", *IEEE International Radar Conference 2015* (*RADAR 2015)*, Washington DC, pp321–325, 9–12 May 2005.
[111] Doerry, Armin W., 'Shaping the spectrum of random-phase radar waveforms', Sandia Report SAND 2012-12-6915, Sept 2012, prod.sandia.gov/techlib/access-control.cgi/2012/126915.pdf.
[112] Kouemou, G., ***Radar Technology***, ISBN 978-953-307-029-2, Chapter 5, pp 410. Dec 2009, http://cdn.intechopen.com/pdfs/6882/InTech-Wideband_noise_radar_based_on_phase _coded_sequences.pdf.
[113] Levanon, N., ***Radar Signals***, John Wiley, New York, 2004.
[114] Sego, D. J. and Griffiths, H. D., 'Tomography using digital broadcast television', *IEEE Radar Conference 2014 (RadarConf 14)*, Cincinnati, OH, May 2014, pp 285.
[115] Skolnik, M. I (ed.), ***Radar Handbook***, McGraw-Hill, New York NY, 1970.
[116] Kelly, E. J., and Wishner, R. P., 'Matched-filter theory for high velocity, accelerating targets', *IEEE Trans. on Military Electronics*, MIL-9, No. 1, pp55-69, 1965.
[117] Olsen, K. E. and Woodbridge, K., 'Performance of a multiband passive bistatic radar processing scheme- Part II', *IEEE Aerospace and Electronics Systems Magazine*, Vol. 27, No. 10, , pp4-14, Nov. 2012.
[118] Kulpa, K. S. and Czekala, Z., 'Masking effect and its removal from PCL radar', *IEE Proc. Radar Sonar Navig*., Vol 152, No. 3, pp174-178, June 2005.
[119] Monzingo, R. A. and Miller, T. W., ***Adaptive Arrays***, SciTech Publishing, Rayleigh NC, corrected reprinting from John Wiley and Sons, NY, 2004.
[120] Ward, J., 'Space-time adaptive processing for airborne radar", MIT/LL Technical Report 1015, No. 13, Dec, 1994.
[121] Carrera, W. G., Goodman, R. S. and Majewski, R. M., ***Spotlight Synthetic Aperture Radar Signal Processing Algorithms***, Artech House, Inc. Norwood MA, 1995.
[122] Mensa, D. L., ***High Resolution Radar Imaging***, Artech House, Inc, Norwood MA, 1983.
[123] Bric, A. J., 'Imaging a BQM-74E target drone using coherent radar cross section measurements', Johns Hopkins Technical Digest, Vol. 18, No. 3, 1997.
[124] Davis, R. M., Fante, R. L., Perry, R. P. 'Phase coded waveforms for radar', MITRE Technical Papers, http://www.mitre.org/sites/default/files/pdf/05_0112.pdf, March 2005.
[125] Smith B. H., 'Generalization of spatially variant apodization to noninteger Nyquist sampling rates', *IEEE Trans. on Image Processing*, Vol. 9, No. 6, pp1088-1093, June 2000.
[126] Stankwitz, H. C., Dalliare, R. J. and Feinup, J. R., 'Nonlinear apodization for sidelobe control in SAR imagery', *IEEE Trans. Aerospace Electronic Systems*, AES-31, No. 1, pp267-279, Jan 1995.
[127] Zhai, W. and Zhang, Y, 'Apply spatially variant apodization to SAR/INSAR image processing', *1st Asian and Pacific Conference on Synthetic Aperture Radar (APSAR 2007)*, Huangshan China**,** pp 54-57, Nov. 2007.
[128] McCorkle, J. W. and Bennett, M., 'Spatially varying aperture weighting for sidelobe reduction and resolution enhancement in imagery' Army Research Laboratory ARL-TR-1662, www.dtic.mil/docs/ citations/ADA355541, Oct 1998.
[129] Iglesias, R. and Mallorqui, J. J., 'Sidelobe cancellation in DInSAR pixel selection with SVA', *IEEE Geoscience and Remote Sensing Letters*, Vol. 10, No. 4, pp 667-671, July 2013.
[130] FEKO EM Simulation Software, web citation http://www.feko.info/
[131] web citation, 'Sidelobe Cancellation', course notes University of Alabama, Huntsville, http://www.ece.uah.edu/ courses/material/EE710-Merv/SLC_11.pdf.
[132] Kraus, J. D., ***Antennas***, Chapter 6, McGraw-Hill, Inc. New York, 1988.
[133] Smith, G., ***Loop Antennas***, Chapter 5, www.mhprofessional.com/.../products/0071475745/0071475745 _chap05.pdf.
[134] Wadell, Brian C., ***Transmission Line Design Handbook***, Artech House, Dedham MA , pp382, 1991.
[135] web citation, http://www.qsl.net/n1bwt/ch7_part4.pdf, ***W1GHZ Microwave Antenna eBook***, Chapter 4 part 4.
[136] Alford A., 'Long slot antennas', *Proc. Natl. Electronics Conf.*, pp 143-155, 1946, via http://www.w1ghz.org/antbook/Long_Slot_Antennas_Alford.pdf.
[137] Sablatzky, N., 'Communicating high speed multimedia via amateur radio – A horizontally polarized omni-directional antenna you can build', http://www.hotarc.org/hsmm-mesh/articles/horizontally_ polarized_omni_plans.pdf.
[138] web citation http://imageevent.com/publicgallery/mostrecent/uhfslottedcylinderslotantenna000
[139] Brown, G. H., 'The turnstile antenna', *Electronics*, Vol. 9, No. 15, pp14-17, April 1936.
[140] Cebnik, L. B. (W4RNL), 'Some notes on turnstile antenna properties', http://w4rnl.net46.net/download/turns.pdf.

[141] Wikipedia entry FR4 https://en.wikipedia.org/wiki/FR-4.
[142] Balanis, C. A., ***Antenna Theory, Analysis and Design, 3rd Ed.***, chapter 14, Wiley, New York NY, 2005.
[143] Bancroft, R., ***Microstrip and Printed Antenna Design***, chapter 2, Scitech Publishing, Inc, Rayleigh NC, 2006.
[144] Jackson, D. R., 'Overview of microstrip antennas', class notes, http://www0.egr.uh.edu/courses/ece/ECE5318/microstrip antennas overview.pdf.
[145] Pihnas, S. and Shtrikman, S., 'Comparison between computed and measured bandwidth of quarter-wave microstrip radiators', *IEEE Trans. Antennas and Propagation*, Vol. 36, No 11. pp1615-1616, Nov 1988.
[146] Ruck, G. T., Barrick, D. E., Stuart, W. D. and Krichbaum, C. K., ***Radar Cross Section Handbook Volume 1***, Plenum Publishing, New York, NY, 1970.
[147] Doerry, A. W., "Reflectors for SAR performance testing", Sandia Report SAND2008-0396, Jan. 2008.
[148] Krishna, R. R., Krishna, M. K., Krishna, R. G. and Sekhar, D., 'Radar cross section prediction for different objects using MATLAB and RCS reduction', *International Journal of Advanced Research in Computer Science and Electronics Engineering*, Vol. 1, issue 5, pp67-75, July 2012.
[149] Deepa, T., 'Linear and nonlinear equalizers', SRM University, http://www.srmuniv.ac.in/sites/default/files/files/Linear&nonlinearequalizers.pdf.
[150] Ettus Corp data sheet, http://www.ettus.com/product/details/LP0410.
[151] Wu, S. and Li, Y., 'Adaptive channel equalization for space-time processing', *IEEE International Radar Conference 1995*, Alexandria VA, pp 624-628, 8-11 May 1995.
[152] Lauritzen, K., Krichene, H. and Talisa, S., 'Hardware limitations of receiver channel-pair cancellation ratio', *IEEE Trans. Aerospace and Electronic Systems*, Vol. 48, No. 1, pp290-303, Jan. 2012
[153] Tisdale N., Kazmierski, T. and Brooks, D., 'Channel mismatch compensation for space-time adaptive processors', *Proceedings of the 2008 Military Communications Conference*, San Diego CA, , pp1-7, May 2008.
[154] USRP online manuals, http://files.ettus.com/uhd_docs/manual/html/sync.html
[155] Sego, D. J., Griffiths, H. and Wicks, M. C., 'Waveform and synthetic aperture design for low frequency tomography', *2011 UNSC-URSI National Radio Science Meeting, Special Session on Waveform Diversity: Multidisciplinary Approaches to Different Sensing Modalities*, Boulder, CO, 5-8 Jan, 2011.
[156] Torres, J. A., Davis, R. M., Kramer, D. R. and Fante, R. L., "Efficient wideband jammer nulling when using stretch processing", *IEEE Trans on Aerospace and Electronic Systems*, Vol. 36, No. 4, pp1167-1177, Oct 2000.
[157] National Telecommunications and Information Agency. http://www.ntia.doc.gov/page/2011/united-states-frequency-allocation-chart.
[158] web citation, TV Fool, http://www.tvfool.com.
[159] web citation, http://broadcastengineersnotebook.files.wordpress.com/2009/03/8-vsb-mask-dtvemissions.pdf , IEEE P1631™/D3, 'Draft recommended practice for measurement of 8-VSB digital television mask transmission compliance for the USA, Feb 2008
[160] web citation, Federal Communications Commission FCC-11-110, https://apps.fcc.gov/edocs public/attachmatch/FCC-11-110A1.pdf
[161] web citation, http://www.outerzone.co.uk/plan_files_05/5692/Cessna_170A_Guillows _kit_1501.pdf
[162] Soumekh, M., 'Wide-bandwidth continuous wave monostatic/bistatic synthetic aperture imaging', *Proc. 1998 International Conference on Image Processing (ICIP 98)*, Chicago, IL, pp361-365, 4-7 Oct. 1998.
[163] Coetzee, S. L., Baker, C. J. and Griffiths, H. D., "Narrow band high resolution radar imaging", *Proceedings of the 2006 IEEE Conference on Radar*, Verona NY, pp 622-625, April 2006.
[164] Sego, D. J. and Griffiths, H, ., 'Tomography using digital broadcast television - flight test and interim results', *IEEE Radar Conference 2016*, Philadelphia PA, pp557-562, 2-6 May 2016.
[165] Moses, R. L., Potter, L. C., Cetin, M., "Wide angle SAR imaging", *Proc SPIE Algorithms for Synthetic Aperture Radar Imagery XI*; E. G. Zelnio and F. D. Garber, Eds. Vol. 5427, pp. 164-175 April 2004.
[166] Rigling, B. D., Moses, R. L. "GTD-based scattering models for bistatic SAR", *Proc. SPIE* 5427, *Algorithms for Synthetic Aperture Radar Imagery XI*, pp 208-219, Sept., 2004.

Chapter 9.0

Appendices

Appendix A. HDTV Autocorrelation Approximation Ensemble Averaged Spectrum.

Derivation of the autocorrelation function for the HDTV waveform based on using the square of the spectrum mask [5.0-15] as the ensemble averaged power spectrum. We start with (5.2-11) the functional description of the spectrum (magnitude) mask.

$$S(f)=\begin{cases} 0 & f > F_p+\frac{F_{sym}}{2}\left(1+\frac{\alpha}{2}\right)-\frac{BW}{2} \\ \sin\left(\frac{\pi\left(\frac{F_{sym}}{4}(2+\alpha)-\left(f+\frac{BW}{2}\right)+F_p\right)}{\alpha F_{sym}}\right) & f > F_p+\frac{F_{sym}}{2}\left(1-\frac{\alpha}{2}\right)-\frac{BW}{2} \quad f \le F_p+\frac{F_{sym}}{2}\left(1+\frac{\alpha}{2}\right)-\frac{BW}{2} \\ 1 & f \ge F_p+\frac{\alpha F_{sym}}{4}-\frac{BW}{2} \quad f \le F_p+\frac{F_{sym}}{2}\left(1-\frac{\alpha}{2}\right)-\frac{BW}{2} \\ \sin\left(\frac{\pi\left(\left(f+\frac{BW}{2}\right)-F_p+\frac{F_{sym}\alpha}{4}\right)}{\alpha F_{sym}}\right) & f > F_p-\frac{\alpha F_{sym}}{4}-\frac{BW}{2} \quad f < F_p+\frac{\alpha F_{sym}}{4}-\frac{BW}{2} \\ 0 & f < F_p-\frac{\alpha F_{sym}}{4}-\frac{BW}{2} \end{cases} \tag{A-1}$$

We write the autocorrelation in terms of the power spectrum as

$$R(\tau)=\int_{-\infty}^{\infty} S(f)^2 e^{j2\pi f\tau}\,df \tag{A-2}$$

From (D-1) we see two regions where the response is identically zero and three nonzero. The three nonzero regions are identified by breakpoints in frequency allowing the integral to be broken into three regions

$$R(\tau)=\int_{f_0}^{f_1}S_1(f)^2e^{j2\pi f\tau}df+\int_{f_1}^{f_2}S_2(f)^2e^{j2\pi f\tau}df+\int_{f_2}^{f_3}S_3(f)^2e^{j2\pi f\tau}df \qquad \text{(A-3)}$$

where

$$\begin{aligned} f_0 &= F_p-\frac{\alpha F_{sym}}{4}-\frac{BW}{2} & f_1 &= F_p+\frac{\alpha F_{sym}}{4}-\frac{BW}{2} \\ f_2 &= F_p+\frac{F_{sym}}{2}\left(1-\frac{\alpha}{2}\right)-\frac{BW}{2} & f_3 &= F_p+\frac{F_{sym}}{2}\left(1+\frac{\alpha}{2}\right)-\frac{BW}{2}. \end{aligned} \qquad \text{(A-4)}$$

Working term-wise, starting with term 1

$$R_1(\tau)=\int_{f_0}^{f_1}\left(\sin\left(\frac{\pi\left(f+\frac{\alpha F_{sym}}{4}-F_p+BW/2\right)}{\alpha F_{sym}}\right)\right)^2e^{j2\pi f\tau}df \qquad \text{(A-5)}$$

where F_{sym} is the symbol frequency (=10.762238E+06), the pilot tone relative frequency F_p (= 309.441E+03), $\alpha = 2BW/F_{sym}$-1 and BW=6.0E+06 is the total channel bandwidth. All the terms in the argument of the sinusoid are constant, but one, so we make a simplifying variable change

$$x=\kappa f+\beta 1 \quad df=\frac{1}{\kappa}dx \quad \kappa=\frac{\pi}{\alpha F_{sym}} \quad \beta 1=\pi\left(\frac{\alpha F_{sym}}{4}-F_p+BW/2\right) \qquad \text{(A-6)}$$

With (A-6) equation (A-5) becomes

$$R(\tau)=\frac{1}{\kappa}\int_{f_0}^{f_1}\sin^2(x)e^{j\frac{2\pi}{\kappa}(x-\beta 1)\tau}dx \qquad \text{(A-7)}$$

Using the cosine double angle identity to put the integrand into a more convenient form

$$\cos(2x)=1-2\sin^2(x) \quad or \quad \sin^2(x)=\frac{1}{2}-\frac{1}{2}\cos(2x) \qquad \text{(A-8)}$$

gives

$$R_1(\tau)=\frac{1}{\kappa}\int_{f_0}^{f_1}\left(\frac{1}{2}-\frac{1}{2}\cos(2x)\right)e^{j\frac{2\pi}{\kappa}(x-\beta 1)\tau}dx \qquad \text{(A-9)}$$

separating into two sub-expressions gives

$$R_1(\tau) = \frac{1}{2\kappa}\int_{f_0}^{f_1} e^{j\frac{2\pi}{\kappa}(x-\beta 1)\tau}\,dx - \frac{1}{2\kappa}\int_{f_0}^{f_1}\cos(2x)e^{j\frac{2\pi}{\kappa}(x-\beta 1)\tau}\,dx \qquad \text{(A-10)}$$

Solving the first is straight forward

$$\frac{1}{2\kappa}\int_{f_0}^{f_1} e^{j\frac{2\pi}{\kappa}(x-\beta 1)\tau}\,dx = \frac{e^{-j\frac{2\pi}{\kappa}\beta 1\tau}}{2\kappa}\int_{f_0}^{f_1} e^{j\frac{2\pi}{\kappa}(x)\tau}\,dx = \frac{e^{-j\frac{2\pi}{\kappa}\beta 1\tau}}{2\kappa}\frac{1}{-j\frac{2\pi}{\kappa}\tau}e^{j\frac{2\pi}{\kappa}x\tau} \qquad \text{(A-11)}$$

Reversing the substitution allows the use of the original limits

$$= \frac{e^{-j\frac{2\pi}{\kappa}\beta 1\tau}}{2\kappa}\frac{1}{j\frac{2\pi}{\kappa}\tau}\left(e^{j\frac{2\pi}{\kappa}(\kappa f_1+\beta 1)\tau} - e^{j\frac{2\pi}{\kappa}(\kappa f_0+\beta 1)\tau}\right) \qquad \text{(A-12)}$$

Bringing the first exponential inside the brackets gives the final form

$$R_{1of1}(\tau) = \frac{1}{j4\pi\tau}\left(e^{j2\pi f_1\tau} - e^{j2\pi f_0\tau}\right) \qquad \text{(A-13)}$$

Moving to the second part of the first term, this expression resembles a form found in the integral tables

$$\int e^{bx}\cos(ax)dx = \frac{e^{bx}}{a^2+b^2}\left(a\sin(ax)+b\cos(ax)\right). \qquad \text{(A-14)}$$

Referring to (A-10) we have a=2 and b= $j(2\pi/\kappa)\tau$, with substitution we have

$$= \frac{-\frac{1}{2\kappa}e^{-j\frac{2\pi}{\kappa}\beta 1\tau}}{\left(4+\left(j\frac{2\pi}{\kappa}\tau\right)^2\right)}e^{j\frac{2\pi}{\kappa}\tau x}\left(2\sin(2x)+j\frac{2\pi}{\kappa}\tau\cos(2x)\right). \qquad \text{(A-15)}$$

Reversing the substitution for x and with some simplification we have, before evaluating the integral limits

$$R_{2of3}(\tau) = \frac{1}{2\kappa\left(4+\left(j\frac{2\pi}{\kappa}\tau\right)^2\right)}e^{j2\pi tf}\left(2\sin\left(2(\kappa f+\beta 1)\right)+\left(j\frac{2\pi}{\kappa}\tau\right)\cos\left(2(\kappa f+\beta 1 f)\right)\right) \qquad \text{(A-16)}$$

The final form of the second part of the first autocorrelation term (subscript *2of1*) is

$$R_{2of1}(\tau) = -\frac{1}{\left(4+\left(j\frac{2\pi}{\kappa}\tau\right)^2\right)}\left[e^{ja_{1\_t1}\tau_1}\left(2b_{1\_t1}+jc_{1\_t1}\tau\right)-e^{ja_{2\_t1}\tau_1}\left(2b_{2\_t1}+jc_{2\_t1}\tau\right)\right] \quad \text{(A-17)}$$

with substitutions defined by

$$\begin{array}{cc} a_{1\_t1}=2\pi f_1 & a_{2\_t1}=2\pi f_0 \\ b_{1\_t1}=\sin(2(\kappa f_1+\beta 1)) & b_{2\_t1}=\sin(2(\kappa f_0+\beta 1)) \\ c_{1\_t1}=\frac{2\pi}{\kappa}\cos(2(\kappa f_1+\beta 1)) & c_{2\_t1}=\frac{2\pi}{\kappa}\cos(2(\kappa f_0+\beta 1)) \end{array}$$

The second integral term is associated with the flat top (unity magnitude) portion of the spectrum mask. It is given by

$$R_2(\tau)=\int_{f_1}^{f_2} e^{j2\pi f\tau}\,df \quad \text{(A-18)}$$

this is more directly evaluated to give

$$R_2(\tau)=\frac{1}{j2\pi\tau}\left(e^{j2\pi f_2\tau}-e^{j2\pi f_1\tau}\right) \quad \text{(A-19)}$$

The third term of (A-3) resembles the first and has a similar approach

$$R_3(\tau)=\int_{f_2}^{f_3}\left(\sin\left(\frac{\pi\left(\frac{F_{sym}}{4}(2+\alpha)-BW/2+F_p-f\right)}{\alpha F_{sym}}\right)\right)^2 e^{j2\pi f\tau}\,df. \quad \text{(A-20)}$$

Substituting for constants and making a change of variable

$$x=\beta 1-\kappa f \quad df=-\frac{1}{\kappa}dx \quad \kappa=\frac{\pi}{\alpha F_{sym}} \quad \beta 2=\pi\left(\frac{\alpha F_{sym}}{4}(2+\alpha)+F_p-BW/2\right) \quad \text{(A-21)}$$

With these substitutions (A-20) becomes

$$R_3(\tau)=-\frac{1}{\kappa}\int_{f_2}^{f_3}(\sin(x))^2 e^{j\frac{2\pi}{\kappa}(\beta 2-x)\tau}\,dx. \quad \text{(A-22)}$$

Making use of the double angle identity again, we have

$$R_3(\tau)=-\frac{1}{\kappa}e^{j\frac{2\pi}{\kappa}\beta 1\tau}\left(\int_{f_2}^{f_3}\frac{1}{2}e^{-j\frac{2\pi}{\kappa}x\tau}\,dx-\frac{1}{2}\int_{f_2}^{f_3}\cos(2x)e^{-j\frac{2\pi}{\kappa}x\tau}\,dx\right) \quad \text{(A-23)}$$

The derivation for the third term continues as the same manner as the $R_1(\tau)$. The first term reduces directly to

$$R_{1of3}(\tau) = \frac{1}{j4\pi\tau}\left(e^{j2\pi f_3\tau} - e^{j2\pi f_2\tau}\right) \tag{A-24}$$

The second term of $R_3(\tau)$ differs from that of $R_1(\tau)$ by a sign and constants. The evaluated integral, before limits are evaluated is

$$R_{2of3}(\tau) = \frac{1}{2\kappa\left(4+\left(-j\frac{2\pi}{\kappa}\tau\right)^2\right)} e^{j2\pi\tau f}\left(2\sin(2(\beta 2-\kappa f))+\left(-j\frac{2\pi}{\kappa}\tau\right)\cos(2(\beta 2-\kappa f))\right). \tag{A-25}$$

With the final substitutions, as in (A-17) we have

$$R_{2of3}(\tau) = \frac{1}{2\kappa\left(4+\left(-j\frac{2\pi}{\kappa}\tau\right)^2\right)}\left(e^{a_{e\_t1}\tau}\left(2b_{3\_t1}-jc_{3\_t1}\tau\right)-e^{a_{4\_t1}\tau}\left(2b_{4\_t1}-jc_{4\_t1}\tau\right)\right) \tag{A-25}$$

with

$$\begin{array}{cc} a_{3\_t1} = 2\pi f_3 & a_{4\_t1} = 2\pi f_2 \\ b_{3\_t1} = \sin(2(\beta 2-\kappa f_3)) & b_{4\_t1} = \sin(2(\beta 2-\kappa f_2)) \\ c_{3\_t1} = \frac{2\pi}{\kappa}\cos(2(\kappa f_1+\beta 1)) & c_{4\_t1} = \frac{2\pi}{\kappa}\cos(2(\beta 2-\kappa f_2)) \end{array}$$

Evaluating (A-26) over the range of delays

$$R(\tau) = R_{1of1}(\tau)+R_{2of1}(\tau)+R_2(\tau)+R_{1of3}(\tau)+R_{2of3}(\tau) \tag{A-26}$$

produces the spectrum seen in Figure 5.2-6. Though not shown, this spectrum exactly matched a numerical result obtained by squaring the voltage spectrum mask and taking the inverse Fourier Transform. Tomographic reconstruction results from using (A-23) are found in Figure 5.2-7.

Appendix B. Triangle Waveform Approximation, Move-Stop-Move.

This appendix includes the mathematical developments of several functions in the main body.

Starting from (5.3-20) the forward transform of the individual spatial measurement is

$$S_{\phi,\theta}(k) = \int_{-\infty}^{\infty} N_c t_p C_s C_r e^{-jk_0\Delta R} A(r,\Delta R) e^{-jkr} dr \tag{B-1}$$

where the main response of the cross correlation of the binary PN code is given by

$$\begin{aligned} A(r,\Delta R) &= 1 - \frac{|\tau c - \Delta R|}{t_p c}; |c\tau - \Delta R| < c t_p \\ A(r,\Delta R) &= 0; otherwise \end{aligned} \tag{B-2}$$

The terms τ and t_p represent, respectively, the delay relative to the direct path reference (11) and the pulse one-way duration (the pulse length is r_p). ΔR is the specific value of τ that corresponds to the scatterer position, range delay. Using B-2 in B-1

$$S_{\phi,\theta}(k) = N_c t_p C_s C_r e^{-jk_0\Delta R} \int_{-\infty}^{\infty} 1 - \frac{|r - \Delta R|}{r_p} e^{-jkr} dr \tag{B-3}$$

Because the range response extent is constrained by the physical length of the triangle pulse, the limits can be decreased to $\Delta R - r_p$ to $\Delta R + r_p$. Simultaneously we make the change of variable $x = |r - \Delta R|$, $dx = dr$. From this (B-3) becomes, including reevaluating limits with the substitution;

$$S_{\phi,\theta}(k) = N_c t_p C_s C_r e^{-jk_0\Delta R} e^{-jk\Delta R} \int_{-r_p}^{r_p} \left(1 - \frac{|x|}{r_p} e^{jkx}\right) dx \tag{B-4}$$

In order to accommodate the absolute value, the integral is split into the sum of two terms; one covering ranges less than 0, the other ranges greater than 0. In the remainder of this section the leading constants in (B.4) are dropped for convenience.

$$S_{\phi,\theta}(k) = \int_{-r_p}^{0} \left(1 + \frac{x}{r_p}\right) e^{jkx} dx + \int_{0}^{r_p} \left(1 - \frac{x}{r_p}\right) e^{jkx} dx \tag{B-5}$$

Each term in (B-5) is further expanded into two terms

$$S_{\phi,\theta}(k) = \int_{-r_p}^{0} e^{jkx} dx + \int_{-r_p}^{0} \frac{x}{r_p} e^{jkx} dx + \int_{0}^{r_p} e^{jkx} dx - \int_{0}^{r_p} \frac{x}{r_p} e^{jkx} dx \tag{B-6}$$

The four terms individually yield

$$\int_{-r_p}^{0} e^{jkx}dx = -\frac{j}{k}\left(1-e^{-jkr_p}\right)$$
$$-\int_{0}^{r_p} \frac{x}{r_p} e^{jkx}dx = -\frac{j}{k}\left(e^{jkr_p}-1\right)$$
$$\int_{-r_p}^{0} \frac{x}{r_p} e^{jkx}dx = \frac{1}{r_p k^2} - \frac{je}{k}e^{-jkr_p} - \frac{1}{r_p k^2}e^{-jkr_p} \quad \text{(B-7)}$$
$$\int_{0}^{r_p} \frac{x}{r_p} e^{jkx}dx = \frac{1}{r_p k^2} + \frac{je}{k}e^{jkr_p} - \frac{1}{r_p k^2}e^{jkr_p}$$

Combining the four terms of (B-7) gives

$$S_{\phi,\theta}(k) = N_c t_p C_s C_r e^{-j(k_0+k)\Delta R}\left(\frac{2}{r_p k^2} - \frac{2}{r_p k^2}\cos(r_p k)\right) \quad \text{(B-8)}$$

where we have used the exponential identity $e^{ax}+e^{-ax}=2\cos(ax)$. Further using the cosine identity

$$S_{\phi,\theta}(k) = 2N_c t_p C_s C_r e^{-j(k_0+k)\Delta R}\frac{\sin\left(\frac{r_p}{2}k\right)^2}{\frac{r_p}{2}k^2}. \quad \text{(B-9)}$$

The result in (B-9) was used as the input to the filtered backprojection algorithm that produced the IPR presented in Figures 5.2-9.

Appendix C. Frequency Domain Derivation of Cross Correlation Product in the Presence of Main Channel and Reference Channel Doppler.

Starting from the exact solution given in (5.3-26), we proceed to develop an approximate functional representation for the compressed waveform; first in the time domain invoking the mainlobe response (as in Appendix A)

$$\chi(\tau) = Z_c \sum_{m=1}^{N_c}\sum_{n=1}^{N_c} K_4\left[u_m u_n^*\right] \quad \text{(C1)}$$

With $|\tau'| < t_p$ (as earlier) and with

$$K4(\tau'<0)=\begin{cases}\dfrac{\sin\left(\dfrac{(\omega_{scat}-\omega_{ref})(t_p-\tau')}{2}\right)}{\dfrac{(\omega_{scat}-\omega_{ref})}{2}}e^{j\alpha}, & |\tau'|<t_p\\ 0, & otherwise\end{cases}$$

$$K4(\tau'>0)=\begin{cases}\dfrac{\sin\left(\dfrac{(\omega_{scat}-\omega_{ref})(t_p+\tau')}{2}\right)}{\dfrac{(\omega_{scat}-\omega_{ref})}{2}}e^{j\alpha}, & |\tau'|<t_p\\ 0, & otherwise\end{cases} \qquad \text{(C-2)}$$

with

$$\begin{aligned}\alpha &= \omega_{scat}(1/2+m)t_p-\omega_{ref}(1/2+n)t_p+(1/2)(3\omega_{ref}-\omega_{scat})\tau'\\ Z_c &= C_rC_se^{-jk_0\Delta R}e^{j\omega_{scat}\frac{R_s}{c}}e^{-j\omega_{ref}\frac{R_b}{c}}\\ \tau' &= \tau-\frac{\Delta R}{c}-(n-m)t_p.\end{aligned} \qquad \text{(C-3)}$$

Evaluating (C-1) produces a peak response at the matched range with time sidelobes extending into positive and negative delay to twice the sample (burst) duration. The peak response is deterministic and the time sidelobes are random and symmetrical about the peak. In the same manner as the move-stop-move case, we constrain the delay to the interval ΔR-r_p to ΔR+r_p: this is equivalent to the time interval such that $|\tau-\Delta R/c| < t_p$. With a little manipulation the exponential term in (C-2) becomes

$$e^{j\alpha}=e^{j\frac{\omega_{scat}-\omega_{ref}}{2}t_p}e^{j\left(\frac{1}{2}(3\omega_{ref}-\omega_{scat})\left(\tau-\frac{\Delta R}{c}\right)\right)}e^{j(\omega_{scat}m-\omega_{ref}n)t_p} \qquad \text{(C-4)}$$

This allows removing the first two terms of (C-4) from the double summation and the triangle approximation means that m=n thus reducing to a single summation. This leaves

$$\chi(\tau>0)=Z_{cc}\frac{\sin\left(\dfrac{(\omega_{scat}-\omega_{ref})\left(t_p-\left(\tau-\dfrac{\Delta R}{c}\right)\right)}{2}\right)}{\dfrac{(\omega_{scat}-\omega_{ref})}{2}}\sum_{m=1}^{N_c}e^{j(\omega_{scat}-\omega_{ref})mt_p}\left[u_mu_m^{*}\right] \qquad \text{(C-5)}$$

where $Z_{cc}=Z_ce^{j\frac{\omega_{scat}-\omega_{ref}}{2}t_p}e^{j\left(\frac{1}{2}(3\omega_{ref}-\omega_{scat})\left(\tau-\frac{\Delta R}{c}\right)\right)}$. The temporal dependence in the argument of the sine in (C-5) allows the use of the small angle approximation,

particularly over the possible range of platform speeds we might consider. With that the sinc becomes

$$\frac{\sin\left(\frac{\left(\omega_{scat}-\omega_{ref}\right)\left(t_p-\left(\tau-\frac{\Delta R}{c}\right)\right)}{2}\right)}{\frac{\left(\omega_{scat}-\omega_{ref}\right)}{2}} \approx \frac{\frac{\left(\omega_{scat}-\omega_{ref}\right)\left(t_p-\left(\tau-\frac{\Delta R}{c}\right)\right)}{2}}{\frac{\left(\omega_{scat}-\omega_{ref}\right)}{2}} \tag{C-6}$$

the right hand side of which reduces to t_p-τ-$\Delta R/c$. The summation in (C-5) can also be simplified. Using the identity

$$\sum_{m=1}^{N} r^n = \frac{1-r^N}{1-r} \tag{C-7}$$

then by substituting $r=e^{jx}$ into (C-7) and understanding that the code elements multiplied with their complex conjugate results in unity (again we have constrained $m=n$ in the main response lobe), the summation in (C-5) becomes

$$N_c \sum_{m=1}^{N_c} e^{j\left(\omega_{scat}-\omega_{ref}\right)mt_p} = \frac{\sin\left(\frac{N_c}{2}\left(\omega_{scat}-\omega_{ref}\right)t_p\right)}{\sin\left(\frac{1}{2}\left(\omega_{scat}-\omega_{ref}\right)t_p\right)} e^{j\frac{(N_c-1)}{2}\left(\omega_{scat}-\omega_{ref}\right)t_p} \tag{C-8}$$

With the small angle approximation again applied to (C-8) it reduces to

$$N_c \sum_{m=1}^{N_c} e^{j\left(\omega_{scat}-\omega_{ref}\right)mt_p} = \frac{\frac{N_c}{2}\left(\omega_{scat}-\omega_{ref}\right)t_p}{\frac{1}{2}\left(\omega_{scat}-\omega_{ref}\right)t_p} e^{j\frac{(N_c-1)}{2}\left(\omega_{scat}-\omega_{ref}\right)t_p} \tag{C-9}$$

Substituting all these into (C-5)

$$\begin{aligned}
\chi(\tau>0) &= \alpha N_c\left(t_p-\left(\tau-\frac{\Delta R}{c}\right)\right)C_r C_s e^{-jk_0\Delta R} e^{j\omega_{scat}\frac{R_s}{c}} e^{-j\omega_{ref}\frac{R_b}{c}} \\
\chi(\tau<0) &= \alpha N_c\left(t_p+\left(\tau-\frac{\Delta R}{c}\right)\right)C_r C_s e^{-jk_0\Delta R} e^{j\omega_{scat}\frac{R_s}{c}} e^{-j\omega_{ref}\frac{R_b}{c}} \\
\alpha &= e^{j\left(\frac{1}{2}(3\omega_{ref}-\omega_{scat})\left(\tau-\frac{\Delta R}{c}\right)\right)} e^{j\frac{N_c}{2}\left(\omega_{scat}-\omega_{ref}\right)t_p}
\end{aligned} \tag{C-10}$$

Equation (C-10) includes the same amplitude response from the move-stop-mode approximation with the same peak response scaling (indeed (C-10) reduces to (C-1) if

platform motion is set to zero) with the addition of terms and cross terms from different platform motions experienced along the two signal paths and two signals mixing. However all of these terms are constant with respect to range except for the envelope term and, as in the case of $\chi_1(\tau)$, one term with a dependency on delay (range).

Computing the forward transform of (C-10) we start by rescaling (C-10) to a range variable (from time) so that

$$t_p - \left(\tau \pm \frac{\Delta R}{c}\right) = t_p\left(1 \pm \frac{\tau - \Delta R/c}{t_p}\right) \text{ and then } t_p\left(1 \pm \frac{c}{c}\frac{\tau - \Delta R/c}{t_p}\right) = t_p\left(1 \pm \frac{r - \Delta R}{r_p}\right) \quad \text{(C-11)}$$

The break at τ=0 in (C-10) occurs at τ=$\Delta R/c$, or r=ΔR so that with the range constraint the forward transform is given by

$$S_{\phi,\theta}(k) = \int_{\Delta R - r_p}^{\Delta R} \chi(r) e^{-jkr} dr + \int_{\Delta R}^{\Delta R + r_p} \chi(r) e^{-jkr} dr. \quad \text{(C-12)}$$

Substituting (C-10) and (C-11) gives

$$S_{\phi,\theta}(k) = Z_k \int_{\Delta R - r_p}^{\Delta R} t_p\left(1 + \frac{r - \Delta R}{r_p}\right) e^{j(\beta(r-\Delta R))} e^{-jkr} dr + Z_k \int_{\Delta R}^{\Delta R + r_p} t_p\left(1 - \frac{r - \Delta R}{r_p}\right) e^{j(\beta(r-\Delta R))} e^{-jkr} dr. \quad \text{(C-13)}$$

with $Z_k = N_c t_p C_r C_s e^{-jk_0 \Delta R} e^{j\omega_{scat}\frac{R_s}{c}} e^{-j\omega_{ref}\frac{R_b}{c}} e^{j\frac{N_c}{2}(\omega_{scat} - \omega_{ref})t_p}$. The same change of variable is made as in Appendix B; x=r-ΔR, dx=dr. With this

$$S_{\phi,\theta}(k) = Z_k \int_{-r_p}^{0} t_p\left(1 + \frac{x}{r_p}\right) e^{j(\beta x)} e^{-jk(x+\Delta R)} dr + Z_k \int_{\Delta R}^{\Delta R + r_p} t_p\left(1 - \frac{x}{r_p}\right) e^{j(\beta x)} e^{-jk(x+\Delta R)} dr. \quad \text{(C-14)}$$

The $e^{-jk\Delta R}$ is factored from both integrals and factored again into a new constant Z_{kk}=Z_k $e^{-jk\Delta R}$ and β=1/2(3ω_{ref}-ω_{scat}). The integrals in (C-14) result in 6 terms which combine to yield

$$S_{\phi,\theta}(k) = Z_{kk} \frac{2}{r_p(\beta - k)^2}\left[1 - \cos\left(2(\beta - k)\frac{r_p}{2}\right)\right] \quad \text{(C-15)}$$

And by using a cosine double angle trigonometric identity gives

$$S_{\phi,\theta}(k) = N_c t_p C_r C_s e^{-j(k_0+k)\Delta R} e^{j\omega_{scat}\frac{R_s}{c}} e^{-j\omega_{ref}\frac{R_b}{c}} e^{j\frac{N_c}{2}(\omega_{scat}-\omega_{ref})t_p} \frac{\sin\left(\frac{r_p}{2}(\beta-k)\right)^2}{\frac{r_p}{2}(\beta-k)^2} \quad \text{(C-16)}$$

In (C-16), and previous, we have only considered the case of perfect isolation for the signal (main channel). In the section below we add a subscript 1 to represent the direct signal leak through contribution. The subscript '2' will indicate the main channel cross correlated (e.g., χ_2) with the reference channel while subscript '1' is the reference channel correlated with the leakage term. This distinguishing notation was not made in Appendix A, but is needed to address the full signal, which includes the direct signal breakthrough, as addressed in the remainder of this section.

The follow section completes the derivation on the effects of platform motion but is related to the material in Section 5.4 where the finite sidelobes/isolation of the main channel relative to the reference channel is introduced and direct signal breakthrough effects, and mitigations, are evaluated.

Forming $\chi(\tau) = \chi_1(\tau)+\chi_2(\tau)$, there is a delay dependence in the reference signal due to Doppler in $\chi_1(\tau)$ due to platform motion relative to the fixed transmitter. Further, referring to Figure 5.4-1, the contribution of χ_1 resembles, or effectively is, a noise floor if the coupling is severe enough. In the frequency domain

$$\Im(\chi(\tau)) = \Im(\chi_1(\tau) + \chi_2(\tau)) = \Im(\chi_1(\tau)) + \Im(\chi_2(\tau)) \quad \text{(C-17)}$$

where $\Im$ represents the forward Fourier transform. Recalling from (section 5.4-5)

$$\chi_1(\tau) = C_{rl} C_r e^{-j\omega_{ref}\tau} \sum_{m=1}^{N_c} \sum_{n=1}^{N_c} K_1 \left[u_m u_n{}^*\right] \quad \text{(C-18)}$$

where K_1 is defined as

$$K_1 = \begin{cases} t_p - \left|\tau - (n-m)t_p\right|, \left|\tau + t_p - (n-m)t_p\right| < t_p \\ 0, otherwise \end{cases} \quad \text{(C-19)}$$

For one-way propagation we would not expect to see any range dependency on the autocorrelation. For $\tau > t_p$ there is an (n, m) pair which satisfies the inequality in (C-19) and contributes to the random time sidelobes. The forward transform of χ_1 is computed over the same range as χ_2 (ΔR-r_p to ΔR+r_p) corresponding to its mainlobe response region (but where ΔR=0). This gives $\chi_1(\tau)$ as

$$A(r, \Delta R = 0) = 1 - \frac{|r - \Delta R|}{r_p} \tag{C-20}$$

over the interval $-r_p$ to r_p. Taking the forward transform over the defined range starts with

$$S1_{\phi,\theta}(k) = \int_{-r_p}^{r_p} N_c t_p C_r C_{rl} e^{j\frac{\omega_{ref}}{c} r} \left(1 - \frac{|r|}{r_p}\right) e^{-jkr} dr. \tag{C-21}$$

(C-21) expands to four terms as we make the same substitution to accommodate the absolute value

$$S1_{\phi,\theta}(k) = N_c t_p C_r C_{rl} \left[\int_{-r_p}^{0} e^{j\left(\frac{\omega_{ref}}{c} - k\right) r} dr + \int_{-r_p}^{0} \frac{r}{r_p} e^{j\left(\frac{\omega_{ref}}{c} - k\right) r} dr + \int_{0}^{r_p} e^{j\left(\frac{\omega_{ref}}{c} - k\right) r} dr + \int_{0}^{r_p} \frac{r}{r_p} e^{j\left(\frac{\omega_{ref}}{c} - k\right) r} dr \right] \tag{C-22}$$

The evaluation is straight forward term wise. Terms 1 and 3 have similar evaluations, the sum of which is

$$T_1 + T_3 = \frac{1}{j\left(\frac{\omega_{rec}}{c} - k\right)} \left[e^{j\left(\frac{\omega_{rec}}{c} - k\right) r_p} - e^{-j\left(\frac{\omega_{rec}}{c} - k\right) r_p} \right] \tag{C-23}$$

Likewise terms 2 and 4 their sum being given by

$$\begin{aligned} T_2 + T_4 = &- \frac{2}{r_p \left(j\left(\frac{\omega_{rec}}{c} - k\right) \right)^2} + \frac{1}{j\left(\frac{\omega_{rec}}{c} - k\right)} \left[e^{-j\left(\frac{\omega_{rec}}{c} - k\right) r_p} - e^{j\left(\frac{\omega_{rec}}{c} - k\right) r_p} \right] + \\ &+ \frac{1}{r_p \left(j\left(\frac{\omega_{rec}}{c} - k\right) \right)^2} \left[e^{-j\left(\frac{\omega_{rec}}{c} - k\right) r_p} + e^{j\left(\frac{\omega_{rec}}{c} - k\right) r_p} \right] \end{aligned} \tag{C-24}$$

By inspection we see that (C-24) contains the terms of (C-23) but of opposite sign, reducing to

$$S1_{\phi,\theta}(k) = -\frac{2}{r_p\left(j\left(\frac{\omega_{rec}}{c}-k\right)\right)^2} + \frac{1}{r_p\left(j\left(\frac{\omega_{rec}}{c}-k\right)\right)^2}\left[e^{-j\left(\frac{\omega_{rec}}{c}-k\right)r_p} + e^{j\left(\frac{\omega_{rec}}{c}-k\right)r_p}\right] \qquad \text{(C-25)}$$

using the cosine - exponential sum identity, the expression in brackets becomes

$$S1_{\phi,\theta}(k) = -\frac{2}{r_p\left(j\left(\frac{\omega_{rec}}{c}-k\right)\right)^2} + \frac{1}{r_p\left(j\left(\frac{\omega_{rec}}{c}-k\right)\right)^2}\left[2\cos\left(\frac{\omega_{rec}}{c}-k\right)r_p\right] \qquad \text{(C-25)}$$

Some rearranging

$$S1_{\phi,\theta}(k) = -\frac{2}{r_p\left(j\left(\frac{\omega_{rec}}{c}-k\right)\right)^2}\left[1-\cos\left(\frac{\omega_{rec}}{c}-k\right)r_p\right] \qquad \text{(C-26)}$$

evaluating the inverse-root(j) changes the sign of the first term and the sine-squared identity replaces the 1-cosine(), resulting in the direct path spectrum with Doppler

$$S1_{\phi,\theta}(k) = N_c t_p C_r C_{rl} \frac{\sin\left(\left(\frac{\omega_{rec}}{c}-k\right)\frac{r_p}{2}\right)^2}{\left(\left(\frac{\omega_{rec}}{c}-k\right)\frac{r_p}{2}\right)^2} \qquad \text{(C-26)}$$

In this development the main and reference antennas are assumed to have a common phase center so that installed path length differences could be ignored. This will not be the case for the antennas when installed in the test aircraft in Section 6.

Appendix D. Triangle Waveform Approximation Exact Motion Solution with Doppler Compensated Reference Channel.

The reference signal Doppler component represents a single source, in the absence of multipath and with antenna installation such that ground returns are masked by structure. Employing position and velocity information from the radar navigation system, necessary for reconstruction, and knowledge of the position of the illuminator, one can correct the

reference channel Doppler contribution. This leaves only a scatterer-based Doppler component. The relations describing the reference and main signal

$$x_{ref}(t,t_0) = C_r A\left(t - \frac{R_b}{c}\right)e^{-jk_0R_b} \text{ and } x_S(t,t_0) = C_s A\left(t - \frac{R_s}{c}\right)e^{j(-k_0R_s+\omega_{scat}t)} \quad \text{(D-1)}$$

We now form (2) using the elements in (D1)

$$\chi(\tau) = \int_0^T C_s A\left(t - \frac{R_s}{c}\right)e^{j(-k_0R_s+\omega_{scat}t)}\left(C_r A\left(t - \frac{R_b}{c} - \tau\right)e^{-jk_0R_b}\right)^* dt. \quad \text{(D-2)}$$

Keeping with prior practice, equation (60) can be simplified by removing all constants, resulting in

$$\chi(\tau) = C_s C_r e^{-jk_0R_s} e^{jk_0R_b} \int_0^T A\left(t - \frac{R_s}{c}\right)e^{j\omega_{scat}t}\left(A\left(t - \frac{R_b}{c} - \tau\right)\right)^* dt. \quad \text{(D-3)}$$

Substituting the expressions for the PN code sequence

$$= Z_c \int_0^T \sum_{m=1}^{N} e^{j\omega_{scat}t} rect\left(\frac{t - \frac{R_s}{c} - mt_p}{t_p}\right)e^{j\phi_m}\left(\sum_{n=1}^{N} rect\left(\frac{t - \frac{R_b}{c} - nt_p - \tau}{t_p}\right)e^{j\phi_n}\right)^* dt \quad \text{(D-4)}$$

with $Z_c = C_s C_r e^{-jk_0\Delta R}$.

The same substitutions are defined as in prior derivations with $t=t'+R_s/c+mt_p$ and $\tau'=\tau-\Delta R/c-(m-n)t_p$. Thus (D-4) becomes

$$\chi(\tau) = Z_c \int_0^T \sum_{m=1}^{N} e^{j\omega_{scat}\left(t'+\frac{R_s}{c}+mt_p\right)} rect\left(\frac{t'}{t_p}\right)e^{j\phi_m}\left(\sum_{n=1}^{N} rect\left(\frac{t'-\tau'}{t_p}\right)e^{j\phi_n}\right)^* dt.' \quad \text{(D-5)}$$

Taking the complex conjugate and interchanging the order of summation and integration

$$\chi(\tau) = Z_c \sum_{m=1}^{N}\sum_{n=1}^{N} e^{j\phi_m} e^{-j\phi_n} \int_0^T e^{j\omega_{scat}\left(t'+\frac{R_s}{c}+mt_p\right)} rect\left(\frac{t'}{t_p}\right) rect\left(\frac{t'-\tau'}{t_p}\right) dt'. \quad \text{(D-6)}$$

The range of the integrand is restricted to the nonzero range of the correlation of the two rect functions, again as shown in Figure 5.2-9, over τ'. The two cases of $\tau'>0$ and $\tau'<0$,

both under the constraint that $|\tau'-t_p|<t_p$, results in the two definite integrals in (D-7), showing just the integral portions of (D-6) for notational convenience:

$$\begin{aligned} t1(\tau'>0) &= e^{j\omega_{scat}\left(\frac{R_s}{c}+mt_p\right)}\int_0^{t_p-\tau'} e^{j\omega_{scat}t'}dt' \\ t2(\tau'<0) &= e^{j\omega_{scat}\left(\frac{R_s}{c}+mt_p\right)}\int_{-\tau'}^{t_p} e^{j\omega_{scat}t'}dt' \end{aligned} \tag{D-7}$$

The solution to the first is given by (with limits evaluated)

$$t1(\tau'>0) = e^{j\omega_{scat}\left(\frac{R_s}{c}+mt_p\right)} e^{j\frac{\omega_{scat}}{2}\left(t_p-\tau'\right)} \frac{\sin\left(\frac{\omega_{scat}}{2}\left(t_p-\tau'\right)\right)}{\frac{\omega_{scat}}{2}} \tag{D-8}$$

Inserting into (D-6), with some simplification, gives

$$\chi(\tau'>0) = Z_c e^{j\omega_{scat}\frac{R_s}{c}} \sum_{m=1}^{N} e^{j\omega_{scat}mt_p} \sum_{n=1}^{N} e^{j\phi_m} e^{-j\phi_n} e^{j\frac{\omega_{scat}}{2}\left(t_p-\tau'\right)} \frac{\sin\left(\frac{\omega_{scat}}{2}\left(t_p-\tau'\right)\right)}{\frac{\omega_{scat}}{2}} \tag{D-9}$$

The solution for $\tau'<0$ is similar

$$\chi(\tau'<0) = Z_c e^{j\omega_{scat}\frac{R_s}{c}} \sum_{m=1}^{N} e^{j\omega_{scat}mt_p} \sum_{n=1}^{N} e^{j\phi_m} e^{-j\phi_n} e^{j\frac{\omega_{scat}}{2}\left(t_p-\tau'\right)} \frac{\sin\left(\frac{\omega_{scat}}{2}\left(t_p+\tau'\right)\right)}{\frac{\omega_{scat}}{2}} \tag{D-10}$$

Finally we write

$$\chi(\tau'>0) = Z_{cc} \sum_{m=1}^{N_c}\sum_{n=1}^{N_c} K_5\left[u_m u_n{}^*\right] \qquad \chi(\tau'<0) = Z_{cc} \sum_{m=1}^{N_c}\sum_{n=1}^{N_c} K_6\left[u_m u_n{}^*\right] \tag{D-11}$$

where

$$K_5 = \begin{cases} \frac{\sin\left(\frac{\omega_{scat}}{2}\left(t_p-\tau'\right)\right)}{\frac{\omega_{scat}}{2}} e^{j\alpha}, |\tau'|<t_p \\ 0, otherwise \end{cases} \qquad K_6 = \begin{cases} \frac{\sin\left(\frac{\omega_{scat}}{2}\left(t_p+|\tau'|\right)\right)}{\frac{\omega_{scat}}{2}} e^{j\alpha}, |\tau'|<t_p \\ 0, otherwise \end{cases} \tag{D-12}$$

and

$$\alpha = \omega_{scat}mt_p - \frac{\omega_{scat}}{2}\left(t_p-\tau'\right) \quad \text{and} \quad Z_{cc} = C_r C_s e^{-jk_0\Delta R} e^{j\omega_{scat}\frac{R_s}{c}}. \tag{D-13}$$

Proceeding to the frequency domain, as earlier we make the approximation that the reconstruction is dominated by the peak response of the compressed waveform. This was

shown to be a reasonable approach in Section 5.2 where only very small changes to the sidelobe structure of the reconstructed point spread function were observed between the complete and approximated waveforms. Again we constrain the response such that $|\tau-\Delta R/c|<t_p$. For this condition to be true m=n on the codes and summation. With this the compressed waveform is given by

$$\chi(\tau'<0)\approx Z_{cc}\sum_{m=1}^{N}\sum_{n=1}^{N}e^{j\phi_m}e^{-j\phi_n}e^{j\omega_{scat}mt_p}e^{j\frac{\omega_{scat}}{2}\left(t_p-\tau-\Delta R/c\right)}\frac{\sin\left(\frac{\omega_{scat}}{2}\left(t_p+\tau-\Delta R/c\right)\right)}{\frac{\omega_{scat}}{2}} \tag{D-14}$$

Applying the small angle approximation to the sinc function, collapsing the double summation to a single one with the *m=n* constraint, and recognizing that the product of the complex code and its complex conjugate produces unity we have

$$\chi(\tau'<0)=Z_{cc}e^{j\frac{\omega_{scat}}{2}\left(t_p-\tau-\frac{\Delta R}{c}\right)}\left(t_p+\left(\tau-\frac{\Delta R}{c}\right)\right)\sum_{m=1}^{N}e^{j\omega_{scat}mt_p}. \tag{D-15}$$

Using the exponential sum identity

$$\sum_{m=1}^{N}e^{jmx}=\frac{1-e^{jNx}}{1-e^{jx}} \qquad \text{or} \qquad \sum_{m=1}^{N}e^{jmx}=\frac{\sin\left(\frac{Nx}{2}\right)}{\sin\left(\frac{x}{2}\right)}e^{j\frac{(N-1)}{2}x} \tag{D-16}$$

then (D-16) gives

$$\chi(\tau'<0)=Z_{cc}e^{j\frac{\omega_{scat}}{2}\left(t_p-\tau-\frac{\Delta R}{c}\right)}\left(t_p+\tau-\frac{\Delta R}{c}\right)\frac{\sin\left(\frac{\omega_{scat}}{2}N_ct_p\right)}{\sin\left(\frac{\omega_{scat}}{2}t_p\right)}e^{j(N_c-1)\frac{\omega_{scat}}{2}t_p} \tag{D-17}$$

Again applying the small angle approximation results in the final time domain form

$$\chi(\tau'<0)=Z_{cc}N_c\left(t_p+\left(\tau-\frac{\Delta R}{c}\right)\right)e^{j\frac{\omega_{scat}}{2}\left(\tau-\frac{\Delta R}{c}\right)}e^{j\frac{N}{2}\omega_{scat}t_p} \tag{D-18}$$

Repeating the process for *t*'>0 results in

$$\chi(\tau'>0)=Z_{cc}N_c\left(t_p-\left(\tau-\frac{\Delta R}{c}\right)\right)e^{j\frac{\omega_{scat}}{2}\left(\tau-\frac{\Delta R}{c}\right)}e^{j\frac{N}{2}\omega_{scat}t_p} \tag{D-19}$$

We note again that (D-18) and (D-19) represent the full response as there is only a single signal component present in each receive channel. The only motion dependence remaining is the scatterer Doppler contribution.

To prepare for the forward transform with respect to range, the results in (D18) and (D-19) are scaled to range (from time). The pulse length term (t_p) is factored from the envelope term, resulting in the familiar triangular envelope form. At the same time the speed of light is factored in the exponential; resulting in an expression that is a function of the Doppler wavenumber ($k_{scat}=\omega_{scat}/c$), though the frequency term is retained as it is a constant and appears in several terms

$$\begin{aligned}\chi(\tau'>0) &= Z_{cc}N_c t_p\left(1-\left(\frac{r-\Delta R}{r_p}\right)\right)e^{-j\frac{\omega_{scat}}{2c}(r-\Delta R)}e^{j\frac{N}{2}\omega_{scat}t_p}\\ \chi(\tau'<0) &= Z_{cc}N_c t_p\left(1+\left(\frac{r-\Delta R}{r_p}\right)\right)e^{-j\frac{\omega_{scat}}{2c}(r-\Delta R)}e^{j\frac{N}{2}\omega_{scat}t_p}\end{aligned} \qquad \text{(D-20)}$$

Forming the forward Fourier transform with respect to range with the limits of the Fourier integral are set by the mainlobe response constraint (as in the earlier appendices), gives

$$S_{\phi,\theta}(k) = Z_{cc}N_c t_p e^{j\frac{N}{2}\omega_{scat}t_p}\left[\begin{array}{l}\int_{\Delta R-r_p}^{\Delta R}\left(1+\frac{r-\Delta R}{r_p}\right)e^{j\left(\frac{\omega_{scat}}{2c}(r-\Delta R)\right)}e^{-jkr}dr+\\ \int_{\Delta R}^{\Delta R+r_p}\left(1-\frac{r-\Delta R}{r_p}\right)e^{j\left(\frac{\omega_{scat}}{2c}(r-\Delta R)\right)}e^{-jkr}dr\end{array}\right]. \qquad \text{(D-21)}$$

Making the change of variable $x=r-\Delta R$, $dx=dr$, then evaluating the limits under the change of variable yields

$$S_{\phi,\theta}(k) = Z_{cc}N_c t_p e^{j\frac{N}{2}\omega_{scat}t_p}e^{-jk\Delta R}\left[\int_{-r_p}^{0}\left(1+\frac{x}{r_p}\right)e^{-jk(\beta+x)}dr+\int_{0}^{r_p}\left(1-\frac{x}{r_p}\right)e^{-jk(\beta+x)}dr\right] \qquad \text{(D-22)}$$

where $\beta=\omega_{scat}/(2c)$. This result is nearly identical in form to that of the Appendix C with the slight exception that the expression in parenthesis in the exponential is ($\beta+x$) instead

of (β-x). The solution follows along the same lines. Equation D-22 can further be decomposed into 4 terms which are evaluated, individually, as

$$\begin{aligned}
&\int_{-r_p}^{0} e^{j(\beta-k)x}dx = \frac{1}{-j(\beta+k)}e^{-j(\beta+k)x}\Big|_{-r_p}^{0} = \frac{1}{-j(\beta+k)}\left(1-e^{j(\beta+k)r_p}\right)\\
&\int_{0}^{r_p} e^{j(\beta-k)x}dx = \frac{1}{-j(\beta+k)}e^{-j(\beta+k)x}\Big|_{0}^{r_p} = \frac{1}{-j(\beta+k)}\left(e^{-j(\beta+k)r_p}-1\right)\\
&\int_{-r_p}^{0} \frac{x}{r_p}e^{j(\beta-k)x}dx = \left(\frac{x}{-j(\beta+k)}-\frac{1}{(-j(\beta+k))^2}\right)e^{-j(\beta+k)x}\Big|_{-r_p}^{0} = \frac{1}{r_p(\beta+k)^2}+\frac{je^{j(\beta+k)r_p}}{(\beta+k)}-\frac{e^{j(\beta+k)r_p}}{r_p(\beta+k)^2}\\
&\int_{0}^{r_p} -\frac{x}{r_p}e^{j(\beta-k)x}dx = \left(\frac{x}{-j(\beta+k)}-\frac{1}{(-j(\beta+k))^2}\right)e^{-j(\beta+k)x}\Big|_{0}^{r_p} = -\frac{je^{-j(\beta+k)r_p}}{(\beta+k)}-\frac{e^{-j(\beta+k)r_p}}{r_p(\beta+k)^2}+\frac{1}{r_p(\beta+k)^2}
\end{aligned} \tag{D-23}$$

The four terms combine to yield

$$S_{\phi,\theta}(k) = Z_{cc}{}'e^{-jk\Delta R}\left(\frac{2}{r_p(\beta+k)^2}-\frac{e^{-j(\beta+k)r_p}}{r_p(\beta+k)^2}-\frac{e^{j(\beta+k)r_p}}{r_p(\beta+k)^2}\right) \tag{D-24}$$

And with a little more manipulation

$$S_{\phi,\theta}(k) = Z_{cc}{}'e^{-jk\Delta R}\left(\frac{2}{r_p(\beta+k)^2}-\frac{2\cos((\beta+k)r_p)}{r_p(\beta+k)^2}\right) = 2Z_{cc}{}'e^{-jk\Delta R}\frac{\sin^2((\beta+k)r_p)}{r_p(\beta+k)^2} \tag{D-25}$$

This result has the satisfying form of the $\sin^2$, as for the triangle waveform for mode-stop-move, with the simple addition of the Doppler dependency as phase constants that are expressly derived from the measurement geometry, as well as a simple shift of the complex spectrum envelope. The full form of the solution is

$$S_{\phi,\theta}(k) = 2C_rC_sN_ct_pe^{-j(k_0+k)\Delta R}e^{j\omega_{scat}\left(\frac{R_s}{c}+\frac{N_ct_p}{2}\right)}\frac{\sin^2\left(\left(\frac{\omega_{scat}}{2c}+k\right)r_p\right)}{r_p\left(\frac{\omega_{scat}}{2c}+k\right)^2}. \tag{D-26}$$

Appendix E. Large Two Dimensional Images and Apodization.

After Section 6.0 was completed additional two dimensional images were focused as part of the paper presented in [164]. These expanded area images were generated primarily to insure that the scene was properly registering against map and photographic data: that the location of scattering centers could be overlaid with map objects such as structures and foliage. These images are presented in this Appendix.

Figure E.1 contains the largest scene focused in two dimensions. The data were selected from Orbit 3 and represents a 40 degree synthetic aperture relative to the scene origin and as projected into the scene X-Y plane. Figure E.1a is a Google Earth overhead view which is the same scale as the reconstructed image in Figure E.1b. The white lines overlaid on the image correspond with features in the photograph. The image itself has been weighted with a two dimensional, -35 dB Taylor (single parameter), convolved with the image after focusing. The intensity scale is based on a linear mapping with the image hard clipped at 20 dB below the peak response. The shadow area representing the river is clearly visible, as are areas which contained trees. The direction of illumination is indicated by the white arrow in Figure E.1b.

Of note is the general absence of features indicating structure returns. The metallic outbuildings are largely, though not exclusively, aligned with the map cardinal axes. The vertical walls would scatter into the ground given the grazing angle of the incident illumination (approximately 1.4 degrees relative to the local horizontal). Likewise the scattering off metallic roofs with shallow pitches did not illuminate the receiver over the synthetic aperture. Should the receiver pass through a region of increased scattering then we would see image reconstruction as dictated by the region angular width. Using a bistatic scattering model from [166] we can reconstruct a flat plate with response dictated by the specular mainlobe based on a three wavelength plate.. Artifacts are introduced onto the elongated IPR include dual peaks in range and cross range with an along range resolution of 10 meters, cross range of ~1 m (with no competing clutter or noise). Fundamentally the large continuous conductor produces a single response at the phase center. Similarly, one could then exercise the model at arbitrary orientation with respect to the collection aperture and produce exotic responses, there are myriad combinations without any sensitivity considerations. We do observe multiple returns in the immediate vicinity of the silo at image center which may be such in Figure 6.79 (a zoomed version

of E.1 with approximately the same length aperture). As a last point, integrating over aperture angles substantially wider than the specular flash of a multiple wavelength conducting panel may result in adding noise to the pixel/voxel which would suppress the observability of the pixel containing the specular flash.

Figures E.2 through E-10 contain 240 m by 240 m reconstructions for orbits 1 through 9. The images are centered on the silo structure that was selected as the scene reference. Each figure contains four images: linear scale (top) and logarithmic scale (bottom), with tapering and dynamic range as noted. All images are reconstructed over the full orbit segment (approximately 90 degrees) and are Nyquist sampled as noted in the plot title.

The images exhibit what might be termed “stringy” behavior. This is attributed, at least in part, to the sidelobe structure of the focused pixel. Referring to Figure 6.79 we see that the principle sidelobes extend along the “hourglass” pattern. Thus nearby pixels which are on this axis will tend to reinforce. However, consideration must also be given to the potential that the locus of scatterers behave in a non-distributed manner and cohere for a response which is of limited angular extent. With this the orientation and shape of the IPR is dependent on the position within the scene and within the collection aperture.

There is a suggestion of periodicity in the images in E.2 through E.10, perhaps most clearly observed in Figure E.10. The several bright scatterers are observed at scene center. The along-range FWHM of the brightest scales to approximately 11m down range and 1-2m cross range (full aperture resolution would be 0.183 m by 0.746 m), suggesting a specular (also the orientation of the response). The three or four scattering centers produce cross range adjacent responses, all of which exhibit a periodic-like structure in range with a period on the order of 35-38 m. Whether this is a modulation effect or multipath-related was not determined. The fact that this effect tends to align with the pseudo-range direction is suggestive of multipath but could also indicate slight mistuning.

a) Google Earth Overhead View

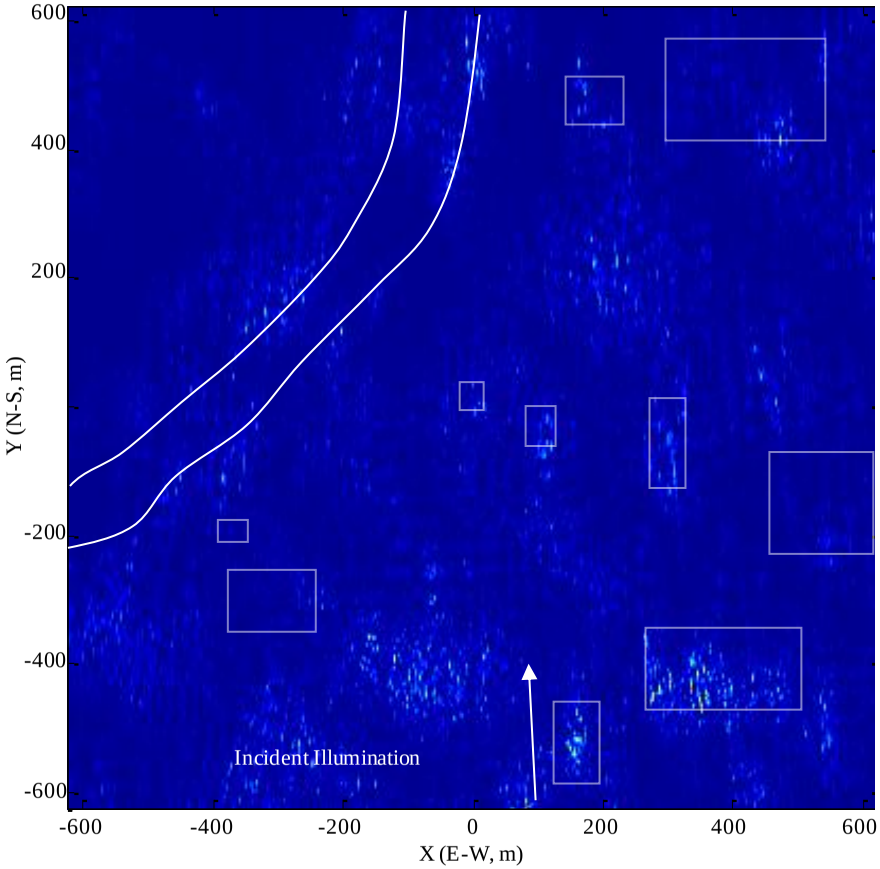

b) 40 Degree Aperture Image

Figure E.1 - 1.25 by 1.25 km Image - 35 dB Taylor, Linear Scale (Orbit 3)

Calculated resolution 0.377m (X), 3.896 m (Y)
Sampled at 0.215 m (X) and 0.916 m (Y)
Focus plane Z=0 (using 44 ft GE local elevation)

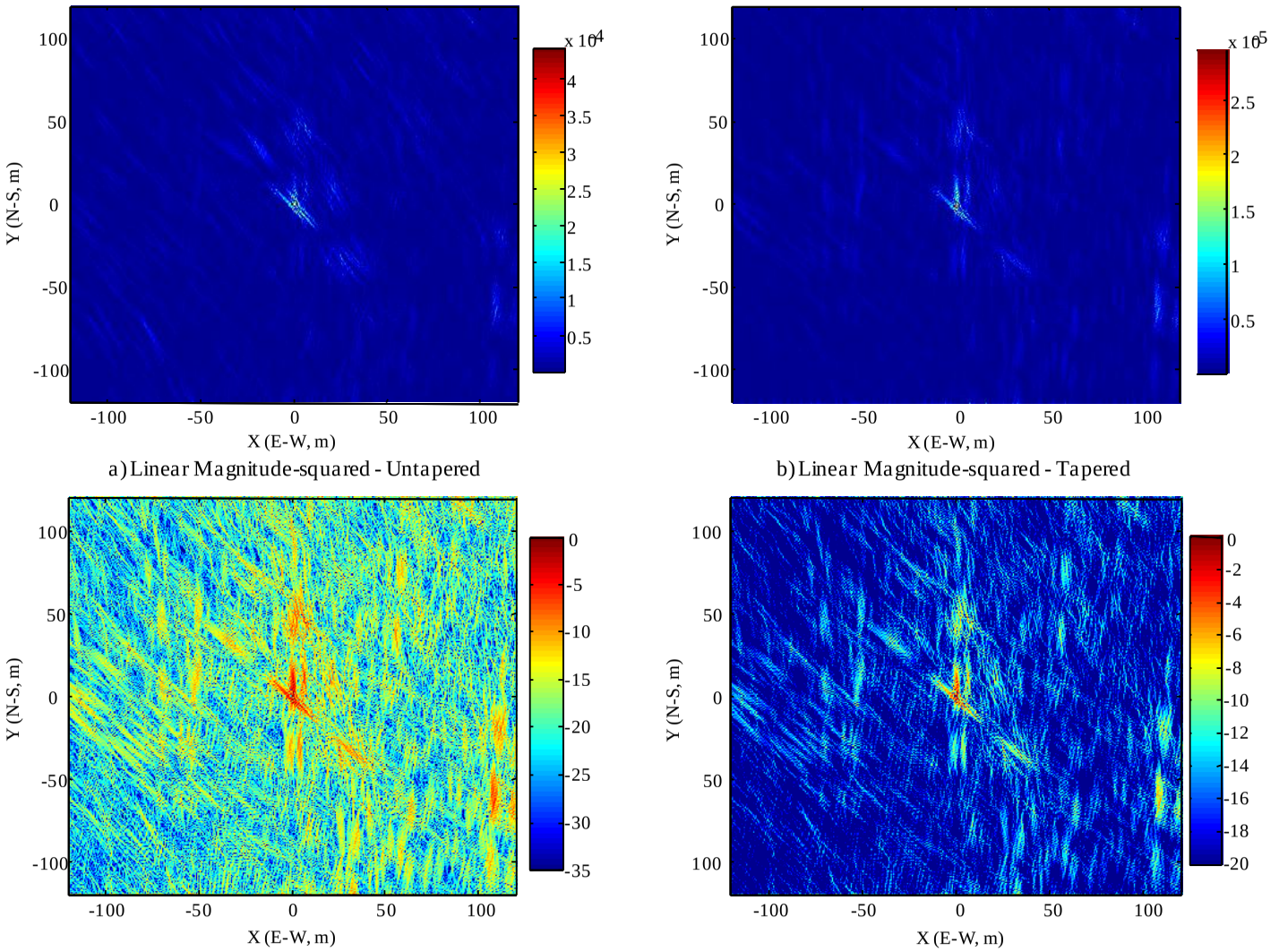

Figure E.2 - Orbit 1 Reconstruction 240 m by 240 m - Sample spacing (X,Y)= (0.236m, 0.755m)

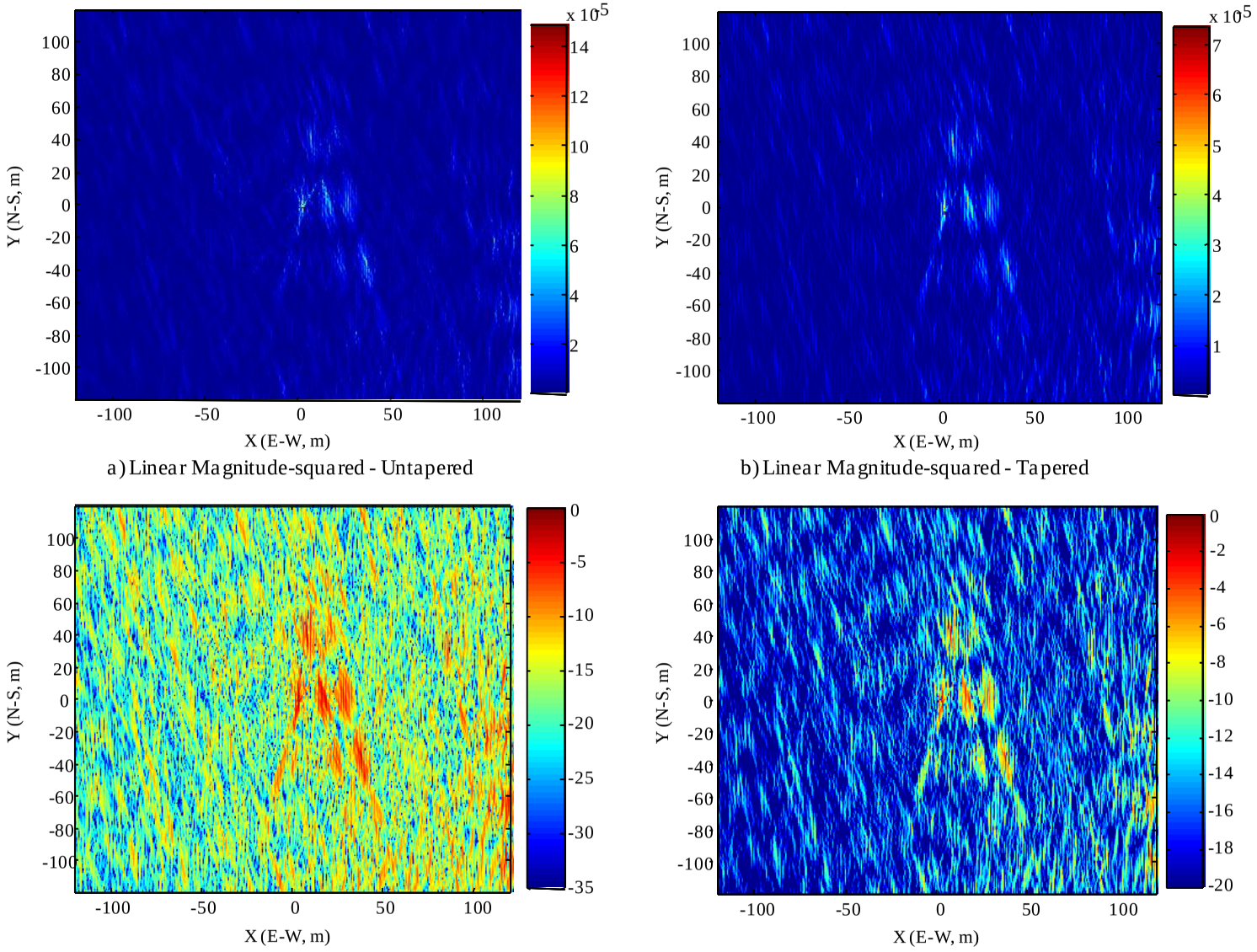

Figure E.3 - Orbit 2 Reconstruction 240m by 240 m - Sample spacing (X,Y)= (0.247m, 1.114m)

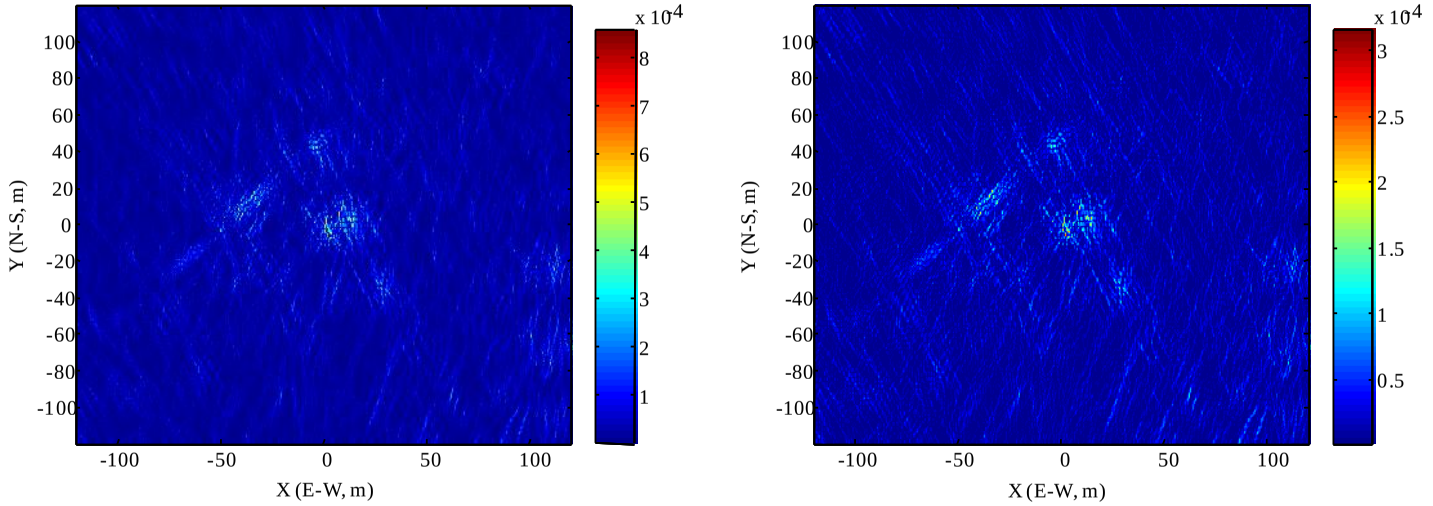

a) Linear Magnitude-squared - Untapered

b) Linear Magnitude-squared - Tapered

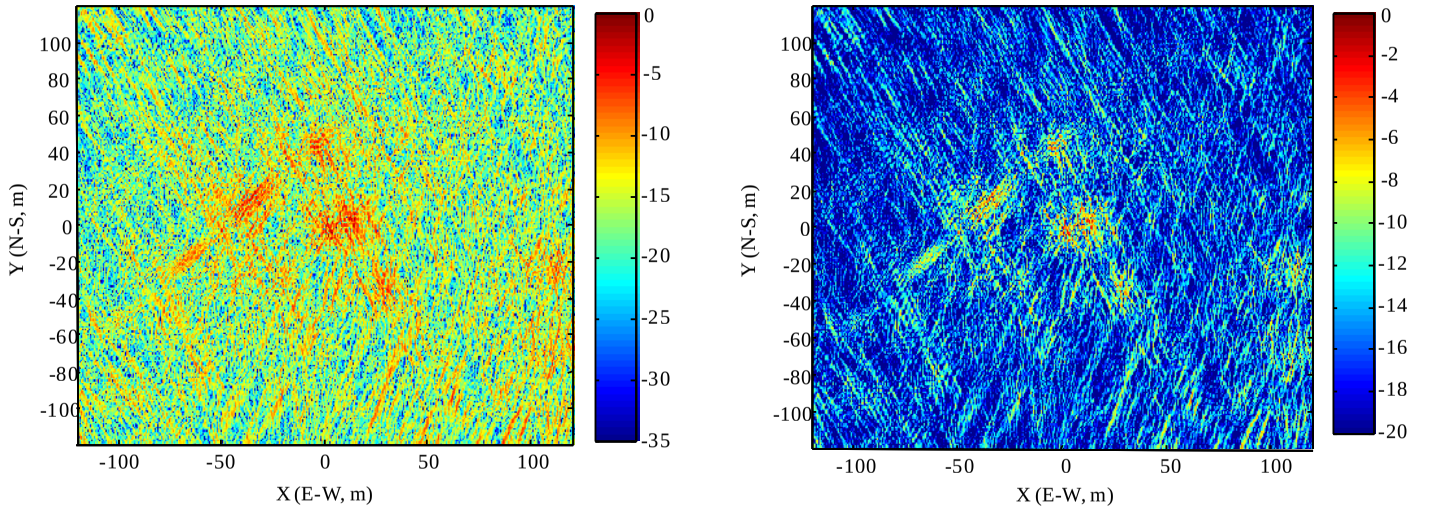

c) Logarithmic Scale - Tapered, Clipped at -35 dB

d) Logarithmic Scale - Tapered, Clipped at -20 dB

Figure E.4 - Orbit 3 Reconstruction 240m by 240 m - Sample spacing (X,Y)= (0.215m, 0.91m)

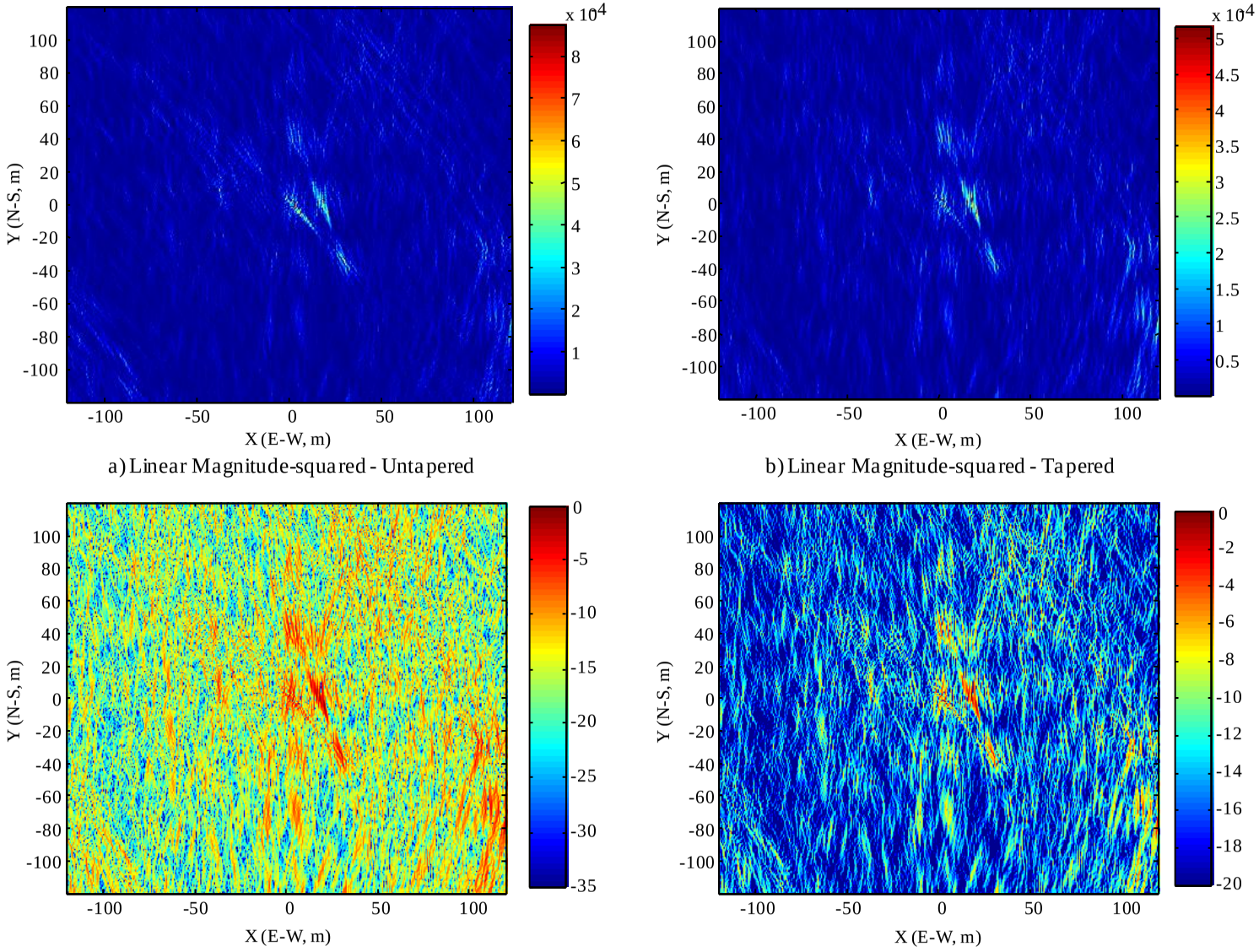

Figure E.5 - Orbit 4 Reconstruction 240m by 240 m - Sample spacing (X,Y)= (0.209m, 0.838m)

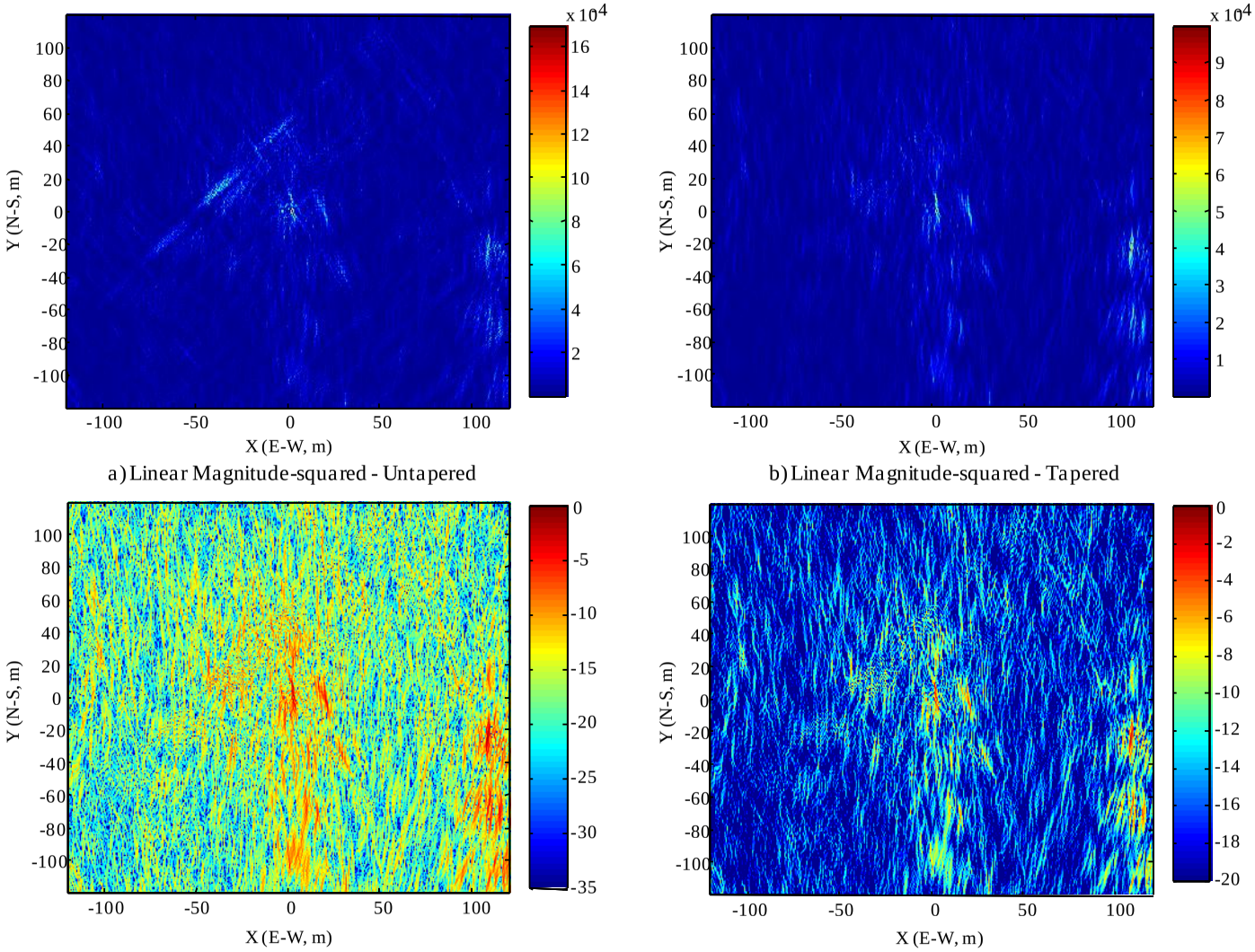

Figure E.6 - Orbit 5 Reconstruction 240m by 240 m - Sample spacing (X,Y)= (0.21, 0.81m)

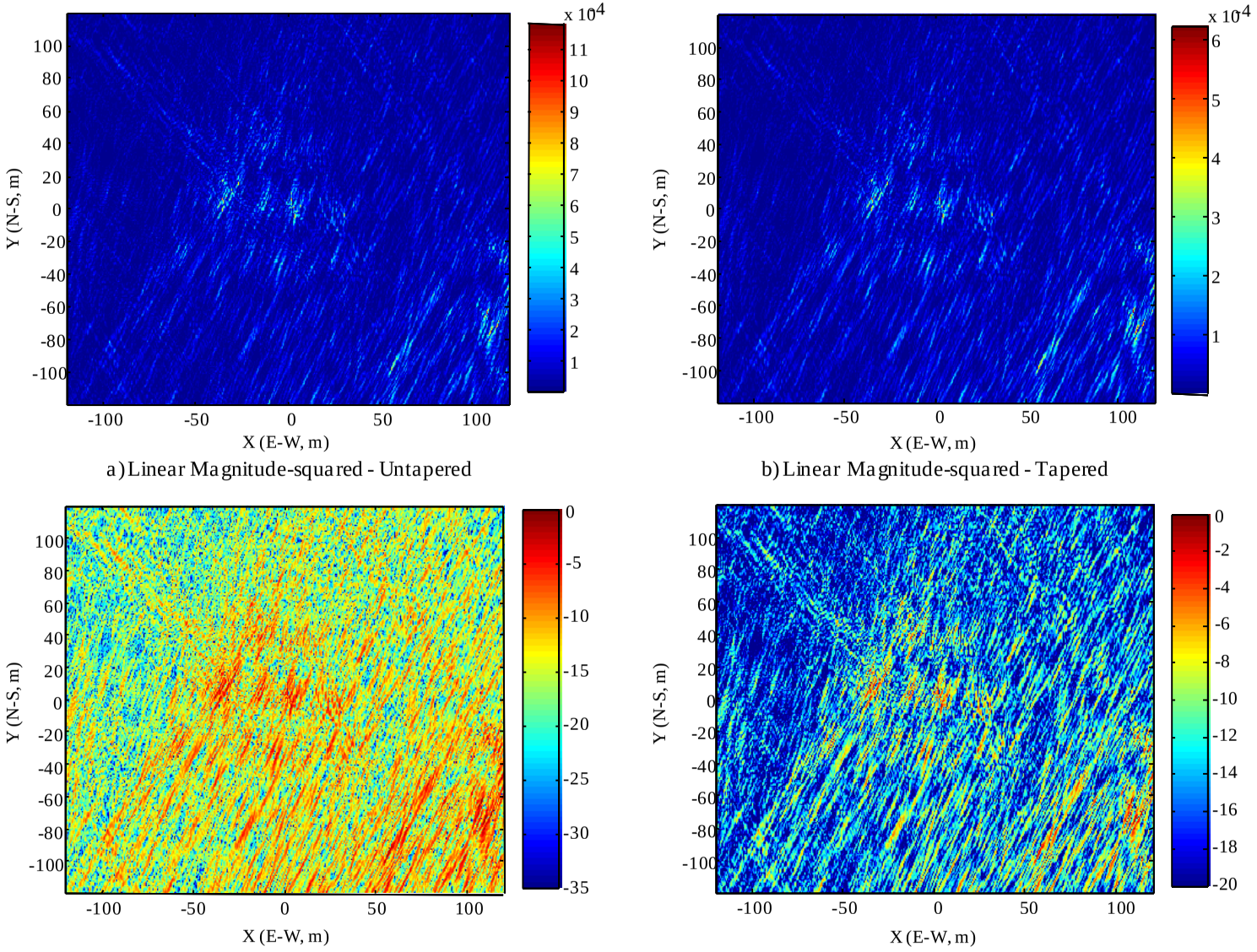

Figure E.7 - Orbit 6 Reconstruction 240m by 240 m - Sample spacing (X,Y)= (0.191m, 0.856m)

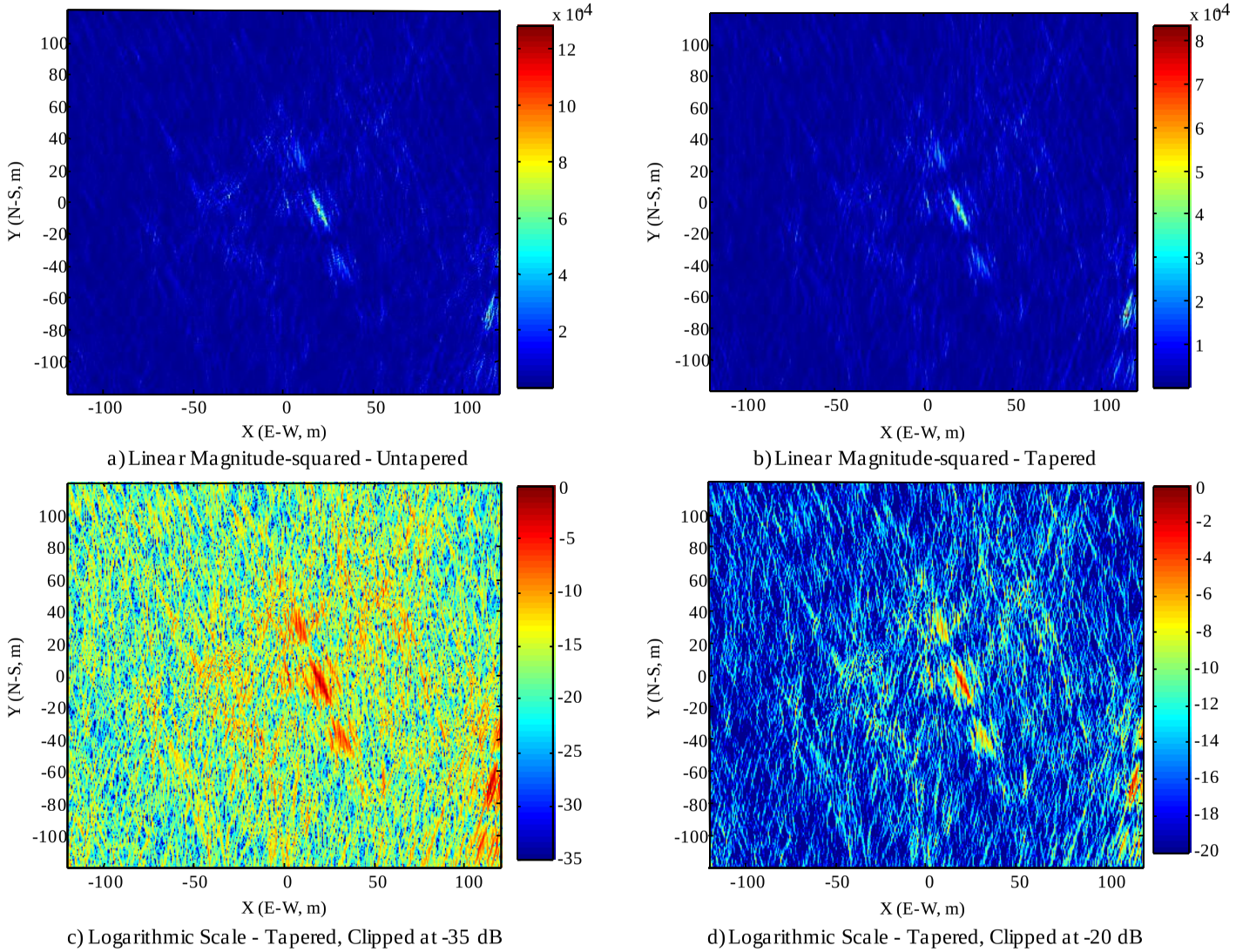

Figure E.8 - Orbit 7 Reconstruction 240m by 240 m - Sample spacing (X,Y)= (0.192m, 0.786m)

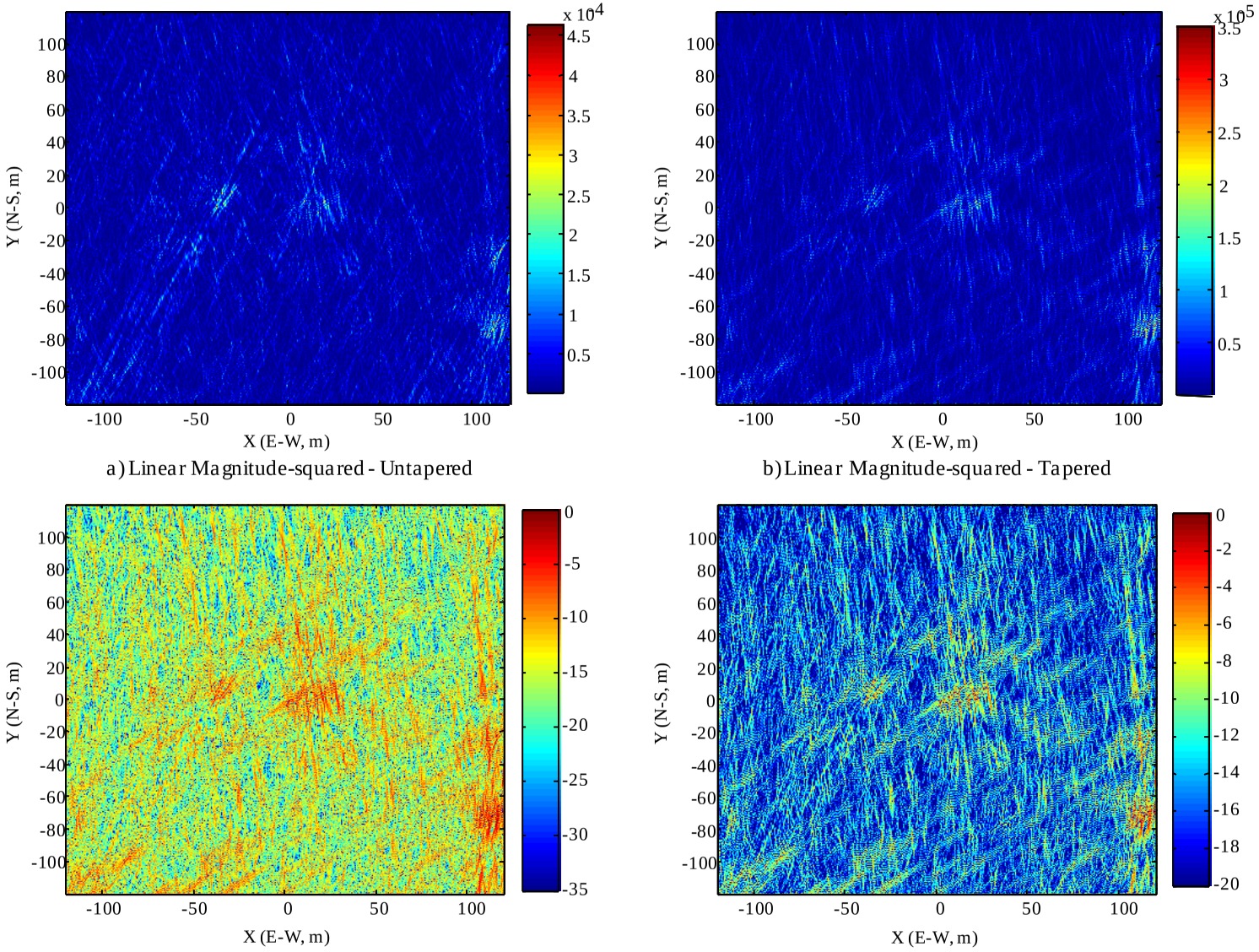

Figure E.9 - Orbit 8 Reconstruction 240m by 240 m - Sample spacing (X,Y)= (0.178m, 0.685m)

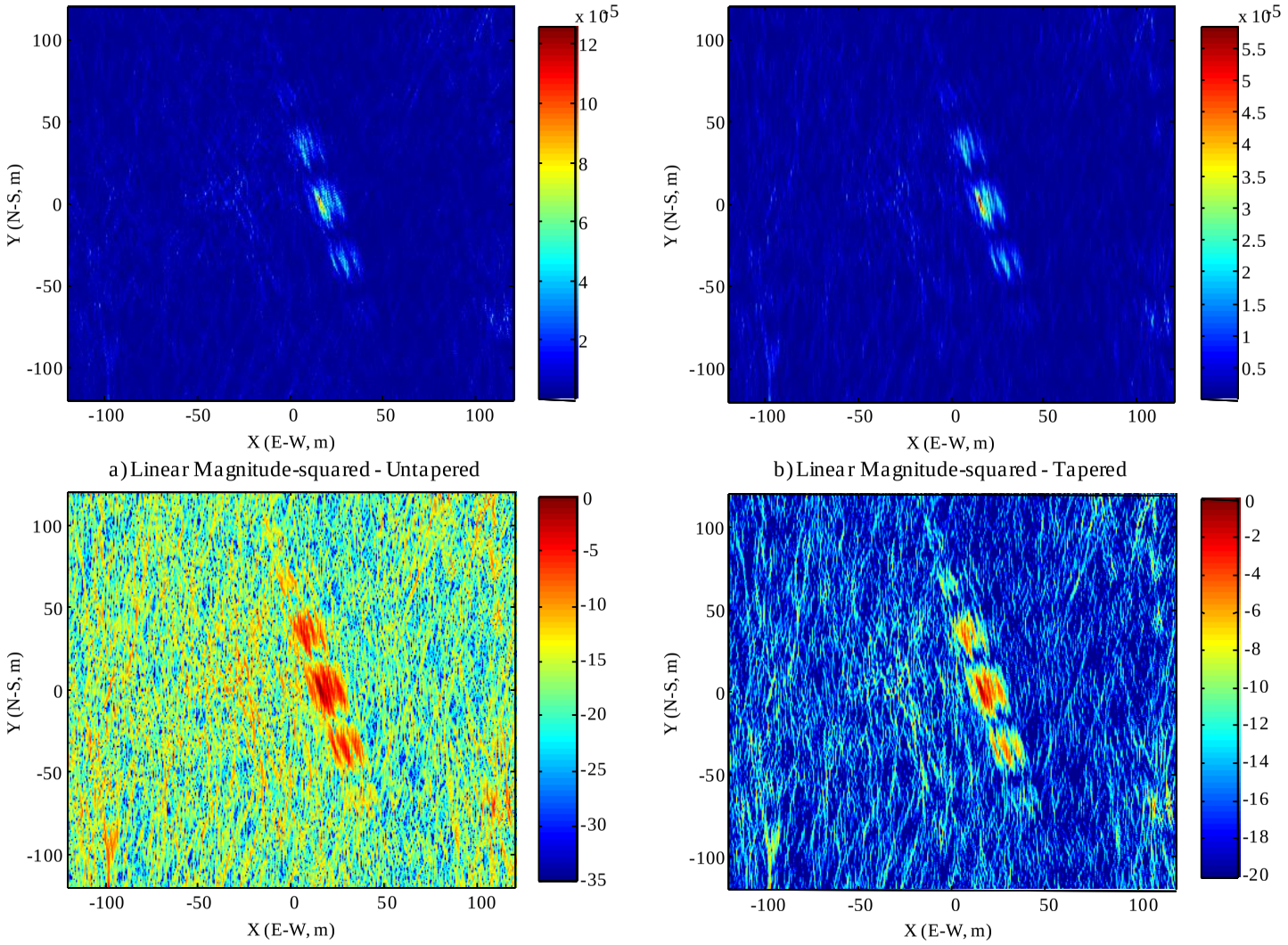

Figure E.10 - Orbit 9 Reconstruction 240m by 240 m - Sample spacing (X,Y)= (0.183m, 0.746m)

The final figure is a compendium of images from the odd orbits with an overhead image of the same scale and with features illustrated. The 240 m by 240 m scene using sample spacing consistent for each spatial aperture, centered on the silo estimated position (the layover is evident in the photograph). After focusing, each image was apodized by convolving a two dimensional 35 dB Taylor with the complex back projected result

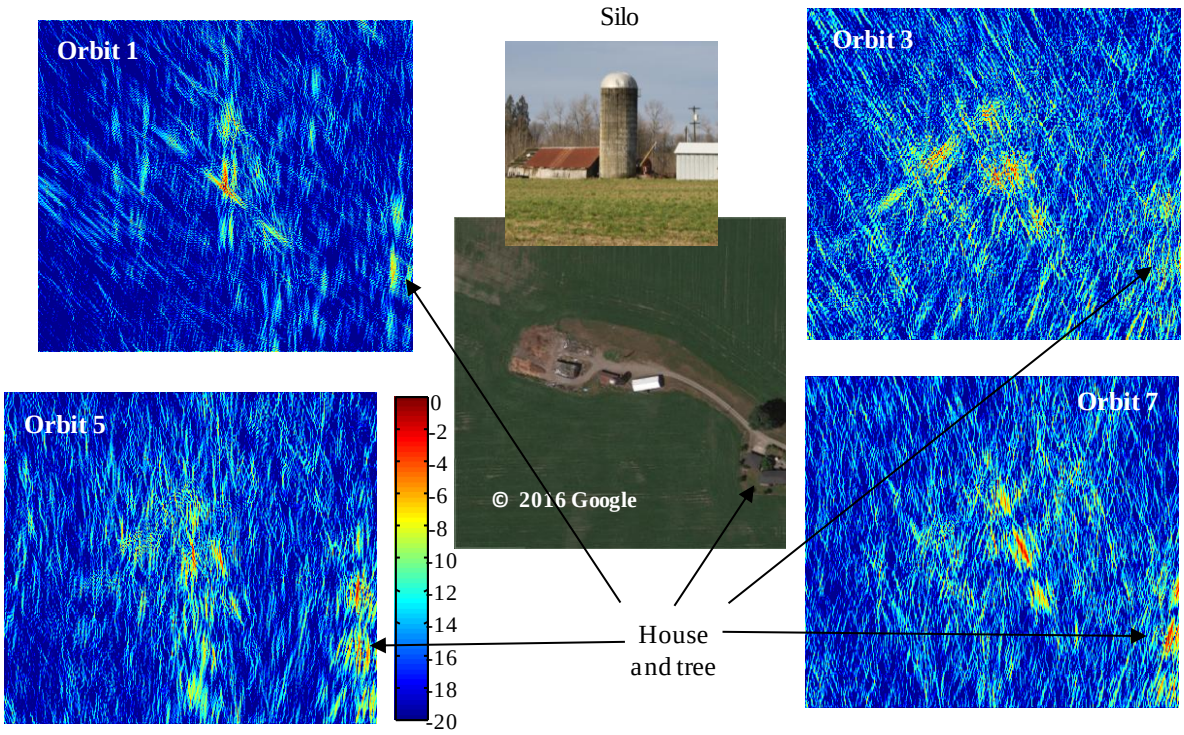

Figure E.11. Enlarged Area around Silo with Features Highlighted – 90 deg. Aperture

The bulk of the discussion of apodization in Chapter 5 was oriented at the tomographic aperture and isotropic scatterer, wherein a circularly symmetric, two-dimensional spatial spectrum was produced. We now address apodization for the partial aperture with the very narrowband illuminating signal. We examine two approaches, first an adaptation of the frequency domain approach described in Chapter 5, the second one more familiar to synthetic aperture radar (SAR) wherein we taper along the collection aperture. This second approach is addressed first.

We modeled a 90 degree aperture in two dimensions using the 400 MHz frequency from Chapter 4 (only for convenience). The aperture was symmetric with respect to the

transmitter line of sight with the geometry configured so that the along-range dimension was parallel to this line of sight (which is coincident with the scene X axis). In this manner the IPR was aligned with range and cross range was defined by the Y axis. The FWHM resolution for the untapered backprojection reconstruction was 2.41 m along range and 0.39 m in cross range with a very sinc-like response. We then applied a taper along the aperture during reconstruction, a -35 dB single parameter Taylor. Results of these two cases are shown in Figure E.12. The taper had the effect of reducing the first sidelobe by about 12 dB (-24.7 dB re peak response) with degradation of resolution to 0.53 m (E.12a). The along-range performance suffered though the effective shortening of the wide angle aperture, generally increasing the close-in sidelobes and reducing resolution to 3.36 m (E.12b). A third curve is overlaid on both plots for a -55 dB Taylor. In this case the resolutions were 0.64 m (along cross range) with a -32.6 dB first sidelobe and 4.82 m (along range).

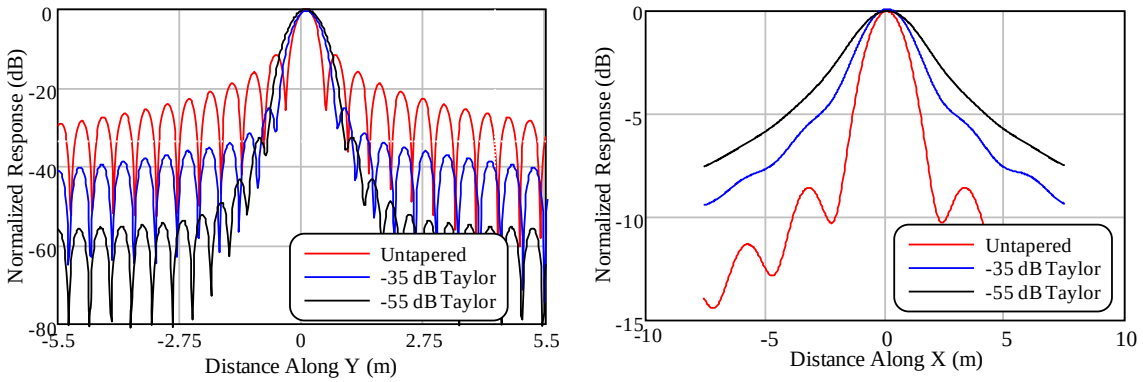

a) Along Y response (Cross Range)

b) Along X response (Down Range)

Figure E.12. Partial Aperture Tapering – Spatial Domain

Figure E.13 is a two dimensional reconstruction, presented as a contour plot, which illustrates the “hourglass” response of the wide angle, partial aperture with tapering applied along the aperture during reconstruction.

The same geometry was employed for assessing frequency domain apodization with partial apertures. The two dimensional reconstruction was performed then forward transformed using a two dimensional FFT, centering the DC term. This is depicted

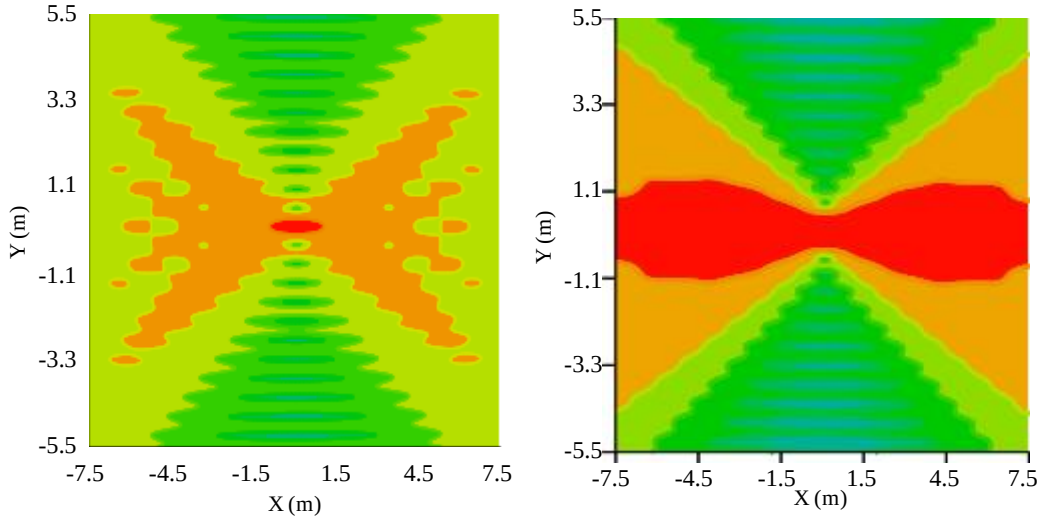

Figure E.13. Partial Aperture Tapering - 2D Reconstruction no Taper and -35 dB Taylor

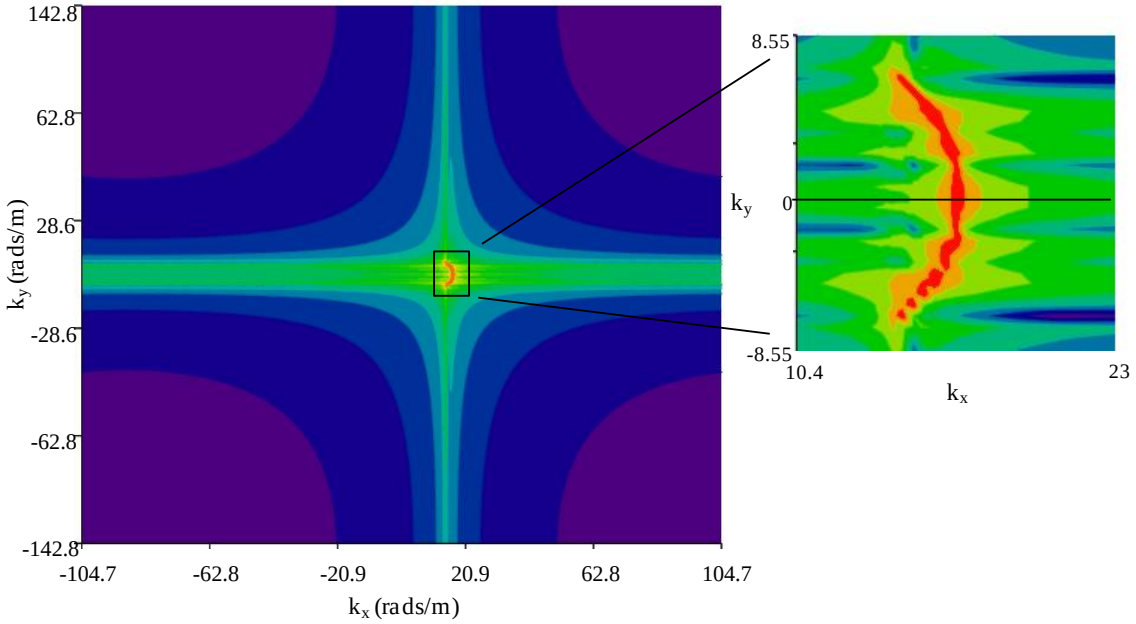

Figure E.14. Partial Aperture Tapering - Frequency Domain

in Figure E.14 with the peak spectral response region extracted as the insert. We begin by defining (calculating) the taper across the full spectral range and applying it likewise. This produces the results in Figure E.15 for a -35 dB Taylor in both dimensions. As would expected this resembles the untapered case in Figure E.12 as the taper exerts virtually no smoothing over the dominant portion of the point scatterer response. The first sidelobe level is at -11.4 dB in cross range. This is essentially the same result obtained in Chapter 5 with the exception of the sidelobe level due to the aperture shape. We followed

this up by first confining the taper to the region of predominant energy along k_y while applying the taper across all k_x, then confining the taper to the dominant energy regions in both k_y and k_x.

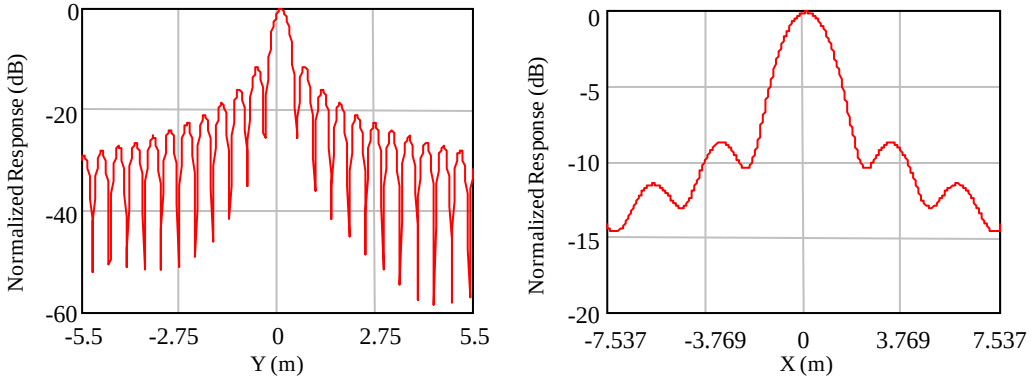

a) Along Y response (Cross Range) b) Along X response (Down Range)

Figure E.15 Apodization Results – 2D Full Frequency Domain Taper

The results from constraining in one dimension are presented in Figure E.16, starting with the weighted spectrum in the frequency domain in E.16a. The Taylor weight is shown parallel to k_y to emphasize the application. Figures E.16b and c contain the cardinal axis results, first for cross range (b) and then along range in c). The FWHM resolution for the -35 dB taper is 0.41 m in cross range while the first sidelobe level is -12.5 dB from the peak response.

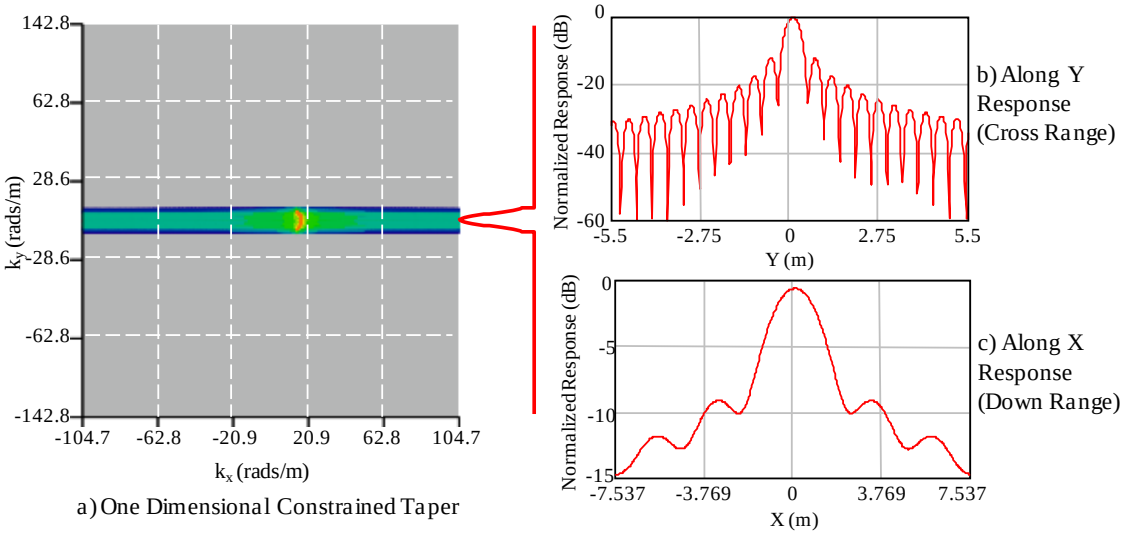

a) One Dimensional Constrained Taper

Figure E.16 Apodization Results – One Dimensional Constrained Taper

The last perturbation evaluated before moving to actual imagery is the application of the constrained tapers in both dimensions. The method is the same as Figure E.16 with results appearing in Figure E.17. The peak cross range sidelobe is at -18.9 dB while resollutionin the same dimension is 0.49 m.

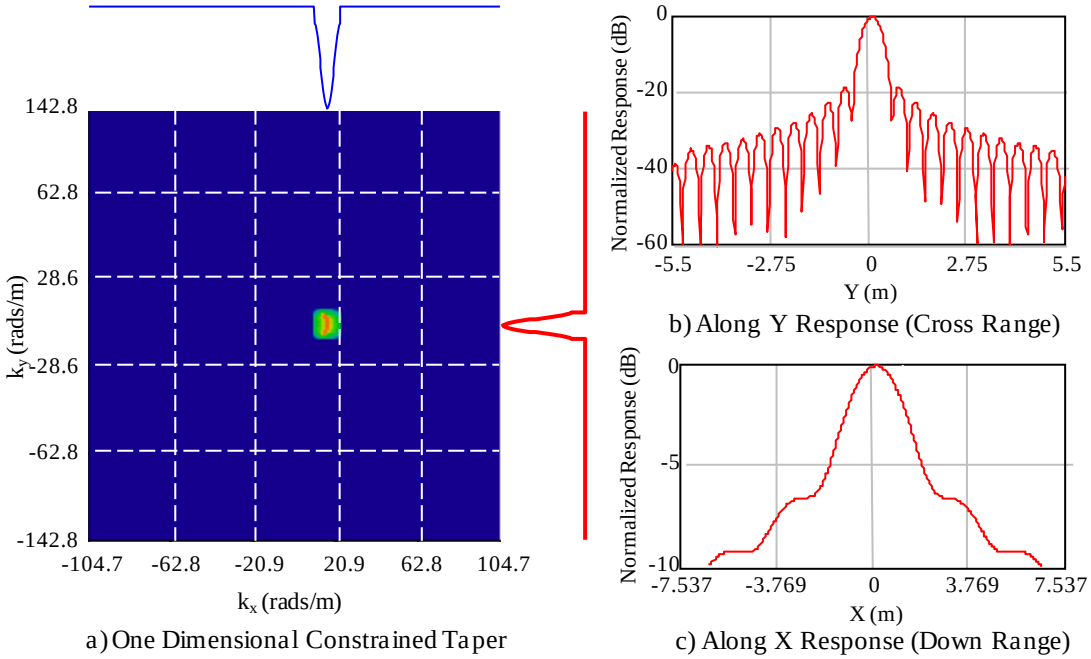

Figure E.17 Apodization Results – Two Dimensional Constrained Taper

The two dimensional frequency domain taper is applied to the image produced from the 40 degree aperture of Orbit 3 (Figure E.1). The 2D FFT is taken on the complex image which is then re-centered (fftshift) placing DC at the center indices. The spatial frequency labeling of the axes is based on the FFT digital frequencies and the sample resolution in the spatial domain. The magnitude-squared spectrum appears in Figure E.18a. The location of the taper to be coincident with the significant energy in the frequency domain is shown in Figure E.18b, a two dimensional -35 dB Taylor separately applied along k_x and k_y. The effect resembles a radial taper and no attempt was made to rescale. The location of the taper was selected to span the significant energy portion of the 2D spectrum without other consideration. The tapered spectrum is shown in Figure E.18c.

Figure E.19a is the original untapered image. Performing the inverse 2D FFT and again re-centering yields the apodized spectrum, power-detected and, like E.19a, presented on a linear scale. Logarithmic scales are used on both Figures E.19c and d with the former clipped at -35 dB and the latter at 20 dB (total dynamic range of the image is 100). The image results show that the geometric mismatch of the taper and the image spectrum has suppressed longer ranges in the image (along Y) through the filtering action at the more negative portion of the y-component of the spectrum.

The single tapered, or single axis constrained approach is illustrated in Figure E.20 with E.20a depicting the one dimensional Taylor weight applied only along k_x in the portion of the spectrum dominated by the image. The weighted magnitude spectrum is shown in Figure E.20b. This is followed by the complex inverse Fourier transform as in Figure E.19 and presented in the same manner. Qualitative assessment shows that the longer range portion of the image is recovered. Also overall contrast is improved with more pixels visible and the dimmer portions seemingly unchanged.

The final example is the case where the weight is applied along the synthetic aperture. Again a -35 dB Taylor is applied. The combination of tapering both along the aperture and during the inverse DFT when the backprojection is steered to the pixel range difference is not shown, again qualitatively, having shown slightly poorer contrast than the along aperture case. As expected a reduction in resolution in the pseudo-range (along Y) dimension is experienced relative to the 1D frequency domain case.

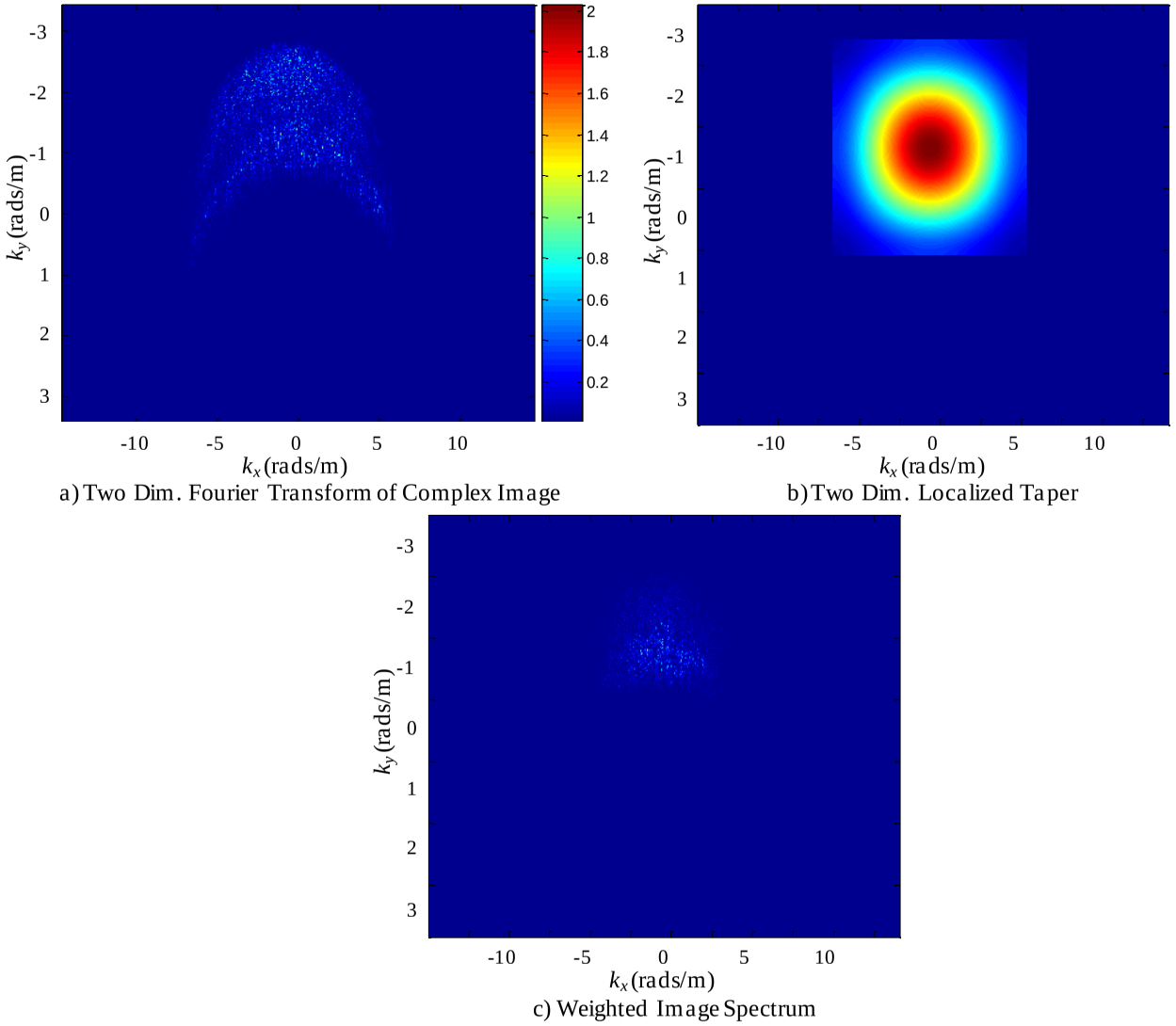

a) Two Dim. Fourier Transform of Complex Image

b) Two Dim. Localized Taper

c) Weighted Image Spectrum

Figure E.18. 2D Frequency Domain Taper with Both Axes Constrained

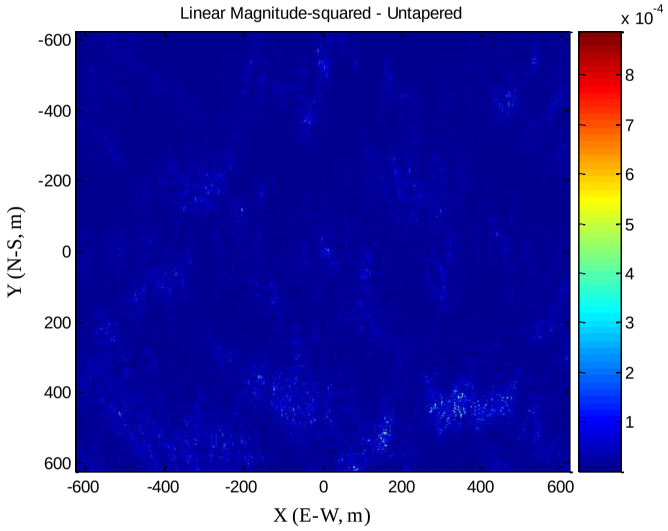

a) Linear Magnitude-squared - Untapered

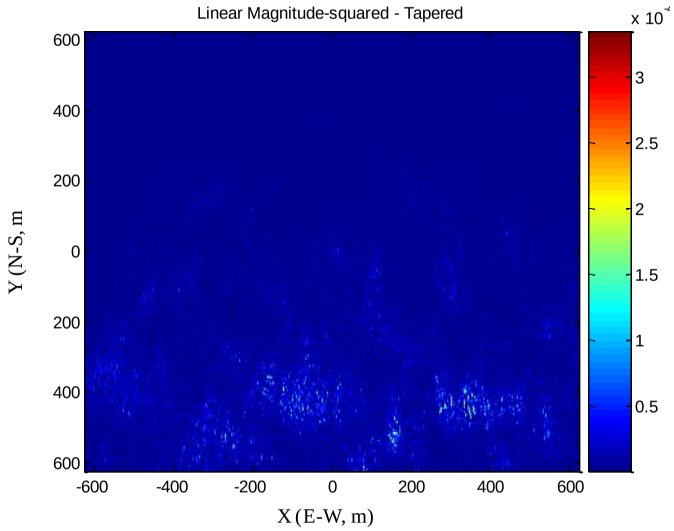

b) Linear Magnitude-squared - Tapered

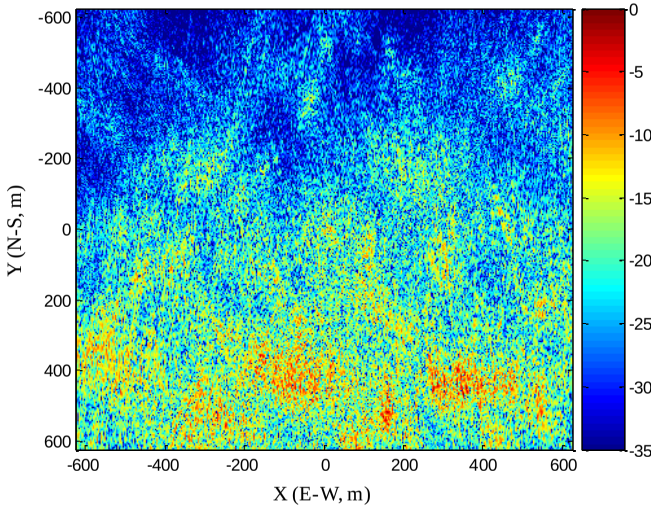

c) Logarithmic Scale - Tapered, Clipped at -35 dB

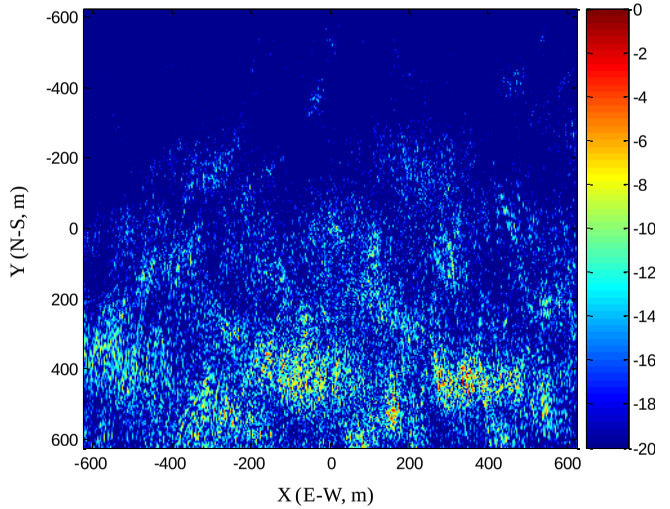

d) Logarithmic Scale - Tapered, Clipped at -20 dB

Figure E.19. Images Resulting from 2D Frequency Domain Taper with Both Axes Constrained

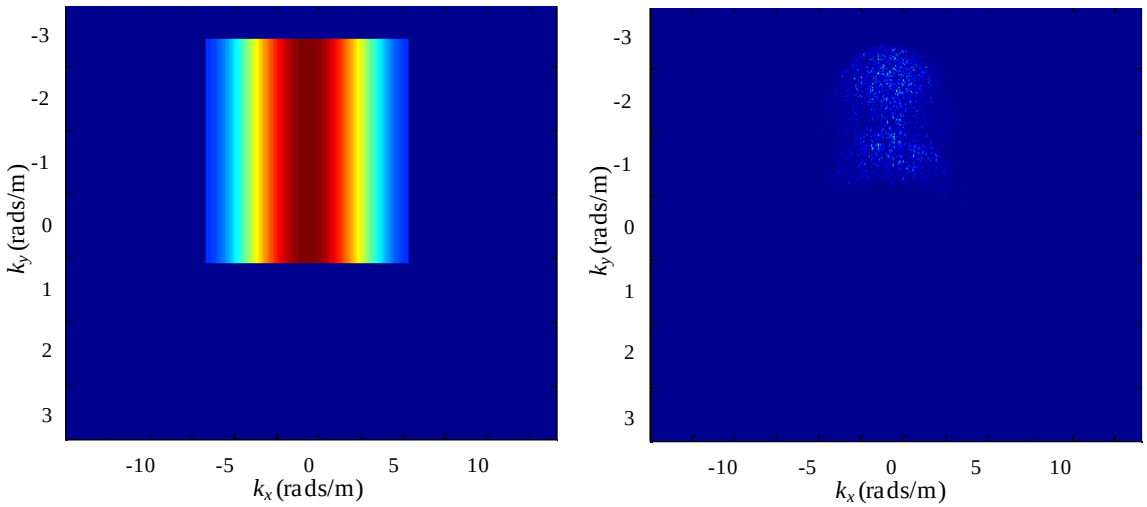

a) Single Frequency Axis Taper (-35 dB Taylor)

b) One Dimensional Weighted Spectrum

Figure E.20. 1D Frequency Domain Taper with A Single Axis Constrained

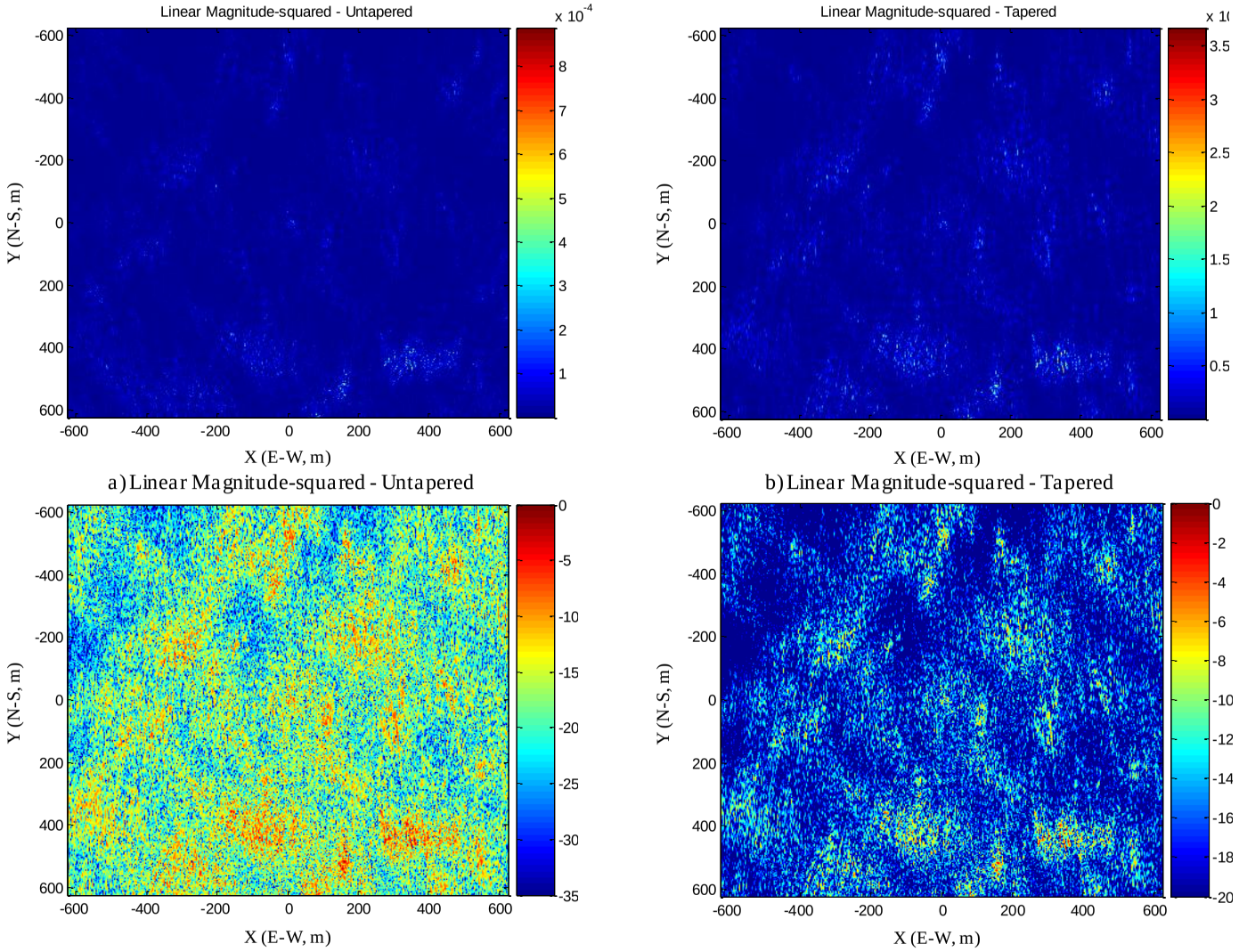

a) Linear Magnitude-squared - Untapered

b) Linear Magnitude-squared - Tapered

c) Logarithmic Scale - Tapered, Clipped at -35 dB

d) Logarithmic Scale - Tapered, Clipped at -20 dB

Figure E.21. Images Resulting from 1D Frequency Domain Taper with One Axis Constrained

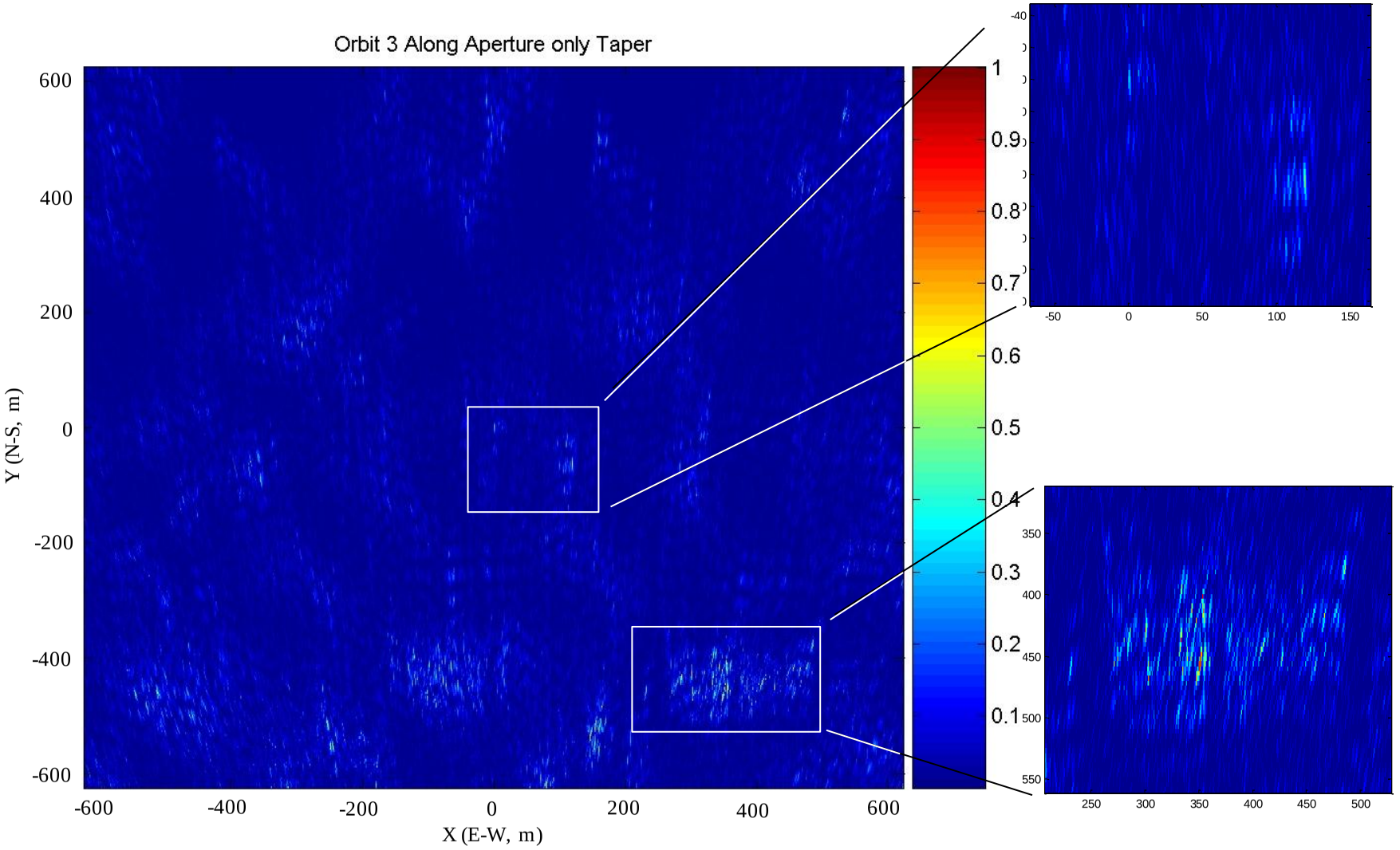

Figure E.22. Images Resulting from Taper Applied Along-Aperture During Reconstruction